Transactions of the ASME, Journal of Heat Transfer (ISSN 0022-1481) is published monthly by The American Society of Mechanical Engineers, Three Park Avenue, New York, NY 10016. Periodicals postage paid at New York, NY and additional mailing offices. POSTMASTER: Send address changes to Transactions of the ASME, Journal of Heat Transfer, c/o THE AMERICAN SOCIETY OF MECHANICAL ENGINEERS, 22 Law Drive, Box 2300, Fairfield, NJ 07007-2300. **CHANGES OF ADDRESS** must be received at Society headquarters seven weeks before they are to be effective. Please send old label and new address.

Journal of Heat Transfer

Published Monthly by ASME

VOLUME 131 • NUMBER 12 • DECEMBER 2009

Special Issue on Molecular-to-Large-Scale Heat Transfer With Multiphase Interfaces

GUEST EDITORIAL

RESEARCH PAPERS

(Contents continued on inside back cover)

This journal is printed on acid-free paper, which exceeds the ANSI Z39.48-1992 specification for permanence of paper and library materials. ♾™
♻ 85% recycled content, including 10% post-consumer fibers.

Journal of Heat Transfer Volume 131, Number 12 DECEMBER 2009

TECHNICAL BRIEFS

The ASME Journal of Heat Transfer is abstracted and indexed in the following:

Applied Science and Technology Index, Chemical Abstracts, Chemical Engineering and Biotechnology Abstracts (Electronic equivalent of Process and Chemical Engineering), Civil Engineering Abstracts, Compendex (The electronic equivalent of Engineering Index), Corrosion Abstracts, Current Contents, E & P Health, Safety, and Environment, Ei EncompassLit, Engineered Materials Abstracts, Engineering Index, Enviroline (The electronic equivalent of Environment Abstracts), Environment Abstracts, Environmental Engineering Abstracts, Environmental Science and Pollution Management, Fluidex, Fuel and Energy Abstracts, Index to Scientific Reviews, INSPEC, International Building Services Abstracts, Mechanical & Transportation Engineering Abstracts, Mechanical Engineering Abstracts, METADEX (The electronic equivalent of Metals Abstracts and Alloys Index), Petroleum Abstracts, Process and Chemical Engineering, Referativnyi Zhurnal, Science Citation Index, SciSearch (The electronic equivalent of Science Citation Index), Theoretical Chemical Engineering

Journal of Heat Transfer

Guest Editorial

Recent Research in Molecular-to-Large-Scale Heat Transfer With Multiphase Interfaces and Their Applications

Heat and mass transfer across multiphase interfaces, or liquid-vapor/gas-solid phase boundaries, represent the most fundamental transport phenomena in diverse applications, which include boiling, two-phase flow, and spray and coating processes, to name a few. The collection of research papers in this special issue of the *Journal of Heat Transfer*, which is indeed topically timely in the current "energy crisis" debate, articulates the current efforts in characterizing the interfacial behavior and advancing the associated basic science as well as applied understanding. The reported work addresses long-standing unresolved issues in ebullient phase-change, capillary-forces driven convection, drop evaporation and/or thin-film cooling, and newer developments that are primarily driven by reductions of spatial scales.

Examining flow boiling in milli- to micro-scale channels in an effort to accommodate and sustain very high heat fluxes for a variety of industrial and electronic cooling applications continues to attract much attention. Four different studies in this issue have dealt with small-scale ducts and addressed questions relating to two-phase flow patterns and their maps, bubble-dynamics induced pressure instabilities and heat transfer, role of heated length on the critical heat flux (CHF), and the application of heat transfer enhancement strategies by producing structured reentrant cavities on the heated surface. Two other papers have explored the effects of altering unstructured surface roughness of a heater, and its wetting characteristics (modified by coatings) on nucleate pool boiling heat transfer. The influence of mesh structures of heat pipe wicks and metal-foam-filled flow ducts on evaporative heat transfer with net vapor generation are the platforms for investigating capillary action at liquid-solid interfaces in two different articles. A two-part publication reports an effort to develop a coupled statistical and mechanistic model for predicting wall heat flux and CHF in subcooled nucleate flow boiling. The enhancement of high heat fluxes for large-scale nuclear energy needs are also addressed in a study on boiling of liquid metals in the presence of magnetic fields, and modeling of liquid-metal thin-film evaporation is carried out in another effort. In three other papers, heat transport at the liquid-vapor-heated-wall interface in liquid mixtures is the subject of an experimental study, boiling of a liquid-mixture droplet in an immiscible liquid is similarly examined, and drop-impact thin-film cooling is numerically modeled. Furthermore, the role of bubble motion (or sliding) is studied experimentally to characterize spatial evolution of gas-liquid interfaces and the consequent heat transfer enhancement.

As is evident from the foregoing, and will be so from a more detailed reading of the collection of research articles in this issue, the study of multiphase interfaces (understanding the associated boundary transport as well as artificially modifying the boundaries) continues to be the fundamental basis for efforts to resolve many different issues in boiling, spray dynamics and coatings, and two-phase flow heat transfer. It is also clear that enhancement of heat transfer is and will be increasingly critical to both large and small (micro-scale and perhaps even smaller) heat exchange systems, and even more so in the emerging arena of the latter. Needless to add that the future bodes well for this field of study, which assumes even greater relevance in the current debate on finding alternative ways of meeting the world's energy needs, and it is hoped that synergistic work would help provide exciting directions and paths for new discoveries in times to come.

In closing, we are grateful for the invitation extended by Professor Yogesh Jaluria, Editor, *Journal of Heat Transfer*, for bringing out this special issue. The resourcefulness and help of Ms. Shefali Patel, assistant to the editor, Rutgers University, in keeping the paper reviews and production of this issue on track, as well as that of the ASME staff (associated with both the print production and the journal's web site) is thankfully acknowledged. And finally, we would like to thank all the authors for their submissions and the reviewers for their impartial and constructive reviews, which are essential to good scholarship.

Milind A. Jog
Guest Editor

Raj M. Manglik
Associate Editor

University of Cincinnati,
Cincinnati, OH

Molecular-to-Large-Scale Heat Transfer With Multiphase Interfaces: Current Status and New Directions

Raj M. Manglik
Fellow ASME

Milind A. Jog
Mem. ASME

Thermal-Fluids and Thermal Processing Laboratory,
University of Cincinnati,
Cincinnati, OH 45221-0072

The scientific understanding of multiphase interfaces and the associated convective mass, momentum, and heat transport across and along their boundaries, provide the fundamental underpinnings of the advancement of boiling heat transfer, two-phase flows, heat pipes, spray cooling, and droplet-film coating, among many other engineering applications. Numerous studies have tried to characterize the interfacial behavior and model their mechanistic influences either directly or implicitly via parametric experimental investigations and/or simulations. The goal of advancing our understanding as well as developing generalized, perhaps "universal," and more accurate phenomenological or mechanistic correlations, for predicting mass, momentum, and heat transfer, continues to engage the worldwide research community. A collection of some such current investigations that are representative of both basic and applied issues in the field is presented in this special issue of the Journal of Heat Transfer. [DOI: 10.1115/1.4000007]

1 Introduction

In multiphase systems and processes, many different interfaces can exist, depending upon which state (gas, liquid, or solid) is finely dispersed in another [1–3]. An interface is fundamentally defined as the region at the contact of two homogeneous phases over which intensive or thermodynamic properties change from those of one phase to that of the other. The stable boundary demarcating this region tends to alter the interface area by virtue of its interfacial free energy [1,2]. The dynamic energy or force balances of interfacial regions, especially those between gas-liquid and solid-liquid interfaces, essentially characterize the gas-/vapor-bubble activity or ebullience in a liquid pool (surface boiling and flow evaporation, for example), and the liquid-droplet transport and its interactions with solid substrates (vapor condensation, spray cooling, and coatings, for example). Likewise, the liquid-liquid interface between two homogeneous but different substances lends to the thermodynamic characterization of binary mixtures and emulsions.

Figure 1 schematically illustrates the inherent role of gas-liquid-solid interfaces in the most fundamental mechanisms that govern the bubble dynamics in ebullient heat transfer and drop-surface interactions in spray cooling and/or coating. While the phase-change process in nucleate boiling is quite complex [4–7], a set of primary functional determinants can be related to the transient behavior of (a) liquid-solid interface, where surface wetting influences cavity activation, and nucleation of embryonic vapor bubbles; and (b) liquid-vapor interface, where the gas-liquid interfacial (or "surface") tension affects Marangoni flow or microconvection, and post-nucleation bubble dynamics (size, shape, and frequency). In the post-departure bubble dynamics, besides the interfacial tension, the shear force at the liquid-vapor interface or viscous interaction also plays a role. Likewise, in the complex drop-impact and postimpact droplet-surface dynamics [8–10], (a) the dynamics of liquid-solid interface or surface wetting influences the spreading, recoil, and re-adhesion or splatter of the postimpact drop film; (b) the evolving liquid-gas interfacial behavior controls liquid film surface curvature evolution, rebound, and drop breakup; and (c) viscous forces influence spreading, retraction, and rebound. The cognizance of these fundamental mechanisms and modeling of the underlying physics, so as to develop more generalized predictive tools for the attendant heat and/or mass transport in boiling or ebullient phase-change, has been the focus of numerous studies (see Refs. [11–26], for example) for more than 7 decades; the concomitant activity in spray-droplet impact on solid surfaces and postimpact dynamics is relatively recent [8–10,27–35].

1.1 Boiling Heat Transfer. The transformational stage for current explorations in boiling and two-phase flow heat transfer was perhaps set by the pioneering works of Nukiyama [36] and Jakob and Fritz [37]. While Nukiyama [36] presented the complete boiling curve, Jakob and Fritz [37] reported one of the earliest discussions of interfacial effects in their study of bubble dynamics and the role of heater surface roughness and nucleation sites on boiling history. It is especially noteworthy that the latter issue continues to engage us [15–17,23,38–43] as we extend our basic understanding and refine the ability to predict heterogeneous bubble nucleation and the interplay of surface cavities and liquid wetting. The maturing evolvement of this knowledge, in many ways, has led to the development of a variety of novel enhanced boiling surfaces and the growth of the new field of enhancement of boiling heat transfer [44–49]. Furthermore, in deciphering boiling heat transfer mechanisms, a crucial mode of exploration is to visually capture and characterize its ebullient signature. Here again, the initial stage was perhaps set in the 1930s by Jakob [11], and the seminal photographic documentation of boiling by Westwater and Santangelo [50], almost 2 decades later, and after another decade the paper by Gaertner [51] re-articulated the need for such scrutiny, which endures to this day [52–58].

The prediction of the pool-boiling curve continues to evoke considerable activity in the literature. While many of the underlying issues, enunciated since the early post-Nukiyama examinations and submissions [6,12–18,24,59–61], have been resolved, to a degree, with increasing refinements in experimentation and modeling, the use of more advanced tools have also opened up newer questions. A case in point, for example, is the prediction of heat transfer in the nucleate pool-boiling regime and the effects of heater surface roughness. As seen in Fig. 2 for a typical set of

Contributed by the Heat Transfer Division of ASME for publication in the JOURNAL OF HEAT TRANSFER. Manuscript received July 29, 2009; final manuscript received August 6, 2009; published online October 15, 2009. Assoc. Editor: Yogesh Jaluria.

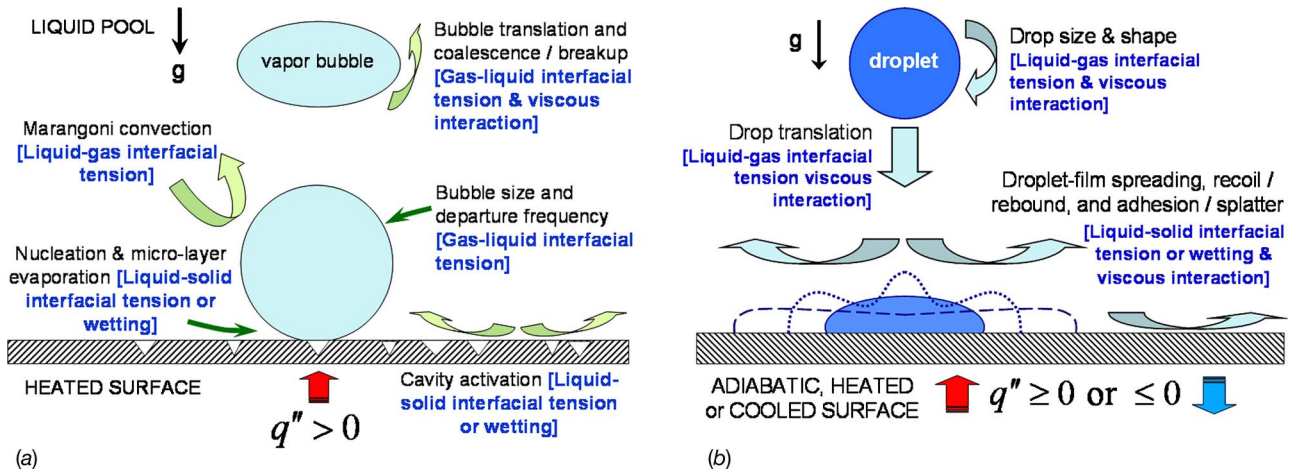

Fig. 1 Schematic representation of the influence of gas-liquid and liquid-solid interfacial properties on (*a*) boiling bubble nucleation and its dynamics and (*b*) drop-impact and postimpact droplet-surface dynamics

saturated (atmospheric pressure) pool-boiling data for water with an electrically heated "rough" cylinder (average surface roughness $R_a \approx 0.225$ μm, rms roughness $R_q = 0.260$ μm, and peak-to-mean surface roughness $R_p = 0.244$ μm) [62], there is considerable scatter in the prediction envelope that spans, among others, the Rohsenow [14] and Cooper [63,64] correlations, respectively, at the lower and higher wall superheat (fixed heat flux) ends of the curve. The difference in ΔT_{sat} ranges from 1.34 K to 2.86 K, respectively, with q''_w varying from 10 kW/m^2 to 100 kW/m^2, which accounts for an uncertainty of $\pm 13.9\%$ from the mean ΔT_{sat} at a fixed wall heat flux. The Cooper [63,64] correlation has been specifically devised for rough surfaces (characterized by R_p), and the adjustable constants (n and C_{sf}) in the Rohsenow [14] correlation consider the surface-fluid interface conditions. In the latter case, n and C_{sf} have been revised as well as new values

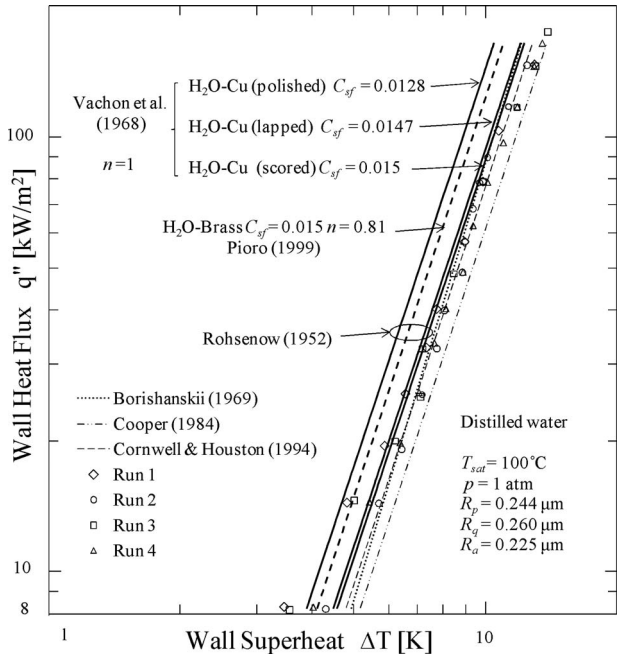

Fig. 2 Prediction on heat transfer in the nucleate pool-boiling regime in water from a cylindrical horizontal heater for saturated conditions at atmospheric pressure from different correlations in the literature and comparison with representative experimental data [62]

added [65–68] to the list originally provided [14]. While the nucleate boiling heat transfer curve for saturated water has generally been described as $q''_w \propto \Delta T^3$, and as pointed out by Bergles [4] some uncertainty prevails due to the imprecision in measurement and several other heater-pool-system parameters, an important issue seems to be the scaling and quantification of heater surface-roughness effects. Can surface roughness (R_a or R_q or R_p) in itself be a definitive correlating variable and represent the liquid-solid interface effects?

Characterizing roughness so as to scale it as a meaningful predictor of nucleate boiling is difficult and perhaps requires renewed consideration and alternative modeling of both its qualitative structure and quantification. The classical studies of Jakob and Fritz [37] and Berenson [38], for example, simply documented the surface qualitatively in terms of the process by which it was treated (sand blast, oxidation, emery grades, etc.; a tradition that persists to the present time [69]) instead of a numerical measure. The subsequent works on refrigerant boiling reported by Danilova and Kupriyanova [70] and Nishikawa et al. [71,72], among others [4,7,40,63], provided some quantification and have suggested the peak-to-mean roughness R_p as a correlating parameter along with reduced-pressure based thermophysical properties of the boiling fluid. Cooper [63] continued this theme to develop a correlation, based on a wide-ranging set of data available at that time, which forms the lower end of the prediction envelope for the conditions of Fig. 2. Roughness is important in as much as it provides active and stable cavities for nucleation, and its size along with liquid-surface wetting have a significant influence [40,73,74], which in turn influences the *nucleation site density* on a heated surface [42,61]. In itself it is perhaps only symptomatic of possible altered boiling performance rather than a definitive predictor. This contention is schematically highlighted in Fig. 3, where four different cases are depicted that have shallow, conical, re-entrant, and a combination set of cavities with the same degree of roughness. Regardless of the surface-roughness measure, the boiling performance of each surface would tend to be different for both wetting and relatively nonwetting liquids. A definitive resolution warrants a different approach by perhaps using current advanced surface characterization tools (fractal and more detailed features enunciation, for example) [24,75,76], or possibly *and preferably* a complete shift to premanufactured, structured, or enhanced boiling surfaces for most applications [44–47,77].

The role of enhanced heat transfer in boiling and two-phase flows as a possible pathway for improving the process and energy efficiency, compellingly articulated by Bergles [46,78], and thereby, alleviating our ever-increasing energy-consumption footprint [79] cannot be overstated. An issue of considerable impor-

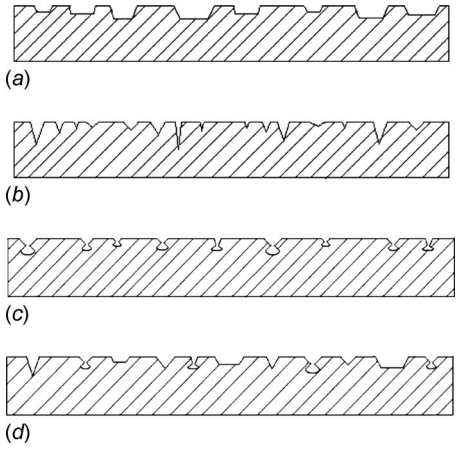

Fig. 3 Schematic representation of surfaces with the same average roughness R_a but different structure of cavities: (*a*) shallow, (*b*) conical, (*c*) re-entrant, and (*d*) combination set of (*a*)–(*c*)-type cavities

tance is the ability to sustain and accommodate very high heat fluxes, which has been accentuated by the rapid developments in microelectronics, microscale devices, and several high-energy density power systems, among others [80,81]. Boiling via immersion cooling provides a viable solution for high volumetric power-density microelectronics and the levels of heat fluxes that can be sustained are represented in Fig. 4. A rather diverse range of heat fluxes and applications are, however, encountered in practice. To cite a few examples: a 10-W microelectronic chip can dissipate 4×10^5 W/m^2 through a 25 mm^2 surface, 1.6×10^7 W/m^2 can be encountered in cooling nozzle throats of liquid-propellant rockets, and a heat input of 3.7×10^9 W/m^2 may be required in millisecond duration carbon sublimation cooling with air-plasma

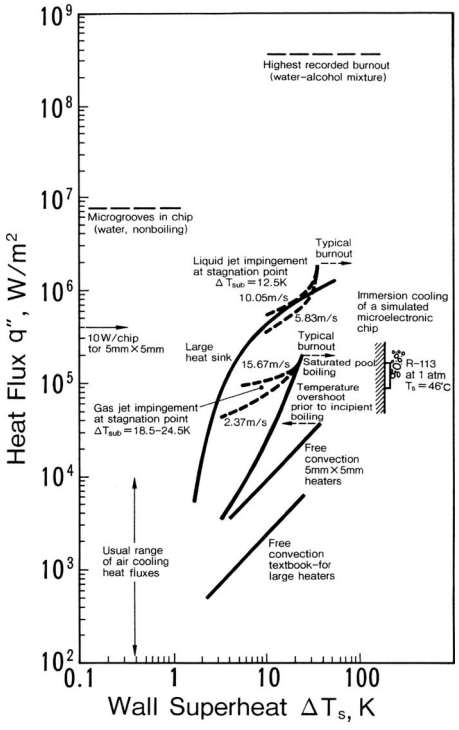

Fig. 4 Different levels of heat flux encountered in chip-level immersion cooling in microelectronic applications and the maximum burnout reported in the literature for uniform heating conditions [80,81]

[80]. Thus, the study of phase-change heat transfer by enhancing pool and/or flow boiling to attain high heat fluxes with lower temperature differences, and especially enhancing the critical heat flux (CHF) limits, has taken on a new urgency. With flow boiling, some current efforts have been directed at reducing the duct dimension by considering millimeter-to-micro-scale diameter channels [22,82] or employing second- and third-generation enhancement techniques [46–48,78], and both have shown promise in increasing boiling performance as well as the CHF.

As demonstrated in an early path-breaking study by Bergles [83], the CHF increases with a decrease in tube diameter. This has been ascribed to higher bubble velocity relative to the liquid and growth of smaller bubbles, which tend to collapse due to close proximity to high liquid subcooling in the small-diameter channel. That heat fluxes of the order of 10^8 W/m^2 can be attained in a tube of diameter 330 μm with very high mass flux and subcooling have also been demonstrated in an extended experimental study by Vandervort et al. [84]. Thus, driven both by the design of miniature heat-exchange devices and the need to accommodate very high heat fluxes, there have been considerable recent investigative interest in microchannel boiling and attendant thermal-hydrodynamic phenomena [22,25]. Likewise, there is renewed interest in employing enhancement techniques and swirl-flow generation in particular (using twisted-tape inserts, for example) [80,85], among others [48,49,86], to elevate the CHF in boiling with net vapor generation.

1.2 Drop-Impact Dynamics and Heat Transfer. Although the postimpact spreading of a droplet impinging on a solid substrate was first captured using smoked glass plates by Worthington [87,88] over a century ago, concerted study of drop-impact dynamics and associated heat transfer has received attention in the literature primarily during the last 3 decades [33]. These investigations have been motivated by various isothermal (ink-jet deposition, spray coating, aerosol drug delivery, agrochemical sprays, etc.) and nonisothermal (heating/cooling and/or phase-change processes in deposition of thermal barrier coatings, spray cooling, quenching, and near net-shape manufacturing, among others) applications. In studying isothermal drop impact on a solid substrate, efforts have been made to correlate the maximum drop-film spread and conditions for rebound and/or splatter with drop Weber number, Reynolds number, and Ohnesorge number [27–30,32,89–93]. In addition to liquid properties (primarily ρ, σ, and μ) and drop velocity, the important roles played by surface energy (hydrophobic or hydrophilic nature of substrate), interfacial tension, and dynamic contact angle variation have been delineated [30,31,90,94,95].

Based on scale estimates of kinetic energy prior to impact, viscous dissipation and surface tension, and employing the principle of conservation of energy, several correlations have been developed for maximum spread for pure liquid droplets impacting on a solid surface at low Weber numbers [27–30,32,89]. However, there is no unanimity in their predictions over a large range of Weber number and for different liquid-substrate combinations. It is recognized that the liquid-solid contact angle is affected by the hydrodynamics in the vicinity of the moving contact line, which in turn influences the drop spreading and shape evolution [96]. Difficulties in modeling such complex interactions have hindered the development of a universal correlation for the maximum drop spread and drop recoil.

The extensions of this work to study and analyze heat transfer during the drop-impact process have been primarily motivated by three types of applications. First, deposition by solidification of impacting liquid where experimental visualization of post-solidification shape, grain microstructure, and porosity measurements have been carried out (see, for example, Refs. [97–102]). Second, evaporation and boiling of liquid spray on high-temperature substrates for quenching applications and in combustion systems, as explored in Refs. [27,103–109], among others. And third, droplet impact on substrates that are below saturation

temperature for spray cooling applications, for example, as reported in Refs. [35,110–114]. Different regimes of drop evaporation and boiling have been identified [103,104,106,110] but predictive correlations for droplet heat transfer are, so far, unavailable.

More recently, numerical simulations of a single impinging drop undergoing cooling/solidification or heating/boiling have been carried out using different surface tracking methods (arbitrary-Lagrangian-Eulerian, volume-of-fluid, and level-set methods). Advancing and receding contact angle information from experiments have been used as input for detailed simulations [29,35,96,109,111,115,116]. It is shown that the computationally predicted droplet shape evolution and surface oscillations are very sensitive to the advancing and receding contact angle values [117,118]. Where detailed temporal contact angle variation is available from experimental measurements, the computational simulations of drop-surface evolution mimic the experimentally observed shape oscillations very well. However, attempts to model the contact angle behavior as a function of the contact line velocity along with substrate and liquid properties have not been successful in achieving the level of accuracy that is needed to use such models in computational simulations [96,117,119–123]. Sikalo et al. [96] and Sanjeev [119] compared the experimentally obtained temporal variations in the advancing and receding contact angles during postimpact spreading and recoil to those predicted by available correlations and found errors in the prediction to be significant. As such, modeling the dynamic contact angle behavior during postimpact spreading and recoil remains a challenge. Furthermore, the stochastic nature of spray atomization, which typically produces nonuniform droplet diameters and velocities, introduces additional challenges to extending the single droplet simulations to spray processes and their applications. Addressing these issues continue to be an active area of research as evidenced by the articles in this special issue.

2 Some Current Studies

Through careful experimentation, computational simulations, and mechanistic and stochastic modeling, efforts are being made to improve our understanding of the fundamental phenomena underlying phase-change processes and multiphase flow. This is exemplified in the articles in this special issue of the Journal of Heat Transfer where heat transport associated with multiphase interfaces is considered at different length scales (molecular-to-large). As pointed out earlier, these processes are governed by interfacial interactions (at the liquid-vapor, liquid-solid, and solid-vapor interfaces), liquid and gas or vapor properties, and substrate surface properties (roughness, wettability, cavity distribution, and geometry) that can have different manifestations at different length scales in various applications. The collection of articles herein also show that the application of phase-change processes and concomitant high heat fluxes is being extended to new and novel engineering systems.

Recognizing its potential for sustaining and accommodating very high heat fluxes, heat transfer and two-phase flow in channels of millimeter-to-micrometer scales have been examined for industrial heat exchange and electronic cooling applications. A variety of flow patterns, which include isolated bubbly flow, confined bubbly flow, slug flow, churn flow, annular flow, and mist flow, and their flow maps have been reported by Martin-Callizo et al. [124] for flow boiling of R-134a in millimeter-scale circular channels. The boiling behavior changes in microscale channels, as the width of the duct becomes comparable to the diameter of a growing or departing bubble. A growing bubble creates a pressure pulse due to the diminished capacity of the microchannel to accommodate the liquid displaced by the bubble, and such pressure instabilities affect bubble growth and associated heat transfer [125]. Furthermore, the effect of heated length on the critical heat flux for microchannel boiling has been correlated by Tanaka et al. [126]. The modification of channel geometry through structured re-entrant cavities on the side walls has been found to decrease the superheat required at the onset of nucleate boiling and increase the heat transfer coefficient but have no effect on the CHF [127].

The role played by surface wettability and roughness, critical interfacial features that influence ebullient phase-change, has been investigated by Nam et al. [128] and Jones et al. [129]. By comparing single bubble departure on bare and Teflon-coated silicon substrates, Nam et al. [128] have shown that the bubble departure diameter is larger and growth times are significantly longer on a hydrophobic surface. Using test surfaces with roughness ranging from 0.03 μm to 10 μm, the effect of roughness on pool-boiling heat transfer was investigated by Jones et al. [129]. While the heat transfer coefficient is found to increase and correlate with roughness, this work further lends credence to the argument made in Sec. 1 for the need of an alternative approach to characterizing roughness. Nevertheless, both these studies [128,129] underscore the role played by substrate properties in multiphase heat transfer and show a possible route to control and/or enhance heat transfer. In a different vein of investigation involving capillary action at liquid-solid interfaces, whether the internal structure and size of a small mesh can change the heat transfer phenomena considerably is explored for a heat pipe wick by Xu et al. [130], and for metal-foam filled tubes by Zhao et al. [131]. Reduction in cell size of metal-foam for a given porosity has been shown to enhance the heat transfer process in the latter study [131].

In a two-part study, Wu et al. [132,133] considered the prediction of the wall heat flux including critical heat flux for subcooled nucleate flow boiling. A statistical approach has been employed to describe bubble interactions so as to predict the distribution of bubble departure radius and the probability of bubble coalescence. This is combined with a deterministic approach for forced convection, transient conduction, and microlayer evaporation to develop a model for CHF prediction. The model is then compared with experimental data obtained using high-speed visualization as well as data available in literature and found to predict the CHF within $\pm 20\%$. Addressing high heat flux needs of nuclear energy applications with boiling of liquid metals, Arias [134] has shown that an imposed magnetic field can make the vapor film unstable and enhance film boiling heat transfer. Tipton and Kihm [135] developed a model for thin film evaporation of alkaline liquid metal (Na) that captures the dispersion force along with an electronic disjoining pressure component that is unique to liquid metals.

That liquid mixtures and bubble-drop interactions reveal complex phase-change phenomena compared with boiling in pure liquids has also been explored in a few studies. Through high resolution measurements, Wagner and Stephan [136] have shown that for pure liquids up to 50–60% of the latent heat flows through the three-phase contact line formed by the liquid-vapor-heated wall interface; for binary mixtures of FC-84 and FC-3284 this ratio is reduced to about 35%. The boiling of a two-phase droplet in an immiscible liquid has been examined by Haustein et al. [137]. Liquid-liquid interfacial tension and liquid properties along with evaporated mass and flow hydrodynamics determine the different stages of boiling. Heat transfer enhancement caused by a sliding bubble on a thin-foil uniform-heat-generation heater has been reported by Hollingsworth et al. [138]. It is shown that the Nusselt number increases with bubble size and reaches a constant value beyond a critical bubble size. Finally, numerical simulation of cooling due to impact of a droplet on a thin film where a bubble is growing has been carried out by Sarkar and Selvam [139].

3 Looking Forward

The questions addressed by the collection of papers in this special issue of the Journal of Heat Transfer and the directions indicated by much of the current literature elsewhere suggest many challenges in advancing our understanding of both boiling heat transfer and droplet dynamics. Of particular interest are the various interfacial phenomena associated with the heat and/or mass

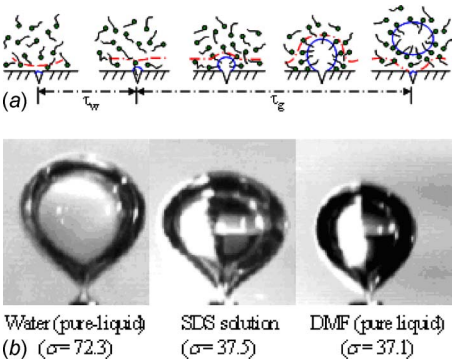

Fig. 5 Liquid-vapor/gas interface dynamics: (*a*) conceptualization of reagent molecular transport at a bubble interface during nucleate boiling (not to scale) and (*b*) the effect of the dynamic surface tension of a surfactant (SDS) solution on the evolved predeparture shape and size of bubbles in an adiabatic air-liquid experiment [141]

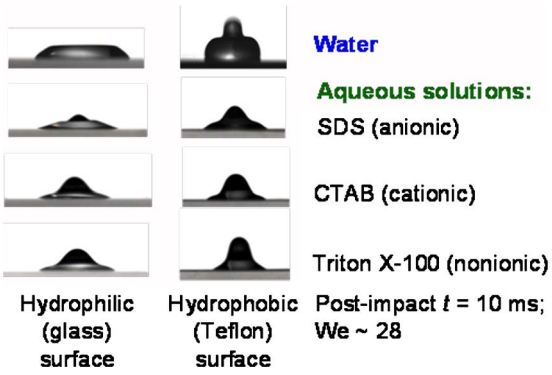

Fig. 6 Postimpact (at t=10 ms) spreading of constant We(~28) droplets of water and aqueous surfactant solutions on glass (hydrophilic) and Teflon (hydrophobic) substrates [95]

transfer at liquid-vapor/gas-solid boundaries, the ability to modulate and eventually control this interfacial transport, and consequently to enhance heat and mass transfer. Altering interfacial properties by either adding reagents in liquid solvents or selectively coating surfaces so as to manipulate the liquid-solid interface (render it hydrophobic or hydrophilic) and/or the gas-liquid interfacial tension continues to attract much research attention in the literature [49,56,140–143].

In the case of nucleate pool-boiling, it has been shown that the dynamic surface tension behavior (time-dependent variation in the gas-liquid interfacial tension) of aqueous solutions of reagents (surfactants and/or surface-active polymers) has a profound effect on bubble formation and departure. This time-dependent behavior can generally be represented by an inverse Ogive curve, where the initial gas-liquid interfacial tension σ is that of the solvent, which then reduces continually with time τ, after a flat plateau period, as reagent molecules adsorb and accumulate at the interface (desorption may also occur) till an equilibrium condition is reached, after which the surface tension becomes constant and the lower plateau in the $\sigma-\tau$ isotherm is attained [141,144]. A conceptualized representation of the molecular time-dependent adsorption-desorption of a reagent around a nucleated growing bubble is illustrated in Fig. 5(*a*), and, as further seen in Fig. 5(*b*), the dynamic surface tension behavior of the surfactant solution lends to a larger bubble than would be anticipated. Even though the two test fluids have the same bulk equilibrium σ value (~37 mN/m), with relatively high bubbling frequency (small τ on the $\sigma-\tau$ isotherm), a larger bubble is seen in aqueous sodium dodecyl sulfate (SDS) solution in comparison to that in a pure liquid (N,N-dimethylformamide or DMF). This is a direct consequence of high σ at short τ in the former case. The surface wetting behavior of the SDS solution, on the other hand, increases to render the heated surface increasingly hydrophilic [141]. This time-dependent apparent decoupling of gas-liquid interfacial tension and liquid-solid interface wetting provides an attractive passive technique to control (enhance or suppress) boiling heat transfer [56,141].

Likewise, in the case of droplet impact on a substrate the consequent liquid-solid interfacial interactions fundamentally dictate the efficacy of a variety of droplet/spray driven process. If the spray-droplet characteristics can be designed au priori so as to achieve the desired coating and/or heating/cooling behavior, it would have an enormous impact on the effective performance of wide-ranging spray applications. Several recent studies [35,95,116,145–149] have shown that surface-active agents (surfactants, polymers, and nanoparticles) added in small amounts to pure liquids hold enormous promise for altering and controlling the drop-surface interactions. The additives change surface wetting, dynamic interfacial tension, and solution rheology. These changes are fundamentally caused at a molecular-scale by the relative bulk molecular dynamics and adsorption-desorption of the additive at the liquid-gas interface, and its physisorption and electrokinetics at the liquid-solid interface [141]. At the macroscale, the dynamics manifests in liquid spreading, recoil dynamics/column fracture, spreading-recoil oscillations, altered rheology, and viscous resistance. Aqueous surfactant solution droplets tend to have a larger spread and a weak recoil compared with water droplets [95,116,119]. This increased liquid-surface contact enhances heat transfer from substrate to the droplet [119].

Gatne et al. [95] have shown that different surfactant solutions with identical equilibrium surface tension and Weber number can have different postimpact spreading/recoil behavior as dictated by the mobility and absorption dynamics of each surfactant. Different types of reagents rendered different spread and recoil characteristics, as represented in Fig. 6 by the results at fixed Weber number (We~28) of three different surfactant (anionic SDS, cationic CTAB, and nonionic Triton X-100) solutions, all of which have the same bulk equilibrium surface tension (σ=~42.5 mN/m). It was observed that higher diffusion and interfacial adsorption-rate (low molecular weight) surfactants promote higher drop spreading factors and weaker oscillations compared with low diffusion/adsorption-rate (high molecular weight) surfactants. Furthermore, polymeric additives can alter the solution rheology and thereby produce a nonlinear viscous behavior (or make the solvent behave as a non-Newtonian liquid). This feature provides another mechanism for simultaneously changing viscous effects and surface wetting so as to control the droplet-surface interactions [149–153].

Another technique to alter the liquid-solid interfacial property is to selectively coat or graft the substrate with different materials so as to make it superhydrophobic or superhydrophilic [49,140,142,143,154]. In one example, it has been shown [140] that a surface coated with a layer of a photocatalyst (titanium dioxide TiO_2, in this case) becomes highly hydrophilic when exposed to ultraviolet (UV) light; conversely, the surface becomes highly hydrophobic when it is shielded from UV light. Pool-boiling experiments in water with a vertical copper cylinder coated with TiO_2 and irradiated with UV light, produced a two-fold increase in the CHF (relative to an uncoated heater). Furthermore, the minimum heat flux (MHF) temperature also increased by 100 K, suggesting an attractive application technique for quench-type cooling as well. Figure 7 illustrates the mechanism for UV-light-induced molecular transformation of the photocatalyst layer and the production of a switchable hydrophilic surface. In another example [142], by grafting a patterned surface in a microchannel control of incipient flow boiling has been sought. The grafted surface, made up of a monolayer of octadecyl-

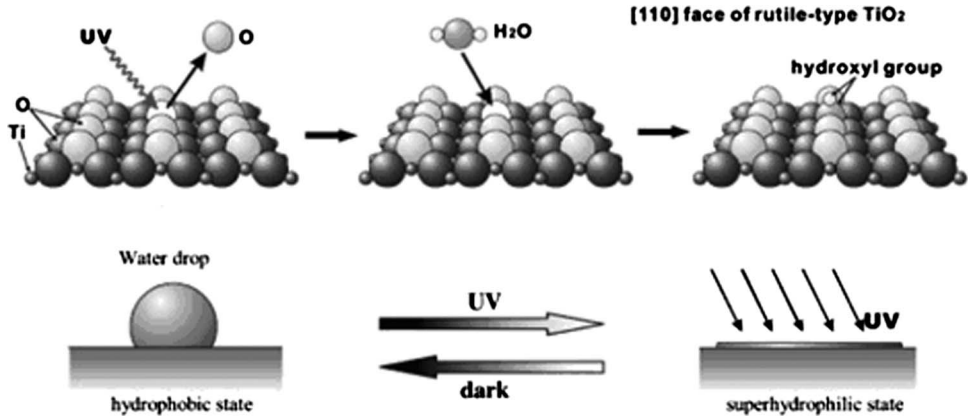

Fig. 7 A switchable hydrophilic surface: mechanism for UV-light-induced molecular transformation of a TiO_2 photocatalyst layer and change of hydrophobic surface to a hydrophilic one and vice versa [140]

trichlorosilane (OTS), was significantly hydrophobic compared with the otherwise hydrophilic glass- and silicon-plate surface of the rectangular microchannel. Artificially roughening a surface with spikelike and pillarlike ordered nanostructures and rendering it to have a "lotus-leaf" effect at the liquid-solid interface [155–157], or making the surface superhydrophobic, is yet another technique that has attracted much attention in droplet dynamics and drop-evaporation studies [143,154]. Under certain conditions the dewetting properties of a lotus leaf have also been found to be reversed to complete wetting [157], thereby providing a different strategy to control interfacial behavior for a variety of both small- and large-scale applications.

The recent quest for small (micro- and nanoscale) devices has, not only, new challenges as well as exciting opportunities. Synergy explorations between molecular chemistry, biology, biochemistry, and materials science, among others, and heat transfer can yield high dividends. In the domain of flow boiling, the use of microchannels provides a possible method to accommodate very high heat fluxes [25,84]. A natural proposition that follows is whether some type of enhancement technique can be engineered and used in very small scales to further improve heat transfer. One such possibility is presented by organic microtwist-ribbons with "tunable" pitch [158], examples of which are depicted in Fig. 8. These novel microscale twisted tapes were synthesized with achiral X-shaped π-conjugated molecules (Figs. 8(*a*) and 8(*b*)) via a solution process from 3,4-dihydroxybenzaldehyde [158]. Their helical pitch could be altered (Fig. 8(*c*)) by precipitating the organic samples at different temperatures. While this particular synthesis is aimed at developing future optoelectronic devices, engineering similar microscale ribbons to promote swirl-enhanced flow boiling (as well as single-phase forced convection) in microchannel heat exchangers [47,85] is certainly not farfetched.

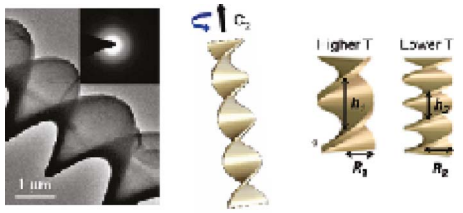

(*a*) (*b*) (*c*)

Fig. 8 Morphology of microscale helical twisted ribbons produced by self-assembled achiral X-shaped π-conjugated molecules synthesized from 3,4-dihydroxybenzaldehyde [158]

4 Looking Back (in Ancient History)

To recall the much quoted George Santayana and his famous observation,

> "Progress, far from consisting in change, depends on retentiveness. … Those who cannot remember the past are condemned to repeat it." [159],

it would be an understatement to suggest that historical antecedents of a field of science and engineering are instructive and illuminating. The past not only provides context to the building blocks of discovery, but often gives insights that sometimes get lost in our selective memory. So is the case with boiling heat transfer, two-phase flows, interfacial phenomena, and their applications in human endeavors. Much of these involve thermal processing in a variety of different forms, which require either the addition or removal of heat and often accompanied with phase-change. In advocating the need for research to achieve a generational change in the development of enhanced heat transfer techniques, Bergles [78] pointed out several challenges especially posed by their usage in the chemical process industry. Remarkably this endeavor has very ancient roots that merit exposition.

In much of the western recounting of history, the use of two-phase processes in machines and engineered applications is ascribed to the steam cannon of Archimedes (~287–212 B.C.E.) and Heron's (~60 C.E.) aeolipile [49,160]. This, however, conspicuously overlooks the substantive archeological and textual evidence of boiling and two-phase flow devices employed for such processes as distillation, material smelting, and medicinal therapy, among others, in the Indian subcontinent that predates this by several centuries [161–166]. Quite sophisticated processes have been described in various Sanskrit texts of ancient India on material and medicinal chemistry, such as *Rasarnavam Rastantram* (~500 B.C.E. or earlier) and Nagarjuna's *Rasaratna Samuchchaya* (~200 C.E.), and medicinal and surgical treatises, such as Sushruta's *Samhita* (~800–600 B.C.E.). A variety of apparatus and devices, some of which have similarities to their modern counterparts, to produce mineral extracts and pharmacological as well as alcoholic brews have been described in ancient Sanskrit texts, and archeological remnants of some have been discovered. Three specific examples are described below.

The production of various brews such as *soma*, *sura*, and *madya* by distillation, involving boiling and condensation, finds numerous descriptions in various ancient Sanskrit treatises. Many different artifacts, associated with their distillation equipment, have been excavated [161,167–170], with some pottery types dat-

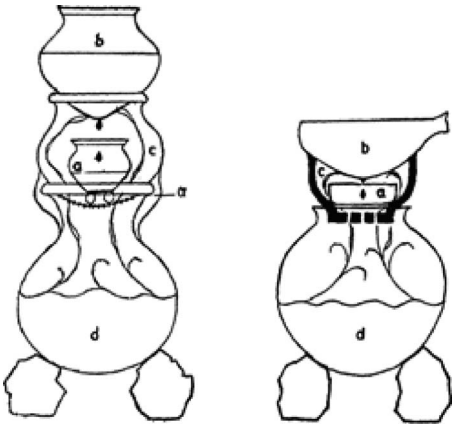

Fig. 9 Reconstructions of two distillation stills from the Hastinapur excavations (~300 B.C.E.), with boiler, condenser, and receiving crucible in one integral structure [167,168,171]

ing back to ca. 2000 B.C.E. A variety of such evidence has prompted Allchin [161] to proclaim:

> "India appears on present evidence to have been the first culture to exploit widespread distillation of alcohol … and … the art of distillation was India's gift to the world!"

Recreations of some later distillation units, based on the artifacts excavated at Hastinapur, Shaikhan Dheri, and Taxila [167–171], are presented in Figs. 9 and 10. Figure 9 gives the reconstruction by Mahdihassan [167,168] of stills from the Hastinapur excavations dating to 300 B.C.E., where the lower pot *d* is the boiler, the upper pot *b* holds the coolant and serves as the condenser, and the middle pot or crucible *a* is the receiver for the distilled liquid; the integral structure is obtained by supporting *a* and *b* with a pot *c* that has a perforated bottom to allow vapor flow and is placed over *d*. Two other distillation systems that have different construction features (with astonishing similarities to modern chemistry-lab apparatus) are depicted in Fig. 10. Here, instead of an integral unit, the boiler and condenser are separated by a tube connecter. The rendering in Fig. 10(*a*) is based on artifacts from Shaikhan Dheri (~200 B.C.E.) [161,169], and that in Fig. 10(*b*) is from the Taxila excavations (~100 B.C.E.) [161,170].

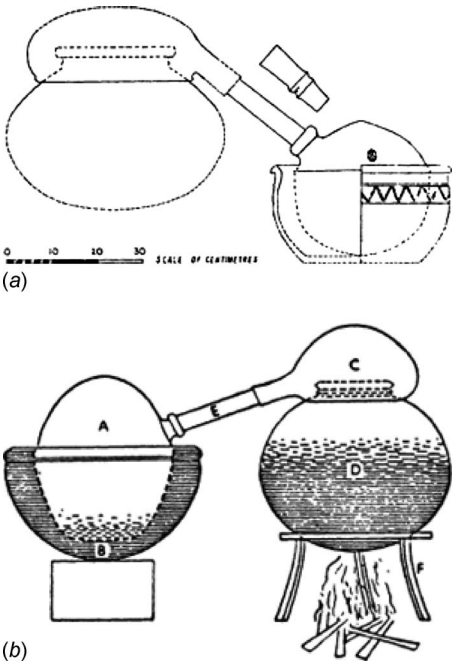

Fig. 10 Rendering of distillation equipment from ancient India composed of a boiler and condenser connected with a tube based on excavated artifacts from (*a*) Shaikhan Dheri (~200 B.C.E.) [161,169] and (b) from Taxila (~100 B.C.E.) [161,170]

In a different but remarkable high-temperature materials processing example, smelting of zinc by distillation was first developed in ancient India [162,172,173]. There is considerable evidence to suggest large-scale zinc extraction with discoveries of distillation equipment and mines dating back to ca. 600 B.C.E. (or possibly much earlier) [162,173]. Excavations at Zawar Mala (in the state of Rajasthan, India) have led Craddock [162] to assert:

> "Zawar can lay claim not only to the earliest high-temperature distillation process in the world, but also to being the direct ancestor of all such techniques in use today. The Zawar process was certainly one of the most sophisticated and technically exacting process developed …"

A representation of the type equipment used for this high-temperature two-phase flow technology (boiling and evaporation at ~1100–1200°C, with zinc-vapor condensation at ~420–550°C [162], which inarguably requires sophisticated and close control of the two-phase processes) is presented in Fig. 11. A photographic record of the zinc smelting furnace, or *kosthi*, is shown in Fig. 11(*a*), and a recreation of the furnace, retort, perforated holding plate, and condenser cup or pot is given in Fig. 11(*b*). Ancient Sanskrit texts, Rasaratna Samuchchaya for example, give elaborate descriptions of the process and equipment, or *yantram*.

The final example points to the use of two-phase flow for medicinal application. The illustration in Fig. 12 is for a device used for an otological therapy, *nadisveda*, in *Ayurveda* (the system of medicinal science of ancient India, which is finding increasing use and reinvention in present times) and described in Sushruta's Samhita (~800–600 B.C.E.) [164]. In this treatment, steam infused with medicinal herb extracts, produced by boiling different plant leaves in a pot of water, was delivered via a fibrous-porous tube directly to the ear canal of a patient. The delivery tube was made of woven grass and wrapped in herbal leaves, and the pipe had bends by which the vapor was "made delightful" [164]. The latter clearly suggests knowledge of convective recirculation and mixing promoted by curved and twisted tubes (modern enhancement techniques [47,85]), and it can perhaps be conjectured that this was also the first ancient usage of a porous duct to promote enhanced mass transfer (infusion of herb extracts into steam flow) by means of wall transpiration.

5 Concluding Remarks

The issues posed by multiphase interfaces, especially those encountered in boiling, two-phase flows, and droplet dynamics and interactions with solid substrates, not only continue to present many challenges but also lend to exciting opportunities for developing new devices and technologies. The latter is particularly driven from new explorations of phenomena occurring at very small scales (micro- to molecular-scales). The advancement of the fundamental science of transport behavior at gas-liquid-solid interfaces in different heat and mass transfer situations is critical for, not only, improving the design of large-scale traditional energy and thermal-processing systems, but also for developing micro-scale devices. The need for greater thermal and convection efficiencies at both ends of the device-size spectrum also requires a transformational advancement in the development and usage of heat and mass transfer enhancement techniques. It is hoped that the directions provided and questions raised by the collection of studies reported in this *special issue* of the Journal of Heat Transfer will be combined with both current synergistic and past experiential knowledge (including very ancient understanding and evidence) to chart future endeavors and development.

(*a*)

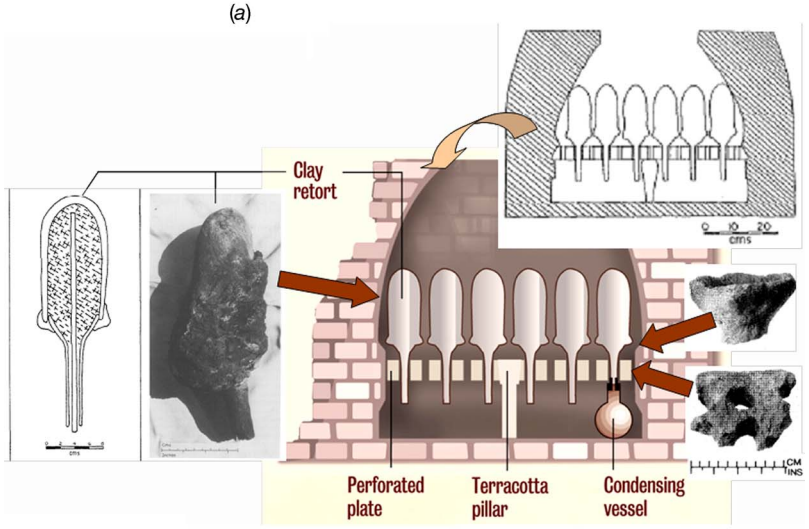

(*b*)

Fig. 11 (*a*) Photograph of Zawar Mala (Rajasthan, India) excavation site [162] showing the ancient zinc smelting furnace, or kosthi, and (*b*) rendering of the furnace depicting various excavated equipment elements (retort, retort-base cup, and perforated holding plate) [162,172]

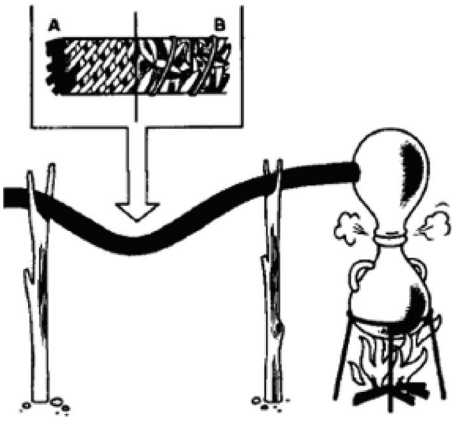

Fig. 12 Depiction of an apparatus for treating certain otological ailments described in Sushruta's Samhita (~800 −600 B.C.E.), consisting of producing herb-extract laden steam by boiling medicinal plants and delivering it to the ear via a curved or twisted tube made of woven grass (section A) and wrapped in herbs (section B) [164]

Acknowledgment

Support in part was provided by the National Science Foundation (Grant No. CBET-0755720) to both authors and by the Department of Energy (NEER Grant No. DE-FG07-07ID14772) to R.M.M. Also, the assistance provided by Mr. A. Athavale in the Thermal-Fluids and Thermal Processing Laboratory is thankfully acknowledged.

References

[1] Jaycock, M. J., and Parfitt, G. D., 1981, *Chemistry of Interfaces*, Ellis Horwood, Chichester, UK.

[2] Myers, D., 1999, *Surfaces, Interfaces, and Colloids*, 2nd ed., Wiley-VCH, New York.

[3] Hunter, R. J., 2001, *Foundations of Colloid Science*, Oxford University Press, Oxford, UK.

[4] Bergles, A. E., 1988, *Fundamentals of Boiling and Evaporation, Two-Phase Flow Heat Exchangers: Thermal-Hydraulic Fundamentals and Design*, S. Kakac, A. E. Bergles, and E. O. Fernandes, eds., Kluwer, The Netherlands, pp. 159–200.

[5] Dhir, V. K., 1998, "Boiling Heat Transfer," Annu. Rev. Fluid Mech., **30**, pp. 365–401.

[6] Kenning, D. B. R., 1999, "What Do We Really Know About Nucleate Boiling?," IMechE Conference Transactions, 6th UK National Heat Transfer Conference, Edinburgh, UK, pp. 143–167.

[7] Collier, J. G., and Thome, J. R., 2001, *Convective Boiling and Condensation*, 3rd ed., Oxford University Press, Oxford, UK.
[8] Clift, R., Grace, J. R., and Weber, M. E., 1978, *Bubbles, Drops, and Particles*, Academic, New York.
[9] Sadhal, S. S., Ayyaswamy, P. S., and Chung, J. N., 1997, *Transport Phenomena With Drops and Bubbles*, Springer, New York.
[10] de Gennes, P., Brochard-Wyard, F., and Quere, D., 2004, *Capillarity and Wetting Phenomena: Drops, Bubbles, Pearls, Waves*, Springer, New York.
[11] Jakob, M., 1936, "Heat Transfer in Evaporation and Condensation—I," Mech. Eng. (Am. Soc. Mech. Eng.), **58**, pp. 643–660.
[12] McAdams, W. H., Kennel, W. E., Mindon, C. S., Carl, R., Picornel, P. M., and Dew, J. E., 1949, "Heat Transfer to Water With Surface Boiling," Ind. Eng. Chem., **41**, pp. 1945–1953.
[13] Morgan, A. I., Bromley, L. A., and Wilke, C. R., 1949, "Effect of Surface Tension on Heat Transfer in Boiling," Ind. Eng. Chem., **41**, pp. 2767–2769.
[14] Rohsenow, W. M., 1952, "A Method of Correlating Heat Transfer Data for Surface Boiling of Liquids," Trans. ASME, **74**(3), pp. 969–976.
[15] Hsu, Y. Y., 1962, "On the Size of Range of Active Nucleation Cavities on a Heating Surface," ASME J. Heat Transfer, **84**, pp. 207–216.
[16] Han, C. -Y., and Griffith, P., 1965, "The Mechanism of Heat Transfer in Nucleate Pool Boiling-Part I: Bubble Initiation, Growth and Departure," Int. J. Heat Mass Transfer, **8**(6), pp. 887–904.
[17] Han, C.-Y., and Griffith, P., 1965, "The Mechanism of Heat Transfer in Nucleate Pool Boiling—Part II: The Heat Flux-Temperature Difference Relation," Int. J. Heat Mass Transfer, **8**(6), pp. 905–914.
[18] Dhir, V. K., and Liaw, S. P., 1989, "Framework for a Unified Model for Nucleate and Transition Pool Boiling," ASME J. Heat Transfer, **111**, pp. 739–746.
[19] Lay, J. H., and Dhir, V. K., 1995, "Shape of a Vapor Stem During Nucleate Boiling of Saturated Liquids," ASME J. Heat Transfer, **117**, pp. 394–401.
[20] Manglik, R. M., and Kraus, A. D., 1996, *Process, Enhanced, and Multiphase Heat Transfer*, Begell House, New York.
[21] Dhir, V. K., 2001, "Numerical Simulation of Pool-Boiling Heat Transfer," AIChE J., **47**(4), pp. 813–834.
[22] Bergles, A. E., Lienhard, J. H., Kendall, G. E., and Griffith, P., 2003, "Boiling and Evaporation in Small Diameter Channels," Heat Transfer Eng., **24**(1), pp. 18–40.
[23] Thomas, O. C., Cavicchi, R. E., and Tarlov, M. J., 2003, "Effect of Surface Wettability on Fast Transient Microboiling Behaviour," Langmuir, **19**, pp. 6168–6177.
[24] Shoji, M., 2004, "Studies of Boiling Chaos: A Review," Int. J. Heat Mass Transfer, **47**(6–7), pp. 1105–1128.
[25] Bergles, A. E., 2008, "Thermal-Hydraulic Phenomena in Microchannels With Boiling," Heat Transfer Res., **39**(4), pp. 327–346.
[26] Subramani, A., Jog, M. A., and Manglik, R. M., 2008, "Air-Water Ebullience Systems: Visualizing Single Bubble to Wave Instability Signatures," ASME J. Heat Transfer, **130**(8), p. 080905.
[27] Chandra, S., and Avedisian, C. T., 1991, "On the Collision of a Droplet With a Solid Surface," Proc. R. Soc. London, Ser. A, **432**(1884), pp. 13–41.
[28] Mundo, C., Sommerfeld, M., and Tropea, C., 1995, "Droplet-Wall Collisions: Experimental Studies of the Deformation and Breakup Process," Int. J. Multiphase Flow, **21**, pp. 151–173.
[29] Pasandideh-Fard, M., Qiao, Y. M., Chandra, S., and Mostaghimi, J., 1996, "Capillary Effects During Droplet Impact on a Solid Surface," Phys. Fluids, **8**(3), pp. 650–658.
[30] Mao, T., Kuhn, D. C. S., and Tran, H., 1997, "Spread and Rebound of Liquid Droplets Upon Impact on Flat Surfaces," AIChE J., **43**(9), pp. 2169–2179.
[31] Park, H., and Carr, W. W., 2003, "Single Drop Impaction on a Solid Surface," AIChE J., **49**(10), pp. 2461–2471.
[32] Ukiwe, C., and Kwok, K. Y., 2005, "On the Maximum Spreading Diameter of Impacting Droplets on Well Prepared Solid Surfaces," Langmuir, **21**, pp. 666–673.
[33] Yarin, A. L., 2006, "Drop Impact Dynamics: Splashing, Spreading, Receding, Bouncing," Annu. Rev. Fluid Mech., **38**, pp. 159–192.
[34] Sikalo, S., and Ganic, E. N., 2006, "Phenomena of Droplet-Surface Interactions," Exp. Therm. Fluid Sci., **31**, pp. 97–110.
[35] Sanjeev, A., Huzayyin, O., Gatne, K. P., Manglik, R. M., and Jog, M. A., 2008, "Short Time Impact and Cooling of Water Droplets Impinging on Hydrophobic and Hydrophilic Surfaces," ASME J. Heat Transfer, **130**(8), p. 080903.
[36] Nukiyama, S., 1966, "The Maximum and Minimum Values of the Heat Q Transmitted From Metal to Boiling Water Under Atmospheric Pressure," Int. J. Heat Mass Transfer, **9**, pp. 1419–1433.
[37] Jakob, M., and Fritz, W., 1931, "Versuche über den Verdampfungsvorgang," Forsch. Geb. Ingenieurwes., **2**, pp. 435–447.
[38] Berenson, P. J., 1962, "Experiments on Pool-Boiling Heat Transfer," Int. J. Heat Mass Transfer, **5**(10), pp. 985–999.
[39] Cooper, M. G., and Lloyd, A. J. P., 1969, "The Microlayer in Nucleate Pool Boiling," Int. J. Heat Mass Transfer, **12**(8), pp. 895–913.
[40] Roy Chowdhury, S. K., and Winterton, R. H. S., 1985, "Surface Effects in Pool Boiling," Int. J. Heat Mass Transfer, **28**(10), pp. 1881–1889.
[41] Bar-Cohen, A., 1992, "Hysteresis Phenomena at the Onset of Nucleate Boiling," ASME Conference on Pool and External Flow Boiling, ASME, New York, pp. 1–14.
[42] Wang, C. H., and Dhir, V. K., 1993, "Effect of Surface Wettability on Active Nucleation Site Density During Pool Boiling of Water on a Vertical Surface," ASME J. Heat Transfer, **115**, pp. 659–669.
[43] Chen, J. C., 2003, "Surface Contact and Its Significance for Multiphase Heat Transfer: Diverse Examples," ASME J. Heat Transfer, **125**(4), pp. 549–566.
[44] Thome, J. R., 1990, *Enhanced Boiling Heat Transfer*, Hemisphere, New York.
[45] Bergles, A. E., 1997, "Enhancement of Pool Boiling," Int. J. Refrig., **20**(8), pp. 545–551.
[46] Bergles, A. E., 2000, "New Frontiers in Enhanced Heat Transfer," *Advances in Enhanced Heat Transfer* (HTD), Vol. 365, R. M. Manglik, T. S. Ravigururajan, A. Muley, R. A. Papar, and J. Kim, eds., ASME, New York, pp. 1–8.
[47] Manglik, R. M., 2003, "Heat Transfer Enhancement," *Heat Transfer Handbook*, A. Bejan and A. D. Kraus, eds., Wiley, New York, Chap. 14.
[48] Manglik, R. M., and Bergles, A. E., 2004, "Enhanced Heat and Mass Transfer in the New Millennium: A Review of the 2001 Literature," J. Enhanced Heat Transfer, **11**(2), pp. 87–118.
[49] Manglik, R. M., 2006, "On the Advancements in Boiling, Two-Phase Flow Heat Transfer, and Interfacial Phenomena," ASME J. Heat Transfer, **128**(12), pp. 1237–1242.
[50] Westwater, J. W., and Santangelo, J. G., 1955, "Photographic Study of Boiling," Ind. Eng. Chem., **47**(8), pp. 1605–1610.
[51] Gaertner, R. F., 1965, "Photographic Study of Nucleate Pool Boiling on a Horizontal Surface," ASME J. Heat Transfer, **87**(1), pp. 17–29.
[52] Basu, N., Warrier, G. R., and Dhir, V. K., 2002, "Onset of Nucleate Boiling and Active Site Density During Subcooled Flow Boiling," ASME J. Heat Transfer, **124**(4), pp. 717–728.
[53] Kulenovic, R., Mertz, R., and Groll, M., 2002, "High Speed Flow Visualization of Pool Boiling From Structured Tubular Heat Transfer Surfaces," Exp. Therm. Fluid Sci., **25**(7), pp. 547–555.
[54] Zhang, J., and Manglik, R. M., 2003, "Visualization of Ebullient Dynamics in Aqueous Surfactant Solutions," ASME J. Heat Transfer, **125**(4), p. 547.
[55] Zhang, J., and Manglik, R. M., 2004, "Effect of Ethoxylation and Molecular Weight of Cationic Surfactants on Nucleate Boiling in Aqueous Solutions," ASME J. Heat Transfer, **126**(1), pp. 34–42.
[56] Zhang, J., and Manglik, R. M., 2005, "Nucleate Pool Boiling of Aqueous Polymer Solutions on a Cylindrical Heater," J. Non-Newtonian Fluid Mech., **125**(2–3), pp. 185–196.
[57] Chen, Y., Groll, M., Mertz, R., and Kulenovic, R., 2005, "Visualization and Mechanisms of Pool Boiling of Propane, Isubutane, and Their Mixtures on Enhanced Tubes With Reentrant Channels," Int. J. Heat Mass Transfer, **48**(12), pp. 2516–2528.
[58] Siedel, S., Cioulachtjian, S., and Bonjour, J., 2008, "Experimental Analysis of Bubble Growth, Departure, and Interactions During Pool Boiling on Artificial Nucleation Sites," Exp. Therm. Fluid Sci., **32**(8), pp. 1504–1511.
[59] Nishikawa, K., 1987, "Historical Developments in the Research of Boiling Heat Transfer," JSME Int. J., **30**(264), pp. 897–905.
[60] Judd, R. L., and Hwang, K. S., 1976, "A Comprehensive Model for Nucleate Heat Transfer Including Microlayer Evaporation," ASME J. Heat Transfer, **98**, pp. 623–629.
[61] Mikiç, B. B., and Rohsenow, W. M., 1969, "A New Correlation of Pool-Boiling Data Including Effect of Heating Surface Characteristics," ASME J. Heat Transfer, **9**(2), pp. 245–250.
[62] Athavale, A., and Manglik, R. M., 2009, "Experiments in Pool Boiling From a Horizontal Cylindrical Heater in Water and Polymeric Aqueous Solutions," University of Cincinnati Report No. TFTPL-09-PR.
[63] Cooper, M. G., 1984, "Heat Flow Rates in Saturated Nucleate Pool Boiling—A Wide-Ranging Examination Using Reduced Properties," *Advances in Heat Transfer*, Vol. 16, J. P. Hartnett, and T. F. Irvines, Jr., eds., Academic, New York, pp. 157–239.
[64] Cooper, M. G., 1984, "Saturated Nucleate Pool Boiling—A Simple Correlation," *First UK National Conference on Heat Transfer*, Vol. 2, Institute of Chemical Engineers, University of Leeds, UK, pp. 785–793.
[65] Vachon, R. I., Nix, G. H., and Tanger, G. E., 1968, "Evaluation of Constants for the Rohsenow Pool-Boiling Correlation," ASME J. Heat Transfer, **90**(2), pp. 239–247.
[66] Pioro, I. L., 1999, "Experimental Evaluation of Constants for the Rohsenow Pool Boiling Correlation," Int. J. Heat Mass Transfer, **42**(11), pp. 2003–2013.
[67] Pioro, I. L., Rohsenow, W., and Doerffer, S. S., 2004, "Nucleate Pool-Boiling Heat Transfer. I: Review of Parametric Effects of Boiling Surface," Int. J. Heat Mass Transfer, **47**(23), pp. 5033–5044.
[68] Pioro, I. L., Rohsenow, W., and Doerffer, S. S., 2004, "Nucleate Pool-Boiling Heat Transfer. II: Assessment of Prediction Methods," Int. J. Heat Mass Transfer, **47**(23), pp. 5045–5057.
[69] Hahne, E., and Barthau, G., 2006, "Heat Transfer and Nucleation in Pool-Boiling," Int. J. Therm. Sci., **45**(3), pp. 209–216.
[70] Danilova, G. N., and Kupriyanova, A. V., 1970, "Boiling Heat Transfer to Freons C318 and 21," Heat Transfer-Sov. Res., **2**(2), pp. 79–83.
[71] Nishikawa, K., Fujita, Y., Ohta, H., and Hidaka, S., 1979, "Heat Transfer in Nucleate Boiling of Freon," Heat Transfer-Jpn. Res., **8**(3), pp. 16–36.
[72] Nishikawa, K., Fujita, Y., Ohta, H., and Hidaka, S., 1982, "Effects of System Pressure and Surface Roughness on Nucleate Boiling Heat Transfer," Memoirs of the Faculty of Engineering, Kyushu University, **42**(2), pp. 95–123.
[73] Marto, P. J., Moulson, J. A., and Maynard, M. D., 1968, "Nucleate Pool Boiling of Nitrogen With Different Surface Conditions," ASME J. Heat Transfer, **90**(4), pp. 437–444.
[74] Singh, A., Mikiç, B. B., and Rohsenow, W. M., 1976, "Active Sites in Boiling," ASME J. Heat Transfer, **98**(3), pp. 401–406.
[75] Fong, R. W. L., McRae, G. A., Coleman, C. E., Nitheanandan, T., and Sanderson, D. B., 2001, "Correlation Between the Critical Heat Flux and the Fractal Surface Roughness of Zirconium Alloy Tubes," J. Enhanced Heat Transfer, **8**(2), pp. 137–146.

[76] Tsujii, K., 1998, *Surface Activity*, Academic, San Diego, CA.
[77] Bergles, A. E., 1999, "Enhanced Heat Transfer: Endless Frontier, or Mature and Routine?," J. Enhanced Heat Transfer, **6**(2–4), pp. 79–88.
[78] Bergles, A. E., 2001, "The Implications and Challenges of Enhanced Heat Transfer for the Chemical Process Industries," Chem. Eng. Res. Des., **79**(4), pp. 437–444.
[79] Manglik, R. M., and Manglik, A., 2009, "Energy Consumption, Economic Efficiency, and Fourth-Generation Technological Innovation for a Sustainable Future," Thermal-Fluids & Thermal Processing Laboratory Report No. TFTPL-EP-09, University of Cincinnati, Cincinnati, OH.
[80] Bergles, A. E., 2003, "High-Flux Processes Through Enhanced Heat Transfer," Rohsenow Symposium, Massachusetts Institute of Technology, Cambridge, MA.
[81] Nakayama, W., and Bergles, A. E., 1990, "Cooling Electronic Equipment: Past, Present and Future," *Heat Transfer in Electronic and Microelectronic Equipment*, A. E. Bergles, ed., Hemisphere, New York, pp. 3–39.
[82] Kandlikar, S. G., 2001, "Critical Heat Flux in Subcooled Flow Boiling—An Assessment of Current Understanding and Future Directions for Research," Multiphase Sci. Technol., **13**(3), pp. 207–232.
[83] Bergles, A. E., 1963, "Subcooled Burnout in Tubes of Small Diameter," ASME Paper No. WAM 63-WA-182.
[84] Vandervort, C. L., Bergles, A. E., and Jensen, M. K., 1994, "An Experimental Study of Critical Heat Flux in Very High Heat Flux Subcooled Boiling," Int. J. Heat Mass Transfer, **37**, pp. 161–173.
[85] Manglik, R. M., and Bergles, A. E., 2002, "Swirl Flow Heat Transfer and Pressure Drop With Twisted-Tape Inserts," *Advances in Heat Transfer*, Vol. 36, J. P. Hartnett, T. F. Irvine, Jr., Y. I. Cho, and G. A. Greene, eds., Academic, San Diego, CA, pp. 183–266.
[86] Chang, S. H., and Baek, W.-P., 2003, "Understanding, Predicting, and Enhancing Critical Heat Flux," Proceedings of the Tenth International Topical Meeting on Nuclear Reactor Thermal Hydraulics (NURETH-10), Seoul, Korea, pp. 1–20.
[87] Worthington, A. M., 1876, "On the Forms Assumed by Drops of Liquid Falling Vertically on a Horizontal Plate," Proc. R. Soc. London, **25**, pp. 261–272.
[88] Worthington, A. M., 1877, "A Second Paper on the Forms Assumed by Drops of Liquid Falling Vertically on a Horizontal Plate," Proc. R. Soc. London, **25**, pp. 498–503.
[89] Asai, A., Shioya, M., Hirasawa, S., and Okazaki, T., 1993, "Impact of an Ink Drop on Paper," J. Imaging Sci. Technol., **37**(2), pp. 205–207.
[90] Rioboo, R., Marengo, M., and Tropea, C., 2001, "Outcomes From a Drop Impact on Solid Surfaces," Atomization Sprays, **11**, pp. 155–165.
[91] Rioboo, R., Marengo, M., and Tropea, C., 2002, "Time Evolution of Droplet Impact Onto Solid, Dry Surfaces," Exp. Fluids, **33**, pp. 12–24.
[92] Roisman, I. V., Rioboo, R., and Tropea, C., 2002, "Normal Impact of a Liquid Drop on a Dry Surface: Model for Spreading and Receding," Proc. R. Soc. London, **A458**, pp. 1411–1430.
[93] Gatne, K. P., 2006, "Experimental Investigation of Droplet Impact Dynamics on Solid Surfaces," MS thesis, University of Cincinnati, Cincinnati, OH.
[94] Gatne, K. P., Manglik, R. M., and Jog, M. A., 2007, "Visualization of Fracture Dynamics of Droplet Recoil on Hydrophobic Surface," ASME J. Heat Transfer, **129**(8), p. 931.
[95] Gatne, K. P., Jog, M. A., and Manglik, R. M., 2009, "Surfactant-Inducted Modification of Low Weber Number Droplet Impact Dynamics," Langmuir, **25**(14), pp. 8122–8130.
[96] Sikalo, S., Wilhelm, H. D., Roisman, I. V., Jakirlic, S., and Tropea, C., 2005, "Dynamic Contact Angle of Spreading Droplets: Experiments and Simulations," Phys. Fluids, **17**(6), p. 062103.
[97] Jones, H., 1971, "Cooling, Freezing, and Substrate Impact of Drops Formed by Rotary Atomization," J. Phys. D, **4**, pp. 1657–1660.
[98] Madejski, J., 1976, "Solidification of Droplets on a Cold Surface," Int. J. Heat Mass Transfer, **19**, pp. 1009–1013.
[99] Wang, G. X., and Matthys, E. F., 1991, "Modeling of Heat Transfer and Solidification During Splat Cooling: Effect of the Splat Thickness and Splat/Substrate Thermal Contact," Int. J. Rapid Solidif., **6**, pp. 141–174.
[100] Bennett, T., and Poulikakos, D., 1993, "Splat-Quench Solidification: Estimating the Maximum Spreading of a Droplet Impacting a Solid Surface," J. Mater. Sci., **28**, pp. 963–970.
[101] Zhao, Z., and Poulikakos, D., 1996, "Heat Transfer and Fluid Dynamics During the Collision of a Liquid Droplet on a Substrate—I. Modeling," Int. J. Heat Mass Transfer, **39**, pp. 2771–2789.
[102] Zhao, Z., and Poulikakos, D., 1996, "Heat Transfer and Fluid Dynamics During the Collision of a Liquid Droplet on a Substrate—II. Experiments," Int. J. Heat Mass Transfer, **39**, pp. 2791–2802.
[103] Bernardin, J. D., Stebbins, C. J., and Mudawar, I., 1997, "Mapping of Impact and Heat Transfer Regimes of Water Drops Impinging on a Polished Surface," Int. J. Heat Mass Transfer, **40**(2), pp. 247–267.
[104] Bernardin, J. D., Stebbins, C. J., and Mudawar, I., 1997, "Effects of Surface Roughness on Water Droplet Impact History and Heat Transfer Regimes," Int. J. Heat Mass Transfer, **40**(1), pp. 73–88.
[105] Ge, Y., and Fan, L. S., 2006, "3-D Modeling of the Dynamics and Heat Transfer Characteristics of Subcooled Droplet Impact on a Surface With Film Boiling," Int. J. Heat Mass Transfer, **49**, pp. 4231–4249.
[106] Mehdizadeh, N. Z., and Chandra, S., 2006, "Boiling During High-Velocity Impact of Water Droplets on a Hot Stainless Steel Surface," Proc. R. Soc. London, Ser. A, **462**, pp. 3115–3131.
[107] Akhtar, S. W., Nasr, G. G., and Yule, A. J., 2007, "Characteristics of Water Droplet Impaction Behavior on a Polished Steel Heated Surface—Part II," Atomization Sprays, **17**, pp. 683–729.
[108] Akhtar, S. W., Nasr, G. G., and Yule, A. J., 2007, "Characteristics of Water Droplet Impaction Behavior on a Polished Steel Heated Surface—Part I," Atomization Sprays, **17**, pp. 659–681.
[109] Nikolopoulos, N., Theodorakakos, A., and Bergeles, G., 2007, "A Numerical Investigation of the Evaporation Process of a Liquid Droplet Impinging Onto a Hot Substrate," Int. J. Heat Mass Transfer, **50**, pp. 303–319.
[110] Lee, J., Kim, J., and Kiger, K. T., 2001, "Time- and Space-Resolved Heat Transfer Characteristics of Single Droplet Cooling Using Microscale Heater Arrays," Int. J. Heat Fluid Flow, **22**, pp. 188–200.
[111] Pasandideh-Fard, M., Aziz, S. D., Chandra, S., and Mostaghimi, J., 2001, "Cooling Effectiveness of a Water Drop Impinging on a Hot Surface," Int. J. Heat Fluid Flow, **22**, pp. 201–210.
[112] Manzello, S. L., and Yang, J. C., 2004, "An Experimental Investigation of Water Droplet Impingement on a Heated Wax Surface," Int. J. Heat Mass Transfer, **47**, pp. 1701–1709.
[113] Tarozzi, L., Muscio, A., and Tartarini, P., 2007, "Experimental Tests of Dropwise Cooling on Infrared-Transparent Media," Exp. Therm. Fluid Sci., **31**, pp. 857–865.
[114] Landero, J. C., and Watkins, A. P., 2008, "Modeling of Steady-State Heat Transfer in a Water Spray Impingement Onto a Heated Wall," Atomization Sprays, **18**, pp. 1–47.
[115] Fukai, J., Shiiba, Y., Yamamoto, T., Miyatake, O., Poulikakos, D., Megaridis, C. M., and Zhao, Z., 1995, "Wetting Effects on the Spreading of a Liquid Droplet Colliding With a Flat Surface: Experiment and Modeling," Phys. Fluids, **7**, pp. 236–247.
[116] Gunjal, P. R., Ranade, V. V., and Chaudhari, R. V., 2005, "Dynamics of Drop Impact on Solid Surfaces: Experiments and VOF Simulations," AIChE J., **51**(1), pp. 59–79.
[117] Manservisi, S., and Scardovelli, R., 2009, "A Variational Approach to the Contact Angle Dynamics of Spreading Droplets," Comput. Fluids, **38**, pp. 406–424.
[118] Lunkad, S. F., Buwa, V. V., and Nigam, K. D. P., 2007, "Numerical Simulations of Drop Impact and Spreading on Horizontal and Inclined Surfaces," Chem. Eng. Sci., **62**(24), pp. 7214–7224.
[119] Sanjeev, A., 2008, "Computational Study of Surfactant-Induced Modification of Droplet Impact Dynamics and Heat Transfer on Hydrophobic and Hydrophilic Surfaces," MS thesis, University of Cincinnati, Cincinnati, OH.
[120] Jiang, T., Oh, S., and Slattery, J. C., 1979, "Correlation for Dynamic Contact Angle," J. Colloid Interface Sci., **69**, pp. 74–77.
[121] Cox, R. G., 1986, "The Dynamics of the Spreading of Liquids on a Solid Surface. Part 1. Viscous Flow," J. Fluid Mech., **168**, pp. 169–194.
[122] Blake, T. D., 1993, "Dynamic Contact Angles and Wetting Kinetics," *Wettability*, J. C. Berg, ed., Marcel Dekker, New York, pp. 251–310.
[123] Blake, T. D., Bracke, M., and Shikhmurzaev, Y. D., 1999, "Experimental Evidence of Nonlocal Hydrodynamic Influence on the Dynamic Contact Angle," Phys. Fluids, **11**, pp. 1995–2007.
[124] Martin-Callizo, C., Palm, B., Owhaib, W., and Ali, R., 2010, "Flow Boiling Visualization of R-134a in a Vertical Channel of Small Diameter," ASME J. Heat Transfer, 132, to be published.
[125] Fogg, D., and Goodson, K. E., 2009, "Bubble-Induced Water Hammer and Cavitation in Microchannel Flow Boiling," ASME J. Heat Transfer, **131**(12), p. 121006.
[126] Tanaka, F., Hibishi, T., and Mishima, K., 2009, "Correlation for Flow Boiling Critical Heat Flux in Thin Rectangular Channels," ASME J. Heat Transfer, **131**(12), p. 121003.
[127] Kuo, C. J., and Peles, Y., 2009, "Flow Boiling of Coolant (HFE-7000) Inside Structured and Plain Wall Microchannels," ASME J. Heat Transfer, **131**(12), p. 121011.
[128] Nam, Y., Wu, J., Warrier, G., and Ju, Y. S., 2009, "Experimental and Numerical Study of Single Bubble Dynamics on a Hydrophobic Surface," ASME J. Heat Transfer, **131**(12), p. 121004.
[129] Jones, B. J., McHale, J. P., and Garimella, S. V., 2009, "The Influence of Surface Roughness on Nucleate Pool Boiling Heat Transfer," ASME J. Heat Transfer, **131**(12), p. 121009.
[130] Xu, J., Zhang, Y., and Ma, H., 2009, "Effect of Internal Wick Structure on Liquid-Vapor Oscillatory Flow and Heat Transfer in an Oscillating Heat Pipe," ASME J. Heat Transfer, **131**(12), p. 121012.
[131] Zhao, C. Y., Lu, W., and Tassou, S. A., 2009, "Flow Boiling Heat Transfer in Horizontal Metal-Foam Tubes," ASME J. Heat Transfer, **131**(12), p. 121002.
[132] Wu, W., Jones, B. G., and Newell, T. A., 2009, "A Statistical Model of Bubble Coalescence and Its Application to Boiling Heat Flux Prediction—Part I: Model Development," ASME J. Heat Transfer, **131**(12), p. 121013.
[133] Wu, W., Jones, B. G., and Newell, T. A., 2009, "A Statistical Model of Bubble Coalescence and Its Application to Boiling Heat Flux Prediction—Part II: Experimental Validation," ASME J. Heat Transfer, **131**(12), p. 121014.
[134] Arias, F. J., 2009, "Magnetohydrodynamic Correction in Film Boiling Heat Transfer on Liquid Metal in Presence of an Ideal Magnetic Field With Particular Reference to Fusion Reactor Project," ASME J. Heat Transfer, **131**(12), p. 124501.
[135] Tipton, J. B., Jr., Kihm, K. D., and Pratt, D. M., 2009, "Modeling Alkaline Liquid Metal (Na) Evaporating Thin Films Using Both Retarded Dispersion and Electronic Force Components," ASME J. Heat Transfer, **131**(12), p. 121015.
[136] Wagner, E., and Stephan, P., 2009, "High Resolution Measurements at Nucleate Boiling of Pure FC-84 and FC-3284 and Its Binary Mixtures," ASME J.

Heat Transfer, **131**(12), p. 121008.
[137] Haustein, H. D., Gany, A., and Elias, E., 2009, "Rapid Boiling of a Two-Phase Droplet in an Immiscible Liquid at High Superheat," ASME J. Heat Transfer, **131**(12), p. 121010.
[138] Hollingsworth, D. K., Witte, L. C., and Figueroa, M., 2009, "Enhancement of Heat Transfer Behind Sliding Bubbles," ASME J. Heat Transfer, **131**(12), p. 121005.
[139] Sarkar, S., and Selvam, R. P., 2009, "Direct Numerical Simulation of Heat Transfer in Spray Cooling Through 3D Multiphase Flow Modeling Using Parallel Computing," ASME J. Heat Transfer, **131**(12), p. 121007.
[140] Takata, Y., Hidaka, S., Masuda, M., and Ito, T., 2003, "Pool Boiling on a Superhydrophilic Surface," Int. J. Energy Res., **27**(2), pp. 111–119.
[141] Zhang, J., and Manglik, R. M., 2005, "Additive Adsorption and Interfacial Characteristics of Nucleate Pool Boiling in Aqueous Surfactant Solutions," ASME J. Heat Transfer, **127**(7), pp. 684–691.
[142] Rioboo, R., Marengo, M., Dall'Olio, S., Voue, M., and De Coninck, J., 2009, "An Innovative Method to Control the Incipient Flow Boiling Through Grafted Surfaces With Chemical Patterns," Langmuir, **25**(11), pp. 6005–6009.
[143] Choi, C.-H., and Kim, C.-J., 2009, "Droplet Evaporation of Pure Water and Protein Solution on Nanostructured Superhydrophobic Surfaces of Varying Heights," Langmuir, **25**(13), pp. 7561–7567.
[144] Chang, C.-H., and Franses, E. I., 1995, "Adsorption Dynamics of Surfactants at the Air/Water Interface: A Critical Review of Mathematical Models, Data, and Mechanisms," Colloids Surf., A, **100**, pp. 1–45.
[145] Mourougou-Candoni, N., Prunet-Foch, B., Legay, F., Vignes-Alder, M., and Wong, K., 1997, "Influence of Dynamic Surface Tension on the Spreading of Surfactant Solution Droplets Impacting Onto a Low-Surface-Energy Solid Substrate," J. Colloid Interface Sci., **192**, pp. 129–141.
[146] Zhang, X., and Basaran, O. A., 1997, "Dynamic Surface Tension Effects in Impact of a Drop With a Solid Surface," J. Colloid Interface Sci., **187**, pp. 166–178.
[147] Bergeron, V., Bonn, D., Martin, J. Y., and Vovelle, L., 2000, "Controlling Droplet Deposition With Polymer Additives," Nature (London), **405**, pp. 772–775.
[148] Crooks, R., Cooper-White, J., and Boger, D. V., 2001, "The Role of Dynamic Surface Tension and Elasticity on the Dynamics of Drop Impact," Chem. Eng. Sci., **56**, pp. 5575–5592.
[149] Bertola, V., 2004, "Drop Impact on a Hot Surface: Effect of a Polymer Additive," Exp. Fluids, **37**, pp. 653–664.
[150] Cooper-White, J. J., Crooks, R. C., and Boger, D. V., 2002, "A Drop Impact Study of Worm-Like Viscoelastic Surfactant Solutions," Colloids Surf., A, **210**, pp. 105–123.
[151] Lampe, J., DiLalla, R., Grimaldi, J., and Rothstein, J. P., 2005, "Impact Dynamics of Drops on Thin Films of Viscoelastic Wormlike Micelle Solutions," J. Non-Newtonian Fluid Mech., **125**, pp. 11–23.
[152] Ariyo, A., 2009, "Experimental Investigation of an Aqueous Polymer Solution Drop Impinging on a Solid Substrate," MS thesis, University of Cincinnati, Cincinnati, OH.
[153] Ariyo, A., Jog, M. A., and Manglik, R. M., 2009, "Droplet Impact Dynamics of Aqueous Polymeric Solutions," Proceedings of the 11th Triennial International Conference on Liquid Atomization and Spray Systems (ICLASS 2009), Vail, CO, Paper No. ICLASS 2009-0066.
[154] Jung, Y. C., and Bhushan, B., 2008, "Dynamic Effects of Bouncing Water Droplets on Superhydrophobic Surfaces," Langmuir, **24**(12), pp. 6262–6269.
[155] Patankar, N. A., 2004, "Mimicking the Lotus Effect: Influence of Double Roughness Structures and Slender Pillars," Langmuir, **20**(19), pp. 8209–8213.
[156] Spori, D. M., Drobek, T., Zürcher, S., Ochsner, M., Sprecher, C., Mühlebach, A., and Spencer, N. D., 2008, "Beyond the Lotus Effect: Roughness Influence on Wetting Over a Wide Surface-Energy Range," Langmuir, **24**(10), pp. 5411–5417.
[157] Zhang, J., Sheng, X., and Jiang, L., 2009, "The Dewetting Properties of Lotus Leaves," Langmuir, **25**(3), pp. 1371–1376.
[158] Chen, H.-B., Zhou, Y., Yin, J., Yan, J., Ma, Y., Wang, L., Cao, Y., Wang, J., and Pei, J., 2009, "Single Organic Microtwist With Tunable Pitch," Langmuir, **25**(10), pp. 5459–5462.
[159] Santayana, G., 1905, *The Life of Reason, or The Phases of Human Progress*, Vol. 1, C. Scribner's Sons, New York; 1998, *The Life of Reason, or The Phases of Human Progress*, republished by Prometheus Books, Amherst, NY.
[160] Bergles, A. E., 1981, "Two-Phase Flow and Heat Transfer," Heat Transfer Eng., **2**(3–4), pp. 101–114.
[161] Allchin, F. R., 1979, "India: The Ancient Home of Distillation?" Man, New Series, **14**(1), pp. 55–63.
[162] Craddock, P. T., 1987, "The Early History of Zinc," Endeavour, **11**(4), pp. 183–191.
[163] Despande, V., 1996, "A Note on Ancient Zinc-Smelting in India and China," Indian J. Hist. Sci., **31**(3), pp. 276–279.
[164] Pothula, V. B., Jones, T. M., and Lesser, T. H. J., 2001, "Otology in Ancient India," J. Laryngol. Otol., **115**, pp. 179–183.
[165] Dwivedi, G., and Dwivedi, S., 2007, "Sushruta—The Clinician—Teacher par Excellence," Indian J. Chest Dis. Allied Sci., **49**(4), pp. 243–244.
[166] Natarajan, K., 2008, "Surgical Instruments and Endoscopes of Susruta, the Sage Surgeon of Ancient India," Indian J. Surg., **70**(5), pp. 219–223.
[167] Mahdihassan, S., 1979, "Distillation Assembly of Pottery in Ancient India With a Single Item of Special Construction," Vishveshvaranand Indological Journal, **17**, pp. 264–266.
[168] Mahdihassan, S., 1972, "The Earliest Distillation Units of Pottery in Indo-Pakistan," Pa. Archaeol., **8**, pp. 159–168.
[169] Dani, A. H., 1966, "Shaikhan Dheri Excavations, 1963 and 1964," Ancient Pakistan, **2**, pp. 17–214.
[170] Marshall, J., 1951, *Taxila*, Cambridge University Press, Cambridge, UK.
[171] Oort, M. S., 2002, "Sura in the Paippalada Samhita of the Atharvaveda," J. Am. Orient. Soc., **122**(2), pp. 355–360.
[172] Craddock, P. T., Gurjar, L. K., and Hegde, K. T. M., 1983, "Zinc Production in Medieval India," World Archaeol., **15**(2), pp. 211–217.
[173] Willies, L., Craddock, P. T., Gurjar, L. J., and Hegde, K. T. M., 1984, "Ancient Lead and Zinc Mining in Rajasthan, India," World Archaeol., **16**(2), pp. 222–233.

Flow Boiling Heat Transfer in Horizontal Metal-Foam Tubes

C. Y. Zhao[1]
e-mail: c.y.zhao@warwick.ac.uk

W. Lu

School of Engineering,
University of Warwick,
Coventry CV4 7AL, UK

S. A. Tassou
School of Engineering and Design,
Brunel University,
Uxbridge,
Middlesex UB8 3PH, UK

The two-phase flow and boiling heat transfer in horizontal metal-foam filled tubes are experimentally investigated. The results show that the heat transfer is almost doubled by reducing the cell size from 20 ppi to 40 ppi for a given porosity, thanks to more surface area and strong flow mixing for the smaller cell size. The boiling heat transfer coefficient keeps steady rising, albeit slowly, by increasing the vapor quality for high mass flow rates, while the same story does not hold for the cases of low mass flow rates. The flow pattern can be indirectly judged through monitoring the cross-sectional wall surface temperature fluctuations and wall-refrigerant temperature difference. As the operating pressure increases, the boiling heat transfer at low vapor quality ($x<0.1$) exhibits similar behavior with pool boiling heat transfer, namely, the heat transfer is enhanced by improving the pressure. However the flow boiling heat transfer is suppressed to some extent as the pressure increases. The heat transfer coefficient of copper foam tubes is approximately three times higher than that of plain tubes. [DOI: 10.1115/1.3216036]

Keywords: metal foam, boiling heat transfer, vapor quality

1 Introduction

Metal foams, as one kind of promising porous materials for heat transfer, have received much attention in recent years. Extensive investigations have been carried out for thermal transport in metal foams [1–15]. Calmidi and Mahajan [1] measured the effective thermal conductivity of aluminum Energy Research and Generation, Inc. (ERG) foams by using both air and water as the fluid phase. The measurement was conducted at low temperatures, so the thermal radiation effect is neglected. An analytical model was also derived by Calmidi and Mahajan [1] based on the two-dimensional hexagonal structure of the metal foam. As an extension of the work of Calmidi and Mahajan, Boomsma and Poulikakos [2] proposed an effective thermal conductivity model based on a three-dimensional idealized cellular structure of a metal foam, and a good agreement with the test data [1] has been achieved. Zhao et al. [3] measured the thermal conductivities of steel alloy (FeCrAlY) foams under a temperature range of 25–500°C. The study showed that the thermal radiation plays a significant role on effective thermal conductivity at high temperatures. Also, to examine the thermal radiation mechanism in metal foams, Zhao et al. [4] conducted the spectral transmittance and reflectance measurements, from which the spectral extinction coefficient was deduced. An analytical model was also built based on the Rosseland diffusion equation and the metal foam microstructures in that paper [4].

Hunt and Tien [5] studied the effects of thermal dispersion on forced convection in metal foams with water as the fluid phase. Lee et al. [6] investigated the application of metal foams as high-performance air-cooled heat sinks in electronics packaging. In their experimental study, they demonstrated that aluminum foams could dissipate heat fluxes up to 100 W/cm^2. Using the fin approach, Lu et al. [7] developed an analytical model to predict the metal foam-assisted heat transfer, where the foam is modeled as interconnected cylinders. Bastarows et al. [8] studied the single-sided heating of a foam-filled channel for electronics cooling applications. The test results showed that brazed foam materials are much more effective at heat removal than epoxy-bonded samples, and that the heat exchange performance is three times more efficient compared with a conventional fin-pin array. Calmidi and Mahajan [9] conducted experimental and numerical investigations on the forced conduction in ERG aluminum foams with air as the fluid phase. Kim et al. [10,11] experimentally studied the heat transport in aluminum foams, and their results showed that the foam material offers a better heat transfer performance compared with that of a louvered array, but at a greater pressure drop. Boomsma and coworker [12,13] studied the pressure drop and heat transfer for the compressed aluminum foams by using water as the coolant. The results showed that the precompression porosity has little effect on the final permeability and foam coefficient, and the postcompression porosity determines the permeability and the overall hydraulic behavior of the compressed foams. Compared with the commercially used heat exchangers, the metal-foam heat exchangers showed a favorable thermal resistance reduction, and hence, a better heat transfer performance. The convective heat transfer and friction drag in a duct inserted with aluminum foams have been experimentally studied by Hwang et al. [14]. Their results showed that both the friction factor and the volumetric heat transfer coefficient increase with decreasing the foam porosity at a fixed Reynolds number. Bhattacharya et al. [15] investigated the permeability and inertial coefficient of aluminum foam samples of different porosities and pore sizes. In their model a parameter of tortuosity was introduced, and the predictions can give quite good agreements with the experimental data. Zhao et al. [16] performed experimental and numerical studies on the forced convection in FeCrAlY and copper foams, wherein in these studies the effect of metal-foam microstructures (foam porosity and cell size) on heat transfer was examined. The natural convections in metal foams have been investigated by Zhao et al. [17] and Phanikumar and Mahajan [18]. Both results showed that the natural convection takes place in a global domain rather than in a single cell, and thereby leads to a high heat transfer capability. Metal-foam tube heat exchangers have been analytically investigated by Zhao and coworkers [19,20], and the results showed that the metal-foam tube heat exchangers have a superior performance to the conventional finned tube heat exchangers.

Although single-phase forced convection in metal foams has been studied to some extent, very little work has been done for boiling heat transfer in metal foams. Ng et al. [21] measured the pool boiling heat transfer for copper foam at subatmospheric pressures. In that paper the heat flux for pool boiling was derived from uniform radiant heaters. To the authors' knowledge, no work has

[1]Corresponding author.

Contributed by the Heat Transfer Division of ASME for publication in the JOURNAL OF HEAT TRANSFER. Manuscript received August 16, 2007; final manuscript received October 20, 2008; published online October 15, 2009.

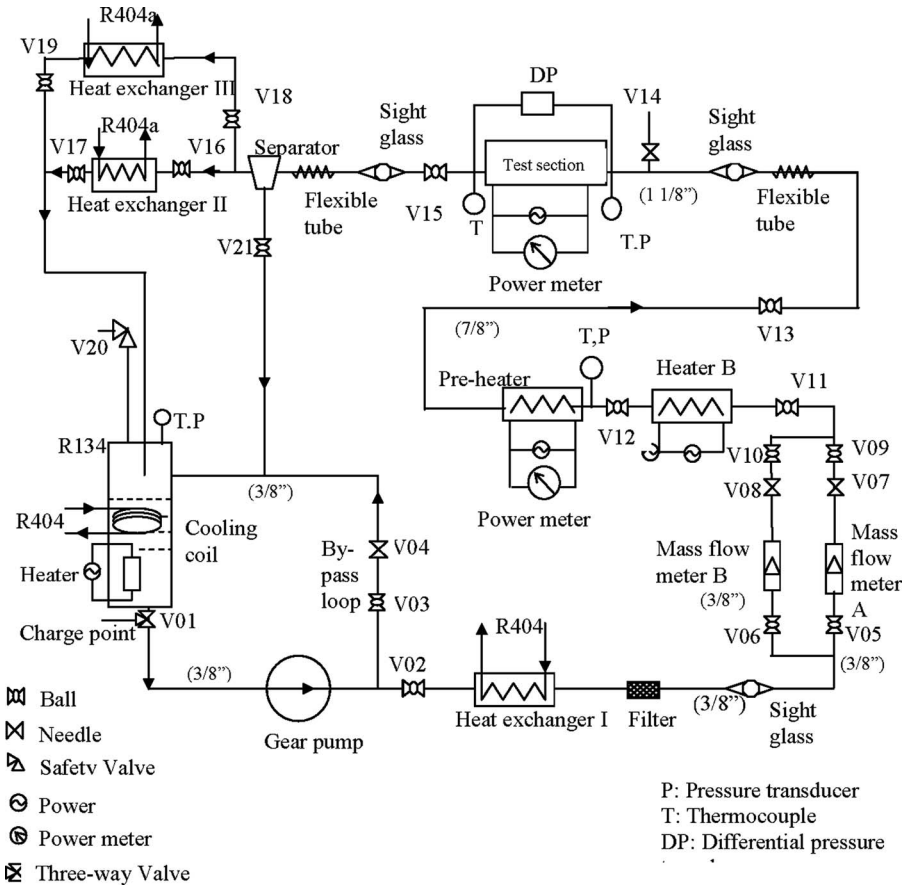

Fig. 1 Schematic diagram of the test rig

been done for flow boiling heat transfer in metal foams, even though some boiling heat transfer investigations have been carried out for porous media such as packed beds or sintered particles [22–28]. The flow boiling mechanism in metal foams is very complicated due to the inherent complexities of boiling heat transfer and unique microstructure of the metal foam. The metal-foam structures not only provide more boiling sites to promote heat transfer, but can also constrain bubble growth and even break up the bubbles when the flow is obstructed by the foam ligaments with different orientation angles. This tends to homogenize the flow field and enhance heat transfer. Some distinctive and interesting boiling transport phenomena would be expected, which could lead to different boiling heat transfer characteristics from those of plain channel flows.

This paper aims to experimentally investigate the boiling flow and heat transfer in metal-foam filled tubes. The effects of heat flux, mass flow rate, operating pressure, and foam microstructures on boiling heat transfer and pressure drop are presented in the paper.

2 Experimental Equipment and Measurement Procedures

Figure 1 shows a schematic diagram of the experimental apparatus that is used in this study. It consists of a gear pump (Tuthill, Llkeston, UK, magnetically-coupled gear pump, TXS5.3PPPN3WN0000 with Asea Brown Boveri Ltd, Zurich (ABB) inverter) for refrigerant (R134a) circulation, mass flow meters, a preheater, a test section, and three chillers: one for subcooling the refrigerant before the flow meters and the other two for condensing the refrigerant, an electrically heated refrigerant reservoir, and an electric power supply system in the test section. The required system pressure can be maintained by an automatically controlled heating system, which can heat the two-phase refrigerant in the reservoir and enhance the pressure when the system pressure is below the required test value. So in the refrigerant reservoir the vapor state refrigerant fills the upper part, while the liquid state refrigerant occupies the lower part. A gear pump is used to circulate the liquid refrigerant. Before the refrigerant enters into the mass flow meters, it is first subcooled in a chiller in case of possible evaporation in pipes. Two Coriolis (KROHNE Ltd., Northants, UK, Optimass Mfs 7150 S03 and S04) mass flow meters are used to measure the refrigerant mass flow rate: one for low flows (0–1 kg/min) and the other one for high flows (1–6 kg/min). A well-insulated preheater is used to control the inlet vapor quality of refrigerant to the test section. The enthalpy of the subcooled refrigerant before the preheater can be determined from its pressure and temperature (*T*-type sheathed thermocouple, with response time of 0.25 s), thus the refrigerant quality and enthalpy at the inlet of test section can be determined by an energy balance on the preheater section. The temperature and pressure of the refrigerant at the inlet and outlet of the test section are measured. The exit quality can be calculated from an energy balance between the imposed heat flux and enthalpy change in the refrigerant across the test section. The pressure drop in the test section is also measured using a differential pressure transducer (OMEGA Engineering Limited, Manchester, UK, PX771A-100DI). A glass tube after the test section is used to facilitate visualization of the flow. After the test tube the refrigerant enters into a separator with the liquid flowing from the bottom of the separator to the refrigerant reservoir and the vapor passing through a condensing heat exchanger, where it condenses to liquid before returning to the reservoir. A computer controlled 60-channel data acquisition system (Solartron Metrology, West Sus-

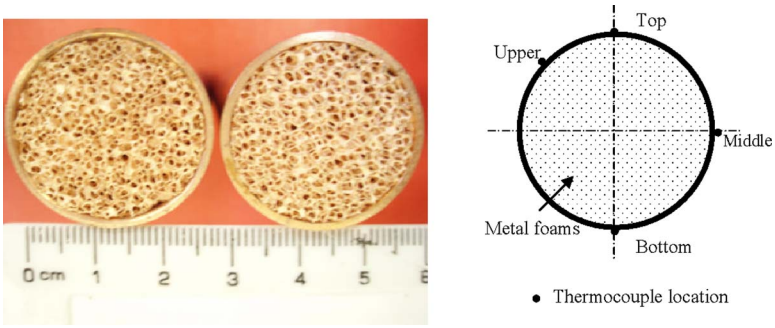

Fig. 2 Test section

sex, UK, IMP3595) with LABVIEW data logging software is used to record and display the experimental data.

The test section is schematically shown in Fig. 2. The tested copper-foam filled tubes are 150 mm long with the inner diameter of 26 mm. The tubes are instrumented with thin foil (0.05–0.10 mm thickness) *T*-type copper-constantan thermocouples (response time of 1 ms), which are attached to the outer surface of the wall at three locations (50 mm, 75 mm, and 100 mm) along the flow direction to monitor the temperature variation along the tubes. At each location, four thermocouples are placed on the circumference of the tube, as shown in Fig. 2. Due to the short tubes, the imposed heat flux only changes the exit vapor quality slightly (<0.04) from the inlet point in the test, so all the measured results are referred to the averaged inlet and outlet vapor qualities in the following results analysis. The inner wall temperatures along the circumference and length of the tube, which are used to obtain the heat transfer coefficients, can be calculated from the measured outer wall temperature and heat flux. The test tubes are heated by a direct current surface heater, which provides controlled and uniform heat fluxes on the surface of the tube. The heater element is coated with thermal epoxy to enhance the thermal contact with the tubes. The test section is insulated with 80 mm *Tancast 8*™ thermal insulation material to minimize heat loss. All measurements are carried out after the test reaches the steady state conditions, and it typically takes 1–2 h to reach steady state after any change in parameters.

3 Uncertainty Analysis

An uncertainty analysis for the measurements has been performed following the method of Kline and McClintock [29]. The uncertainty for the heat transfer coefficient can be mainly attributed to the input heat flux and temperature measurement. Then the uncertainty of the heat transfer coefficient can be expressed as

$$\frac{\delta h}{h} = \sqrt{\left(\frac{\delta q_w}{q_w}\right)^2 + \left(\frac{\delta \Delta T}{\Delta T}\right)^2}$$

The uncertainty of the heat flux is estimated as less than 5% by considering the accuracy (0.5%) of the programmable power meter (Hameg HM8115-2), the estimated uncertainty caused by axial heat conduction, and the geometric uncertainty of the test tubes and heat loss through the insulations. The uncertainty of ΔT (temperature difference between the averaged inner wall surface temperature and the fluid average temperature) is around 0.5°C by taking into account the accuracy of thermocouples (0.1°C) and the estimated uncertainty caused by the contact thermal resistance of thermocouple attachment. Therefore, the uncertainty in the temperature difference ΔT is 10% based on the typical ΔT of 5°C. Therefore, the uncertainty in heat transfer coefficient is less than 12% from the above equation. Similar analysis can be done for the pressure drop. Finally, the uncertainties for the heat transfer coefficient and pressure drop are calculated to be 12% and 5.8%, respectively.

4 Experimental Results and Discussions

4.1 Pressure Drop. In this study the pressure drop has been measured by pressure transducers. For the metal foam with the microstructure of 20 ppi (pore number per inch) and 90% porosity, Fig. 3 shows the variation in the pressure drop per unit length as a function of the vapor quality for a series of mass flow rates. It can be seen that the pressure drop nonlinearly increases as the vapor quality rises. This is the reason why the void fraction substantially increases with the vapor quality, and this causes higher vapor velocity, which leads to the higher pressure drop. For a given porosity (90%) and mass flow rate (106 $kg/m^2 s$), the effect of metal-foam cell size on the pressure drop is presented in Fig. 4. As the cell size becomes smaller (40 ppi), the pressure drop significantly increases, and this implies that the two-phase flow encounters much more flow resistance for smaller cell size due to

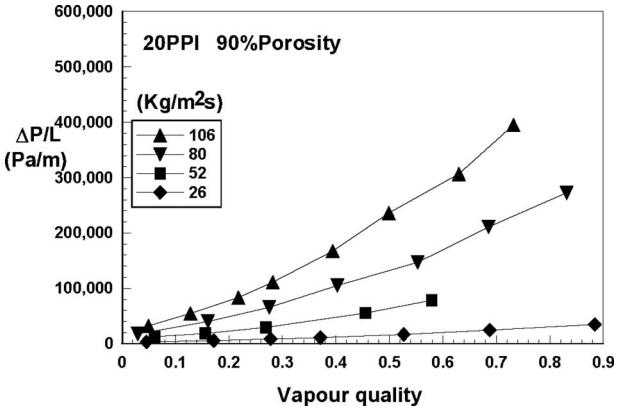

Fig. 3 Variation in the pressure drop per unit length as a function of the vapor quality

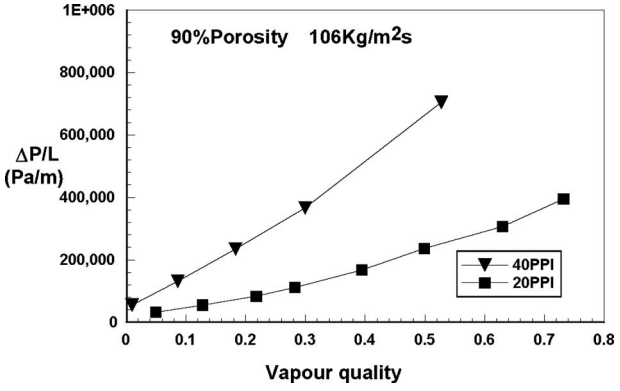

Fig. 4 Effect of metal-foam cell size on the pressure drop

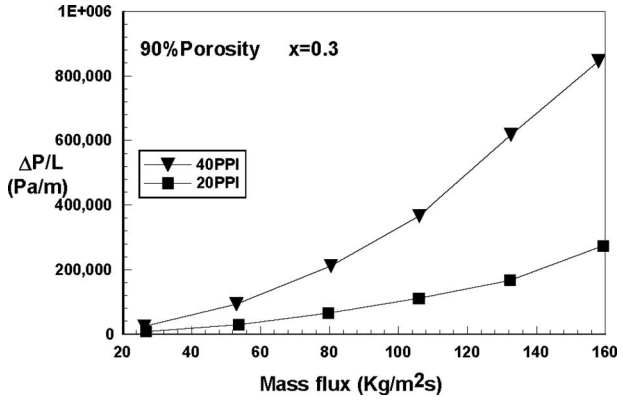

Fig. 5 Variation in the pressure drop as a function of the mass flow rate

the presence of metal-foam structures. This result is similar to the situation for the single-phase flow [9,16]. The flow resistance in metal-foam channels mainly comprises three parts: channel surface drag resistance, Darcy viscous resistance, and form resistance induced by metal-foam structures. The latter two parts are caused by the presence of foam structures. For detailed analysis on flow resistance in metal foams, interested readers can refer to Ref. [16]. For a given porosity (90%) and vapor quality ($x=0.3$), the variation in the pressure drop as a function of the mass flow rate is shown in Fig. 5 for two different cell sizes. As expected, the pressure drop increases as the mass flow rate rises. Figure 6 presents the effect of the operating pressure on the pressure drop. As the operating pressure rises, the vapor density gets higher, and this leads to a lower vapor velocity for a higher operating pressure, thereby causing less pressure drop.

4.2 Temperature Fluctuations and Flow Patterns in Metal Foams. As well known, the two-phase flow exhibits different flow patterns such as slug flow, wavy flow, annular flow, etc., under different conditions, i.e., mass flow rates, vapor quality, heat flux, etc. For the flow boiling heat transfer in plain tubes, the flow patterns can be directly visualized through optical techniques. The investigations [30,31] showed that the flow pattern is mainly governed by the mass flow rates and vapor qualities. However, for two-phase flow in metal-foam tubes studied in this paper, the presence of metal-foam structures blocks the direct view on the flow patterns inside. This problem can be partially addressed by monitoring and analyzing the wall temperature distributions. For the metal-foam tube with 20 ppi and 90% porosity, Figs. 7 and 8 present the wall temperature's fluctuations with time for two different mass flow rates at the middle cross section of the tube. In both figures (and the following figures), the legends "Top," "middle," and "bottom" refers to the top, middle, and bottom wall temperatures over the cross section, as shown in Fig. 2. Figures 7(*a*) and 7(*b*) show the variation in the wall temperature for vapor quality at $x=0.18$ and $x=0.53$, respectively, for the low mass flow rate of 26 kg/m^2 s. Both figures reveal that the wall temperature at the bottom is pretty stable, while the temperatures at the top and middle exhibit strong fluctuations, particularly for the case of vapor quality $x=0.18$. This implies that the lower part of the tube is always filled with liquid refrigerant, but this may not be the case for the upper part of the tube. The different wall temperature behavior is determined by different two-phase flow patterns. The flow pattern in Fig. 7(*a*) can be judged as a slug/wavy flow from the measured wall temperatures. The upper part of the tube is occupied by liquid or vapor intermittently, thereby causing strong temperature fluctuations. As the vapor quality increases from 0.18 to 0.53, the two-phase flow pattern gradually changes to stratified wavy flow, where the upper part is vapor. Therefore the top wall temperature fluctuation diminishes, but the wall temperature at the middle point shows to be more fluctuant. Figures 8(*a*) and 8(*b*) show the variation in the wall temperature fluctuation for vapor quality at $x=0.22$ and $x=0.63$, respectively, for the high mass flow rate of 106 kg/m^2 s. Both figures indicate that the temperature distributions are more uniformly distributed, and the high velocity causes the wall temperatures to fluctuate at a much smaller magnitude but with a higher frequency. This wall temperature distribution indicates that the flow pattern is more like annular flow, being the whole tube wall surface is wetted by the liquid phase.

Figures 9(*a*) and 9(*b*) present the distribution of temperature difference between the wall surface and refrigerant for two different mass flow rates. The wall temperature exhibits large difference over the cross section for the smaller mass flow rate $m=26$ kg/m^2 s, particularly at the high vapor quality regime. The flow pattern at this smaller mass flow rate is believed to be strati-

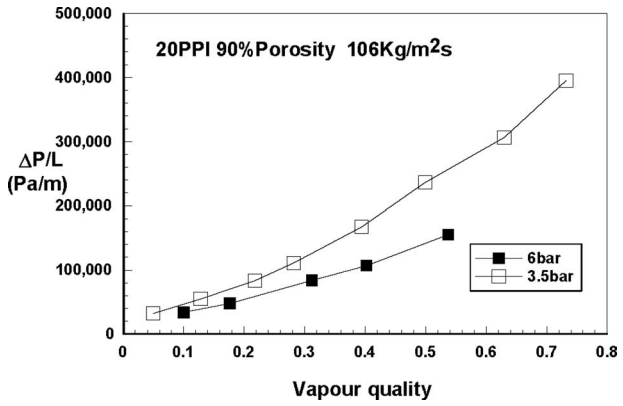

Fig. 6 Effect of operating pressure on the pressure drop

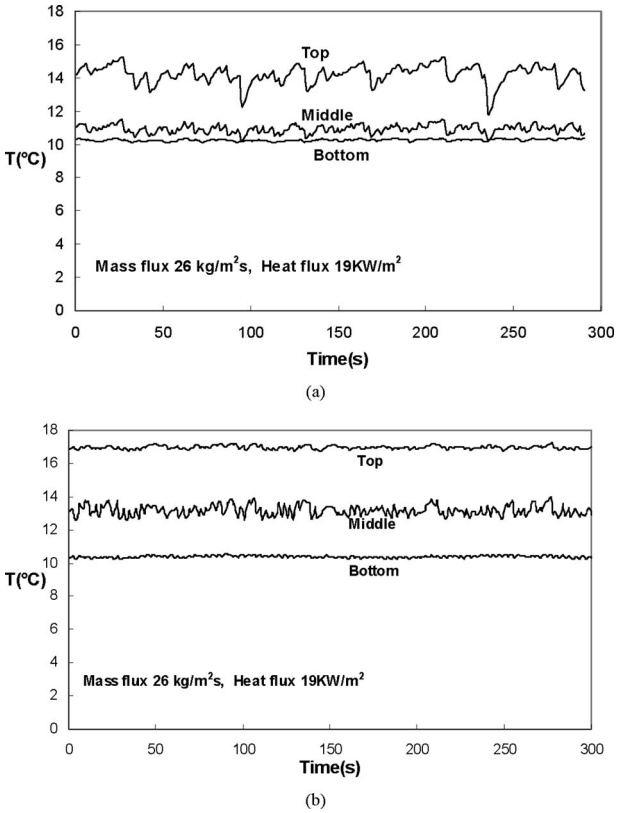

Fig. 7 Wall temperature's fluctuations with time for vapor quality at (*a*) $x=0.18$ and (*b*) $x=0.53$ for the mass flow rate of 26 kg/m^2 s

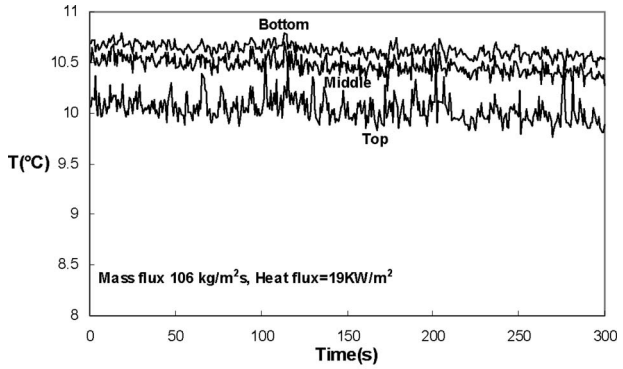

(a)

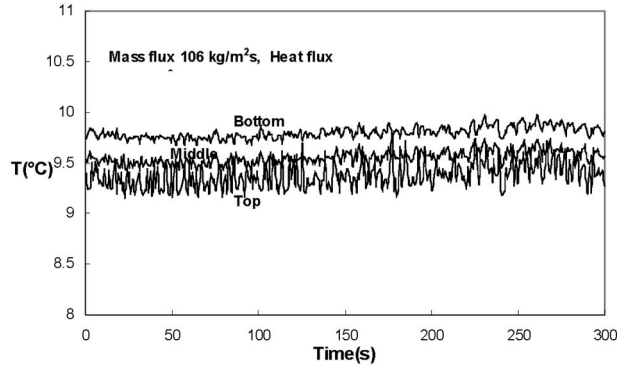

(b)

Fig. 8 Wall temperature's fluctuations for vapor quality at (*a*) $x=0.22$ and (*b*) $x=0.63$ for the high mass flow rate of 106 kg/m² s

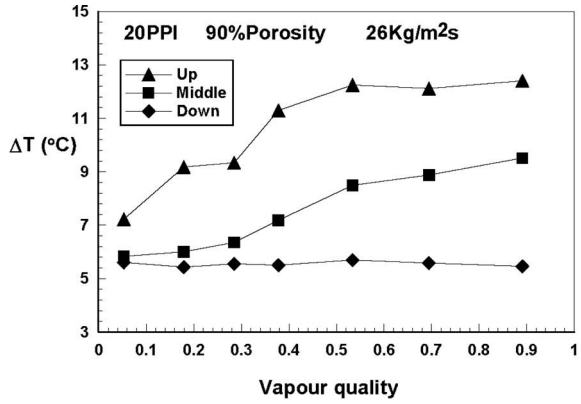

(a)

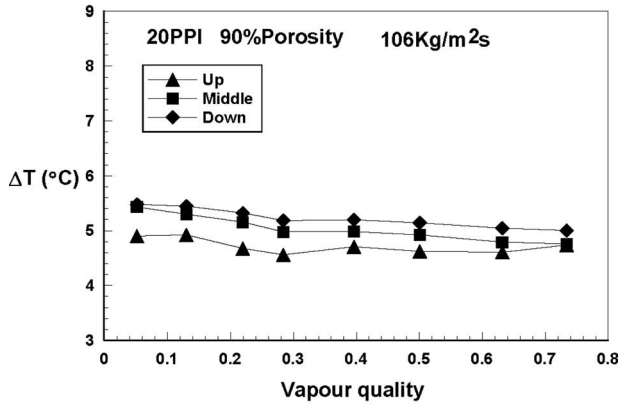

(b)

Fig. 9 Temperature difference between the wall surface and refrigerant for two different mass flow rates

fied wavy flow for the majority of the vapor flow regime. The upper part of the tube is occupied by vapor, while the lower part is liquid. Even though the liquid and vapor maintain the same saturation temperature, the tube wall temperature is quite different along the circumference due to the different local heat transfer coefficient caused by liquid or vapor. This flow pattern determines the measured temperature distribution, namely, the temperature difference ΔT in the upper part of the tube is higher than that in the lower part of the circumference of the tube, though the metal-foam structure tends to homogenize the temperature distribution over the cross section. For the larger mass flow rate of 106 kg/m² s, the temperature difference over the cross section is dramatically reduced. The flow pattern for this case should be more like annular flow, thus a thin liquid film adheres to the whole wall surface, and also under the help of metal-foam structure the wall temperature exhibits pretty uniform distribution over the cross section.

4.3 Heat Transfer Coefficient. In this paper the overall heat transfer coefficient h is defined as

$$h = \frac{q}{\Delta T}$$

where q is the uniform heat flux applied on the tube surface, and ΔT is the temperature difference between the averaged inner wall surface and refrigerant. The inner wall surface temperature can be deduced based on one-dimensional conduction assumption from the measured outer wall surface temperature. Without elsewhere stated, the metal-foam material is 92 Cu with 8% Ag for the following measurement results.

4.3.1 Effect of Vapor Quality. Figures 10(*a*) and 10(*b*) show the variation in the heat transfer coefficient with the vapor quality for two different cell-sized foam tubes, respectively. One interesting observation from the figure is that the heat transfer coefficient exhibits different behaviors as the vapor quality rises. For low mass flow rates, the heat transfer coefficient becomes smaller as the vapor quality rises. As indicated earlier, the flow pattern should be stratified wavy flow for low mass flow rates, so more metal-foam structure and tube wall surfaces are occupied by the vapor as the vapor quality rises, and this reduces the heat transfer capability. For high mass flow rates, the flow pattern is more like annular flow as the vapor quality rises, so the heat transfer coefficient keeps steady rising, albeit slowly.

4.3.2 Effects of Metal-Foam Cell Size. The effect of cell size on boiling heat transfer is shown in Figs. 11(*a*) and 11(*b*) for different vapor qualities and mass flow rates, respectively. Both figures show that the heat transfer is dramatically enhanced by reducing the cell size from 20 ppi to 40 ppi. A metal foam with smaller cell size can provide more surface areas and boiling sites, and it can also enhance the flow mixing and break up the large bubbles, thereby increasing the heat transfer coefficient. Both figures show that the boiling heat transfer coefficients for 40 ppi metal-foam tubes are nearly twice those of 20 ppi foam tubes.

4.3.3 Effect of Mass Flow Rates. The effect of mass flow rates on heat transfer is shown in Fig. 11(*b*). The heat transfer coefficient moderately increases with the mass flow rates, which is a typical convective flow boiling characteristic. In horizontal metal-foam tubes, the metal-foam structures not only provide more boiling sites to promote heat transfer, but can also constrain bubble growth and even break up the bubbles when the flow is obstructed by the foam ligaments with different orientation angles. This tends to homogenize the flow field and enhance heat transfer.

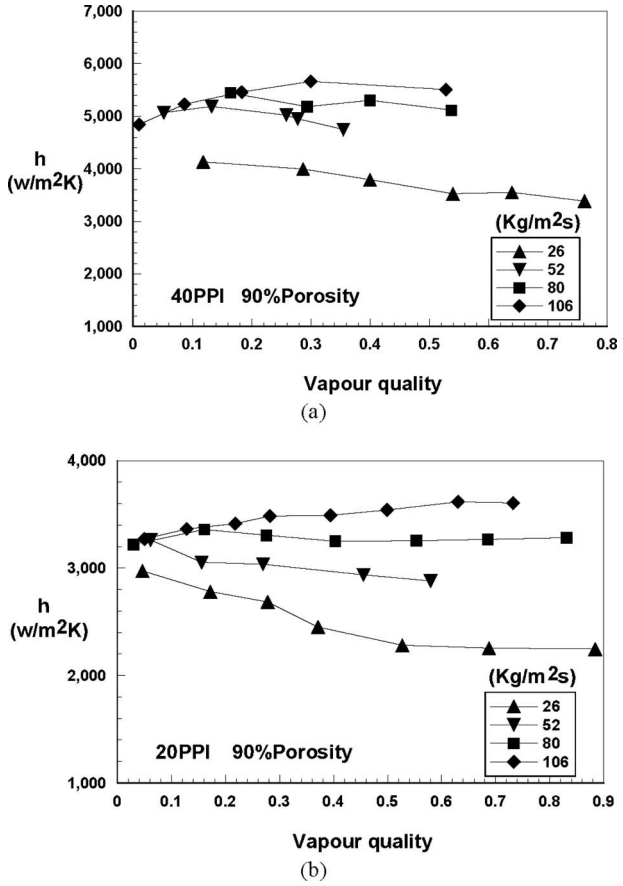

Fig. 10 Variation in the heat transfer coefficient with the vapor quality for two different cell-sized foam tubes

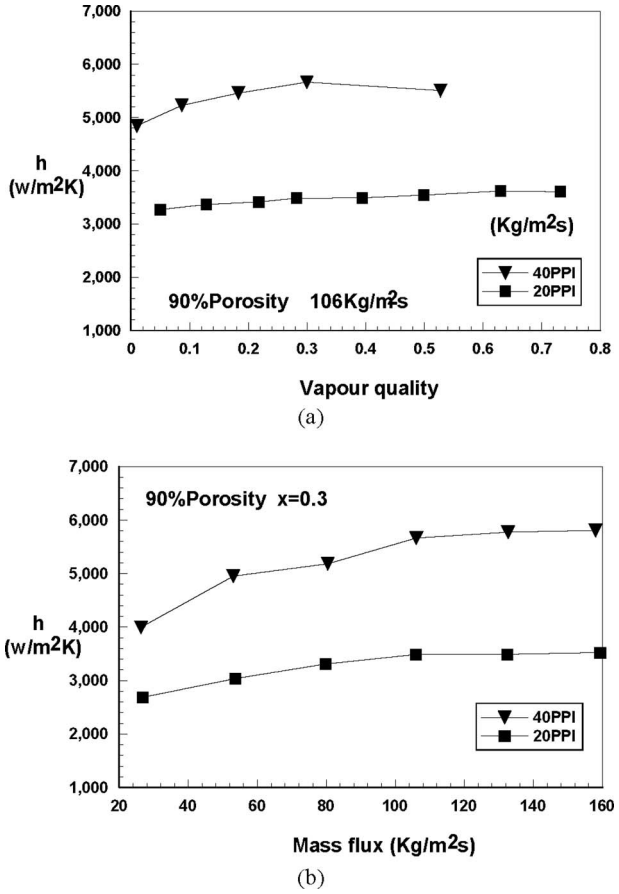

Fig. 11 Effect of cell size on boiling heat transfer: (*a*) for different vapor qualities and (*b*) for different mass flow rates

4.3.4 Effect of Heat Flux. The effect of heat flux on boiling heat transfer is shown in Fig. 12. For the single-phase flow, it is known that the heat flux has no effect on the heat transfer coefficient; however, the same story does not necessarily hold for boiling heat transfer. Figure 12 shows that the heat flux plays a very moderate role on boiling heat transfer, and this implies that the convective heat transfer plays a dominant role for the case of high mass flow rate of 106 kg/m^2 s.

4.3.5 Effect of Operating Pressure. The effect of refrigerant pressure on boiling heat transfer is shown in Fig. 13. It is noted that the boiling heat transfer coefficient of pressure of 6.0 bar is higher than that of 3.5 bar for small vapor quality $x=0.1$. This observation is in line with the pool boiling heat transfer, where the heat transfer coefficient increases with the refrigerant pressure, and it implies that the heat transfer exhibits pool boiling heat transfer characteristics for small vapor quality $x \leq 0.1$. However, the story is different for larger vapor qualities. As the vapor quality rises, the vapor velocity for the low pressure is higher due to the small vapor density, and this consequently causes higher heat transfer coefficient for the case of pressure of 3.5 bar. Also Fig. 13 shows that the heat transfer coefficient almost remains unchanged with the increase in vapor quality for the higher pressure of 6.0 bar, whereas it keeps steady increasing as the vapor quality rises for the lower pressure of 3.5 bar. For the high pressure of 6.0 bar, the diminishing liquid effect is offset by the enhancing vapor convective effect as the vapor quality rises. However, for the low pressure of 3.5 bar, the heat transfer enhancing effect of vapor convection outstrips the diminishing effect of the lacking liquid, and this leads to the steady increasing heat transfer behavior as the vapor quality rises.

4.3.6 Effect of Metal Foam Materials. In order to examine the metal-foam material effect on the heat transfer, measurements have been conducted for two different metal-foam material tubes. Figure 14 presents the comparison of boiling heat transfer between the two different material foam tubes. The boiling heat transfer coefficient of the metal-foam tube with 14 Ag and 86 Cu is around 30% higher than that of pure copper-foam tube. The different metal-foam composition has a direct effect on its overall thermal conductivity, and perhaps more importantly, it will directly affect the attachment quality with the tubes, which plays a key role on heat transfer.

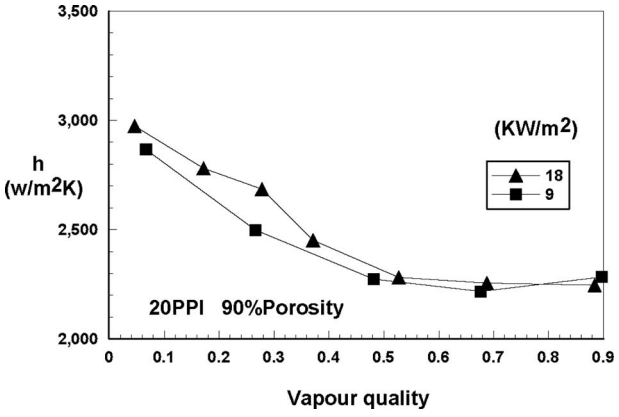

Fig. 12 Effect of heat flux on boiling heat transfer

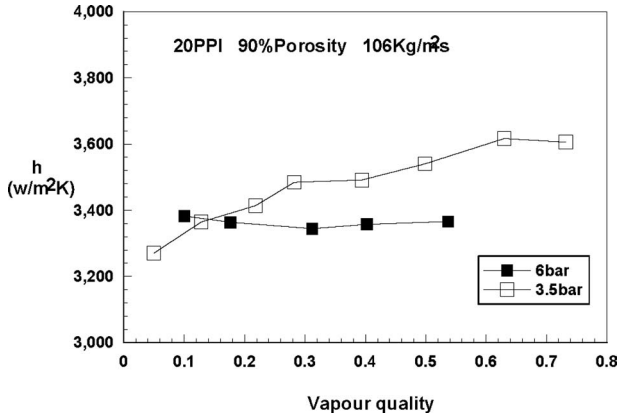

Fig. 13 Effect of refrigerant pressure on boiling heat transfer

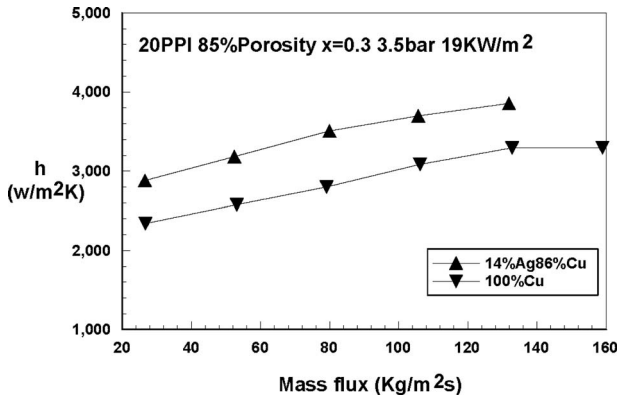

Fig. 14 Comparison of heat transfer between the two different material foam tubes

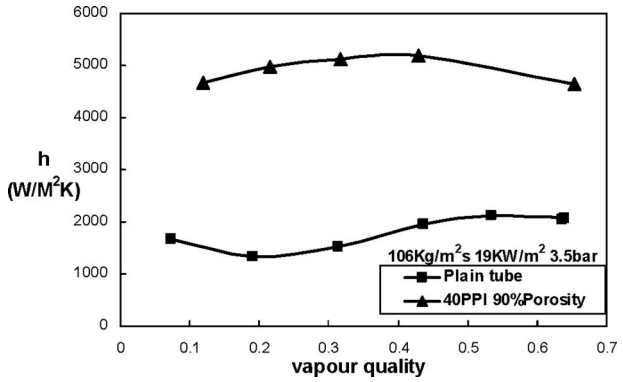

Fig. 15 Comparison of heat transfer coefficient between plain and copper foam tubes

4.3.7 Comparison With the Plain Tubes. To reveal the enhancing effect compared with the plain tubes, Fig. 15 presents the comparison of heat transfer coefficient for copper tubes. Approximately the heat transfer coefficient of foam tubes is three times higher than that of plain tubes. The combining quality (contact thermal resistance) between the tube surface and metal-foam structure is considered as the main cause to limit the enhancing effect [32]. Also the imperfection (deficiency) of metal-foam structures, such as broken foam structures, constrains the enhancing effect.

5 Conclusions

In this paper the boiling heat transfer in horizontal metal-foam tubes is experimentally investigated. Some conclusions can be drawn as follows:

(1) The pressure drop nonlinearly increases with the vapor quality and mass flow rates. The metal-foam cell size has a significant effect on the pressure drop, and the pressure drop is doubled by reducing the cell size from 20 ppi to 40 ppi. Higher operating pressure can reduce the pressure drop due to lower vapor velocity.
(2) The flow pattern can be indirectly judged through monitoring the cross-sectional wall surface temperature fluctuations and wall-refrigerant temperature difference. The flow patterns that occurred inside the metal-foam tubes should be the stratified or slug wavy flow for low mass flow rates and the annular flow for high mass flow rates as the vapor quality rises.
(3) For different mass flow rates, the heat transfer coefficient exhibits different behaviors as the vapor quality rises. For lower mass flow rates, the heat transfer coefficient becomes smaller with the increase in the vapor quality, while the reverse situation holds for higher mass flow rates. The different heat transfer behaviors can be attributed to different flow patterns.
(4) The heat transfer coefficient of foam tubes is approximately three times higher than that of plain tubes. The combining quality (contact thermal resistance) between the tube surface and metal-foam structure and the broken foam structures are considered as the main causes that limit the enhancing effect.
(5) Metal-foam cell size plays a significant role on boiling heat transfer, and the heat transfer coefficients can be nearly doubled as the cell size decreases from 20 ppi to 40 ppi due to the increased surface area density and flow mixing.

Acknowledgment

This work is supported by the Engineering and Physical Science Research Council (EPSRC-GB) (Grant Nos. EP/F061439/1 and GR/T24364/01) and the National Natural Science Foundation of China (Grant No. 50576069). The authors also wish to thank the assistance of Mr. Ian Stirling of Porvair PLC for providing the test samples.

Nomenclature

d = tube diameter (m)
h = heat transfer coefficient (W/m^2 K)
L = length (m)
m = mass flux (kg/m^2 s)
P = pressure (Pa)
ΔP = pressure difference (Pa)
q = heat flux (W/m^2)
T = temperature (°C)
ΔT = temperature difference (°C)
u = fluid velocity (m/s)
x = vapor quality

References

[1] Calmidi, V. V., and Mahajan, R. L., 1999, "The Effective Thermal Conductivity of High Porosity Fibrous Metal Foams," ASME J. Heat Transfer, **121**, pp. 466–471.
[2] Boomsma, K., and Poulikakos, D., 2001, "On the Effective Thermal Conductivity of a Three-Dimensionally Structured Fluid-Saturated Metal Foam," Int. J. Heat Mass Transfer, **44**, pp. 827–836.
[3] Zhao, C. Y., Lu, T. J., Hodson, H. P., and Jackson, J. D., 2004, "The Temperature Dependence of Effective Thermal Conductivity of Open-Celled Steel Alloy Foams," Mater. Sci. Eng., A, **367**, pp. 123–131.
[4] Zhao, C. Y., Lu, T. J., and Hodson, H. P., 2004, "Thermal Radiation in Metal Foams With Open Cells," Int. J. Heat Mass Transfer, **47**, pp. 2927–2939.
[5] Hunt, M. L., and Tien, C. L., 1988, "Effects of Thermal Dispersion on Forced

Convection in Fibrous Media," Int. J. Heat Mass Transfer, **31**, pp. 301–309.
[6] Lee, Y. C., Zhang, W., Xie, H., and Mahajan, R. L., 1993, "Cooling of a FCHIP Package With 100 W 1 cm^2 Chip," *Proceedings of the 1993 ASME International Electronic Packaging Conference*, New York, Vol. 1, pp. 419–423.
[7] Lu, T. J., Stone, H. A., and Ashby, M. F., 1998, "Heat Transfer in Open-Celled Metal Foams," Acta Mater., **46**, pp. 3619–3635.
[8] Bastarows, A. F., Evans, A. G., and Stone, H. A., 1998, "Evaluation of Cellular Metal Heat Dissipation Media," Harvard University, Technical Report No. MECH-325.
[9] Calmidi, V. V., and Mahajan, R. L., 2000, "Forced Convection in High Porosity Metal Foams," ASME J. Heat Transfer, **122**, pp. 557–565.
[10] Kim, S. Y., Paek, J. W., and Kang, B. H., 2000, "Flow and Heat Transfer Correlations for Porous Fin in a Plate-Fin Heat Exchanger," ASME J. Heat Transfer, **122**, pp. 572–578.
[11] Kim, S. Y., Kang, B. H., and Kim, J. H., 2001, "Forced Convection From Aluminum Foam Materials in an Asymmetrically Heated Channel," Int. J. Heat Mass Transfer, **44**, pp. 1451–1454.
[12] Boomsma, K., and Poulikakos, D., 2001, "The Effects of Compression and Pore Size Variations on the Liquid Flow Characteristics in Metal Foams," ASME J. Fluids Eng., **124**, pp. 263–272.
[13] Boomsma, K., 2002, Metal Foams as Novel Compact High Performance Heat Exchangers for the Cooling of Electronics, Ph.D. thesis, Swiss Federal Institute of Technology, Zurich.
[14] Hwang, J. J., Hwang, G. J., Yeh, R. H., and Chao, C. H., 2002, "Measurement of Interstitial Convective Heat Transfer and Frictional Drag for Flow Across Metal Foams," ASME J. Heat Transfer, **124**, pp. 120–129.
[15] Bhattacharya, A., Calmidi, V. V., and Mahajan, R. L., 2002, "Thermophysical Properties of High Porosity Metal Foams," Int. J. Heat Mass Transfer, **45**, pp. 1017–1031.
[16] Zhao, C. Y., Kim, T., Lu, T. J., and Hodson, H. P., 2004, "Thermal Transport in High Porosity Cellular Metal Foams," J. Thermophys. Heat Transfer, **18**(3), pp. 309–317.
[17] Zhao, C. Y., Lu, T. J., and Hodson, H. P., 2005, "Natural Convection in Metal Foams With Open Cells," Int. J. Heat Mass Transfer, **48**, pp. 2452–2463.
[18] Phanikumar, M. S., and Mahajan, R. L., 2002, "Non-Darcy Natural Convection in High Porosity Metal Foams," Int. J. Heat Mass Transfer, **45**, pp. 3781–3793.
[19] Zhao, C. Y., Lu, W., and Tassou, S. A., 2006, "Thermal Analysis on Metal-Foam Filled Heat Exchangers, II. Tube Heat Exchangers," Int. J. Heat Mass Transfer, **49**, pp. 2762–2770.
[20] Lu, W., Zhao, C. Y., and Tassou, S. A., 2006, "Thermal Analysis on Metal-Foam Filled Heat Exchangers, I. Metal-Foam Filled Pipes," Int. J. Heat Mass Transfer, **49**, pp. 2751–2761.
[21] Ng, K. C., Anutosh, C., Sai, M. A., and Wang, X. L., 2006, "New Pool Boiling Data for Water With Copper-Foam Metal at Sub-Atmospheric Pressures: Experiments and Correlation," Appl. Therm. Eng., **26**, pp. 1286–1290.
[22] Rojas, M. E., de Andrés, M. C., and González, L., 2008, "Designing Capillary Systems to Enhance Heat Transfer in LS3 Parabolic Trough Collectors for Direct Steam Generator," Sol. Energy, **82**, pp. 53–60.
[23] Miscevic, M., Rahli, O., Tadrist, L., and Topin, F., 2006, "Experiments on Flows, Boiling and Heat Transfer in Porous Media: Emphasis on Bottom Injection," Nucl. Eng. Des., **236**, pp. 2084–2103.
[24] Kaya, T., and Goldak, J., 2006, "Numerical Analysis of Heat and Mass Transfer in the Capillary Structure of a Loop Heat Pipe," Int. J. Heat Mass Transfer, **49**, pp. 3211–3220.
[25] Imke, U., 2004, "Porous Media Simplified Simulation of Single- and Two-Phase Flow Heat Transfer in Micro-Channel Heat Exchangers," Chem. Eng. J., **101**, pp. 295–302.
[26] Chen, Z. Q., Cheng, P., and Zhao, T. S., 2000, "An Experimental Study of Two Phase Flow and Boiling Heat Transfer in Bi-Dispersed Porous Channels," Int. Commun. Heat Mass Transfer, **27**, pp. 293–302.
[27] Liao, Q., and Zhao, T. S., 2000, "A Visual Study of Phase-Change Heat Transfer in a Two-Dimensional Porous Structure With a Partial Heating Boundary," Int. J. Heat Mass Transfer, **43**, pp. 1089–1102.
[28] Qu, W., and Mudawar, I., 2003, "Flow Boiling Heat Transfer in Two-Phase Micro-Channel Heat Sinks—I. Experimental Investigation and Assessment of Correlation Methods," Int. J. Heat Mass Transfer, **46**, pp. 2755–2771.
[29] Kline, S. J., and McClintock, F. A., 1953, "Describing Uncertainties in Single-Sample Experiments," J. Mech. Eng., **75**, pp. 3–8.
[30] Kattan, N., Thome, J. R., and Favrat, D., 1998, "Flow Boiling in Horizontal Tubes: Part 1—Development of a Diabatic Two-Phase Flow Pattern Map," ASME J. Heat Transfer, **120**(1), pp. 140–147.
[31] Wojtan, L., Ursenbacher, T., and Thome, J. R., 2005, "Investigation of Flow Boiling in Horizontal Tubes: Part I—A New Diabatic Two-Phase Flow Pattern Map," Int. J. Heat Mass Transfer, **48**, pp. 2955–2969.
[32] Lu, W., Zhao, C. Y., Xu, Z. Y., and Tassou, S., 2007, "The R134a Vapour Flow Heat Transfer in Horizontal Metal-Foam Tubes," Tenth UK National Heat Transfer Conference, Edinburg, UK.

Futoshi Tanaka[1]
Graduate School of Energy Science,
Kyoto University;
and Mitsubishi Heavy Industries, LTD.,
16-5, Konan 2-Chome, Minato-ku,
Tokyo 108-8215, Japan
e-mail: f_tanaka@mhi.co.jp

Takashi Hibiki
School of Nuclear Engineering,
Purdue University,
Nuclear Engineering Building,
Room 132C, 400 Central Drive,
West Lafayette, IN 47907-2017
e-mail: hibiki@ecn.purdue.edu

Kaichiro Mishima
Research Reactor Institute,
Kyoto University,
Kumatori, Sennan,
Osaka 590-0494, Japan;
and Institute of Nuclear Safety System,
Incorporated,
64 Sata, Mihama-cho, Mikata-gun,
Fukui 919-1205 Japan
e-mail: mishima@rri.kyoto-u.ac.jp;
mishima.kaichiro@inss.co.jp

Correlation for Flow Boiling Critical Heat Flux in Thin Rectangular Channels

The effect of heated length on critical heat flux (CHF) in thin rectangular channels under atmospheric pressure has been studied. CHF in small channels has been widely studied in the last decades but most of the studies are based on flow in round tubes and number of studies focused on rectangular channels is relatively small. Although basic triggering mechanisms, which lead to CHF in thin rectangular channels, are similar to that of tubes, applicability of thermal hydraulic correlations developed for tubes to rectangular channels are questionable since heat transfer in rectangular channels are affected by the existence of nonheated walls and the noncircular geometry of channel circumference. Several studies of CHF in thin rectangular channels have been reported in relation to thermal hydraulic design of research reactors and neutron source targets and correlations have been proposed, but the studies mostly focus on geometrical conditions of the application of interest and therefore effect of channel parameters exceeding their interest is not fully understood. In his study, CHF data for thin rectangular channels have been collected from previous studies and the effect of heated length on CHF was examined. Existing correlations were verified with data with positive quality outlet flow but none of the correlations successfully reproduced the data for a wide range of heated lengths. A new CHF correlation for quality region applicable to a wide range of heated lengths has been developed based on the collected data. [DOI: 10.1115/1.3216037]

Keywords: critical heat flux, heated length, correlation, flooding, rectangular channel

1 Introduction

It is known that the critical heat flux (CHF) in forced convective flow in channels is related with the heated length of the channel. Based on results from forced convection heat transfer studies, previous investigators have most frequently used the ratio of heated length to the inside equivalent diameter of the channel L/D_e as the characteristic dimensionless length to correlate the impact of heated length. Generally, CHF increases as L/D_e decreases and this tendency becomes more significant at small L/D_e conditions [1]. On the other hand, regarding channels with large L/D_e, experiments show the presence of a threshold beyond which the CHF is practically independent of L/D_e [2]. Although many researchers have reported values of L/D_e beyond which it does not show significant effect, it is not clear what this limiting value is, or whether L/D_e is the appropriate parameter to characterize the effect of heated length. Furthermore, it is clear that, since the L/D_e is related directly to the flow development along the heated area, the impact of L/D_e is not a constant, but is also related to flow parameters and fluid properties.

CHF has been widely studied in the last decades both analytically and experimentally but most of the studies are related to flow in round tubes. Although basic triggering mechanisms of CHF in thin rectangular channels may be similar to those in tubes, applicability of correlations developed for tubes to other geometry is questionable due to the existence of nonheated walls and the noncircular geometry of the channel circumference in rectangular channels. Several studies focusing on CHF in thin rectangular channels have been performed in relation to research reactors and neutron source targets [3–13], but these studies mainly focus only on the geometry of the application and therefore geometrical effects covering a wide range of heated lengths has not been fully revealed. Recently, CHF in minichannels have been widely studied in relation to design of compact heat sinks for electrical devices such as computer processors and CHF correlations for small channels have been developed [14–17]. Studies on heat transfer in minichannels mostly focus on conditions with relatively short heated lengths simulating their application.

Katto [18] studied general features of forced convection flow CHF in rectangular channels and recognized that it can be classified into four regimes as in the same way as for round tubes. The four regimes vary with mass velocities and are different in ways flow and geometrical parameters affect the CHF. CHF for various L/D_e can be predicted by one of the four correlations applicable to each flow regime. However, Katto reported that CHF in very small L/D_e channels shows unique tendency and deviates from the proposed correlations. Sudo [7] studied the effect of channel length on CHF under high subcooling and high velocities and found out that CHF increases with decreasing L/D_e especially where L/D_e is smaller than 20. They reported that the high CHF values in small L/D_e channels are results of high heat transfer coefficient of forced convection flow due to short heated lengths. Sudo et al. [8] also performed analytical studies of CHF in positive quality regions. Based on the results of the semi-analytical CHF model developed, they reported that in this region, the effect of heated length and channel gap size is significant and longer heated lengths and smaller gap sizes result in low CHF values. In vertical upflow channels, CHF is limited by flooding at the channel outlet as the inlet mass flux condition approaches to zero. Mishima and Nishihara [4] studied CHF in thin rectangular channels and reported that at near zero mass flux conditions, CHF can be predicted by the following equation based on the flooding correlation of Wallis [19] and the heat and mass balance in the channel

[1]Corresponding author.

Contributed by the Heat Transfer Division of ASME for publication in the JOURNAL OF HEAT TRANSFER. Manuscript received September 11, 2007; final manuscript received December 22, 2008; published online October 15, 2009. Review conducted by Peter Vadasz.

Table 1 CHF data sets of thin rectangular channels investigated in this study

Database	s (mm)	w (mm)	w_H (mm)	L/D_e	P (MPa)	G (kg/m^2 s)	$\Delta T_{in,sub}$ (K)	$x_{eq,out}$
Mishima et al. [5]	1.0	4.0	3.0	179	0.1	0–200	40–80	0.17–1.0
Mishima and Nishihara [4]	2.4	4.0	3.0	77	0.1	0–100	15–75	0.17–1.0
Tanaka et al. [11]	1.0	4.0	3.0	50	0.1	0–2500	40–80	–0.04–1.0
Tanaka et al. [11]	1.5	4.0	3.0	34	0.1	25–4000	40–80	–0.06–0.21
Sudo et al. [9]	2.8	5.0	4.0	174	0.1	0–110	30–60	0.35–1.0
Sudo et al. [9]	2.25	5.0	4.0	71	0.1	0–470	25–80	0.08–1.0

All CHF data were obtained in two-side heated rectangular channels with upward flowing water.

$$q = \frac{C^2 h_{fg} A \sqrt{\rho_g \Delta\rho D g}}{A_H [1 + (\rho_g/\rho_l)^{1/4}]^2} \quad (1)$$

where C is a coefficient determined by the geometry of the channel top entry. Qualitatively speaking, flooding CHF decreases with increasing L/D_e and therefore, CHF is low for large L/D_e channels when compared under very low mass flux conditions. On the other hand, in channel with very small L/D_e, flooding CHF increases with decreasing L/D_e and approaches pool boiling CHF. In forced convection flow, Mishima and Nishihara [4] reported that CHF is caused by dryout of the liquid film just after the flow regime transits from churn to annular flow.

The purpose of this study is to propose a CHF correlation for thin rectangular channels applicable to a wide range of heated lengths. The study evaluates the applicability of existing correlations to predict CHF in thin rectangular channels using water as a working fluid. A CHF correlation for thin rectangular channels using water that is applicable to a wide range of heated length is developed.

2 Investigation of CHF Data and Correlations in Quality Region

2.1 Effect of Channel Length on CHF. CHF in thin rectangular channels of various L/D_e values have been collected from previous studies and compared to investigate the effect of heated length. CHF is known to be affected by parameters such as flow orientation, heated circumference, and pressure. To focus on the channel length effect in thin rectangular channels, experimental data obtained in two-sided heated rectangular channels with vertical upward flowing water under atmospheric pressure were selected. Available data sets meeting the condition are listed in Table 1. All of the data are obtained in single channel flow test section with directly heated walls constructed by SUS304 or Inconel alloy plates. Data of Tanaka et al. [11] were obtained by increasing the heat flux stepwise at 3% each step, until a sudden temperature rise of the heated wall was detected. Error associated with heater input was ±2%, and therefore the uncertainties of measured CHFs are ±3.5%. Error associated with inlet mass flow rate was ±3%. Uncertainties of other data sources are not provided in the literature and therefore are unknown.

Figure 1 shows variation in CHF with mass flux in thin rectangular channels. In this figure, data obtained in different channel geometries are plotted with different symbols to see the variation in data along with L/D_e. In the low mass flux region ($G < 200$ kg/m^2 s), the data vary significantly with L/D_e of the channel and channels with L/D_e larger than 170 shows lower CHF compared with channels with L/D_e below 100. Lower CHF values for large L/D_e channels under very low mass flux condition can be explained by the effect of L/D_e on flooding conditions which trigger CHF. Under fixed inlet flow and heat flux condition, superficial vapor velocity at the channel outlet caused by boiling in the channel increases with increasing L/D_e. For this reason, channels with large L/D_e will reach flooding condition at a low heat flux compared with channels with small L/D_e, and result in lower CHF value. It should also be noted that in the low mass flux region, CHF is affected by L/D_e rather than the heated length solely.

Comparison of mass flux with exit quality of CHF in various channel geometries is shown in Fig. 2. Generally, exit quality of CHF decreases with increasing mass flux. When inlet mass flux is fixed, channels with large L/D_e show high exit quality of CHF. Furthermore, in channels with similar L/D_e values, CHF tends to occur at higher exit quality conditions for channels with longer heated lengths when the inlet mass flux is the same.

The superficial liquid and vapor velocities at the channel outlet at CHF condition are compared on a flow regime map in Fig. 3.

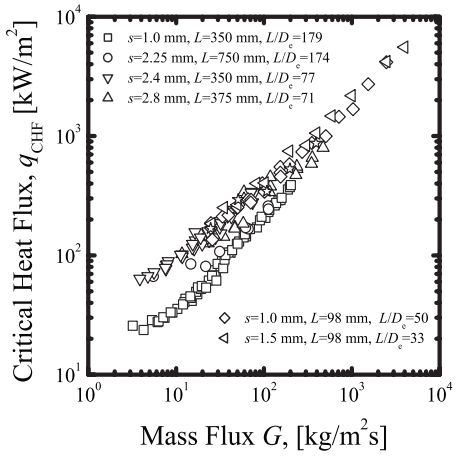

Fig. 1 Variation in CHF with mass flux in thin rectangular channels

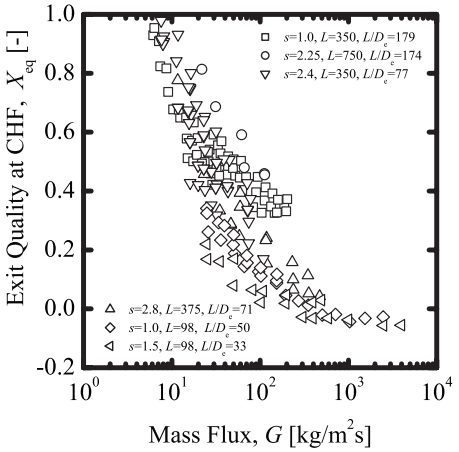

Fig. 2 Variation in exit quality of CHF with mass flux in thin rectangular channels

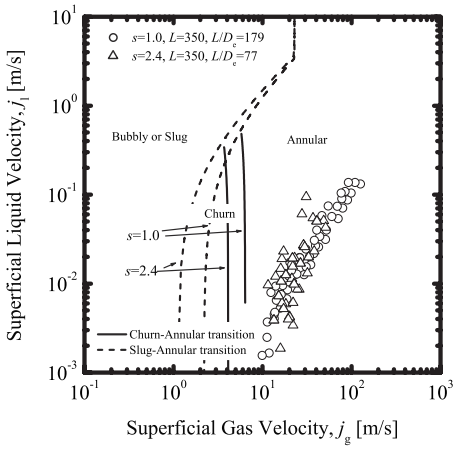

Fig. 3 Comparison of CHF conditions with the flow regime map

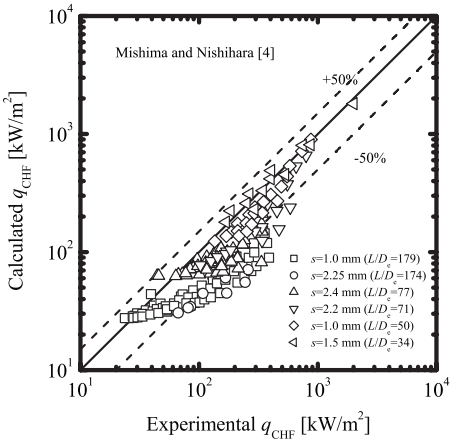

Fig. 5 Comparison of saturated CHF data with the correlation of Mishima and Nishihara [4]

Superficial liquid and vapor velocities were calculated for each data and were plotted on the flow regime map of narrow rectangular channels developed by Hibiki and Mishima [20]. Even though the flow regime map of Hibiki and Mishima [20] is based on adiabatic flow, the flow transition criteria will give us an idea of the flow pattern at CHF. Superficial velocities for the data were calculated based on thermally equivalent quality, so data plotted on Fig. 3 are limited to CHF with positive outlet quality conditions. For all data, flow pattern at CHF is annular flow. Similar tendency was observed for other positive quality CHF data collected.

2.2 Evaluation of Existing Correlations. Existing CHF correlations were compared with data in order to investigate the accuracy of reproducing the effect of L/D_e. Four correlations for thin rectangular channels developed by Katto [18], Mishima and Nishihara [4], Sudo [8], and Wright et al. [13], and four correlations for minichannels developed by Zhang et al. [14], Kuan and Kandlikar [15], Qu and Mudawar [16], and Wojtan et al. [17] were compared with the data. Within the eight correlations, the correlation of Katto [18], Mishima and Nishihara [4], Sudo [8], Zhang et al. [14], and Qu and Mudawar [16] reproduced the data fairly good while others showed relatively large deviation from the data. Comparisons of the data with the predicted values of these five correlations are shown in Figs. 4–8, respectively.

Figure 4 shows comparison of the data with the correlation of Katto [18]. This correlation consists of four correlations, each corresponding to a regime where different burnout mechanisms take place. The general form of the correlation was originally proposed for round and annular channels, assuming that CHF can be correlated by four nondimensional numbers Bo, We_L, ρ_v/ρ_l, and L/D_e. CHF data obtained in rectangular channels were analyzed and a generalized correlation was proposed by introducing

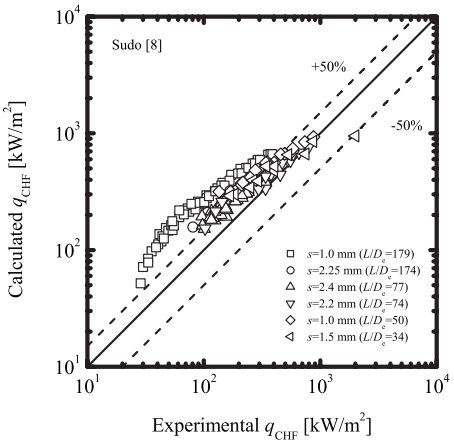

Fig. 6 Comparison of saturated CHF data with the correlation of Sudo [8]

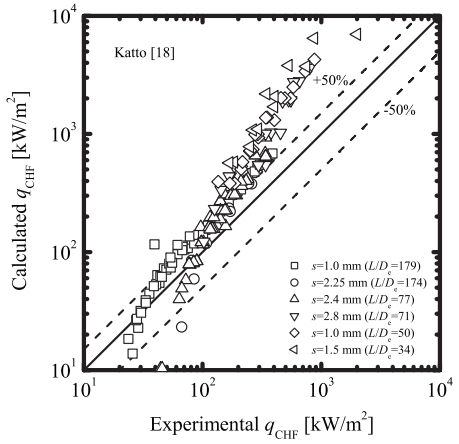

Fig. 4 Comparison of saturated CHF data with the correlation of Katto [18]

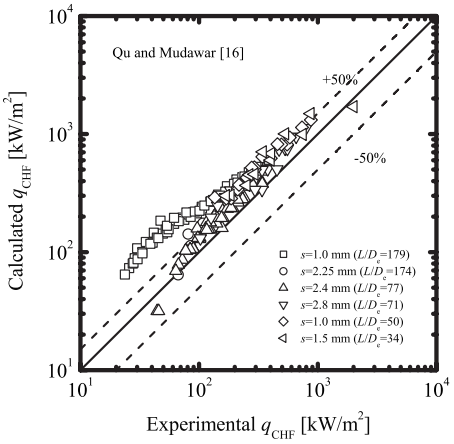

Fig. 7 Comparison of saturated CHF data with the correlation of Qu and Mudawar [16]

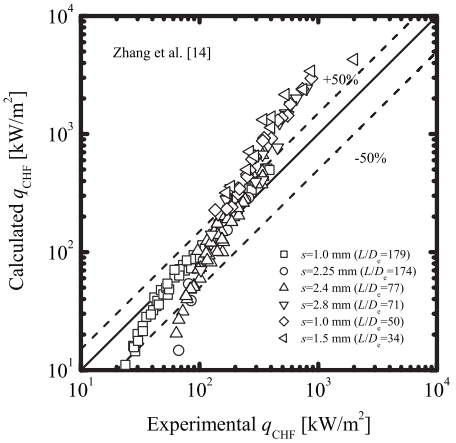

Fig. 8 Comparison of saturated CHF data with the correlation of Zhang et al. [14]

Table 2 Assessment of saturated CHF correlations

Database			Mean deviation (%)				
Reference	Gap (mm)	L/D_e	Katto (1981)	Mishima (1987)	Sudo (1986)	Qu (2004)	Zhang (2006)
Mishima et al. [5]	1.0	179	54.1	45.5	167.0	148.8	18.3
Mishima and Nishihara [4]	2.4	77	54.8	37.5	51.2	31.0	23.6
Tanaka et al. [11]	1.0	50	236.1	23.5	58.8	69.5	121.3
Tanaka et al. [11]	1.5	34	369.1	11.4	37.0	62.5	184.7
Sudo et al. [9]	2.8	174	31.0	66.0	80.4	48.1	21.3
Sudo et al. [9]	2.25	71	191.3	40.0	31.6	54.4	103.3
Average among database			156.1	37.3	71.0	67.5	78.7

the heated equivalent diameter for rectangular channels. As it can be seen in Fig. 4, the correlation of Katto tends to over estimate the CHF, especially for high heat flux values.

Figure 5 shows comparison of the data with the correlation of Mishima and Nishihara [4]. This correlation is based on the observation of flow pattern transition near burnout. In the churn flow regime, dry patches on the heated surface are quenched by the passage of liquid bridges. But when the flow pattern transits to annular flow, dry patches are no longer quenched due to the absence of liquid bridges. Figure 5 shows that for channels with relatively large L/D_e, the correlation of Mishima and Nishihara [4] tends to underestimate the CHF with increasing CHF values. However, fairly good correlation can be seen with the data in a wide range of heat flux for channels with small L/D_e.

Figure 6 shows comparison of the data with the correlation of Sudo [8]. The correlation of Sudo overestimates the data for most of the region. The correlation of Sudo is based on an analytical model, assuming that the burnout is triggered by the dryout of the liquid sublayer underneath the vapor blanket. Sudo considered that, in relatively low mass flux and saturated two phase flow, the flow is annular flow with vapor blankets formed in the liquid layer.

Figure 7 shows comparison of the data with the correlation of Zhang et al. [14]. The calculated CHF values in the figure are results when the hydraulic equivalent diameter is chosen as the characteristic diameter. Zhang's correlation underestimates the CHF for low CHF values, but this may be due to the fact that the calculated CHF converges to zero at very low mass flux condition while the actual CHF approaches to flooding CHF value. The correlation of Zhang overestimates the CHF for small L/D_e channels.

Figure 8 shows comparison of the correlation of Qu and Mudawar [16] with the data. This correlation is based on data obtained in parallel rectangular channels, which results in relatively large flow instabilities compared with flow in singular channels. The correlation tends to overpredict the CHF for thin rectangular channels.

Evaluation results of the five correlations are tabulated in Table 2. Mean deviations of the correlation from the data are listed for each database. Among the five correlations, the correlation of Mishima and Nishihara [4] reproduced the CHF with the least mean deviation. The average mean deviation with the data sets was 37.3% and the maximum mean deviation was 66.0%, which was the case for data obtained in the $L/D_e=174$ channel. The correlation of Mishima and Nishihara reproduces the CHF for channels with small L/D_e fairly well (within the mean deviation of 25% for $L/D_e<50$), whereas the mean deviation tends to increase with L/D_e. The correlation of Qu and Mudawar [16] has an average mean deviation of 67.5%, which is the second smallest of the correlations compared in this study. The correlation of Qu and Mudawar showed large deviation from the data of Mishima et al. [5]. The correlation of Sudo [8] has an average mean deviation of 71.0%. The correlation of Sudo tends to deviate largely from the data in channels with L/D_e over 100, especially from the data of $L/D_e=179$. The correlation of Zhang et al. [14] gives an average mean deviation of 78.7% when the hydraulic equivalent diameter is chosen as the characteristic diameter. Additionally, the average mean deviation was 114.9% when the heated equivalent diameter is chosen as the characteristic diameter. The use of hydraulic equivalent diameter therefore seems better when applying the correlation of Zhang to rectangular channels. However, the correlation of Zhang fails to predict CHF in channels with L/D_e below 50 while it reproduces the data quite well for channels with relatively large L/D_e. Finally, the correlation of Katto [18] gives an average mean deviation of 156.1%. The correlation of Katto tends to deviates from the data in channels with L/D_e below 50.

Regarding other CHF correlations, the correlations of Wright et al. [13] and Wojtan et al. [17] showed large deviation from the data. The correlation of Wright et al. [13] is based on the data obtained in aluminum heated surfaces and takes into account the Biot number. On the other hand, data compared in this study were obtained in the test sections with SUS304 or Inconel alloy heated surfaces and this may be the reason this correlation did not reproduce the data well. The correlation of Wojtan et al. [17] is based on the data obtained in minichannels using refrigerants R-134a and R-235fa, and the correlation seems not applicable to water. The equation used in the correlation of Kuan and Kandilkar [15] did not have solutions for some of the flow conditions of the data compared in this study. Their correlation may have limitations when applying to channels with a channel height of a few millimeters.

3 Development of New CHF Correlation

Eight correlations have been compared with saturated CHF data in thin rectangular channels with various databases but none of them seem to successfully predict the CHF over a wide range of L/D_e. A new correlation for saturated CHF in thin rectangular channels has been developed based on the existing data discussed above.

CHF is strongly affected by the inlet mass flux, and mass flux is a dominant parameter to correlate CHF. In channels where a water plenum is set at the channel top, CHF approaches the heat flux obtained by the flooding condition at the outlet, which is independent with inlet mass flux, at near zero mass flux conditions. The CHF correlation was therefore assumed to have the following form

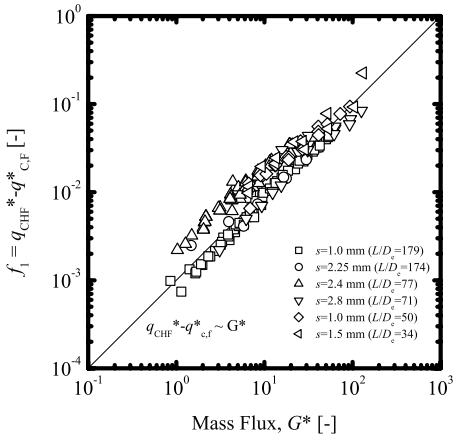

Fig. 9 Comparison of force convection related CHF term with the mass flux

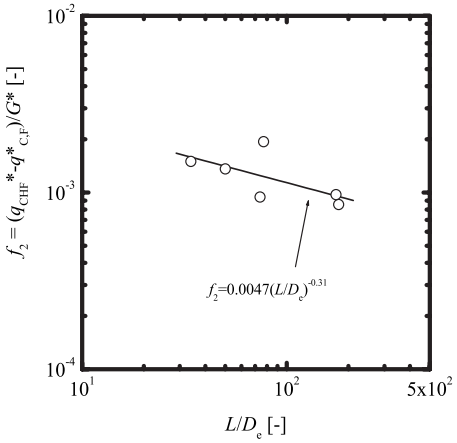

Fig. 10 Determination of L/D_e dependency in thin rectangular channels

$$q_{CHF}^* = q_{CHF,F}^* + f_1(G^*) \tag{2}$$

where q_{CHF}^* is the nondimensional CHF, $q_{CHF,F}^*$ is the nondimensional flooding heat flux, and f_1 is a function of the mass flux, which represents the contribution of forced convective flow on CHF. Nondimensional heat and mass fluxes used in this correlation are defined as

$$q^* = q/(h_{fg}\sqrt{\lambda\rho_g g\Delta\rho}) \tag{3}$$

$$G^* = G/\sqrt{\lambda\rho_g g\Delta\rho} \tag{4}$$

$$\lambda = \sqrt{\sigma/g\Delta\rho} \tag{5}$$

Flooding heat flux $q_{CHF,F}^*$ is unique for each test section and if this value is known, f_1 can be calculated as $q_{CHF}^* - q_{CHF,F}^*$ for each of the CHF data. Among the six data sets for thin rectangular channels, five data sets included the CHF at zero mass flux condition, which gives the experimental value of $q_{CHF,F}^*$. For one data set, experimental value of $q_{CHF,F}^*$ did not exist so the value was estimated by extrapolating the CHF data at low mass flux conditions. Figure 9 shows the relation of f_1 and G^*. For each data sets, the relation of f_1 and G^* is almost linear and the relationship holds for a wide range of G^*. This implies that the ratio of f_1 and G^* is approximately constant for each channel geometries, regardless of the flow conditions such as mass flux and inlet subcooling. f_1 was therefore assumed to be simply express as

$$f_1 = G^* f_2(L/D_e) \tag{6}$$

where f_2 is a function of L/D_e. To investigate the relation of f_2 and L/D_e, f_2 was calculated for all of the data and the average value for each channel geometries were compared with L/D_e. Figure 10 shows the relation of the mean value of f_2 with L/D_e. f_2 decreases with increasing L/D_e, and the two parameters can be correlated as follows:

$$f_2 = 0.0047(L/D_e)^{-0.31} \tag{7}$$

Summarizing Eqs. (2)–(7), the CHF correlation for thin rectangular channel was concluded to be described as

$$q_{CHF}^* = q_{CHF,F}^* + 0.0047G^*(L/D_e)^{-0.31} \tag{8}$$

The flooding CHF term $q_{CHF,F}^*$ in Eq. (8) can be calculated by Eq. (1) if the parameter C for thin rectangular channels is known. Figure 11 shows the values of C for each channel geometry of the database calculated by the flooding CHF value and Eq. (1). During the calculation of C, the channel width was chosen as the characteristic length of the flooding, because in thin rectangular channels, liquid mainly flows down the side walls as liquid film and the velocity profile along the wide walls impact the flooding condition. As it can be seen in Fig. 11, C is approximately 0.71 for thin rectangular channels. Applying this constant value, the flooding CHF term $q_{CHF,F}^*$ can be calculated by the equation below, which is derived from Eq. (1) and the definition of the nondimensional heat flux described in Eq. (3), as

$$q_{CHF,F}^* = \frac{(0.71)^2 A\sqrt{D/\lambda}}{A_H[1 + (\rho_g/\rho_l)^{1/4}]^2} \tag{9}$$

Here, the characteristic length D is represented by the channel width.

Now that the flooding CHF in thin rectangular channels can be calculated, saturated CHF in thin rectangular channels can be predicted as

$$q^* = \frac{(0.71)^2 A\sqrt{D/\lambda}}{A_H[1 + (\rho_g/\rho_l)^{1/4}]^2} + 0.0047G^*(L/D_e)^{-0.31} \tag{10}$$

where q^*, G^*, and λ are defined by Eqs. (3)–(5), respectively and D is represented by the channel width. The new correlation was evaluated by the CHF database tabulated in Table 1 and the results are summarized in Table 3. The average of the mean deviation of each data set is 18.7%. The new correlation predicts all the data with a mean deviation of 17.0%, and succeeds to reproduce CHF within ±32% deviation with 90% confidence. The maximum deviation is +80%, which was with the data obtained under relatively high mass flux condition. Figure 12 compares the CHF data and predicted values with the new correlation. The new correlation succeeds to predict the CHF within a fairly small error for

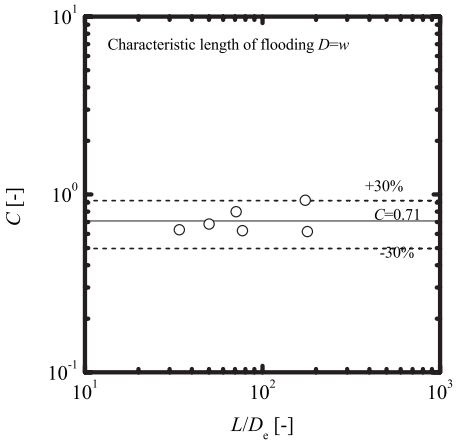

Fig. 11 Comparison of parameter C with L/D_e

Table 3 Assessment of the new developed CHF correlations

Database			
Reference	Gap (mm)	L/D_e	Mean deviation (%)
Mishima et al.	1.0	179	17.7
Mishima and Nishihara	2.4	77	13.0
Tanaka et al.	1.0	50	12.1
Tanaka et al.	1.5	34	24.8
Sudo et al.	2.8	174	14.5
Sudo et al.	2.25	71	30.2
Average among database			18.7

channels with various values of L/D_e. Generally, the new correlation tends to deviate from the data at relatively high inlet mass flux conditions, which is considered to be near the region where CHF mechanism transits from dryout to burnout type. When limited to mass flux conditions below 200 kg/m^2 s, the new correlation reproduces the CHF within ±50% error. Applicable range of the new correlation to predict CHF within ±50% error is tabulated in Table 4. Figure 13 shows a comparison of the CHF data obtained in channels with different heated lengths but the same cross sectional geometry. The figure indicates that CHF decreases with increasing L/D_e when the mass flux is fixed and the new correlation reproduces this tendency fairly well. In Fig. 14, calculation lines of the new correlation are plotted as a function of L/D_e. CHF decreases with increasing L/D_e and the new correlation reproduces the effect of L/D_e for either of the mass flux conditions compared in the figure.

The new developed correlation has been compared with data for working fluid other than water to seek its applicability to other fluids. The correlation was compared with the data of Wojtan et al. [17], which was obtained in single circular minichannels for R-134a and R-245fa. Figure 15 shows comparison of the predicted CHF with the data. The new correlation predicts the CHF fairly well within ±40% error, even though the correlation was based solely on data for water. However, CHF data for thin rectangular channels for fluids other than water are limited at this time and therefore applicability of the correlation to other fluids has uncertainty.

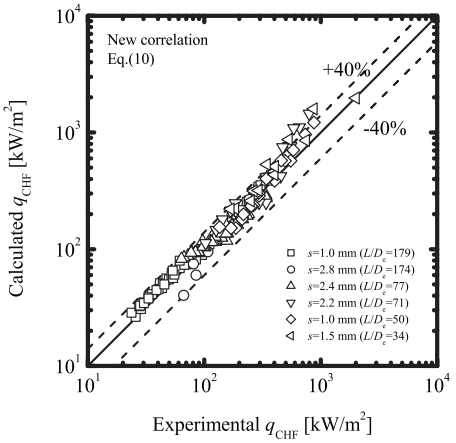

Fig. 12 Evaluation of the new developed correlation with saturated CHF data

Table 4 Applicable range of the new correlation

Parameter	Range
Channel gap, s (mm)	1–2.8
Channel length, L/D_e	34–179
Inlet subcool, ΔT_{sub} (K)	20–80
Exit quality, x_{eq}	0.05–1
Mass flux, G (kg/m^2 s)	0–200

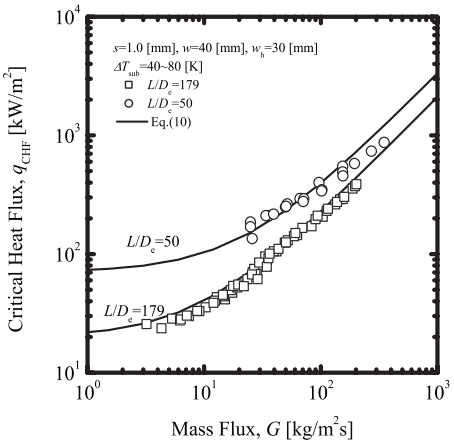

Fig. 13 Comparison of the new correlation with CHF data obtained in channels with different heated length

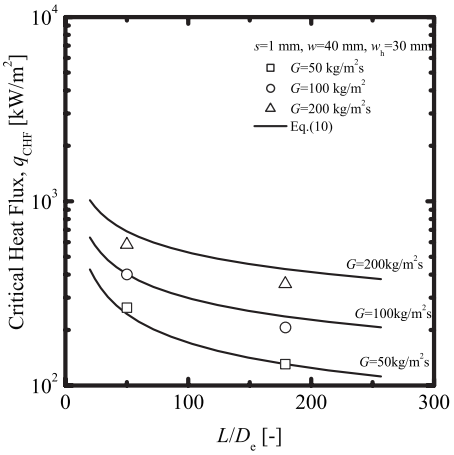

Fig. 14 Effect of heated length on CHF in different mass flux conditions

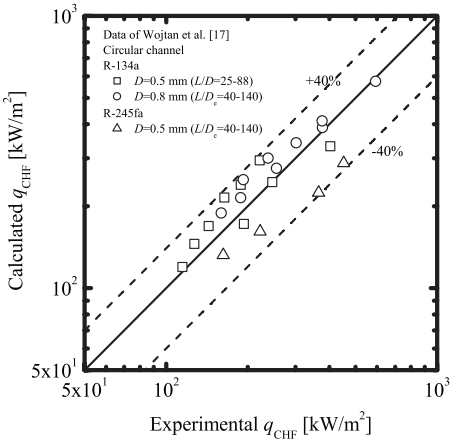

Fig. 15 Comparison of the new correlation with CHF data for working fluids other than water

4 Conclusions

CHF in thin rectangular channels has been studied based on existing data for water obtained under atmospheric pressure. Existing CHF correlations were examined to seek the applicability to thin rectangular channels but none seem to cover the CHF for a wide range of heated lengths. A new CHF correlation applicable in positive quality region that takes into account the heated length was developed. Detailed conclusions can be drawn as follows:

(1) Under low mass flux conditions, the CHF is highly affected by the L/D_e of the channel. Channels with larger L/D_e values tend to result in low CHF. Under fixed inlet flow and heat flux condition, superficial vapor velocity at the channel outlet increases with increasing L/D_e. It is considered that channels with large L/D_e will reach flooding condition or annular flow transition at a lower heat flux compared with channels with small L/D_e values, and result in lower CHF.
(2) CHF correlations for rectangular channels and minichannels were compared with the existing data for thin rectangular channels. The correlation of Mishima and Nishihara [4] reproduced the saturated CHF data within the smallest mean deviation. Some correlation show good agreement with data for particular channel geometries but none successfully predicted the CHF for a wide range of L/D_e.
(3) A new CHF correlation for thin rectangular channels applicable to a wide range of heated length has been developed. The correlation reproduced saturated CHF in low mass flux conditions within $\pm 50\%$ error and a mean deviation of 17%, which is less than half of the value of the existing correlations. Applicable range of the correlation is shown in Table 4.

Nomenclature

A = cross sectional area of channel
A_H = heated area
C = coefficient
Bo = Boiling number
D = characteristic length or diameter
D_e = hydraulic equivalent diameter of channel
ΔT_{sub} = subcooled temperature
f_1, f_2 = function
g = gravitation acceleration
G = mass flux
h_{fg} = latent heat of evaporation
L = length from channel inlet
P = pressure
q = heat flux
s = gap clearance
w = channel width
w_H = heated channel width
We = Weber number
x_{eq} = thermodynamic equilibrium quality

Greek Symbols

$\Delta\rho$ = differential density (ρ_l-ρ_g)
λ = critical wavelength
ρ = density

Subscripts

CHF = critical heat flux
F = flooding condition
g = saturated vapor
in = inlet of channel
l = saturated liquid
L = length from channel inlet
out = outlet of channel

References

[1] Nariai, H., Inasaka, F., and Shimura, T., 1987, "Critical Heat Flux of Subcooled Flow Boiling in Narrow Tube," ASME-JSME Thermal Engineering Conference, Honolulu, HI, Mar. 22–27.
[2] Boyd, R. D., 1985, "Subcooled Flow Boiling Critical Heat Flux (CHF) and Its Application to Fusion Energy Components. Part II: A Review of Micro-Convective, Experimental, and Correlational Aspects," Fusion Technol., **7**, pp. 31–52.
[3] Gambill, W. R., and Bundy, R. D., 1964, "Heat Transfer Studies of Water Flow in Thin Rectangular Channels," Nucl. Sci. Eng., **18**, pp. 69–79.
[4] Mishima, K., and Nishihara, H., 1987, "Effect of Channel Geometry on Critical Heat Flux for Low Pressure Water," Int. J. Heat Mass Transfer, **30**, pp. 1169–1182.
[5] Mishima, K., Hibiki, T., and Nishihara, H., 1996. "Experimental Study on Critical Heat Flux in Laterally Non-Uniformly Heated Rectangular Channels," Second European Thermal-Sciences (EUROTHERM) and 14th UIT National Heat Transfer Conference, May 29–31.
[6] Gambill, W. R., and Mochizuki, T., 1988, "Advanced Neutron Source Design: Burnout Heat Flux Correlation Development," ANS/ENS 1988 International Conference, pp. 298–300.
[7] Sudo, Y., 1997, "Effect of Channel Length on Critical Heat Flux Under Conditions of High Subcooling and High Velocity in Short Heated Channels," Trans. Jpn. Soc. Mech. Eng., **63**, pp. 1667–1673.
[8] Sudo, Y., 1996, "Study on Critical Heat Flux in Rectangular Channels Heated From One or Both Sides at Pressures Ranging From 0.1 to 14 MPa," ASME J. Heat Transfer, **118**, pp. 680–688.
[9] Sudo, Y., Miyata, K., Ikawa, H., Ogaswara, M., and Kaminaga, M., 1985, "Core Heat Transfer for JRR-3 to be Upgraded at 20 MWt: Part II," Japan Atomic Energy Research Institute Report No. JAERI-M 85-126.
[10] Oh, C. H., and Englert, S. B., 1993, "Critical Heat Flux for Low Boiling in Vertical Uniformly Heated Thin Rectangular Channels," Int. J. Heat Mass Transfer, **36**, pp. 325–335.
[11] Tanaka, F., Hibiki, T., Saito, Y., Takeda, T., and Mishima, K., 2001, "Thermal-Hydraulic Design Concept of Spallation Neutron Source," J. Nucl. Sci. Technol., **38**, pp. 832–843.
[12] Kureta, M., and Akimoto, H., 2002, "Critical Heat Flux Correlation for Subcooled Boiling Flow in Narrow Channels," Int. J. Heat Mass Transfer, **45**, pp. 4107–4115.
[13] Wright, C. T., O'Brien, J. E., and Spall, R. E., 2008, "A New Critical Heat Flux Correlation for Vertical Water Flow Through Multiple Thin Rectangular Channels," Int. J. Heat Mass Transfer, **51**, pp. 1071–1084.
[14] Zhang, W., Hibiki, T., Mishima, K., and Mi, Y., 2006, "Correlation of Critical Heat Flux for Flow Boiling of Water in Mini-Channels," Int. J. Heat Mass Transfer, **49**, pp. 1058–1072.
[15] Kuan, W. K., and Kandlikar, S. G., 2008, "Experimental Study and Model on Critical Heat Flux of Refrigerant-123 and Water in Microchannels," ASME J. Heat Transfer, **130**, pp. 034503.
[16] Qu, W., and Mudawar, I., 2004, "Measurement and Correlation of Critical Heat Flux in Two-Phase Micro-Channel Heat Sinks," Int. J. Heat Mass Transfer, **47**, pp. 2045–2059.
[17] Wojtan, L., Revellin, R., and Thome, J. R., 2006, "Investigation of Saturated Critical Heat Flux in a Single Uniformly Heated Microchannel," Exp. Therm. Fluid Sci., **30**, pp. 765–774.
[18] Katto, Y., 1981, "General Features of CHF of Forced Convection Boiling in Uniformly Heated Rectangular Channels," Int. J. Heat Mass Transfer, **24**, pp. 1413–1419.
[19] Wallis, G. B., 1969, *One-Dimensional Two-Phase Flow*, McGraw-Hill, New York.
[20] Hibiki, T., and Mishima, K., 2001, "Flow Regime Criteria for Upward Two-Phase Flow in Vertical Narrow Rectangular Channels," Nucl. Eng. Des., **203**, pp. 117–131.

Experimental and Numerical Study of Single Bubble Dynamics on a Hydrophobic Surface

Youngsuk Nam
Jinfeng Wu
Gopinath Warrier
Y. Sungtaek Ju

Department of Mechanical and Aerospace Engineering,
University of California,
Los Angeles, CA 90095

The growth and departure of single bubbles on two smooth surfaces with very different wettabilities are studied using high-speed video microscopy and numerical simulations. Isolated artificial cavities of approximately 10 μm diameter are microfabricated on both a bare and a Teflon-coated silicon substrate to serve as nucleation sites. The bubble departure diameter is observed to be almost 3 times larger and the growth period almost 60 times longer for the hydrophobic surface than for the hydrophilic surface. The waiting period is practically zero for the hydrophobic surface because a small residual bubble nucleus is left behind on the cavity from a previous ebullition cycle. The experimental results are consistent with our numerical simulation results. Bubble nucleation occurs on nominally smooth hydrophobic regions with root mean square roughness (R_q) less than 1 nm even at superheat as small as 3°C. Liquid subcooling significantly affects bubble growth on the hydrophobic surface due to increased bubble surface area. Fundamental understanding of bubble dynamics on heated hydrophobic surfaces will facilitate the development of chemically patterned surfaces with enhanced boiling heat transfer performance and novel phase-change based micro-actuators and energy harvesters.
[DOI: 10.1115/1.3216038]

Keywords: single bubble, hydrophobic surface, nucleate boiling, dynamics, wettability, phase change

1 Introduction

Fundamental understanding of bubble nucleation and growth on heated surfaces is essential to predict boiling heat transfer performance and design bubble-driven microfluidic devices. Past studies have identified surface wettability as one of the most important factors affecting bubble nucleation and growth dynamics. The recent studies of Dhir [1,2] provide a good summary of the current understanding.

The effect of surface wettability on bubble growth can be inferred from the previous empirical correlations. Fritz [3] derived the following semi-empirical relation between the bubble departure diameter and contact angle by balancing the buoyancy force with the surface tension force

$$D_d = 0.0208\varphi\sqrt{\frac{\sigma}{g(\rho_l - \rho_v)}} \tag{1}$$

Equation (1) illustrates that the bubble departure diameter increases with increasing contact angle. For the bubble release frequency, Zuber [4] suggested the following relation:

$$fD_d = 0.59\left[\frac{\sigma g(\rho_l - \rho_v)}{\rho_l^2}\right]^{1/4} \tag{2}$$

By combining Eq. (2) with Eq. (1), the bubble release frequency can also be related with surface wettability. However, it should be noted that the above correlations were obtained from a rather limited set of data and their validity, especially for hydrophobic surfaces, has not yet been fully established.

Abarajith and Dhir [5] conducted numerical simulations to investigate the effect of contact angle on single bubble growth dynamics. Their study showed that as the contact angle increased from 0 deg to 90 deg, the bubble departure diameter and growth period increased substantially. Nonetheless, the accuracy of numerical simulations remains limited due to challenges associated with modeling dynamic contact angles and microlayers.

Experiments of single bubble dynamics have been conducted over a limited range of contact angles because most studies have used a polished silicon or copper substrate as the heating surface. Qiu and co-workers [6,7] conducted single bubble experiments on a silicon wafer with a 55 deg static contact angle, and measured the bubble departure diameter and bubble growth period while changing the superheat and subcooling from 6°C to 9°C and 0°C to 3°C under both earth and low gravity levels. They also reported changes in dynamic contact angles during the ebullition cycle.

Takata et al. [8] reported a study of boiling on superhydrophobic surfaces made of fine particles of nickel and polytetrafluoroethylene (PTFE). However, they only made a rather qualitative observation that the film boiling occurs even at very small superheat because generated bubbles merge into a vapor film without departing from the surface.

In the present study, we report a detailed study of single bubble nucleation, growth, and departure dynamics on a hydrophobic surface.

2 Experimental Setup

Figure 1 shows the schematic of our experimental setup, which is similar to the one used by Qiu and co-workers [6,7]. The setup consists of a polycarbonate test chamber (d_c=200 mm and h_c=93 mm), a quartz window (d_w=50.8 mm), and a G-10 base. De-ionized, filtered, and degassed water is used as the test liquid. Two cartridge heaters are immersed in the liquid to control the subcooling level, and two K-type thermocouple probes are used to monitor the liquid temperature. The test chamber is thermally insulated by a melamine foam sheet. Bubble images are captured using a high-speed camera (1220 5PS) equipped with a zoom lens (105 mm f/2.8D AF Micro Nikkor).

A bare silicon wafer and a Teflon-coated silicon wafer are used as the heating surfaces. At the center of each wafer, a microcavity

Manuscript received September 28, 2007; final manuscript received March 28, 2008; published online October 15, 2009.

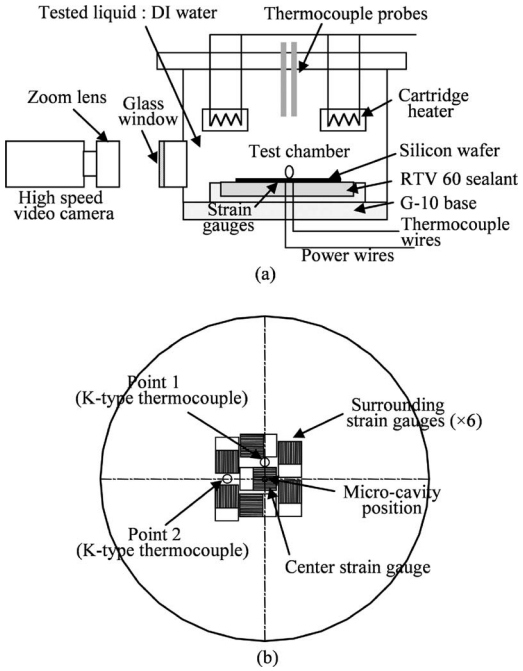

Fig. 1 Schematic diagram of the experimental setup: (*a*) the whole setup and (*b*) the silicon wafer instrumented with strain gauge heaters and thermocouple wires

is fabricated using the deep reactive ion etching (DRIE) technique. The diameter of the cavity is about 15 μm for the bare silicon wafer and 7 μm for the Teflon-coated wafer. Both cavities have a depth of approximately 20 μm. As in Fig. 1(*b*), a set of planar strain gauge heaters (7×7 mm^2 and 120 Ω) and K-type thermocouple wires are attached to the back side of the wafers to control and measure the wafer temperature. The wafer and wires are mounted on a G-10 base using RTV 60 sealant.

3 Hydrophobic Coating With Teflon Solution

A thin, smooth hydrophobic layer required for the single bubble experiment is generated using a Teflon amorphous fluoropolymer (AF) solution, which is made by dissolving 2% (by weight) Teflon amorphous fluoropolymer resin (Du Pont Polymers) into FC40 solvent (3M Fluorinert Electronic Liquid). This solution is spin-coated on a silicon substrate at 2000 rpm for 30 s. Subsequently, the substrate is baked at 180°C for 10 min to dry the solvent, and then annealed at 340°C for 2 h to improve the surface uniformity and the adhesion characteristic. The thickness of the Teflon layer is measured to be about 200 nm, and the static contact angle with water is about 120 deg at room temperature. To measure the static contact angle, a droplet (~5 μL) of de-ionized and filtered water is placed on the surface and the contact angle is measured using a goniometer (First Ten Angstroms 4000A). One of the captured droplet images is shown in Fig. 2(*a*). The surface topography and roughness of the Teflon-coated surface is measured using an atomic force microscope and the results are given in Fig. 2. The root mean square roughness of profile (R_q) is measured to be 0.418 nm, and the peak-to-peak height (R_y) is 2.086 nm.

4 Estimation of the Wall Superheat

To measure the superheat, thermocouples are attached to the silicon wafers. However, measuring the accurate superheat at a microcavity is quite challenging because of the small size of the cavity. In case of the bare silicon wafer, one central and six sur-

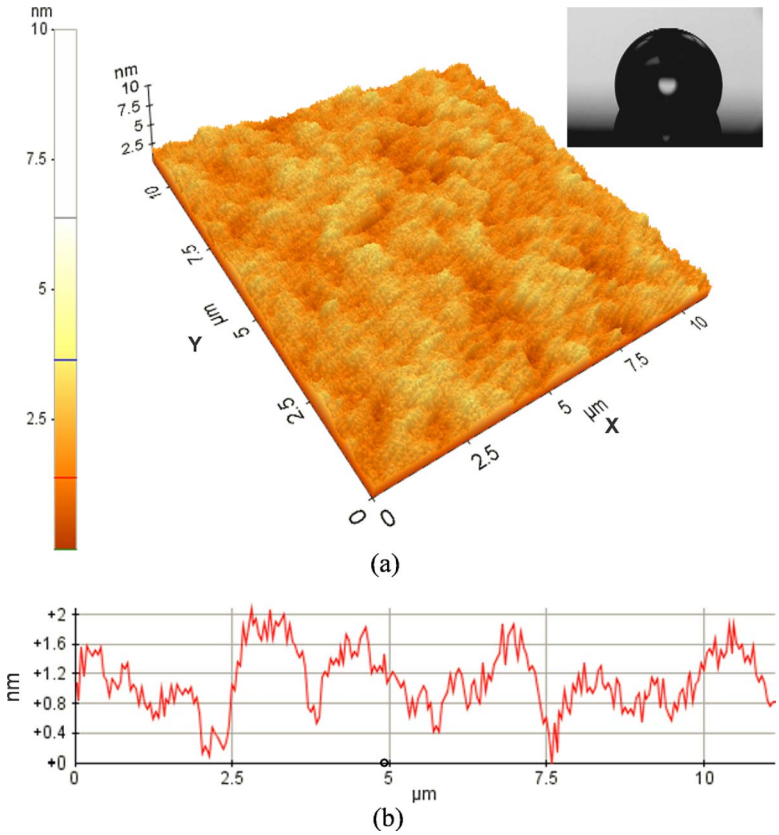

Fig. 2 Surface topography of Teflon-coated wafer: (*a*) 3D surface topography and the water droplet placed on this surface and (*b*) the line profile at *Y*=5.5 μm

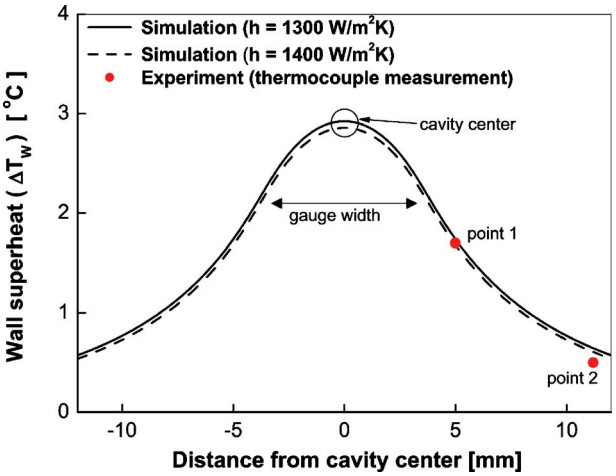

Fig. 3 Temperature distributions on the silicon wafer surface

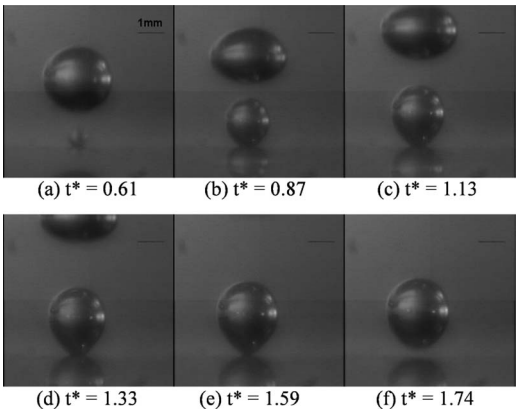

Fig. 4 Selected images of the single bubble during one ebullition cycle (heating surface: bare silicon wafer, ΔT_w=4.0°C, ΔT_{sub}=1.5°C, p=1 atm, $t^*=t/t_0$, and $t_0=1.6\times10^{-2}$ s)

rounding heating elements are used simultaneously to obtain a uniform temperature distribution around the center cavity (see Fig. 1(*b*)). However, on the Teflon-coated wafer, this heater arrangement tends to generate unexpected bubbles on the nominally smooth surrounding surface with no artificial cavity. To minimize any undesired bubble nucleation, only the center heating element is activated. The resulting superheat at the cavity is estimated using finite element simulations.

The calculated 3D model consists of a 7×7 mm^2 constantan heating element (the center element), a 100 mm-diameter silicon wafer, and a 15 mm-thick RTV 60 silicone layer. The convective heat transfer coefficient (h) of the top surface of the wafer is estimated between 1300–1400 W/m^2 K based on the previous experimental data [9]. The adiabatic condition is applied at the boundaries of the RTV silicone layer. Figure 3 shows predicted temperature distributions, which agree well with the measured values at points 1 and 2.

The bubble nucleation on nanoscopically smooth surfaces is very interesting but still not a well understood topic. A previous study also reported bubble nucleation on "smooth" surfaces at modest superheats, raising questions about the validity of existing nucleation models. Theofanous et al. [10] reported that bubble nucleation occurs at around 12–17°C of superheat on nanoscale fresh titanium thin films. The authors later argued (Dinh et al. [11]) that the presence of nanoscale inhomogeneities rather than microscopic cavities is responsible for such "premature" nucleation. In a recent unpublished study, we microfabricated isolated hydrophobic patches of 15–100 μm in width and 200 nm in thickness on a silicon surface. On these hydrophobic patterns, we observed reproducible and stable bubble nucleation at 6–9°C of superheat. This provides more direct experimental evidence that smooth hydrophobic surfaces can serve as effective bubble nucleation sites.

5 Results and Discussion

5.1 Bubble Departure Diameter and Growth Period. Figures 4 and 5 display selected frames of the bubble growth images during one ebullition cycle, and Figs. 6 and 7 show the bubble growth history on the bare silicon wafer and the Teflon-coated wafer. In Fig. 7, the base diameter and height are separately presented instead of the bubble equilibrium diameter because the bubble shape is far from spherical. To compare the two cases, characteristic length (l_0), velocity (u_0), and time (t_0) are introduced as follows [12]:

$$l_0=\sqrt{\frac{\sigma}{g(\rho_l-\rho_v)}},\quad u_0=\sqrt{g\cdot l_0},\quad t_0=\frac{l_0}{u_0} \tag{3}$$

As seen from Figs. 4–7, a single bubble generated on the Teflon-coated wafer has about 3 times larger bubble departure diameter and 60 times longer bubble growth period than one on the bare silicon wafer. This can be explained by balancing forces acting on a bubble. When a bubble grows, the buoyancy force acts as the main upward force while the surface tension force counteracts it. Additionally, when the surrounding liquid is stationary, the viscous drag also opposes the buoyancy force.

On the surfaces with high contact angles, the large bubble base area leads to increased downward surface tension force. Consequently a large volume is required for a bubble to depart from the surface, and the bubble has a large departure diameter and a long growth period. The horizontal component of the surface tension force is also worthy of notice. For a contact angle greater than 90 deg, the force changes its direction and opposes the shrinking of the bubble base. Therefore, the bubble can maintain its large base

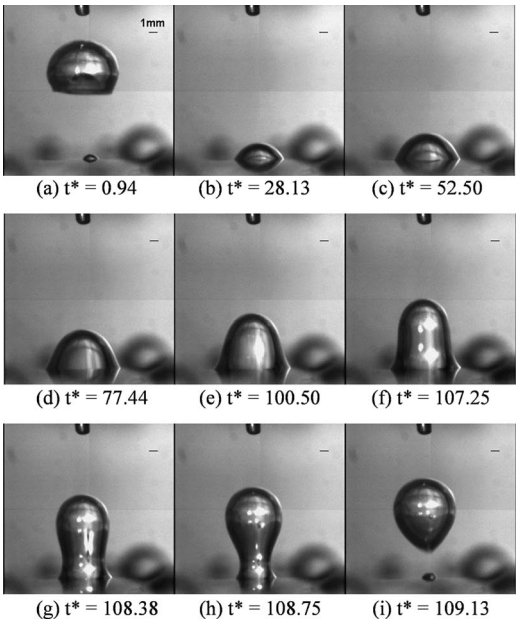

Fig. 5 Selected images of the single bubble during one ebullition cycle (heating surface: Teflon-coated silicon wafer, ΔT_w =2.9°C, ΔT_{sub}=0°C, p=1 atm, $t^*=t/t_0$, and $t_0=1.6\times10^{-2}$ s)

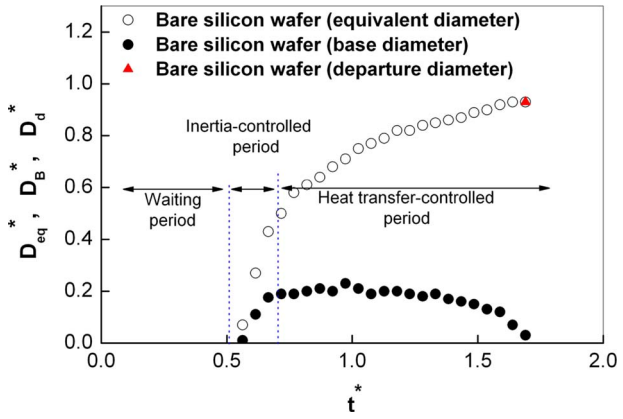

Fig. 6 Bubble growth history during one ebullition cycle (heating surface: bare silicon wafer, $\Delta T_w=4.0°C$, $\Delta T_{sub}=1.5°C$, $p=1$ atm, $t^*=t/t_0$, $t_0=1.6\times10^{-2}$ s, $D_{eq}^*=D_{eq}/l_0$, $D_B^*=D_B/l_0$, $D_d^*=D_d/l_0$, and $l_0=2.5\times10^{-3}$ m)

diameter for a long time and have an extremely long growth period.

Table 1 shows the measured dynamic contact angles on our bare and Teflon-coated silicon wafers. In both cases, the dynamic contact angles measured during the base shrinking period are larger than the ones observed during the base expansion period. A previous study [7] on single bubble dynamics reported higher contact angles for bare silicon wafers than is obtained for the present wafer due presumably to differences in surface preparation methods. This may explain why the previous study observed larger bubble departure diameters and longer growth periods than the present study.

The bubble departure diameter and growth period are calculated using Eqs. (1) and (2) with the measured ranges of dynamic contact angles as input parameters. As shown in Table 2, the predicted values compare favorably with the data for the bare silicon surface. Our data, however, do suggest that the validity of the existing correlation for the bubble growth period is severely limited for hydrophobic surfaces.

5.2 Bubble Growth Dynamics. On substrates with moderate contact angles, the bubble growth period can divided into three stages: the waiting period, the inertia-controlled period, and the heat transfer-controlled period [13–17]. Figure 6 shows that the bubble growth on a bare silicon wafer can be well explained by these three stages. However, Fig. 7 reveals that the bubble growth

Table 1 Changes in dynamic contact angles during bubble ebullition cycle

Tested wafer	Receding contact angle (during base expansion) (deg)	Advancing contact angle (during base shrinking) (deg)
Bare silicon wafer	33–43	39–46
Teflon-coated silicon wafer	118–125	126–134
Bare silicon wafer [7]	45–51	55–61

mechanism on a hydrophobic surface cannot be clearly characterized using the same stages. For example, the bubble departs from the surface after a short necking period and leaves behind a small nucleus on the surface, which then continues to grow into a new bubble. As a result, no waiting period is observed. Also, rapid bubble expansion out of the cavity, which typically occurs during the inertia-controlled period for hydrophilic surfaces, is not observed on the Teflon surface.

To clarify the relative effect of the viscous force versus the surface tension force, the capillary numbers ($Ca=\mu v_h/\sigma$) are calculated in Fig. 8. Here, μ is the viscosity coefficient of water and v_h is the growth rate of the bubble height. Figure 8 illustrates the increased effect of the surface tension force as well as the distinct bubble growth patterns on a hydrophobic surface. On the bare silicon wafer, the capillary number is gradually decreased from the inertia-controlled period to the heat transfer-controlled period.

Table 2 Normalized bubble departure diameters and bubble growth periods: experimental results and calculated values by Eqs. (1) and (2)

	Silicon wafer		Teflon-coated wafer	
	Present exp.	Eqs. (1) and (2) [3 and 4]	Present exp.	Eqs. (1) and (2) [3 and 4]
Departure diameter (D_d^*)	0.93	0.78–0.93	2.67	2.53–2.70
Growth period (t^*)	1.69	1.33–1.56	109.13	4.28–4.56

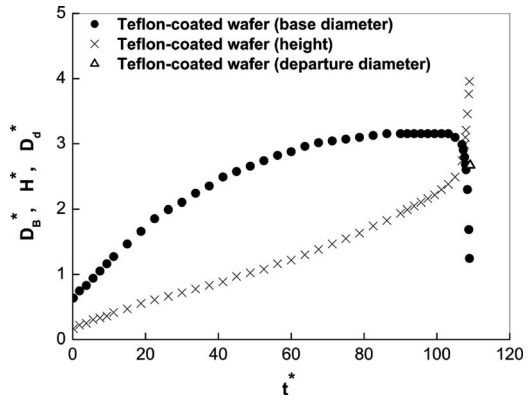

Fig. 7 Bubble growth history during one ebullition cycle (heating surface: Teflon-coated silicon wafer, $\Delta T_w=2.9°C$, $\Delta T_{sub}=0°C$, $p=1$ atm, $t^*=t/t_0$, $t_0=1.6\times10^{-2}$ s, $D_B^*=D_B/l_0$, $H^*=H/l_0$, $D_d^*=D_d/l_0$, and $l_0=2.5\times10^{-3}$ m)

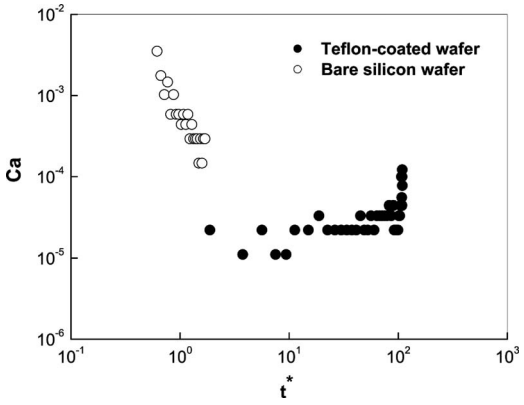

Fig. 8 Temporal change in capillary number during one ebullition cycle ($t^*=t/t_0$, $t_0=1.6\times10^{-2}$ s, and logarithmic scale)

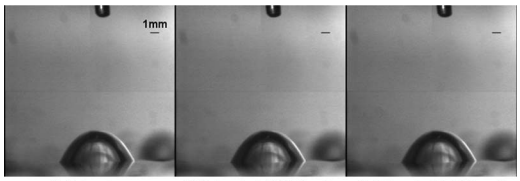

Fig. 9 Selected images of the single bubble in subcooled liquid (heating surface: Teflon-coated wafer, ΔT_w=2.9°C, ΔT_{sub}=2.5°C, and p=1 atm)

However, on the Teflon-coated wafer, the capillary number is almost constant before the lift-off period, and then starts to increase.

6 Subcooling Effects

Figures 9 and 10 show the bubble images on the Teflon-coated wafer under two different subcooling conditions. Only the time difference is presented because there was no ebullition cycle. In Fig. 9, the nucleated bubble stops growing and remains on the surface. In this specific case, the bubble is stationary because evaporation at the bubble base is balanced by condensation occurring at the top of the bubble. In Fig. 10, despite high superheat and active bubble merging, bubbles still cannot depart from the surface. This figure also shows many small bubbles generated on the nominally smooth surrounding region with no cavity. The effect of subcooling becomes more significant on a hydrophobic surface than on a hydrophilic surface because of the increased condensation area of larger bubbles. Qiu and Dhir [6] reported that even subcooling as small as 0.3°C led to an increase in the bubble growth period from 9 s to 15 s under low gravity condition due to the large bubble size. Takata et al. [8] also observed that, on superhydrophobic surfaces with a static contact angle of 152 deg, bubbles immediately form a vapor film under a subcooled liquid.

7 Numerical Simulation

To further elucidate our experimental results, numerical simulations are conducted under the conditions of ΔT_w=2.9°C, ΔT_{sub}=0°C, p=1 atm, and φ=120 deg. The vapor-liquid interface is captured by the level set method. The details of the model are described in Son et al. [12]. In addition, the moving mesh method is incorporated into the computational framework [18]. The natural convection temperature distribution [19] and stationary flow field conditions are adopted as the initial conditions.

The accuracy of the simulation is limited by the following simplifications. Evaporation from the microlayer and the change in wall temperature are neglected throughout the simulation. Furthermore, the contact angle is assumed to be fixed at 120 deg in the simulation, while the dynamic contact angles range from 118 deg to 134 deg in the experiment (see Table 1). Finally, the simulation results are obtained only during the first ebullition cycle, while experimental data are measured after reaching steady state. Since simulating a large bubble on a hydrophobic surface requires a larger computational domain than a small bubble on a hydrophilic surface, multiple-cycle calculations are not performed in this study in order to limit calculation time and cost.

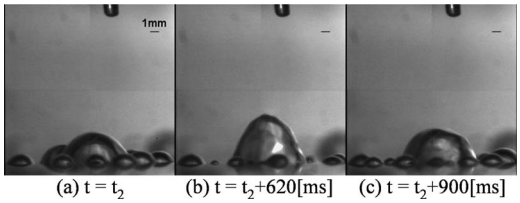

Fig. 10 Selected images of the single bubble in subcooled liquid (heating surface: Teflon-coated wafer, ΔT_w=4.6°C, ΔT_{sub}=3.5°C, and p=1 atm)

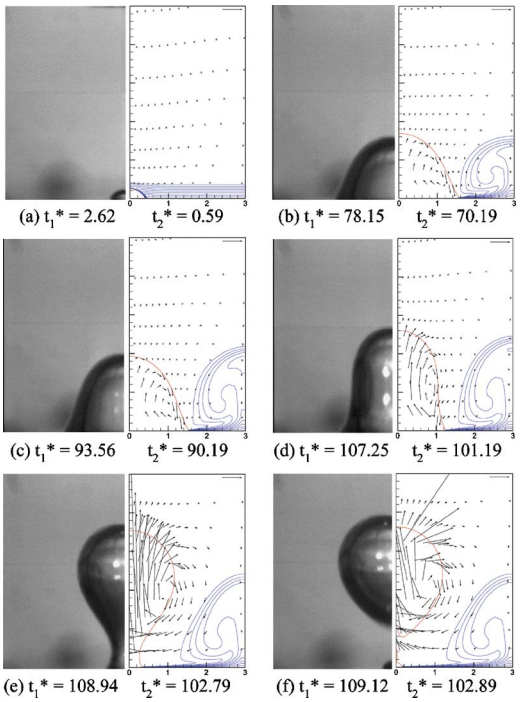

Fig. 11 Bubble shapes, temperature distributions, and velocity vectors (φ=120 deg, ΔT_w=2.9°C, ΔT_{sub}=0°C, p=1 atm, $t^*=t/t_0$, $t_0=1.6\times10^{-2}$ s, t_1^*=experimental data, and t_2^*=numerical data)

In spite of these limitations, the simulation provides strong qualitative support to the experimental findings and gives the detailed information of flow, temperature, and pressure distributions. Figure 11 shows the evolution of the bubble interface, temperature distributions, and normalized velocity vectors ($\mathbf{u}^*=\mathbf{u}/u_0$). The experimental and numerical results are presented side by side. Here, the simulated bubble shapes correspond well with the experimental results. The predicted growth period and bubble departure diameter are only 5 and 7% less than the eperimental data, respectively. Some difference in the growth rate is understandable considering the simplifications mentioned above.

As in the experiment, when a bubble grows, the base also expands, and the vortex in the liquid forms to flow upward, away from the bubble. Initially, the bubble grows fast, and then downward flow of the surrounding liquid compresses the thermal layer near the interface. Since only a small portion of the interface is surrounded by the superheated liquid, bubble growth then slows down. Similar to Fig. 5, the interface starts to be distorted after the base reaches its maximum value. The base shrinks very rapidly and the bubble starts to lift off as it breaks off at the bubble neck near the heating surface. The residual bubble nucleus remains on the surface and starts to grow as a second bubble.

Figure 12 represents the pressure distributions. The pressure at the top of the domain is set to be zero and is scaled by the product of vapor density and the square of characteristic velocity ($p^*=p/p_0$, $p_0=\rho_v u_0^2$). When the bubble growth rate is very small and inertia force is ignored, the surface tension balances the pressure difference through the interface. An insignificant pressure variation exists inside the bubble, so the pressure difference along the interface in the liquid side is proportional to the interfacial curvature variation at different locations. As the bubble grows, the pressure difference also increases between the top of the bubble and the location close to the wall in the liquid. When it reaches a

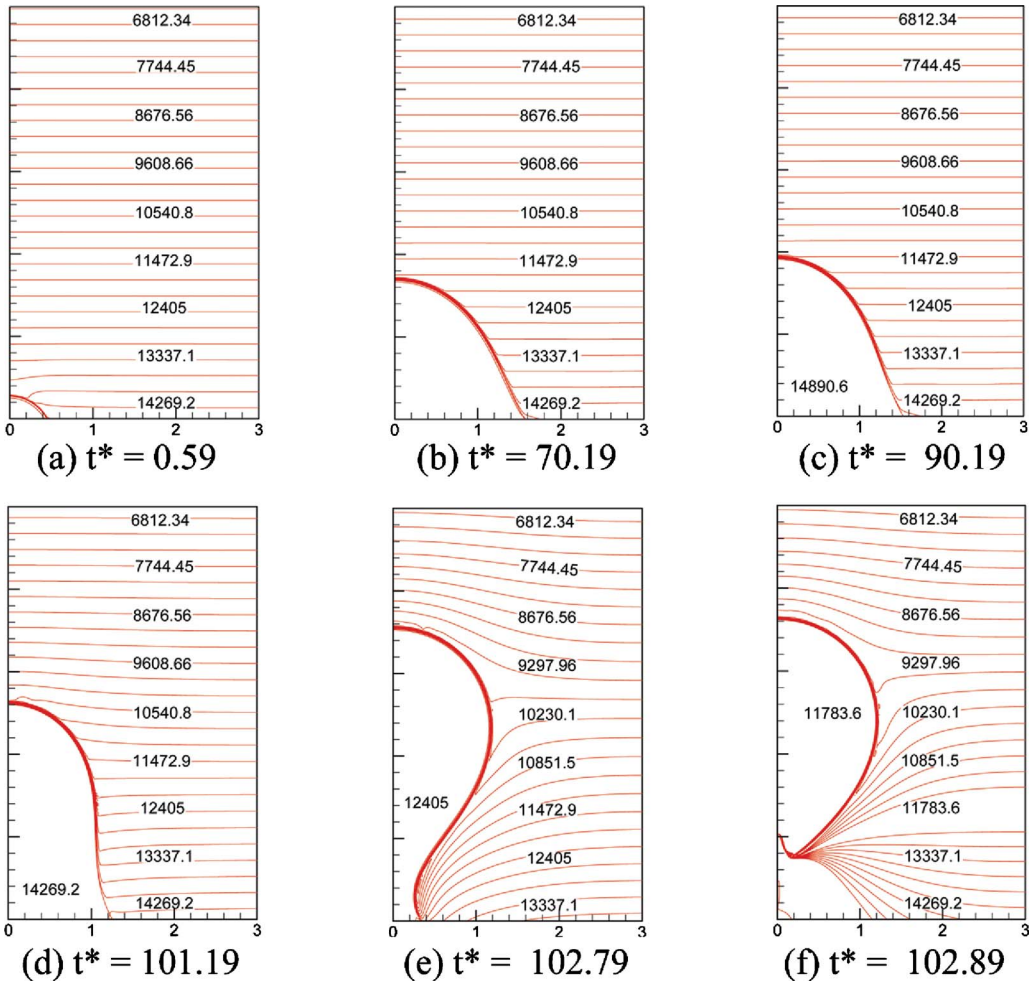

Fig. 12 Bubble shapes and pressure distributions (φ=120 deg, ΔT_w=2.9°C, ΔT_{sub}=0°C, p=1 atm, $t^*=t/t_0$, and $t_0=1.6\times10^{-2}$ s)

certain value, the curvature at the location close to the wall has to adjust itself to balance the pressure difference since the fixed contact angle does not allow the shape to change at the junction of three phases. The resulting liquid flow accelerates the shrinking of the bubble base.

8 Conclusions

The nucleation, growth, and departure of single bubbles are studied on two smooth surfaces with very different wettabilities. To our knowledge, this is the first quantitative study of single bubble dynamics on a hydrophobic surface having a contact angle greater than 100 deg. The bubble on the Teflon-coated wafer has about 3 times larger departure diameter and 60 times longer growth period than one on the bare silicon wafer. On the hydrophobic surface, the bubble departs from the surface after a short necking period and leaves behind a small residual bubble nucleus on the surface, which then grows in the next cycle. As a result, no waiting period is observed. In addition, liquid subcooling significantly impedes bubble growth on the hydrophobic surface due to the increased bubble surface area. The experimental findings are qualitatively consistent with the results of numerical simulations and the calculated bubble growth period and departure diameter are 5% and 7% less than the experimental values, respectively. Accurate models for dynamic contact angle changes and microlayer evaporation will be required to improve the accuracy of numerical simulations.

Acknowledgment

The authors are grateful to Dr. M.-T. Hung for his help with the microfabrication of artificial cavities.

Nomenclature

Ca = capillary number
D_{eq} = equivalent bubble diameter, m
D_B = bubble base diameter, m
D_d = bubble departure diameter, m
d_c = test chamber diameter, mm
d_w = quartz window diameter, mm
f = bubble release frequency, 1/s
g = gravitational acceleration at any level, m/s^2
h = convective heat transfer coefficient, W/m^2 K
h_c = test chamber height, mm
H = bubble height, m
l_0 = characteristic length, m
P = pressure, atm
R_q = root mean square roughness of profile, nm
R_y = peak-peak height roughness of profile, nm
t = time, s
t_0 = characteristic time, s
T = temperature, K
$\mathbf{u}$ = velocity vector
u_0 = characteristic velocity, m/s

v_h = growth rate of bubble height, m/s
μ = liquid viscosity coefficient, N s/m^2
ρ = density, kg/m^3
σ = surface tension, N/m
φ = apparent contact angle, deg

Subscripts

l,v = liquid and vapor phases
sub = subcooling
w = wall

References

[1] Dhir, V. K., 2006, "Mechanistic Prediction of Nucleate Boiling Heat Transfer-Achievable or a Hopeless Task?" ASME J. Heat Transfer, **128**(1), pp. 1–12.
[2] Dhir, V. K., 2001, "Numerical Simulations of Pool-Boiling Heat Transfer," AIChE J., **47**(4), pp. 813–834.
[3] Frtiz, W., 1935, "Maximum Volume of Vapor Bubbles," Phys. Z., **36**, pp. 379–384.
[4] Zuber, N., 1959, "Hydrodynamic Aspect of Boiling Heat Transfer," Ph.D. thesis, University of California, Los Angeles.
[5] Abarajith, H. S., and Dhir, V. K., 2002, "Effect of Contact Angle on the Dynamics of a Single Bubble During Pool Boiling," *Proceedings of the IMECE 2002 ASME International Mechanical Engineering Congress and Exposition*, New Orleans.
[6] Qiu, D. M., and Dhir, V. K., 2002, "Single Bubble Dynamics During Pool Boiling Under Low Gravity Conditions," J. Thermophys. Heat Transfer, **16**(3), pp. 336–345.
[7] Qiu, D. M., Dhir, V. K., Hasan, M. M., Chao, D., Neumann, E., Yee, G., and Witherow, J., 1999, "Single Bubble Dynamics During Nucleate Boiling Under Microgravity Conditions," Engineering Foundation Conference on Microgravity Fluid Physics and Heat Transfer, Honolulu, HI.
[8] Takata, Y., Hidaka, S., and Uraguchi, T., 2006, "Boiling Feature on a Super Water-Repellent Surface," Heat Transfer Eng., **27**(8), pp. 25–30.
[9] Nishikawa, K., Fujita, Y., Uchida, S., and Ohta, H., 1983, "Effect of Heating Surface Orientation on Nucleate Boiling Heat Transfer," *Proceedings of the ASME-JSME Thermal Engineering Joint Conference*, Honolulu, Vol. 1, pp. 129–136.
[10] Theofanous, T. G., Tu, J. P., Dinh, A. T., and Dinh, T. N., 2002, "The Boiling Crisis Phenomenon Part I: Nucleation and Nucleate Boiling Heat Transfer," Exp. Therm. Fluid Sci., **26**, pp. 775–792.
[11] Dinh, T. N., Tu, J. P., Dinh, A. T., and Theofanous, T. G., 2003, "Nucleation Phenomena in Boiling on Nanoscopically Smooth Surfaces," *Proceedings of the 41st Aerospace Sciences Meeting and Exhibit*, Reno, NV, Jan. 6–9.
[12] Son, G., Dhir, V. K., and Ramanujapu, N., 1999, "Dynamics and Heat Transfer Associated With a Single Bubble During Nucleate Boiling on a Horizontal Surface," ASME J. Heat Transfer, **121**(3), pp. 623–631.
[13] Carey, V. P., 1992, *Liquid-Vapor Phase Change Phenomena*, Hemisphere, Washington, DC.
[14] Mikic, B. B., and Rohsenow, W. M., 1969, "Bubble Growth Rates in Non-Uniform Temperature Field," Prog. Heat Mass Transfer, **2**, pp. 283–292.
[15] Strutt, J. W., and Rayleigh, A., 1920, "On the Pressure Developed in a Liquid During the Collapse of a Spherical Cavity," *Scientific Papers*, Vol. 6, Cambridge University Press, Cambridge, UK.
[16] Plesset, M. S., and Zwick, S. A., 1954, "The Growth of Vapor Bubbles in Superheated Liquids," J. Appl. Phys., **25**, pp. 493–500.
[17] Scriven, L. E., 1959, "On the Dynamics of Phase Growth," Chem. Eng. Sci., **10**, pp. 1–13.
[18] Wu, J., Dhir, V. K., and Qian, J., 2007, "Numerical Simulation of Subcooled Nucleate Boiling by Coupling Level-Set Method With Moving Mesh Method," Numer. Heat Transfer, Part B, **51**, pp. 535–563.
[19] Mills, A. F., 1995, *Basic Heat and Mass Transfer*, Irwin, Chicago.

Enhancement of Heat Transfer Behind Sliding Bubbles

D. Keith Hollingsworth

Larry C. Witte

Marcelino Figueroa

Department of Mechanical Engineering,
University of Houston,
Houston, TX 77204-4006

The time-dependent temperature distribution on an inclined, thin-foil uniform-heat-generation heater was used to infer the heat transfer enhancement caused by the passage of an FC-87 bubble sliding beneath the lower surface of the heater. A two-camera system was used: One camera recorded color images of a liquid crystal layer applied to the upper (dry) side of the heater while a second camera simultaneously recorded the position, size, and shape of the bubble from below. The temperature response of the heater could then be correlated directly to the bubble characteristics at any given time during its passage. The data along the line bisecting the bubble wake from the nine bubbles comprising 54 bubble images were analyzed. The heat transfer in the wake behind the sliding cap-shaped bubbles is very effective compared with the natural convection that occurs before the passage of the bubble. The maximum values of heat transfer coefficient in the range of 2500 $W/m^2 K$ were produced in very sharply peaked curves. The point of maximum cooling measured as a fraction of the local driving temperature difference before the bubble passage was identified and correlated with some success to the streamwise length of the bubble. The location of the maximum heat transfer coefficient was reasonably correlated with bubble width. The level of the maximum heat transfer coefficient when cast as a Nusselt number based on bubble width grew to a saturation value as the bubble moved across the plate. A constant value of Nusselt number requires that the heat transfer coefficient falls as the bubble grows past some critical bubble size. This behavior was observed for the larger cap-shaped bubbles. [DOI: 10.1115/1.3216039]

Keywords: sliding bubbles, enhancement, wakes

1 Introduction

Boiling heat transfer occurs in a wide variety of engineering applications such as energy conversion systems, manufacturing processes, and cooling of advanced electronic systems. Nucleate boiling provides an attractive means of cooling temperature-sensitive, high heat-flux devices because it can sustain a large heat-flux over a small and relatively stable temperature difference. The design of high-density computer chips and compact heat exchangers require reliable predictions of the initiation of boiling and of the heat transfer rate that follows for a variety of surfaces and convective fields assuring that a surface designed to operate in boiling is in fact doing so is of extreme importance. For example, it is well known that boiling can be delayed on heat-flux-controlled surfaces so that large and potentially damaging, *overshoots* in surface temperature can occur. In addition to eliminating temperature overshoot, there is also a need for flows that combine single-phase convection and boiling so that heat transfer is enhanced beyond the rates that occur in boiling alone.

Many convective situations involve bubbles forming at one place in a device and, after detachment, moving along adjacent surfaces. This has become known as the *sliding-bubble* phenomenon. Sliding bubbles can dramatically increase the local heat transfer rate from the surface on which they slide. Cornwell and Schuller [1] observed that sliding bubbles enhanced heat transfer is a shell-and-tube heat exchanger that experiences boiling over some or all of its tubes. Later, Cornwell [2] produced a surprising result. With all the tubes in a tube bank at the same heat-flux, the upstream tubes were in nucleate flow-boiling while the downstream tubes experienced no boiling at all. Clearly the heat transfer coefficient h on the downstream tubes had to be high enough to hold the surface temperature T_w below that required for the onset of boiling while supporting a heat-flux that should have resulting in boiling. Cornwell postulated that high h on the downstream tubes resulted from heat transfer into bubbles that nucleated on the upstream tubes and *slid* around the walls of the downstream tubes. Furthermore, at higher heat fluxes, boiling initiated on the downstream tubes *with no reported temperature* overshoot. This implies that for higher fluxes, the downstream h values are so high that little change in T_w is experienced once boiling initiates.

A recent work has shown that the importance of the sliding-bubble phenomenon extends beyond the external-flow surfaces of heat exchangers and surfaces that experience pool boiling. For example, Klausner [3] discussed sliding bubbles in the context of forced convection boiling inside tubes, a common industrial heat transfer application that is not commonly associated with this mechanism.

A sliding-bubble can induce at least three significant mechanisms that enhance heat transfer. The bubble displaces liquid and acts almost like a bluff body moving through the liquid, so a local enhancement in convection around the bubble can occur. Also, it was long known that sliding bubbles can create a thin liquid *microlayer* between the bubble and the surface on which it slides [4,5]. As the bubble slides, the microlayer evaporates and is replenished by liquid trapped under the upstream edge of the bubble. Finally, the bubble induces substantial mixing in its wake, giving a sustained increase in heat-flux behind the bubble.

Addlesee and co-workers [6–8] examined the fluid dynamics of sliding bubbles and the accompanying heat transfer implications. They also investigated the velocity of bubbles as they rise under an inclined plate and the film thickness that separates the bubble from the surface. Yan and co-workers [9,10] also undertook studies that seek to explain the enhancement mechanisms of sliding bubbles. Yan was the first to apply liquid crystal thermography to the measurement of surface temperature fields that develop around sliding bubbles. Kenning et al. [11] mapped the surface temperature imprint from a bubble sliding through saturated water using

Contributed by the Heat Transfer Division of ASME for publication in the JOURNAL OF HEAT TRANSFER. Manuscript received February 12, 2008; final manuscript received March 24, 2009; published online October 15, 2009. Review conducted by Yogesh Jaluria.

liquid crystals. Because the liquid was saturated, the amount of heat transferred to the bubble could be estimated from the observed volume increase in the bubble.

In a work reported later, Kenning and Bustnes [12] reported the studies of the injection of steam bubbles into saturated water under a thin heater coated with a liquid crystal at inclinations of 15 deg, 30 deg, and 45 deg from horizontal. The data for only one bubble at 15 deg were reported, which are reasonably close to the data contained in this paper for FC-72 at 12 deg inclination. Liquid crystal measurements before, during, and after bubble passage were presented. Their experiments involved a series of bubbles being injected rather than a single bubble. The authors noted that "the interval between injected vapor bubbles could not be longer than 5 s and thermal disturbances from a preceding bubble were sometimes present that could not be detected by eye in the live, unprocessed image." The present work as reported in this paper involves the injection of a single bubble so that there was ample time for all disturbances to damp out before another experiment was performed. Indeed, Kenning and Bustnes noted that the temperature field in front of the bubble revealed small-scale disturbances in both the heat transfer coefficients and the heat-flux maps. They note that the nature of the thermal boundary layer ahead of the bubble prior to the passage of the bubble affects the convective heat transfer to the curved interface of the bubble, which they claim is the dominant mode of heat transfer in their experiments. They observe that this effect has not been examined systematically in experiments on isolated bubbles. Our work reported in this paper addresses this issue directly. In our work, the temperature field in front of the bubble depended on the natural convection field generated by the liquid itself as it was exposed to the heated wall. The natural convective field was carefully measured and it was used as the baseline against which the enhancement of heat transfer as the bubble passed was measured.

Kenning and Bustnes also noted that there was an area of intense cooling directly behind the bubble and even in the far-field there were indications of thermal disturbance. We did not observe the disturbances in the far-field in our experiments probably because we injected a single bubble into a flow that was undisturbed by the passage of previous bubbles.

In a precursor work to this study, Bayazit and co-workers [13,14] used thermochromic liquid crystals on a 51 μm thick stainless steel foil to study the heat transfer mechanisms generated by a sliding-bubble. Using FC-87 as the working fluid, they injected single FC-87 vapor bubbles under a constant heat-flux surface that was inclined at 12 deg from the horizontal. A camera mounted from above recorded the color change in the liquid crystal surface while a bottom-mounted camera recorded the bubble dynamics. Using these images, the bubble position, size, and velocity were determined. Also, the bubble coordinates were mapped onto the top surface to analyze the temperature drop in comparison to the bubble position. The convective heat transfer coefficient h was determined in relation to the position of the sliding-bubble and it was determined that the highest h occurs in the wake of the bubble. In the wake, the h reached a max value that ranged from 500 W/m^2 K to 800 W/m^2 K. Bayazit [13] found h in the wake of the bubble to be six to seven times higher than that due to natural convection.

Qui and Dhir [15] studied the heat transfer enhancement under a sliding-bubble on a silicon test surface heated by microgauge heaters and instrumented with thermocouples. Vapor bubbles of PF-5060 were created from an artificial cavity. Silvered glass particles were added to the fluid to enable flow visualization. They observed a transition from spherical to elliptical bubbles and they found that vortices in the bubble wake enhanced the heat transfer continuously by bringing cooler liquid from the pool nearer to the surface.

Thorncroft and Klausner [16] examined the effect of a gas bubble sliding during forced convection boiling. The flow facility was vertical with a transparent test section. They concluded that sliding bubbles enhance heat transfer significantly, up to 52%, even during single-phase convection. They also showed that the turbulence induced by bubble injection was a significant heat transfer enhancement mechanism.

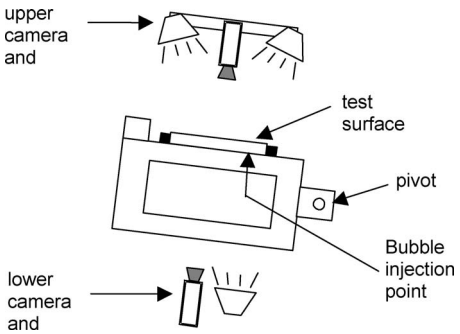

Fig. 1 Schematic drawing of the test apparatus

The outstanding issues regarding the heat transfer enhancement caused by the passage of a sliding-bubble are (1) the fluid dynamics of the microlayer, our ability to predict its thickness and the heat-flux through it; (2) the relative importance of the energy flow through the microlayer in the context of bubble growth; and (3) the fluid dynamics and surface energy flux associated with the wake. While past work understandably tends to focus on the first two items, this paper builds on the work of Bayazit and coworkers [13,14] by presenting the results of a thermographic study of the wake heat transfer behind cap-shaped bubbles. This presentation is based on centerline temperature and heat transfer coefficient distributions on a uniform-heat-generation surface.

2 Experimental Apparatus and Procedure

2.1 Apparatus. Figure 1 shows a schematic of the apparatus developed by Bayazit [13] to investigate sliding-bubble heat transfer. The same apparatus with slight modifications was used in the studies reported herein (see Figueroa [17]). It consists of a rectangular chamber (approximately $40\times20\times19$ cm^3) made of thin aluminum plates. The chamber can be rotated about a pivot point to give different heater inclination angles relative to the horizontal. The test fluid is FC-87, a perfluorocarbon fluid manufactured by 3M Corporation (St. Paul, MN). FC-87 has a boiling point of 30.0°C at 1 atm.

Two sidewalls and the bottom were equipped with glass windows for lighting and photography. The openings in the chamber allowed injection of vapor bubbles, removal of vapor produced in the chamber, and placement of pressure transducers and thermocouples. The bubbles of FC-87 vapor were injected just below the lower end of the heated surface by a vapor generation system designed to allow control of the frequency and size of the bubbles. The ability to produce a single bubble of a consistent and substantial size, as opposed to an uncontrolled stream of bubbles, is a nontrivial technical issue. FC-87 vapor was produced in a 1 cc syringe with an electrically heated nichrome wire inserted through the syringe walls. A set screw as employed to "squeeze" a small amount of vapor into the chamber through a 16.24 cm long needle. The bubbles were injected about 15 cm below the heater. When they reached the heater, they were estimated to be about 0.5 mm in diameter.

2.2 Test Surface. A 51 μm thick by 21.0×16.8 cm^2 stainless steel foil served as the electrically heated test surface and was mounted on top of the chamber. The test fluid touched the bottom face of the test surface, and a thermochromic liquid crystal (TLC) was applied to the upper (dry) face of the heater. The application was by airbrush: a layer of black paint followed by a layer of micro-encapsulated thermochromic liquid crystals from Hallcrest, Inc. (Glenview, IL). The foil was heated by a dc power supply

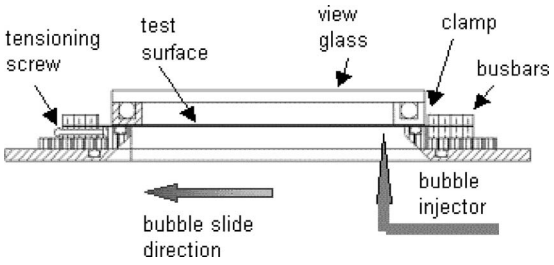

Fig. 2 Detailed sketch of test surface

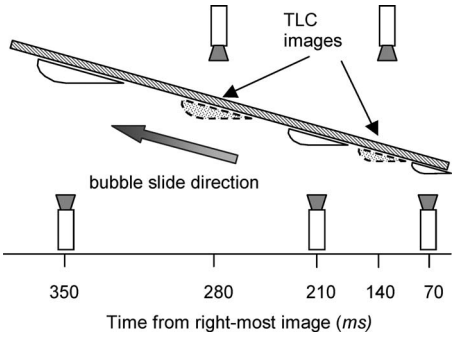

Fig. 3 Timing of lower and upper image sequences: The positions of the bubbles drawn in dashed lines are interpolated

capable of 12 V and 200 A. Further details of the design can be found in Bayazit [13]. Figure 2 shows a side view of the assembly with the various components labeled. Those include a tensioning mechanism to hold the foil as flat as possible and a sealing system to prevent leakage to the outside of the chamber. This system included an aluminum frame that clamped the edges of the foil. The frame was water-cooled to remove the energy generated within the clamped edges of the foil. A glass window attached to the frame allowed viewing of the TLC surface as well as providing a stagnant air gap above the test surface to minimize heat losses to the atmosphere.

2.3 Imaging Technique and Data Acquisition. In the UH Heat Transfer Laboratory, various experiments have employed wide-band calibrated liquid crystal thermography. For examples see Hollingsworth and co-workers [18–22]. The TLC used here was calibrated according to the procedure of Hay and Hollingsworth [18,19] over a range of 30.2–40.6°C. The first-order, 95% confidence, uncertainty was less than ±0.5°C below 33°C, rose to ±0.8°C at 35°C, and was ±1.2°C at 40.6°C.

Two 15 W fluorescent light bulbs were used to light the TLC surface; while a single 15 W bulb lighted the lower surface (bubble view). An upper light stand, fixed to the pivot arms of the chamber, held the upper camera and lights at fixed a position relative to the test surface regardless of the inclination angle. The data acquisition system consisted of a Matrox Meteor MC II dual-camera color frame grabber board and a Matrox G-4 video card installed in an Intel Pentium computer. A pair of digital video sequences was acquired from the bottom and the top of the heated surface by alternating image acquisition from two cameras. A software was developed for grabbing the images and sequencing them in time. A Pulnix charge-coupled device (CCD) color camera with a Navitar lens acquired the TLC images. The bottom camera was a Pulnix CCD unit with Fujinon lens and an external shutter control. The bottom camera was synchronized with a signal generated by the top camera. The field size in pixels for the digitized images from both cameras was 640×480. The dimensions for the square pixels were 217 μm/pixel for the TLC surface and 231 μm/pixel for the bubble images.

The image sequencing produced an interlaced TLC image from the upper camera followed by an interlaced bubble image from the lower camera at a net framing rate of 14.29 frames/s, less than the nominal 30 frames/s because of latency in the acquisition board and the control software. As shown in Fig. 3, the result is two digital video sequences, each sequence having frames separated by 140 ms. The sequences are offset in time by 70 ms.

To colocate the bubble with its TLC temperature, the position of the bubble (as given by three points on the bubble surface) for every bubble image in a run was mapped from the lower to the upper surface, and the position of the bubble for each TLC image in the run was computed from a nonlinear interpolation of the known mapped points. Typical uncertainty for locating the bubble in the TLC image was ±5 pixels or ±1.09 mm.

Additional data acquisition equipment included a pressure transducer connected to the upper wall of the apparatus to insure the pressure there remained at atmospheric and a thermocouple probe with a true ice-bath junction to measure the bulk fluid temperature far from the test surface.

3 Results

The top and bottom camera outputs were combined as explained in Sec. 2.3 to create histories of the surface temperature and the bubble location. Thus at any time, the position of the bubble could be ascertained along with the corresponding temperature response of the surface below and behind it. The heater surface was inclined at 9 deg for all the test runs reported here. For all runs, the bulk temperature of the FC-87 was held as near as possible to 27°C ranging from 26.2°C to 27.4°C. For these conditions it was found that a range of heat fluxes from 805 W/m^2 to 1083 W/m^2 allowed for a range of average surface temperatures that fell into the range of the liquid crystal. An example sequence of the liquid crystal images is shown in Fig. 4. The position of the bubble is shown by an ellipse in all cases for convenience. As the bubble grows, it transforms from a small near-spherical shape to an oval shape and finally to a cap shape, see Fig. 5, as it moves under the heater surface.

3.1 Precursor Field. Prior to the introduction and passage of a bubble under the inclined surface, a weak natural convection flow was established. Care was taken to allow the temperature field to come to equilibrium before a bubble was introduced because it is this natural convection temperature distribution that provides the reference for the enhancement of heat transfer as the bubble passes under the surface. This temperature distribution is

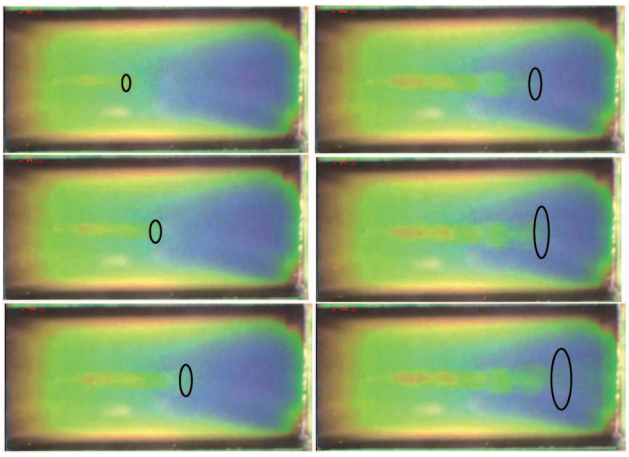

Fig. 4 Sequence of liquid crystal images for a typical sliding-bubble: The position of the bubble is shown with an ellipse in each image—the images are 140 ms apart and the bubble motion is to the right

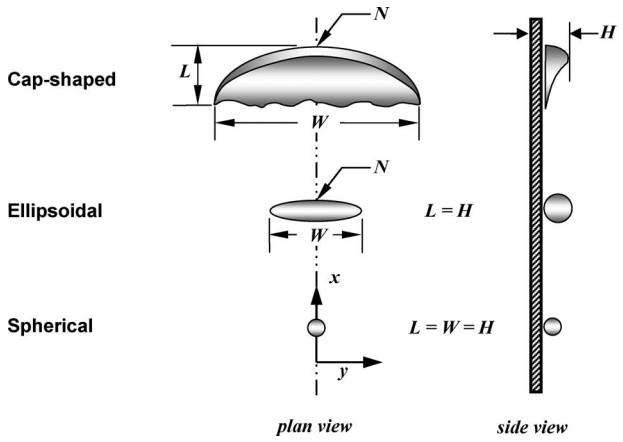

Fig. 5 Sketch of sliding bubbles, showing how length (*L*), width (*W*), and height (*H*) are defined: *N* refers to the bubble nose

the "precursor" temperature field. The parameters describing the precursor field for the nine runs in this study are given in Table 1. Here, T_{avg} is the average surface temperature along the centerline of the plate over its length. The last column gives the surface superheat divided by the bulk fluid subcooling.

Figure 6 shows the results of one of the runs for the precursor field along with the measured surface temperature ($T_w(x)$) and local Nusselt number (Nu_x) distributions. A curve representing a local Nusselt number calculated on the basis of a natural convection correlation for a vertical uniform-heat-flux surface [23] corrected for inclination angle is included as a reference

$$Nu_x = \left(\frac{Pr}{4 + 9Pr^{1/2} + 10Pr} \right)^{1/5} (Gr_x^* Pr)^{1/5} \quad (1)$$

$$Gr_x^* \equiv \frac{g \sin \phi \beta}{k\nu^2} \dot{q}_0'' x^4 \quad (2)$$

where the local heat transfer coefficient is found by dividing the heat-flux by the difference between the local surface and far-field fluid temperatures. The measurements were made along a line that bisects the bubble as it passed under the surface.

While Fig. 6 shows reasonable agreement between the experimental and calculated Nu_x in general this was not the case. This surface is inclined at only 9 deg so that the angle correction from a vertical surface is severe. Also, the construction of the enclosure did not allow for a smooth approach and departure of the naturally circulating fluid in the vicinity of the test surface. Finally, the cooling clamp securing the surface drew energy from the edges of the test surface. This tend to produce measured Nu_x that were too high at both ends of the heater surface. Thus an equation such as Eq. (1) cannot be used to establish a precursor field for a comparison to the experiments. In what follows, only the experimentally determined precursor field was used as the reference for heat transfer enhancement caused by bubble passage.

Table 1 Parameters for the precursor field

Run	T_∞	T_{avg}	Heating rate (W/m^2)	$T_{avg} - T_{sat} / T_{sat} - T_{sub}$
1	27.0	42.4	814	4.13
2	27.4	42.3	993	4.73
3	26.6	40.8	825	3.18
4	27.5	41.6	805	4.64
5	27.5	41.0	805	4.40
6	26.8	39.8	1026	3.06
7	25.7	42.2	1083	2.84
8	26.3	38.9	961	2.41
9	25.9	40.0	1005	2.44

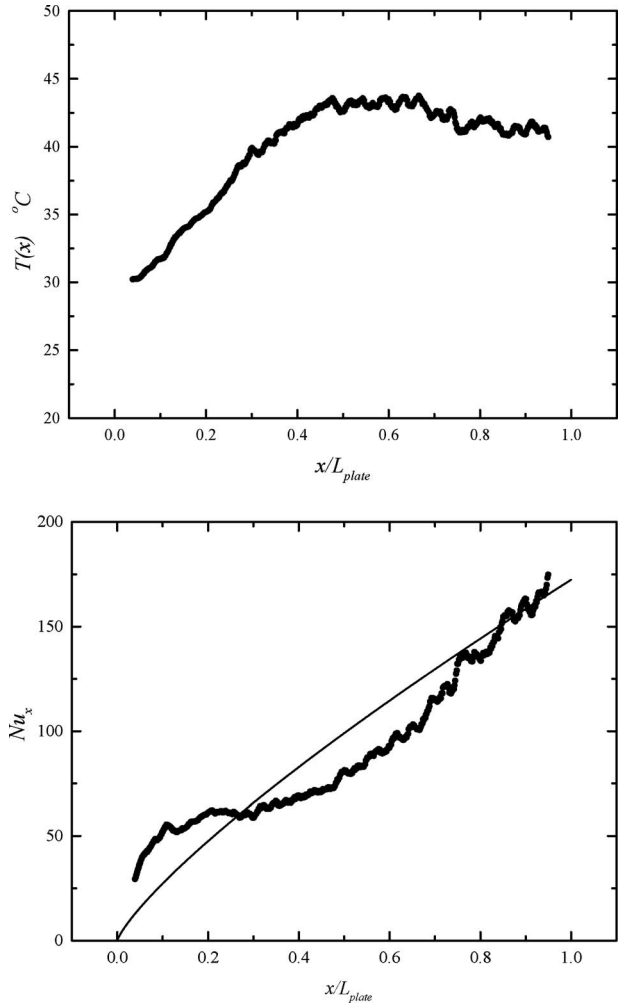

Fig. 6 The liquid crystal image (top), the temperature distribution (middle), and the local Nusselt number (bottom) for run 6—T_∞=26.8°C and wall flux of 1026 W/m^2: The smooth line represents Eq. (1)

3.2 Heat Transfer Enhancement. We begin our examination of the heat transfer enhancement by presenting a typical series of temperature distributions as a cap-shaped vapor bubble moves across the surface. Figure 7 shows the distributions of driving temperature difference $T_w(x) - T_\infty$ plotted against dimensionless plate position x/L_{plate} for six positions of the bubble. Included is the distribution created by the "boundary layer" precursor field. The positions of the bubbles at the selected times are shown on the plot as shaded boxes.

The most interesting feature of Fig. 7 is that once a bubble has passed and created a temperature depression behind it, the level of that depression remains virtually constant even though the bubble has moved significantly away from that location. Given that the precursor temperature field varies with x, the magnitude of the temperature reduction also varies with x. Equation (3) was devised to express the surface temperature rise above the bulk fluid value after the bubble passage as a fraction of the local value produced by the precursor field

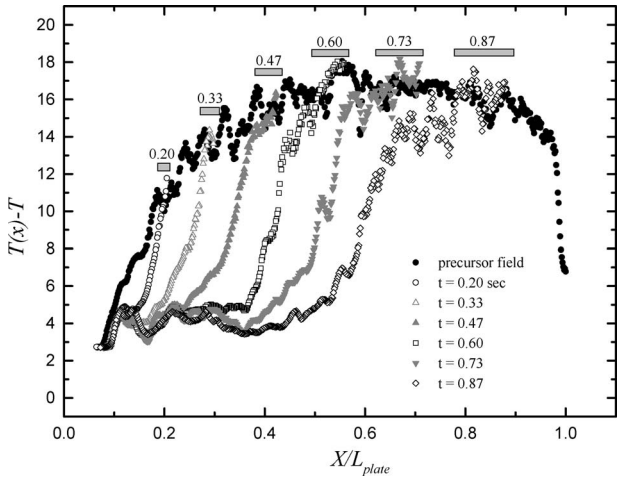

Fig. 7 Temperature distributions at various times for run 4: Times in the legend are in seconds and the shaded bars represent the location of the bubble at the time indicated in the legend

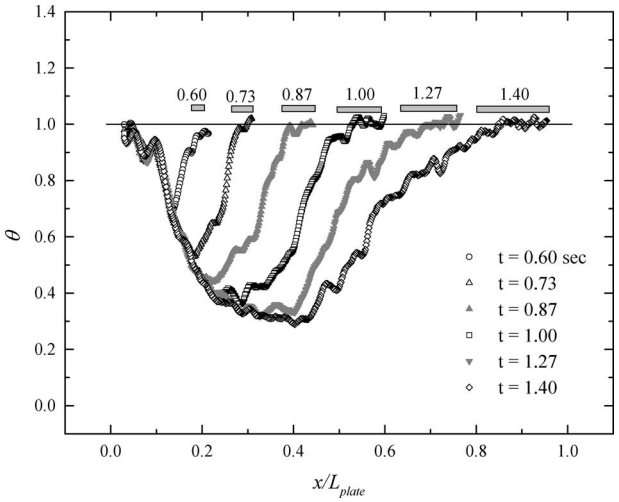

Fig. 9 Nondimensional temperature distribution for run 7

$$\theta = \frac{T(x) - T_x}{T_{\text{boundary layer}}(x) - T_\infty} \tag{3}$$

Figure 8 shows the data from run 4, the same data as shown in Fig. 7, plotted in terms of Eq. (3). These data are from a run with the lowest heat-flux and the second highest ratio of superheat to subcooling. Figure 9 is presented to show that for the case of the highest heat-flux and one of the lowest ratios of superheat to subcooling, run 7, the data behave in the same general way. However, the data from run 7 are somewhat smoother and the curves are perhaps more angular with more clearly defined minima.

3.3 Scaling Concepts. The fact that all the θ curves "nest" to the left is because the region of uniform and sustained surface temperature seen in Fig. 6 occurs where the surface temperature produced by the precursor field is still rising with x. Eventually, a streamwise position is reached for each bubble position where a minimum in θ occurs and the temperature recovers as the back of the bubble is approached. It is natural to ask if this minimum θ position scales on a characteristic bubble dimension. In this study the length of the bubble, i.e., the distance along a bisecting line from the nose of the bubble to the trailing edge was directly measured. Figure 5 shows how the dimensions of the bubble were defined. W is the width of the bubble measured transverse to the flow direction and L is the length of the bubble measured from the nose of the bubble to the trailing edge directly behind the nose. H is the height of the bubble; it was not measured in this study. As the bubble grows in the streamwise direction, the heater surface area beneath the wake increases as well. Does this behavior indicate that the wake length as given by the position of the maximum fractional temperature *depression* (minimum θ) scales on the bubble length? One way to test this hypothesis is to find the length of the wake region measured from the front of the bubble to the point where the fractional surface temperature θ is a minimum, call it Δx_θ, then form a ratio with the length of the bubble, which is $\Delta x_\theta / L$. The argument here is that if a bubble moves into a precursor field with a nonuniform surface temperature, the maximum fractional surface temperature depression is a more appropriate descriptor of the local thermal wake strength.

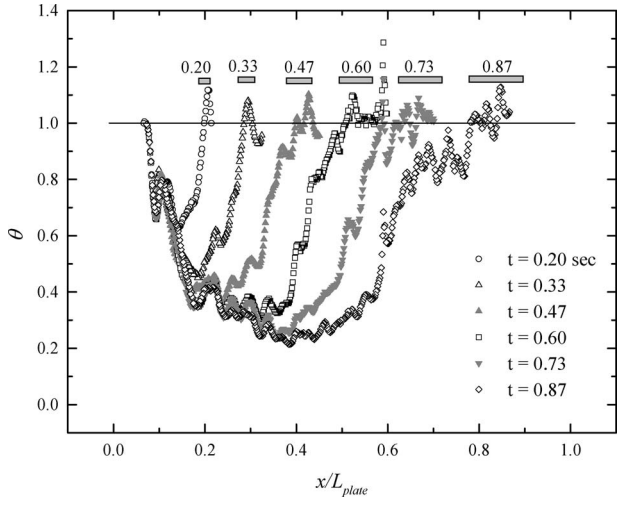

Fig. 8 Nondimensional temperature distribution for run 4

Figure 10 shows $\Delta x_\theta / L$ plotted against a Reynolds number based on bubble velocity and length Re_L for all nine runs from Table 1. A $\Delta x_\theta / L$ of unity represents the rear of the bubble. For runs 1–6, the data cluster about an increasing trend for Re_L as shown by the upper dashed line. Runs 8 and 9 cluster about a trend with a markedly lower intercept. Run 7 produces results in between. This segregation follows the trend in the ratio of superheat to subcooling shown in Table 1.

Example uncertainty estimates are shown for run 1 and are dominated by the position uncertainty of ± 1.09 mm as it affects length and velocity measurements and by noise in the θ curves near the minimum value. While the wake heat transfer is a purely single-phase phenomenon, the shape of the bubble, and most particularly its height, is not. In this experiment, height was not measured but Fig. 10 suggests that as the superheat to subcooling is reduced and the minimum θ point shifts toward the bubble. The height of the bubble may be reduced as it grows from a less superheated near-wall layer and into a more subcooled far-field fluid. Fluid moving over the peak of the bubble may be deposited into the wake nearer to the rear of the bubble. An attempt to scale Δx_θ on the bubble width W did not produce a significant improvement.

The temperature response illustrated in Figs. 7 and 8 clearly demonstrate that the heat transfer is significantly enhanced in the wake region behind the sliding bubbles. The extent of the enhancement can be found by computing the heat transfer coefficients that correspond to the position of the bubble as it slides under the heater. The convective heat transfer coefficient $h(x,t)$

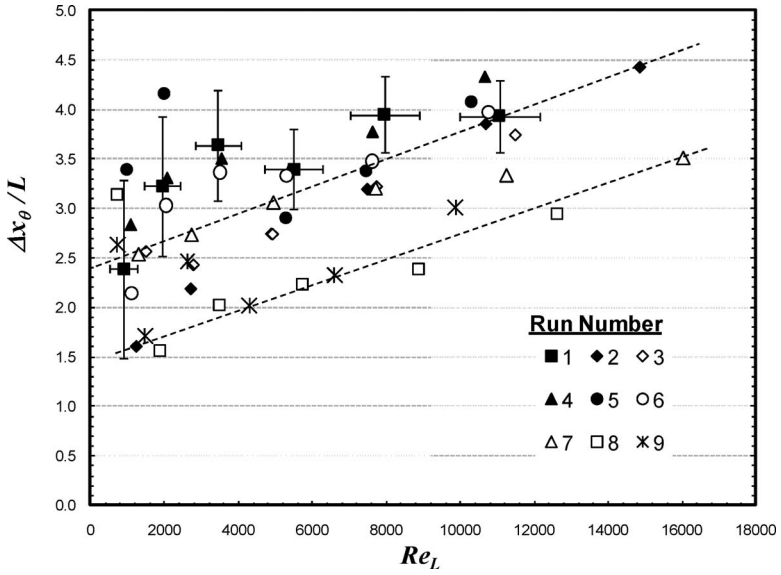

Fig. 10 Distance to minimum fractional surface temperature scaled on bubble length

was determined from the data for each bubble position on the foil surface. The instantaneous heat transfer coefficient at a point on the plate is defined as

$$h(x,t) \equiv \frac{\dot{Q}''_{\text{conv}}}{T_w(x,t) - T_\infty} \tag{4}$$

$T_w(x,t)$ is the temperature of the foil surface at a particular position and time. The heat-flux from the wetted side of the test surface $\dot{Q}''_{\text{conv}}$ is determined by performing an energy balance on a differential volume on the foil surface assuming no lateral heat flow within the foil. Therefore

$$\dot{Q}''_{\text{conv}} = \dot{Q}''_e - \frac{dU''}{dt} = \dot{Q}''_e - \rho_{\text{ss}} \tau_w c_{\text{ss}} \frac{\partial T(x,t)}{\partial t} \tag{5}$$

where $\dot{Q}''_e$ is the internal energy generation and U'' is the stored internal energy of the foil at a given position on the foil, both per unit wetted surface area. For the foil surface, the rate of energy storage per unit area is computed from the time derivative of the measured temperatures where ρ_{ss} is the density of the foil, τ_w is the thickness of the foil surface, and c_{ss} is the specific heat of the foil. The time derivative of the wall temperature in Eq. (5) can be approximated from the data by a quotient of finite differences so that the resulting formulation of $h(x,t)$ is

$$h(x,t) \equiv \frac{\dot{Q}''_e - \rho_{\text{ss}} \tau_w c_{\text{ss}} \left(\dfrac{T(x,t) - T(x,t-\Delta t)}{\Delta t} \right)}{T(x,t) - T_\infty} \tag{6}$$

By this method, the streamwise distribution of heat transfer coefficient for selected times (bubble positions) was computed for the nine runs in Table 1. The results for runs 4 and 7 are shown in Figs. 11 and 12, respectively. The values for the precursor natural boundary layer are labeled "precursor field."

These plots show that the local heat transfer in the wake reaches a peak where the high temperature gradient begins immediately adjacent to the region of uniform surface temperature. The surface heat-flux is dominated by the rate of removal of stored energy as opposed to the electrical generation rate and this location is where the time derivative of temperature is the largest. The scaling concept that was discussed earlier in connection with the maximum degree of cooling achieved in the wake can be applied to these data as well. The length along the bubble centerline from the front of the bubble to the location of maximum h was found to be well approximated by the bubble width for developed bubbles, which is $\Delta x_h / W \approx 1$. This result is shown in Fig. 13 plotted against the bubble Reynolds number based on width Re_w. Example uncertainty estimates are again shown for run 1 and are dominated by the position uncertainty. These uncertainty levels apply to the other runs as well and are not shown so that run symbols are not obscured. Again, runs 8 and 9 are those with the lowest ratios of superheat to subcooling produce data, which gen-

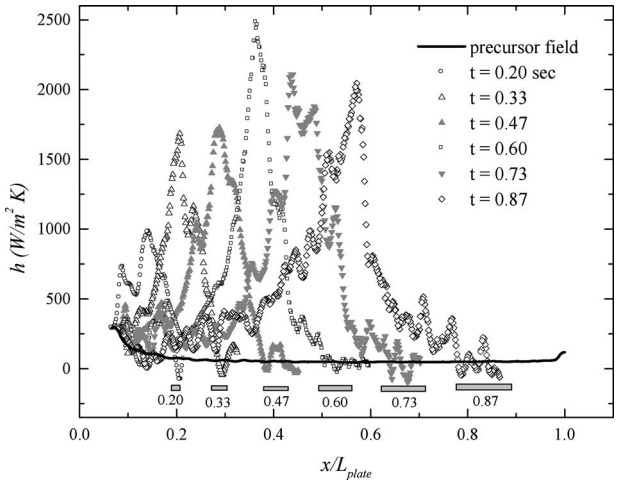

Fig. 11 Heat transfer coefficients for run 4 (corresponds to Fig. 7)

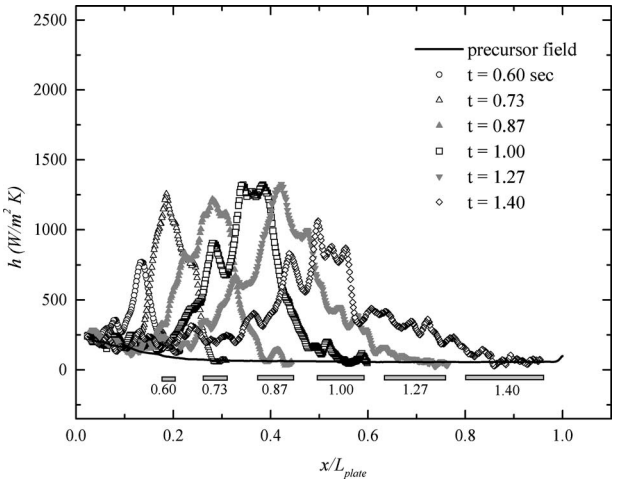

Fig. 12 Heat transfer coefficients for run 7 (corresponds to Fig. 8)

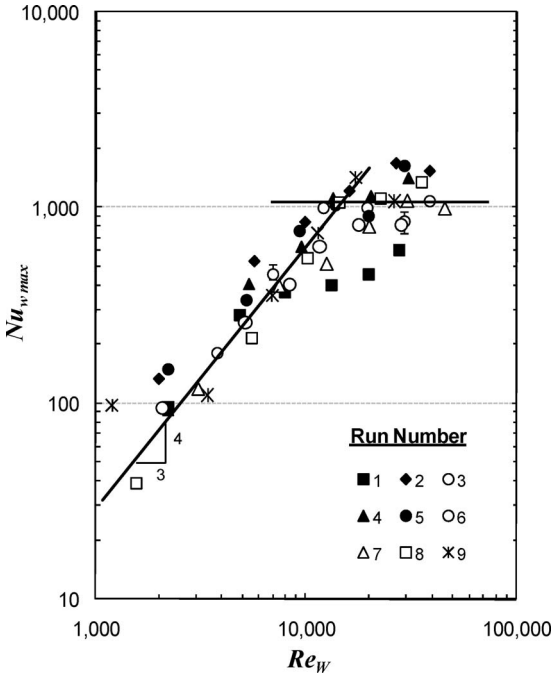

Fig. 14 Maximum Nusselt number versus width-based Reynolds number

erally approach from below the others but the discrepancy is not large at higher Re_w. The better collapse for h seen in Fig. 12 as opposed to θ in Fig. 9 may be due to the absence in Fig. 13 of any directly scaling dependence on the precursor surface temperature.

Figure 14 is a graph of the maximum width-based Nusselt number $Nu_W \equiv h_{w,\max} W/k$ obtained from each bubble image in all nine runs. Here, $Nu_{w,\max}$ is plotted against Re_w on a log-log scale. The results suggest two phases of development: An initial phase where the $Nu_{w,\max}$ displays a power-law growth with a power of approximately 1.33 and a fully developed phase beyond a Re_w of approximately 15,000. Given that the bubble continues to grow, the plateau in $Nu_{w,\max}$ required that the dimensional heat transfer coefficient must reach a maximum and then decrease with increasing bubble size. Also, the value of the plateau is very much in question as different runs produce plateaus between 450 and 1600. Figures 10 and 11 demonstrate both observations: The decrease in h for larger bubbles and two very different general levels for the maximum dimensional h. The different plateau values of Nu_w are likely due to variations in the capacity of the bubble to bring cold far-field fluid near the wall in the wake. Obvious candidates include differences in bubble height and differences in the thickness of the precursor boundary layer Given that the different plateau values are very much grouped by run and not scattered within a run, the behavior of the precursor boundary layer is the likely culprit.

Although we have shown that the heat transfer enhancement along the center line of the bubble scales best with the width of the bubble, at least up to the point where large cap-shaped bubbles have evolved, we speculate that the height of the bubble is a more likely parameter that controls the enhancement of heat transfer in the wake behind the bubble. However, we did not measure the height of the bubbles in this study so we could not attempt a correlation along these lines. As bubbles evolve from spherical to

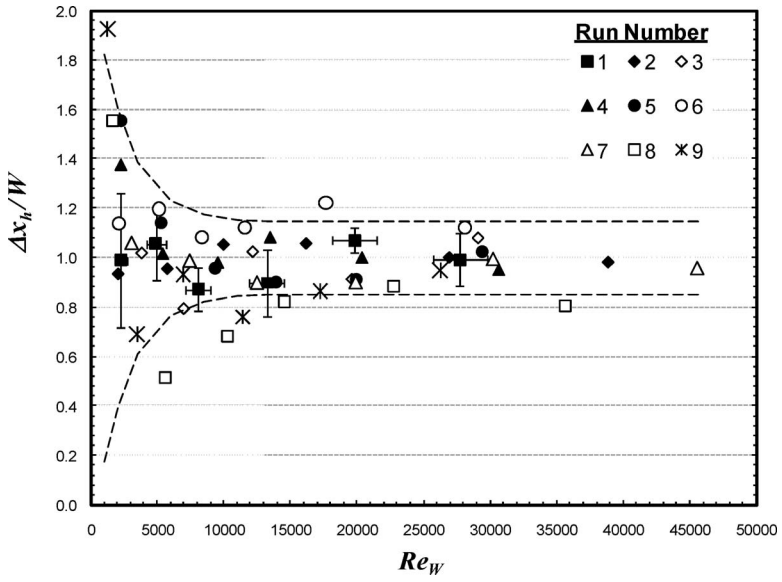

Fig. 13 Distance to location of maximum heat transfer coefficient scaled on bubble width

elliptical to cap-shaped, the data of Li et al. [24] in which photos of height of the bubble were obtained along with plan and frontal views, indicated that the maximum height of the bubble occurs at the centerline and drops off toward zero toward the transverse edges of the bubble. As the height drops off, so does the extent of the enhancement of heat transfer in the wake falling to zero enhancement near the transverse edge of the bubble. This accounts for the triangular region in the wake where enhancement clearly occurs. The motion of the liquid over the height of the bubble tends to bring cooler liquid down into the wake region thus causing the enhancement of heat transfer that is proportional to the height at any point along the transverse dimension of the bubble. As the height drops off, the length of the affected area drops as well.

4 Conclusions

The heat transfer in the wake behind sliding cap-shaped bubbles is very effective compared with the natural convection that occurs before the passage of the bubble. Liquid crystal thermography provides time-dependent surface temperature measurements of fine spatial resolution that allow detailed analysis of the wake structure. This paper presents the beginning of such an analysis by considering what can be learned by looking only at the data lying along the line bisecting the bubble wake. The data from the nine bubbles comprising 54 bubble images were analyzed and some preliminary conclusions can be drawn. Perhaps the most important overall conclusion is the importance of the surface thermal boundary condition. These data show that heat transfer coefficient values of 2500 W/m^2K can be produced for this fluid but in very sharply peaked curves that move with the bubble. Heat transfer coefficients are functions of the details of the flow field, fluid properties, and the surface boundary condition. The capacity of the heater to deliver energy (in this case through depletion of the energy stored in a thin-foil) is likely to be an important determinant of the coefficient produced—a thinner foil or a thick uniform-temperature surface may behave differently. In any case, the ability to measure (or correctly model for those attempting a predictive computation model) the time-dependent local surface heat-flux is paramount.

Our results indicate that the details of the precursor boundary layer are also important. We attempted to include the pre-existing surface temperature distribution through our definition of θ as a thermal wake structure descriptor. Our attempt to correlate the location of the minimum θ met with limited success; we believe we are hampered here by the lack of bubble height measurements and of thermal boundary layer thickness measurements. We consider the ratio of the average superheat to the average subcooling of the precursor flow to provide an indication of the capacity of the bubble to grow into the cooler extremes of the boundary layer where condensation on the lower surface of the bubble may limit its height.

The location of the maximum h was found to be reasonably correlated with bubble width—in fact one bubble width behind the nose of the bubble. However, two or three of the data sets were not as well correlated as the others, again perhaps due to the bubble height varying with the details of the precursor flow. Finally, the level of the maximum h was explored through the definition of a bubble-width-based Nusselt number. Presented in this way, the Nusselt numbers for the peaks in the temperature curves grow as a power-law function of Reynolds number to a saturation value, which again appears to be a function of the precursor flow and perhaps the bubble height. However, the fact that a plateau value in the product of h and W is produced for a given run means that h falls as W increases past some critical bubble size. This behavior is indeed observed in graphs of h versus streamwise position and leads to the interesting possibility that an optimum bubble size exists—at least for the boundary condition employed here.

Acknowledgment

This work was supported in part by the State of Texas Advanced Research Program Grant, ARP under Contract No. 003652-762.

Nomenclature

c_{ss} = specific heat of stainless foil, J/kg °C
g = gravitational constant, m/s^2
Gr_L^* = heat-flux-based Grashof number
h = convective heat transfer coefficient, W/m^2 K
k = thermal conductivity, W/m^2 K
L_{plate} = foil length, mm
L = bubble length in the x-direction, mm
Nu_x = local Nusselt number$\equiv hx/k$
$Nu_{w\,max}$ = Nusselt number based on maximum h and bubble width for each bubble image$\equiv h_{max}W/k$
Pr = Prandtl number
$\dot{q}''$ = heat-flux per unit area, W/m^2
$\dot{Q}''_{conv}$ = convective flux for h computation, W/m^2
$\dot{Q}''_e$ = internal heat generation per unit area, W/m^2
Re_L = Reynolds number based on bubble length$\equiv u_{bubble}L/\nu$
Re_w = Reynolds number based on bubble width$\equiv u_{bubble}W/\nu$
T_w = wall temperature, °C
$T_{boundary\ layer}$ = temperature of the precursor flow, °C
T_∞ = bulk fluid temperature far from the test surface, °C
T_{avg} = average wall temperature along the foil centerline, °C
T_{sat} = saturation temperature, °C
T_{sub} = temperature of the subcooled liquid, °C
t = time, s
u_{bubble} = bubble velocity, mm/s
U'' = internal energy per unit surface area of foil, J/m^2
W = bubble width, transverse to flow direction, mm
x = direction of bubble motion, mm

Greek Symbols

β = coefficient of thermal expansion, K^{-1}
Δx_h = distance from front of bubble to the point of maximum h, mm
Δx_θ = distance from the front of bubble to the point of minimum temperature, mm
ϕ = heater inclination angle from the vertical, arc deg
ρ_{ss} = density of stainless foil, kg/m^3
θ = dimensionless temperature
τ_{ss} = foil thickness, μm
ν = kinematic viscosity, m^2/s

References

[1] Cornwell, K., and Schuller, R. B., 1982, "A Study of Boiling Outside a Tube Bundle Using High Speed Photography," Int. J. Heat Mass Transfer, **25**(5), pp. 683–690.
[2] Cornwell, K., 1991, "The Influence of Bubbly Flow on Boiling From a Tube Bundle," Int. J. Heat Mass Transfer, **33**, pp. 2579–2584.
[3] Klausner, J., 2000, "Bubble Forces and Detachment Models," Keynote Address, *Engineering Foundation Conference Boiling 2000: Phenomena and Emerging Applications*, Begell House, Reading, CT.
[4] Cooper, M. G., and Lloyd, A. J. P., 1969, "The Microlayer in Nucleate Pool Boiling," Int. J. Heat Mass Transfer, **12**, pp. 895–913.
[5] Koffman, L. D., and Plesset, M. S., 1983, "Experimental Observations of the Microlayer in Vapor Bubble Growth on a Heated Solid," ASME J. Heat Transfer, **105**, pp. 625–632.
[6] Addlesee, A. J., Cornwell, K., and Peace, D. G., 1989, "Fluid Dynamics of Sliding Bubbles and Heat Transfer Implications," *Pool Boiling, Proceedings of Eurotherm Seminar 8*, , Paderborn, Germany, pp. 57–64.

[7] Addlesee, A. J., and Cornwell, K., 1997, "Liquid Film Thickness Above a Bubble Rising Under an Inclined Plate," Chem. Eng. Res. Des., **75**, pp. 663–667.
[8] Addlesee, A. J., and Cornwell, K., 1999, "The Velocity of Bubbles Rising Under an Inclined Plate," Transactions of the ImechE Conference, 6th UK National Conference on Heat Transfer, pp. 231–236.
[9] Yan, Y., and Kenning, D. B. R., 1994, "Heat Transfer Near Sliding Vapour Bubbles in Boiling," *Proceedings of the 10th International Heat Transfer Conference*, pp. 195–200.
[10] Yan, Y., Kenning, D. B. R., Grant, I. A., and Cornwell, K., 1996, "Heat Transfer to Sliding Bubbles Under Plane and Curved Surfaces," 4th UK National Conference on Heat Transfer, Manchester, UK, Paper No. IMechE C510/118, pp. 295–299.
[11] Kenning, D. B. R., Bustnes, O. E., and Yan, Y., 2000, "Heat Transfer to a Sliding Vapor Bubble," *Proceedings of ASME Boiling 2000 Conference*, Vol. 104, pp. 82–89.
[12] Kenning, D. B. R., and Bustnes, O. E., 2009, "Liquid Crystal Studies of Sliding Vapour Bubbles," Heat Mass Transfer, **45**(7), pp. 867–880.
[13] Bayazit, B. B., 2000, "A Thermographic Analysis of the Heat Transfer Mechanisms Generated by a Sliding Bubble," MS thesis, University of Houston, Houston TX.
[14] Bayazit, B. B., Hollingsworth, D. K., and Witte, L. C., 2003, "Heat Transfer Enhancement Caused by Sliding Bubbles," ASME J. Heat Transfer, **125**(3), pp. 503–509.
[15] Qui, D., and Dhir, V. K., 2002, "Experimental Study of Flow Pattern and Heat Transfer Associated With a Bubble Sliding on Downward Facing Inclined Surfaces," Exp. Therm. Fluid Sci., **26**, pp. 605–616.
[16] Thorncroft, G. E., and Klausner, J. F., 1999, "The Influence of Vapor-Bubble Sliding on Forced Convection Boiling Heat Transfer," ASME J. Heat Transfer, **121**, pp. 73–79.
[17] Figueroa, M., 2005, "The Evolution of the Microlayer Thickness Above a Sliding, Vapor Bubble," MS thesis, University of Houston, Houston TX.
[18] Hay, J. L., and Hollingsworth, D. K., 1996, "A Comparison of Trichromic Systems for Use in the Calibration of Polymer-Dispersed Thermochromic Liquid Crystals," Exp. Therm. Fluid Sci., **12**, pp. 1–12.
[19] Hay, J. L., and Hollingsworth, D. K., 1998, "Calibration of Micro-Encapsulated Liquid Crystals Using Hue Angle and a Dimensionless Temperature," Exp. Therm. Fluid Sci., **18**, pp. 251–257.
[20] Dukle, N. M., and Hollingsworth, D. K., 1996, "Liquid Crystal Images of the Transition From Jet-Impingement Convection to Nucleate Boiling, Part 1: Monotonic Distribution of the Convection Coefficient," Exp. Therm. Fluid Sci., **12**, pp. 274–287.
[21] Dukle, N. M., and Hollingsworth, D. K., 1996, "Liquid Crystal Images of the Transition From Jet-Impingement Convection to Nucleate Boiling, Part 2: Nonmonotonic Distribution of the Convection Coefficient," Exp. Therm. Fluid Sci., **12**, pp. 288–297.
[22] Dalrymple, N. E., Dukle, N. M., and Hollingsworth, D. K., 1995, "The Behavior of a Boiling Front in Jet-Impingement Boiling," *Proceedings of ASME/JSME Thermal Engineering Conference*, Vol. 2, pp. 339–346.
[23] Kays, W. M., Crawford, M. E., and Weigand, B., 1994, *Convective Heat and Mass Transfer*, 4th ed., McGraw-Hill, New York.
[24] Li, X., Hollingsworth, D. K., and Witte, L. C., 2006, "The Thickness of the Liquid Microlayer Between a Cap-Shaped Sliding Bubble and a Heated Wall: Experimental Measurements," ASME J. Heat Trans, **128**, pp. 934–944.

Bubble-Induced Water Hammer and Cavitation in Microchannel Flow Boiling

David W. Fogg
Creare Inc,
P.O. Box 71,
Hanover, NH 03755
e-mail: dwf@creare.com

Kenneth E. Goodson
Department of Mechanical Engineering,
Stanford University,
Building 530, Room 224,
Stanford, CA 94305

While microchannel flow boiling has received much research attention, past work has not considered the impact of acoustic waves generated by rapidly nucleating bubbles. The present work provides a theoretical framework for these pressure waves, which resembles classical "water hammer" theory and predicts a strong influence on bubble nucleation rates and effective convection coefficients. These pressure waves result directly from confinement in microchannel geometries, reflect from geometrical transitions, and superimpose to create large transients in the static liquid pressure. Feedback from the pressure waves inhibits bubble growth rates, reducing the effective heat transfer. Pressure depressions generated by the propagating pressure pulses can cause other bubbles to grow at lower than expected wall temperatures. The additional nucleation enhances heat transfer over short times but increased flow instability may inhibit heat transfer over longer periods. The limited quantitative measurements available in the literature indicate confined bubble growth rates in microchannels are significantly lower than those predicted by the classical Rayleigh–Plesset equation. The present model predicts confined bubble growth rates to within ± 20%. A nondimensional number indicative of the relative magnitude of the water hammer pressure to bubble pressure is proposed to characterize the transitions from conventional to microchannel flow boiling. [DOI: 10.1115/1.3216381]

Keywords: microchannel, flow boiling, confinement, two-phase heat transfer, bubble acoustics, water hammer

1 Introduction

The semiconductor industry continues to increase the total number, number density, and power density of transistors in microprocessors. The resulting trend in device design is leading to highly nonuniform heat generation and increasing power consumption by the chips [1]. In the near future, forced air convection will be replaced by liquid microchannel cooling technologies in an effort to drive the resistance of the chip package down and allow larger heat exchangers to be located remotely in the computer chassis. Two-phase microchannel cooling promises increased performance by further reducing the package resistance while still allowing a remote exchanger to reject the waste heat to the environment.

Notwithstanding the concentrated research effort in this field, fundamental challenges in controlling the pressure and temperature fluctuations remain, preventing accurate predictions of performance and reliability. Oscillations in temperature and pressure have been observed in both single channels [2] and multichannel arrays [3,4]. Qu and Mudawar [3] observed pressure drop and parallel channel instabilities in an array of 21 231×712 μm^2 rectangular channels. The pressure drop instability is a result of the flow rate response of the flow delivery system to pressure changes in the test section. Frequencies are usually very low on the order of 0.1 Hz. In the parallel channel instability, the flow redistributes itself in response to an increased pressure drop in a few channels due to nonuniform vapor generation. Peles [4] also observed parallel channel and pressure drop instabilities in 13 channel arrays of 50–200 μm triangular channels. A flow excursion instability resulting from flow regime transitions and a compound relaxation instability from rapid bubble growth were also observed. Peles [4] noted that the instabilities were more pronounced in the microchannels than they are for large channels. Zhang et al. [2] observed pressure oscillations and periodic vapor generation in single rectangular microchannels measuring 44 μm and 113 μm in hydraulic diameter under constant applied heat flux and constant inlet velocity boundary conditions. The resulting oscillations were classified a compound relaxation instability similar to bumping and geysering and was associated with the rapid vapor generation characteristic of microchannels. For detailed descriptions of two-phase flow instabilities refer to Boure et al. [5] or Carey [6].

Understanding the dynamic behavior of microchannel flow boiling is a major challenge, as the metrology and modeling for these flows are still in their infancy relative to larger scale systems. Due to the spatial constraints of the system, measurements have been limited to inlet and outlet pressures from commercial pressure taps, flow rates with commercial flow meters, wall temperatures with IR thermometry or microfabricated thermistors, and high speed video imaging [2,3,7–10]. The inability to directly measure flow parameters in the channel itself leads to a great deal of uncertainty as it forces assumptions to be made in order to interpolate local values from those measured externally. Research is ongoing to identify techniques to measure parameters such as void fraction [11,12] and local liquid temperature [12] but further work is required before they can be applied to obtain reliable quantitative values.

Numerical and analytical studies can provide insight into these flows in the absence of direct experimental evidence. To date, the bulk of microchannel two-phase research has been experimental, but several analytical and numerical studies have been performed. Chavan et al. [13] analytically examined the stability of two-phase forced convection in microchannels using a homogeneous flow linear stability model. This model was previously applied to macroscale flows. The model predicts the pressure response for a single channel to perturbations in inlet velocity and Chavan concludes that microchannel forced convective boiling is only stable for low subcooling and low applied heat fluxes. Consequently,

Contributed by the Heat Transfer Division of ASME for publication in the JOURNAL OF HEAT TRANSFER. Manuscript received February 13, 2008; final manuscript received October 7, 2008; published online October 15, 2009.

these systems are inherently unstable at practical operating conditions. Zhang et al. [10] modeled a single channel using a steady-state one-dimensional homogeneous model in which conjugate wall conduction was considered. The model showed reasonable agreement with experimental single channel data. This model was later extended to estimate the thermal performance for 3D logic architectures [14]. Ajaev and Homsy [15] numerically investigated constrained vapor bubbles next to a heated wall. The simulations included 2D and 3D steady bubbles in which condensation at colder regions of the interface balanced the evaporation at the heated regions, as well as the growth of a 2D bubble under higher thermal loads. Mukherjee and Kandlikar [16] used a level set method to simulate the growth of constrained bubbles in a superheated liquid showing good agreement with experiments in interface growth rates and overall bubble shape. The model was later used to investigate the role of inlet constrictions on the ejection of vapor bubbles from microchannels [17].

One assumption common to all of these models is that the liquid is incompressible. They also neglect the bubble nucleation process assuming a bubble already exists. Homogeneous models do not consider individual bubbles but treat the two-phase mixture as a single pseudofluid. It has been speculated that the rapid growth of bubbles in microchannels generates pressure pulses within the channel [18], but little to no research, either experimental or analytical, has focused on this aspect of confined flow boiling. Rapid gas production during severe accidents in light water reactors are known to generate significant water hammer pulses in macroscale systems [19]. This analysis examines the role liquid compressibility plays in the nucleation, growth, and associated heat transfer of vapor bubbles in confined channels. The results indicate the heat and mass transfer during nucleate boiling in microchannels is inhibited by the confined geometry. Single bubbles can also trigger additional nucleation elsewhere in the channel leading to increased flow instability. This analysis identifies a nondimensional parameter to characterize the transition from conventional to microscale flow boiling.

2 Numerical Model

The following one-dimensional fully compressible Lagrangian–Eulerian finite-volume scheme is formulated to investigate the effect confined geometries have on microchannel flow boiling. The channels considered for the numerical model are square in cross section. The Rayleigh–Plesset model, described in detail later, is used to predict the growth of a spherical bubble. This growth model has been used extensively in other fields such as cavitation [20], sonoluminescence [21], and boiling [22]. The simulations are restricted to bubble diameters less than 50% of the channel diameter to avoid situations where the walls cause the bubbles to become nonspherical.

In this model, the liquid is captured with the Eulerian elements, while each bubble is tracked as a single Lagrangian structure. The Lagrangian–Eulerian approach allows a coarser discretization in the Eulerian grids thereby increasing the maximum allowable time step, while at the same time, retaining subelement resolution for the size and location of the bubbles. A fully discretized two- or three-dimensional compressible model requires extremely short time steps to avoid CFL instability issues.

2.1 Nucleation. For a two-phase microchannel heat exchanger to be effective for applications such as microprocessor cooling, boiling must occur well below the kinetic limit for homogeneous nucleation. In a practical heat exchanger, wall structures serve as heterogeneous nucleation sites. Nucleation starts because vapor embryos trapped in wall cavities are conducive to growth under the appropriate conditions. A nucleation site activates when the internal vapor pressure in a wall cavity exceeds the combination of surface tension and the external pressure,

$$P_b \geq P_l + \frac{2\sigma}{r_{\mathrm{ns}}} \tag{1}$$

The pressure inside the cavity is at the vapor pressure at the local wall temperature. The criterion can be rewritten as

$$T_w \geq T_{\mathrm{sat}}\left(P_l + \frac{2\sigma}{r_{\mathrm{ns}}}\right) \tag{2}$$

2.2 Bubble Initial Conditions. Initially, the interface is stationary,

$$\dot{r}_b = 0 \tag{3}$$

The nucleating bubble is treated as a sphere throughout the simulated growth and the initial volume is

$$V_b = \frac{4}{3}\pi r_{\mathrm{ns}}^3 \tag{4}$$

The bubble temperature is the local wall temperature, $T_b = T_w$, while pressure is the saturation pressure at the bubble temperature, $P_b = P_{sat}(T_b)$, and mass is obtained from the ideal gas law:

$$m_b = \frac{P_b V_b}{R T_b} \tag{5}$$

2.3 Heat and Mass Transfer. After a bubble has nucleated, heat and mass transfer between the liquid and the vapor are monitored. During the early inertia-controlled stage of growth, the vapor inside the bubble remains isothermal due to the thin thermal boundary layer surrounding the bubble. The bubble pressure remains constant for an isothermal bubble. As the bubble grows into the thermally controlled regime, transport of energy across the thermal boundary layer surrounding the bubble eventually limits the evaporation process.

To accurately capture the heat and mass transfer into a bubble growing in a microchannel, the full three-dimensional thermal convection problem should be solved, but this is computationally expensive and time consuming. In this study, the heat transfer rate is calculated as

$$\dot{q}_{\mathrm{lv}} = A_{b,s} h_{\mathrm{tp}} (T_w - T_b) \tag{6}$$

The two-phase heat transfer coefficient, h_{tp}, can be determined from a microchannel heat transfer correlation [23,24] or taken as a fixed effective value.

Considering the correlations are not derived for single bubble physics, the heat transfer coefficient in this study is a constant. Significant insight into the expected behavior can be obtained with this one-dimensional model by examining reasonable limits to the thermal transport. Infinite heat transfer, corresponding to an isothermal bubble at the nucleation temperature, provides the upper limit to the heat transfer into the bubble, while an effective two-phase heat transfer coefficient on the order of the single-phase convective coefficient serves as the lower limit. The heat transfer coefficient for a single bubble should be greater than the spatially averaged heat transfer coefficient typically reported for flow boiling in a microchannel. Except for the section where the effect of the heat transfer coefficient is evaluated, the analysis presented in this article assumes infinite heat transfer corresponding to inertia-controlled growth.

Mass transfer into the bubble is calculated directly from the heat transfer to the bubble and an enthalpy balance. The model accounts for the sensible heat required to raise the vaporized liquid to the bubble temperature, any temperature changes to the previous mass in the bubble, and the latent heat of vaporization, i_{lv}.

$$\frac{dm_b}{dt} = \frac{\dot{q}_{\mathrm{lv}} - m_b C p_v \dfrac{dT_b}{dt}}{C p_l (T_b - T_l) + i_{\mathrm{lv}}} \tag{7}$$

The saturated vapor inside the bubble is modeled as an ideal gas. Changes in pressure with respect to temperature are given by the Clausius–Clapeyron equation [25].

$$\left(\frac{dP_b}{dT_b}\right)_{\text{sat}} = \frac{i_{\text{lv}}}{T_b(v_v - v_l)} \tag{8}$$

Differentiating the ideal gas law and substituting Eq. (8) provides the expression for the change in temperature with respect to specific volume

$$\left(\frac{dT_b}{dv_v}\right)_{\text{sat}} = \frac{P_b}{R - \dfrac{v_v i_{\text{lv}}}{T_b(v_v - v_l)}} \tag{9}$$

The bubble pressure is the saturation pressure at the bubble temperature. For many fluids including water, the saturation pressure is well correlated with the saturation temperature using a form derived from the Clapeyron equation [25].

$$\ln P_{\text{sat}} = \frac{T_c \ln P_c}{T_c - T_{\text{boil}}}\left(1 - \frac{T_{\text{boil}}}{T_b}\right) \tag{10}$$

where pressures are in bars and temperatures are in Kelvin.

2.4 Interface Velocity. The Rayleigh–Plesset equation models the growth or collapse of a spherical bubble from an active nucleation site in an infinite incompressible fluid [20].

$$\frac{P_b(t) - P_l(t)}{\rho_f} = r_b\ddot{r}_b + \frac{3}{2}(\dot{r}_b)^2 + \frac{4\eta_l \dot{r}_b}{r_b} + \frac{2\sigma}{\rho_l r_b} \tag{11}$$

The driving pressure gradient, $P_b - P_l - 2\sigma/r_b$, between the vapor and liquid can vary in time. In order to remain consistent with the geometry for which Rayleigh–Plesset equation was derived, the bubble is assumed to grow as a sphere. Consequently, the results presented correspond to early bubble growth where the shapes of bubbles in square channels have yet to be influenced by the walls. The accuracy of the Rayleigh–Plesset model should be questioned for bubbles that have grown to the size of the channel. As the interface approaches a wall, the interface velocity would be better approximated by a lubrication theory approach.

2.5 Liquid. The liquid is captured using staggered Eulerian grids consisting of the channel with the bubble volumes subtracted from each cell in which a bubble or part of a bubble exists. The linearized equation of state (Eq. (15)) accounts for the compressibility of the liquid, and changes in volume are captured through the use of the local void fraction, α. The grids are one-dimensional with cell divisions in the streamwise direction. Each element is uniform in length but can have different transverse dimensions allowing for varying channel cross sections. The staggered grid avoids the odd-even numerical instability arising from pressure-velocity coupling in centrally differenced convection terms [26]. The pressure grid is used to calculate density, pressure, enthalpy, and temperature, while the velocity grid is used only for liquid velocity.

2.6 Equations. The numerical approach solves the one-dimensional Navier–Stokes equations along with the convective energy equation and an appropriate equation of state.

$$\frac{\partial(\rho_l \alpha)}{\partial t} + \frac{1}{A_{\text{ch}}}\frac{\partial}{\partial z}(\rho_l U_l \alpha A_{\text{ch}}) = \sum_{k=1}^{nb} \frac{d\rho_{v,k}}{dt}\frac{A_{b,k}}{A_{\text{ch}}} \tag{12}$$

$$\frac{\partial}{\partial t}(\rho_l U_l \alpha) + \frac{1}{A_{\text{ch}}}\frac{\partial}{\partial z}(\rho_l U_l^2 \alpha A_{\text{ch}}) = -\frac{\partial P_l}{\partial z} + \frac{1}{A_{\text{ch}}}\frac{\partial}{\partial z}\sum \mathcal{F} \tag{13}$$

$$\frac{\partial}{\partial t}(\rho_l i_l \alpha) + \frac{1}{A_{\text{ch}}}\frac{\partial}{\partial z}(\rho_l U_l i_l \alpha A_{\text{ch}}) = \frac{1}{A_{\text{ch}}}\left(P_h h_{\text{tp}}(T_w - T_l) - \frac{\partial \dot{q}_{\text{lv}}}{\partial z}\right) \tag{14}$$

$$P_l = P_{l,0} + a_l^2(\rho_l - \rho_{l,0}) \tag{15}$$

These equations account for mass transfer between the phases and any forces, $\mathcal{F}$, including viscous shear, imposed on the liquid by the liquid-vapor or liquid-wall interfaces. The equation of state is a linearization about a reference point of 1 atm at room temperature for a liquid speed of sound, a_l. The bubble interactions with the liquid grids change the cell volumes and flux areas through the local void fraction, α.

2.7 Solution Algorithm. The numerical model is solved with an iterative segregated system. Semi-implicit temporal discretization prevents large overshoots in pressure and void dependent quantities, such as two-phase frictional pressure drop and heat transfer coefficient, while centrally differenced spatial discretization allows propagation in both directions. A tridiagonal matrix algorithm (TDMA) [26] solves each matrix system.

For each time step, the wall temperature, liquid density, liquid velocity, and liquid enthalpy or temperature are solved in order in an iterative loop. The new wall temperatures and liquid pressures are used to determine if any new nucleation sites have become active. Any new bubbles are initialized and the evolution of existing bubbles is calculated. A time step is considered to converge when the difference norm of the residuals has fallen by at least three orders of magnitude and total mass and energy are conserved to within 0.1%.

A grid convergence study was performed to determine the influence discretization has on the prediction of bubble growth rates. Eulerian grids of 75, 150, and 300 elements were used to predict the growth of a bubble with a constant pressure of 1.8 bar in a 2 cm long channel. Little difference was observed between the grids with 150 and 300 elements. Grid densities of 150 elements/cm are used for the remaining simulations.

3 Results and Discussion

3.1 Initial Bubble Growth. For this discussion, *confinement* in any direction refers to an obstruction preventing the liquid from moving in a direction, while *constrained* indicates the bubble interface is pressed against the obstruction preventing further growth in that direction. A truly unconfined bubble only exists in theory as practical systems are enclosed by boundaries. However, many systems are large enough that bubble growth is well approximated by the theory for unconfined bubbles. This is not the case for microchannels.

Let's review unconfined inertia-controlled bubble growth before exploring bubbles in microchannels. An *unconfined* isothermal bubble grows according to the Rayleigh–Plesset equation (Eq. (11)). For isothermal or inertia-controlled bubble growth, the heat transfer is sufficient to maintain a constant bubble pressure. After an initial period of acceleration, the interface asymptotes to a constant velocity presuming $r_b \gg r_{b,0}$.

$$\dot{r}_b = \left[\frac{2(P_b - P_l)}{3\rho_l}\right]^{1/2} \tag{16}$$

In this situation, the volume of the spherical bubble increases as t^3 because the volume goes as r_b^3.

Now assume the bubble is constrained in one dimension, by a pair of parallel walls in a high-aspect ratio channel for example. Such a bubble takes on the shape of a squat cylinder or a pancake. The diameter is free to grow but the thickness is restricted by the spacing of the parallel walls. If there is adequate heat transfer to keep the bubble pressure constant, the free interface still asymptotes to a constant velocity. The free portion of the interface remains inertia-controlled even though part of the interface is constrained. Neglecting wall friction this velocity is given by Eq. (16). In this case the volume grows with t^2 since the bubble is constrained by the spacing of the parallel walls. Following this rationale, the volume of an inertia-controlled bubble constrained in two dimensions, say by the four walls of a long rectangular

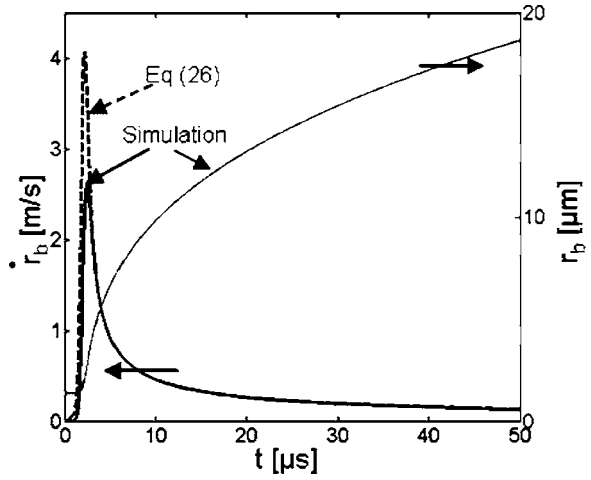

Fig. 1 Growth history for a bubble nucleating from a cavity (d_{ns}=2.75 μm, T_b-T_w=20 K) in a 100 μm square microchannel

channel, increases linearly with time. As discussed later, experiments by Fogg and Goodson [27] demonstrated that these trends do not hold for confined boiling in microchannels.

The radial growth for a confined bubble nucleating from a 2.75 μm diameter cavity in a 100 μm square channel is depicted in Fig. 1. Inertia-controlled growth is dominated by the liquid inertia. During this stage, heat and mass transfer are sufficient to maintain the bubble pressure at its initial value. After an acceleration period the interface velocity asymptotes to the value given by Eq. (16).

At some point, the channel confinement significantly affects growth. For water the specific volume of the liquid phase is three orders of magnitude smaller than the vapor phase. As a bubble grows, the liquid pressure increases to accommodate the rapidly displaced volume of liquid. The capacity of the channel to deal with this liquid diminishes with decreasing cross-sectional area. The increase in pressure propagates axially through the channel both upstream and downstream.

The resulting *confinement pressure*, P_{con}, comes from the rapid reduction in volume available for the liquid to occupy. It arises in the numerical model from terms involving $d(\rho\alpha)/dt$. Note that P_{con} is not influenced by the water bulk velocity. The additional term corresponding to the P_{con} superimposes onto the frictional and accelerational contributions to the pressure profile.

One can derive a simple expression for P_{con}, by considering a control mass of liquid surrounding a growing bubble, which is compressing the liquid. Symmetry allows the analysis to consider only $\frac{1}{2}$ of the bubble. The control mass should be sized, $dx=a_l dt$, such that any change in pressure due to the expanding bubble propagates right to the edge of the control mass. Since P_{con} depends on the change in volume, smearing the bubble into a rectangular volume, which spans the channel cross section, simplifies the analysis without changing the results for this one-dimensional derivation.

The choice of the control mass ensures that

$$V_l d\rho_l = -\rho_l dV_l \tag{17}$$

An increase in the volumetric growth rate of the bubble causes the volume of the control mass to shrink at $\frac{1}{2}$ the rate of the bubble growth.

$$\frac{d\dot{V}_b}{2} = -d\dot{V}_l \tag{18}$$

Although liquids are highly incompressible, they still are slightly compressible. The change in liquid pressure with respect to a change in density is

$$\frac{dP}{d\rho_l} = a_l^2 \tag{19}$$

After combining Eqs. (17)–(19) and recalling that $dx=a_l dt$, the change in pressure due to confinement, dP_{con}, is

$$dP_{\text{con}} = \frac{\rho_l a_l d\dot{V}_b}{2A_{\text{ch}}} \tag{20}$$

By integrating Eq. (20) from the initial condition of ($P_{\text{con}}=0$ and $\dot{V}_b=0$), the confinement pressure as a function of bubble volumetric growth rate is obtained.

$$P_{\text{con}} = \frac{\rho_l a_l \dot{V}_b}{2A_{\text{ch}}} \tag{21}$$

This derivation is remarkably similar to a piston compressing liquid in a one-dimensional duct [28]. The piston velocity corresponds to

$$\overline{\dot{r}_b} = \frac{\dot{V}_b}{2A_{\text{ch}}} \tag{22}$$

and P_{con} can be rewritten as

$$P_{\text{con}} = \rho_l \overline{\dot{r}_b} a_l \tag{23}$$

This pressure is the same form as the Joukowsky pressure [29] from water hammer theory. Thus, a bubble growing rapidly in a microchannel is comparable to a fast closing valve in a pipe, except the induced water hammer pressure influences bubble expansion. Increasing thermal loads and decreasing channel cross section exacerbate these water hammer effects. Although Eq. (23) provides the instantaneous liquid pressure, the maximum liquid pressure is estimated from the bubble pressure using the equality in Eq. (1). The confinement pressure can also be thought of as a bubble-generated acoustic pulse. Equation (22) corresponds to the particle velocity in one-dimensional acoustics and Eq. (23) is the sound pressure. The specific acoustic impedance is $P_{\text{con}}/\overline{\dot{r}_b}=\rho_l a_l$.

One should note that the derivation above does not assume a particular growth behavior for the bubble. Since the confinement pressure depends on the volumetric growth rate, Eq. (21) can be applied to either inertia- or thermal-controlled growth. Of the two regimes, inertia-controlled growth will yield the higher confinement pressures for a given wall superheat.

If the water hammer or acoustic pulse reflections are neglected, confined bubble growth reaches a steady state when the effective bubble driving pressure balances the confinement pressure.

$$P_b - P_{f,0} - \frac{2\sigma}{r_b} = \frac{\rho_f a_f \dot{V}_b}{2A_{\text{ch}}} \tag{24}$$

When the interface is not constrained, the bubble remains spherical and the volumetric growth rate is

$$\dot{V}_b = 4\pi r_b^2 \dot{r}_b \tag{25}$$

Substituting Eq. (25) into Eq. (24) and specifying $P_b-P_{l,0}=2\sigma/r_{\text{ns}}$ yields the radial growth rate as a function of bubble radius,

$$\dot{r}_b = \frac{\sigma A_{\text{ch}}(1 - r_{\text{ns}}/r_b)}{\pi\rho_l a_l r_{\text{ns}} r_b^2} \tag{26}$$

As shown in Fig. 1, Eq. (26) agrees with the numerical solution once the liquid pressure reaches steady state.

For a high-aspect ratio channel, the walls quickly constrain the

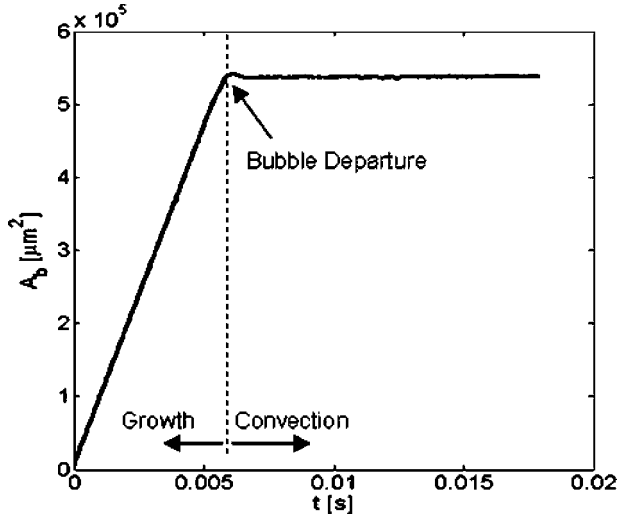

Fig. 2 Measured visible area of a pancake-shaped bubble growing in a 1000 μm by a 25 μm channel. Note the area grows linearly for this confined bubble and constrained in one dimension.

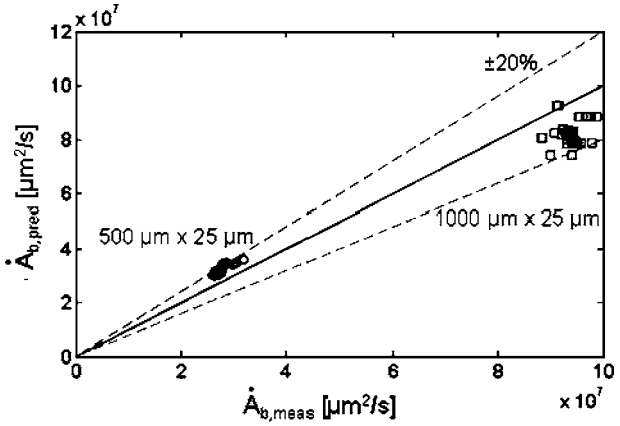

Fig. 3 Bubble growth rates measured in Ref. [29] are predicted within ±20% by the confinement pressure model

interface in one direction. In this case, the interface curvature is fixed by the critical channel dimension and the volumetric growth is, approximately,

$$\dot{V} = 2\pi r_b \dot{r}_b H_{\text{ch}} \tag{27}$$

The resulting radial growth rate in the unconstrained dimensions is

$$\dot{r}_b = \frac{2\sigma W_{\text{ch}}(1 - 2r_{\text{ns}}/H_{\text{ch}})}{\pi \rho_l a_l r_{\text{ns}} r_b} \tag{28}$$

Note the volumetric growth rate is constant because the effective driving pressure no longer varies with bubble radius.

Data collected by Fogg and Goodson [27] support this result. In the experiment, single inertia-controlled bubbles are simulated by injecting air through a 10–15 μm orifice in the center of high-aspect microchannels (1000×25 μm^2 and 500×25 μm^2). The supply air pressure, liquid flow rate, and liquid pressure drop are recorded by a data acquisition system, while a high-speed camera captures the bubble growth at 5000 fps. The measured evolution of the unconstrained cross-sectional bubble area is shown in Fig. 2. Unlike an unconfined bubble, constrained between infinite parallel plates, the pancake-shaped bubbles do not grow volumetrically as t^2 but rather linearly with time as predicted by Eqs. (27) and (28). As shown in Fig. 3, the model estimates the growth rates well. The ability to predict not only the temporal trend but also the growth rate indicates the model captures the key physics of confined bubble growth. Lee et al. [30] also measured constant volumetric growth rates for thermally grown pancake bubbles. This trend agrees with that predicted by the model, but may be associated with the temporal variation in the bubble pressure, which is not directly measured.

Reducing the channel cross-sectional area affects bubble growth as shown in Fig. 4. In all cases, initial growth is dominated by liquid inertia and channel confinement is negligible. Eventually the bubble grows large enough such that confinement pressure becomes significant relative to the bubble pressure, thereby retarding growth. The radius at which the confinement effect becomes noticeable scales with channel cross section. None of the bubble interface velocities in Fig. 4 reach the Rayleigh–Plesset asymptotic velocity (Eq. (16)) because feedback from the confinement pressure retards the volumetric growth. For a given wall superheat, the volumetric growth rate of bubbles in smaller channels is lower than that of bubbles in larger channels since the confinement pressure feedback occurs earlier in the growth process.

This result is particularly interesting since bubble growth in microchannels is often characterized as "explosive" [31] or "rapid" [32], yet this analysis predicts that microchannel bubble growth only appears rapid because of the relative scale of the channels to the bubbles. As shown in Table 1, the few measurements of interface velocities reported in the literature are lower than the Rayleigh–Plesset equation predictions for unconfined inertia-controlled growth at equivalent heating conditions. Although these studies seem to support the confinement pressure theory, they were not designed to capture the parametric dependence pertaining to growth velocities in microchannels. Based on the measurements reported, one is unable to determine whether the bubbles experience inertia- or thermal-controlled growth. The limited observations are insufficient to draw reliable conclusions.

Figure 5 illustrates the wall superheat effect on bubble growth. The pressure difference driving interface motion increases with temperature and leads to faster bubble growth. Surface tension is responsible for the time lag from the initiation of growth to the rapid acceleration of the interface. At the higher wall superheats

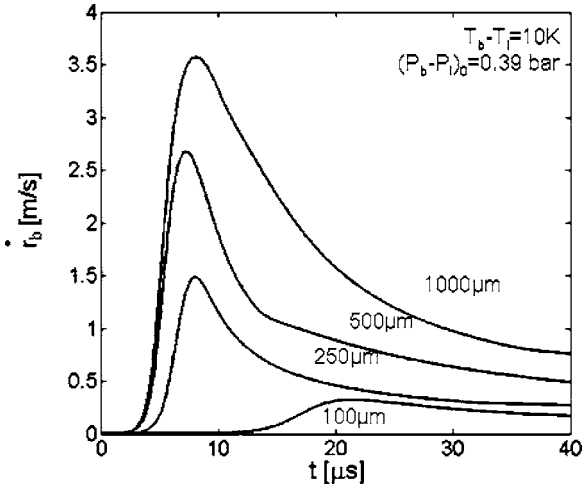

Fig. 4 The effect of reducing the channel cross-sectional area for bubbles nucleating at a wall superheat of 10 K, corresponding to a bubble overpressures of 0.39 bar. None of the bubble interfaces reach the asymptotic Rayleigh–Plesset velocity (Eq. (16)) before confinement retards growth.

Table 1 Comparison to interface velocities in the literature

Reference	Channel	Fluid	Max wall superheat (K)	Liquid pressure (kPa)	Max interface velocity (m/s)	Rayleigh–Plesset velocity (Eq. (16)) (m/s)
[31]	200–310 μm triangular	Water	6	101[a]	0.3	3.8
[40]	990×207 μm^2 rectangular	Water	9.5	101[a]	3.5	5.0
[41]	D_h=51.7 μm trapezoidal	Water	23	210	0.045	8.7

[a]Pressure not reported and assumed to be atmospheric.

the curvature of the bubble embryo is higher, and small increases in bubble radius rapidly reduce the opposing Laplace pressure, $2\sigma/r_b$. Higher superheats also lead to increased mass transfer.

One of the most significant unknowns in this model is the effective heat transfer coefficient. Existing experiments evaluate only average heat transfer. No microchannel studies for single bubbles have even been attempted. Lacking quality experimental data, models must assume a fixed value, as done in this study, or rely on heat transfer correlations [23,24] which are also time and spatially averaged.

Figure 6 shows how the heat transfer coefficient influences bubbles growing in water in a 100 μm square channel. The lowest value, 50 kW/m^2 approximates the value for single-phase liquid flow and serves as a lower limit. The upper limit corresponds to infinite heat transfer maintaining a constant bubble temperature and pressure. At lower heat transfer coefficients, bubble expansion reduces the bubble pressure and temperature due to insufficient phase change. However, heat transfer during inertia-controlled bubble growth is nearly infinite. After time, the superheat in thermal boundary layer becomes depleted and limits growth. From the analysis of Plesset and Zwick [22], this boundary layer grows roughly as the square root of time, $\delta_{\text{th}}\approx(\Lambda_l t)^{1/2}$ for a bubble in an otherwise quiescent infinite liquid at uniform superheat. For microchannels, the proximity of multiple walls enhances heat transfer. The Kandlikar correlation [33] predicts two-phase time-averaged microchannel heat transfer coefficients on the order of 100 kW/m^2 to 1 MW/m^2 for water depending on flow and heating conditions and channel geometry. The initial value for the heat transfer coefficient during bubble growth is much higher than the single-phase value and should be higher than the average heat transfer coefficients for microchannel flow boiling. Considering average h_{tp} is on the order of several hundred kW/m^2, the assumption of inertia-controlled growth for a small bubble appears reasonable. One should note that the confinement pressure depends on the volumetric growth rate of the bubble, whether or not bubble growth is inertia-controlled or heat transfer-controlled. The choice of a particular heat transfer coefficient merely changes the amplitude and evolution of the bubble-induced pressure pulse.

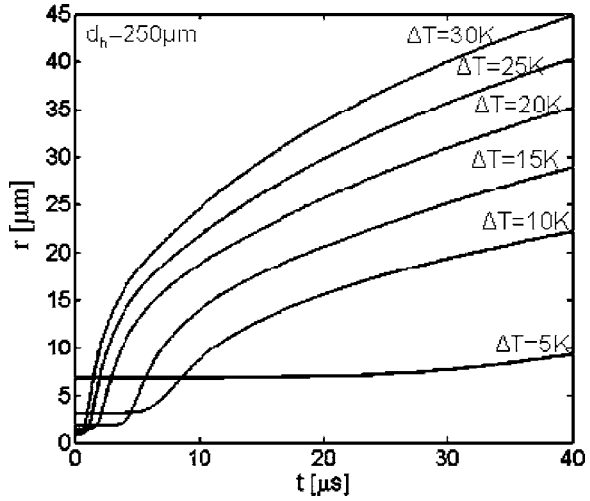

Fig. 5 The influence of wall superheat on a bubble growing in a square 250 μm channel

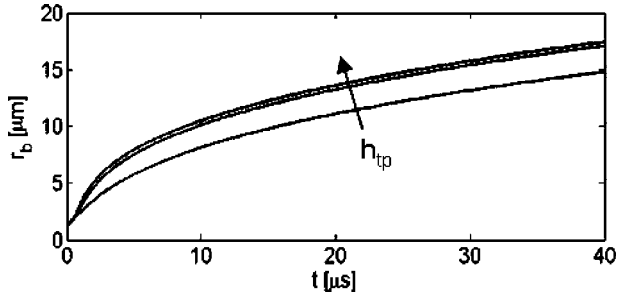

Fig. 6 The effect of heat transfer coefficient on bubble growth. The lines correspond to h_{tp}=50 kW/m^2, 500 kW/m^2, 5 MW/m^2, and 50 MW/m^2. The largest two lines are virtually on top of each other.

3.2 Heat Transfer. The majority heat transferred in flow boiling is due to phase change. The instantaneous heat transfer rate into the bubble is

$$\dot{q}_b = \rho_v \dot{V}_b i_{\text{lv}} \tag{29}$$

For an isothermal bubble ρ_v remains constant and the heat transfer rate is directly proportional to bubble growth. As discussed in Sec. 3.1, the bubble volumetric growth rate in microchannels is reduced from that in large channels because the confinement pressure retards growth. Thus, two-phase heat transfer is reduced for nucleate boiling in microchannels.

3.3 Channel Systems. The confinement pressure propagates through channel systems as water hammer or acoustic pressures travel through piping and duct systems. The pulses propagate both upstream and downstream. Microchannel heat exchangers contain various components including manifolds and headers, reducing and expansion junctions, inlet and outlet ports, as well as the tubing connecting the heat exchangers to the pump, reservoirs, and condenser. The combination of these various geometries dictates pressure pulse propagation.

To demonstrate the role geometry plays in pulse propagation and the ultimate impact on microchannel flow boiling, two single channel chip designs with different manifolds are simulated. The simulation includes system components from the channel up to inlet and outlet tubing. Both manifold geometries, shown in Fig. 7, are from single microchannel experiments [2,34]. The primary difference between the two designs lies in the manifold-to-channel transition. In the first design, the manifold suddenly steps down to the channel size, while in the second, the manifold tapers to the channel dimensions. The channels are 100 μm square and 2 cm long. The straight rectangular manifolds measure 600 μm wide, 250 μm deep, and 1 cm long [2]. The rectangular portions of the tapered manifolds measure 1000 μm wide by 100 μm deep and 9 mm long. They taper to the channel width over 1 mm creating a manifold 1 cm in total length [34]. The dimensions of the other components are summarized in Table 2. De-ionized water flowing

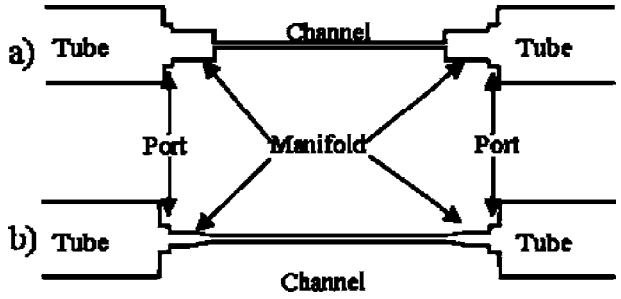

Fig. 7 Schematic of experimental manifold designs used in simulations to determine effect system design

at a Re=0.66 serves as the working fluid.

Figure 8 shows the pressure evolution inside the two channel systems for a bubble, located 1.45 cm ($z=0$) from the inlet manifold-channel junction, nucleating at a superheat of 20 K. This superheat corresponds to an initial pressure difference of $P_b - P_{l,0}=0.91$ bar. The bubble remains isothermal throughout its growth. At $t=3.5$ μs, the initial pulse reaches the transition to the outlet manifold. The reflected and transmitted portions of the pulse are seen propagating shortly thereafter. For the straight manifold, the portion of the pulse transmitted to the manifold is 12.5% of the pulse magnitude. The tapered manifold transmits 18.4% due to the more gradual area reduction. The reflections are inverted due to the expansion, locally reducing the liquid pressure. The pressure remains positive because they are superimposed on the incoming portion of the initial pulse.

At 10.5 μs, the upstream side of the initial pulse reaches the inlet manifolds. The reflections off the outlet manifolds have reached the bubble. An isothermal bubble approximates a constant pressure boundary leading to full reflections of incoming pulses.

By 16 μs, the initial pulse has reflected off the inlet manifold. The ratios of the reflected and transmitted pulses for each manifold design are the same as that for those at the outlet manifolds. The downstream pulse has also reflected off the manifold-port junction. Note that the pulse amplitudes transmitted into the tubing are negligible due to the large expansion between the ports and the tubing.

Direct experimental evidence of water hammer propagation in microchannel systems is difficult to obtain due to the spatial constraints imposed by the channels. The common measurement of inlet and outlet pressure in the tubing connected to the manifolds is incapable of capturing these pressure fluctuations due to the large expansions reflecting the pulses back into the system. The large cross-sectional area of the tubing readily absorbs any transmitted portion greatly reducing the measurable amplitude. A high-speed pressure sensor located in the microchannel itself needs to be developed to directly measure the water hammer pulses.

At 27 μs, multiple reflections have superimposed near the channel inlet to create a depression in the local liquid pressure below the operating pressure. As the bubble grows, the liquid pressure profile evolves ($t=44$ μs) with the confinement pressure propagation dictated by the channel system geometry. In the final set of profiles ($t=56$ μs), the multiple reflections superimpose creating a large pressure depression. In the straight manifold this depression is 10.0% of the bubble overpressure, $2\sigma/r_{ns}$, below the baseline pressure. For the tapered manifold, it is 14.4% below the baseline.

Figure 9 depicts the time history of the radial velocity and local liquid pressure for the bubble in the straight channel. After the initial acceleration, the bubble grows according to Eq. (26) until the first reflection off the manifold-channel junction returns to the bubble location. The bubble responds to the reduction in local liquid pressure by increasing its growth rate. This interface velocity remains at the increased level after the arrival of the manifold reflection because the bubble continues to emit a pressure front that negatively reflects back to the bubble location. Clearly, the channel system geometry significantly influences how the bubble-induced water hammer pressures propagate in microchannel systems influencing bubble growth, departure, convection, and nucleation. This feedback from the reflections of the bubble-induced water hammer indicates the channel system geometry can be engineered to manipulate the bubble growth and heat transfer rates.

3.4 Bubble Nucleation and Growth. The confinement pressure inhibits bubble growth but its subsequent propagation has the potential to promote additional nucleation. Water hammers are known to cause cavitation and water column separation [35]. Column separation in conventional channels usually occurs at one end of the water column when the liquid inertia essentially pulls the column away from a boundary creating a large void. Cavitation regions with low void fraction, known as dispersive column separation, are created by the propagation of a negative pulse slightly less than the local saturation pressure. Two negative pulses passing each other can lead to intermediate column separation as the superposition reduces the local pressure below the vapor pressure. Cavitation has been induced in small diameter channels with low-frequency ultrasound [36]. What remains to be answered is whether or not pressure depressions from water hammer reflections in microchannels can initiate and sustain boiling at normally inactive nucleation sites.

Figure 10 compares the local liquid pressure at $z=-11.4$ mm for the two channel systems in Sec. 3.3. In general, the evolution of the pressure is similar in both channels since the lengths and cross sections are comparable, but the taper does vary the reflections from the channel-manifold junction slightly. In the end, the tapered manifold leads to deeper troughs and higher peaks in the pressure for the situation simulated. The peaks in the liquid pressure can deactivate nucleation sites by forcing liquid into the cavities and flooding them. The troughs, on the other hand, have the potential to lead to additional nucleation.

As discussed before, a nucleation site will become active when the vapor pressure in a cavity exceeds the combination of surface tension and external pressure. Consequently, the pressure troughs should be capable of triggering bubble nucleation within the channel. Figure 11 displays the axial pressure distribution after the deepest trough has passed $z=-11.4$ mm in the tapered manifold design. As the trough passes ($t=56$ μs), a bubble nucleates from a 2.44 μm diameter cavity prescribed at $z=-11.4$ mm. The pressure increase due to the second bubble emerges in the confined channel. At $t=63$ μs, two pressure reflections are superimposed between the two bubbles to create a large pressure increase. A short while later, these pressure waves reflect off the bubbles creating another pressure trough, although this one is above the op-

Table 2 Dimensions of the microchannel systems depicted in Fig. 7. All lengths are in mm.

	Tubing			Port			Manifold			Taper				Channel		
System	W	H	L	W	H	L	W	H	L	W_1	W_2	H	L	W	H	L
A	2.8	2.8	20	1	1	0.5	0.6	0.25	10			NA		0.10	0.10	20
B	2.8	2.8	20	1	1	0.5	1	0.10	9	1	0.10	0.10	1	0.10	0.10	20

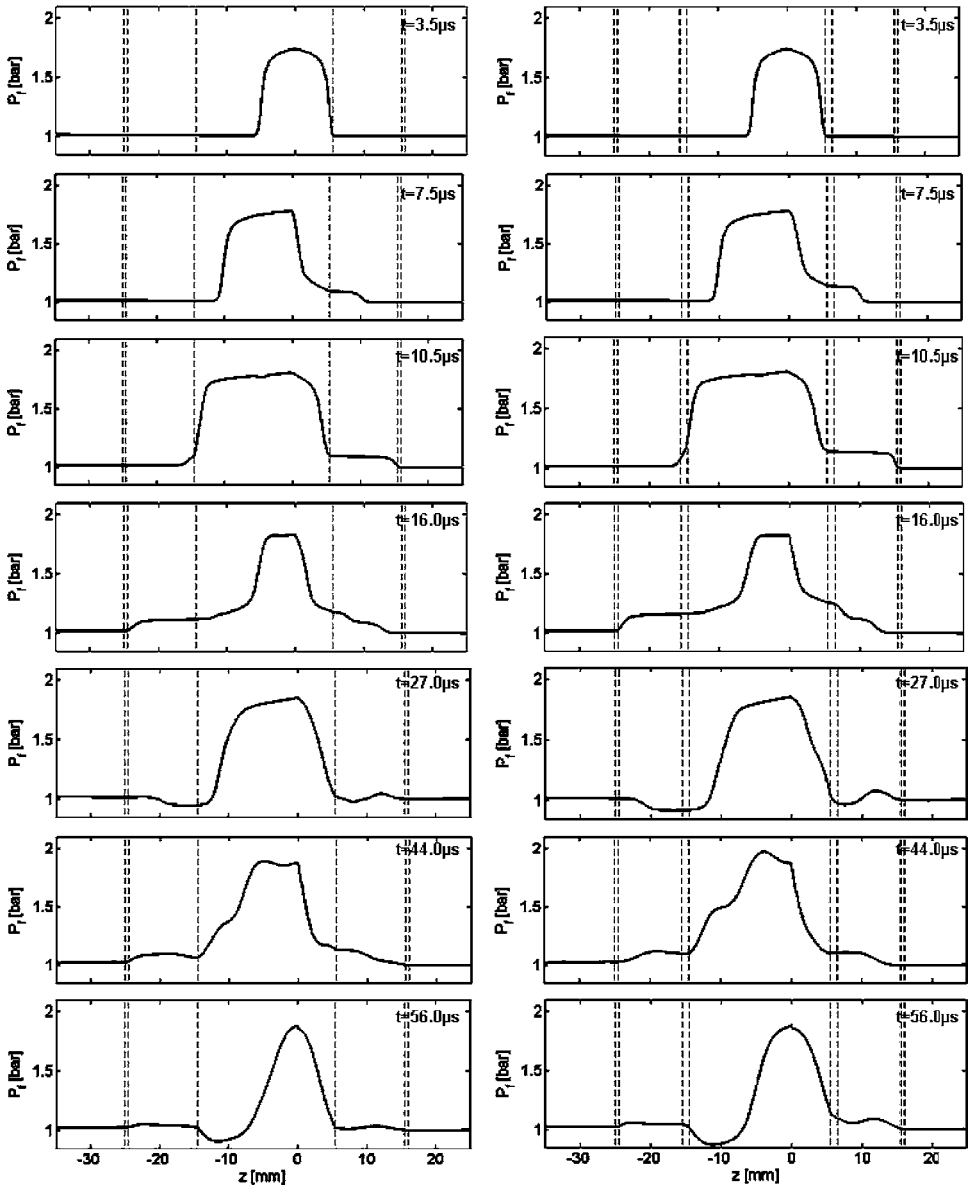

Fig. 8 Evolution of liquid pressure pulses in microchannel systems caused by the nucleation and growth of a single bubble. Straight manifold design (left) and tapered manifold design (right). The bubble nucleates at at $z=0$ for a wall superheat of 20 K and experiences inertia-controlled growth at a constant pressure throughout the simulation. The dashed lines denote axial locations with changes in channel geometry.

erating pressure. Figure 12 compares the time evolution of the liquid pressure for the tapered system with and without secondary nucleation at a location ($z=-6$ mm) between the two possible nucleation sites. The second bubble causes the maximum pressure to increase because the confinement pressure of the second bubble is added to the existing pressure. The oscillation period decreases since the pulse propagation length is between the two bubbles (11.4 mm) instead of the first bubble and the inlet manifold (15 mm).

Since the propagation of the acoustic pressures is dictated by a linear differential equation, the contributions of several bubbles superimpose in a channel. As displayed in Fig. 13, the bubble-induced water hammer from the second bubble influences the growth of the first bubble. For this case, the interface velocity of the first bubble is slightly affected by the second bubble, but the net effect on the bubble radius is negligible.

Because of the transient nature of the liquid pressure, the size of the nucleation site determines whether or not net bubble growth is realized at the secondary nucleation site. For a local wall superheat of 20 K, Fig. 14 plots the resulting bubble growth for nucleation sites of diameter 2.392 μm, 2.415 μm, and 2.557 μm from which bubbles start to grow once the local liquid pressure drops below 0.868 bar, 0.878 bar, and 0.936 bar, respectively. The minimum activation diameter for these conditions with the liquid pressure history in Fig. 10 is 2.3886 μm. Less than 30 nm means the difference between a bubble that continues to grow and one that collapses. If the nucleation site diameter is fixed, this corresponds to only a few tenths of a Kelvin in wall temperature. Therefore, for most wall temperatures greater than the minimum activation temperature, secondary bubbles will nucleate, grow, and depart in microchannels.

The additional nucleation and bubble growth generated by bubble-induced water hammer could have profound impacts on device performance. Vapor generated at lower than expected wall

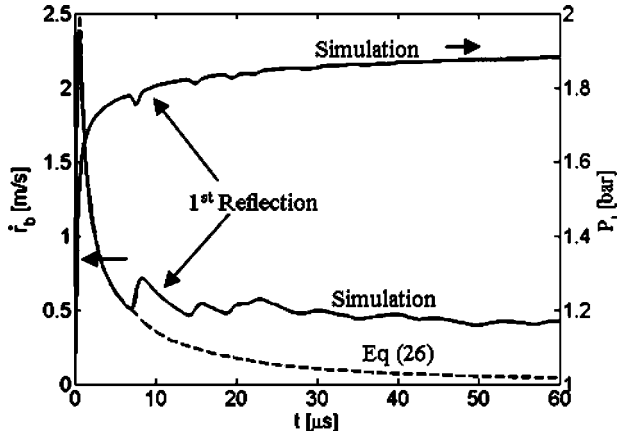

Fig. 9 Time history of the bubble radial velocity in the straight manifold channel. The negative water hammer reflections effectively increase the bubble growth rate.

temperatures improves heat transfer over short time periods. The thermal performance of similar channel geometries with different manifolds can vary significantly due to magnitudes of reflected water hammer pulses. Flow redistribution and associated instabilities will increase due to the increased channel pressure drop tied to the additional nucleation. In single microchannels, water hammer pulses can generate groups of bubbles at once similar to the compound relaxation instability observed by Zhang et al. [2]. The strong dependence on the overall system geometry makes it difficult to quantitatively compare results between different devices with the same channel dimensions.

3.5 Confinement Number. Microchannel flow boiling researchers have yet to identify a nondimensional parameter to describe the transition from conventional channels to microchannels. In the schemes proposed by Kandlikar and Grande [37] or Mehendale et al. [38], the size effect on flow boiling is characterized only by channel hydraulic diameter. For example, Kandlikar and Grande [37] classified flow boiling in channels as follows:

conventional channels: $d_h > 3$ mm
minichannels: 200 μm $< d_h \leq 3$ mm
microchannels: 10 μm $< d_h \leq 200$ μm
transition channels: 0.1 μm $< d_h \leq 10$ μm
molecular nanochannels: $d_h \leq 0.1$ μm

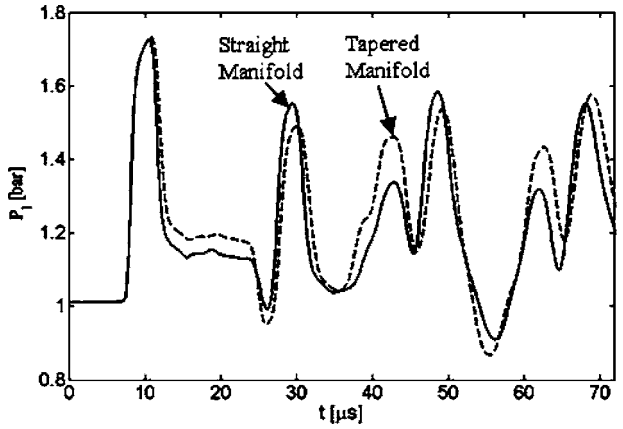

Fig. 10 Time evolution for the local liquid pressure at $z = -11.4$ mm. The bubbles nucleate at $T_{sup} = 20$ K in both systems. The minimum P_l for the straight manifold is 0.909 bar and 0.866 bar for the tapered manifold.

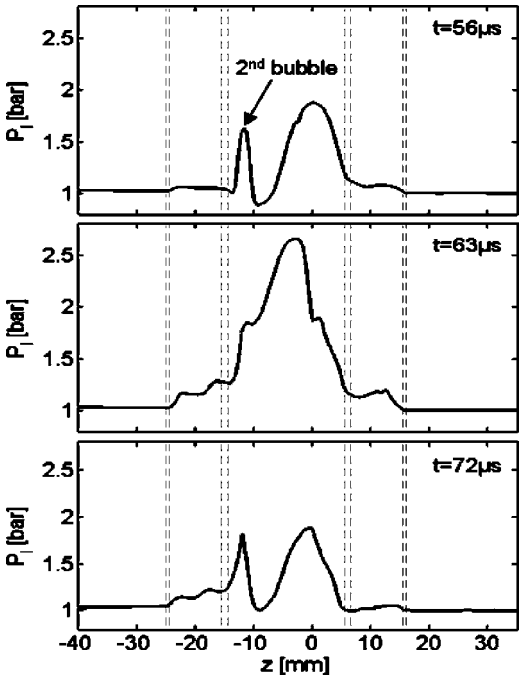

Fig. 11 The evolution of the static liquid pressure in the tapered channel if a 2.44 μm diameter cavity is located at $z = -11.4$ mm

Both classification schemes are based solely on qualitative experimental observations and do not necessarily reflect natural regime transitions due to fundamental physical phenomena.

A better system would predict phenomenological transitions using nondimensional numbers which may include the geometry, fluid properties, and other parameters indicative of shifts in the dominant physical mechanisms. Kew and Cornwell [39] recommended a confinement number,

$$\mathrm{Co}_{\mathrm{KC}} = \left[\frac{\sigma}{g(\rho_l - \rho_v) d_h^2} \right]^{1/2} \tag{30}$$

to differentiate between macroscale and microscale flow boiling. They found the flow characteristics and heat transfer were significantly different than macrochannel predictions when $\mathrm{Co}_{\mathrm{KC}} > 0.5$. For water at atmospheric pressure the transition based on this criterion is approximately 5 mm. The applicability of this number is questionable as scaling analysis typically indicates buoyancy is negligible for microchannels.

The increase in local liquid pressure is a fundamental confine-

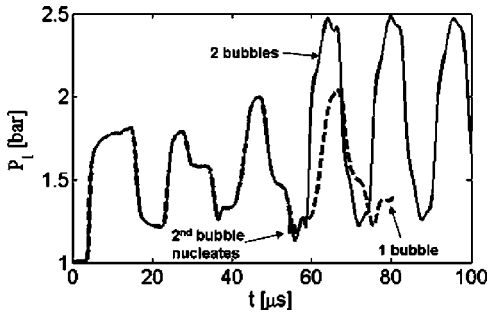

Fig. 12 Time history comparison of the liquid pressure at $z = -6$ mm for the tapered manifold channel with (solid line) and without (dashed line) additional nucleation from a 2.44 μm cavity at $z = -11.4$ mm

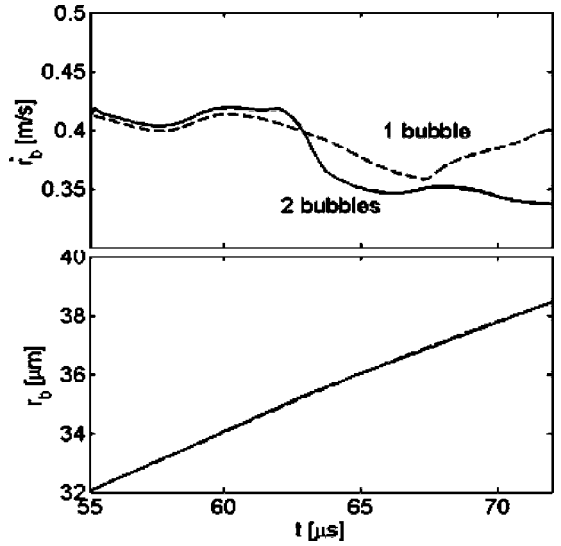

Fig. 13 Interaction of the second bubble in the tapered manifold channel with the growth of the first bubble

ment effect, presenting an opportunity to define a nondimensional number as the ratio of the confinement pressure to the bubble overpressure,

$$\mathrm{Co}_{\mathrm{FG}} \equiv \frac{P_{\mathrm{con}}}{P_b - P_{l,0}} \tag{31}$$

This number indicates magnitude of the feedback from the confinement pressure and can characterize the transition from conventional channels to microchannels. For channels large enough that the increases to the local liquid pressure are negligible, $P_{\mathrm{con}} \ll P_b - P_{l,0}$, $\mathrm{Co}_{\mathrm{FG}}$ is small. Large values for $\mathrm{Co}_{\mathrm{FG}}$ correspond to systems where the induced liquid pressure significantly inhibits volumetric growth.

Equation (31) can be applied to more than just single bubbles. The definition is rather general and can easily be applied to practical channel conditions at any instant in time. Since the confinement pressure is driven by the change in local liquid fraction, one could treat a pair of closely spaced bubbles that are about to coalesce as a single void. The volumetric growth rate of the combined void would then be used in Eq. (21). Furthermore, Eq. (31) could be applied to thermally controlled bubbles simply by using the saturation pressure, which corresponds to the instantaneous bubble temperature, for P_b. Only the parameter $P_{l,0}$ is fixed as it represents the liquid pressure the bubble would see if it is unconfined.

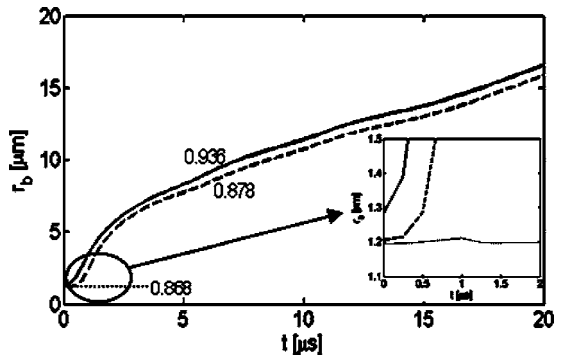

Fig. 14 The growth history for bubbles at $z=-11.4$ mm from sites nucleating at liquid pressures of 0.868 bar, 0.878 bar, and 0.936 bar for a $T_w=393.15$ K. These nucleation sites measure 2.392 μm, 2.415 μm and 2.557 μm in diameter, respectively.

For a certain set of assumptions, $\mathrm{Co}_{\mathrm{FG}}$ can be used to analytically estimate when a bubble becomes confined. Consider a relatively small inertia-controlled bubble that is not affected by channel confinement. The volumetric growth rate is determined by the interface velocity (Eq. (16)). The bubble overpressure can be approximated as $(P_b - P_{l,0}) = 2\sigma / r_{\mathrm{ns}}$. Substituting this relation and Eq. (21) into Eq. (31) allows the confinement number to be rewritten as

$$\mathrm{Co}_{\mathrm{FG}} = \frac{a_l \mathcal{G} r_b}{2A_{\mathrm{ch}}} \left(\frac{\rho_l r_{\mathrm{ns}}}{3\sigma} \right)^{0.5} \leq C_{\mathrm{con}} \tag{32}$$

The shape factor $\mathcal{G}$ accounts for the bubble geometry, which is introduced through the volumetric growth rate in Eq. (16). For a sphere $\mathcal{G} = 4\pi r_b$, while for a pancake-shaped bubble constrained in one dimension $\mathcal{G} = 2\pi H_{\mathrm{ch}}$. Equation (32) contains parameters representing the channel and bubble geometries as well as fluid properties. After specifying a confinement threshold, C_{con}, a confinement bubble diameter can be defined. For reference, the maximum radial velocity, noted in Fig. 1, for bubbles with superheats from 5 K to 30 K in channels (100 $\mu\mathrm{m} \leq d_h \leq 1$ mm) correspond to $0.11 < C_{\mathrm{con}} < 0.41$. The peak radial velocity occurs after P_{con} overcomes the driving pressure.

Ultimately, the threshold, C_{con}, at which channel confinement significantly influences bubble growth must be determined from experimental data. Such experiments need to measure both bubble growth and pressure over the growth cycle of single bubbles. A measurement of the bubble pressure is virtually impossible in heat transfer studies. With the exception of Ref. [29], the authors are unaware of any other study in the literature which monitors both these parameters for single bubbles in small channels. Furthermore, the range of channel diameters in Ref. [29] is insufficient to ascertain the confinement threshold. In lieu of an experimentally determined C_{con}, a logical choice is 0.1 indicating P_{con} is at least one order of magnitude less than the bubble driving pressure. This somewhat arbitrary value appears reasonable based on the simulation results. Eventually suitable experiments will need to be performed to properly characterize the true transition from an unconstrained bubble to a confined one.

Utilizing Eq. (27) one can define a critical nondimensional bubble cross section where the bubble begins to become confined. For a spherical bubble in a liquid, this is a function of the liquid properties and wall superheat.

$$A_b^* \equiv \frac{\pi r_b^2}{A_{\mathrm{ch}}} = \frac{C_{\mathrm{con}}}{2a_l} \left(\frac{3\sigma}{\rho_l r_{\mathrm{ns}}} \right)^{0.5} \tag{33}$$

The critical value increases with superheat because P_{con} based on the Rayleigh–Plesset asymptotic velocity (Eq. (16)) increases only with $P_b^{1/2}$. For a threshold value of $C_{\mathrm{con}} = 0.1$, the nondimensional critical confinement bubble radius, $r_b^* = 2r_b/d_h$, for water in a square channel is approximately 2% of d_h. Hence, P_{con} becomes important for $r_b = 1$ μm, 10 μm, and 100 μm for $d_h = 100$ μm, 1 mm, and 1 cm, respectively. Assuming a bubble essentially stops growing once it departs from the wall, the effects of P_{con} are not realized for channels where the bubble departure diameter is less than the critical confinement diameter. These values qualitatively agree with experimental observations. For channels on the order of a few hundreds of micrometers, confinement is always observed. Millimeter-sized channels are reported to exhibit both conventional and microchannel behavior, while larger channels are well modeled by conventional theory. Note the above discussion assumes bubble pressure remains constant throughout the growth process. If bubble growth becomes thermally controlled, bubble growth slows, which would allow the bubble to become larger before the confinement pressure becomes significant.

4 Conclusions

Bubble-induced water hammers or acoustic pulses are one of the first confinement effects to be modeled. The additional acoustic pressure inherent to microchannel flow boiling plays an important role in the dynamic behavior of the flows. Depending on the level of superheat, the analysis predicts the amplitude of the acoustic pressure may be on the order of an atmosphere. The initial increase in liquid pressure due to channel confinement feeds back and reduces the bubble growth rate. Because growth diminishes with cross-sectional area, less heat is transferred as d_h decreases, provided all other conditions are identical. Consequently, microchannels do not improve the heat transfer for single bubbles during the early stages of nucleate boiling. The equations describing the generation of these acoustic pressures lead to a nondimensional number, $\mathrm{Co}_{\mathrm{FG}}$, capable of predicting when bubble growth and heat transfer will be significantly inhibited in microchannels.

The limited capacity to accommodate the mass displaced during the growth of a single bubble can lead to large pressure perturbations to the steady-state flow profile. The initial pressure waves inhibit further nucleation and growth and may deactivate potential nucleation sites, while the reflected waves decrease the local pressure to levels that can allow nucleation in regions incompressible analysis does not predict.

The design of a microchannel heat exchanger, including all components up to the inlet and outlet tubing, significantly influences the nucleation characteristics in the channels themselves. Sites that would not normally generate bubbles can become active due to the pressure depressions created by the reflected acoustic pressures. As a result, the boiling heat transfer characteristics of microchannel systems are tied to the system design. Although the error due to water hammer effects may fall within the experimental error of the measurements, the influence of liquid compressibility on metrics such as heat transfer rate and mass quality have yet to be quantified. Studies of identical microchannels and channel arrays may have vastly different heat transfer results due to differences in the manifold and tubing designs making it extremely difficult to compare the different data sets. Even different chips from the same processing batch might have large differences in performance due to the random distribution of potential nucleation sites within the channels.

The bubble-induced water hammer provides an additional design factor previous unidentified. Its impact is amplified with increasing thermal loads or diminishing channel dimensions. Increases in flow instability directly compete against the additional evaporation and associated heat transfer. Whether future channels will be manufactured to amplify or dissipate these pressure pulses depends on the net benefit imposed by these opposing effects.

Acknowledgment

Dr. Fogg was supported by the Naval Nuclear Propulsion Fellowship Program sponsored by Naval Reactors Division of the U.S. Department of Energy. The authors acknowledge the support of the Interconnect Focus Center, one of five research centers funded under the Focus Center Research Program, a Semiconductor Research Corporation program, and appreciate support from the Semiconductor Research Corporation through Task 1445.

Nomenclature

a = sound speed (m)
Co = confinement number
Cp = specific heat (J/kg K)
C_{con} = confinement threshold
d_h = hydraulic diameter (m)
$\mathcal{F}$ = force (N)
$\mathcal{G}$ = geometry factor (m)
h = heat transfer coefficient (W/m K)
H = height (m)
i = enthalpy (J/kg)
L = length (m)
m = mass (kg)
nb = number of bubbles
P = pressure (Pa)
P_h = heated perimeter (m)
q = heat transfer (J)
r = radius (m)
R = specific gas constant (J/kg K)
T = time (s)
T = temperature (K)
U = axial velocity (m/s)
V = volume (m^3)
W = width (m)
z = axial coordinate (m)
α = void fraction
δ_{th} = thermal boundary layer thickness (m)
Λ = thermal diffusivity (m^2/s)
η = kinematic viscosity (m^2/s)
ρ = density (kg/m^3)
σ = surface tension (N/m)
υ = specific volume (m^3/kg)

Subscripts

0 = reference value
b = bubble
boil = boiling at standard temperature and pressure
b,s = bubble surface
c = critical property
ch = channel
con = confinement
FG = Fogg–Goodson
KC = Kew–Cornwell
l = liquid
lv = liquid-to-vapor
meas = measured
ns = nucleation site
pred = predicted
RP = Rayleigh–Plesset
sat = saturation
sup = superheat
tp = two-phase
v = vapor
w = wall

References

[1] Prasher, R. S., Chang, J. Y., Sauciuc, I., Narasimhan, S., Chau, D., Chrysler, G., Myers, A., Prstic, S., and Hu, C., 2005, "Electronic Package Technology Development," Intel Technol. J., **9**(4), pp. 285–296.
[2] Zhang, L., Koo, J.-M., Jiang, L., Goodson, K. E., Santiago, J. G., and Kenny, T. W., 2001, "Study of Boiling Regimes and Transient Signal Measurements in Microchannels," 11th International Conference on Solid-State Sensors and Actuators, Munich, Germany, pp. 1514–1517.
[3] Qu, W. A., and Mudawar, I., 2002, "Transport Phenomena in Two-Phase Micro-Channel Heat Sinks," ASME Paper No. IMECE2002-33711.
[4] Peles, Y., 2003, "Two-Phase Boiling Flow in Microchannels—Instabilities Issues and Flow Regime Mapping," ASME Paper No. ICMM2003-1069.
[5] Boure, J. A., Bergles, A. E., and Tong, L. S., 1973, "Review of Two-Phase Instability," Nucl. Eng. Des., **25**, pp. 165–192.
[6] Carey, V., 1992, *Liquid-Vapor Phase-Change Phenomena*, Taylor & Francis, London.
[7] Balasubramanian, P., and Kandlikar, S. G., 2003, "High Speed Photographic Observation of Flow Patterns During Flow Boiling in Single Rectangular Minichannel," ASME Paper No. HT2003-47175.
[8] Hetsroni, G., Klein, D., Mosyak, A., Segal, Z., and Pogrebnyak, E., 2003, "Convective Boiling in Parallel Micro-Channels," ASME Paper No. ICMM2003-1007.
[9] Jiang, L., Wong, M., and Zohar, Y., 2001, "Forced Convection Boiling in a Microchannel Heat Sink," J. Microelectromech. Syst., **10**(1), pp. 80–87.
[10] Zhang, L., Koo, J. M., Jiang, L., Asheghi, M., Goodson, K. E., Santiago, J. G., and Kenny, T. W., 2002, "Measurements and Modeling of Two-Phase Flow in Microchannels With Nearly-Constant Heat Flux Boundary Conditions," J. Microelectromech. Syst., **11**, pp. 12–19.

[11] Lee, M., Wong, M., and Zohar, Y., 2003, "Integrated Micro-Heat-Pipe Fabrication Technology," J. Microelectromech. Syst., **12**(2), pp. 138–146.
[12] Fogg, D., Flynn, R., Hidrovo, C., Zhang, L., and Goodson, K., 2004, "Fluorescent Imaging of Void Fraction in Two-Phase Microchannels," Pisa, Italy, Paper No. SGK07.
[13] Chavan, N., Bhattacharya, A., and Iyer, K., 2005, "Modeling of Two-Phase Flow Instabilities in Microchannels," Paper No. ICMM2005-75048.
[14] Koo, J. M., Im, S., Jiang, L., and Goodson, K. E., 2005, "Integrated Microchannel Cooling for Three-Dimensional Electronic Architectures," ASME J. Heat Transfer, **127**, pp. 49–58.
[15] Ajaev, V. S., and Homsy, G. M., 2003, "Mathematical Modeling of Constrained Vapor Bubbles," ASME Paper No. ICMM2003-1072.
[16] Mukherjee, A., and Kandlikar, S. G., 2004, "Numerical Study of the Growth of a Vapor Bubble During Flow Boiling of Water in Microchannels," ASME Paper No. ICMM2004-2382.
[17] Mukherjee, A., and Kandlikar, S. G., 2005, "Numerical Study of the Effect of Inlet Constriction on Bubble Growth During Flow Boiling in Microchannels," ASME Paper No. ICMM2005-75143.
[18] Zhang, J. T., Peng, X. F., and Peterson, G. P., 2000, "Analysis of Phase Change Mechanisms in Microchannels Using Cluster Nucleation Theory," Microscale Thermophys. Eng., **4**(3), pp. 177–187.
[19] Inasaka, F., Adachi, M., Shiozaki, K., Aya, I., and Nariai, H., 2005, "Water Hammer Caused by Rapid Gas Production in Severe Accident in a Light Water Reactor," JSME Int. J., Ser. B, **48**(1), pp. 48–55.
[20] Brennen, C. E., 1995, *Cavitation and Bubble Dynamics*, Oxford University Press, New York.
[21] Lu, X., Properetti, A., Toegel, R., and Lohse, D., 2003, "Harmonic Enhancement of Single-Bubble Luminescence," Phys. Rev. E, **67**, p. 056310.
[22] Plesset, M. S., and Zwick, S. A., 1952, "A Nonsteady Heat Diffusion Problem With Spherical Symmetry," J. Appl. Phys., **23**(1), pp. 95–98.
[23] Lee, J., and Mudawar, I., 2005, "Two-Phase Flow in High-Heat-Flux Micro-Channel Heat Sink for Refrigeration Cooling Applications: Part II—Heat Transfer Characteristics," Int. J. Heat Mass Transfer, **48**, pp. 941–955.
[24] Qu, W., and Mudawar, I., 2003, "Flow Boiling Heat Transfer in Two-Phase Micro-Channel Heat Sinks—I Experimental Investigation and Assessment of Correlation Methods," Int. J. Heat Mass Transfer, **46**, pp. 2755–2771.
[25] Wark, K., 1995, *Advanced Thermodynamics for Engineers*, McGraw-Hill, New York.
[26] Ferziger, J. H., and Peric, M., 2002, *Computational Methods for Fluid Dynamics*, Springer-Verlag, New York.
[27] Fogg, D., and Goodson, K. E., 2006, "The Effects of Liquid Compressibility on the Nucleation and Growth of Bubbles in Forced Convective Flow Boiling Within Microchannels," ASME Paper No. ICNMM2006-96208.
[28] Sabersky, R., Acosta, A. J., Hauptmann, E. G., and Gates, E. M., 1999, *Fluid Flow*, Prentice-Hall, Upper Saddle River, NJ.
[29] Ghidaoui, M. S., Zhao, M., Mcinnis, D. A., and Axworthy, D. H., 2005, "A Review of Water Hammer Theory and Practice," Appl. Mech. Rev., **58**, pp. 49–76.
[30] Lee, M., Cheung, L. S. L., Lee, Y. K., and Zohar, Y., 2005, "Height Effect on Nucleation-Site Activity and Size-Dependent Bubble Dynamics in Microchannel Convective Boiling," J. Micromech. Microeng., **15**, pp. 2121–2129.
[31] Hetsroni, G., Klein, D., Mosyak, A., Segal, Z., and Pogrebnyak, E., 2003, "Convective Boiling in Parallel Micro-Channels," Microscale Thermophys. Eng., **8**, pp. 403–421.
[32] Kandlikar, S. G., 2004, "Heat Transfer Mechanisms During Flow Boiling in Microchannels," ASME J. Heat Transfer, **126**, pp. 8–16.
[33] Kandlikar, S. G., 1990, "A General Correlation for Saturated Two-Phase Flow Boiling Heat Transfer Inside Horizontal and Vertical Tubes," ASME J. Heat Transfer, **112**, pp. 219–228.
[34] Kramer, T., Flynn, R. D., Fogg, D. W., Wang, E. N., Hidrovo, C. H., Goodson, K. E., Prasher, R. S., Chau, D. S., and Narasimhan, S., 2004, "Microchannel Experimental Structure for Measuring Temperature Fields During Convective Boiling," ASME Paper No. IMECE2004-61936.
[35] Bergant, A., Simpson, A. R., and Tijsseling, A. S., 2006, "Water Hammer With Column Separation: A Historical Review," J. Fluids Struct., **22**(2), pp. 135–171.
[36] Lam, K. W., Drake, J. M., and Cobbold, R. S. C., 1999, "Generation and Maintenance of Bubbles in Small Tubes by Low-Frequency Ultrasound," J. Acoust. Soc. Am., **106**(6), pp. 3719–3729.
[37] Kandlikar, S. G., and Grande, W. J., 2002, "Evolution of Microchannel Flow Passages-Thermohydraulic Performance and Fabrication Technology," Heat Transfer Eng., **25**(1), pp. 3–17.
[38] Mehendale, S. S., Jacobi, A. M., and Shah, R. K., 2000, "Fluid Flow and Heat Transfer at Micro- and Meso-Scales With Application to Heat Exchanger Design," Appl. Mech. Rev., **53**(7), pp. 175–193.
[39] Kew, P., and Cornwell, K., 1997, "Correlations for Predictions of Boiling Heat Transfer in Small Diameter Channels," Appl. Therm. Eng., **17**, pp. 705–715.
[40] Balasubramanian, P., and Kandlikar, S. G., 2005, "Experimental Study of Flow Patterns Pressure Drop, and Flow Instabilities in Parallel Rectangular Minichannels," Heat Transfer Eng., **26**(3), pp. 20–27.
[41] Li, H. Y., Lee, P. C., Tseng, F. G., and Pan, C., 2004, "Two-Phase Flow Phenomena for Boiling in Two Parallel Microchannels," ASME Paper No. ICMM2004-2384.

Direct Numerical Simulation of Heat Transfer in Spray Cooling Through 3D Multiphase Flow Modeling Using Parallel Computing

Suranjan Sarkar

R. Panneer Selvam
e-mail: rps@uark.edu

Computational Mechanics Laboratory,
University of Arkansas,
Bell 4190,
Fayetteville, AR 72701

Thermal management issues have become a major bottleneck for further miniaturization and increased power consumption of electronics. Power electronics require more increasing use of high heat flux cooling technologies. Spray cooling with phase change has the advantage of large amount of heat transfer from the hot surface of many power electronics. Spray cooling is a complex phenomenon due to the interaction of liquid, vapor, and phase change at small length scale. A good understanding of the underlying physics and the heat removal process in spray cooling through numerical modeling is needed to design efficient spray cooling system. A computational fluid dynamics based 3D multiphase model for spray cooling is developed here in parallel computing environment using multigrid conjugate gradient solver. This model considers the effect of surface tension, gravity, phase change, and viscosity. The level set method is used to capture the movement of the liquid-vapor interface. The governing equations are solved using finite difference method. Spray cooling is studied using this model, where a vapor bubble is growing in a thin liquid film on a hot surface and a droplet is impacting on the thin film. The symmetry boundary condition considered on four sides of the domain effectively represents a large spray made up of multiple equally sized droplets and bubbles and their interaction. Studies have also been performed for different wall superheats in the absence of vapor bubble to compare the effect of two-phase heat transfer compared to single-phase in spray cooling. The computed interface, temperature, and heat flux distributions at different times over the domain are visualized for better understanding of the heat removal mechanism. [DOI: 10.1115/1.3220142]

Keywords: spray cooling, multiphase flow modeling, heat transfer, parallel computing, CFD, direct numerical simulation

1 Introduction

Spray cooling is a high heat flux ($>100\ W/cm^2$) thermal management technique that is capable of dissipating heat fluxes of $100\ W/cm^2$ using fluorinert [1] and over $1000\ W/cm^2$ using water [2]. This technique is very effective in cooling high power electronic devices such as laser diode arrays, radar systems, and many other applications. In spray cooling, the liquid is forced through a small orifice that shatters into a dispersion of fine droplets, which then impact on a heated surface. The droplets impinge, spread on the surface, and evaporate, thus forming a thin liquid film. With time, bubbles nucleate on the surface inside the thin liquid film. Droplets impinge and interact further with the growing bubbles within the film and results in high heat removal through conduction, convection, and phase change. The spray cooling process is sketched in Fig. 1. The heat removal is very high than pool boiling because of less resistance to the removal of vapor from the hot surface. Other advantages of spray cooling include uniformly cooled surfaces, low droplet velocity, and no temperature overshoot.

Several experiments have been conducted using spray cooling in recent years [3,4] and various designs of spray cooling devices are emerging. However, the theoretical understanding of spray cooling heat transfer is not well known because of the simultaneous interaction of spray droplets, thin film surface evaporation, nucleation, convection, and phase change. Another complication in understanding heat transfer mechanism is the small scales at which it occurs. Direct experimentation, therefore, has been limited in its ability to provide much more than empirical heat transfer correlations. Therefore, numerical modeling is invaluable because several aspects can be studied very quickly and at minimum cost. Recent advances in computational power and efficiency have led to a proliferation of numerical methods that seek to directly simulate interface transport mechanisms of multiphase flows. Only limited work is available in the related area of bubble dynamics [5,6], pool boiling [7–9], and droplet impact [10] on a hot plate. The current status of spray cooling modeling and methods to solve multiphase flow is presented by Selvam et al. [11] and Sarkar [12]. However, research on the multiphase simulation of spray cooling, especially in 3D, is seriously lacking in the literature.

Direct simulation based on fluid dynamics principles that represent detailed aspects of the spray cooling process (schematic shown in Fig. 1) such as droplet ejection, its interaction in transit to the heater surface, droplet impact on the liquid film, and vapor bubble growth and departure are beyond computational capabilities at this time. Selvam et al. [13] determined that by reducing the complexity of the problem and modeling the effects of droplet impact on bubble growth in a thin film (circular portion in Fig. 1)

Contributed by the Heat Transfer Division of ASME for publication in the JOURNAL OF HEAT TRANSFER. Manuscript received February 13, 2008; final manuscript received December 13, 2008; published online October 15, 2009. Review conducted by Yogesh Jaluria.

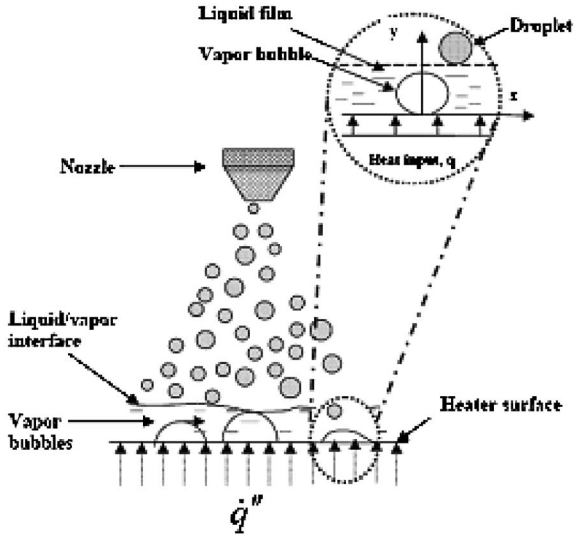

Fig. 1 Schematic diagram of spray cooling phenomena

immensely helps in understanding the phenomena. The liquid film thickness in spray cooling is 40–150 μm [4,14], much smaller compared to the film thickness observed in pool boiling (7.5 mm) [7]. The theoretical understanding of nucleate boiling in thin film (40–150 μm) is not available at this time. Bubble growth and droplet impact on bubble in spray cooling are 3D in nature and hence a 3D multiphase modeling is essential for the quantitative prediction of flow field and heat transfer. The major concern for implementing 3D model is its very high computation time in a serial computer. A 3D multiphase flow model is implemented here in distributed parallel computing environment. The spray cooling phenomena has been studied using the 3D multiphase flow model to predict and illustrate the two-phase heat transfer process after the spray droplets impact on growing vapor bubbles inside a thin liquid film (44 μm). Studies are also performed for different wall superheats without the vapor bubble to understand the single-phase heat transfer process and to compare the heat flux with the two-phase heat transfer in presence of droplet impact.

2 Numerical Formulation of 3D Multiphase Flow Using Level Set Method

2.1 Multiphase Flow Modeling. A 3D multiphase model incorporating surface tension, gravity, and viscosity is developed. The interface is captured by the level set function φ introduced by Sussman et al. [5] and later modified by Son and Dhir [7] to include phase change. The function φ is defined as a positive or negative distance from the interface, and similar to that of Son and Dhir [7], the negative is chosen for the vapor phase and positive is chosen for the liquid.

2.2 Assumptions of the 3D Model. To develop the 3D multiphase flow model for spray cooling, the following assumptions are made:

(1) Modeling the effects of droplet impact on bubble growth in a thin film of 40–150 μm on hot surface would aid in better understanding the heat transfer mechanisms associated with spray cooling.
(2) The flow is assumed to be incompressible.
(3) In spite of droplet interaction with liquid thin film the flow is laminar.
(4) The fluid properties, i.e., density, viscosity, and thermal conductivity, are constant in both liquid and vapor phases.
(5) The vapor phase as well as the interface is maintained at the saturation temperature of the liquid.
(6) The thermal conductivity at the vapor phase is zero
(7) The wall temperature, i.e., the temperature of heater surface, was always constant.
(8) The contact angle of vapor bubble on solid wall is kept constant as 90 deg.

2.3 Governing Equations. The Navier–Stokes equations, considering the effect of surface tension, gravity, and phase change at the interface, are as follows:

$$\rho(\partial_t u + u \cdot \nabla u) = -\nabla p + \rho g - \sigma\kappa \nabla H + \nabla \cdot \mu \nabla u + \nabla \cdot \mu \nabla u^T \tag{1}$$

where u is the velocity vector, ρ is the density, g is the gravity, H is the Heaviside function, μ is the dynamic viscosity, and κ is the thermal conductivity. The energy conservation equation can be stated as

$$\rho c_{pl}(\partial_t T + u \cdot \nabla T) = \nabla \cdot k \nabla T - \rho(u_{\text{int}} - u)h_{fg} \cdot \nabla H \tag{2a}$$

where c_{pl} is the specific heat of the liquid at constant pressure. To calculate for the interfacial velocity, a Newtonian iteration algorithm was developed by Juric and Tryggvason [15] that requires expensive computations and there is no explicit relation exists between the interfacial velocity and temperature. To avoid such difficulty in solving the energy equation, the interfacial velocity u_{int} is extracted from Eq. (2*a*). Finally, the energy equation coupled with the interface temperature condition is considered below as Eqs. (2*b*) and (2*c*) as suggested by Son [16].

$$\rho c_{pl}(\partial_t T + u \cdot \nabla T) = \nabla \cdot k \nabla T \quad \text{for} \quad H > 0 \tag{2b}$$

$$T = T_{\text{sat}}(p_v) \quad \text{for} \quad H = 0 \tag{2c}$$

where p_v is the pressure of the vapor phase, and T_{sat} is the saturation temperature. Mass conservation equation is used as

$$\nabla \cdot u = m \cdot \nabla \rho / \rho^2 \tag{3}$$

where

$$\rho = \rho_v + (\rho_l - \rho_v)H \tag{4}$$

where ρ_l and ρ_v are the densities of the vapor, and m is the mass flux. The value of μ and k are calculated using the similar relation as used in Eq. (4) as suggested by Son [17] to prevent instabilities at the interface. Evaluation of varying properties using different interpolation schemes is discussed by Patankar [18]. H is the Heaviside function and is defined as

$$\begin{gathered} H = 1 \quad \text{if} \quad \varphi \geq 1.5h, \quad H = 0 \quad \text{if} \quad \varphi \leq -1.5h \\ H = 0.5 + \varphi/(3h) + \sin[2\pi\varphi/(3h)]/(2\pi) \quad \text{if} \quad |\varphi| \leq 1.5h \end{gathered} \tag{5}$$

where h is a grid spacing. Equation (5) implies that the interface separating two phases is replaced by a transition region of finite thickness to avoid numerical instabilities at the interface for larger density differences in its two sides. H is a step function chosen to smooth over three greed spacing (+1.5h to −1.5h) as suggested by Sussman et al. [5]. The volume source term is included in the continuity (Eq. (3)), derived from conditions of continuity and energy balance at the interface

$$m = \rho(u_{\text{int}} - u) = k \nabla T / h_{fg} \tag{6}$$

where u_{int} is the interface velocity vector, and h_{fg} is the latent heat of vaporization. In the level set formulation, the level set function φ is advanced and reinitialized as

$$\partial_t \varphi = -u_{\text{int}} \cdot \nabla \varphi \tag{7}$$

$$\partial_t \varphi = \varphi_0(1 - |\nabla \varphi|)/\sqrt{(\varphi_0{}^2 + h^2)} \tag{8}$$

where φ_0 is a solution of Eq. (7).

The surface tension effect is considered in the momentum equation by using a step function H (H=0 in vapor and H=1 in liquid) and κ is the interfacial curvature expressed for 3D as

$$\kappa = \nabla \cdot (\nabla\varphi/|\nabla\varphi|)$$
$$= (\varphi_x{}^2\varphi_{yy} - 2\varphi_x\varphi_y\varphi_{xy} + \varphi_y{}^2\varphi_{xx} + \varphi_x{}^2\varphi_{zz} - 2\varphi_x\varphi_z\varphi_{xz} + \varphi_z{}^2\varphi_{xx} + \varphi_y{}^2\varphi_{zz} - 2\varphi_y\varphi_z\varphi_{yz} + \varphi_z{}^2\varphi_{yy})/(\varphi_x{}^2 + \varphi_y{}^2 + \varphi_z{}^2)^{3/2} \quad (9)$$

Here the subscripts are in differentiation with respect to φ. The surface tension force $\sigma\kappa\nabla H$ is implemented in the volume form to avoid the need for explicit description of the interface as suggested by Brackbill et al. [19].

2.4 Nondimensional Form of the Governing Equations. The nondimensional form of the above set of equations is derived using the characteristic length l_r, velocity u_r, time t_r, and dimensionless temperature T^*. They are defined, as suggested by Son and Dhir [7], as

$$l_r = \sqrt{\sigma/g(\rho_l - \rho_v)}, \quad u_r = \sqrt{gl_r}, \quad t_r = l_r/u_r, \quad \text{and} \quad T^* = (T - T_{\text{sat}})/(T_w - T_{\text{sat}}) \quad (10)$$

The reference values are taken in such a way that the gravity force becomes unity, that is, Froude number (Fr) equal to 1 and the Bond number (Bo) is just above 1.0 if the density ratio of the liquid to vapor is larger. In addition, considering ρ^*, k^*, μ^*, and $c_p{}^*$ of liquid as reference values, the nondimensional equations are expressed as:

$$\rho^*(\partial_t u^* + u^* \cdot \nabla u^*) = -\nabla p^* + \rho^* g^* - \kappa^* \nabla H^*/\text{Bo} + (\nabla \cdot \mu^* \nabla u^* + \nabla \cdot \mu^* \nabla u^{*T})/\text{Re} \quad (11)$$

$$\rho^* c^*_{pl}(\partial_t T^* + u^* \cdot \nabla T^*) = (\nabla \cdot k^* \nabla T)/\text{Pe} \quad (12)$$

$$\nabla \cdot u = \text{Ja} \cdot k^* \nabla T^* \cdot \nabla \rho^*/(\text{Pe} \cdot \rho^{*2}) \quad (13)$$

$$u^*_{\text{int}} = u^* + \text{Ja} \cdot k \nabla T^*/(\text{Pe} \cdot \rho^*) \quad (14)$$

where $\text{Re} = \rho_l u_r l_r/\mu_l$, $\text{Bo} = \rho_l g l_r/\sigma$, $\text{Ja} = c_{pl}\Delta T/h_{fg}$, $\text{Pr} = c_{pl}\mu_l/k_l$, $\text{Pe} = \text{Re}$, $\text{Pr} = \rho_l u_r l_r c_{pl}/k_l$. g_y represents unit gravitational force in the y-direction.

2.5 Numerical Solution. Highly nonlinear equations (Eqs. (1), (2*a*)–(2*c*), (3), (7), and (8)) are discretized using finite difference method on a staggered grid system. All variables except pressure are stored at the grid points and pressure is stored at the cell center. The diffusion terms are considered implicitly and the convection and source terms are considered explicitly in time. For spatial approximations all terms are considered using second-order central difference and the convection term by a second-order ENO method. The discretized equations are solved by the preconditioned conjugate gradient (PCG), multigrid (MG), and multigrid conjugate gradient (MGCG) solvers in an iterative form to compare the solver efficiency. Spray cooling is studied by MGCG using MG level 5. At each time-step the equations are solved sequentially in the following order: (a) solve the momentum equation (Eq. (1)) for velocities; (b) correct the velocity to take the pressure effect; (c) solve the pressure equation to satisfy continuity; (d) update the velocities to include the new pressure effect; (e) solve for the temperature equation (Eq. (2)), (f) solve for the distance function (Eq. (7)), (g) reinitialize the distance function as per (Eq. (8)), and go to next time-step. Time-steps for the computation is chosen such that the Courant-Friedrichs-Lewy (CFL) condition $[\Delta t \le \min(h/(|u| + |v| + |w|)10^{-6})]$ is satisfied.

3 Implementation of Multiphase Flow Model in Parallel Computing Environment

3.1 Message Passing Environment and Domain Decomposition:. For a standard problem of 3D spray cooling to solve, it requires almost 30–50 days using PCG solver in a serial computer. This is nowhere close to the practical turnaround time. This is because of the use of a large number of grid points in 3D problem (e.g., 129 grids in each direction gives rise to more than 2×10^6 cells in 3D compared to 16,000 cells in 2D). So the implementation of 3D model in parallel computing environment is a must to reduce the turnaround time. Message passing interface (MPI) [20] is used to exchange data among processors through communications by sending and receiving messages. Domain decomposition (DD) technique [21] is used in the parallel implementation. The problem is first decomposed into several domains and then each task performed on a part of the data simultaneously. The boundary values of several domains are transferred from one processor to the other. First the code is written to have DD in one direction and then in three. The 1D DD worked very well for PCG solvers but it is not very efficient for MG solvers. The number of levels that can be used in 1D DD gets reduced as the number of processors is increased. Hence 3D DD is preferred for multigrid solvers.

Table 1 Convergence rate and CPU time for different solvers in parallel computing

Solver	MG level used	Number of iterations for convergence	CPU time for solving 20 time-steps of bubble growth problem
MGCG	5	5–9	83
MGCG	3	8–14	93
MGCG	2	14–24	153
PCG	-	26–32	335
MG	-	200	912

3.2 Efficient Solvers for Distributed Parallel Computing. The PCG solver looses its efficiency when more processors are used, as reported in Ref. [21]. MG solver is very efficient for computational fluid dynamics (CFD) applications. In the current model the MG solvers are also not converging for certain time-steps. Therefore, MGCG solvers [22] are also considered where the MG is considered as a preconditioner for the PCG. For MG calculations the incomplete Cholesky decomposition is used to reduce the high frequency errors. The MG solvers are efficient for reducing the individual domains error and CG for reducing the interface domain error. Table 1 shows the convergence rate for MGCG solver with different number of levels (subdomains) used to solve a bubble growth problem for 20 time-steps using eight processors. The table also includes results for PCG and MG solver for comparison. A grid size of $65 \times 65 \times 65$ is used for all calculations. The MGCG solver is found to be up to four times faster compared to PCG solver and implemented in the 3D model in parallel computing.

3.3 Performance Enhancement Using MGCG Solver in Parallel Computing. The time required to complete the 20 time-steps of a standard spray cooling problem is observed for different solvers and number of processors. An estimation of completion time for the benchmark problem (with 10,000 time steps) is made based on the time required for solving 20 time-steps. For smaller problem size ($65 \times 65 \times 65$ grid sizes), use of PCG solver in serial computing is found to take almost 105 h (more than 4 days) to solve the problem. In contrast, using MGCG solver with more than three levels (L) and using eight or more number of processors, the same result is achieved within 10 h. So the turnaround time of the problem is improved by almost ten times. The advantage of using MGCG solver is even more prominent when the problem size is bigger ($129 \times 129 \times 129$ grids). For bigger problems, the 3D multiphase model with PCG solver in serial computing would take almost 1427 h, i.e., 60 days, to solve the problem. When MGCG solver (level 5) is used with 32 numbers of processors, the same result can be achieved within 30 h. So the turnaround time of bigger problem is improved by 45–50 times and ideal to solve the challenging multiphase flow problem more efficiently using MGCG solver with higher levels in parallel com-

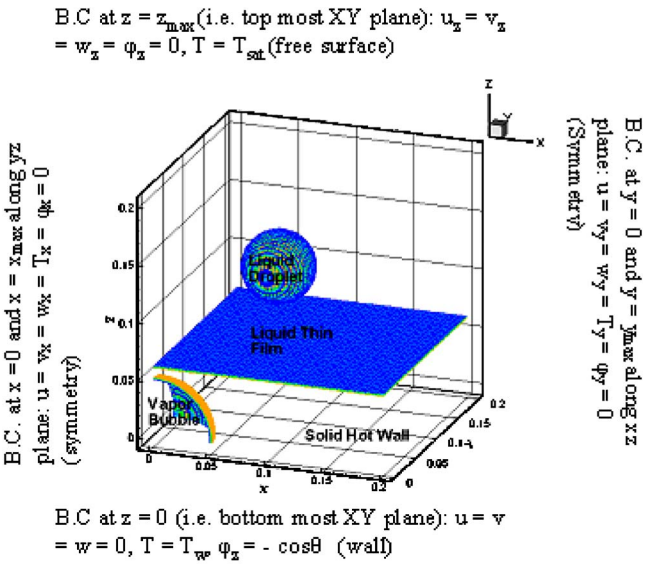

Fig. 2 Initial and boundary conditions

puting. The speedup is observed to be significant, up to 32 processors for larger problems and up to eight processors for smaller problems, before communication overhead to become significant to affect the speedup.

4 3D Modeling of Liquid Droplet Impact on Thin Liquid Film With Growing Vapor Bubble

4.1 Simulation Details. Properties of FC-72 (a dielectric coolant) at $T_{sat}=53°C$ is considered for 3D modeling of droplet impact on growing bubble in thin liquid film. The computed reference values are as follows: reference length $l_r=736.2$ μm, reference velocity $u_r=85$ mm/s, reference time $t_r=8.66$ ms, and $\Delta T=10°C$. The nondimensional numbers are as follows: Re $=218$, Bo$=1$ (or We$=1$), Pe$=2050$, Ja$=0.127$, and Ec$=6.6\times10^{-7}$. The liquid-to-vapor density ratio (ρ_l/ρ_v) is 138. For numerical stability issues, the density ratio of 20 is used in the computations. The computed results using higher density ratios have similar trends of heat flux but the time-steps needed to be used is much smaller. As the goal of this study to investigate the heat transfer mechanism during spray cooling, the use of density ratio of 20 instead of 138 serves the purpose. The above data refer to spray cooling experiments performed by Lin and Ponnappan [4] using FC-72 of $T_{sat}=53°C$. A computational domain of $0.2\times0.2\times0.2$ units ($147.2\times147.2\times147.2$ μm^3) is considered. Appropriate grid sizes for studying the droplet-bubble dynamics are chosen using grid convergence studies. The dependence of heat transfer for different grid points is checked and $129\times129\times129$ grids are observed to be optimum. Therefore, the computational domain is discretized by $129\times129\times129$ mesh for this study (grid size is 1.14 μm). Computation is done with a time-step of 86.6 ns (5×10^{-6} units) for 20,000 time-steps. The MGCG solver with multigrid level 5 is used.

4.2 Initial and Boundary Conditions. The 3D multiphase flow model developed here simulates the droplet and bubble interaction in thin liquid film over hot surface. The typical initial condition including computational domain and the boundary conditions for the governing equations are shown below in Fig. 2. A droplet radius of 0.03 (22.086 μm) falling down with a velocity of 40 (3.4 m/s) units located at 0.13 (95.706 μm) units above the hot wall is introduced. These parameters are close to the 40 μm diameter of the spray falling with a velocity of 10 m/s reported by Baysinger [23] from experiment. The frequency of the falling droplet is suggested to be 1 kHz (1 ms interval) [24]. The initial temperature of the droplet is assumed to be T_{sat}. The bubble growth process is too slow than the droplet impact. Therefore, a sufficiently grown bubble with a radius of 0.05 (36.81 μm) nondimensional units is placed on one corner of the domain over hot wall within a thin liquid layer of 0.06 (44.172 μm) nondimensional units. This is done to capture the droplet-bubble interaction within a reasonable time due to very high computational overhead of the 3D model. The initial temperature distribution of the liquid film is considered to be varying linearly from the surface to 0.012 (8.834 μm) units above the surface.

Though a single representative droplet-bubble interaction has been modeled, the symmetry boundary condition considered on four sides of the domain indeed represents that the same process is taking place on the other sides of the wall. In effect, a large spray made up of multiple equally sized droplets and bubbles have been considered and the associated spray cooling heat transfer due to their interaction has been modeled in this simulation.

4.3 Results and Discussions. The initial condition considered for droplet impact study on thin liquid film with growing bubble is shown in Figs. 3(*a*)–3(*d*)(i). Figs. 3(*a*) and 3(*b*)(i) show the initial liquid-vapor interface in 3D and first planar views, respectively. The orientation of the axes in Figs. 3(*a*) and 3(*b*)(i) are different for better visualization. The initial temperature and heat flux contour on the heated surface are shown in Figs. 3(*c*) and 3(*d*)(i).

To illustrate systematically the heat transfer in spray cooling in time sequences, the shape of the liquid-vapor region, the temperature contours on the first plane above the heated surface, and the heat flux over the hot surface are plotted for several times in Figs. 3(*a*)–3(*d*)(ii and iii). The computed heat transfer rates are captured and visualized at several instants of times after droplet impact when liquid and vapors are trying to find equilibrium. This helps to understand the heat transfer process in spray cooling. Due to space restriction, only plots are shown when high heat transfer occurs. It is assumed that there is some initial temperature distribution in the liquid region and the initial Nu is 79.36. From the average Nu versus time plot (not shown here) it is observed that the Nu starts increasing from 79.36–101.28 in 0.0063 (54.56 μs) time and reaches its maximum to 119 in 0.0106 (91.80 μs) dimensionless time. That is the time when the maximum heat transfer occurs. Observing closely Fig. 3(*a*)(ii and iii) it is revealed that after the liquid droplet impact on the liquid layer with vapor bubble in it, the droplet spreads on the top of the liquid layer, and due to impact the thin liquid layer above the bubble expands and tears away, as shown in Figs. 3(*a*) and 3(*b*)(ii), at 54.56 μs and the average Nu reaches 101.28. The temperature contour very close to the hot surface and the corresponding heat flux contour on the hot surface at this time instant is shown in Figs. 3(*c*) and 3(*d*)(ii), respectively. It is observed that due to droplet impact very cold liquid droplet mixed with the liquid layer touches the hot surface and high heat is removed from the hot surface due to instant conduction from the hot wall to the cooler liquid. This is evident from the circular cold patch in Fig. 4(*c*)(ii). Although the average Nu reaches 101.28, the local Nu at this region reaches from 120–420 and in a very small area it reaches even up to 490 as found from the heat flux contour in Fig. 3(*c*)(ii). With time the cooler liquid starts to spread and move towards the dry area where the vapor was growing, as shown in Figs. 3(*a*) and 3(*b*)(iii) at 77.94 μs. The temperature and heat flux contours (Figs. 3(*c*) and 3(*d*)(iii)) shows the cooling of the hot surface at some region due to the high heat transfer. Heat flux contour on the hot surface (Fig. 3(*d*)(iii)) reveals that the local Nu is around 420–490 in a larger portion of the moving liquid (compared to Nu of 120–420 after 54.56 μs). As a result the corresponding average Nu increases and reaches to its maximum value of 119.0 at 77.94 μs. Thus the highest heat flux occurs after the vapor bubble breaks due to droplet impact and the cooler liquid spreads with time on the dry hot surface vacated by the bubble. The flow changes in a very short

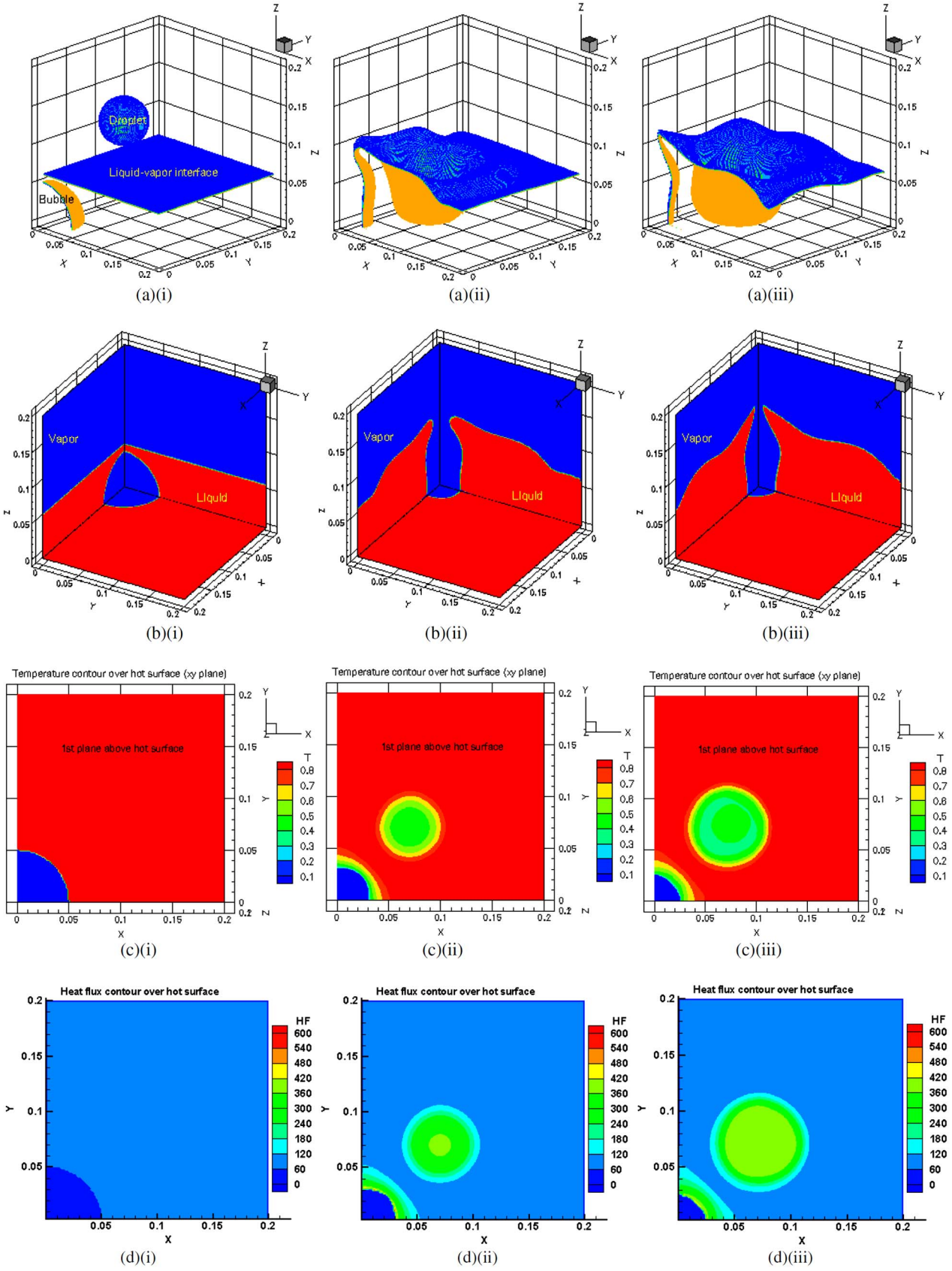

Fig. 3 (*a*) **Overall shape of the liquid droplet and vapor bubble and** (*b*) **shape of liquid and vapor layers at the first plane in all directions,** (*c*) **temperature contour on the first plane above the hot surface** (*xy* **plane), and** (*d*) **heat flux contour over the hot surface at different times:** (i) **plot at 0.087** μ**s (initial condition),** (ii) **plot at 54.56** μ**s (droplet impact) and** (iii) **plot at 77.94** μ**s (some time after droplet impact when cold liquid spreads over the hot surface—transient conduction)**

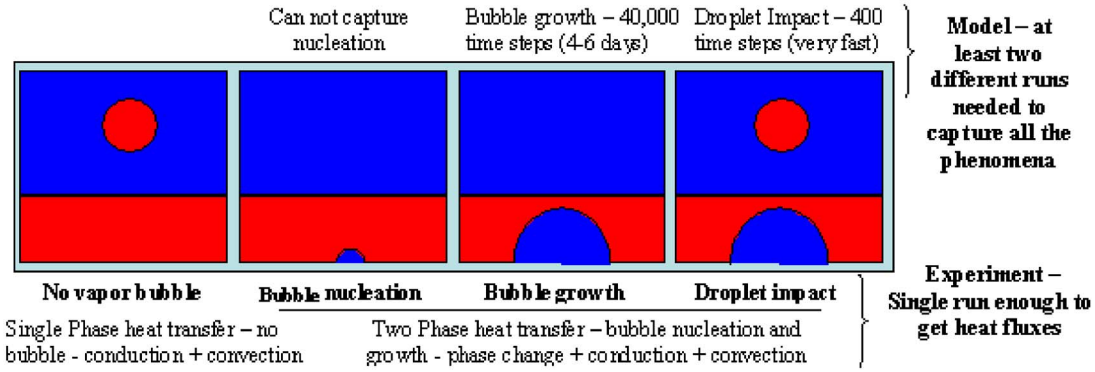

Fig. 4 Stages in spray cooling and capability of multiphase flow modeling to capture these stages

time due to the interaction of the surface tension, viscosity, gravity, and phase change. The cooler liquid takes away a lot of heat while spreading on the hot surface.

4.4 Mechanism of Spray Cooling. Several mechanisms of spray cooling heat transfer have been proposed in the literature. Pais et al. [25] suggested that due to high temperature gradient between the hot surface and the liquid layer, a thin film is developed and the high heat transfer occurs due to evaporation at the liquid-vapor interface of the thin film. Rini et al. [26] and Pais et al. [27] suggested that the key mechanism of spray cooling is "secondary nucleation," which creates numerous bubble nucleation sites in the film when droplet impingement at the liquid/vapor interface results to vapor bubble fracture and vapor entrainment in the liquid film. A recent review paper by Silk et al. [28] summarizes the proposed heat transfer mechanisms in spray cooling research community and analyzes the applicability and limitations of each of them.

From the current study the transient conduction is found to be the main mechanism of high heat transfer. When the vapor bubble breaks due to liquid droplet impact the cooler liquid spreads in the dry hot area and heat is conducted from the wall to the liquid layer with time. This transient conduction in a very short time is the one which produces the high heat flux. To bring cooler liquid to the heated surface in a very short time, vapor bubble collapse due to droplet impact is necessary. Importance of transient conduction mechanism indicates the usefulness of efficient fluid removal system to bring new cooler liquid on the heated surface. This research group is developing new spray cooling and other multiphase cooling devices for smaller and larger areas using this concept. Preliminary results are very promising indicating up to 30–40% heat transfer enhancement compared to heat flux data available in literature.

5 Single-Phase and Two-Phase Heat Transfer in Spray Cooling: 3D Model versus Experiment

Spray cooling process is stochastic in nature and the heat transfer associated with it varies depending on different combinations of droplet-bubble distance, droplet impinging timing, bubble size, droplet velocity, wall superheat, and many other parameters. However, wall superheats and droplet velocity are two major controlling parameters. So these two parameters are kept similar to what Lin et al. [4] have used. The single-phase and two-phase heat transfer was studied for spray cooling using the 3D multiphase model and the predicted heat flux is compared with the experimental results.

In actual spray cooling the single-phase heat transfer occurs before the formation of the vapor bubble on the hot surface. During this period the heat transfer occurs through conduction and convection. The phase change mode of heat transfer is totally absent at this time. When the conditions are favorable for nucleation on the hot surface the nucleation starts to occur. The vapor bubble grows and the two-phase heat transfer comes into play due to phase change along with conduction and convection. Thus the spray cooling phenomena can be described as a combination of four different stages, as illustrated in Fig. 4, i.e., (a) single-phase heat transfer in the absence of vapor bubble, (b) bubble nucleation, (c) bubble growth, and (d) droplet impact. In spray cooling experiment, a single run with increasing wall superheat from 5–40°C is enough to acquire all the data to draw its characteristic spray cooling curve. Unfortunately, any macroscopic multiphase flow model is not capable of capturing the bubble nucleation, as it is a molecular level process. For this reason, all the stages of spray cooling cannot be captured in a single simulation run. However, a vapor bubble of some initial size could be introduced into or omitted from the model as needed to mimic single-phase and two-phase heat transfers, respectively. As the bubble growth process is too slow compared to the droplet impact, a sufficiently grown bubble was considered in simulation to capture the droplet-bubble interaction and corresponding heat transfer.

To compare the heat flux calculated from the 3D model with the experimental data, two sets of runs are performed. The first set considers both droplet and vapor bubble (two-phase) and the second set consider only droplet and no vapor bubble (single-phase). Two sets have been studied for different wall superheats of 10°C, 20°C, 30°C, and 40°C. The droplet velocity is kept constant at 115 nondimensional units, which is equal to 9.8 m/s. This droplet velocity is chosen as to compare with spray cooling experimental results from Lin et al. [4], where a droplet velocity of 10 m/s was used. A spray cooling characteristic curve (Fig. 5) is plotted with single- and two-phase heat transfers from the 3D multiphase model. An experimental heat flux data of Lin et al. [4] for the similar parameters as used in this model is also plotted for comparison. The slope for two-phase heat transfer is higher compared to single-phase heat transfer. The experimental heat flux curve is observed to be a smooth transition from single-phase heat transfer regime to two-phase heat transfer regime and it correlates well with the results from our model. Below 10°C wall superheat the heat flux curve is predominantly single-phase and after that it is predominantly two-phase. This behavior is similar to actual spray cooling. So this model can predict the spray cooling phenomena and associated heat transfer reasonably well. However, the comparison with experiment is not to match the data very precisely but to check whether this model can predict the spray cooling heat transfer reasonably well and if it can identify the single- and two-phase regimes of heat transfer. Future work is underway to implement multiple droplet-bubble interactions and use of horizontal convective velocity in the current model. Then a very realistic comparison between the model and experiment can be performed.

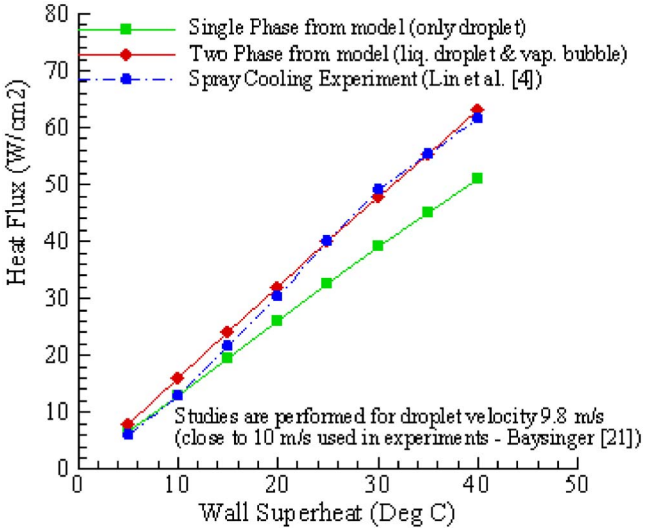

Fig. 5 Comparison of heat flux in spray cooling: 3D model versus experiment

6 Conclusions

A 3D computer model for multiphase flow of spray cooling with parallel computing is reported in this paper. Level set method is used to capture the liquid-vapor interface. The spray cooling phenomena, and single-phase versus two-phase heat transfer in spray cooling has been studied using this model. From the study the following conclusions are made:

(i) Conduction, convection, phase change, and droplet impact all interacts simultaneously in spray cooling. High heat flux occurs at the time instant when cold liquid droplet, after impacting, mixes with the thin liquid film and hits the hot surface. At the same time thin liquid film breaks due to droplet impact and merges with the vapor over the liquid film. The maximum heat flux occurs after bubble merging due to transient conduction when the cold liquid moves with time from all directions over the dry hot surface vacated by the vapor bubble. This represents the actual behavior in spray cooling.

(ii) The heat flux contour over the hot plate gives the detail picture of local heat transfers occurring in different places over the hot surface along with the average Nu. In this aspect 3D multiphase flow model is realistic, gives quantitative heat transfer prediction, and provides actual visualization of flow field and associated heat transfer at micrometer length scale that is very hard to capture from experiments. This study will be extended in future to include the interaction of multiple droplets introduced at different times with bubbles of different sizes, which is more realistic to stochastic spray cooling process.

(iii) The model can predict both the single- and two-phase heat transfers in spray cooling. The slope of two-phase heat flux is higher compared to that of single-phase. Comparison with experimental data by Lin et al. [4] indicated that this model is well capable of simulating the spray cooling phenomena and predicting the associated heat transfer.

(iv) This specific study is for modeling heat transfer in thin film but the computational challenges addressed here is quite similar to what has been seen to model many other phase change processes. Therefore it is believed that the use of parallel computation and more efficient MGCG solver would make the modeling of larger phase change problems more feasible.

Acknowledgement

We acknowledge the support received from the ONR (Grant No. N00014-05-1-0889) through the University of Arkansas to perform this work. We also acknowledge the computational resource of Red Diamond cluster (128 dual 64-bit Intel® Xeon™ processors), which allowed us to perform the 3D distributed parallel computing. Funding for Red Diamond is supplied through NSF Instrumentation Grant (Grant No. 0421099) and additional support from the University of Arkansas.

Nomenclature

Bo = Bond number, $\rho_l g l_r^2/\sigma$
c_p = specific heat at constant pressure (J/kg K)
h = grid spacing (m)
h_{fg} = latent heat of evaporation (j/kg)
Ja = Jacob number $= c_{pl}\Delta T/h_{fg}$
K = thermal conductivity (W/m K)
l_r = characteristic length, $\sqrt{\sigma/g(\rho_l-\rho_v)}$ (m)
m = mass flux vector ($g/m^3/m^2$ s)
Nu = Nusselt number, $ql_r/(\Delta T k_l)$
p = Pressure (Pascal)
Pe = Peclet number, $\rho_l u_r l_r c_{pl}/k_l$
Pr = Prandtl number, $c_{pl}\mu_l/k_l$
q = heat flux (W/m^2)
Re = Reynolds number, $\rho_l u_r l_r/\mu_l$
T = temperature (K)
T^* = dimensionless temperature, $(T-T_{sat})/(T_w-T_{sat})$
ΔT = temperature difference, T_w-T_{sat}
t = time (s)
g = gravity vector (m/s^2)
H = step function
t_r = characteristic time, l_r/u_r (s)
u = velocity vector (u,v) (m/s)
u_{int} = interface velocity vector (m/s)
u_r = characteristic velocity, $\sqrt{gl_r}$ (m/s)
α = thermal diffusivity (m^2/s)
κ = interfacial curvature
μ = dynamic viscosity (N s/m^2)
ρ = density (g/m^3)
σ = surface tension (N/m)
φ = level set function

Subscripts

int = interface
l, v = liquid, vapor
sat, w = saturation, wall

References

[1] Mudawar, I., 2001, "Assessment of High Heat-Flux Thermal Management Schemes," IEEE Trans. Compon. Packag. Technol., **24**, pp. 122–141.
[2] Yang, J., Chow, L. C., and Paris, M. R., 1996, "Nucleate Boiling Heat Transfer in Spray Cooling," ASME J. Heat Transfer, **118**, pp. 668–671.
[3] Chow, L. C., Sehembey, M. S., and Paris, M. R., 1997, "High Heat Flux Spray Cooling," Annu. Rev. Heat Transfer, **8**, pp. 291–318.
[4] Lin, L., and Ponnappan, R., 2003, "Heat Transfer Characteristics of Spray Cooling in a Close Loop," Int. J. Heat Mass Transfer, **46**, pp. 3737–3746.
[5] Sussman, M., Smereka, P., and Osher, S., 1994, "A Level Set Approach for Computing Solutions to Incompressible Two-Phase Flow," J. Comput. Phys., **114**, pp. 146–159.
[6] Tryggvason, G., Bunner, B., Esmaeeli, A., Juric, D., Al-Rawahi, N., Tauber, W., Han, J., Nas, J., and Jan, Y.-J., 2001, "A Front-Tracking Method for the Computations of Multiphase Flow," J. Comput. Phys., **169**, pp. 708–759.
[7] Son, G., and Dhir, V. K., 1998, "Numerical Simulation of Film Boiling Near Critical Pressures With a Level Set Method," ASME J. Heat Transfer, **120**, pp. 183–192.
[8] Yoon, H. Y., Koshizuka, S., and Oka, Y., 2001, "Direct Calculation of Bubble Growth, Departure, and Rise in Nucleate Pool Boiling," Int. J. Multiphase Flow, **27**, pp. 277–298.
[9] Welch, S. W. J., and Wilson, J., 2000, "A Volume of Fluid Based Method for Fluid Flows With Phase Change," J. Comput. Phys., **160**, pp. 662–682.
[10] Pasandideh-Fard, M., Aziz, S. D., Chandra, S., and Mostaghimi, J., 2001,

"Cooling Effectiveness of Water Drop Impinging on Hot Surface," Int. J. Heat Mass Transfer, **22**, pp. 201–210.
[11] Selvam, R. P., Sarkar, S., and Sarkar, M., 2007, "Modeling Multiphase Flow and Heat Transfer—Current Status and Future Challenges," Invited paper in the *Proceedings of the Seventh Asian Computational Fluid Dynamics Conference*, IISC, Bangalore, India, Nov. 26–30.
[12] Sarkar, S., 2008, "3-D Multiphase Flow Modeling of Spray Cooling in Parallel Computing," Ph.D. thesis, University of Arkansas, Fayetteville, AR.
[13] Selvam, R. P., Lin, L., and Ponnappan, R., 2006, "Direct Simulation of Spray Cooling: Effect of Vapor Bubble Growth and Liquid Droplet Impact on Heat Transfer," Int. J. Heat Mass Transfer, **49**, pp. 4265–4278.
[14] Pautsch, A. G., and Shedd, T. A., 2005, "Spray Impingement Cooling With Single- and Multiple-Nozzle Arrays—Part I: Heat Transfer Data Using FC-72," Int. J. Heat Mass Transfer, **48**, pp. 3167–3175.
[15] Juric, D., and Tryggvason, G., 1998, "Computations of Boiling Flows," Int. J. Multiphase Flow, **24**, pp. 387–410.
[16] Son, G., 2001, "A Numerical Method for Bubble Motion With Phase Change," Numer. Heat Transfer, Part B, **39**, pp. 509–523.
[17] Son, G., 2005, "A Level Set Method for Incompressible Two-Fluid Flows With Immersed Solid Boundaries," Numer. Heat Transfer, Part B, **47**, pp. 473–489.
[18] Patankar, S. V., 1980, *Numerical Heat Transfer and Fluid Flow*, Hemisphere, Washington, DC.
[19] Brackbill, J. U., Kothe, D. B., and Zamach, C., 1992, "A Continuum Method for Modeling Surface Tension," J. Comput. Phys., **100**, pp. 335–354.
[20] Gropp, W., Lusk, E., and Skjellum, A., 1999, *Using MPI: Portable Parallel Programming With the Message-Passing Interface*, 2nd ed., MIT, Cambridge, MA.
[21] Ferziger, J. H., and Peric, M., 2002, *Computational Methods for Fluid Dynamics*, Springer, New York.
[22] Selvam, R. P., 1996, "Multigrid Methods for Computational Wind Engineering," Computational Mechanics Laboratory, Department of Civil Engineering, University of Arkansas, Report No. 19961.
[23] Baysinger, K. M., 2004, "Design of a Microgravity Spray Cooling Experiment," AIAA Paper No. AIAA-2004-0966.
[24] Harris, R. J., 2004, private communications, University of Dayton Research Institute, Dayton, OH.
[25] Pais, M. R., Tilton, D., and Chow, L. C., 1989, "High Heat Flux, Low Superheat Evaporative Spray Cooling," AIAA Paper No. AIAA 89-024.
[26] Rini, D., Chen, R.-H., and Chow, L., 2002, "Bubble Behavior and Nucleate Boiling Heat Transfer in Saturated FC-72 Spray Cooling," ASME J. Heat Transfer, **124**, pp. 63–72.
[27] Pais, M., Chow, L., and Mahefkey, E., 1992, "Surface Roughness and Its Effects on the Heat Transfer Mechanism of Spray Cooling," ASME J. Heat Transfer, **114**, pp. 211–219.
[28] Silk, E. A., Golliher, E. L., and Selvam, R. P., 2008, "Spray Cooling Heat Transfer: Technology Overview and Assessment of Future Challenges for Micro-Gravity Application," Energy Convers. Manage., **49**, pp. 453–468.

High-Resolution Measurements at Nucleate Boiling of Pure FC-84 and FC-3284 and Its Binary Mixtures

Enno Wagner
Weingartenstrasse 33,
D-64367 Mühltal, Germany
e-mail: enno.wagner@gmx.de

Peter Stephan[1]
Department of Mechanical Engineering,
Institute of Technical Thermodynamics,
Technische Universität Darmstadt,
D-64287 Darmstadt, Germany
e-mail: pstephan@ttd.tu-darmstadt.de

*In a special boiling cell, vapor bubbles are generated at single nucleation sites on top of a 20 μm thick stainless steel heating foil. An infrared camera captures the rear side of the heating foil for analyzing the temperature distribution. The bubble shape is recorded through side windows with a high-speed camera. Global measurements were conducted, with the pure fluids FC-84 and FC-3284 and with its binary mixtures of 0.25, 0.5, and 0.75 mole fraction. The heat transfer coefficient (HTC) in a binary mixture is less than the HTC in either of the single component fluid alone. Applying the correlation of Schlünder showed good agreement with the measurements (1982, "Über den Wärmeübergang bei der Blasenverdampfung von Gemischen," Verfahrenstechnik, **16**(9), pp. 692–698). Furthermore, local measurements were arranged with high lateral and temporal resolution for single bubble events. The wall heat flux was computed and analyzed, especially at the three-phase-contact line between liquid, vapor, and heated wall. The bubble volume and the vapor production rate were also investigated. For pure fluids, up to 50–60% of the latent heat flows through the three-phase-contact region. For mixtures, this ratio is clearly reduced and is about 35%.* [DOI: 10.1115/1.3220143]

Keywords: nucleate boiling, binary mixtures, single nucleation site, thin metallic foil heater, local wall temperature, local wall heat flux, three-phase contact line evaporation

1 Introduction

Nucleate boiling of binary mixtures is a well established process in the chemical industry, petrochemistry, and food industry. For the calculation of the heat transfer coefficient, many empirical correlations are available that predict the well known effect that the nucleate boiling heat transfer coefficient (HTC) of a binary mixture is typically lower than the coefficients of the pure fluids. The first researchers to do extensive experiments with binary mixtures were Bonilla and Perry in the 1940s. They found that the heat transfer coefficient α of a binary mixture of water and ethanol is much lower than the ideal heat transfer coefficient α_{id}, which is defined as the average mole ratio between the heat transfer coefficients of the pure fluids [1]. Baehr and Stephan [2] explained this effect with the local change in the mixture concentration close to the bubble. Because the more volatile component will evaporate more easily, the vapor in the bubble will contain a higher concentration of this component than the liquid in the bulk. Thus, the fluid close to the wall (especially near the bubble foot where the highest evaporation takes place) becomes locally poor in the more volatile component. The local saturation temperature increases and less energy can be transferred at the same heat flux rate: the HTC decreases. Schlünder [3] developed a model that describes the reduction in the global heat transfer coefficient for nucleate boiling of binary mixtures. In his model, it is assumed that there is a concentration gradient from the phase interface to the bulk liquid due to the reasons mentioned above. Therefore, a back diffusion of the less volatile component from the phase interface into the bulk is taking place. This effect is qualified through the mass transfer coefficient β_0. The ratio between the real and the ideal HTC is expressed as follows:

$$\frac{\alpha}{\alpha_{id}} = \frac{1}{1 + \frac{\alpha_{id}}{\dot{q}}(T_{S2} - T_{S1})\widetilde{(y_1 - y_2)}\left[1 - \exp\left(\frac{-B_0\dot{q}}{\rho_l \beta_0 \Delta h_v}\right)\right]} \quad (1)$$

The only coefficient that has to be fitted to experiments is the parameter B_0, which is in the order of 1. With the model of Schlünder [3], it is also possible to show that the heat transfer coefficient of mixtures is less affected by pressure and heat flux than the heat transfer coefficients of pure fluids.

More recently, experiments were carried out by Schlindwein et al. [4] who observed a binary mixture of FC-87 and FC-72. They analyzed the global heat transfer coefficient and compared it with different correlations for pure fluids, e.g., from Rohsenow, Cooper, and Stephan/Abdelsalam. Since all of these correlations are based on empirical data, large differences can appear when different fluids or heater surfaces are used. In Ref. [4], the correlation of Cooper fits very well to the experimental data. Since their fluids were very simliar to the fluids used in this article and because the correlation of Cooper is very simple, it was used for the validation of the presented experiments. The equation is given below:

$$\alpha = 55 p_r^b (-0{,}4343 \ln(p_r))^{-0.55} M^{-0.5} q^{0.67} \quad (2)$$

where $p_r = p/p_c$ is the reduced pressure and $b = 0.12 - 0.2 \log(R_p)$ is a function of the surface roughness.

However, all of these correlations are predominantly experiment based and need large amounts of experimental data for validation. With new fluids or new surfaces, the models may fail. Thus, our basic understanding of the complex transport phenomena is still not sufficient to build a comprehensive theory or accurately predict nucleate boiling heat transfer [5]. Stephan [5] explained that this is due to different transport phenomena from the nanometer to the millimeter scale, which strongly interact with each other in a transient process with very small response time. Since modern measurement technologies with very high lateral

[1]Corresponding author.

Manuscript received February 15, 2008; final manuscript received January 12, 2009; published online October 15, 2009. Review conducted by Yogesh Jaluria.

and temporal resolution and powerful numerical methods are available, it is possible to include microscale mechanisms in theoretical and experimental research.

A general approach of thin film evaporation using the disjoinig pressure concept was laid in the 1970s by Wayner et al. [6]. From that model, the heat and mass transfer could be computed near the tiny contact region where the liquid-vapor interface meets the heated wall. Here, the curvature changes and the heat resistance is very low. Thus, extreme heat fluxes appear in a region with about 1 μm lateral extension. The heated wall, which is in direct contact with the vapor, holds an adsorbed film of about 2 nm thickness. It cannot evaporate, and in the inner region of the bubble the heat flux is almost zero.

Since that time, different groups have developed numerical models where the calculation of the so called *microregion* is included in the calculation of single bubble growth on heated walls (*macroregion*). Dhir et al. [7] conducted numerical calculations of entire bubble cycles growing and departing from a heated wall and bubble coalescence using a free bubble surface. The microregion heat flux was computed with a simplified assumption of constant wall temperature and with a parametrized dynamic contact angle function. Fujita and Bai [8] also presented a transient model for bubble growth and departure, assuming constant wall temperature and constant contact angle. Stephan and Hammer [9] developed a quasistationary model of bubble growth on a heated surface. In an iterative process, the equations for mass, momentum, and energy balance were solved and coupled between the micro- and macroregion. The temperature distribution in the wall was also computed. It shows that spatial and temporal fluctuations of the wall temperature have a non-negligible influence on the heat transfer. Fuchs and Stephan [10] extended the model to calculate the entire bubble cycle including bubble contraction, displacement, and rise in the liquid. The local heat fluxes between heater and bubble (microregion), between heater and fluid, and between fluid and vapor bubble were computed for the entire bubble cycle. It was discovered that about 30–40% of the latent heat is flowing through this tiny region near the contact line. Kern and Stephan [11] developed a model also based on the model of Stephan and Hammer [9] and included the mass transfer of binary mixture evaporation. Kern analyzed the effect of Marangoni convection, variation in the fluid properties, and differences in the saturation temperature. He showed that the Marangoni convection and the variation in the fluid properties in binary mixtures have only a small influence on the heat transfer rates. However, the increase in the saturation temperature due to the concentration gradient at the interface has a strong influence on the nucleate boiling heat transfer of binary mixtures. The local heat flux through the microregion is reduced by about 30% in the case of binary mixture evaporation in contrast to pure fluids. The mass transfer is also lower, which is why the interface curvature and the contact angle are reduced.

For validation of these theoretical predictions, local temperature observations at the heater surface have been carried out by different groups. Kenning et al. [12–14] used thermocromic liquid crystals (TLCs) to obtain a high spatial temperature resulution at the rear side of a thin metallic foil heater. When bubbles grow in the liquid, on top of the foil, a spreading cold spot could be visualized by the TLCs. While the TLCs provide lateral resolution in the range of some microns, the temperature signal is always alleviated due to the thermal inertia of the TLC substance itself. Thus, the local effects of contact line evaporation were blurred and the observation was hindered. Shoji et al. [15] used silicon plates of 200 μm thickness with artificial nucleation sites. These microbores had different shapes and varying diameter (5–100 μm) and cavity depths (20–80 μm). The plate was heated by a Nd-YAG laser and the heater's back side was recorded with an IR camera. The lateral and temporal resolution was not high enough to observe local effects. The bubble rate at the artificial nucleation sites shows irregularities and fluctuations to some extent.

The problems of high bubble frequencies, and thus strong signal attenuation, have been avoided in some experiments at the author's institute. Hoehmann and Stephan [16] observed a steady state evaporating liquid meniscus on top of a very thin heating foil. They used unencapsulated TLCs to visualize an obvious temperature drop near the three-phase contact line, caused by strong evaporation. The lateral resolution of his measurement technique was 0.8 μm, and the temperature drop occurred in a region of about 40 μm. In Ref. [17], the contact line evaporation of a steady state vapor bubble was observed during a parabolic flight experiment, and this was also with unencapsulated TLCs. In almost zero gravity, the bubble did not detach and the temperature profile could develop at the 10 μm thick heating foil. Close to the contact line, a temperature drop occurred with about 5 K amplitude. In the center of the bubble, the temperature increased continuously, the reason being that there is almost no heat flux into the wall, except for electrical heat input. These results agree qualitatively well with the theory of Wayner et al. [6].

Current research is focused on the quantitative validation of numerical results. In Ref. [18], entire bubble cycles of water at atmospheric pressure were observed ontop of a 6 μm titanium foil heater. The back side was observed using an IR high-speed camera with a 40 μm lateral extension and a 1000 Hz frame rate. The temperature images have been used to compute the heat flux from the heater into the bubble applying an energy balance for every pixel element. Golobic et al. [18] showed high local heat fluxes close to the contact line during the first milliseconds of bubble growth. When the bubbles have reached their maximum foot diameter, the local heat flux decreases significantly. In the center of the bubbles, a certain heat flux was visible in all cases due to unclarified reasons. Unfortunately, the authors did not discuss the measurement errors, since these calculations are very sensitive to unknown exact electric heat input. Very similar experiments were also conducted at the authors' institute [19,20]. An IR camera was recording the rear side of a 50 μm thick heating foil, running at 1000 Hz, with 14.5 μm lateral extension. In these experiments, the local heat flux at the contact line was clearly visible as a ring shaped region with very high heat fluxes. During the change from receding to advancing contact angle, the heat flux also decreases significantly. However, in the center of the bubble, there was almost no heat flux at all times. Additionally, in Ref. [20], the entire bubble cycle was analyzed using the shadow method for the bubble volume identification. The heat flux through the microregion was then compared with the total latent heat of the bubble: about 30% of the latent heat is flowing through this tiny contact region. This fits quite well the calculations of Fuchs and Stephan [10].

To the authors' knowledge, no one has tried to observe the microscale effects of contact line evaporation when binary mixtures are evaporated instead of pure fluids. The numerical results of Kern and Stephan [11] have not been validated yet. For that reason, the measurement technique described above was used to analyze the local heat transfer mechanism near the contact line for a binary mixture of FC-84 and FC-3284. With global measurements, the mixture effects were visualized first. Then, a detailed analysis of the contact line heat flux was carried out using the methods that have been tested previously for pure fluids.

2 Experimental Setup and Procedure

In contrast to several other boiling experiments, a new experimental concept has been developed. Thus, it is possible to carry out conventional boiling experiments to determine the global HTC. Additionally local measurements at isolated single bubble events can be analyzed.

2.1 Design of the Boiling Cell. The boiling device basically consists of the boiling cell itself and a special electric foil heater at the bottom.

In Fig. 1, a sketch of the boiling cell is shown. The cell has a volume of about 80 ml and is made of brass. The complete cell is

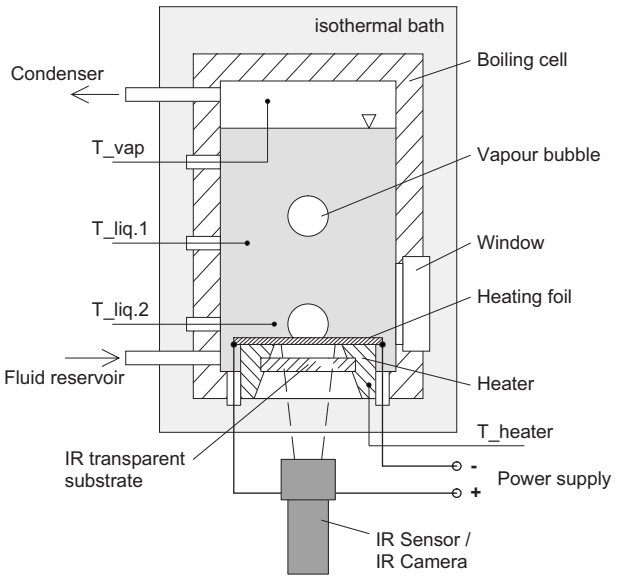

Fig. 1 Design of the boiling cell with an electric foil heater

dunked into an isothermal bath to guarantee stable thermal conditions, even at low heat flux. The heater is mounted in the bottom plate of the cell, which consists basically of a copper platform. The heating foil is fixed on top of this block and contacted with two electrodes. The heater has a separate cooling system to avoid nucleate boiling at unwanted hot spots, especially at the electrodes. The vapor bubbles are generated at the center of the heating foil. The temperature of the foil is recorded from the rear site with an IR sensor for global measurements or with a high-speed IR camera in the case of high-resolution local measurement. The bubble shape is accessible through windows in the side walls. Two thermocouples and one PT100 resistance thermometer ($T_{\mathrm{liq.1}}$) give information about the temperature in the boiling cell. Another thermocouple is used to control the heater block temperature. The condenser and the fluid reservoir for volume compensation and pressure adjustment are placed in a separate chamber not shown in Fig. 1. More details about the experimental setup are given in Refs. [19,20].

2.2 Experimental Procedure. Fluorinert fluids such as FC-84 and FC-3284 have the affinity to dissolve huge amounts of noncondensable gases like air. This will affect the nucleate boiling performance as reported in Refs. [21,22]. However, a degassing procedure must be conducted, which is not trivial when binary mixtures are used. For pure fluids, the general approach is to boil the fluid for some hours and exhaust the noncondensable gases at the highest point above the condensator. Separation due to higher density of the fluorinert vapor can be applied in this case. When binary mixtures are boiled, it is not possible to exhaust a vapor/gas mixture out of the system. Since the vapor will always contain a higher concentration of the more volatile component, removing vapor will lead to a shift of the mole fraction. Thus, when binary mixtures are used, the noncondensable gases must be removed before filling. During the boiling procedure, the system must be closed. Here, the mixture was made by weighting out the components under air contact. Then, a degassing procedure was applied, which is recommended in Ref. [23] for heat pipe fluids. Therefore, the liquid mixture is filled into a round bottom flask, closed and frozen with liquid nitrogen. When the fluid is completely frozen, the vapor pressure tends toward zero and the flask can be evacuated. When unfreezing, the dissolved gas will bubble out of the liquid. It can be removed with the vacuum pump after refreezing the liquid again. The gases will be removed after two to three freezing cycles.

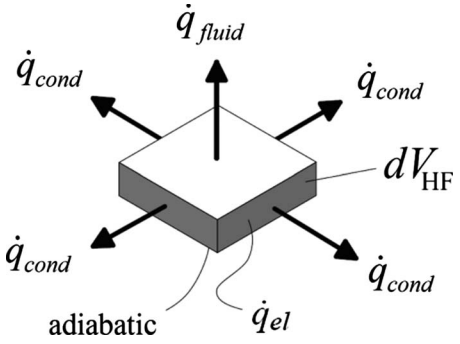

Fig. 2 Energy balance of one single pixel element

The boiling procedure was carried out as recommended in Ref. [24] always with decreasing heat flux to avoid the known effect of hysteresis when changing between nucleate boiling and natural convection. The heat flux was always adjusted by controlling the electric current. Thus, fluctuations caused by varying temperature, and subsequently varying voltage drop of the connections and cables, could be avoided.

2.3 Experimental Based Data Analysis. For the local measurements, the rear site of the heating foil is captured with an IR camera providing high-resolution temperature fields. From this, the local heat flux distribution from the heater into the fluid $\dot{q}_{\mathrm{fluid}}$ is estimated.

Therefore, a discretization algorithm like the one suggested by Alifanov [25] is used. The heating foil is divided into the pixel elements dV_{HF} of the IR images as shown in Fig. 2. For each pixel, an energy balance is applied using Fourier's equation:

$$\delta\rho c\frac{\partial T}{\partial \tau}=\lambda\left(\frac{\partial^2 T}{\partial x^2}+\frac{\partial^2 T}{\partial y^2}\right)+\dot{q}_{\mathrm{el}}-\dot{q}_{\mathrm{fluid}} \tag{3}$$

Thus, the lateral heat conduction $\dot{q}_{\mathrm{cond}}$ is taken into account. For the calculation, it was assumed that the back side of the heating foil is adiabatic and that the temperature is constant within the volume of the pixel elements dV_{HF}.

The heat flux $\dot{q}_{\mathrm{el}}$ is calculated using only the electric current I, to avoid errors due to unknown voltage drops at the electrode-heater contact. Therefore, the resistance of the heating foil is calculated using the specific electric resistance, which is a temperature dependent material constant. With this, the transient heat storage in the foil material is included through the temperature difference between two time steps:

$$\frac{\partial T}{\partial \tau}=\frac{T_{i+1}-T_i}{\Delta\tau} \tag{4}$$

The spatial derivation of second order on the right hand side (heat conduction) was also approximated by discrete elements.

$$\frac{\partial^2 T}{\partial x^2}\approx\frac{T_{x+1}-2T_x+T_{x-1}}{(\Delta x)^2} \tag{5}$$

Due to the problem of all inverse heat conduction problems, the signal noise of the camera signal will be attenuated and disturb the data analysis. Therefore, a filter technique based on the discrete cosine transformation (DCT) is used. The error made through the noise could be strongly reduced. For more information, see also Ref. [19].

For computing the total microregion heat flux, a threshold of 4×10^4 W/m^2 was applied to the $\dot{q}_{\mathrm{fluid}}$ values of all pixels. Only values higher than the threshold were allocated to the microregion evaporation. The total microregion heat flux $\dot{Q}_{\mathrm{mic}}$ is the sum of these values.

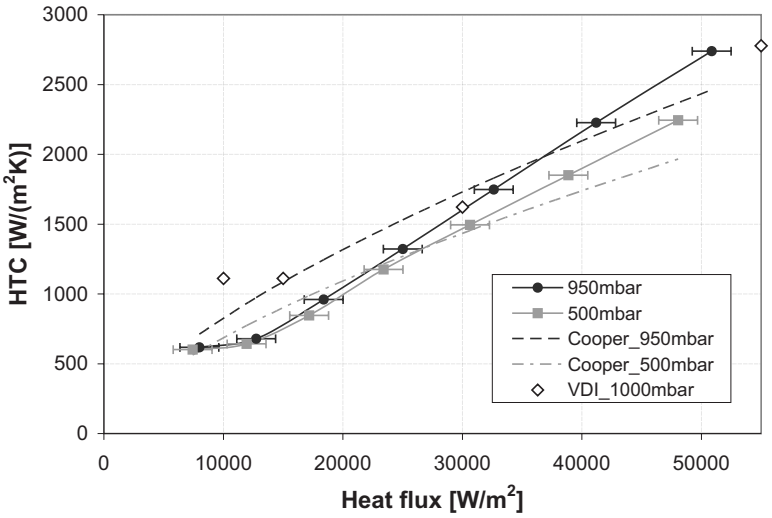

Fig. 3 HTCs for FC-84, measurements, and calculations

2.4 Estimation of the Measurement Errors. It should be mentioned that the presented data include measurement errors that are partly non-negligible. For the determination of the (global) heat transfer coefficient α, the heat flux and the temperature of the heating foil, as well as the saturation temperature, must be known.

$$\alpha = \frac{q_{\mathrm{el}}}{t_w - t_{\mathrm{sat}}} \tag{6}$$

Generally, two classes of measurement errors must be considered. The first class is the absolute measurement error, which is dependent on the system configuration. When measurements are compared with data from other authors, these errors will cause a continuous offset of the values. When different fluids or conditions are observed in the same system, the absolute errors will cancel each other out. In this case, the second class of errors decides: The statistical measurement errors will lead to a variance between the measurement points and the true values. It is recommended to repeat the measurements several times for a reduction in this variance, which can be expressed by the standard derivation.

2.4.1 Heat Flux. The heat flux is the most important input value of the nucleate boiling system. Electrical power is converted into heat by Ohm's law when electric current is flowing through the resistance of the heating foil.

$$\dot{Q}_{\mathrm{el}} = P_{\mathrm{el}} = U \cdot I \tag{7}$$

However, only the voltage drop U of the entire heating foil and the current I are available for the measurement. The heat flux $\dot{q}_{\mathrm{el}}$ is not directly known. The heat that is produced in a certain area of interest is where the nucleate boiling process takes place. When the heat flux $\dot{q}_{\mathrm{el}}$ is calculated in a global way by the ratio of the total heat flux $\dot{Q}_{\mathrm{el}}$ to the entire area of the heating foil, a non-negligible error will occur. At the contact area between the electrodes and the heating foil, additional contact resistances must be taken into account, which are not known; about 30% of the electric power is converted into heat at these sites. For that reason, the authors decided to calculate the heat flux only with the electric current I, which is the same in all cables and resistances of the circuit.

$$\dot{q}_{\mathrm{el}} = \frac{I^2 \cdot \rho_{20}(1 + \alpha_{20}(t_w - 20))}{b_f^2 \cdot s_f \cdot 10^6} \tag{8}$$

Here, the index f stands for the heating foil. For the following values, the maximum errors are estimated in a conservative way. The electric current I is given by the power source in a quite accurate range of about 10 mA. The specific resistance of the heating foil ρ_f is taken from the literature, and for stainless steel (X5 CrNi 18 9) the value is 0.73 $\Omega\,\mathrm{mm}^2/\mathrm{m}$ at 20 °C [26]. The electric resistance is also a function of the temperature. It can be assumed with $\alpha_{20} = 0.005\ 1/\mathrm{K}$. For the heater temperature t_w, an error of about 0.5 K is assumed, which is estimated conservatively on the basis of the error of the thermocouple itself (± 0.1 K) and the applied calibration method of the IR camera. The thickness s_f of the heating foil is 20 μm with a tolerance of 1 μm. The width of the foil b_f is 20 mm with a tolerance of 0.1 mm.

For the estimation of the total measurement error of the heat flux, an error propagation recommended in Ref. [27] was used.

$$\Delta\dot{q}_{\mathrm{el}} = \frac{\partial\dot{q}_{\mathrm{el}}}{\partial I}\Delta I + \frac{\partial\dot{q}_{\mathrm{el}}}{\partial\rho}\Delta\rho + \frac{\partial\dot{q}_{\mathrm{el}}}{\partial\alpha_{20}}\Delta\alpha_{20} + \frac{\partial\dot{q}_{\mathrm{el}}}{\partial T_w}\Delta T_w + \frac{\partial\dot{q}_{\mathrm{el}}}{\partial b}\Delta b + \frac{\partial\dot{q}_{\mathrm{el}}}{\partial s}\Delta s \tag{9}$$

With the above mentioned data the heat flux was calculated for a standard experiment with FC-84 at 500 mbars, $t_{\mathrm{sat}} = 62.5$ °C, $t_w = 82.5$ °C, and 12 A heating current. The calculated heat flux is

$$\dot{q}_{\mathrm{el}} = 17250 \pm 1625\ \mathrm{W/m}^2 \tag{10}$$

The absolute measurement error for the heat flux is therefore

$$\frac{\Delta\dot{q}_{\mathrm{el}}}{\dot{q}_{\mathrm{el}}} = 0.188 \tag{11}$$

This uncertainty of maximum $\pm 9.4\%$ is a result of the maximum errors of the wall temperature measurement and the further parameters included in Eq. (8). The uncertainty decreases below this value for higher heat fluxes, as shown in Fig. 3, where error bars are included.

2.4.2 Temperature Measurements. The main temperature in the boiling cell ($T_{\mathrm{liq.1}}$) is measured with a Pt100 sensor. It was calibrated with a reference sensor from the DKD,[2] and its accuracy is about 0.1 K. All other temperature sensors are calibrated with this sensor. The IR sensor has the highest error with about 0.5 K given from the manufacturer. The IR camera was calibrated in situ with special calibration polynomials for every pixel element. Thus, the error could be assumed with about 0.5 K, like the IR sensor.

[2]DKD: German Calibration Service.

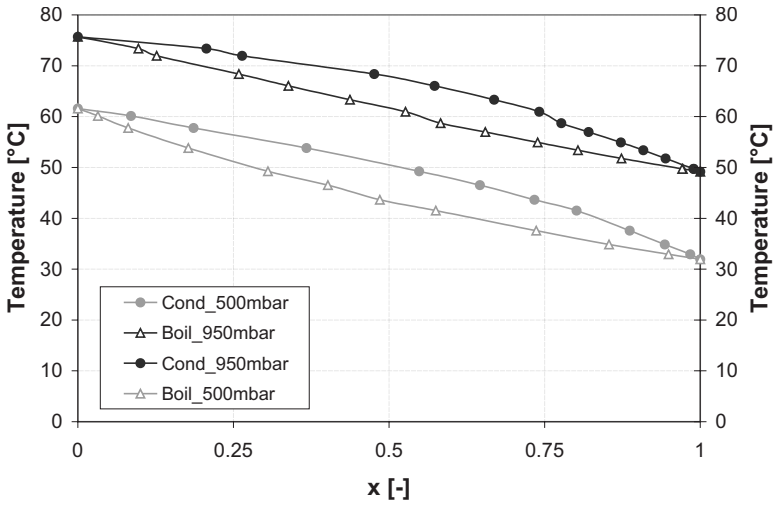

Fig. 4 Boiling and condensation curves of FC-84/FC-3284 binary mixtures at 500 mbar and 950 mbar absolute pressures

2.4.3 Pressure. The system pressure is not directly involved in Eq. (6). However, the saturation temperature t_{sat} is calculated from the measurement of the system pressure. The accuracy is about 5 mbars, which leads to a temperature error of 0.25 K. The error of the saturation temperature, which is calculated with a polynomial, is about 0.2 K. Thus, the overall temperature error of the saturation temperature is 0.45 K.

2.5 Standard Experiment. Before experiments with mixture effects will be compared, it is recommended to check the general reliability of the boiling curves. Therefore, a standard experiment has been defined, which is carried out with FC-84 at 500 mbars and 950 mbars.

In Fig. 3, the heat transfer coefficient α (HTC) is plotted versus the heat flux for the fluid FC-84. The HTC was calculated with Eq. (6). Two measurements at 500 mbars and 950 mbars are plotted. The curves of Cooper were calculated with the correlation given in Eq. (2). Additionally, measurements from the VDI-Wärmeatlas [28] are taken, which were recorded at 1000 mbars. The error bars at measured curves display the absolute measurement error, which was calculated in Sec. 2.4.1. The standard deviation of the HTC is about 1% calculated from several runs at the same system parameters.

The differences between the measurements and calculations are generally larger at low heat fluxes. The reason for this differences at low heat fluxes might have various reasons. One reason might be that at low heat fluxes, when natural convection still dominates, the test cell confinement might influence the overall heat transfer. Another reason might be the uncertainty of Cooper's correlation, which is not specified for our case. At 35 kW/m^2, the correlation of Cooper fits very well with the measured points. The gradient of the curves also shows little differences between calculated and measured data, but the spreading of the curves with different pressure is qualitatively right. The measured points from the VDI-Wärmeatlas show good agreement at higher heat flux. Altogether it can be concluded that the measured data are in an acceptable range compared with correlations and other measurements. Divergences in the range of small heat fluxes might be a result of different boiling cell designs. In the experiments of this article, a very thin heater plate is used with a relative wide extension at the bottom plate of the boiling cell. This could reduce the HTC of the convective flow in the cell.

3 Experimental Results

For the analysis of binary mixture experiments, the boiling and condensation points of different mixture compositions must be known. For that reason, the boiling and condensation curves have been recorded for the mixture of FC-84/FC-3284.[3]

From Fig. 4, it is clear that the differences between the saturation temperatures of the pure fluids are about 25 K at 950 mbars and even 30 K at 500 mbars. The 0.5*M* mixture shows a temperature difference between the boiling and condensation curves of about 7 K. These temperature differences should be sufficient to investigate certain mixture effects.

3.1 Global Measurements. At first, global measurements were conducted where the heat flux is plotted versus superheat of the heater plate. Conventional boiling curves are used to compare the characteristics of the pure fluids with the binary mixture.

In Fig. 5, boiling curves are plotted for all examined fluids at 500 mbar system pressure. The subcooling of the fluid is about 1.5–2 K in each experiment, and the curves were recorded with successive decreasing heat flux. It is obvious that the runs with binary mixtures show generally a higher wall superheat. The 0.5*M* mixture shows the highest wall superheat, while the 0.25*M* and 0.75*M* mixtures work with medium superheat. The curves of the pure fluids, FC-84 and FC-3284, show the lowest wall superheat and are close together at one point. It is remarkable that all curves show an anomaly at the change-over between nucleate boiling and natural convection, which was only observed at low system pressures. A possible explanation could be the following: With decreasing heat flux, the wall superheat increases again when the majority of the nucleation sites extinguish. It seems that a minimum heat flux is required for the nucleation site activity. In this special case, the effect might be caused by the very small thickness of the heating foil. The heat must be supplied locally with relatively high rates because the heat transfer from adjacent regions is not possible. In the following diagrams, the boiling curves are transformed to analyze the HTCs.

The curves in Fig. 6 show the HTCs as a function of wall heat flux. The characteristic is now more linear and the change-over from nucleate boiling to natural convection seems to be undisturbed. It is noticeable that the curves of the pure fluids are very close to each other, and the difference is actually indeterminable. The curves of the binary mixtures all show reduced HTCs. The 0.5*M* mixture shows the lowest values, and the 0.25*M* and 0.75*M* mixtures show medium HTCs. The mixture effect is clearly visible, and it is reproduciable at higher pressure (see Fig. 7). At

[3]The data were recorded within the scope of a cooperative DFG boiling project at the RWTH Aachen, Chair of Thermal Process Engineering.

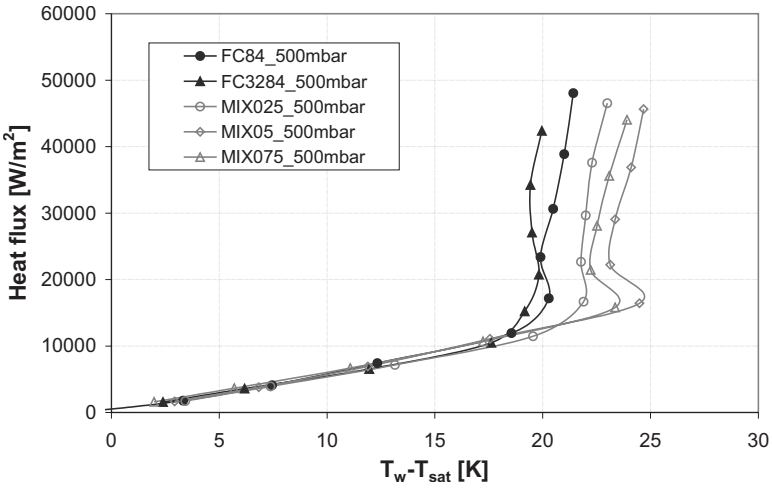

Fig. 5 Boiling curves for FC-84 and FC-3284 and a binary mixture with x = 0.5, all at 500 mbar system pressure

950 mbars, the effect is even more pronounced. While the pure fluid shows linear behavior, the mixtures show curved progression. This is an indication for the closeness to the critical point where film boiling starts. From the curves in Figs. 6 and 7, the HTC values could be determined at 40,000 kW.

In Fig. 8, the HTCs are plotted for 500 mbars and 950 mbars as a function of the mole fraction x (of the more volatile component FC-3284). The mixture effect is clearly observable; the HTCs of the 0.25M, 0.5M, and 0.75M mixtures show an obvious difference between the ideal and the measured HTC. The correlation of Schlünder [3] seems to predict this effect quite well for two different pressures. It is remarkable that the 0.25M mixture has a higher HTC as predicted by the correlation of Schlünder [3]. This particularity of flourinerts is also visible in the results presented by Schlindwein et al. [4], and it was found in other experiments at the authors' institute. As mentioned by Schlünder et al.[4], the difference between the HTCs of varying pressure is less pronounced for a binary mixture. This behavior is clear from the measurement points, but the model does not reflect this. For the presented data, the factor B_0 was set to 1.0; for the mass transfer coefficient β_0 the value 3×10^{-4} m/s was used. Thus, the correlation meets the measured data in a quite acceptable range.

3.2 Local Measurements. In this row of experiments, isolated bubbles were observed growing at one defined location. Therefore, different experiments were performed to activate single nucleation sites. As presented in previous reports, experiments with artificial nucleation sites were performed. In the present article, a bore produced with a focused ion beam (FIB) with a diameter of 10 μm and a depth of 15 μm was observed. This artificial nucleation site provided a reproducible bubble generation site for adjusting the measurement equipment. On the other hand, the bubble dynamics were not very regular. Often double bubbles were created and vertical coalescence occurred. Thus, the temperature and heat flux interpretation was possible but not in a good-looking way. Much better characteristics in a quite presentable style were obtained by the use of a coincidentally activated nucleation site on top of a plain stainless steel surface. After intense boiling with high current, the heat flux was successively reduced until this nucleation site was the only one active. It shows very high reproducibility, and after refilling the boiling cell, it was possible to activate the exact same nucleation site again with a different fluid. Therefore, the presented results in the following are produced with this natural nucleation site.

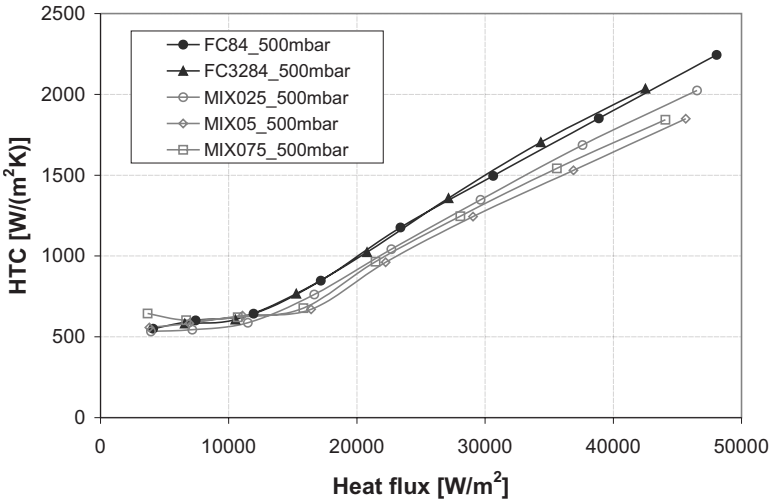

Fig. 6 Graph of heat transfer coefficients for FC-84 and FC-3284 and binary mixtures with x=0.25, x=0.5, and x=0.75, all at 500 mbar system pressure

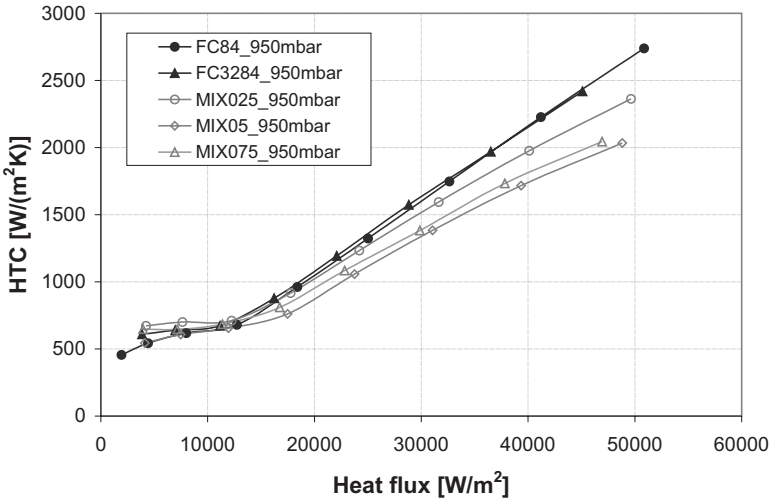

Fig. 7 Graph of heat transfer coefficients for FC-84 and FC-3284 and binary mixtures with $x=0.25$, $x=0.5$, and $x=0.75$, all at 950 mbar system pressure

For the local measurements, the IR sensor was replaced with an IR high-speed camera, which runs at 978 Hz. The spatial resolution was 14.5 μm.

It was possible to analyze the progression of the temperature field underneath growing and departing vapor bubbles. In Figs. 9–16, the bubble development is plotted for the pure fluid FC-3284, boiling at one single nucleation site at 500 mbars, as a representative example. The heat flux was 12,900 W/m^2. The first picture shows the bubble shape, visible from the shadow pictures. The second picture shows the temperature distribution, which was recorded with the IR camera. The third picture presents the temperature line profile along the line, which is visible in the temperature picture on the left. The line was placed in a way that the center of the line lies at the center of the bubble foot. Thus, almost symmetrical temperature profiles could be displayed. The fourth picture shows the heat flux picture calculated as described in Sec. 2.3. The time step between two figures is about 2(1.956) ms.

It has to be mentioned that the heat flux pictures are actually not exactly concurrent with the temperature fields. The temperature difference between two time steps is calculated by using the subsequent temperature picture. Thus, the heat flux pictures are a little bit in the future of the temperature pictures. However, the heat flux pictures obviously display where the bubble foot is located: A ring of very high heat flux is clearly visible close to the contact line at the bubble foot. This was predicted from numerical simulations [11,9]. During the first milliseconds, the bubble grows very fast, and very high heat flux rates around 250 kW/m^2 occur. At 62 ms, the bubble has reached its maximum foot diameter of about 2 mm, noticeable at the edges in the temperature line profile. The maximum heat flux at the contact line is only about 80 kW/m^2 at this moment. With decreasing bubble foot diameter, the contact-line heat flux increases again up to 170 kW/m^2 just before the bubble detachment. Another thing is remarkable: During the backward sliding contact line, the inner region of the bubble heats up (Figs. 13–16) until it has reached 54°C just before detachment. This effect might be caused by a neglectable heat flux $\dot{q}_{\text{fluid}}$ from the foil into the fluid. Since there is still the same heat input $\dot{q}_{\text{el}}$, the thin heating foil heats up very quick. The observed effect is a possible evidence of the numerical predictions that the heat flux is almost zero inside the bubble. The heat flux pictures also show insignificant heat flux within the inner region.

These effects have been reported before in Refs. [19,20]. However, the current questions are as follows: Is there an influence on

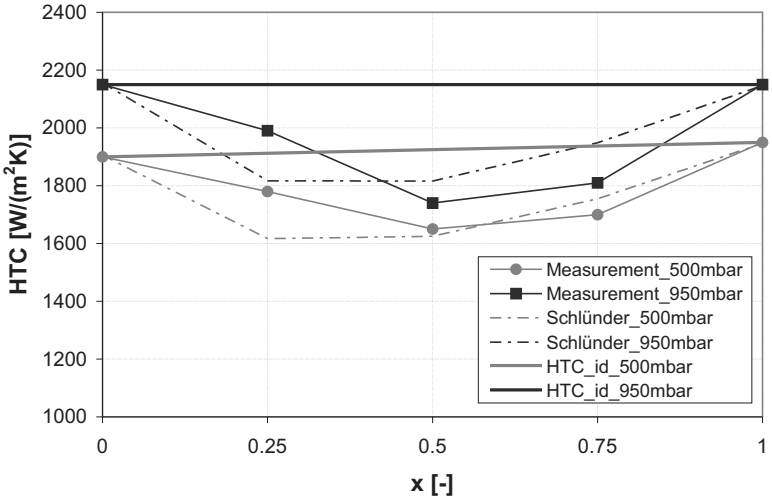

Fig. 8 HTCs as a function of the mole fraction x of the more volatile component FC-3284

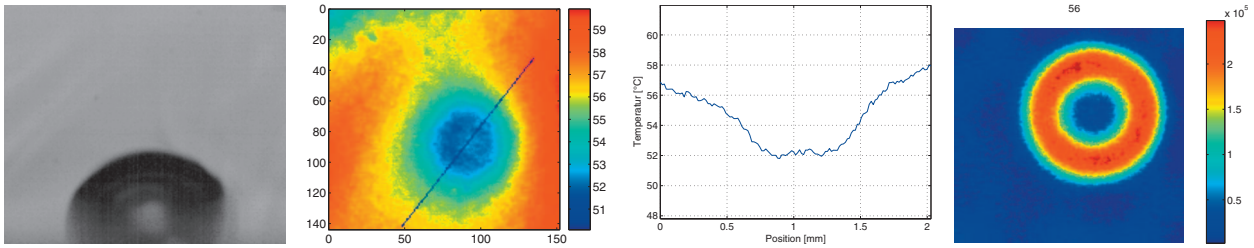

(*a*) (*b*) (*c*) (*d*)

Fig. 9 Bubble shape, IR temperature field (°C), temperature line profile, and heat flux distribution (W/m^2) at τ=56 ms

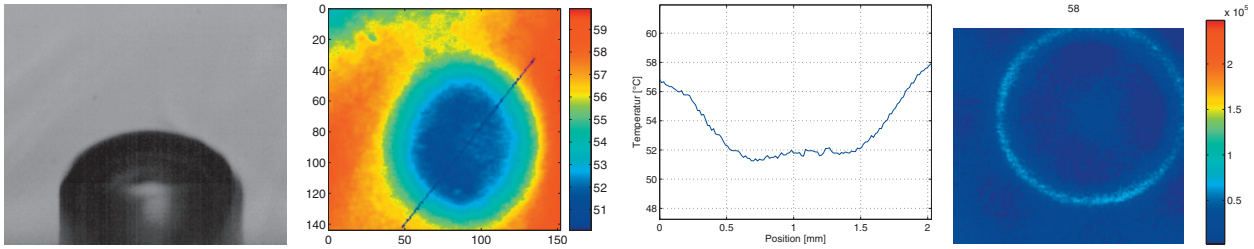

(*a*) (*b*) (*c*) (*d*)

Fig. 10 Bubble shape, IR temperature field (°C), temperature line profile, and heat flux distribution (W/m^2) at τ=58 ms

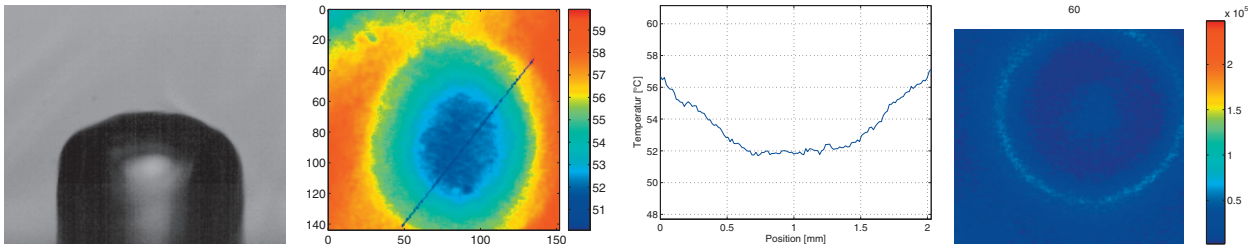

(*a*) (*b*) (*c*) (*d*)

Fig. 11 Bubble shape, IR temperature field (°C), temperature line profile, and heat flux distribution (W/m^2) at τ=60 ms

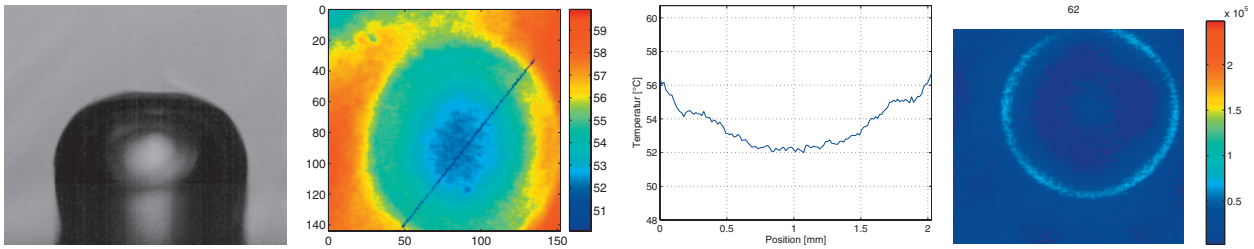

(*a*) (*b*) (*c*) (*d*)

Fig. 12 Bubble shape, IR temperature field (°C), temperature line profile, and heat flux distribution (W/m^2) at τ=62 ms

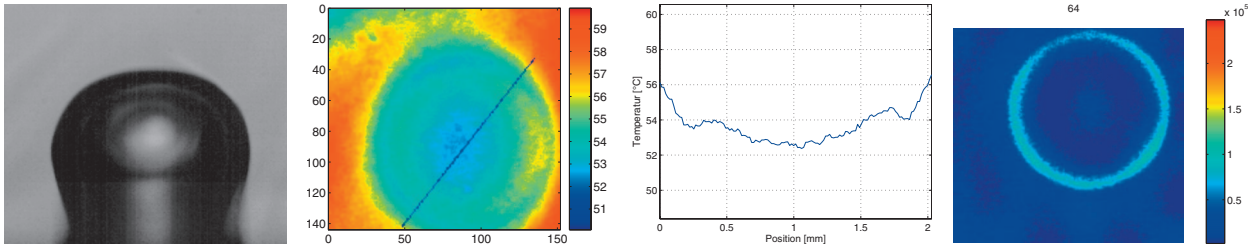

(*a*) (*b*) (*c*) (*d*)

Fig. 13 Bubble shape, IR temperature field (°C), temperature line profile, and heat flux distribution (W/m^2) at τ=64 ms

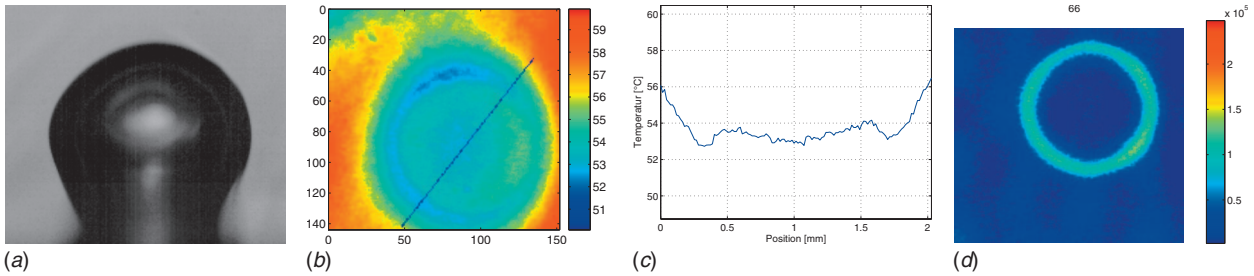

Fig. 14 Bubble shape, IR temperature field (°C), temperature line profile, and heat flux distribution (W/m^2) at τ=66 ms

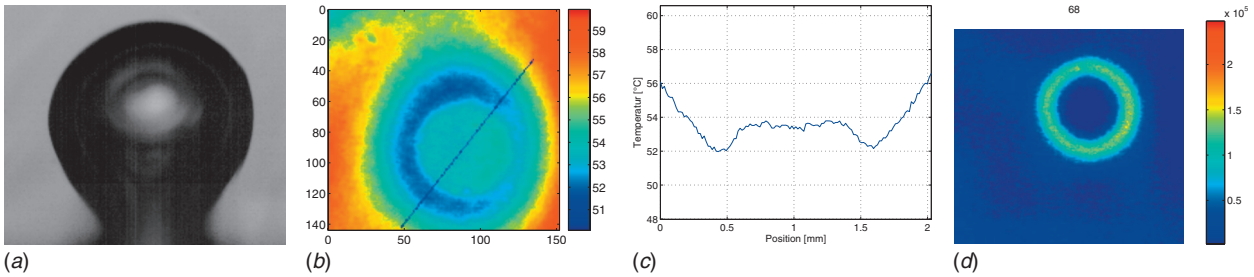

Fig. 15 Bubble shape, IR temperature field (°C), temperature line profile, and heat flux distribution (W/m^2) at τ=68 ms

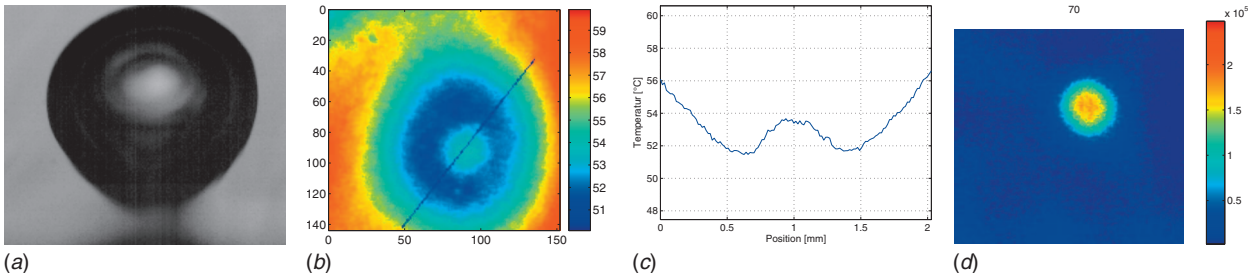

Fig. 16 Bubble shape, IR temperature field (°C), temperature line profile, and heat flux distribution (W/m^2) at τ=70 ms

the contact-line heat flux when binary mixtures are boiled instead of pure fluids? Is it possible to show a reduction in the contact-line heat flux of about 30%, which was calculated by Kern and Stephan [11]? Is the measurement accuracy high enough to display heat flux changes in the submicron range?

To find an answer to these questions, a single bubble experiment was conducted where the pure fluids FC-84 and FC-3284 were compared with a 0.5*M* mixture in the same experimental setup. It succeeded in activating the same nucleation site after changing the working fluid. Thus, all camera adjustments and calibration data could be used for the entire test series. However, the nucleation site activity always shows little instabilities and fluctuating behavior.

In Fig. 17, the bubble departure diameters, bubble frequency, and wall superheat of the three fluids are displayed as a function of the wall heat flux. As reported in a previous publication [19], the bubble diameter is predominantly influenced by the system pressure and not by the heat flux. Here, the diameters are in the range of about 2 mm (except one run with FC-3284, which shows partially an increase in the bubble diameters; huge bubbles with diameters up to 3.4 mm occur exceptionally in this case). FC-84 and the 0.5*M* mixture show almost constant diameters. Thus, the effect of reduced bubble diameters of binary mixtures, which was presented in Ref. [29], is not obvious in this case.

The bubble frequencies are also displayed as a function of the wall heat flux. Here, the correlation is obvious: With increasing heat flux, the bubble generation rate increases almost linear with a steep gradient. For the mixture, generally higher heat flux rates must be adjusted to generate single bubbles at the nucleation site. Since the bubble sizes were comparable with the pure fluids, higher frequencies level off to guarantee the heat removal from the wall.

In the bottom diagram of Fig. 17, the local wall superheats are shown as a function of temperature. Therefore, the temperature fields of Figs. 9–16 were used. The temperature fields were locally averaged over a region that was individually adjusted to the maximum bubble foot diameter. For the plots in Fig. 17, the temperature values were additionally averaged over a time sequence of 200 ms. Thus, the data represent the local medium wall superheats of the single bubble events. It is obvious that the binary mixture shows much higher wall superheat than the pure fluids. In combination with the effects of the bubble departure diameter and the bubble frequency, some interpretation of mixture effects is allowed: With the binary mixture, generally higher heat flux rates are necessary to obtain the activation of single bubbles at the nucleation site. This comes along with higher wall superheat and higher bubble frequency. The bubble departure diameter remains in a similar range as during pure fluid experiments. Thus, for the generation of a bubble with a special volume, the binary mixture requires a higher temperature gradient than the pure fluids. The heat transfer resistance, and therefore the work to produce a bubble, is obviously higher for the mixture.

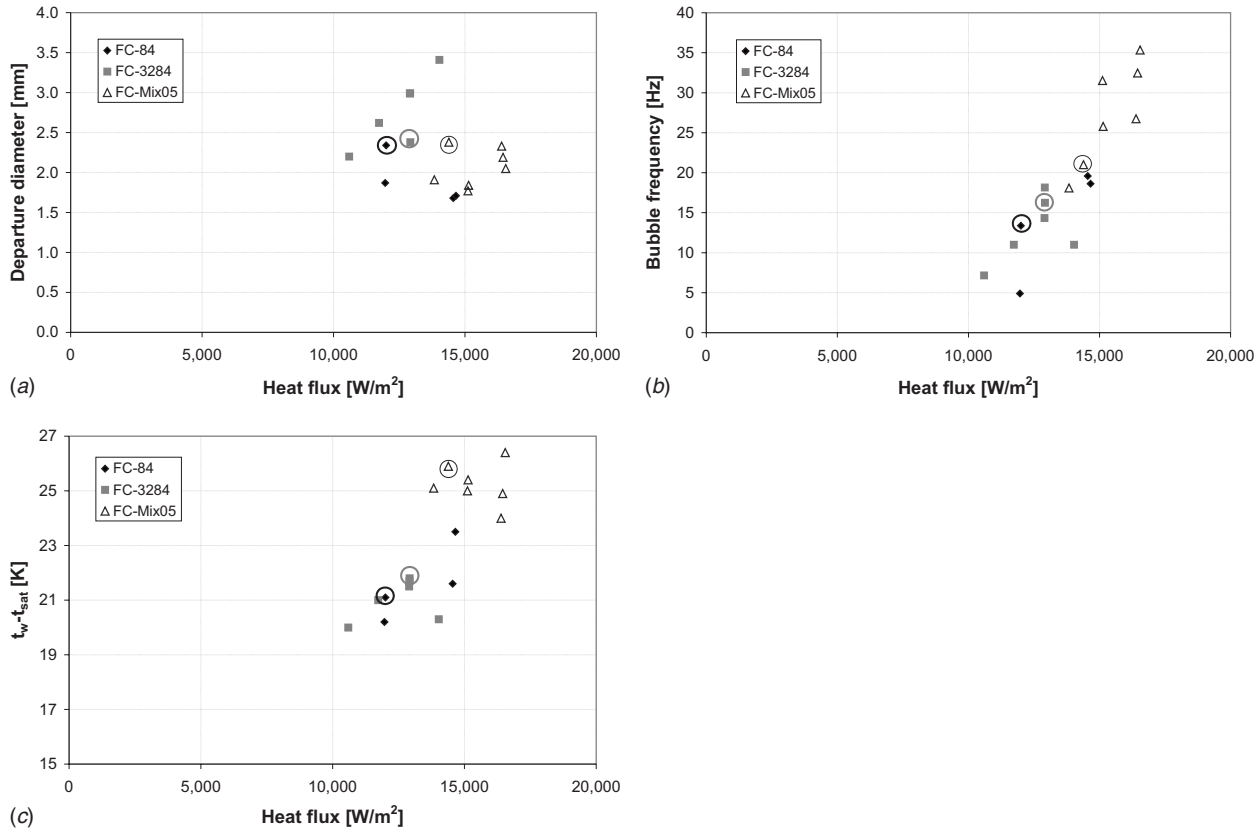

Fig. 17 Measurement results of single bubble test series with FC-84, FC-3284, and a 0.5*M* binary mixture at 500 mbars. Top: bubble departure diameter; center: bubble frequency; bottom: wall superheat; all as a function of heat flux.

For the detailed analysis and comparison, three measurements have been chosen with similar bubble diameters and heat flux rates. The elected experiments are labeled with circles of the corresponding graey scale.

In Fig. 18, single bubble cycles are displayed for FC-84 (top), FC-3284 (middle), and the 0.5*M* mixture (bottom). For better clearness, the timeline is shifted and the onset of bubble growth is set at 1 ms for each experiment. The development of the bubble volume is analyzed with a polynominal ($V_{\text{bub,poly}}$) that was fitted through the measurement points ($V_{\text{bub,meas}}$). The total evaporation heat flux into the bubble $\dot{Q}_B$ is also displayed and the heat flux through the contact region (microregion) $\dot{Q}_{\text{mic}}$. A similar way of the measurement analysis has been presented in Ref. [20]. Therefore, the bubble volume was determined by image processing of the bubble shape pictures. From the volume difference ΔV_B between two time steps, the evaporation heat flux $\dot{Q}_B$ was calculated using the density of the vapor ρ_v and the latent heat Δh_v. The microregion heat flux $\dot{Q}_{\text{mic}}$ is calculated from the heat flux pictures in Figs. 9–16. With a threshold of 4×10^4 W/m^2, only the values of the visible ring were taken into account and summed up for every picture. The ratio of the microregion heat flux to the evaporation heat flux $\dot{Q}_{\text{mic}}/\dot{Q}_B$ is additionally displayed.

The development of a bubble growing on the heating foil can be divided into three periods. During the first milliseconds, very fast explosionlike bubble growth is observable. The highest heat flux rates and the steepest increase in the bubble volume occur in this moment. For pure fluids in this experiment (FC-84 and FC-3284), about 30% of the total evaporation heat was flowing through the microregion during this first event of bubble growth; for the mixture (FC-84/FC-3284, $x=0.5$), the ratio was less than 20%. In the second period, the bubble foot diameter reached its maximum extension and the constriction began. The dynamic contact angle changed from "receding" (expansion) to "advancing" (contraction). Here, a minimum in the microregion heat flux occurred, and the curve of the bubble volume turned into a more flat slope. Only less than 10% of the heat was flowing through the microregion for the observed pure fluids (FC-84 and FC-3284); in terms of the binary mixture (FC-84/FC-3284, $x=0.5$), the ratio approached 0%. The reason for the reduced microregion heat flux is not yet fully understood because the bubble contraction at the bubble food is a very complex process. It was observed that the velocity of the contact-line movement has an influence on the microregion heat flux. Thus during very low contact-line velocity, the lowest microregion heat flux occurs. The last period was characterized through the bubble detachment with advancing contact angle. The microregion heat flux had a second maximum, while the over all heat flux decreased continuously. Thus, the ratio of the microregion heat flux reached high values between 40% and 60% for the observed pure fluids. For the mixture in this experiment, the microregion ratio was obviously reduced and reached not more than 35%. This can be explained by the theory of the mixture effect: As a result of very high heat fluxes close to the contact line, the adjacent region changed its mixture concentration very quick. A higher concentration of FC-84 increased the local saturation temperature, and this increased the heat transfer resistance. More heat had to flow through other regions, and the ratio of the microregion heat flux was obviously reduced. The reduction in the microregion heat flux agreed quite well with the numerical results of Kern and Stephan [11].

4 Summary and Conclusion

A test section was built where nucleate boiling can be performed on top of a metallic foil heater with a thickness of 20 μm. The temperature of the heater was recorded from the rear side by IR thermography. Global measurements were conducted using an

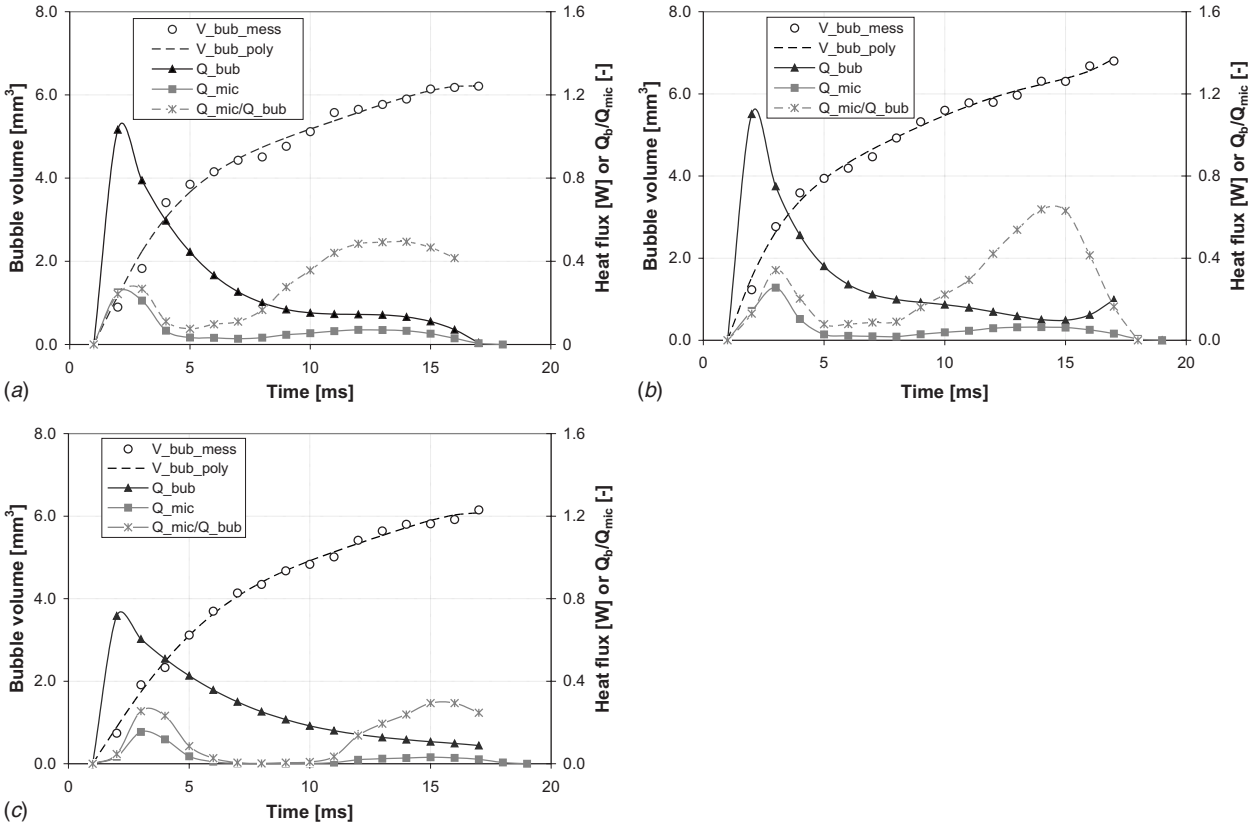

Fig. 18 Time progression of measured bubble volume ($V_{bub,meas}$), fitted polynominal ($V_{bub,poly}$), latent heat flux ($\dot{Q}_{bub}$), microregion heat flux ($\dot{Q}_{mic}$), and ration of microregion heat flux ($\dot{Q}_{mic}/\dot{Q}_{bub}$) during bubble growth. Top: FC-84 at 12,000 W/m²; center: FC-3284 at 12,900 W/m²; bottom: FC-mix, x=0.5 at 14,400 W/m².

IR sensor for receiving the mean heater temperature. The fluids FC-84, FC-3284, and binary mixtures with mole fractions of x =0.25, 0.5, and 0.75 were observed at 500 mbar and 950 mbar absolute pressures. Local measurements were conducted with only one active nucleation site generating isolated bubbles. The heater temperature was recorded with a high-speed IR camera providing high temporal and spatial resolutions. The local distribution of heat flux from the heater into the fluid, especially through the microregion at the contact line, could be computed from the IR temperature fields. From that, the heat transferred through this region could be analyzed for the pure fluids and for one mixture with a mole fraction of x=0.5.

In Table 1, some important fluid properties are listed along with the main results from the global measurements. The pure fluids FC-3284 and FC-84 are very similar and the properties vary in a range of only 10%. Thus, the influence of the fluid properties on the heat transfer may not be significant. The more volatile fluid FC-3284 shows the highest latent heat and the highest heat transfer coefficients during the global measurements. However, this difference is also less than 10% and should fall in the range of the measurement accuracy. For the binary mixture, instead of the saturation temperature, the bubble point (bp) was experimentally determined. The fluid properties of the mixture are the ideal (id) properties. They are calculated from the pure fluid properties and weighted by means of the mole fraction. During the experiments, the mixture shows a HTC reduction of more than 20%, which was reproducible in different experiments. The mixture effect is obvious and is confirmed by the correlation of Schlünder.[3].

In Table 2, an overview is given about the main experimental results of the local measurements. From a test series where more than 100 single bubbles were analyzed, three representative bubbles were chosen that have a similar bubble departure diameter. The heat flux and the bubble frequency of the elected bubbles were also in a typical range (compare Fig. 17). For these bubbles, the progression of the bubble volume V_{bub}, the total evaporation heat flux $\dot{Q}_{bub}$, and the microregion heat flux $\dot{Q}_{mic}$ are plotted in a similar way as presented by Fuchs et al. [10]. The curves given by Fuchs et al. [10] show little deviant behavior compared to the measurement results. $\dot{Q}_{mic}$, for example, increases continuously and has a maximum just before departure. This development is caused by an almost constant dynamic contact angle and spherical

Table 1 Fluid properties at 500 mbars and summary of the global measurement results

	FC-84	FC-3284	FC-mix
T_{sat}	62.5°C	32.2°C	45.5°C (bp)
Δh_v	90.0 J/g	105.0 J/g	97.5 J/g (id)
$\sigma_{20°C}$	12.0 mN/m	13.0 mN/m	12.5 mN/m (id)
$HTC_{40\ kW/m^2}$	1940 W/m² K	2100 W/m² K	1650 W/m² K
$\Delta T_{40\ kW/m^2}$	21.1 K	19.8 K	24.5 K

Table 2 Summary of the local measurement results at 500 mbars

	FC-84	FC-3284	FC-mix
$\dot{q}_{el}$	12,000 W/m²	12,900 W/m²	14,400 W/m²
$\Delta T_{local,m}$	22.3 K	23.0 K	26.7 K
d_B	2.29 mm	2.25 mm	2.21 mm
f_B	13.4 Hz	16.2 Hz	21.0 K
$\dot{Q}_{mic,m}/\dot{Q}_B$	30.0%	28.1%	13.2%

bubbles until departure. The free surface behavior of the bubble constriction is not implemented in the model. The averaged ratio of the microregion heat flux $\dot{Q}_{\mathrm{mic}}/\dot{Q}_B$ shows good agreement between measurement and computation.

The binary mixture shows an obviously reduced microregion heat flux in all periods. Thus, to form a bubble with a given size (comparable to the pure fluids), more heat has to flow through the phase interface between liquid and vapor. Because of a local concentration gradient of the more volatile component in this direction, the heat transfer resistance is increased. Therefore, higher wall superheat is required to force the heat flux. Higher wall superheat again requires a higher wall heat flux. This additional heat will be removed by an increase in the bubble frequency.

Acknowledgment

The authors gratefully thank the German Science Foundation (DFG) for financial support of the project within the joint program "Nucleate Boiling of Mixtures," where the groups of Professor Auracher and Professor Ziegler in Berlin, Leipertz in Erlangen and Marquardt in Aachen collaborate. Sincere thanks goes to all participants of this program for fruitful discussions and support. We thank Professor A. Pfennig from the Chair of Thermal Process Engineering at RWTH Aachen, who determined the boiling and condensation curves for different mixture concentrations.

Nomenclature

b = coefficient of Cooper
b_f = width heating foil (m)
B_0 = coefficient of Schlünder
c = heat capacity (J/kg K)
d_B = bubble diameter (m)
f_B = bubble frequency (Hz)
I = electrical current (A)
M = molar mass (kg/mole)
p = system pressure (bar)
p_c = critical pressure (bar)
p_r = normalized pressure
$\dot{q}$ = heat flux ($\mathrm{W/m^2}$)
$\dot{Q}_B$ = total heat flux in bubble (W)
$\dot{q}_{\mathrm{el}}$ = electrical heat flux ($\mathrm{W/m^2}$)
$\dot{Q}_{\mathrm{el}}$ = electrical power (W)
$\dot{Q}_{\mathrm{mic}}$ = microregion heat flux (W)
$\dot{q}_{\mathrm{fluid}}$ = heat flux wall fluid ($\mathrm{W/m^2}$)
R_p = surface roughness (μm)
s_f = thickness of heating foil (m)
t_w = wall temperature (°C)
t_{sat} = saturation temperature (°C)
T_{S1} = saturation temp. FC-3284 (°C)
T_{S2} = saturation temp. FC-84 (°C)
U = voltage (V)
x = first extension heater (m)
y = second extension heater (m)
$\tilde{y}_1$ = mole fraction vapor, FC-3284
$\tilde{y}_2$ = mole fraction vapor, FC-84

Greek Symbols

α = heat transfer coefficient HTC ($\mathrm{W/m^2\,K}$)
α_{20} = temperature coefficient (1/K)
α_{id} = ideal HTC ($\mathrm{W/m^2\,K}$)
β_0 = mass transfer coefficient (m/s)
δ = thickness (m)
Δ = difference
Δh_v = latent heat (J/kg K)
ΔT = wall superheat (K)
∂ = partial
λ = thermal conductivity (W/m K)
ρ = density ($\mathrm{kg/m^3}$)
ρ_{20} = electric resistivity ($\Omega\mathrm{mm^2/m}$)
ρ_l = liquid density ($\mathrm{kg/m^3}$)
σ = surface tension (N/m)

References

[1] Bonilla, C., and Perry, C., 1941, "Heat Transmission to Boiling Binary Mixtures," Trans. Am. Inst. Chem. Eng., **37**, pp. 662–669.
[2] Baehr, H., and Stephan, K., 2006, *Wärme- und Stoffüberragung*, 5th ed., Springer-Verlag, Berlin.
[3] Schlünder, E., 1982, "Über den Wärmeübergang bei der Blasenverdampfung von Gemischen," Verfahrenstechnik, **16**(9), pp. 692–698.
[4] Schlindwein, A. R., Martin, F. O., Jr., Misale, M., and Passos, J. C., 2006, "Nucleate Boiling of FC-87/FC-72 Zeotropic Mixtures on a Horizontal Copper Disc," ECI International Conference on Boiling Heat Transfer.
[5] Stephan, P., 2007, "Transient Transport Phenomena During Bubble Growth, Detachment and Rise in a Nucleate Boiling Process," Fourth International Berlin Workshop on Transport Phenomena With Moving Boundaries.
[6] Wayner, P., Kao, Y., and Croix, L. L., 1976, "The Interline Heat Transfer Coefficient on an Evaporating Wetting Film," Int. J. Heat Mass Transfer, **19**, pp. 487–492.
[7] Dhir, V. K., 2000, "Numerical Simulations of Pool-Boiling Heat Transfer," AIChE J., **47**, pp. 813–834.
[8] Fujita, Y., and Bai, Q., 1998, "Numerical Simulation of the Growth for an Isolated Bubble in Nucleate Boiling," *Proceedings of the 11th Heat Transfer Conference*, J. S. Lee, ed., pp. 437–442.
[9] Stephan, P., and Hammer, J., 1994, "A New Model for Nucleate Boiling Heat Transfer," Heat Mass Transfer, **30**, pp. 119–125.
[10] Fuchs, T., Kern, J., and Stephan, P., 2006, "A Transient Nucleate Boiling Model Including Microscale Effects and Wall Heat Transfer," ASME J. Heat Transfer, **128**, pp. 1257–1265.
[11] Kern, J., and Stephan, P., 2003, "Theoretical Model for Nucleate Boiling Heat and Mass Transfer of Binary Mixtures," ASME J. Heat Transfer, **125**, pp. 1106–1115.
[12] Kenning, D., 1991, "Wall Temperature Patterns in Nucleate Boiling," Int. J. Heat Mass Transfer, **35**, pp. 73–86.
[13] Kenning, D., and Yan, Y., 1996, "Pool Boiling Heat Transfer on a Thin Plate: Features Revealed by Liquid Crystal Thermography," Int. J. Heat Mass Transfer, **39**, pp. 3117–3137.
[14] Kenning, D., Kono, T., and Wienecke, M., 2001, "Investigation of Boiling Heat Transfer by Liquid Crystal Thermography," Exp. Therm. Fluid Sci., **25**, pp. 219–229.
[15] Shoji, M., Zhang, L., and Chatpun, S., 2005, "Nucleation Site Interaction in Pool Nucleate Boiling—Serial Experiments Using Artificial Boiling Surfaces," Sixth World Conference on Experimental Heat Transfer, Fluid Mechanics, and Thermodynamics.
[16] Hoehmann, C., and Stephan, P., 2002, "Microscale Temperature Measurement at an Evaporating Liquid Meniscus," Exp. Therm. Fluid Sci., **26**, pp. 157–162.
[17] Wagner, E., Sodtke, C., Schweizer, N., and Stephan, P., 2006, "Experimental Study of Nucleate Boiling Heat Transfer Under Low Gravity Conditions Using TLCs for High Resolution Temperature Measurements," Heat Mass Transfer, **42**, pp. 875–883.
[18] Golobic, I., Petkovsek, J., Baselj, M., Papez, A., and Kenning, D., 2006, "Experimental Determination of Transient Wall Temperature Distributions Close to Growing Vapor Bubbles," ECI International Conference on Boiling Heat Transfer.
[19] Wagner, E., Sprenger, A., Stephan, P., Koeppen, O., Ziegler, F., and Auracher, H., 2007, "Nucleate Boiling at Single Artificial Cavities: Bubble Dynamics and Local Temperature Measurements," Sixth International Conference on Multiphase Flow ICMF 2007.
[20] Wagner, E., Stephan, P., Koeppen, O., and Auracher, H., 2007, "High Resolution Temperature Measurements at Moving Vapor/Liquid and Vapor/Liquid/Solid Interfaces During Bubble Growth in Nucleate Boiling," Fourth International Berlin Workshop on Transport Phenomena With Moving Boundaries.
[21] Henry, C., Kim, J., and McQuillen, J., 2006, "Dissolved Gas Effects on Thermocapillary Convection During Boiling in Reduced Gravity Environments," Heat Mass Transfer, **42**, pp. 919–928.
[22] You, S., Somon, T., Bar-Cohem, A., and Hong, Y., 1995, "Effects of Dissolved Gas Content on Pool Boiling of a Highly Wetting Fluid," ASME J. Heat Transfer, **117**, pp. 687–692.
[23] Dunn, P., and Reay, D., 1994, *Heat Pipes*, 4th ed., Elsevier Science Ltd., Oxford, England.
[24] Gorenflo, D., Goetz, J., and Bier, K., 1982, "Vorschlag fr eine Standard-Apparatur zur Messung des Wärmeübergangs beim Blasensieden," Waerme-Stoffuebertrag., **16**, pp. 69–78.
[25] Alifanov, O., 1994, *Inverse Heat Transfer Problems*, Springer-Verlag, Berlin.
[26] 2006, "Informationsstelle Edelstahl Rostfrei—Eigenschaften," www.edelstahl-rostfrei.de
[27] Schoene, A., 1997, *Messtechnik*, 2nd ed., Springer-Verlag, Berlin.
[28] 2002, *VDI-Wärmeatlas: Berechnungsblätter für den Wärmeübergang*, 10th ed. Springer-Verlag, Berlin.
[29] Bednar, W., and Bier, K., 1994, *Wärmebergang beim Blasensieden von binren Kohlenwasserstoffgemischen*, VDI, Düsseldorf.

The Influence of Surface Roughness on Nucleate Pool Boiling Heat Transfer

Benjamin J. Jones

John P. McHale

Suresh V. Garimella[1]
e-mail: sureshg@purdue.edu

NSF Cooling Technologies Research Center,
School of Mechanical Engineering,
and Birck Nanotechnology Center,
Purdue University,
585 Purdue Mall,
West Lafayette, IN 47907-2088

The effect of surface roughness on pool boiling heat transfer is experimentally explored over a wide range of roughness values in water and Fluorinert™ FC-77, two fluids with different thermal properties and wetting characteristics. The test surfaces ranged from a polished surface (R_a between 0.027 μm and 0.038 μm) to electrical discharge machined (EDM) surfaces with a roughness (R_a) ranging from 1.08 μm to 10.0 μm. Different trends were observed in the heat transfer coefficient with respect to the surface roughness between the two fluids on the same set of surfaces. For FC-77, the heat transfer coefficient was found to continually increase with increasing roughness. For water, on the other hand, EDM surfaces of intermediate roughness displayed similar heat transfer coefficients that were higher than for the polished surface, while the roughest surface showed the highest heat transfer coefficients. The heat transfer coefficients were more strongly influenced by surface roughness with FC-77 than with water. For FC-77, the roughest surface produced 210% higher heat transfer coefficients than the polished surface while for water, a more modest 100% enhancement was measured between the same set of surfaces. Although the results highlight the inadequacy of characterizing nucleate pool boiling data using R_a, the observed effect of roughness was correlated using $h \propto R_a^m$ as has been done in several prior studies. The experimental results were compared with predictions from several widely used correlations in the literature.
[DOI: 10.1115/1.3220144]

Keywords: nucleate pool boiling, heat transfer, surface roughness

1 Introduction

Surface roughness has long been known to have a significant impact on the boiling process. In 1936, Jakob [1] reported that both surface roughness and the level of corrosion and oxidation of the surface dramatically influence the boiling curve. At the time, the bubble incipience process was not well understood. By the late 1950s, one of the prevailing theories was that bubbles emanate from cavities containing entrapped vapor [2]. The experiments by Clark et al. [3] provided strong evidence for the theory that bubbles do indeed emanate from cavities and other surface imperfections. The theoretical analysis by Bankoff [4] further substantiated the vapor entrapment theory by showing that only unwetted cavities can serve as nucleation sites, and that only cavities of a certain shape can serve as vapor traps [5]. The role of cavities was further elucidated by Griffith and Wallis [6], who showed that the cavity radius determines the superheat required for bubble nucleation in a uniformly superheated liquid, with larger cavities requiring lower wall superheats. Hsu [7] extended this analysis to include the effects of the thermal boundary layer and showed that only a certain range of cavity sizes can serve as active nucleation sites.

The realization of the importance of cavities spurred interest in using roughened surfaces as a means of increasing the number of nucleation sites and size of cavities, thus enhancing boiling heat transfer. Several investigations into the effect of surface roughness were carried out in the 1950s and 1960s. Corty and Foust [8] investigated a variety of copper and nickel surfaces prepared with different levels of polishing. They found that the surface roughness not only affected the superheat required for incipience but also the slope of the boiling curve. Rougher surfaces resulted in lower superheats for a given heat flux, which was attributed to the presence of larger unwetted cavities on the rougher surfaces. Similar conclusions were reached by other researchers: Kurihara and Myers [9], who studied a variety of fluids boiling from copper surfaces with differing levels of polish; Hsu and Schmidt [10], who studied the boiling of water from stainless steel surfaces; and Marto and Rohsenow [11] who studied the boiling of sodium from surfaces prepared using a variety of different techniques. Berenson [12] studied the boiling of *n*-pentane on surfaces of varying roughness and found large variations in the heat transfer coefficient, of up to 600%, due to the differences in surface characteristics.

The increased understanding of the role of surface condition has also led to commercially available enhanced surfaces for improved boiling performance. Many of these boiling enhancements are designed to create re-entrant-type cavity structures which are more difficult for the liquid to fully wet than simple cavity shapes and, based on the analysis of Griffith and Wallis [6], are believed to serve as more stable nucleation sites. Therefore, these enhanced surface geometries typically lead to better boiling performance compared with roughened surfaces produced by conventional machining processes. A wide variety of industrial applications, however, still utilize surfaces produced using conventional machining processes and these surfaces remain the focus of the present work. Good reviews of enhanced boiling surfaces have been provided by Webb [13,14].

For surfaces produced using conventional manufacturing techniques, several researchers have noted the inability of commonly used surface roughness parameters, such as the rms roughness (R_q) or average roughness (R_a), to explain the variation in observed nucleate boiling heat transfer characteristics. Berenson [12] noted that the rms surface roughness itself was not the best indicator of the resulting performance since lapped surfaces had much higher heat transfer coefficients than rougher surfaces produced

[1]Corresponding author.

Manuscript received April 15, 2008; final manuscript received May 6, 2009; published online October 15, 2009. Review conducted by Yogesh Jaluria.

with emery paper. Bier et al. [15] reached a similar conclusion after studying the boiling of R11 and R115 from surfaces prepared using various techniques over a range of pressures. Chowdhury and Winterton [16] suggested that rougher surfaces would yield higher nucleate pool boiling heat transfer coefficients if a consistent method of surface preparation is used, but the results from other investigators have not shown such a trend. Vachon et al. [17] investigated boiling from unidirectionally polished and chemically etched surfaces of varying roughness in water. The results from the polished surfaces indicated that roughening the surfaces only improved the boiling performance up to a certain point. The best heat transfer performance was obtained with an 1 μm rms surface roughness, and further roughening of the surface yielded no additional benefit. The results from the chemically etched surfaces were more varied and showed the inadequacy of using rms roughness to characterize boiling surfaces.

Several researchers have also noted an apparent maximum heat transfer coefficient with respect to surface roughness as observed by Vachon et al. [17]. Kravchenko and Ostruovskiy [18] studied various organic fluids and nitrogen boiling from stainless steel tubes. Their results indicated that vertical tubes with a roughness average (R_a) greater than 0.58 μm do not experience any further improvement in the heat transfer coefficient. Grigoriev et al. [19] studied the boiling of helium for surfaces of varying roughness and also noted that once a surface was sufficiently rough, additional roughening yielded no benefit. Many other researchers, however, have not observed such an apparent maximum heat transfer coefficient, and this variety of results may simply indicate the inadequacy of correlating nucleate boiling heat transfer data using surface roughness parameters.

Recognizing the deficiencies of characterizing boiling surfaces with surface roughness parameters, several researchers have attempted to characterize the surfaces in a more mechanistic fashion by measuring cavity sizes and shapes using optical or electron microscopy [20–23]. Using an optical microscope, Wang and Dhir [23,24] characterized the cavity structures on polished copper surfaces and developed a wetting criterion for determining the active cavity size distribution. Their theoretical analysis agreed well with experimental results. However, such an approach is only tractable on very smooth surfaces on which the number of cavities is relatively small. Attempts to characterize stochastically rough surfaces have been met with marginal success. Qi et al. [25] and Luke [26,27] have developed methods for determining active cavity size distributions from 3D profilometry data of boiling surfaces. However, the simplistic treatment of the surface structure and the wetting phenomenon used in the analyses has limited the utility of such predictions.

While numerous investigators have reported on the inefficacy of correlating nucleate boiling data using surface roughness parameters, some researchers have reported success in correlating the general trend of increasing heat transfer coefficients with increased roughness. Stephan [28], in his investigation of boiling of R11 from copper surfaces of varying roughness, found that the influence of surface roughness on the heat transfer coefficient at a fixed heat flux could be represented with $h \propto R_{p,\mathrm{old}}^{0.133}$, where $R_{p,\mathrm{old}}$ is the German "Glättungstiefe" defined by DIN 4762/1:1960. Danilova and Bel'skii [29] found a somewhat different dependence of $h \propto R_z^{0.2}$ when studying R12 and R113 boiling from tube surfaces prepared using various techniques. Both these studies [28,29] were conducted at low reduced pressure. Nishikawa et al. [30,31] extended the study of roughness to a wide range of reduced pressure and found that the effect of surface roughness on the heat transfer coefficient diminishes as the pressure approaches the critical pressure. They found that the relation $h \propto R_{p,\mathrm{old}}^{0.2(1-P_r)}$ best represented their experimental data.

A relationship of the form $h \propto R^m$ does not adequately explain many of the previously discussed anomalies when correlating nucleate pool boiling data using surface roughness parameters. Nonetheless, it does provide a simple framework for incorporating the influence of surface roughness into nucleate pool boiling correlations; and indeed several correlations have accounted for the surface roughness effect using such relationships, including the popular Cooper [32,33] and Gorenflo [34] correlations.

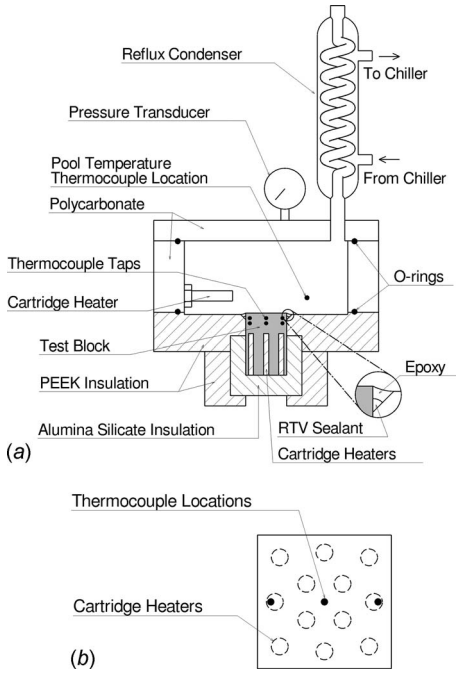

Fig. 1 (*a*) Schematic of pool boiling facility and (*b*) top view of test block showing the locations of thermocouples and cartridge heaters

Due to the importance of accurately accounting for the influence of surface roughness when correlating nucleate boiling data, and given the wide variety of conclusions that have been reached in previous investigations, further research is warranted. The goal of the present work is to provide additional insights into the role of surface roughness on nucleate pool boiling with an experimental exploration using two fluids with widely differing thermal properties and wetting characteristics: water and FC-77, a perfluorinated dielectric fluid. Widely used nucleate pool boiling correlations are evaluated against the experimental results. In particular, the capability of the correlations to account for the effect of surface roughness is of prime interest in this study.

2 Experimental Setup

2.1 Test Facility. The pool boiling test facility is shown in Fig. 1(*a*). The 25.4×25.4 mm^2 test surface is prepared on top of an aluminum test block. Heat is supplied through 12 cartridge heaters embedded in the test block. The arrangement of the cartridge heaters is shown in Fig. 1(*b*). Numerical simulations were performed to ensure that the cartridge heaters supplied heat uniformly to the test surface. Six thermocouple taps were drilled into the test block at two different vertical and three horizontal locations as shown in Fig. 1. Surface temperature measurements were determined by extrapolating the thermocouple readings. Type-T, 0.8 mm diameter sheathed thermocouples were used. All thermocouples were referenced to 0°C using a dry-block ice point reference chamber and the thermocouples were calibrated using a dry-block thermocouple calibration unit. The estimated uncertainty in the thermocouple measurements is 0.3°C, while the estimated uncertainty in the extrapolated surface temperature ranges from 0.3°C at low heat fluxes to 0.6°C at higher heat fluxes.

A high temperature thermoplastic, PEEK, was chosen as an insulation material due to its combination of low thermal conductivity ($\sim$0.28 W/m K), high temperature resistance (up to

250°C), and good machinability. A ceramic (alumina silicate) sheath served as the insulation material around the hottest portion of the test block. The liquid pool was enclosed by clear polycarbonate walls to allow for direct observation of the boiling process. A thermocouple located in the pool (see Fig. 1(*a*)) was used to measure the liquid pool temperature. Cartridge heaters installed inside the pool provided additional heat to maintain the liquid at the saturation temperature. Vapor generated from the boiling process flowed into a Graham-type condenser. The vapor inside the condenser was cooled and condensed using water from a chiller, with the condensate draining back into the pool, and the outlet open to the atmosphere in order to maintain atmospheric pressure inside the pool. Since, under high vapor loads, the condenser can become clogged with liquid, a pressure transducer monitors the pool pressure to ensure that it is indeed at atmospheric pressure throughout the experiments.

Establishing an effective seal between the test piece and the insulation proved to be difficult. Any gap or crack in this interface can result in unwanted nucleation sites. A solution to this problem was devised using an epoxy sealing technique. A very slight chamfer in the insulation block around the test surface formed a groove which provided space for a bead of sealant (as shown in the inset of Fig. 1(*a*)). A small bead of silicone RTV sealant was first applied to the bottom of the groove. A low-viscosity, slow-cure epoxy filled the remaining portion of the groove. The RTV prevents the epoxy from wicking down the clearance gap between the test piece and insulation, thus allowing for easier removal of the test piece. Although undesirable nucleation sites were still occasionally detected with this technique, repeated testing indicated that these occasional unwanted nucleation sites have little effect on the results obtained.

The surface heat flux was determined by correcting the electrical power input by the amount of estimated heat loss. Although the axial pairs of thermocouples in the aluminum block could be used to measure the surface heat flux directly, this results in unacceptable errors in the measurement due to tolerances in the placement of the thermocouples and the thermocouple measurement uncertainties. Therefore, a 3D numerical simulation was performed to estimate the heat losses. The PEEK and ceramic insulation as well as the test block were included in the model and boundary conditions representative of the experimental test conditions were applied (uniform boiler surface temperature, uniform heat generation region for the cartridge heaters, and natural convection boundary conditions for the exterior surfaces). The numerically estimated heat losses were in reasonable agreement with the heat losses estimated based on thermocouple readings when considering the errors associated with this estimate. The heat losses were found to be less than 15% of the electrical power input for moderate to high heat fluxes ($q > 120$ kW/m^2).

2.2 Test Surfaces. A total of six test pieces of varying surface roughness were fabricated. Separate test pieces were manufactured with a polished surface for use in the water and FC-77 experiments. In both cases, the polishing was achieved using successively finer grits of sandpaper. The other test pieces were manufactured with surfaces roughened to varying degrees. The surfaces were first fly-cut and then roughened using ram-type electrical discharge machining (EDM). In the EDM process, the machine parameters can be controlled to produce surfaces with different roughness. Enough surface material was removed with EDM so that the final roughness was solely due to the EDM process rather than the original machining operation.

The surface roughness of the test surfaces was measured with either a probe-type surface profilometer or an optical profilometer. Several scans were performed in different locations on each surface. The roughness average (R_a), RMS roughness (R_q), maximum profile peak height (R_p), and five-point average maximum height (R_z) were evaluated according to ASME B46.1-1995 standards and are reported in Table 1. No single roughness parameter has been shown to be superior for characterizing boiling surfaces and several surface parameters are being reported simply to allow an easier comparison to previous studies. However, it should be noted that the definition of some of these surface parameters has changed over time. For example, R_p currently has congruent definitions in the ASME, ISO, and DIN standards, although the current definition differs from $R_{p,\mathrm{old}}$ in DIN 4762/1:1960, which has been used by Stephan [28] among many other researchers. For the remainder of this paper, the roughness average (R_a) will be used to identify the different surfaces under study.

Table 1 Surface roughness measurements

	Surface roughness parameters			
Surface preparation	R_a (μm)	R_q (μm)	R_p (μm)	R_z (μm)
Polished (water)	0.038	0.062	0.81	0.58
Polished (FC-77)	0.027	0.039	0.18	0.35
EDM	1.08	1.37	6.09	8.24
	2.22	2.81	12.0	16.7
	5.89	7.37	24.5	37.1
	10.0	12.5	32.4	56.5

The surface topography of four of the surfaces, as measured with the optical profilometer, is shown in Fig. 2. The polished surface (Fig. 2(*a*)) is seen to be quite smooth with a few small cavities distributed across the surface. EDM tends to form an irregular pattern of cavities on the surface (Figs. 2(*b*)–2(*d*)). The cavities are larger and more numerous on the EDM surfaces compared with the polished surface. The EDM surfaces with larger roughness form larger cavities than those with smaller RMS roughness.

2.3 Experimental Procedure. Deionized water and FC-77 were used as the test fluids; relevant thermophysical properties of the FC-77 are as follows: $T_{\mathrm{sat}} \approx 100.3$°C, $\rho = 1592$ kg/m^3, $\mu = 4.42 \times 10^4$ kg/m s, $k_l = 0.057$ W/m K, $h_{fg} = 89$ kJ/kg, $c_{p,l} = 1.170$ kJ/kg K, and $\sigma = 0.0057$ N/m [35,36]. The liquid was degassed by boiling for approximately 2 h prior to each experiment, either using the immersed cartridge heaters in the pool (for the FC-77 experiments) or in an external degassing reservoir (for the water experiments). During the experiments, heat losses from the pool required additional heat to be supplied through the immersed cartridge heaters to maintain the liquid at the saturation temperature. To mitigate undesirable convective currents induced by the immersed heaters, the power setting for the cartridge heaters was maintained as low as possible while maintaining the pool to within 0.5°C of the saturation temperature. At high heat fluxes, the pool cartridge heaters were turned off as the test piece provided enough heat by itself to maintain the desired pool temperature.

The thermocouple readings were recorded with a data acquisition system. All reported values of the surface temperature represent the average over an interval of at least 1 min, after the surface temperature had reached equilibrium. Experiments were conducted both in order of increasing and decreasing heat flux to check for boiling hysteresis. The boiling process was observed through the front polycarbonate wall using a high-speed camera system with a macro lens. Illumination was provided by two fiber-optic illuminators and a halogen light source in the water experiments. A green laser light sheet served as the illumination source for the FC-77 experiments as this light source provided higher intensity and more uniform illumination that was necessary to resolve the smaller and more numerous vapor bubbles observed in the FC-77 experiments compared with the experiments in water. Images were recorded at frame rates between 8000 and 12,000 fps.

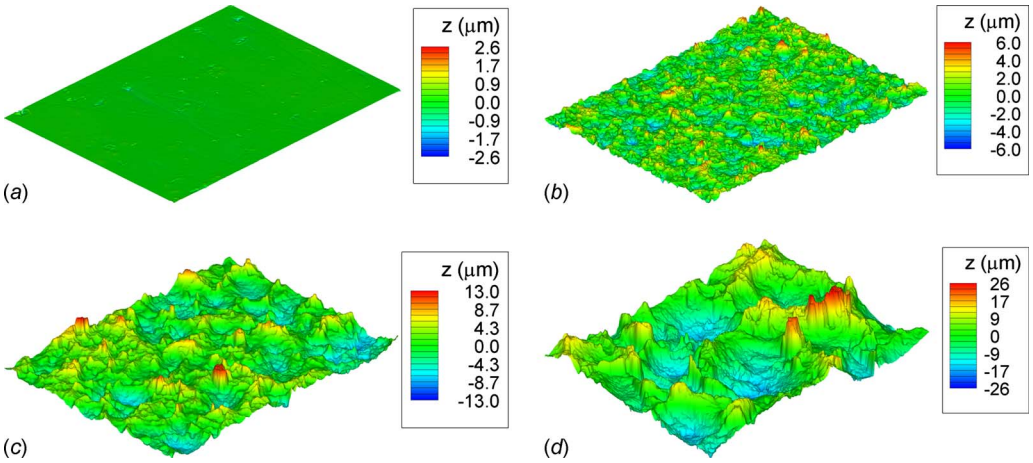

Fig. 2 Surface topography of test surfaces over an area of 400×300 μm^2 as measured by an optical profilometer: (*a*) 0.038 μm polished surface, (*b*) 1.08 μm EDM surface, (*c*) 2.22 μm EDM surface, and (*d*) 5.89 μm EDM surface

3 Experimental Results

The boiling curves for water are shown in Fig. 3. The results are shown for data obtained in order of increasing heat flux (i.e., traversing "up" the boiling curve). As seen in Fig. 3(*a*), the roughest EDM surface (10.0 μm) resulted in the lowest superheat at a given heat flux while the polished test piece (0.038 μm) was associated with the highest superheat. The other EDM test surfaces of intermediate roughness (1.08 μm, 2.22 μm, and 5.89 μm) performed similarly, resulting in lower superheats than the polished test piece but higher superheats than the roughest EDM surface. The 5.89 μm surface had slightly higher superheats than the 1.08 μm and 2.22 μm surfaces at lower heat fluxes but the results show negligible difference in superheat at higher heat fluxes. Boiling incipience occurred at a superheat of approximately 5°C for the roughest EDM surface (10.0 μm), 7°C for the other EDM surfaces (1.08 μm, 2.22 μm, and 5.89 μm), and 11°C for the polished surface. This may be attributed to the rougher surfaces having larger active cavity sizes, which result in lower wall superheats at incipience. The heat transfer coefficients show a similar trend (Fig. 3(*b*)). The roughest EDM surface achieved the highest heat transfer coefficient for a given heat flux while the polished test piece resulted in the lowest. The 1.08 μm, 2.22 μm, and 5.89 μm surfaces showed approximately a 60% improvement in the heat transfer coefficient over the polished surface at a given heat flux, while the 10.0 μm EDM surface provided approximately a 100% improvement.

As discussed earlier, several researchers have concluded that once a surface is sufficiently rough, there is no benefit to additional roughening [17–19]. If the 10.0 μm surface is excluded, the current study would support this conclusion as there is no additional enhancement beyond $R_a = 1.08$ μm. It is possible that if the roughness were increased significantly in the past studies, a trend similar to the findings in the current study may have held true. However, it is currently unclear why the 10.0 μm surface performs markedly better than the other EDM surfaces (in repeated tests), and it is difficult to conclusively address this issue. The roughest EDM surface had a lower incipience superheat and higher heat transfer coefficients than the other EDM surfaces. The surface area in contact with the fluid for the 10.0 μm EDM surface, estimated from the optical profilometer data, was only ap-

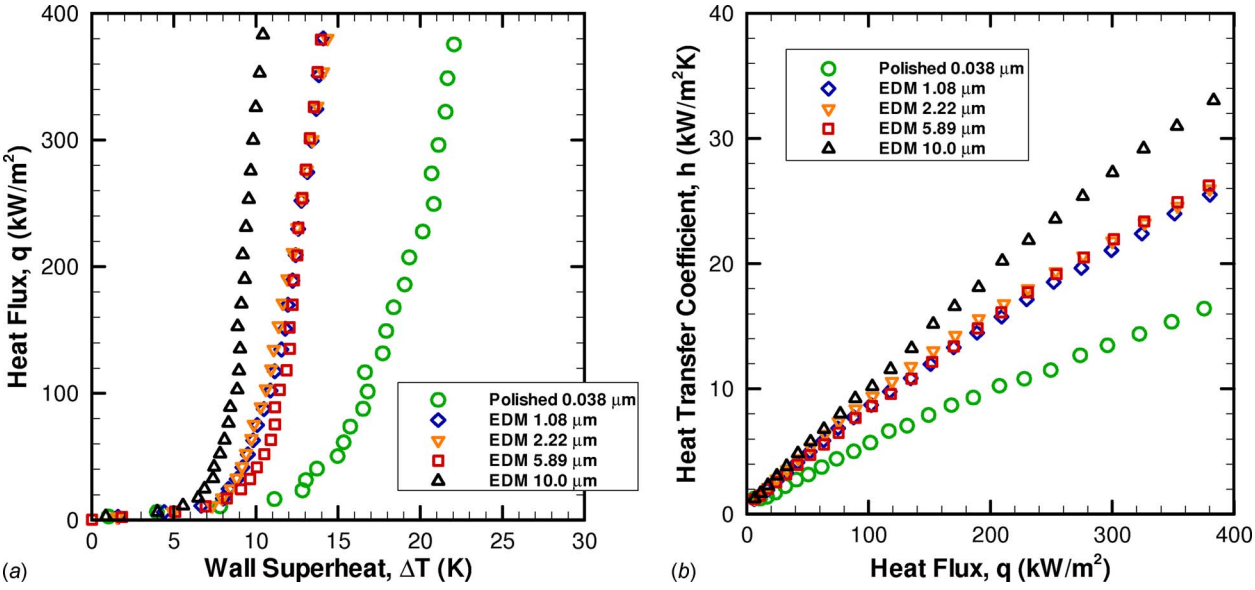

Fig. 3 Boiling curves for water: (*a*) heat flux versus wall superheat and (*b*) heat transfer coefficient versus heat flux

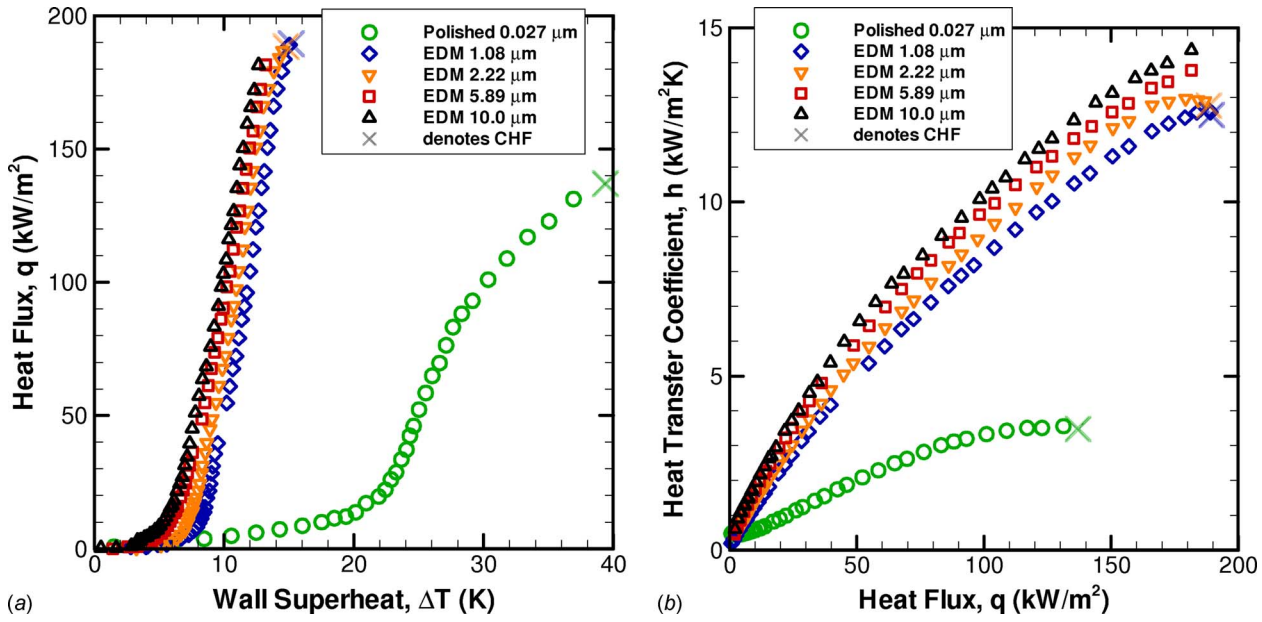

Fig. 4 Boiling curves for FC-77: (*a*) heat flux versus wall superheat and (*b*) heat transfer coefficient versus heat flux

proximately 1% greater than for the 5.89 μm surface. Therefore, a surface area enhancement does not explain the higher heat transfer coefficients observed. It appears that the 10.0 μm EDM surface has larger active cavities and a higher active cavity density than the other EDM surfaces. These results, as other researchers have concluded, highlight the inadequacy in using standard surface roughness parameters to characterize boiling surfaces.

The boiling curves for FC-77 are shown in Fig. 4. The results are shown for data obtained in order of decreasing heat flux (i.e., traversing "down" the boiling curve). Hysteresis effects (i.e., comparison of data obtained while traversing "up" the boiling curve versus "down" the curve) are discussed later in this section. Unlike the results in water, a trend of continuously increasing heat transfer coefficients with respect to surface roughness, for a given heat flux, is observed in the FC-77 experiments. There also appears to be a larger dependence of heat transfer coefficient on surface roughness for FC-77 than for water. The improvements in heat transfer coefficient range from 150% for the 1.08 μm surface to 210% for the 10.0 μm surface above the values obtained for the polished surface, at a fixed heat flux. The differences in the observed trends in the heat transfer coefficient between water and FC-77 may be attributed to the differences in wetting behavior of the two fluids as well as the cavity size distribution presented by the surfaces. Since FC-77 is more highly wetting than water, smaller cavities are preferred for nucleation. For instance, it is possible that the 1.08 μm and 5.89 μm surfaces have a similar number of the larger cavities that cause nucleation in water, yet the 5.89 μm surface may have a greater number of the smaller cavities that cause nucleation in FC-77. However, evaluation of the surfaces for cavity size distribution is not straightforward even when detailed 3D surface profiles are available, and the reasons for the observed differences between water and FC-77 need further study.

The value of critical heat flux, depicted with an $\times$ in Fig. 4, was experimentally determined for the polished, 1.08 μm, and 2.22 μm surfaces in FC-77. It can be seen in Fig. 4(*b*) that the boiling curves tend to flatten out as critical heat flux is approached, as is most apparent with the polished surface. The polished surface exhibited a critical heat flux of 137 kW/m^2, while higher and nearly identical values of critical heat flux of 189 and 188 kW/m^2 were observed for the 1.08 μm and 2.22 μm EDM surfaces, respectively, showing an almost 40% improvement. Due to the limit on the condenser capability with respect to maximum vapor generation rates, the experiments were not run to critical heat flux values with the two roughest surfaces for FC-77 and for any of the surfaces in water.

Additional experiments were conducted to check for boiling hysteresis (see Fig. 5). For water (Fig. 5(*a*)), the roughest EDM test piece showed no discernible hysteresis, with the results obtained during increasing ($q\uparrow$) and decreasing ($q\downarrow$) heat flux being nearly identical. However, some extent of hysteresis was observed for the polished test piece in water. At the incipience heat flux ($\sim$15 kW/m^2), the wall superheat is approximately 10.8°C in the direction of increasing heat flux ($q\uparrow$), while it was only 9.5°C for decreasing heat flux ($q\downarrow$). The maximum disparity in the superheat between the increasing and decreasing curves occurs at a heat flux of 2.0 W/cm^2, corresponding to a temperature overshoot of 2.3°C. Hysteresis has generally not been reported in the literature for water at atmospheric pressure, although such effects have been observed for water at subatmospheric pressures [37].

Large hysteresis effects on smooth surfaces have been widely reported for FC fluids [38–40] and highly wetting fluids in general [8,41]. Accordingly, a large temperature overshoot of 16.8°C was observed for the polished surface (see Fig. 5(*b*)). The EDM surfaces also exhibit noticeable hysteresis effects with FC-77. A maximum temperature overshoot of 16.2°C was measured for the 1.08 μm EDM surface, which is comparable to the measured overshoot for the polished surface, although much lower surface temperatures are obtained with the EDM surface. The 10.0 μm EDM surface had a much reduced, although still significant, temperature overshoot of 5.6°C. It should also be noted that past boiling history has been shown to have a strong influence on the observed hysteresis [8,38,42], although this has not been studied in detail in the present work.

Photographs of the boiling process taken with the high-speed camera system are shown in Fig. 6 for water and in Fig. 7 for FC-77. At low heat fluxes close to the incipience heat flux (50 kW/m^2 for water and 20 kW/m^2 for FC-77 as seen in Figs. 6 and 7, respectively), significantly more active nucleation sites can be observed in the roughened EDM surface relative to the polished surface. Furthermore, the 5.89 μm EDM surface has a smaller bubble departure diameter and a higher bubble emission frequency than the polished surface. The reasons for the differ-

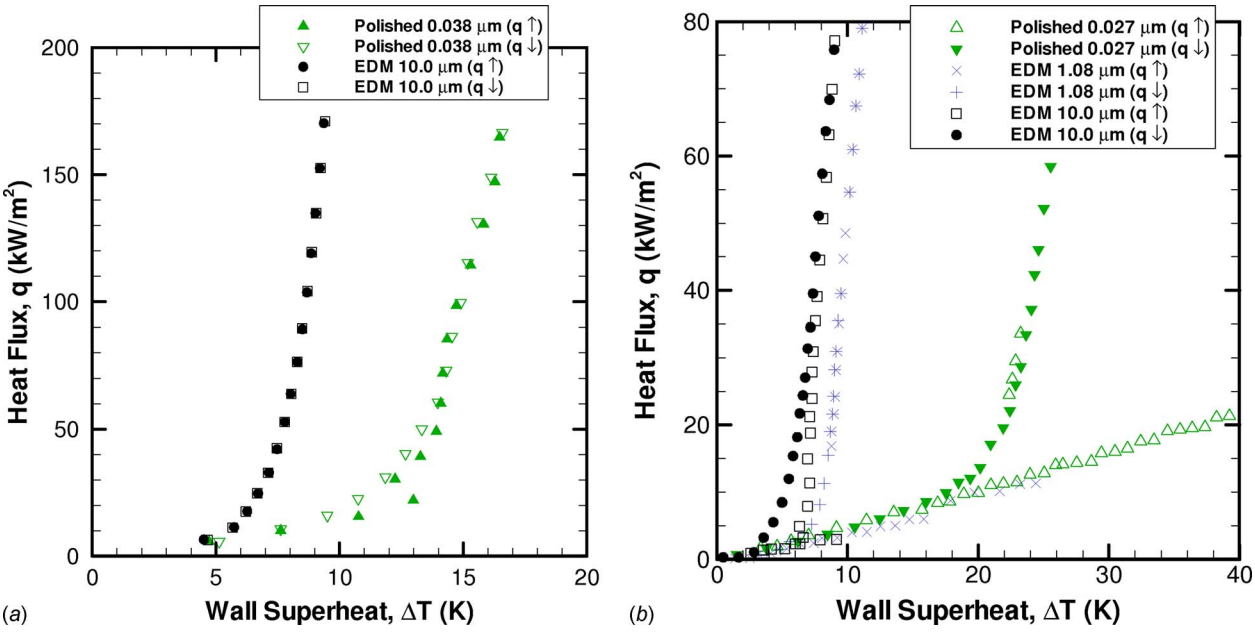

Fig. 5 Boiling curves showing the hysteresis effect for (*a*) water and (*b*) FC-77, where $q\uparrow$ indicates data obtained in order of increasing heat flux and $q\downarrow$ indicates those in order of decreasing heat flux. It is noted that a smaller heat flux increment was used experimentally than is indicated in (*b*); only a fraction of the data are included to improve readability of the figure.

ences in bubble departure size for the different surfaces were explained by Hatton and Hall [43]. Hatton and Hall considered all of the forces acting on a bubble during the growth process. For small cavity sizes, the bubble departure size is mainly determined by a balance between the buoyancy and the dynamic inertial forces. As the cavity size increases, the inertial forces decrease and the bubble departure diameter decreases, which explains the decreased bubble diameters from the EDM surfaces. For large cavities, a balance between buoyancy and surface tension forces determines the departure size.

At higher heat fluxes, the sizes of bubbles issuing from the smooth surface are similar to those issuing from the roughened surface due to a merging of bubbles from adjacent nucleation sites. This is most clearly seen in Fig. 6 at a heat flux of 100 kW/m^2 for water and in Fig. 7 at a heat flux of 80 kW/m^2 for FC-77. As the heat flux is further increased, vapor slugs and columns are formed, as can be observed in the last row of photographs in Fig. 6. For water at 210 kW/m^2, it is still apparent that the roughened surface has a greater number of active nucleation

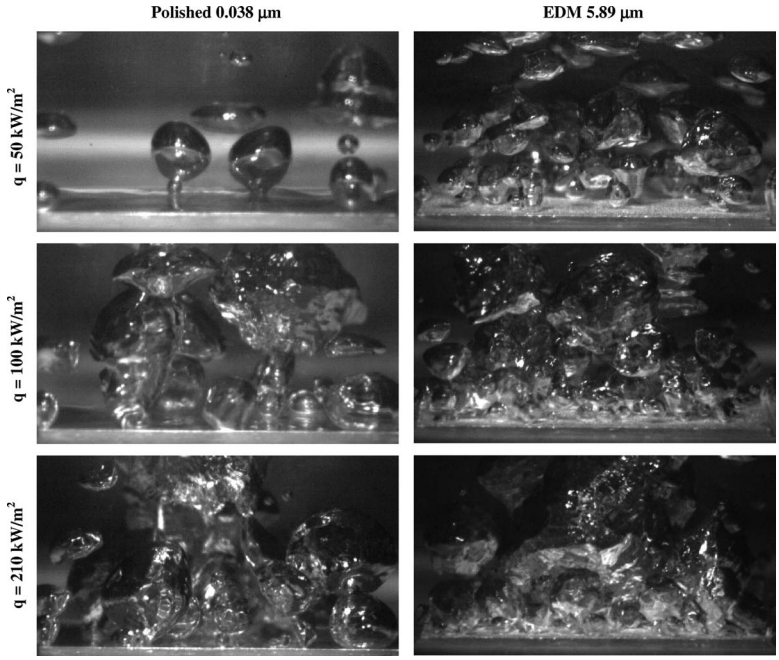

Fig. 6 Photographs of the boiling process in water for varying heat flux and surface roughness. The physical width of each image is approximately 25 mm.

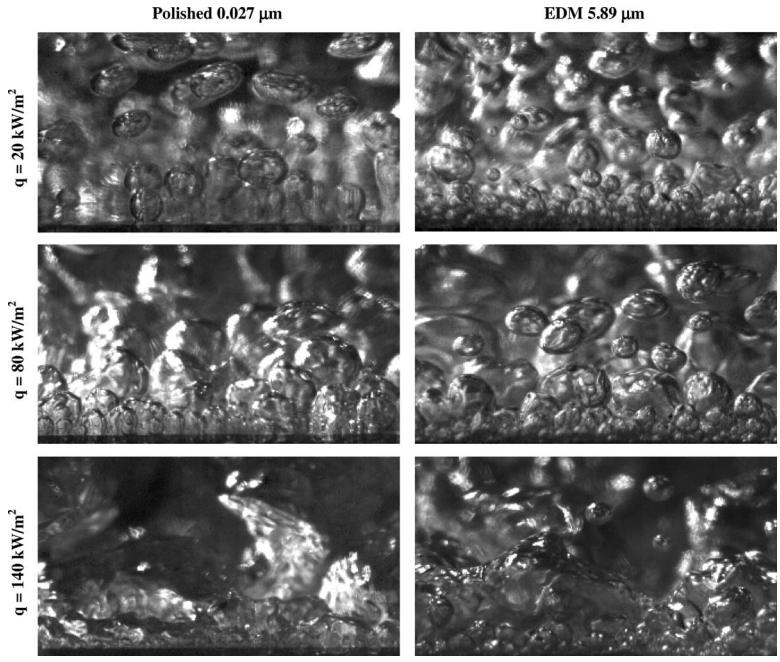

Fig. 7 Photographs of the boiling process in FC-77 for varying heat flux and surface roughness. The physical width of each image is approximately 7.3 mm.

sites than the polished surface. For FC-77 at 140 kW/m^2, both the polished and rough surfaces are close to being blanketed by the vapor as the heat flux is approaching the critical value.

Some other interesting visual differences in the boiling behavior between water and FC-77 were also observed. For water, bubbles first nucleated from a single site and as the heat flux was incrementally increased, additional nucleate sites became active, more or less randomly distributed across the test surface. For FC-77, however, nucleation sites tended to spread from the initial bubble-generating site as the heat flux was increased while the rest of the surface remained free of active centers (although this is not evident in Fig. 7 since only a small portion of the surface is shown). The boiling patch would continue to grow until the heat flux was sufficient to activate sites across the entire surface. This patchwise boiling phenomenon has been previously reported by other investigators such as Corty and Foust [8] and Bergles and Chyu [42].

4 Discussion

4.1 Influence of Surface Roughness on the Boiling Curve. It is well known that nucleate boiling heat transfer can be well represented by an exponential relationship given by $h \propto q^n$, where n is a function of pressure and surface characteristics. As was mentioned earlier, several researchers have also noted that the dependence of heat transfer coefficient on surface roughness (at a fixed heat flux) can be modeled by an exponential relation, $h \propto R^m$, where R is some measure of the surface roughness. Putting these two relationships together yields

$$h = CR^m q^n \tag{1}$$

where C is a constant. As Eq. (1) indicates, surface roughness can both change the magnitude of the heat transfer coefficient and change the slope of its variation with heat flux since the exponent n is also dependent on roughness. In this section, the $h \propto R^m$ relationship is first examined, followed by the influence of surface roughness on the slope of the h versus q variation.

The effect on heat transfer coefficient of the surface roughness at different heat fluxes is illustrated in Fig. 8. An exponential curve represents the experimental results reasonably well, with some deviation from the trend exhibited in Fig. 8(a) by the 5.89 μm surface in water. The roughness exponent m changes only mildly with heat flux. For water, the roughness exponent is 0.09 at 50 kW/m^2 and 100 kW/m^2 and increases slightly to $m = 0.11$ at a heat flux of 300 kW/m^2. With FC-77 (see Fig. 8(b)), a greater dependence of surface roughness on the heat transfer coefficient is seen than with water, resulting in higher roughness exponents ranging from $m = 0.21$ at 20 kW/m^2 to $m = 0.19$ at 80 kW/m^2. The EDM surfaces for FC-77 seem to be better represented by a different slope than the overall curve (the latter includes the polished surface). The roughness exponents for the EDM surfaces alone range from $m = 0.15$ at 20 kW/m^2 to $m = 0.09$ at 80 kW/m^2.

The results indicate that the surface roughness exponent is not a constant across different fluid-surface combinations. Since it is well known that the wettablity of the fluid has important consequences on the nucleation behavior [23], it is reasonable to hypothesize that m is also a function of the contact angle. Although contact angles were not measured in the current study, FC-77 is highly wetting on most metal surfaces while water is moderately wetting. Therefore, it may be proposed that highly wetting fluids are well represented by a roughness exponent $m = 0.2$ while for moderately wetting fluids, $m = 0.1$ is more appropriate. However, it is noted that the difference in slopes between the overall curves and the EDM-only curves for FC-77 and the anomalously low value of the heat transfer coefficient for the 5.89 μm surface in water cannot be reconciled if m is simply a function of contact angle (θ). This further illustrates the weakness in using R_a to correlate the nucleate boiling data and highlights the deficiencies in models of the form $h \propto R^m$. That said, although the model does not account for all of the inconsistencies that numerous other authors have observed when trying to correlate the effects of roughness, it does serve as a useful basis for developing nucleate boiling correlations, as will be further discussed later.

Table 2 provides a summary of findings in the literature regarding the dependence of heat transfer coefficient on surface roughness. Most of the studies were conducted using refrigerants with

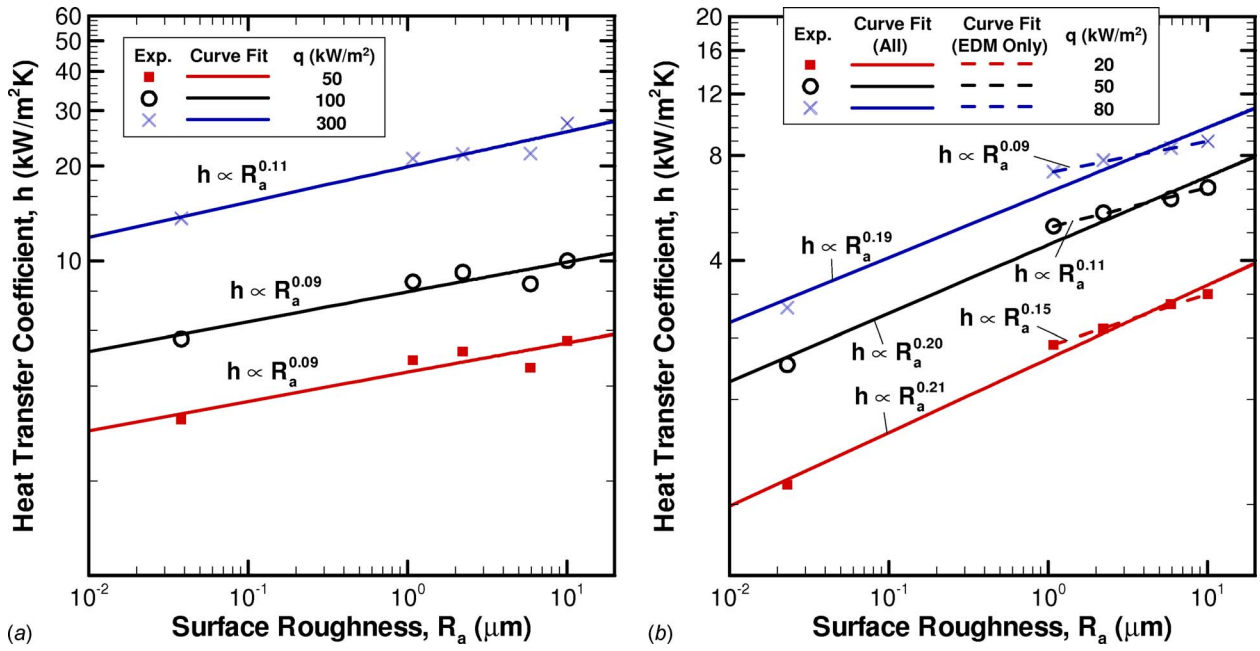

Fig. 8 Dependence of heat transfer coefficient on surface roughness for (*a*) water and (*b*) FC-77. The solid lines represent a curve fit through all five experimental data points (one polished surface and four EDM surfaces). The dashed lines in (*b*) represent a curve fit to only the four EDM surfaces (excluding the 0.027 μm polished surface).

the exception of Fedders [44] and the current study, where water is considered. Moreover, most past studies were conducted at low reduced pressure and only in the study by Nishikawa et al. [30,31] was a wide range of reduced pressures investigated. As stated earlier, Nishikawa et al. found that $m=0.2(1-P_r)$, which reduces to $m\approx 0.2$ at low reduced pressures. This seems to agree well with the findings of Danilova and Bel'skii [29] and Ribatski and Jabardo [45], but conflicts with the value proposed by Stephan [28]. A surface roughness exponent of $m=0.2$ also agrees with the current results in FC-77. If the hypothesis that $m=f(\theta)$ holds, this is not entirely surprising since most refrigerants are highly wetting on metal surface. Of the results in water, Fedders [45] found m to range from 0.10 to 0.133, which agrees reasonably well with the present m values (0.09 to 0.11) for water. However, these m values in water also agree with Stephan's [28] $m=0.133$ in R11, which does not support the claim that m is a function of θ. Thus, more experimental investigations are needed to clarify whether $m=f(\theta)$ is an adequate generalization of the influence of surface roughness.

Table 2 Dependence of heat transfer coefficient on surface roughness

Author(s)	Dependence	Pressure	Heat flux (W/m^2)	Fluid(s)	Heater type	Surface material	Surface preparation	Roughness (μm)
Stephan [28]	$h\propto R_{p,\mathrm{old}}^{0.133}$	$P_r=0.023$	5×10^4	R-11	horizontal cylinder, horizontal plate	copper	not specified	$0.15<R_{p,\mathrm{old}}<7.9$
Danilova and Bel'skii [29]	$h\propto R_z^{0.2}$	$0.118<P_r<0.155$	10^4	R-12, R-114	horizontal cylinder	cooper, steel	sandpaper, sandblasted, turning, etc.	$0.3<R_z<58$
Nishikawa et al. [30,31]	$h\propto R_{p,\mathrm{old}}^{0.2(1-P_r)}$	$0.08<P_r<0.9$	10^5	R-12, R-113, R-114	horizontal plate	copper	emery cloth	$0.022<R_{p,\mathrm{old}}<4.31$
Fedders [44]	$h\propto R_{p,\mathrm{old}}^{0.133}$	$0.012<P_r<0.089$	5×10^4	water	horizontal cylinder	stainless steel	sandpaper, sandblasted	$0.18<R_{p,\mathrm{old}}<3.6$
	$h\propto R_{p,\mathrm{old}}^{0.12}$	$P_r=0.012$	10^6					
	$h\propto R_{p,\mathrm{old}}^{0.10}$	$P_r=0.089$						
Ribatski and Jabardo [45]	$h\propto R_a^{0.2}$	$0.008<P_r<0.260$	not specified	R-11, R-123, R-12, R-134a, R-22	horizontal cylinder	copper, brass, stainless steel	sandpaper, sandblasted	$0.02<R_a<3.3$
Current work	$h\propto R_a^{0.1}$	$P_r=0.0046$	5×10^4 to 3×10^5	water	horizontal plate	aluminum	sandpaper, EDM	$0.038<R_a<10.0$
	$h\propto R_a^{0.2}$	$P_r=0.064$	2×10^4 to 8×10^4	FC-77				$0.027<R_a<10.0$

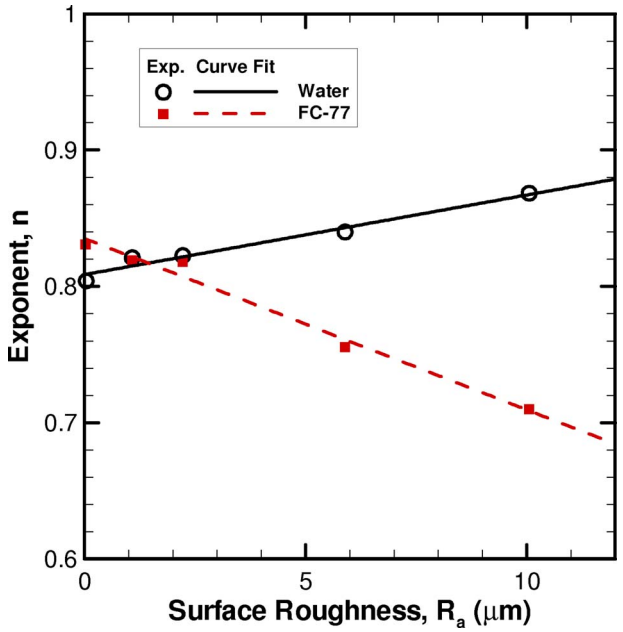

Fig. 9 Dependence of heat flux exponent *n* in the relationship $h \propto q^n$ on surface roughness

From Table 2 it does not appear that heater type (horizontal cylinder versus horizontal flat plate) has a discernible effect on the surface roughness exponent. Stephan [28] studied both horizontal cylinders and flat surfaces and found that a roughness exponent of $m=0.133$ was representative of both heater types. Few studies have investigated the effects of surface roughness on vertical cylinders and flat plates. Although Chun and Kang's [46] study of surfaces over a small range of surface roughness (R_q between 0.0151 μm and 0.0609 μm) found that vertical tubes are affected by surface roughness to a greater extent than horizontal tubes, there is no further confirmation in the literature of this trend, and it is currently unclear that a modification in surface roughness exponent m is needed to account for tube orientation.

The role of the surface material on the surface roughness exponent is not conclusive. In Danilova and Bel'skii's [29] study, both copper and steel surfaces were used and no noticeable difference in the trend of heat transfer coefficient with surface roughness was noted for the two surface materials. While Ribatski and Jabardo [45] also studied a variety of surface materials, most of their work on the effects of surface roughness dealt with copper surfaces. Since the surface material and other surface characteristics (degree of oxidation, coatings, etc.) influence the contact angle θ, the choice of material may influence m if it is indeed a function of θ. However, to the authors' knowledge, this has not been experimentally explored in detail.

The present results show that the heat flux exponent n changes with roughness since the exponent m in the relationship $h \propto R^m$ was found to change with heat flux. The relationship between n and R_a thus warrants a closer investigation. As shown in Fig. 9, the exponent n is found to vary linearly with surface roughness from 0.80 for the polished to 0.87 for the roughest EDM surfaces in water; the corresponding variation in n for FC-77 is from 0.83 to 0.71.

The findings from the present work may be compared with a number of studies in the literature. The data provided by Vachon et al. [17,47,48] for water at atmospheric pressure suggest exponents n in the relationship $h \propto q^n$ in the same range as the present study. However, data by Vachon et al. for chemically etched surfaces exhibit higher exponents n than their data for the unidirectional polished surfaces despite having similar surface roughness. The experimental data for water by Kurihara and Myers [9,49] show a much stronger dependence on surface roughness on the slope of the boiling curve than observed in the current study. As determined from the data provided in Ref. [49], the exponent n varies from 0.76 to 0.95 from the smoothest to the roughest surface. Although Kurihara and Myers [9] did not state the surface roughness, it was implied that the rms roughness was less than 1.2 μm. Based on these comparisons, it does not appear that n can be adequately correlated with surface roughness. However for the current results, the ability to predict the change in the exponent n with roughness is of secondary importance since only small changes in the slope were noted (n ranging from 0.80 to 0.87 for R_a ranging from 0.038 μm to 10.0 μm, respectively, in water).

4.2 Nucleate Boiling Correlations. The complex liquid-vapor-surface phenomena involved in nucleate pool boiling heat transfer has rendered the development of a predictive model difficult, as is evident from the large number of nucleate boiling correlations that have been proposed over the past several decades (see Table 3). Many of these correlations have theoretical underpinnings, such as the correlation by Forster and Zuber [50]; however, their utility is limited by the failure to adequately account for surface effects. One of the earliest correlations developed specifically to handle a wide variety of fluids and surfaces is the Rohsenow [51] correlation, which uses empirical factors to account for the surface-fluid combination. Constants for several surface-fluid combinations have been provided by various authors [52,53]. However, the usefulness of the Rohsenow correlation is also limited as it requires experimental data on the fluid-surface combination of interest as inputs.

Several correlations have been formulated in terms of nucleation site densities to represent the influence of different surface characteristics on heat transfer. These include the correlations by Tien [54], Leinhard [55], and Mikic and Rohsenow [56]. However, since the nucleation site densities are generally not known a priori, most of these correlations require empirical fits to determine these parameters and other associated constants. Although these correlations are still of some theoretical significance, their utility in many engineering environments is limited.

As noted earlier, several investigators have observed a $h \propto R^m$ dependence and correlations adopting a form similar to Eq. (1) have been proposed. These include the correlations by Danilova [57], Nishikawa et al. [31], Cooper [32,33], Gorenflo [34], Leiner [58], and Ribatski and Jabardo [45]. Most of these correlations provide predictions of nucleate pool boiling heat transfer coefficients without the need for experimental data as inputs; thus, these correlations have proven quite useful in many engineering applications. The Danilova, Nishikawa, and Ribatski and Jabardo correlations were developed specifically for refrigerants; while the Cooper, Gorenflo, and Leiner correlations were designed for a broader range of fluids. Since it is highly desirable to have a single correlation that provides accurate predictions for a wide variety of fluid-surface combinations, further discussion in this work is limited to the Cooper, Gorenflo, and Leiner correlations. The suitability of each of these correlations for predicting the nucleate pool boiling heat transfer coefficients from the present work for two fluids (water and FC-77) with significantly different wetting characteristics and thermal properties over a wide range of surface roughness is assessed.

4.3 Cooper Correlation. Cooper [59] noticed that although many correlations had different algebraic forms, they produced similar numerical predictions and similar trends. He showed that many of these correlations could be reformulated using reduced properties, resulting in a simpler formulation without much loss in accuracy [32,33]. The Cooper correlation (see Table 3) accounts for the surface roughness effect using the relation developed by Nishikawa et al. [30,31]. However, Cooper reformulated the $(8R_{p,\mathrm{old}})^{0.2(1-P_r)}$ relationship suggested by Nishikawa et al. into $P_r^{0.12-0.2\log_{10}R_p}$. Cooper [33] found that the reformulated expression matched the original expression by Nishikawa et al. within

Table 3 Nucleate boiling correlations

Author(s)	Correlation
Forster and Zuber [50]	$q = Ck_l \ \mathrm{Pr}_l^b \left[\frac{h_{fg}\rho_v}{c_{p,l}\rho_l\sqrt{\pi\alpha_l}} \left(\frac{\Delta P}{2\sigma}\right)^{0.5} \left(\frac{\Delta P}{\rho_l}\right)^{0.25} \right] \left[\frac{\rho_l}{\mu_l} \left(\frac{\Delta T c_{p,l}\rho_l\sqrt{\pi\alpha_l}}{h_{fg}\rho_v} \right)^2 \right]^a$
Rohsenow [51]	$q = \mu_l h_{fg} \sqrt{\frac{g(\rho_l - \rho_v)}{\sigma}} \left[\frac{c_{p,l}\Delta T}{C h_{fg} \ \mathrm{Pr}_l^b} \right]^a$
Tien [54]	$q = Ck_l \ \mathrm{Pr}_l^{0.33} N^{0.5} \Delta T$
Lienhard [55]	$q = Ck_l \ \mathrm{Pr}^{1/3} \frac{\sqrt{\sigma g(\rho_l - \rho_v)/\rho_l^2}}{\sqrt{\sigma g(\rho_l - \rho_v)/\rho_l^2\|_{\mathrm{H_2O}}}} N^{1/3} (\Delta T)^{5/4}$
Mikic and Rohsenow [56]	$q = C(k_l\rho_l c_{p,l} f)^{1/2} d_0^2 N \Delta T$
Danilova [57]	$h = C\left(\frac{R_z}{R_{z0}}\right)^{0.2} (0.14 + 2.2P_r) q^{0.75}$
Nishikawa et al. [31]	$h = \left(31.4 \frac{P_c^{0.2}}{M^{0.1} T_c^{0.9}} \right) (8R_{p,\mathrm{old}})^{(1-P_r)/5} \left[\frac{P_r^{0.23}}{(1 - 0.99P_r)^{0.9}} \right] q^{0.8}$
Cooper [32,33]	$h = C(P_r^{0.12 - 0.2 \log_{10} R_{p,\mathrm{old}}})(-\log_{10} P_r)^{-0.55} M^{-0.5} q^{0.67}$; $C = 55$ for horizontal aluminum surfaces
Gorenflo [34]	$\frac{h}{h_0} = CF(P_r)\left(\frac{q}{q_0}\right)^n; \quad C = \left(\frac{R_a}{R_{a0}}\right)^{0.133}; \quad R_{a0} = 0.4 \ \mu\mathrm{m}$ $F(P_r) = 1.73P_r^{0.27} + \left(6.1 + \frac{0.68}{1 - P_r}\right) P_r^2$ and $n = 0.9 - 0.3P_r^{0.15}$ for water $F(P_r) = 1.2P_r^{0.27} + \left(2.5 + \frac{1}{1 - P_r}\right) P_r$ and $n = 0.9 - 0.3P_r^{0.3}$ for all other fluids
Leiner [58]	$\frac{h}{P_c\sqrt{\Re/T_c}} = 0.6161 C^{0.1512} K^{0.4894} \left[\frac{R_a}{(k_B T_c/P_c)^{1/3}} \right]^{0.133} F'(P_r) \left(\frac{q}{P_c\sqrt{\Re T_c}} \right)^n$ $F'(P_r) = 43000^{n-0.75} \left[1.2P_r^{0.27} + \left(2.5 + \frac{1}{1 - P_r}\right) P_r \right]; \quad n = 0.9 - 0.3P_r^{0.3}$ $C = \frac{c_{p,l}}{\Re}\|_{P_r = 0.1}; \quad K = -T_r \ln\left(\frac{P_r}{1 - T_r}\right)\|_{P_r = 0.1}$
Ribatski and Jabardo [45]	$h = CR_a^{0.2} P_r^{0.45} [-\log(P_r)]^{-0.8} M^{-0.5} q^n$

3% over the pressure ($0.08 < P_r < 0.9$) and surface roughness ($0.22 \ \mu\mathrm{m} < R_{p,\mathrm{old}} < 4.31 \ \mu\mathrm{m}$) ranges studied. It should be noted that $R_{p,\mathrm{old}}$ used in the Cooper correlation is defined by DIN 4762/1:1960. Gorenflo [34] suggested the conversion $R_a \approx 0.4R_{p,\mathrm{old}}$, which is adopted in this work.

A comparison between the experimental data from the present work and predictions from the Cooper correlation is shown in Fig. 10. The Cooper correlation predicts heat transfer coefficients for FC-77 with mean absolute errors (MAEs) ranging from 12.9% for the roughest EDM surface to 33.4% for the polished surface with an overall MAE of 24.1%. Here, the mean absolute error is defined as

$$MAE = \frac{1}{N} \sum_{i=1}^{N} \frac{|h_{\mathrm{corr},i} - h_{\mathrm{exp},i}|}{h_{\mathrm{exp},i}} \tag{2}$$

where i represents an experimental data point at a given heat flux.

For water under the given experimental conditions, the predictive capability of the Cooper correlation is poor, with MAEs ranging from 44.4% to 324% for the polished and roughest EDM surfaces, respectively. The poor predictions result from the reformulation of the roughness relationship of Nishikawa et al. At a fixed heat flux, the Cooper correlation predicts 13.6 times higher heat transfer coefficients on the roughest surface (10.0 μm) compared with the smoothest (0.038 μm), while the original relationship by Nishikawa et al. predicts a more modest increase by a factor of 3. Cooper did not consider such a low reduced pressure ($P_r = 0.0046$) as was used in the present study when reformulating the surface roughness relation of Nishikawa et al. At a reduced pressure of $P_r = 0.064$ corresponding to the FC-77 experiments, Cooper's reformulation matches the relation of Nishikawa et al. within 20% over the surfaces studied. For this reason, the Cooper correlation is not recommended for reduced pressures much below $P_r = 0.08$.

4.4 Gorenflo Correlation. The Gorenflo [34] correlation is shown in Table 3. Following Stephan's work [28], Gorenflo accounted for surface roughness using $h \propto R_a^{0.133}$. The Gorenflo correlation requires knowledge of a reference heat transfer coefficient, h_0, at a given reference heat flux, q_0. For water, a reference value of $h_0 = 5600 \ \mathrm{W/m^2\,K}$ at $q_0 = 20{,}000 \ \mathrm{W/m^2}$ was obtained from the VDI Heat Atlas [34]. For fluids for which no suitable experimental data are available, such as FC-77, Gorenflo recommended using the Stephan and Preußer correlation (as cited in Ref. [34]), although greater uncertainties can be expected in the following prediction.

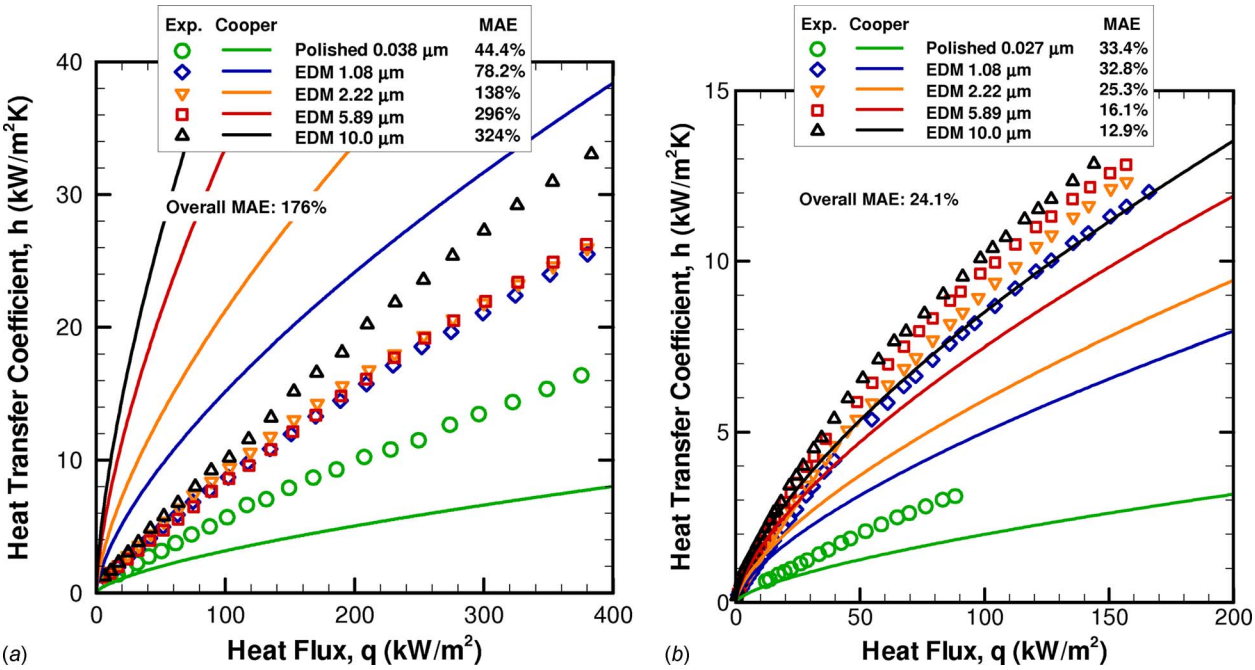

Fig. 10 Comparison between experimental data and predictions from the Cooper correlation [32,33] for (*a*) water and (*b*) FC-77

$$\frac{hd_0}{k_l} = 0.1\left(\frac{q_0 d_0}{k_l T_{\text{sat}}}\right)^{0.674}\left(\frac{\rho_v}{\rho_l}\right)^{0.156}\left(\frac{h_{fg}d_0^2}{\alpha_l^2}\right)^{0.371}\left(\frac{\alpha_l^2\rho_l}{\sigma d_0}\right)^{0.350} \times\left(\frac{\mu_l c_{p,l}}{k_l}\right)^{-0.16} \tag{3}$$

where

$$d_0 = 0.0149\theta\sqrt{\frac{2\sigma}{g(\rho_l-\rho_v)}} \tag{4}$$

Gorenflo suggested evaluating h using fluid properties at a pressure $P_r=0.03$ and then converting to h_0 at the reference pressure of $P_{r0}=0.1$ through the use of the $F(P_r)$ equation shown in Table

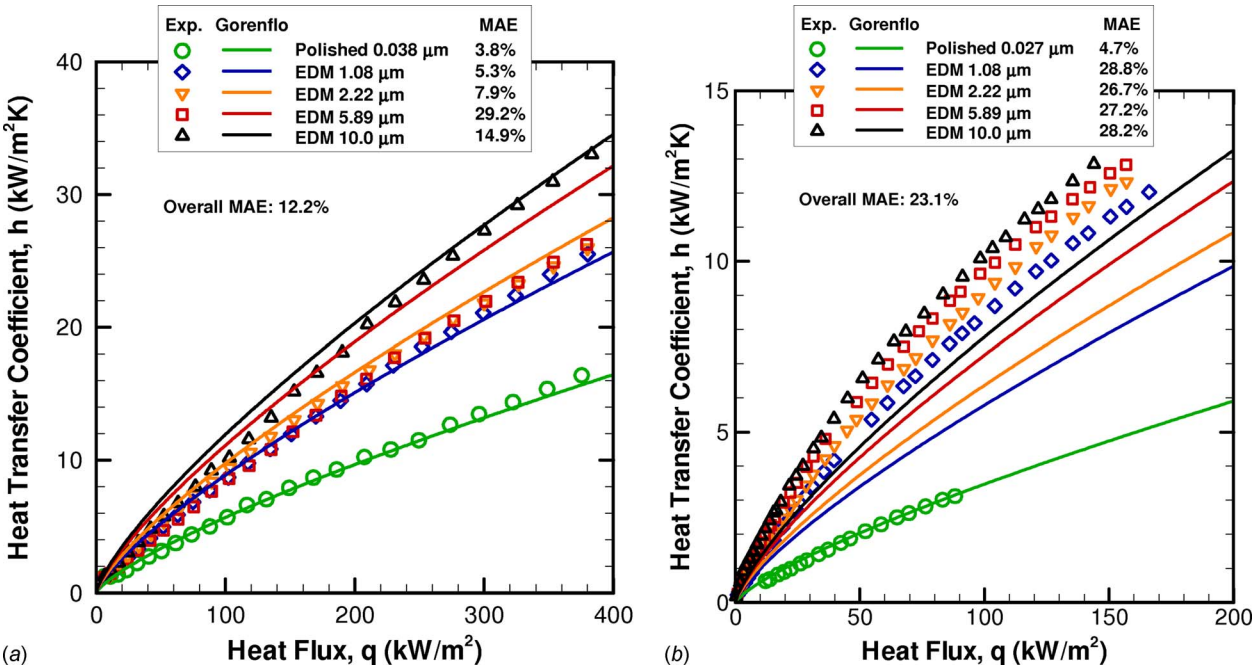

Fig. 11 Comparison between experimental data and predictions from the Gorenflo correlation [34] for (*a*) water and (*b*) FC-77

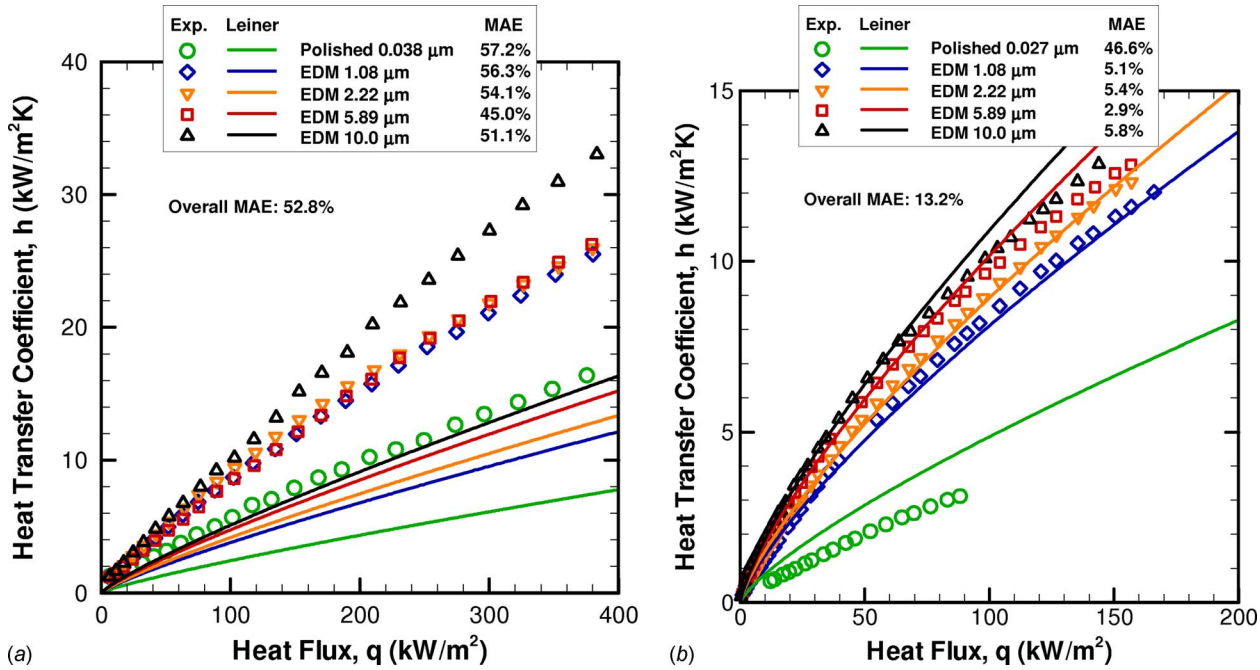

Fig. 12 Comparison between experimental data and predictions from the Leiner correlation [59] for (*a*) water and (*b*) FC-77

3. For FC-77, the estimated reference heat transfer coefficient is $h_0 = 1840$ W/m^2 K at $q_0 = 20{,}000$ W/m^2.

A comparison between the Gorenflo correlation and the experimental results for water and FC-77 is shown in Fig. 11. The Gorenflo correlation predicts the experimental results in water quite well, with a MAE of only 3.8% for the polished surface and an overall MAE of 12.2%. For FC-77, the predictions are less accurate, particularly for the EDM surface with MAEs in the range of 26–29%, although the predictions for the polished surface are quite good with a MAE of 4.7%.

4.5 Leiner Correlation. The reliance on reference values reduces the utility of the Gorenflo correlation as reference values are only available for a limited number of fluids. Leiner [56] addressed this issue by using the principles of thermodynamic similarity to further develop the Gorenflo correlation by removing the need for reference values (see Table 3). It should be noted that the pressure function, $F'(P_r)$, was specifically developed for fluids other than water, and so the Leiner correlation is not expected to offer accurate predictions of boiling in water. In this case, the Gorenflo correlation should provide better predictions.

The comparison between the Leiner correlation and experimental results is shown in Fig. 12. As expected, the Leiner correlation is not particularly accurate for water, with MAEs of approximately 50%. The Leiner correlation fares much better with FC-77 with MAEs around 5% for the EDM surfaces, but the correlation significantly overpredicts heat transfer coefficients for the polished surface with a MAE of 46.6%. Although the Leiner correlation has a lower overall MAE than the Gorenfo correlation for FC-77 (13.2% versus 23.1%), this is probably influenced by the fact that four EDM surfaces (where the Leiner correlation provides the best predictions) and only one polished surfaces (where the Gorenflo provides the best predictions) were considered in the present work. Thus, despite the lower overall MAE of the Leiner correlation, it is inconclusive whether much additional accuracy is provided by the Leiner correlation over the Gorenflo correlation for FC-77.

The main problem with the Gorenflo and Leiner correlations' predictions for FC-77 is that neither accurately accounts for the influence of surface roughness. Both correlations use Stephan's recommendation of $m = 0.133$, which is closer to the $m = 0.1$ found for water in this study, but differs from the $m = 0.2$ found for FC-77. If the Gorenflo correlation in Table 3 is modified so that factor C becomes

$$C = \left(\frac{R_a}{R_{a0}}\right)^{0.2} \tag{5}$$

then the overall MAE for FC-77 is reduced from 23.1% to 15.8%. If a reference heat transfer coefficient $h_0 = 2160$ W/m^2 K at $q_0 = 20{,}000$ W/m^2, which more closely matches the experimental results, is used instead of $h_0 = 1840$ W/m^2 K as estimated by the Stephan and Preußer correlation [34], the MAE is further reduced to 6.7%. Modifying the Leiner correlation to account for a surface roughness exponent $m = 0.2$ requires more manipulation, but it can be shown that

$$\frac{h}{P_c\sqrt{\bar{\mathfrak{R}}/T_c}} = 0.6161C^{0.1512}K^{0.4894}F'(P_r) \times \left(\frac{q}{P_c\sqrt{\bar{\mathfrak{R}}T_c}}\right)^n \left\{\frac{R_a^{0.2}}{R_{a0}^{0.067}[(k_BT_c/P_c)^{1/3}]^{0.133}}\right\} \tag{6}$$

The overall MAE for FC-77 increases from 13.2% to 18.2% when using Eq. (6) instead of the original Leiner correlation, although the predictions are notably improved for the polished surface, with an MAE of 21.1%.

For water, the Gorenflo correlation clearly provides the best predictive capabilities. From the discussion above, the modified Gorenflo correlation provided the lowest errors for FC-77. However, given the limited number of surfaces tested, and considering the wide range of conclusions from other researchers regarding the influence of roughness on nucleate boiling, it is unclear whether a modification to the Gorenflo correlation for FC-77 will lead to a general improvement in accuracy. Further, it is unclear whether any general improvement in predictive capability can be achieved when using standard surface roughness parameters to account for the effects of surface characteristics on boiling heat transfer. Although it has been proposed that the relationship $h \propto R^m$ where $m = f(\theta)$ may lead to an improvement in predictions, more experimental data are needed to conclusively establish this dependence. Moreover, the current experimental data indicate

general weaknesses in using $h \propto R^m$ to account for surface roughness, and it is therefore recommended that future research focus on developing new methods of characterizing boiling surfaces.

5 Conclusions

Pool boiling at atmospheric pressure from surfaces with a wide range of surface roughness in two fluids with differing wetting characteristics was experimentally explored. For water, the results indicate little improvement in heat transfer coefficient for roughness beyond $R_a = 1.08$ μm, except for a very rough 10.0 μm surface, which had significantly higher heat transfer coefficients. On the same set of surfaces, FC-77 exhibited a different trend with continuously increasing heat transfer coefficient with respect to surface roughness, at a fixed heat flux. The general trend of increasing heat transfer coefficient with surface roughness was correlated using $h \propto R^m$. The results indicate a stronger dependence on surface roughness for FC-77 with $m = 0.2$ compared with $m = 0.1$ for water.

The experimental results were compared with predictions from widely used nucleate boiling correlations. Due to differences in the surface roughness exponent for the two fluids, no single correlation provides entirely satisfactory predictions. The Gorenflo correlation provided the lowest errors for water. For FC-77, the lowest errors were obtained using a modified Gorenflo correlation with a surface roughness exponent of $m = 0.2$. Due to the numerous deficiencies associated with correlating nucleate boiling data using surface roughness parameters, it is recommended that future research focus on developing new techniques for characterizing boiling surfaces.

Acknowledgment

Dr. Dong Liu, Dr. Tailian Chen, Dr. Poh-Seng Lee, and Dr. Stefan Bertsch are thanked for their helpful and insightful discussions. Funding from the Indiana 21st Century Research and Technology Fund, and the Cooling Technologies Research Center, an NSF IUCRC at Purdue University, is gratefully acknowledged.

Nomenclature

a, b, C, K = empirical constants
c_p = specific heat
d_0 = bubble departure diameter
F, F' = pressure functions
f = bubble emission frequency
g = acceleration due to gravity
h = heat transfer coefficient
h_{fg} = heat of vaporization
k = thermal conductivity
k_B = Boltzmann constant, $k_B = 1.3807 \times 10^{-23}$ J/K
M = molecular weight
m = surface roughness exponent
N = active nucleation site density
n = heat flux exponent
P = pressure
ΔP = excess pressure corresponding to wall superheat, $\Delta P = P_w - P_{sat}$
Pr = Prandtl number, $\mathrm{Pr} = c_p \mu / k$
$\mathfrak{R}$ = universal gas constant, $\mathfrak{R} = 8.314$ kJ/K kmol
$\overline{\mathfrak{R}}$ = specific gas constant, $\overline{\mathfrak{R}} = \mathfrak{R}/M$
R_a, R_p, R_q, R_z = roughness parameters according to ASME B46.1–1995
$R_{p,\mathrm{old}}$ = "Glättungstiefe" according to DIN 4762/1:1960
q = heat flux
T = temperature
ΔT = wall superheat, $\Delta T = T_w - T_{sat}$

Greek

α = thermal diffusivity, $\alpha = k/\rho c_p$
θ = contact angle
μ = dynamic viscosity
ρ = density
σ = surface tension

Subscripts

c = critical
corr = correlation
exp = experiment
l = liquid
r = reduced
sat = saturation
v = vapor
w = wall
0 = reference

References

[1] Jakob, M., 1936, "Heat Transfer in Evaporation and Condensation—I," Mech. Eng. (Am. Soc. Mech. Eng.), **58**, pp. 643–660.
[2] Westwater, J. W., 1958, "Boiling Heat Transfer," Am. Sci., **47**, pp. 427–446.
[3] Clark, H. B., Strenge, P. S., and Westwater, J. W., 1959, "Active Sites for Nucleate Boiling," Chem. Eng. Prog., Symp. Ser., **55**(29), pp. 103–110.
[4] Bankoff, S. G., 1958, "Ebullition From Solid Surfaces in the Absence of a Pre-Existing Gaseous Phase," Trans. ASME, **79**, pp. 735–740.
[5] Bankoff, S. G., 1958, "Entrapment of Gas in the Spreading of a Liquid Over a Rough Surface," AIChE J., **4**(1), pp. 24–26.
[6] Griffith, P., and Wallis, J. D., 1960, "The Role of Surface Conditions in Nucleate Boiling," Chem. Eng. Prog., Symp. Ser., **56**(30), pp. 49–63.
[7] Hsu, Y. Y., 1962, "On the Size Range of Active Nucleation Cavities on a Heating Surface," ASME J. Heat Transfer, **84**, pp. 207–216.
[8] Corty, C., and Foust, A. S., 1955, "Surface Variables in Nucleate Boiling," Chem. Eng. Prog., Symp. Ser., **51**(17), pp. 1–12.
[9] Kurihara, H. M., and Myers, J. E., 1960, "The Effects of Superheat and Surface Roughness on Boiling Coefficients," AIChE J., **6**(1), pp. 83–91.
[10] Hsu, S. T., and Schmidt, F. W., 1961, "Measured Variations in Local Surface Temperatures in Pool Boiling of Water," ASME J. Heat Transfer, **83**, pp. 254–260.
[11] Marto, P. J., and Rohsenow, W. M., 1966, "Effects of Surface Conditions on Nucleate Pool Boiling of Sodium," ASME J. Heat Transfer, **88**, pp. 196–204.
[12] Berenson, P. J., 1962, "Experiments on Pool-Boiling Heat Transfer," Int. J. Heat Mass Transfer, **5**, pp. 985–999.
[13] Webb, R. L., 1981, "The Evolution of Enhanced Surface Geometries for Nucleate Boiling," Heat Transfer Eng., **2**, pp. 46–69.
[14] Webb, R. L., 2004, "Odyssey of the Enhanced Boiling Surface," ASME J. Heat Transfer, **126**, pp. 1051–1059.
[15] Bier, K., Gorenflo, D., Salam, M., and Tanes, Y., 1978, "Pool Boiling Heat Transfer and Size of Active Nucleation Centers for Horizontal Plates With Different Surface Roughness," *Proceedings of the Sixth International Heat Transfer Conference*, Toronto, Canada, Vol. 1, pp. 151–156.
[16] Chowdhury, S. K. R., and Winterton, R. H. S., 1985, "Surface Effects in Pool Boiling," Int. J. Heat Mass Transfer, **28**(10), pp. 1881–1889.
[17] Vachon, R. I., Tanger, G. E., Davis, D. L., and Nix, G. H., 1968, "Pool Boiling on Polished and Chemically Etched Stainless-Steel Surfaces," ASME J. Heat Transfer, **80**, pp. 231–238.
[18] Kravchenko, V. A., and Ostrovskiy, Yu. N., 1979, "Effect of Surface Roughness on Boiling Heat Transfer to Light Hydrocarbons and Nitrogen," Heat Transfer-Sov. Res., **11**(1), pp. 133–137.
[19] Grigoriev, V. A., Pavlov, Yu. M., and Ametistov, Ye. V., 1974, "An Investigation of Nucleate Boiling Heat Transfer of Helium," *Proceedings of the Fifth International Heat Transfer Conference*, Tokyo, Japan, pp. 45–49.
[20] Yang, S. R., and Kim, R. H., 1988, "A Mathematical Model of the Pool Boiling Nucleation Site Density in Terms of the Surface Characteristics," Int. J. Heat Mass Transfer, **31**(6), pp. 1127–1135.
[21] Cornwell, K., 1977, "Naturally Formed Boiling Site Cavities," Lett. Heat Mass Transfer, **4**, pp. 63–72.
[22] Shoukri, M., and Judd, R. L., 1975, "Nucleation Site Activation in Saturated Boiling," ASME J. Heat Transfer, **97**, pp. 93–98.
[23] Wang, C. H., and Dhir, V. K., 1993, "Effect of Surface Wettability on Active Nucleation Site Density During Pool Boiling of Water on a Vertical Surface," ASME J. Heat Transfer, **115**, pp. 659–669.
[24] Wang, C. H., and Dhir, V. K., 1993, "On the Gas Entrapment and Nucleation Site Density During Pool Boiling of Saturated Water," ASME J. Heat Transfer, **115**, pp. 670–679.
[25] Qi, Y., Klausner, J. F., and Mei, R., 2004, "Role of Surface Structure in Heterogeneous Nucleation," Int. J. Heat Mass Transfer, **47**, pp. 3097–3107.
[26] Luke, A., 2004, "Active and Potential Bubble Nucleation Sites on Different Structured Heated Surfaces," Chem. Eng. Res. Des., **82**, pp. 462–470.
[27] Luke, A., 2006, "Preparation, Measurement and Analysis of Microstructure of Evaporator Surfaces," Int. J. Therm. Sci., **45**, pp. 237–256.
[28] Stephan, K., 1963, "Mechanismus und Modellgesetz des Wärmeübergangs bei der Blasenverdampfung," Chem.-Ing.-Tech., **35**(11), pp. 775–784.
[29] Danilova, G. N., and Bel'skii, V. K., 1965, "Study of Heat Transfer on Boiling

of Freon 113 and Freon 12 on Pipes of Differing Roughness," Kholodil'naia Tekhnika, **4**, pp. 24–28.
[30] Nishikawa, K., Fujita, Y., Ohta, H., and Hidaka, S., 1982, "Effect of the Surface Roughness on the Nucleate Boiling Heat Transfer Over the Wide Range of Pressure," *Proceedings of the Seventh International Heat Transfer Conference*, München, Germany, Vol. 4, pp. 61–66.
[31] Nishikawa, K., Fujita, Y., Ohta, H., and Hidaka, S., 1982, "Effects of System Pressure and Surface Roughness on Nucleate Boiling Heat Transfer," Memoirs of the Faculty of Engineering, Kyushu University, **42**(2), pp. 95–111.
[32] Cooper, M. G., 1984, "Saturation Nucleate Pool Boiling—A Simple Correlation," First UK National Conference on Heat Transfer, University of Leeds, pp. 785–793.
[33] Cooper, M. G., 1984, "Heat Flow Rates in Saturated Nucleate Pool Boiling—A Wide-Ranging Examination Using Reduced Properties," Adv. Heat Transfer, **16**, pp. 157–239.
[34] Gorenflo, D., 1993, "Pool Boiling," *VDI Heat Atlas*, VDI Verlag, Düsseldorf.
[35] 3M Corporation, 1986, Fluorinert Liquids Product Manual, Industrial Chemical Products Division.
[36] 3M Corporation, 2000, Fluorinert Electronic Liquid FC-77 Product Information No. 98-0212-2309-8 (HB), Specialty Materials Division.
[37] Raben, I. A., Beaubouef, R. T., and Commerford, G. E., 1965, "A Study of Heat Transfer in Nucleate Pool Boiling of Water at Low Pressure," Chem. Eng. Prog., Symp. Ser., **61**(57), pp. 249–257.
[38] Anderson, T. M., and Mudawar, I., 1989, "Microelectronic Cooling by Enhanced Pool Boiling of a Dielectric Fluorocarbon Liquid," ASME J. Heat Transfer, **111**, pp. 752–759.
[39] Baldwin, C. S., Bhavnani, S. H., and Jaeger, R. C., 2000, "Toward Optimizing Enhanced Surfaces for Passive Immersion Cooled Heat Sinks," IEEE Trans. Compon. Packag. Tech., **23**(1), pp. 70–79.
[40] Parker, J. L., and El-Genk, M. S., 2005, "Enhanced Saturation and Subcooled Boiling of FC-72 Dielectric Liquid," Int. J. Heat Mass Transfer, **48**, pp. 3736–3752.
[41] Bhavnani, S. H., Tsai, C.-P., Jaegar, R. C., and Eison, D. L., 1993, "An Integral Heat Sink for Cooling Microelectronic Components," ASME J. Electron. Packag., **115**, pp. 284–291.
[42] Bergles, A. E., and Chyu, M. C., 1982, "Characteristics of Nucleate Pool Boiling From Porous Metallic Coatings," ASME J. Heat Transfer, **104**, pp. 279–285.
[43] Hatton, A. P., and Hall, I. S., 1966, "Photographic Study of Boiling on Prepared Surfaces," *Proceedings of the Third International Heat Transfer Conference*, Chicago, IL, Vol. 4, pp. 24–37.
[44] Fedders, H., 1971, "Messung des Wärmeüberganges beim Blasensieden von Wasser an metallischen Rohren," Kernforschungsanlage Jülich Report No. Jül-740-RB.
[45] Ribatski, G., and Jabardo, J. M. S., 2003, "Experimental Study of Nucleate Boiling of Halocarbon Refrigerants on Cylindrical Surfaces," Int. J. Heat Mass Transfer, **46**, pp. 4439–4451.
[46] Chun, M.-H., and Kang, M.-G., 1998, "Effects of Heat Exchanger Tube Parameters on Nucleate Pool Boiling Heat Transfer," ASME J. Heat Transfer, **120**(2), pp. 468–476.
[47] Vachon, R. I., Tanger, G. E., Nix, G. H., and Davis, D. L., 1965, "Pool Boiling of Water From Mechanically Polished and Chemically Etched Stainless Steel Surfaces," Auburn Research Foundation Report No. IV.
[48] Vachon, R. I., Tanger, G. E., Nix, G. H., and Goree, L. H., 1966, "Pool Boiling of Water on 304 Stainless Steel Etched With Hydrochloric Acid," Auburn Research Foundation Report No. VI.
[49] Kurihara, H. M., 1956, "Fundamental Factors Affecting Boiling Coefficients," Ph.D. thesis, Purdue University, Lafayette, IN.
[50] Forster, H. K., and Zuber, N., 1955, "Dynamics of Vapor Bubbles and Boiling Heat Transfer," AIChE J., **1**(4), pp. 531–535.
[51] Rohsenow, W. M., 1952, "A Method of Correlating Heat-Transfer Data for Surface Boiling of Liquids," Trans. ASME, **74**, pp. 969–976.
[52] Vachon, R. I., Nix, G. H., and Tanger, G. E., 1968, "Evaluation of Constants for the Rohsenow Pool-Boiling Correlation," ASME J. Heat Transfer, **90**, pp. 239–247.
[53] Pioro, I. L., 1999, "Experimental Evaluation of Constants for the Rohsenow Pool Boiling Correlation," Int. J. Heat Mass Transfer, **42**, pp. 2003–2013.
[54] Tien, C. L., 1962, "A Hydrodynamic Model for Nucleate Pool Boiling," Int. J. Heat Mass Transfer, **5**, pp. 533–540.
[55] Lienhard, J. H., 1963, "A Semi-Rational Nucleate Boiling Heat Flux Correlation," Int. J. Heat Mass Transfer, **6**, pp. 215–219.
[56] Mikic, B. B., and Rohsenow, W. M., 1969, "A New Correlation of Pool-Boiling Data Including the Effect of Heating Surface Characteristics," ASME J. Heat Transfer, **91**, pp. 245–250.
[57] Danilova, G. N., 1970, "Correlation of Boiling Heat Transfer Data for Freons," Heat Transfer-Sov. Res., **2**(2), pp. 73–78.
[58] Leiner, W., 1994, "Heat Transfer by Nucleate Pool Boiling—General Correlation Based on Thermodynamic Similarity," Int. J. Heat Mass Transfer, **37**(5), pp. 763–769.
[59] Cooper, M. G., 1982, "Correlations for Nucleate Boiling—Formulation Using Reduced Properties," PCH, PhysicoChem. Hydrodyn., **3**(2), pp. 89–111.

Rapid Boiling of a Two-Phase Droplet in an Immiscible Liquid at High Superheat

Herman D. Haustein
Mem. ASME
Faculty of Mechanical Engineering,
Technion Israel Institute of Technology,
Haifa 32000, Israel
e-mail: herman@tx.technion.ac.il

Alon Gany
Professor Lena and Ben Fohrman Chair
Mem. ASME
Faculty of Aerospace Engineering,
Technion Israel Institute of Technology,
Haifa 32000, Israel
e-mail: gany@tx.technion.ac.il

Ezra Elias
Professor T. Segal Chair
Faculty of Mechanical Engineering,
Technion Israel Institute of Technology,
Haifa 32000, Israel
e-mail: merezra@tx.technion.ac.il

This work studies experimentally the rapid boiling of a droplet rising in a host liquid environment, within a range of superheats ($0.2<J_a^*<0.5$) not previously investigated. The direct-contact rapid-boiling process has many advantages in the fields of heat exchange and multiphase flow. By taking into account the superheat, heat transfer, and hydrodynamics of the multiphase-droplet the aim of this study is to create greater insight into the character of this transient-boiling process, for the first time. The sudden depressurization of a water column led to the rapid boiling of liquid propane droplets rising by buoyancy. During this millisecond boiling distinct stages were identified. Appropriate critical times for the transition between stages were defined by a simplified model, among these a novel criterion for the sudden pause in boiling caused by the engulfing liquid-film's collapse. Good agreement was found between these predicted time-points and measured changes in the boiling profile. This form of boiling, though being very rapid and sustaining high heat transfer rates, is still calm in nature, therefore, more predictable and widely applicable. Understanding this form of boiling suggests that the "design" of the boiling curve may be possible by setting the initial parameters.
[DOI: 10.1115/1.3220146]

Keywords: rapid boiling, rapid phase transfer, two-phase droplet, three-fluid system, superheat, depressurization, vaporization, liquid propane droplets

1 Introduction

This paper studies experimentally the direct-contact rapid-boiling process of a multiphase-droplet in an immiscible host liquid (a three-fluid system). We define our boiling as direct-contact because heat is transferred to the droplets from the host liquid environment, directly through the liquid-liquid interface, as in direct-contact heat exchangers. This form of heat exchange has the advantage of maximizing the contact area, while avoiding fouling and wall resistance.

In order to create rapid-boiling, a high level of superheat is required. This superheating is obtained through sudden depressurization. There are numerous works dealing with boiling due to depressurization. Notable among these is the experimental work of Hewitt and Parker [1], which deals with the initial bubble growth (0.5–2 mm). However, the pressure gradients in Ref. [1] were small (0.01 bar/ms), and therefore, the boiling rate was limited by the depressurization rate (the system was at a quasi-equilibrium state with no real superheating), as in the majority of work in this area (see Appendix A). Since our goal was to obtain a boiling curve based on true boiling dynamics, only experiments in which the depressurization completed before 10% mass boiling occurred (depressurization rates on the scale of 1 atm/ms) were taken into account.

The maximum level of superheat obtained may conveniently be presented in a normalized nondimensional form, expressing the ratio of excess energy to latent heat (see Eq. (1)). This equation is the normalized Jakob number, proposed as a means of comparison between different works conducted in this field.

$$J_a^* = \frac{c_p(T_\infty - T_{\text{sat}})}{h_{fg}} = \text{Ja}\frac{\rho_v}{\rho_l}, \quad 0 \le J_a^* \le 1 \tag{1}$$

On the one hand, numerous researchers [2–4] have studied the subject of explosive boiling of a droplet. This is in fact boiling close to the superheat limit, the practical temperature of homogeneous nucleation ($J_a^* \approx 0.5-0.8$). This form of boiling is unique: it is of a violent nature (generates a pressure wave), it is very fast (on the order of microseconds), and most of the dynamics are inertial controlled. The instability mechanism driving this form of boiling is quite different from the calm boiling that was encountered in the current study.

On the other hand, the problem of the gradual direct-contact boiling of a multiphase-droplet, in an immiscible host liquid at little or no superheat ($J_a^* \approx 0-0.1$), has also been well covered, since the early work of Sideman and Taitel [5]. A good overview of this range is given in Table 1 of Ref. [6]. Notable among these is the analytical/numerical work of Oguz and Sadhal [7]. However, their analysis was conducted under the assumption of Stokes-flow and slow growth of the multiphase-droplet, relevant only to the initial stages of boiling (up to 2% mass fraction) and/or low-superheat levels.

Additional research exists on the growth of a vapor bubble within its own liquid (a two-fluid system) at partial superheat. Experiments have been conducted [8,9] close to our range of superheating ($J_a^* \approx 0.1-0.2$). Theoretical analysis of the two-fluid system is well covered in several works [10,11]. The existing body of work, both theoretical and experimental, is reviewed and compared by Lee and Merte [12]. However, the three-fluid system considered here cannot be well described by this theory as additional/different boundary conditions are present. This is especially evident when the multiphase-droplet is considered under translation motion leading to convective heat transfer.

Manuscript received September 11, 2008; final manuscript received February 25, 2009; published online October 15, 2009.

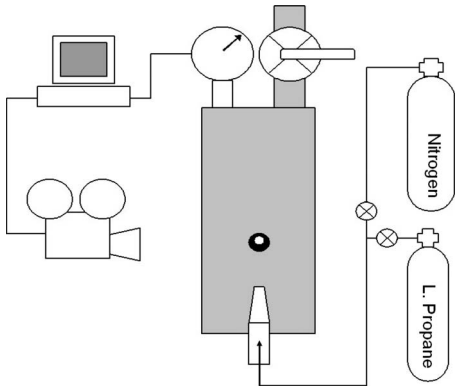

Fig. 1 Schematic of the water column experiment setup

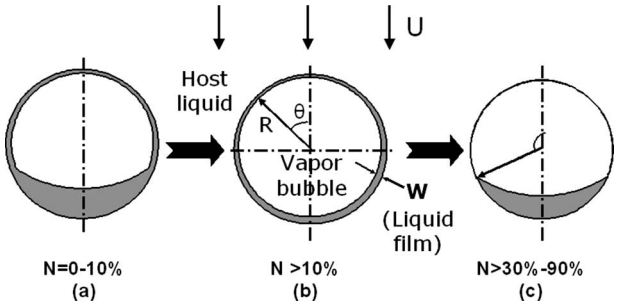

Fig. 2 Configurations at different levels of boiling (*N*): (*a*) initial (observed), (*b*) rapid (observed and predicted), and (*c*) liquid-film collapse (predicted)

It seems, therefore, that the boiling of a multiphase-droplet rising in an immiscible liquid environment has not been studied in the range of medium to high superheats ($0.2<J_a^*<0.5$). It can only be assumed that this is due to certain technical difficulties related with the creation and observation of boiling dynamics. Boiling within this range is widely applicable due to high rates of heat and mass transfer, calm nature, and distinct boiling stages. The latter suggests that boiling rates and time length of different boiling regimes can be controlled by the selection of liquids and the dictation of initial conditions, thereby enabling the design of the rapid-boiling curve. Fields of relevance for this form of boiling include the rapid increase in flow compressibility (gas void-fraction) and the direct-contact heat exchange, among others; while suggested applications range from alternative marine propulsion methods to local microchip-cooling. Further understanding of the problem within this range will extend existing applications and possibly create new ones.

2 Experimental Setup

The boiling fluid was liquid propane, chosen for its suitable properties (given in Ref. [13]): low solubility in water and low boiling temperature at atmospheric pressure (231 K) resulting in high superheat ($J_a^*\approx 0.25-0.45$). The host liquid was water.

The propane was introduced as multiphase-droplets 0.8–2.5 mm in diameter with a vapor bubble nucleus varying in size. This nucleus was flow generated, and therefore, its size was not easily controlled. The droplets were introduced through a nozzle, with a diameter of 0.4 mm, into a water column. Nitrogen was used as an "injector" gas to control injection velocity (source pressure). The water column was made of transparent polymethyl methacrylate (PMMA) that has a similar optical diffraction to water, thereby reducing distortion. A schematic of the experimental setup is presented in Fig. 1. Superheating (tension) was obtained by sudden depressurization. The pressure was released by the manual opening of a 2 in. ball tap on a 1 in. port. The majority of the pressure drop (80%) occurred within 10 ms. This "drop-time" was sufficiently fast for our mode of boiling, as discussed in Appendix A. Pressure was measured via a fast response piezoresistive pressure transducer connected via a data acquisition module to a computer, at rates of 0.35–1 kHz. The droplet's boiling was visually recorded, at the same rate as the pressure measurement, using a high speed camera and frame grabber. The column was backlit by a diffuse light source through a lattice; this was done in order to enhance the borders of the droplets, following the method used in Ref. [5]. The column was slowly and completely filled by the host liquid, water. This was done to minimize entrapped air and was found to be very significant, as gas volume dampens the dynamic response of the system, thereby slowing the pressure drop. De-aeration was considered to be unnecessarily complicating.

2.1 Conducting the Experiment. The host liquid temperature was measured at the beginning and end of every experiment. The focus/exposure and scale (pixels to millimeters) were set and recorded. The pressure transducer was calibrated to the ambient pressure. Subsequently the column was pressurized to propane's saturation pressure at ambient temperature. After which more propane was injected, creating a line of droplets spaced 3–7 cm apart. The propane droplets were at equilibrium with the host liquid up until depressurization. Each multiphase-droplet has a vapor bubble within it so nucleation is not required for boiling. This vapor nucleus was generated by cavitation in the flow through the injection nozzle. At some point the ball tap was opened, causing the pressure to drop and boiling to ensue. The pressure drop was recorded and the boiling was filmed.

From the images the different diameters were obtained as well as the rise velocity. From this data the pressure readings were finely synchronized to the images. This led to an estimated time-shift error of one time step, ± 1.4 ms. The error estimation for the photographs is ± 0.1 mm, as high photographic resolution was used, -17 pixels/mm and above. Lastly, the accuracy of pressure reading is ± 5 kPa, due to initial calibration and sensor accuracy.

3 Results

Numerous experiments were conducted within a range of conditions ($R=0.5-1.35$ mm, $T_\infty=288-316$ K, and $p=1-4$ atm), among these eighteen, with the fastest depressurization and no significant pressure oscillations, were selected for analysis. Experiment conditions could not be reproduced exactly, as some parameters were not directly controlled, but close conditions resulted in similar behavior.

3.1 Configuration. From initial results it seems that for the system considered (propane-water) the two-phase droplet's preferred configuration is engulfment, i.e., that the vapor bubble is surrounded by its liquid-film. The static condition for engulfment, due to surface energy considerations, as described by Mori [14] and by Johnson and Sadhal [15] is given in Eq. (2)

$$S_p = \sigma_h - (\sigma_l + \sigma_{lh}) > 0 \tag{2}$$

S_p is the spreading coefficient, a positive value indicates that the bubble seeks to be covered by the liquid-film. According to the surface tension values for propane, (from the literature [13,16]: liquid-vapor is 15 mN/m, liquid-water is around 46 mN/m, and water-vapor around 70 mN/m) it seems that this is the preferred configuration. Allowing for weakly dynamic conditions—the Bond number (gravity) and capillary number (cross-flow shear) that is small but not negligible, lead to the configurations shown in Fig. 2. In Fig. 2(*a*), gravity and surface tension define the shape. As boiling causes the vapor bubble to inflate, the liquid-film thins and surface tension plays the dominant role (see Fig. 2(*b*)). When the liquid-film reaches a crucial thickness, shear may cause it to collapse and remain so, in spite of a positive spreading coefficient,

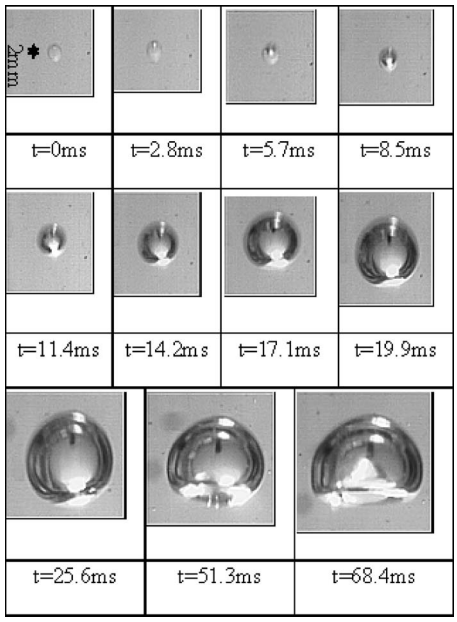

Fig. 3 The photographic boiling sequence of propane two-phase droplet in water (0.3 mm bubble in a 2.1 mm droplet initially, within an environment at $T_\infty = 303$ K); boiling completes around 35 ms—last two frames are after completion

see Fig. 2(*c*). Although not all the configurations can be observed (see first four frames of Fig. 3), some strong evidence of their existence has been found and will be presented.

Although the bubble is initially at the top part of the multiphase-droplet, once boiling begins and the liquid-film thins, concentricity is closely maintained. Even in cases where additional nuclei existed, they centered and joined to one bubble within the first 10 ms. The engulfed configuration is only observable in the initial stages of boiling. When the film thickness reduces below 100 μm (around 10% mass boiled), it becomes visibly indistinguishable.

3.2 Sequence of Boiling. Through the data collected during the boiling process, the transient sequence of events in this boiling was revealed. Let us look at a characteristic behavior of a 2.1 mm diameter multiphase-droplet with a 0.3 mm bubble nucleus at $T_\infty = 303$ K, shown in Fig. 3 (unless stated otherwise, all mentioned values refer to this experiment). Superheat was 80% of its maximum value; the superheat comprised around 40% of the required latent heat for complete boiling ($J_a^* \approx 0.4$).

After the tap was opened, the pressure dropped at an average rate of around 1 atm/ms, the drop-time (90–10%) lasting around 11 ms (shown in Fig. 4). Toward the end of the depressurization the decay was closely exponential, with several oscillations following. The first overshoot is seen around 35 ms.

During the depressurization, boiling commenced at a very slow rate. In Fig. 4(*b*) it can be seen that around 7 ms there exists the first inflection-point in the boiling rate (hereafter t_1), following it boiling increases to an intermediate rate of around 0.06 g/s (interface radial velocity is 0.2 m/s). Then, around 15–17 ms, a second inflection-point (t_2) is evident, beyond which the boiling rate reaches a maximum of 0.11 g/s (interface radial velocity is 0.25 m/s). This high boiling rate is roughly linear on the normalized mass/time graph, see Fig. 5. It shall be defined as the nominal rapid-boiling rate (N_n'). The nominal boiling rate is maintained until a point in time when we see a sudden drop in the boiling rate (t_3)—boiling is almost completely halted, due to the liquid-film collapse. Beyond this point in time boiling resumes at an ever growing rate until all the liquid has transitioned to vapor, this concave boiling curve is typical of the spherical-cap shape that

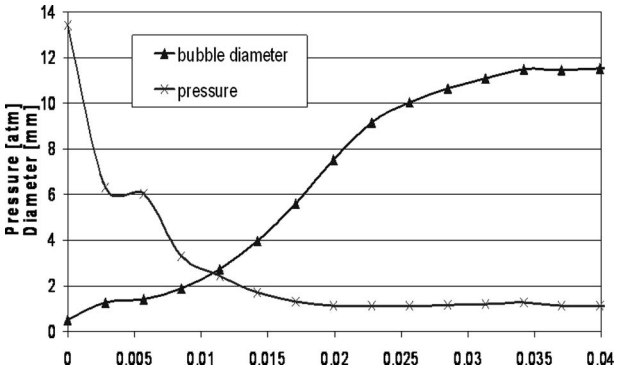

Fig. 4 Pressure and bubble diameter of a typical multiphase-droplet boiling

follows t_3. The focus of this study is on the boiling occurring up to t_3, the liquid-film collapse is an adverse effect that is preferably avoided. For this purpose a virtual time-point was defined at which boiling would complete (90%) following the nominal boiling rate (t_{fn}).

Initially the multiphase-droplet rises at around 15 cm/s. At the instance of pressure drop the vapor bubble expands. At the same time, the multiphase-droplet undergoes acceleration due to the instant pressure gradient (see Fig. 4). Initially the bubble accelerates faster than the droplet and attempts to "break away" from it; this can be seen in the second frame of Fig. 3. Surface tension pulls the bubble back in as the whole multiphase-droplet catches up with it. In the rise velocity graph oscillations at a frequency around 100 Hz are evident. These seem to be caused by the multiphase-droplet's dynamic response to pressure/buoyancy forces (acceleration) and then to the drag forces generated by its velocity increase (deceleration), repeatedly. Alternatively, these

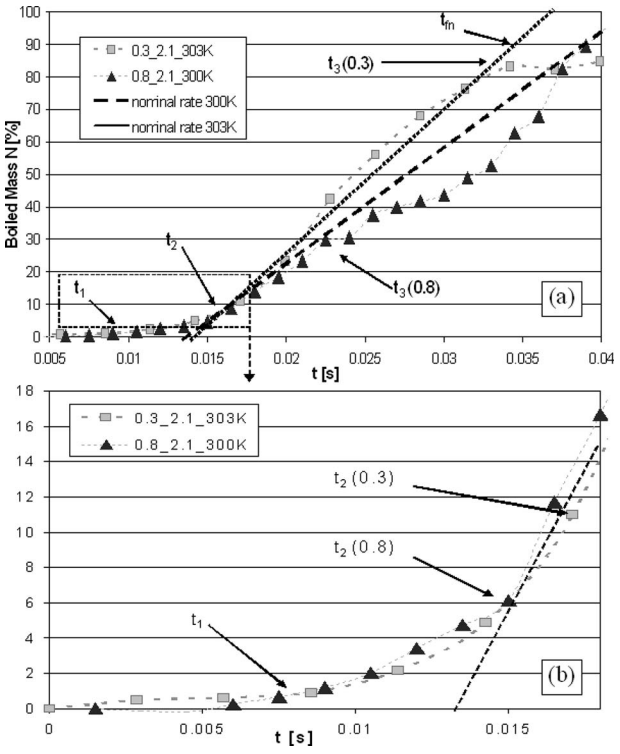

Fig. 5 The calculated boiled mass for a multiphase-droplet: with early collapse ($D_i = 0.8$ mm, $D_o = 2.1$ mm, at 300 K) and with late collapse ($D_i = 0.3$ mm, $D_o = 2.1$ mm, at 303 K)

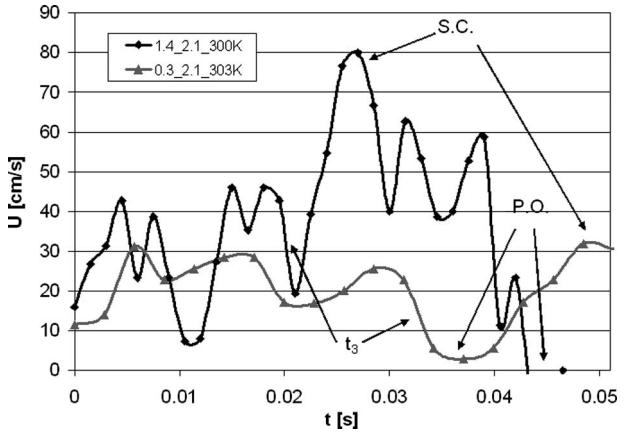

Fig. 6 The velocity measured for two different droplets: with a large and a small initial bubble (t_3—liquid-film collapse, S.C.—transition to spherical-cap shape, and P.O.—pressure overshoot)

drag oscillations are close to the theoretical vortex-shedding frequency and may be caused by it; this remains to be established. Other oscillations exist at a much lower frequency—around 40 Hz, these coincide with the pressure oscillations following the depressurization of the system (the first pressure overshoot is indicated in Fig. 6). Superimposing these frequencies dictate the bubble velocity. Additionally, bubble growth and velocity lead to conditions where spherical bubbles can no longer exist and there is transition to the new stable shape, either ellipsoid or spherical-cap. In Fig. 6 there appear to be two very different cases, one in which the initial bubble was large, leading to high accelerations and liquid-film collapse (t_3), while the other had a small initial bubble and the conditions were calmer; in this case the collapse was not evident during boiling.

4 Analysis

4.1 Analysis Method. In the analysis of the experimental data several assumptions were made.

1. Since the focus is on the rapid boiling (t_1–t_3), one-dimensional spherical configuration was assumed (see Fig. 2).
2. All heat transferred to the two-phase droplet is consumed by boiling (no heating of the vapor during the rapid boiling).
3. There is only thermal conduction through the liquid-film, as it is very thin during the rapid-boiling stage.
4. The penetration depth of the temperature drop into the liquid-film is at least an order of magnitude smaller than the droplet radius, therefore, the curvature may be neglected.
5. The thermal convection coefficient is the instantaneous value, averaged over the sphere. The correlation employed (Eq. (3)) is that of Battya et al. [17] for a boiling two-phase droplet at low superheat. This correlation was found to be suitable, as it is based on the experimental work of Song et al. [5], where, according to our understanding, the engulfed configuration existed. Furthermore, it gives reasonable values and incorporates the Jakob number, making it more suitable for the high-superheat range, as well

$$\mathrm{Nu} = 0.64\mathrm{Pe}^{0.5}\mathrm{Ja}^{-0.35} \tag{3}$$

6. Vapor pressure in the bubble is equal to the far field pressure during the boiling process. The bubble dynamics are reasonably slow—this assumption leads to a pressure error no larger than 2% according to the Rayleigh–Plesset equation.
7. It follows from assumption 6 that vapor temperature is roughly equal to the saturation temperature at the far field pressure. This assumption is generally acceptable for given boiling rates.
8. The depressurization rate is not a relevant factor, as only cases in which 90% of the pressure drop completed before significant boiling were considered (see Appendix A). This allowed gas expansion to be neglected in the analysis.
9. The temperature could not be measured at different locations, due to technical difficulties. However, the temperature can be closely estimated, as described in Sec. 4.2.
10. The two-phase droplet is taken as a growing solid sphere in all flow/drag analysis, due to being covered in a liquid-film throughout the majority of the boiling process.

4.2 Analysis. Initially, boiling relies entirely on the consumption of the liquid's increasing amount of superheat, due to the depressurization. This energy is brought to the boiling front in part by the conduction through the liquid-film and in part through the stretching of the liquid-film, leading to the exposure of a "new" superheated liquid (radial moving boundary). This would be represented by an additional "convective" term in the energy equation, and it is most significant in the initial stages as it is proportional to $1/R_b(t)$. As a first-order analysis this convection is not considered. During this stage the transient temperature profile in the liquid-film can be calculated according to the one-dimensional semi-infinite conduction equation (Eq. (4)).

$$\frac{T(x,t) - T_b(t)}{T_\infty - T_b(t)} = \mathrm{erf}\left(\frac{x}{2\sqrt{\alpha t}}\right) \tag{4}$$

When the temperature gradient reaches the outer interface (liquid-host interface) at the point in time designated t_1 in Fig. 5, convective heat transfer joins in raising the overall boiling rate. This is the instance when Eq. (4) equals 0.99 (first temperature drop). Beyond this point the semi-infinite assumption required by this equation is no longer valid.

$$\mathbb{R}_l(t) = \frac{1}{4\pi k}\left(\frac{1}{R_{\mathrm{lv}}(t)} - \frac{1}{R_{\mathrm{lh}}(t)}\right) \tag{5a}$$

$$\mathbb{R}_h(t) = \frac{1}{h4\pi R_{\mathrm{lh}}^2(t)} \tag{5b}$$

About 17 ms after initiation we reach the second critical time, designated t_2, at which the conduction thermal resistance reduces to the order of the convection resistance, $\mathbb{R}_l/\mathbb{R}_h \approx 2$, as defined in Eqs. (5*a*) and (5*b*). It is important to note that while t_1 and t_3 are specific points in time, t_2 has a physical meaning as the short period of time in which these thermal resistances are on the same scale. From this time on boiling is mostly convection controlled, and it is strongly influenced by the rise velocity. The overall thermal resistance is generally reduced, and t_2 is characterized by a significant increase in the boiling rate.

While the dominant thermal resistance is the conduction through the liquid-film, the boiling curve roughly coincides with the known universal solution for vapor bubble growth in a two-fluid system. As the liquid-film thins, thermal conduction resistance is reduced and convection resistance plays a more dominant role causing the departure from the universal solution and its negative second derivative (falling rate); this is shown in Fig. 7. This experimental deviation from the classical two-fluid theory, in cases of convection, has been observed by others even at low superheats (Fig. 1 of Ref. [18]).

As seen in Sec. 3, the rise velocity oscillates. The resulting accelerations directly affect the drag force, in other words, the drag oscillates, too. Recognizing that the drag creates shear, the main cause for liquid-film collapse, means that collapse will occur when the drag obtains a local maximum. When the liquid-film collapses (t_3 in Fig. 5), it is usually followed by a jump in rise

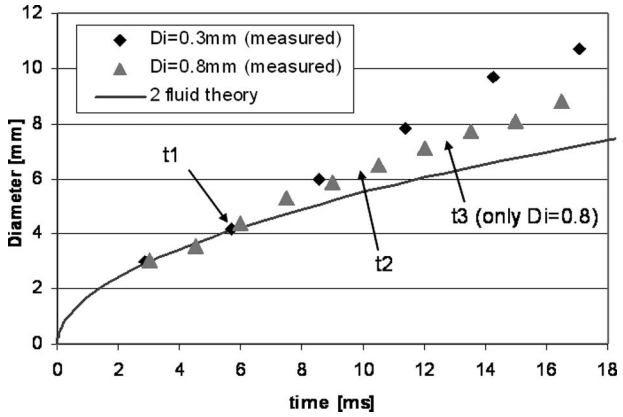

Fig. 7 Vapor bubble growth experiments versus the two-fluid system theory (due to initial delay, experiments' time shifted by 6 ms)

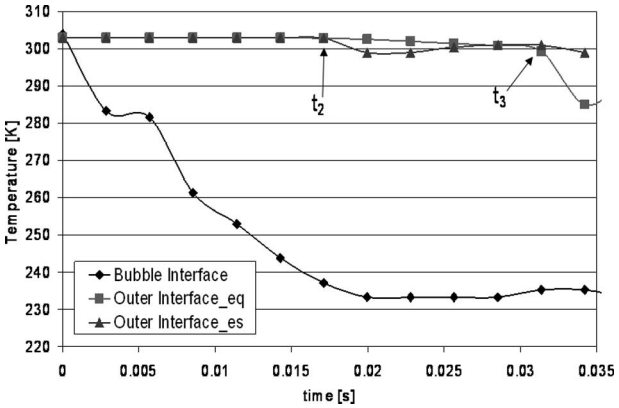

Fig. 8 The temperature evolution prediction at the boiling front and outer surfaces of the liquid-film (eq—interface equilibrium and es—energy summation)

velocity. This is due to the downward motion of the liquid causing an upward motion of the vapor. This in turn leads to further acceleration and transition to the spherical-cap shape. This collapse, although not visible, has been confirmed through numerous experiments in which a sudden cease in the rapid boiling has occurred. Accordingly, experiments with higher velocities and, consequently, shear, experienced earlier collapse. The collapse of such a liquid-film on a somewhat larger scale has been observed by Mori [14] under slower, nonboiling conditions. To properly predict such a film collapse the expression for the drag force needs to be found. Due to the Reynolds numbers considered (200–4000) vortex shedding needs to be taken into account, therefore, a more general approach was employed. Let us consider the momentum equation for a multiphase-droplet rising and boiling within a host liquid of greater density ($\rho_h > \rho_l$). Since the boiling liquid moves with the vapor bubble they are both considered a single entity with varying density. This means that their mass is constant (m_o) as no mass transfer occurs with the immiscible host liquid. In the most general form the equation of motion of this entity is

$$m_o \frac{dU}{dt} = -F_d + F_b - F_g - F_p \tag{6}$$

A simple scale analysis clarifies the fact that the buoyancy term ($F_b \approx \rho_l \times g \times V_b$) renders the gravity term (F_g) negligible very early in the boiling process (from around $R/R_o \approx 2$). Additionally, the local pressure gradient term (F_p) can be incorporated into the drag force term (F_d) to create a new total-drag-force term ($F_D{}^*$). The examination of the buoyancy term (F_b) reveals monotonous growth acting in the same direction as the rise velocity. As seen before, the velocities depicted in Fig. 6 show oscillations. This would require an oscillating total-drag-force term ($F_D{}^*$), as it is the only force than can vary significantly in value. The consideration of the total-drag-force term in numerous experiments shows that liquid-film collapse follows a local maximum of this term. Some additional scaling led to the definition of a nondimensional critical drag (D_c) given in Eq. (7). This critical drag functions as a criterion for the collapse of the liquid-film.

$$F_D{}^* \propto D_c = \left(-\frac{dU(t)}{dt}\frac{1}{g}\right)\left(\frac{R(t)}{W(t)}\right)\frac{10^{-3}}{(J_a^*)^4} \tag{7}$$

At t_3, the instant of liquid-film collapse, a D_c value of 100, applies to experiments over a wide range of initial conditions ($D_i = 0.3–2.3$ mm, $D_o = 2–2.7$ mm, $T_\infty = 294–316$ K, and $p_\infty = 1–3$ atm), within the time-shift error. Though this criterion is not easily predicted, it is readily measured for the monitoring of the boiling process. After the collapse the remaining liquid settles at the base of the bubble, reducing the heat transfer surface area and ending the rapid-boiling stage. The collapse usually leads to the transition to a spherical-cap shape. The remaining liquid later boils at a slower though increasing rate (concave line) that is characteristic of the spherical-cap shape.

4.3 Temperature Evolution. According to the assumptions made, the temperature at the bubble interface follows the saturation curve. On the other hand, the outer interface temperature (T_{lh}) does not reduce significantly, due to the high convection coefficient values. This temperature was calculated using two different methods: by assuming equilibrium on the outer interface and by summing up the droplet's energy. Beyond t_3 nonuniform temperature exists on the outer interface (partially engulfed configuration), and therefore, the prediction of T_{lh} is not relevant.

Based on the predicted temperature in the liquid-film shown in Fig. 8, and its instantaneous thickness, the superheat remaining within the liquid-film can roughly be estimated (linear temperature profile). Furthermore, assuming uniform ideal gas-vapor density within the bubble, the mass flux at any given moment can be evaluated; these are shown in Fig. 9.

During the depressurization there is an increase in superheat, i.e., superheating. In parallel there begins a consumption of this energy by the rapid boiling. Initially the boiling relies on the superheat alone, but around t_2 the heat transfer becomes significant and the mass flux reaches a maximum value of 0.6 $kg/s*m^2$. As the superheat is consumed by boiling, the mass flux reduces, in spite of high heat transfer. From this it can be understood that

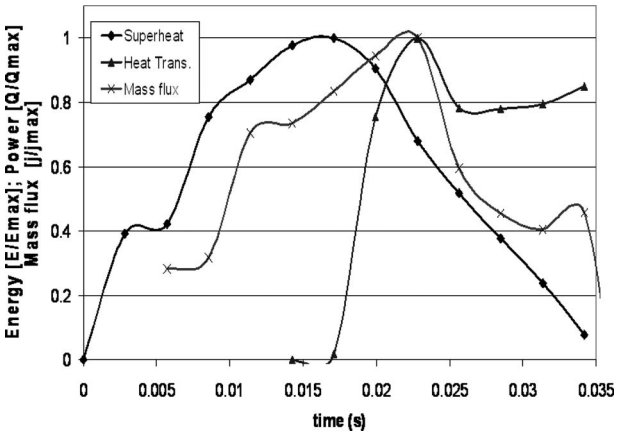

Fig. 9 The normalized form of the superheat, heat transfer, and the resulting mass flux

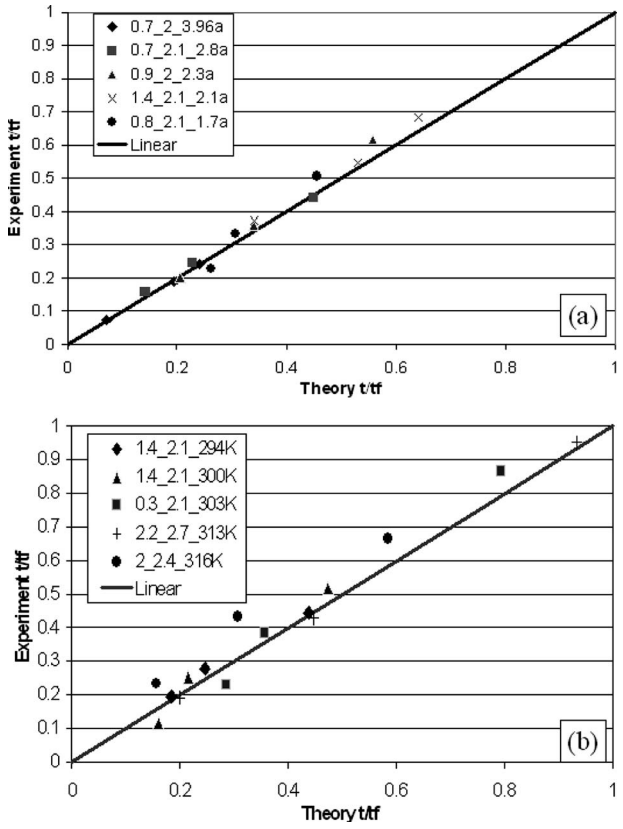

Fig. 10 The comparison of predicted critical times (t_1-t_2-t_3, accordingly) with observed ones: (*a*) ambient pressure variation $0.2<J_a^*<0.35$ and (*b*) ambient temperature variation $0.3<J_a^*<0.45$

high-superheat levels are needed to maintain high boiling rates, and that rapid boiling cannot exist due to heat transfer alone. Although the precision of the values in Figs. 8 and 9 is debatable, due to the inaccuracy in the simplified analysis model, the qualitative behavior is evident.

5 Discussion

The case of boiling of a multiphase-droplet within a third (host) immiscible liquid was considered experimentally, at high-superheat levels ($0.2<J_a^*<0.45$), for the first time. This led to the definition of rapid-boiling, a form of boiling completing (t_f) within several milliseconds. This form of boiling is orders of magnitude faster than low-superheat boiling, on the one hand, and calmer and slower than very-high-superheat explosive boiling (t_f <1 ms), on the other. In this form of boiling transient stages, such as the temperature-gradient development or the transient hydrodynamics (wake evolution, vortex shedding, and liquid-film collapse), define the boiling curve. Several of these transient-boiling stages were observed. Additionally, bubble growth rate is on the same scale as the cross-flow velocity and neither is negligible in the resulting flow field.

The emphasis of this study was to recognize the critical time-points (t_1, t_2, and t_3) between the stages and successfully predict them. The predictions are given in Eqs. (4), (5), and (7), accordingly. Comparison with experiments is shown in Fig. 10. From the figure it is clear that the simple analysis model employed predicts these time-points quite well. At higher J_a^* (Fig. 10(*a*)) there seems to be greater deviation. However, this is artificial and it is caused by the normalization of time-points by t_f that significantly decreases with the increase in superheat. Deviation is still on the order of estimated timescale error.

The sudden depressurization (tension) led to the immediate availability of superheat for boiling and significant "heat absorption" in later stages, resulting in a rapid boiling. This superheat is used to "fuel" the initial stages of boiling, prior to the external heat transfer (before t_1). In addition, it establishes high boiling rates by implementing and maintaining strong temperature gradients, by this means drawing substantial heat from the environment (250 kW/m^2, 30 W per droplet), especially during the convection heat transfer stage (after t_2).

After the convection stage, a sudden end to the rapid boiling was measured (at t_3). From the understanding of the multiphase-droplet configuration this detection of a sudden pause in boiling, usually accompanied by a leap in velocity, is believed to be due to the collapse of the liquid-film surrounding the bubble (drastic decrease in heat transfer surface). A novel liquid-film collapse criterion was defined in Eq. (7). From the consideration of Fig. 10 it is clear that this criterion always predicts collapse slightly before it occurs (t_3 is always above the theory line), thus enabling its avoidance.

These two opposing forces, heat transfer versus film collapse, determine the rate and final level of boiling obtained within the rapid stage. How they are dictated by the parameters of the system (boiling liquid, environmental temperature, background pressure, initial droplet size, and internal bubble nucleus size) is yet to be determined. Current research is aimed at developing an analytical/empirical model for this type of boiling—allowing the prediction of the boiling curve as a function of the initial conditions. This development may enable the heat transfer engineer to design a "tailored" boiling curve, choosing the location and the rate of boiling, for a specific application's requirements.

We believe that it is essential to study this new range of boiling further. Several questions have risen in the course of this study. There remains the question of the source of drag oscillations (believed to be vortex shedding), the time-scale of the transition to a spherical-cap shape, the effect of stretching on the temperature-gradient development, and other related transient effects. This form of boiling requires further study as it has a high potential for micro-/high speed applications, both in the fields of heat transfer and multiphase flow. It could be greatly beneficial to recognize, characterize, and realize such applications.

Acknowledgment

We would like to thank the staff at the Fine Rocket Propulsion Lab: Doron Harlev and Eliahu Ashkenazi, the lab engineers. We would also like to thank Prof. Arthur Shavit and Dr. Michael Shusser for their contribution to this research.

Nomenclature

c_p = specific heat (J/kg K)
D = droplet outer diameter (m)
D_c = critical drag collapse criterion—see Eq. (7)
h = thermal convection coefficient (W/m^2 K)
Ja = Jakob number—superheat number ($J_a=\rho_l c_{pl}\Delta T/\rho_v L$)
k = thermal conductivity (W/m K)
L = latent heat of vaporization (J/kg)
N = boiled mass (%)
Nu = Nusselt number—nondimensional thermal number ($Nu=hD/k$)
p = pressure (Pa)
Pe = Peclet number $Pe=Re\times Pr$
Pr = Prandtl number—ratio of diffusivities ($Pr=\mu/\rho\alpha$)
R = radius (m)
$\dot{R}$ = interface velocity $=dR/dt$(m/s)
$\mathbb{R}$ = thermal resistance (W/K)

Re = Reynolds number—nondimensional flow number (Re$=2\rho_h UR/\mu_h$)
t = time (s)
T = temperature (K)
ΔT = liquid superheat (K)
U = rise velocity (m/s)
V = volume (m^3)
W = liquid-film thickness (m)
x = Cartesian coordinate (m)

Greek Symbols

α = thermal diffusivity (m^2/s)
η = mass boiling fraction ($(kg_v - kg_{vi})/kg_{li}$)
θ = angle (measured from the rear of droplet)
μ = dynamic viscosity (kg/m s)
ρ = density (kg/m^3)
σ = surface tension (N/m)

Subscripts

b = gas-vapor bubble
h = host liquid
i = initial
lh = liquid-host interface
lv = liquid-vapor interface
l = droplet liquid
sat = saturation
v = vapor
∞ = far field

Appendix A

A.1 Choosing a Fast Depressurization Mechanism. For our experiment we expected rapid-boiling (order of milliseconds). Our goal was to obtain the true boiling rate based on boiling dynamics and not the quasisteady pressure-controlled boiling, as is often the case in the literature available, see experimental/theoretical works in Fig. 2.9 of the book by Brennen [19] or the theory/experiment comparisons of Ref. [20].

Therefore, a mechanism that provided the fastest possible rate of depressurization was required, with pressure drop completing before significant boiling occurred. Ball taps of different sizes on different size ports and a plug release were considered. Their depressurization rates are presented in Fig. 11, where a drop-time (90–10%) of 5 ms was attained with a 2 in. ball tap on a 1 in. port. From known depressurization rates of shock tubes, punctured diaphragms, and plug releases appearing in Ref. [21], the maximum attained drop-time, within the above pressure/temperature conditions, is about 3 ms. Therefore, the pressure drop rate attained with the current mechanism was acceptable, especially, considering the use of standard, reusable "off the shelf" parts.

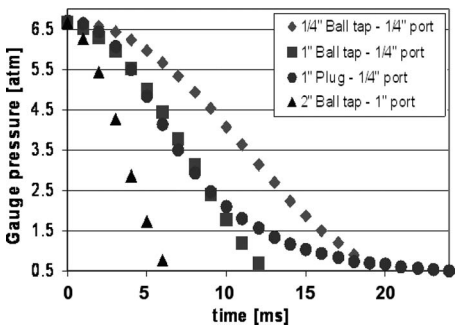

Fig. 11 The depressurization rate for different ball taps and a plug on different size ports

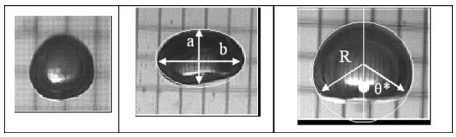

Fig. 12 Parameters of observed shapes of multiphase-droplets: sphere, ellipsoid, and truncate sphere (spherical-cap)

Appendix B

B.1 Shape Correction. During analysis, the distortion of the spherical droplet bubble was observed: ellipsoids and spherical-cap shapes were also analyzed. Ellipsoids appeared at lower J_a^* when boiling was slower and this intermediate shape was stable. The spherical-cap shape was usually observed in the latter stages of boiling at $J_a^* > 0.26$, it is closely approximated by a truncate sphere shape, as shown in Fig. 12.

The volume of these shapes was calculated using Eqs. (B1) and (B2).

The volume of an ellipsoid

$$V = \frac{\pi}{6} ab^2 \tag{B1}$$

The volume of a truncate sphere

$$V = \tfrac{2}{3}\pi R^3 \left(1 + \cos\,\theta^* + \tfrac{1}{2}\sin^2\,\theta^* \times \cos\,\theta^*\right) \tag{B2}$$

where θ^* is the cut-off angle of the sphere of radius R.

References

[1] Hewitt, H. C., and Parker, J. D., 1968, "Bubble Growth and Collapse in Liquid Nitrogen," ASME J. Heat Transfer, **90**, pp. 22–26.
[2] Shepherd, J. E., and Sturtevant, B., 1982, "Rapid Evaporation at the Superheat Limit," J. Fluid Mech., **121**, pp. 379–402.
[3] Frost, D. L., 1988, "Dynamics of Exploding Boiling of a Droplet," Phys. Fluids, **31**, pp. 2554–2561.
[4] Shusser, M., and Weihs, D., 1999, "Explosive Boiling of a Liquid Droplet," Int. J. Multiphase Flow, **25**, pp. 1561–1573.
[5] Sideman, S., and Taitel, Y., 1964, "Direct-Contact Heat Transfer With Change of Phase: Evaporation of Drops in an Immiscible Liquid Medium," Int. J. Heat Mass Transfer, **7**, pp. 1273–1289.
[6] Song, M., Steiff, A., and Weinspach, P. M., 1999, "Direct-Contact Heat Transfer With Change of Phase: A Population Balance Model," Chem. Eng. Sci., **54**, pp. 3861–3871.
[7] Oguz, H. N., and Sadhal, S. S., 1987, "Growth and Collapse of Translating Compound Multiphase Drops: Analysis of Fluid Mechanics and Heat Transfer," J. Fluid Mech., **179**, pp. 105–136.
[8] Kosky, P. G., 1968, "Bubble Growth Measurements in Uniformly Superheated Liquids," Numer. Eng. Sci., **23**, pp. 695–706.
[9] Boherer, T. H., 1973, "Bubble Growth in Highly Superheated Liquids," MS thesis, Chemical Engineering, Purdue University, West Lafayette, IN.
[10] Mikic, B. B., Rohsenow, W. M., and Griffith, P., 1970, "On Bubble Growth Rate," Int. J. Heat Mass Transfer, **13**, pp. 657–666.
[11] Prosperetti, A., and Plesset, M., 1978, "Vapor-Bubble Growth in a Superheated Liquid," J. Fluid Mech., **85**, pp. 349–368.
[12] Lee, H. S., and Merte, H., Jr., 1996, "Spherical Vapor Bubble Growth in Uniformly Superheated Liquids," Int. J. Heat Mass Transfer, **39**, pp. 2427–2447.
[13] Younglove, B. A., and Ely, J. F., 1987, "Thermophysical Properties of Fluids II. Methane, Propane, Isobutane and n-Butane," J. Phys. Chem. Ref. Data, **16**, pp. 670–685.
[14] Mori, Y. H., 1978, "Configuration of Gas-Liquid Two-Phase Bubbles in Immiscible Liquid Media," Int. J. Multiphase Flow, **4**, pp. 383–396.
[15] Johnson, E. R., and Sadhal, S. S., 1985, "Fluid Mechanics of Compound Multiphase Drops and Bubbles," Annu. Rev. Fluid Mech., **17**, pp. 289–320.
[16] Wiegand, G., and Franck, E. U., 1994, "Interfacial Tension Between Water and Non-Polar Fluids Up to 473 K and 2800 Bar," Ber. Bunsenges. Phys. Chem., **98**, pp. 809–817.
[17] Battya, P., Ragharan, V. R., and Seetharamu, K. N., 1984, "Parametric Studies on Direct Contact Evaporation of a Drop in an Immiscible Liquid," Int. J. Heat Mass Transfer, **27**, pp. 263–272.
[18] Ivashnev, O. E., and Smirnov, N. N., 2004, "Thermal Growth of a Vapor Bubble Moving in a Superheated Liquid," Fluid Dyn., **39**, pp. 414–428.
[19] Brennen, C. E., 1995, *Cavitation and Bubble Dynamics*, Oxford University Press, London.
[20] Jones, O. C., Jr., and Zuber, N., 1978, "Bubble Growth of Variable Pressure Fields," ASME J. Heat Transfer, **100**, pp. 453–459.
[21] Borkar, G. S., Lienhard, J. H., and Trela, M., 1977, "A Rapid Hot Water Depressurization Experiment," Report No. EPRI NP-527.

Flow Boiling of Coolant (HFE-7000) Inside Structured and Plain Wall Microchannels

C.-J. Kuo

Y. Peles[1]
e-mail: pelesy@rpi.edu

Department of Mechanical, Aerospace and Nuclear Engineering,
Rensselaer Polytechnic Institute,
Troy, NY 12180

Flow boiling was experimentally studied using coolant HFE-7000 for two types of parallel microchannels: a plain-wall microchannel and a microchannel with structured reentrant cavities on the side walls. Flow morphologies, boiling inceptions, heat transfer coefficients, and critical heat fluxes were obtained and studied for mass fluxes ranging from $G=164$ kg/m^2 s to $G=3025$ kg/m^2 s and mass qualities (energy definition) ranging from $x=-0.25$ to $x=1$. Comparisons of the performance of the enhanced and plain-wall microchannels were carried out. It was found that reentrant cavities were effective in reducing the superheat at the onset of nucleate boiling and increasing the heat transfer coefficient. However, they did not seem to increase the critical heat flux.
[DOI: 10.1115/1.3220674]

Keywords: flow boiling, subcooled boiling, nucleate boiling heat transfer, critical heat flux, MEMS, microchannel

1 Introduction

Flow boiling is associated with a very high heat transfer coefficient and has been extensively studied for numerous cooling applications in conventional scale system [1–8]. Because of the continuous advances in electronic technology and the corresponding power density increase, flow boiling in microdomains has been a topic of great interest in the last decade [9–16]. Key engineering parameters that are typically examined include onset of nucleate boiling (ONB), heat transfer coefficient, critical heat flux (CHF) conditions, flow patterns, and flow instabilities.

In conventional scale, structured reentrant cavities have been effective in reducing ONB, increasing heat transfer coefficient, and increasing CHF [17,18]. Several studies have been conducted to examine the performance of the reentrant cavity at the microscale [14,15,19–24]. Koşar et al. [14] and Kuo and Peles [15] studied the thermal performance and flow boiling patterns in reentrant-cavity microchannel using water. They argued that reentrant cavities can promote bubble nucleation in microchannels, and thus, enhance heat transfer. Kuo and Peles [25,26] conducted studies of flow boiling instability of water in microchannels, and Bhavnani and co-workers [22–24] conducted similar experiments with dielectric fluid FC-72. Their results suggest that flow boiling instability can be mitigated by forming structured reentrant cavities in the channel wall and suppressing the frequently cited rapid bubble growth, which in turn increased CHF value. Certain flow conditions and fluid properties, such as surface tension and mass flux have also been shown to affect bubble nucleation in both macro- and microscale channels [27–31].

The current paper presents a study of flow boiling using coolant HFE-7000 through an array of five parallel microchannels in two types of devices: one with reentrant cavities on the side walls and another with plain side walls. Flow boiling was recorded for both subcooled and saturated boiling for mass quality $-0.25<x<1$, mass flux ranging from $G=164$ kg/m^2 s to $G=3025$ kg/m^2 s, and heat flux up to 150.4 W/cm^2. Flow patterns, boiling inception, heat transfer coefficient, and CHF were obtained and studied. Comparison between the two microchannel devices are presented and discussed.

2 Device Overview

The microchannel device consists of five parallel microchannels, which are 10,000 μm long, 200 μm wide, and 250 μm deep, spaced 200 μm apart. For the reentrant-cavity microchannel, each sidewall encompasses an array of reentrant cavities spaced 100 μm apart (100 cavities on each side of the 10,000 μm long microchannel). An acute angle connects the 7.5 μm mouth to the 50 μm inside diameter reentrant body. A scanning electron microscope (SEM) image of the reentrant cavities is shown in Fig. 1(*a*). In order to minimize ambient heat losses, air gaps were formed on the two ends of the side walls, and inlet and exit plenums were etched on the thin silicon substrate ($\sim$150 μm). On the top, a Pyrex substrate sealed the device and allowed flow visualization. Figure 1(*b*) depicts a CAD model of the heater and thermistors on the backside of the device. For local temperature measurement, three thermistors, which are 10 μm wide and 300 μm long (Fig. 1(*c*)), were located 3400 μm, 6700 μm, and 10,000 μm downstream the channel inlet together with electrical connecting vias. On top of the thermistor layers, a 1 μm silicon oxide layer was deposited for electrical insulation. A heater was then formed on top of the oxide layer to deliver the heating power to the microchannels.

3 Device Fabrication, Experimental Apparatus, and Procedures

3.1 Microchannel Fabrication Method. The microelectromechanical system (MEMS) devices were micromachined on a polished double-sided *n*-type ⟨100⟩ single crystal silicon wafer employing techniques adapted from integrated circuit (IC) manufacturing. A 1 μm thick high-quality oxide film was deposited on both sides of the silicon wafer to shield the bare wafer surface during processing and to serve as an electrical insulator. A layer of 150 Å thick titanium was deposited by a CVC 601 sputter deposition system and patterned on the backside of the wafer to form the thermistors. Electrical connectors of 0.2 μm aluminum containing 1% silicon and 4% copper were subsequently formed in order to create electrical connections to the thermistors. Follow-

[1]Corresponding author.

Contributed by the Heat Transfer Division of ASME for publication in the JOURNAL OF HEAT TRANSFER. Manuscript received November 13, 2008; final manuscript received May 19, 2009; published online October 15, 2009.

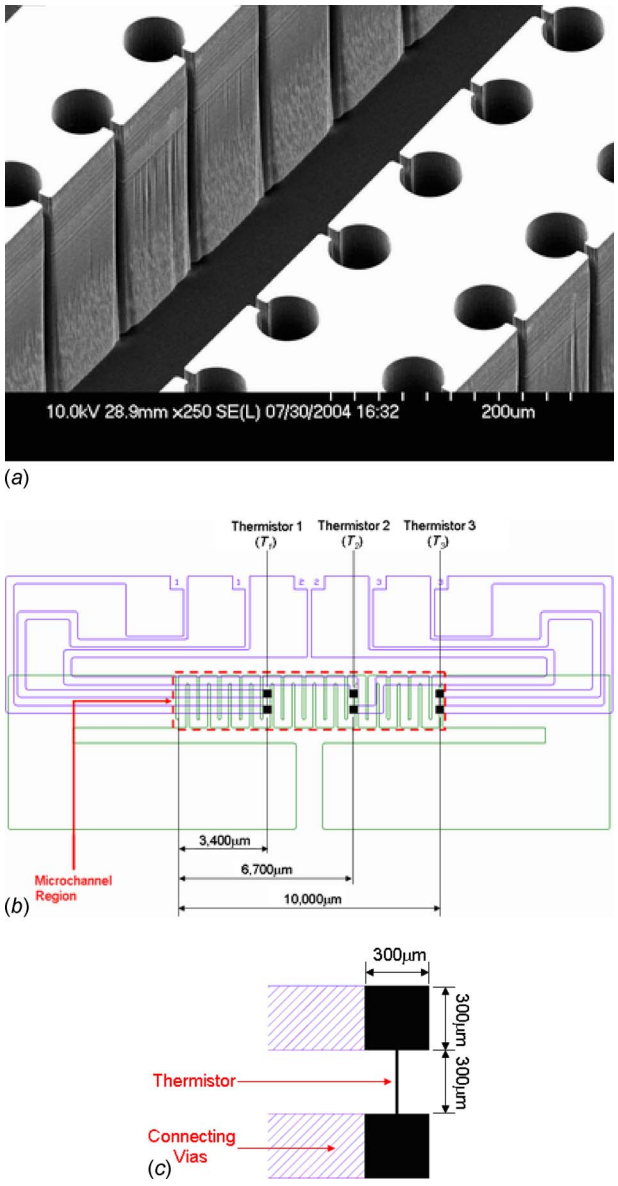

Fig. 1 (*a*) **A SEM image of the reentrant cavities,** (*b*) **a CAD model of the heater and the thermistors on the backside of the microdevice, and** (*c*) **a CAD model of a single thermistor**

ing, a 1 μm thick plasma enhanced chemical vapor deposition (PECVD) oxide was deposited to insulate the thermistors and vias from the lower layer. The heater was then formed on top of the oxide layer by CVC sputtering deposition. A 70 Å thick layer of titanium was initially deposited to enhance adhesion characteristics and was followed by sputtering a 1 μm thick layer of Al-1%Si-4%Cu. Subsequent photolithography and concomitant wet bench processing created the heater on the backside of the wafer. Another 1 μm thick PECVD oxide was deposited to protect the back side features during further processing.

Next, the microchannels were formed on the top side of the wafer. The reentrant cavities on the channel wall were also created through the same step. The wafer was taken through a photolithography step and a reactive ion etching (RIE) oxide removal process to mask certain areas on the wafer, which were not to be etched during the deep reactive ion etching (DRIE) process. The wafer was consequently etched in a DRIE process, and silicon was removed from places not protected by the photoresist/oxide mask. The 2D structure of microchannels and reentrant cavities was then formed. The DRIE process formed deep vertical trenches on the silicon wafer with a characteristic scalloped sidewall possessing a peak-to-peak roughness of ~0.3 μm. A profilometer and SEM were employed to measure and record various dimensions of the device.

The wafer was flipped, and the backside was then processed to create an inlet, outlet, side air gap, and pressure port taps for the transducers. A photolithography step, followed by a buffered oxide etch (BOE) (6:1) oxide removal process, was carried out to create a pattern mask. The wafer was then etched-through in a DRIE process to create the fluidic ports. Thereafter, electrical contacts/pads were opened on the backside of the wafer by performing another round of photolithography and RIE processing. Finally, the processed wafer was stripped of any remaining resist or oxide layers and anodically bonded to a 1 mm thick polished Pyrex (glass) wafer to form a sealed device. After successful completion of the bonding process, the processed stack was diesawed to separate the devices from the parent wafer.

The MEMS device was packaged by sandwiching it between two plates. The fluidic seals were forged using miniature "*o*-rings," while the external electrical connections to the thermistors and the heater were achieved from beneath through spring-loaded pins, which connected the thermistors and the heater to electrical pads residing away from the main microchannel body.

3.2 Experimental Test Rig. The setup, as shown in Fig. 2, consists of three primary subsystems: the flow loop section, instrumentation, and a data acquisition system. The test section houses the MEMS microchannel devices and its fluidic and thermal packaging module. The microchannel device is mounted on the fluidic packaging module through *o*-rings to ensure a complete leak-free system. The fluidic packaging delivers the working fluid and access to the pressure transducers. The heater, which is fabricated on the device backside, is wired (through electric pads) to the power supply. The thermistors are also connected to a National Instruments SCXI-1000 series data acquisition system.

The main flow loop includes the microchannel device, a pulseless gear pump, a reservoir, which consists of a deaerator unit and a heating element to control the inlet temperature, and a flow meter. The test section heater is connected to a power supply with an adjustable dc current to provide power to the device. The thermistors output signals are recorded by the data acquisition system. Simultaneously, the inlet pressure and test section pressure drop are collected, and the boiling process in the microchannels is recorded by a Phantom V4.2 high-speed camera (maximum frame rate of 90,000 frames/s, and 2 μs exposure time) mounted over a Leica DMLM microscope. Calibration of the thermistors is performed prior to the experiment by placing the device in an oven and establishing the resistance-temperature curve for each individual sensor.

3.3 Experimental Procedures and Data Reduction. The coolant HFE-7000 was first degassed at atmospheric pressure (T_{sat}=34°C) for at least 24 h. Then, the system was pressurized by helium to p=143 kPa (T_{sat}=45°C). The liquid flow rate was fixed at desired values, and experiments were conducted after steady thermal-hydraulic conditions were reached. The electrical resistances of the thermistors were also measured at room temperature. During the experiment, voltage was applied in 0.5 V increments to the test section heater, and the resistance data for the heater and the thermistors were recorded once steady thermal-hydraulic state was reached, at which the liquid flow rate, heat input, and resistance data remained constant. Flow visualization was also performed through the experiment. Flow morphologies, boiling inception, flow instability, and critical heat flux were recorded. The heat flux was then decrease in 0.5 V decrements, and the heat input, thermistor resistance, and flow morphologies were once again recorded. The procedure was repeated for different flow rates.

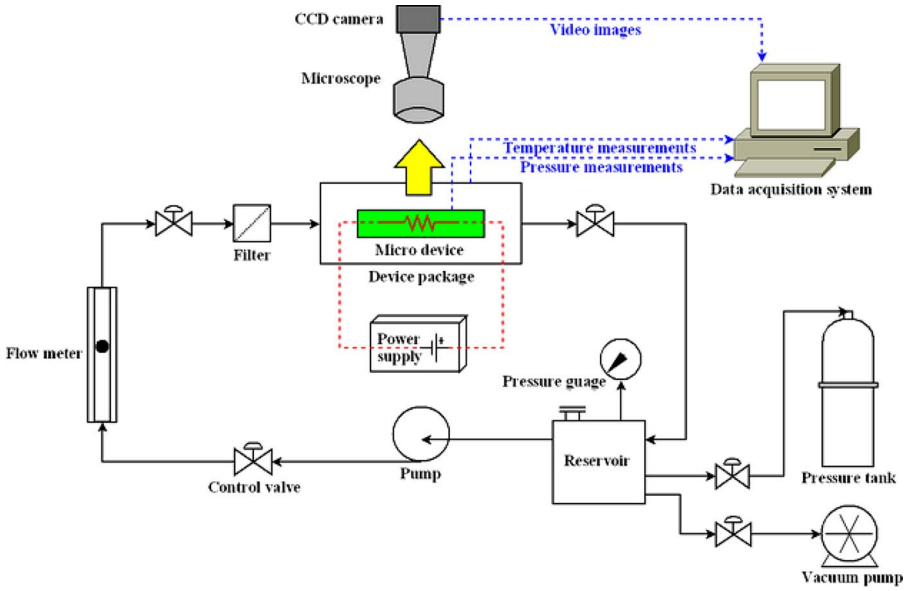

Fig. 2 Experiment setup

To estimate heat losses, electrical power was applied to the test section after evacuating the coolant from the test loop. Once the temperature of the test section became steady, the temperature difference between the ambient and test section was recorded with the corresponding power. The plot of power versus temperature difference was used to calculate the heat loss ($\dot{Q}_{\text{loss}}$) associated with each experimental data point. The average heat loss was estimated to be about 8%.

Data obtained from the voltage, current, and pressure measurements were used to calculate the average single- and two-phase temperatures and the heat transfer coefficients. The electrical input power P and heater resistance R were determined by the measured voltage V and current I, respectively, with

$$P = V \times I \tag{1}$$

and

$$R = V/I \tag{2}$$

The electrical resistance-temperature calibration curves of the thermistors were used for determining the thermistor temperature for each local position $T_{\text{thermistor}}$. The local surface temperature (T_1, T_2, T_3) at the base of the microchannels was then calculated as

$$T_1, T_2, T_3 = T_{\text{thermistor}} - \frac{(P - \dot{Q}_{\text{loss}}) \cdot t}{k_s A_p} \tag{3}$$

where t, k_s, and A_p are the substrate thickness, thermal conductivity of silicon, and the platform area, respectively.

Applying fin analysis, the overall fin efficiency is defined as

$$\eta_o = \frac{5\eta_f A_f + (A_t - 5A_f)}{A_t} \tag{4}$$

where $\eta_f = \tanh(mH)/mH$, $m = \sqrt{h2(L_0 + W)/k_s W L_0}$, $A_f = 2HL_0$, $A_t = 5L_0(W + 2H)$, and L_0, W, H, and k_s are the channel length, width, height, and substrate conductivity, respectively.

The overall fin efficiency was iteratively estimated through Eq. (4) to be equal or larger than 95%. Thus, the effective heat flux q''_{eff} and the channel wall heat flux q''_{ch} were defined as

$$q''_{\text{eff}} = \frac{P - \dot{Q}_{\text{loss}}}{A_p} \tag{5}$$

$$q''_{\text{ch}} = \frac{P - \dot{Q}_{\text{loss}}}{A_t} \tag{6}$$

where A_t is the total channel surface area. The local mass quality at a distance L from the inlet is obtained by

$$x = \frac{(P - \dot{Q}_{\text{loss}})(L/L_0) - GA_s c_p (T_{\text{sat}} - T_{\text{in}})}{GA_s h_{fg}} \tag{7}$$

where G, A_s, c_p, and h_{fg} are the mass flux, total channel cross section area, specific heat, and latent heat of vaporization, respectively. The thermodynamic quality x is defined using energy balance. The negative value of x corresponds to situations where the heat transfer into the flow is less than what it takes to warm up the entire liquid flow to saturation temperature. These situations still allow inception of nucleate boiling flow regimes. The negative values of thermodynamic quality x should not be confused with the true vapor quality X (define as ratio of cross-sectional vapor mass flow rate to total mass flow rate) that is often used in the two-phase literature.

Local heat transfer coefficient h can be obtained through the local surface temperature T, the mean liquid temperature T_l, and q''_{ch} according to

$$h = \frac{q''_{\text{ch}}}{T - T_l} \tag{8}$$

where T_l is obtained by energy balance. To evaluate the heat transfer during the flow boiling process, the two-phase heat transfer coefficient h_{tp} is also defined

$$h_{tp} = \frac{q''_{\text{ch}}}{T - T_{\text{sat}}} \tag{9}$$

Finally, the mean absolute error (MAE) is used to compare the experimental results with correlations according to the following expression

$$\text{MAE} = \frac{1}{M} \sum_{i=1}^{i=M} \frac{|U_{\text{exp}} - U_{\text{theo}}|}{U_{\text{exp}}} \times 100\% \tag{10}$$

where U and M are the parameter under investigation and number of samples, respectively.

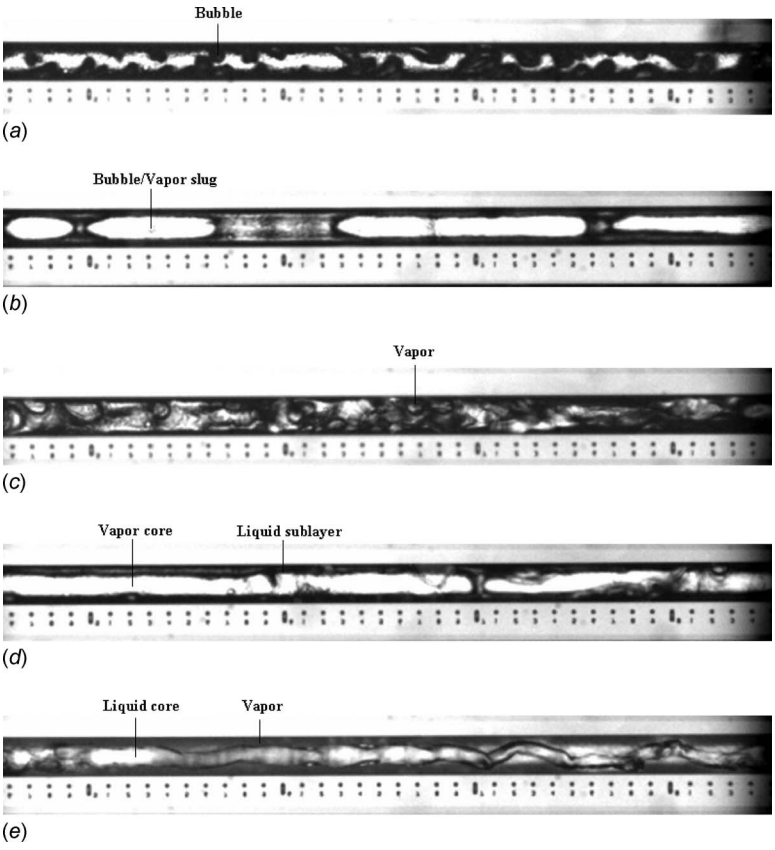

Fig. 3 Flow morphologies: (*a*) bubbly flow for $G=1615$ kg/m^2 s, $q''_{eff}=65.8$ W/cm^2, and $x=-0.08$; (*b*) oscillating single-phase liquid/single bubble/slug tail for $G=303$ kg/m^2 s, $q''_{eff}=11.9$ W/cm^2, and $x=-0.08$; (*c*) churn flow for $G=303$ kg/m^2 s, $q''_{eff}=34.4$ W/cm^2, and $x=0.23$; (*d*) wispy annular flow for $G=303$ kg/m^2 s, $q''_{eff}=38.9$ W/cm^2, and $x=0.28$; (*e*) inverted annular flow for $G=303$ kg/m^2 s, $q''_{eff}=53.0$ W/cm^2, and $x=0.75$.

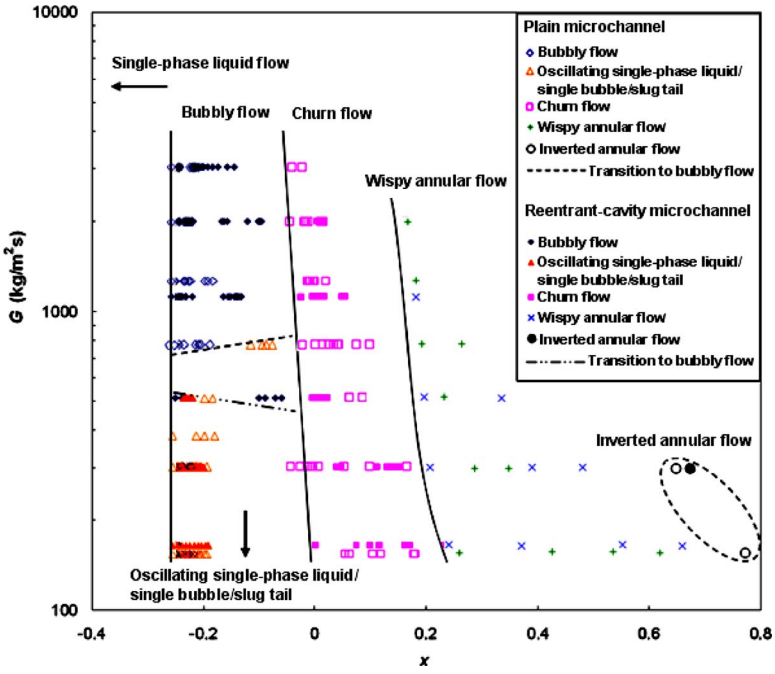

Fig. 4 Flow map for $G=154-3025$ kg/m^2 s

3.4 Uncertainty Analysis. The uncertainties of the measured values are obtained from the manufacturers' specification sheets, while the uncertainties of the derived parameters are calculated using the method developed by Kline and McClintock [32]. Uncertainty in the mass flux (G), total heat flux (q''), temperature (T), mass quality (x), and heat transfer coefficient (h) are estimated to be ±3%, ±1%, ±1°C, ±3%, and ±9%, respectively. Considering that the heat losses in this study are estimated (see Sec. 3.3) to be about 8%, the uncertainty in q''_{eff} or q''_{ch} is estimated as ±4%.

4 Results and Discussion

4.1 Flow Morphologies. Flow patterns similar to conventional scale channel (except for the oscillating single-phase liquid/single bubble/slug tail discussed below) were observed for the plain microchannels and the microchannels with reentrant cavities: single-phase liquid flow, bubbly flow (Fig. 3(*a*)), oscillating single-phase liquid/single bubble/slug tail (Fig. 3(*b*)), churn flow (Fig. 3(*c*)), wispy annular flow (Fig. 3(*d*)), and inverted annular flow (Fig. 3(*e*)). A flow map (Fig. 4) is also presented to identify the relationship between flow patterns and mass flux/mass quality for both microchannels. At low mass fluxes, oscillating single-phase liquid/single bubble/slug tail was noticeable immediately following boiling inception, where a single bubble grew rapidly, formed a vapor slug, which occupied the entire microchannel cross section, and expanded both downstream and upstream. The vapor slug then traveled downstream and the microchannel was temporally occupied by liquid. This type of intermitted flow boiling characteristic is often termed as rapid bubble growth in some studies, and is an important flow boiling instability mode in microchannels [25]. The rapid bubble growth flow pattern appeared in both plain and enhanced microchannels for low mass fluxes. However, it extended to higher mass flux in the plain microchannel ($G \leq 514$ kg/m^2 s for structured surface microchannels and $G \leq 779$ kg/m^2 s for plain microchannels). For higher mass flux, during subcooled flow boiling, a much less violent bubble formation was observed with small bubbles departing from the wall, forming a bubbly flow. In this regime, a more uniform bubble nucleation process was generally observed for the microchannels with reentrant cavities. For both types of microchannels, during the transition to saturated flow boiling, a churn flow pattern was also observed. For low mass fluxes, flow oscillation ceased to exist with the transition to churn flow at higher mass qualities. This suggested that flow oscillation in microchannels for low surface tension fluid is not as violent as for water and is not necessarily associated with premature CHF conditions (see Sec. 4.3). Wispy annular flow patterns prevailed as the mass quality further increased. When the thermal-hydraulic condition approaches CHF, inverted annular flow was observed for low mass fluxes (G

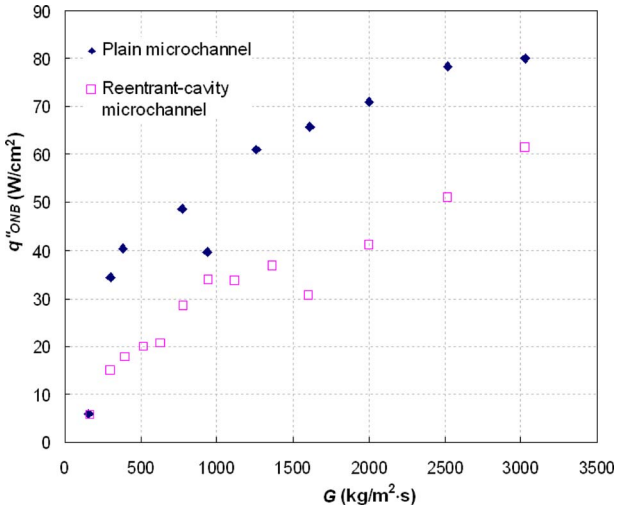

Fig. 5 Effective heat flux at ONB for different mass fluxes

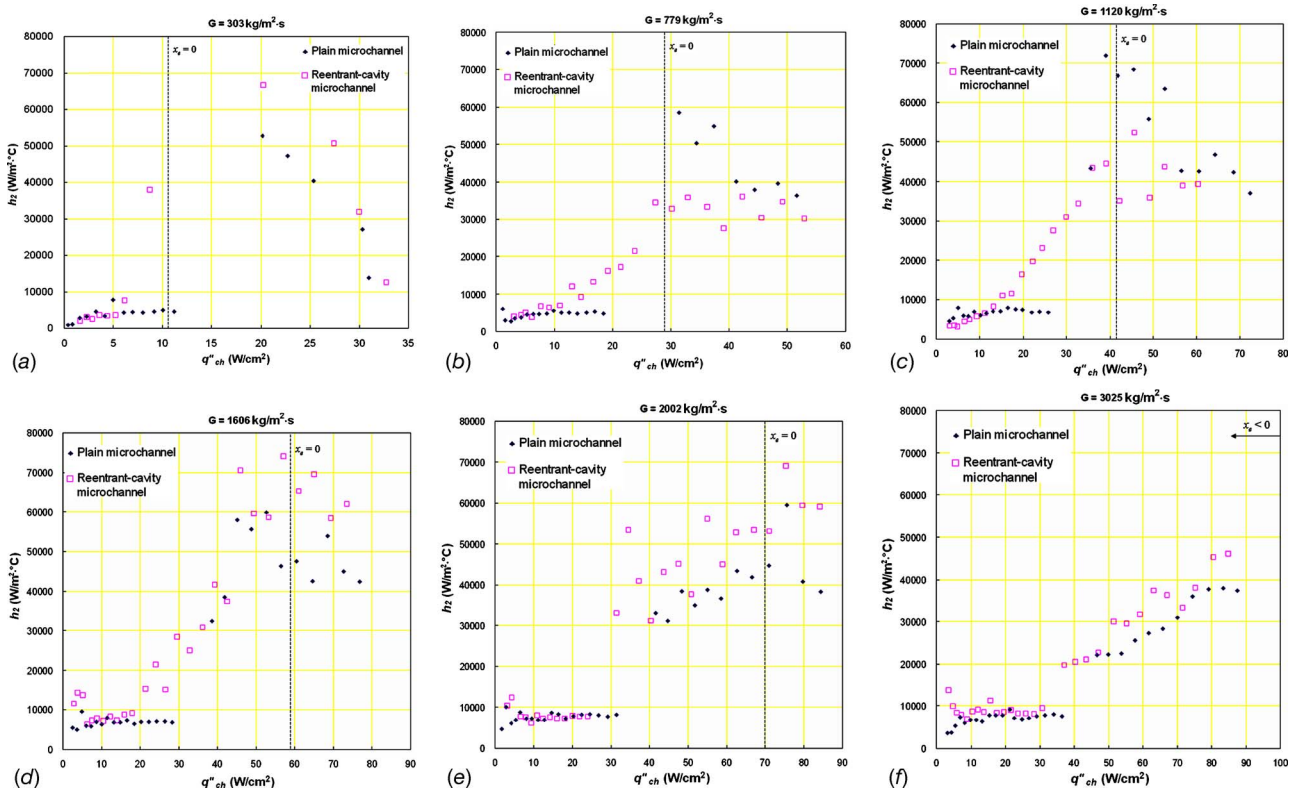

Fig. 6 Heat transfer coefficient as a function of channel heat flux for different mass fluxes

≤ 389 kg/m^2 s) for both microchannels, which was characterized by a liquid core surrounded by vapor sublayers. However, while the heat transfer coefficient decreased, the surface temperature was steady and did not indicate CHF. It appears that very thin liquid layers were presented adjacent to channel walls. The increase in surface temperature indicates that some dry spots started to form on the channel walls. It also appears that the liquid core was adjacent to the insolated top Pyrex surface, which suggests that the void fraction was significantly higher than it appears on Fig. 3(*e*) as indicated by high vapor mass quality (Fig. 4). CHF was observed in close proximity to the inverted annular flow.

Figure 5 shows the heat flux at ONB as a function of mass flux for both types of microchannels. Significant lower heat flux at boiling inception was observed for the microchannels with reentrant cavities. These results are consistent with existing studies for flow boiling in macroscale channels [17,18]. Likewise, a study performed by the current authors on similar device using water [15] showed the same trend (i.e., reentrant cavities provided much lower heat flux at ONB). It was suggested that the reentrant cavities are very effective in triggering boiling at much lower superheated surface temperatures than plain channels. As a result, the microchannels with reentrant cavities had a longer and more stable subcooled boiling region.

4.2 Heat Transfer Coefficient. The local heat transfer coefficient as a function of channel heat flux for both microchannels is shown in Fig. 6. Note that the heat transfer coefficient h is defined based on the wall to mean liquid temperature difference

$$h = q''/(T - T_l) = \begin{cases} q''/(\Delta T_{\text{sat}} + \Delta T_{\text{sub}}) & \text{for } T_l < T_{\text{sat}} (x < 0) \\ q''/\Delta T_{\text{sat}} & \text{for } T_l = T_{\text{sat}} (x \geq 0) \end{cases} \tag{11}$$

Low heat transfer coefficients ($h < 10{,}000$ W/m^2 k) were observed for single-phase flow. Suppression of boiling inception (temperature overshoot) is apparent for the plain microchannels, as discussed in Sec. 4.1, which is shown by an extended single-phase region. For mass fluxes below 1120 kg/m^2 s, as the channel heat flux increased, a sudden increase in the heat transfer coefficient for the plain microchannels was detected, accompanied with boiling inception at local mass quality of $x \sim 0$. For this device, subcooled flow boiling merely existed for $G \leq 779$ kg/m^2 s. As indicated in Sec. 4.1, rapid bubble growth was observed for low mass fluxes especially in the plain channel as a result of high superheat temperature. It was argued by Kuo and Peles [33] that in microchannels, the heat transfer enhancement during nucleate boiling was associated with vigorous flow agitation of the bulk laminar liquid flow caused by the bubble formation and motion. For plain microchannels, at the stage where bubble grew hastily and form slug or annular flow downstream, the sudden liquid mixing caused by the rapid bubble growth enhanced the heat transfer coefficient significantly. However, this enhancement is rarely manageable as it often associated with flow instability. For mass fluxes higher than 1606 kg/m^2 s, significant enhancements of heat transfer coefficient were observed (–30%) for the reentrant-cavity microchannel compared with the plain microchannel. This result is in agreement with the previous study of Kuo and Peles on water boiling flow in similar microchannels [15], in which the heat transfer coefficient was enhanced by up to 30% for reentrant-cavity microchannel compared with plain microchannel for high mass fluxes ($G \geq 303$ kg/m^2 s for water). The enhanced heat transfer coefficient was a result of a more consistent and uniform distribution of bubbles for high mass flux.

As the channel heat flux further increased ($x > 0$), a transition to churn flow, and later to wispy annular flow patterns, was observed, as indicated in Sec. 4.1, and convective boiling began to prevail. With the transition to saturated flow boiling and the corresponding flow pattern transition, bubble nucleation gradually diminished and the reentrant cavities ceased to be active; under these conditions, the reentrant-cavity microchannel did not seem to perform better than the plain microchannel. This was especially significant for high mass qualities, as shown in Figs. 6(*a*)–6(*c*). The result concurs with flow visualization, where the flow patterns for both channels showed good agreement.

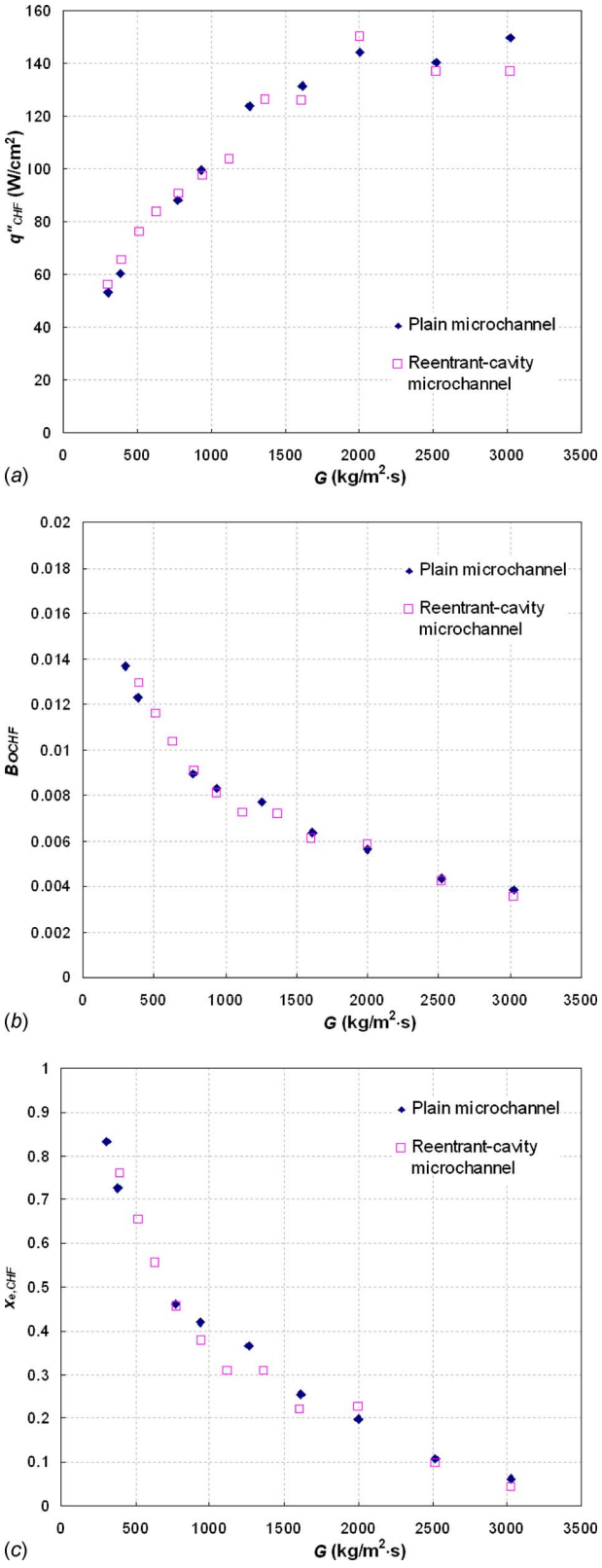

Fig. 7 (*a*) q''_{CHF}, (*b*) Bo_{CHF}, and (*c*) $x_{e,CHF}$ as a function of mass flux

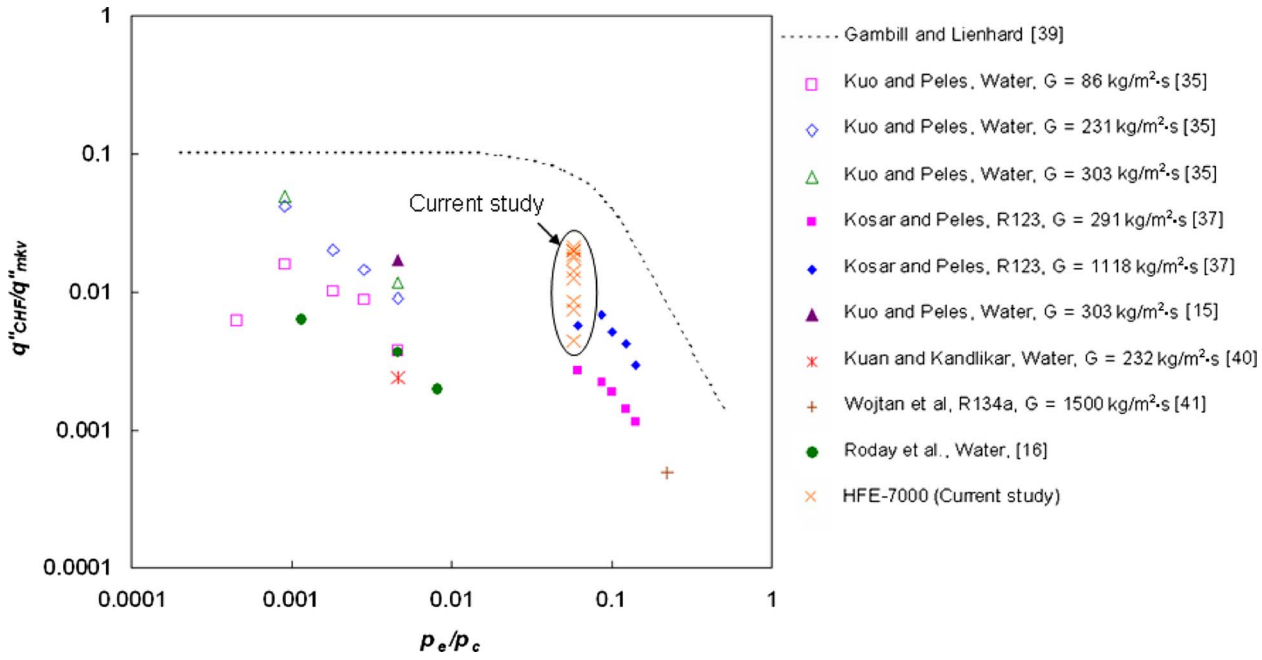

Fig. 8 The ratio of the highest measured critical heat flux to the maximum heat flux from the kinetic theory q''_{CHF}/q''_{mkv} as a function of dimensionless exit pressure p_e/p_c

4.3 Critical Heat Flux. In conventional scale, the CHF condition is primarily a function of mass flux (G), exit quality (x_e), system pressure (p), channel hydraulic diameter (d_h), channel length (L), and fluid properties [34]. The dependency of q''_{CHF} on mass flux and channel exit quality are examined here. Figure 7(a) shows q''_{CHF} as a function of mass flux for both types of microchannels. Very similar values of q''_{CHF} were observed for the plain microchannels and the channels with reentrant cavities. As indicated in Sec. 4.1, the annular and inverted annular flow patterns at the channel exit and the relatively high exit quality at CHF conditions, suggests that CHF is triggered by liquid dryout. Without the premature CHF caused by boiling instability, the heat transfer mechanisms are similar for both microchannels at conditions immediately prior to dryout, and, thus, the CHF values are similar. Note that for the low mass fluxes, the CHF was not affected by the rapid bubble growth flow pattern at low mass qualities. This somewhat contradicts early studies [25,35], which indicated that flow oscillation can trigger premature CHF. It appeared that the rapid bubble growth observed at low qualities and low mass fluxes is not sufficiently violent to trigger premature CHF. Once the mass quality increases beyond a certain threshold ($x \geq 0$), flow oscillations are suppressed and are no longer detrimental factors controlling CHF.

It is also shown in Fig. 7(a) that CHF increases with mass flux for both microchannels. The functional dependency of CHF and mass flux can be reduced to

$$q''_{CHF} = 3.03 \times G^{0.5} \tag{12}$$

with a MAE of 8.5%. Boiling number at CHF condition (Bo_{CHF}) were also obtained. Kuo and Peles [35] suggested that the Bo_{CHF} is constant for water in plain microchannels, while in the current investigation, Bo_{CHF} decreased with mass flux (Fig. 7(b)).

It has been argued that for dryout mechanism, the exit quality at CHF conditions ($x_{e,CHF}$) decreases with increasing mass flux [36,37]. The reduction in $x_{e,CHF}$ at high mass fluxes for dryout mechanism is suggested to be a result of increased droplet entrainment in the vapor core depleting liquid from the wall [36] or interfacial wave instabilities induced by shear or surface tension forces [38]. Figure 7(c) shows $x_{e,CHF}$ as a function of mass flux for both microchannel devices. Significant reduction in exit qualities with increasing mass flux can be observed for flow boiling of HFE-7000. The results concur with the data of Koşar and Peles [37] for R123 in 223 μm hydraulic diameter microchannels. However, they conflict with the data of Kuo and Peles [35] for water flow boiling in plain microchannels, which suggested CHF to be independent of mass quality. The contradicting conclusion may be a result of considerably smaller surface tension of coolant such as HFE-7000 and R123 than water. Considering the surface tension to be an important variable determining the liquid entrainment and the interfacial waves, the droplet and interface wave formations for HFE-7000 are very different from water.

Gambill and Lienhard [39] proposed that a practical limitation of the maximum heat flux exists for boiling. They suggested that the maximum achievable CHF for $p_e/p_c < 0.01$ is 10% of the maximum heat flux calculated from the kinetic theory. Figure 8 shows the ratio of the critical heat flux to the maximum heat flux from the kinetic theory q''_{CHF}/q''_{mkv} as a function of dimensionless exit pressure p_e/p_c. Results from several previous studies for CHF in microchannels using water and different coolants are also presented [15,16,35,37,40,41]. The CHF data of the present study are much lower than Gambill and Lienhard's limitation, which might suggest that the CHF in microchannels are fundamentally lower than in conventional scale channel. However, in the current study, a maximum q''_{CHF}/q''_{mkv} value of 0.02 was obtained for $p_e/p_c \cong 0.058$ and $G = 3025$ kg/m^2 s, which is considerably higher than the values obtained by Koşar and Peles [37] for a similar p_e/p_c value. Higher q''_{CHF}/q''_{mkv} value was obtained as the mass flux increased for the same system pressure. The results show that higher heat flux is achievable in microchannel with higher mass flux or different working fluid. Further studies are needed to be conducted at even higher mass fluxes to explore the heat flux limitation in microchannels.

5 Conclusion

Flow boiling in parallel microchannels with low surface tension fluid HFE-7000 was experimentally studied. Two types of microchannels were examined: plain-wall microchannel and microchannel with structured reentrant cavities on the side walls. Flow mor-

phologies, boiling inceptions, heat transfer coefficients, and critical heat fluxes were obtained and studied for mass fluxes ranging from $G=164$ kg/m^2 s to $G=3025$ kg/m^2 s. Comparisons between the enhanced and plain-wall microchannels were performed. The key findings of this study are as follows:

1. Similar flow patterns were observed for both microchannels: bubbly flow, oscillating single-phase liquid/single bubble/slug tail, churn flow, wispy annular flow, and inverted annular flow. However, transition lines between flow patterns showed some discrepancy between the two devices. It was observed that oscillating single-phase liquid/single bubble/slug tail extend to higher mass fluxes in the plain microchannel.
2. Delay of boiling was observed for flow boiling in the plain microchannels, while the wall superheat was found to be significantly reduced at ONB for the reentrant-cavity microchannels.
3. Rapid bubble growth caused a step wise increase in the heat transfer coefficient for low mass flux in the plain microchannel.
4. Heat transfer coefficient was found to be enhanced by up to 30% for the reentrant-cavity microchannel compared with the plain microchannel. However, this enhancement diminished at high mass qualities where convective boiling prevailed.
5. Dryout was established to be the CHF mechanism under the current thermal-hydraulic condition. This concurs with the annular flow pattern and the heat transfer performance prior to CHF conditions for both microchannels. Without the premature CHF caused by boiling instability, reentrant cavities did not enhance the CHF for HFE-7000.

Acknowledgment

This work was supported by the Office of Naval Research (program officer: Dr. Marl Spector). The microdevice was fabricated in Cornell Nanofabrication Facility (CNF), a member of the National Nanotechnology Infrastructure Network, which is supported by the National Science Foundation (NSF) under Grant No. ECS-0335765, Cornell University, its users, and the industrial affiliates. The authors would like to extend their gratitude to the staff and students of the CNF.

Nomenclature

A_p = platform area (heating surface area above the heater) (m^2)
A_s = total channel cross section area (m^2)
A_t = total channel surface area (m^2)
Bo = Boiling number, q''/Gh_{fg}
G = mass flux (kg/m^2 s)
H = channel height m
h = heat transfer coefficient (W/m^2 °C)
h_{fg} = latent heat of vaporization (J/kg)
h_{sp} = single-phase heat transfer coefficient (W/m^2 °C)
I = electrical current (A)
k_s = thermal conductivity of the substrate (silicon) (W/m °C)
L = distance from the inlet of the microchannel (m)
L_0 = channel length (m)
p = pressure (kPa)
P = electrical power (W)
q'' = heat flux (W/cm^2)
q''_{ch} = channel wall heat flux (W/cm^2)
q''_{eff} = effective heat flux (W/cm^2)
$\dot{Q}_{loss}$ = heat loss (W)
R = electrical resistance (Ω)
Re = Reynolds number, $vD\rho/\mu$
t = thickness of the silicon substrate (m)
T = local surface temperature (°C)
T_{in} = inlet temperature (°C)
T_l = mean liquid temperature (°C)
$T_{thermistor}$ = thermistor temperature (°C)
ΔT_w = wall superheat, $T-T$ (°C)
ΔT_{sat} = saturation superheat, $T-T_{sat}$ (°C)
ΔT_{sub} = subcooled temperature, $T_{sat}-T$ (°C)
V = electrical voltage (V)
W = channel width (m)
v = velocity (m/s)
X = true vapor mass quality
x = (thermodynamic) local mass quality

Greek

ρ = density (m^3/s)
μ = viscosity (N s/m^2)
σ = surface tension (N/m)

Subscripts

ch = channel
eff = effective
l = liquid
sat = saturation
sub = subcooled
tp = two-phase
v = vapor

References

[1] Thome, J. R., 1990, *Enhanced Boiling Heat Transfer*, Hemisphere, Washington, DC.
[2] Zeng, L. Z., and Klausner, J. F., 1993, "Nucleation Site Density in Forced Convection Boiling," ASME J. Heat Transfer, **115**, pp. 215–221.
[3] Del Valle, V. H. M., and Kenning, D. B. R., 1985, "Subcooled Flow Boiling at High Heat Flux," Int. J. Heat Mass Transfer, **28**, pp. 1907–1920.
[4] Kandlikar, S. G., 1990, "A General Correlation for Two-Phase Flow Boiling Heat Transfer Inside Horizontal and Vertical Tubes," ASME J. Heat Transfer, **112**, pp. 219–228.
[5] Kandlikar, S. G., 1991, "Development of a Flow Boiling Map for Subcooled and Saturated Flow Boiling of Different Fluids Inside Circular Tubes," ASME J. Heat Transfer, **113**, pp. 190–200.
[6] Liu, Z., and Winterton, R. H. S., 1991, "A General Correlation for Saturated and Subcooled Flow Boiling in Tubes and Annuli, Based on a Nucleate Pool Boiling Equation," Int. J. Heat Mass Transfer, **34**, pp. 2759–2766.
[7] Warrier, G. R., and Dhir, V. K., 2006, "Heat Transfer and Wall Heat Flux Partitioning During Subcooled Flow Nucleate Boiling—A Review," ASME J. Heat Transfer, **128**, pp. 1243–1256.
[8] Kandlikar, S. G., 2007, "Discussion: Heat Transfer and Wall Heat Flux Partitioning During Subcooled Flow Nucleate Boiling—A Review," ASME J. Heat Transfer, **129**, pp. 1300–1301.
[9] Jiang, L., Wong, M., and Zohar, Y., 2001, "Forced Convection Boiling in Microchannel Heat Sink," J. Microelectromech. Syst., **10**(1), pp. 80–87.
[10] Zhang, L., Koo, J., Jiang, L., Asheghi, M., Goodson, K. E., and Santiago, J. G., 2002, "Measurements and Modeling of Two-Phase Flow in Microchannels With Nearly Constant Heat Flux Boundary Conditions," J. Microelectromech. Syst., **11**(1), pp. 12–19.
[11] Kandlikar, S. G., 2002, "Fundamental Issues Related to Flow Boiling in Minichannels and Microchannels," Exp. Therm. Fluid Sci., **26**, pp. 389–407.
[12] Qu, W., and Mudawar, I., 2003, "Flow Boiling Heat Transfer in Two-Phase Micro-Channel Heat Sinks—I. Experimental Investigation and Assessment of Correlation Methods," Int. J. Heat Mass Transfer, **46**, pp. 2755–2771.
[13] Qu, W., and Mudawar, I., 2003, "Flow Boiling Heat Transfer in Two-Phase Micro-Channel Heat Sinks—II. Annular Two-Phase Flow Model," Int. J. Heat Mass Transfer, **46**, pp. 2773–2784.
[14] Koşar, A., Kuo, C.-J., and Peles, Y., 2005, "Boiling Heat Transfer in Rectangular Microchannels With Reentrant Cavities," Int. J. Heat Mass Transfer, **48**(23–24), pp. 4867–4886.
[15] Kuo, C.-J., and Peles, Y., 2007, "Local Measurement of Flow Boiling in Structured Surface Microchannels," Int. J. Heat Mass Transfer, **50**(23–24), pp. 4513–4526.
[16] Roday, A. P., Borca-Tasciuc, T., and Jensen, M. K., 2008, "The Critical Heat Flux Condition With Water in a Uniformly Heated Microtube," ASME J. Heat Transfer, **130**, pp. 012901.
[17] Roser, R., Thonon, B., and Mercier, P., 1999, "Experimental Investigations on Boiling of N-Pentane Across a Horizontal Tube Bundle: Two-Phase Flow and Heat Transfer Characteristics," Int. J. Refrig., **22**, pp. 536–547.
[18] Chang, J. Y., and You, S. M., 1997, "Boiling Heat Transfer Phenomena From

Micro-Porous Surfaces in Saturated FC-72," Int. J. Heat Mass Transfer, **40**(18), pp. 4437–4447.
[19] Zhang, L., Wang, E. N., Goodson, K. E., and Kenny, T. W., 2005, "Phase Change Phenomena in Silicon Microchannels," Int. J. Heat Mass Transfer, **48**(8), pp. 1572–1582.
[20] Koşar, A., Kuo, C.-J., and Peles, Y., 2005, "Reduced Pressure Boiling Heat Transfer in Rectangular Microchannels With Interconnected Reentrant Cavities," ASME J. Heat Transfer, **127**(10), pp. 1106–1114.
[21] Kuo, C.-J., Koşar, A., Peles, Y., Virost, S., Mishra, C., and Jensen, M. K., 2005, "Bubble Dynamics During Boiling in Enhanced Surface Microchannels," J. Microelectromech. Syst., **15**(6), pp. 1514–1527.
[22] Pate, D. T., Jones, R. J., and Bhavnani, S. H., 2006, "Cavity-Induced Two-Phase Heat Transfer in Silicon Microchannels," *Thermomechanical Phenomena in Electronic Systems, Proceedings of the 10th Intersociety Conference on Thermal and Thermomechanical Phenomena and Emerging Technologies in Electronic Systems (ITherm 2006)*, pp. 71–78.
[23] Jones, R. J., Pate, D. T., and Bhavnani, S. H., 2007, "Control of Instabilities in Two-Phase Microchannel Flow Using Artificial Nucleation Sites," *Proceedings of the ASME InterPack Conference (IPack 2007)*, pp. 247–358.
[24] Naveenan, T., Jones, R. J., Pate, D. T., and Bhavnani, S. H., 2008, "Thermal Characteristics of Two-Phase Flow of a Dielectric Fluid of Surface-Augmented Microchannels," 11th IEEE Intersociety Conference on Thermal and Thermomechanical Phenomena in Electronic System (ITherm 2008), pp. 189–196.
[25] Kuo, C.-J., and Peles, Y., 2008, "Flow Boiling Instabilities in Microchannels and Means for Mitigation by Reentrant Cavities," ASME J. Heat Transfer, **130**(7), p. 072402.
[26] Kuo, C.-J., and Peles, Y., 2009, "Pressure Effect on Flow Boiling Instabilities in Parallel Microchannels," Int. J. Heat Mass Transfer, **52**(1-2), pp.271–280.
[27] Yin, C.-P., Yan, Y.-Y., Lin, T.-F., and Yang, B.-C., 2000, "Subcooled Flow Boiling Heat Transfer of R-134a and Bubble Characteristics in a Horizontal Annular Duct," Int. J. Heat Mass Transfer, **43**(11), pp. 1885–1896.
[28] Lie, Y. M., and Lin, T. F., 2006, "Subcooled Flow Boiling Heat Transfer and Associated Bubble Characteristics of R-134a in a Narrow Annular Duct," Int. J. Heat Mass Transfer, **49**(13–14), pp. 2077–2089.
[29] Martin-Callizo, C., Palm, B., and Owhaib, W., 2007, "Subcooled Flow Boiling of R-134-a in Vertical Channels of Small Diameter," Int. J. Multiphase Flow, **33**, pp. 822–832.
[30] Bertsch, S. S., Groll, E. A., and Garimella, S. V., 2008, "Refrigerant Flow Boiling Heat Transfer in Parallel Microchannels as a Function of Local Vapor Quality," Int. J. Heat Mass Transfer, **51**, pp. 4775–4787.
[31] Revellin, R., Agostini, B., Ursenbacher, T., and Thome, J. R., 2008, "Experimental Investigation of Velocity and Length of Elongated Bubbles for Flow of R-134a in a 0.5 MM Microchannel," Exp. Therm. Fluid Sci., **32**, pp. 870–881.
[32] Kline, S., and McClintock, F. A., 1953, "Describing Uncertainties in Single-Sample Experiments," Mech. Eng. (Am. Soc. Mech. Eng.), **75**(1), pp. 3–8.
[33] Kuo, C.-J., 2009, "Flow Boiling in Structured Surface Microchannels," Ph.D. dissertation, Rensselaer Polytechnic Institute, Troy, NY.
[34] Collier, J. G., and Thome, J. R., 1994, *Convective Boiling and Condensation*, 3rd ed., Oxford University Press, New York.
[35] Kuo, C.-J., and Peles, Y., 2008, "Critical Heat Flux of Water at Sub-Atmospheric Pressures in Microchannels," ASME J. Heat Transfer, **130**(7), p. 072403.
[36] Carey, V. P., 1992, *Liquid-Vapor Phase-Change Phenomena*, Taylor and Francis, London.
[37] Koşar, A., and Peles, Y., 2007, "Critical Heat Flux of R-123 in Silicon-Based Microchannels," ASME J. Heat Transfer, **129**(7), pp. 844–851.
[38] Revellin, R., and Thome, J. R., 2008, "A Theoretical Model for the Prediction of the Critical Heat Flux in Heated Microchannels," Int. J. Heat Mass Transfer, **51**(5-6), pp. 1216–1225.
[39] Gambill, W. R., and Lienhard, J. H., 1987, "An Upper Bound for the Critical Boiling Heat Flux," *Proceedings of ASME-JSME Thermal Engineering Joint Conference*, Vol. 3, pp. 621–626.
[40] Kuan, W. K., and Kandlikar, S. G., 2006, "Experimental Study on Saturated Flow Boiling Critical Heat Flux in Microchannels," *Proceedings of the 4th International Conference on Nanochannels, Microchannels and Minichannels*, pp. 45–52.
[41] Wojtan, L., Revellin, R., and Thome, J. R., 2006, "Investigation of Saturated Critical Heat Flux in a Single, Uniformly Heated Microchannel," Exp. Therm. Fluid Sci., **30**(8), pp. 765–774.

Effect of Internal Wick Structure on Liquid-Vapor Oscillatory Flow and Heat Transfer in an Oscillating Heat Pipe

Jiajun Xu

Yuwen Zhang[1]
Fellow ASME
e-mail: zhangyu@missouri.edu

Hongbin Ma

Department of Mechanical and Aerospace Engineering,
University of Missouri,
Columbia, MO 65211

Liquid-vapor oscillating flow and heat transfer in a vertically placed oscillating heat pipe (OHP) with a sintered particle wick structure are analyzed in this paper. The oscillatory flow of the liquid slug is driven by the variations in pressures in the vapor plug due to evaporation and condensation. The evaporation and condensation heat transfer coefficients are obtained by solving the microfilm evaporation and condensation on the sintered particles. The sensible heat transfer between the liquid slug and the channel wall are obtained by analytical solution or empirical correlations depending on whether the liquid flow is laminar or turbulent. The effects of the sintered particles wick structure on the oscillatory flow, as well as sensible and latent heat transfer, are analyzed and compared with the results without wick structure. A parametric study on the oscillatory flow and heat transfer in the OHP with sintered particle wick structure is also performed.
[DOI: 10.1115/1.3222736]

1 Introduction

Oscillating heat pipe (OHP) is a very promising heat transfer device that can be utilized to transfer a large amount of heat from the heating section to the cooling section. It is potentially very useful for the chipset industry where the large amount of heat is generated and needs to be transferred within a limited time and area. In addition to its excellent heat transfer capability, it also posses advantages over the conventional heat pipe that include its simple structure and absence of friction between liquid and vapor phases [1,2].

OHP is made up of a long, continuous capillary tube bent into many turns with sufficiently small inner diameter to ensure the formation of liquid slugs. If the diameter is too large, the liquid and vapor phases tend to stratify [3]. Due to the oscillation of the working fluid in the axial direction of the tube, heat is transported from the heating section to the cooling section via latent and sensible heat, which is dominant when the flow pattern in the OHP is slug flow [4,5]. At the cold state, the liquid slugs in the OHPs are in their equilibrium positions. If triggered by the starting pulse, the liquid slugs depart from their equilibrium positions and oscillation is initiated. The heat input, acting as the driving force, increases the pressure of the vapor plug in the evaporator section. Meanwhile, the condensation that takes place in the condenser section results in decreasing vapor pressure in the condenser section. The pressure difference between two ends of the liquid slug causes liquid slug to move from the evaporator section to the condenser section. The movement of the liquid slug causes expansion of the vapor plug with higher pressure and compression of the vapor plug with low pressure so that the pressure difference between the two ends of the liquid slug decreases as the liquid slug moves. The pressure difference can also change its sign as the movement of the liquid causes the vapor plugs that was originally in the evaporator (condenser) section moves to the condenser (evaporator) section. This process is repeated and the oscillation of the liquid plugs and vapor bubbles in the OHP can be sustained.

Dobson and Harms [6] developed a simple mathematical model to study the behavior of an OHP with an open-end. They reported that the oscillating behavior would be different for different initial conditions. Zhang and Faghri [7] investigated the heat transfer process in an oscillating heat pipe with an open-end by considering the thin film evaporation and condensation. Wong et al. [8] proposed a theoretical model of OHP based on a Lagrange approach in which the flow was modeled under adiabatic condition. Hosoda et al. [9] reported a simplified numerical model of an OHP in which temperature and pressures are calculated by solving the momentum and energy equations for a two-dimensional two-phase flow. Experimental results were used as initial conditions for the model. The numerical results for pressure in the OHP are higher than the experimental results and the model did show that propagation of vapor plugs induced fluid flow in the capillary tubes. Shafii et al. [5] developed a theoretical model to simulate the behavior of the liquid slugs and the vapor plugs in both closed- and open-loop OHPs with two turns. They concluded that the number of vapor plugs was reduced to the number of heating section no matter how many vapor slugs were initially in the OHP. Based on their research, the OHP with even turns is symmetric and can be modeled as several *U*-shaped channels. Zhang et al. [10] analyzed the liquid-vapor oscillating flow in a *U*-shaped miniature channel. Xu and Zhang [11] studied sensible and latent heat transfer during liquid-vapor flow in a *U*-Shaped miniature tube.

Wick structure is commonly used in conventional heat pipes to provide capillary force to return liquid from the condenser section to the evaporator section [12]. In order to achieve the maximum heat transport through the heat pipe, the geometry of the wick must be optimized. For example, a higher capillary pressure can be achieved by small pore size but large pore size results in lower liquid pressure drop in the wick. Therefore, many different types of wick structures have been developed in order to optimize the performance of the conventional heat pipes. The commonly used wick structures in a heat pipe include grooved, sintered particles, mesh, and screened wick structure. The sintered particle wick structure is manufactured by packing the tiny metal particles in powder form between the inner heat pipe wall and a mandrel. This assembly is then heated until the metal spheres are sintered to each other and to the inner wall of the heat pipe. The effective

[1]Corresponding author.
Manuscript received January 13, 2009; final manuscript received April 9, 2009; published online October 15, 2009. Review conducted by Louis C. Chow.

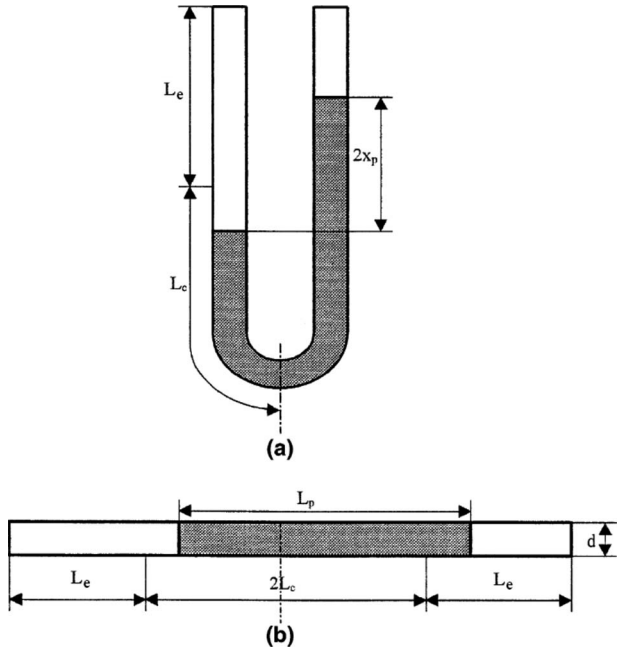

Fig. 1 Physical model

thermal conductivity of sintered particle wick is much higher than other wick structure, however, the permeability of the sintered particles wick structure is relatively low [12].

Based on the experience in conventional heat pipes, it will be logical to assume that the heat transfer performance of an OHP will be improved by adding wick structures. Zuo et al. [13] prototyped an OHP with sintered metal wicks and it achieved high heat fluxes. The wick aided the distribution of liquid throughout the OHP and provides more nucleation sites for bubbles to form. Holley and Faghri [14] analyzed the OHP with capillary wick and developed a model to determine the contribution of adding a sintered particle wick structure. Empirical correlation was used in their work to obtain boiling heat transfer coefficient from the surface of the wick structure. In this paper, liquid-vapor flow and heat transfer in a miniature *U*-shaped miniature channel will be analyzed and the effects of wick structure on heat transfer performance will be investigated.

2 Physical Model for Oscillatory Flow

A schematic diagram of the physical model is shown in Fig. 1. The inner surface of a *U*-shaped miniature channel is coated with a layer of sintered metal particles. The inner diameter of the miniature tube measured from the surface of the sintered wick is d and its total length is $2L$. The two ends of the *U*-shaped miniature channel are sealed. The two evaporator sections have a length of L_e locating near the two ends of the tube. The part between the two evaporation sections is the condensation section with a length of $2L_c$, which is located at the bottom of the *U*-shaped tube. The wall temperatures at the heating and cooling sections are T_e and T_c, respectively. The length of the liquid slug is L_p and the displacement of the liquid slug is represented by x_p, which is zero when the liquid slug is exactly in the middle of the *U*-shaped miniature channel. The displacement is positive when the liquid slug shifts to the right side; when it shifts to the left side the displacement is negative.

If the initial value of displacement x_{p0} is positive, part of the vapor plug in the left side is in contact with the condenser section; condensation in the left part will cause the pressure of the left vapor plug p_1 to decrease. The pressure difference between the two vapor plug will cause the liquid slug moving to the left direction and it will leave a liquid layer behind. Evaporation of the liquid layer left behind on the surface of the sintered wicks causes the pressure of the right vapor plug p_2 to increase and the pressure difference between the two ends of the liquid slug is further increased. When the displacement x_p becomes zero, there is neither evaporation nor condensation in two vapor plugs but the liquid slug keeps moving due to its inertia. When the liquid moves to the left side ($x_p<0$), the pressure difference changes its sign. The oscillation of the liquid slug can be maintained by alternative evaporation and condensation in the two vapor plugs.

The displacement of liquid slug [10] can be expressed as following:

$$A_c L_p \rho_l \frac{d^2 x_p}{dt^2} = (p_{v1} - p_{v2})A_c - 2\rho_l g A_c x_p - \pi d L_p \tau_p \tag{1}$$

where $A_c = \pi d^2/4$ is the cross-sectional area of the tube and $\tau_p = C_l \rho_l v_l^2/2$ is the shear stress acting between the liquid slug and the tube, where the friction coefficient can be determined by

$$C_l = \begin{cases} 16/\mathrm{Re} & \mathrm{Re} \le 2000 \\ 0.078\ \mathrm{Re}^{-0.2} & \mathrm{Re} > 2000 \end{cases} \tag{2}$$

Utilizing the first law of thermodynamics to the two vapor plugs, one obtains

$$\frac{d(m_{v1} c_v T_{v1})}{dt} = c_p T_{v1} \frac{dm_{v1}}{dt} - p_v \frac{\pi}{4} d^2 \frac{dx_p}{dt} \tag{3}$$

$$\frac{d(m_{v2} c_v T_{v2})}{dt} = c_p T_{v2} \frac{dm_{v2}}{dt} + p_v \frac{\pi}{4} d^2 \frac{dx_p}{dt} \tag{4}$$

It is assumed that the behaviors of the vapor plugs can be modeled using ideal gas law, i.e.,

$$p_{v1}(L_e + x_p)\frac{\pi}{4} d^2 = m_{v1} R T_{v1} \tag{5}$$

$$p_{v2}(L_e - x_p)\frac{\pi}{4} d^2 = m_{v2} R T_{v2} \tag{6}$$

The masses of two vapor plugs [10] can be obtained from Eqs. (3)–(6) as

$$m_{v1} = C_1 p_{v1}^{1/\gamma}(L_e + x_p) \tag{7}$$

$$m_{v2} = C_2 p_{v2}^{1/\gamma}(L_e - x_p) \tag{8}$$

where C_1 and C_2 are integral constants. Since the structure of the *U*-shaped channel is symmetric, the two integral constants are the same, i.e., $C_1 = C_2 = C$. The temperatures of the two vapor plugs can be obtained by substituting Eqs. (7) and (8) into Eqs. (5) and (6), i.e.,

$$T_{v1} = \frac{\pi d^2}{4CR} p_{v1}^{(\gamma-1)/\gamma} \tag{9}$$

$$T_{v2} = \frac{\pi d^2}{4CR} p_{v2}^{(\gamma-1)/\gamma} \tag{10}$$

To determine the integration constant, it is necessary to choose a reference state of the *U*-shaped miniature channel. At the reference state, the pressures of both vapor plugs are p_0, the temperatures of both vapor plugs are T_0, and the displacement of the liquid slug is x_{p0}. According to Eqs. (9) and (10), the integration constant can be expressed in term of reference state as

$$C_1 = C_2 = C = \frac{\pi d^2}{4RT_0} p_0^{(\gamma-1)/\gamma} \tag{11}$$

Substituting Eq. (11) into Eqs. (7)–(10), the masses and temperatures of the two vapor plugs can be expressed as

$$m_{v1} = \frac{\pi d^2 p_0}{4RT_0}\left(\frac{p_{v1}}{p_0}\right)^{1/\gamma}(L_e + x_p) \tag{12}$$

$$m_{v2} = \frac{\pi d^2 p_0}{4RT_0}\left(\frac{p_{v2}}{p_0}\right)^{1/\gamma}(L_e - x_p) \tag{13}$$

$$T_{v1} = T_0\left(\frac{p_{v1}}{p_0}\right)^{(\gamma-1)/\gamma} \tag{14}$$

$$T_{v2} = T_0\left(\frac{p_{v2}}{p_0}\right)^{(\gamma-1)/\gamma} \tag{15}$$

The masses of the vapor plugs increase due to evaporation and decrease due to condensation

$$\frac{dm_{v1}}{dt} = \begin{cases} -h_c \pi d x_p (T_{v1} - T_c)/h_{fg}, & x_p > 0 \\ -h_e \pi d (L_e + x_p)(T_e - T_{v1})/h_{fg}, & x_p < 0 \end{cases} \tag{16}$$

$$\frac{dm_{v2}}{dt} = \begin{cases} h_e \pi d (L_e - x_p)(T_e - T_{v2})/h_{fg}, & x_p > 0 \\ h_c \pi d x_p (T_{v2} - T_c)/h_{fg}, & x_p < 0 \end{cases} \tag{17}$$

where the heat transfer coefficients in the evaporator and condenser sections, h_e and h_c, must be obtained by solving evaporation and condensation on the top of the sintered particle wick structure.

The reference state of the *U*-shaped miniature channel is chosen to be the initial state of the system in this work, i.e.,

$$x_p = x_{p0}, \quad t = 0 \tag{18}$$

$$p_1 = p_2 = p_0, \quad t = 0 \tag{19}$$

$$T_1 = T_2 = T_0, \quad t = 0 \tag{20}$$

$$m_{v1} = \frac{\pi d^2 p_0}{4RT_0}(L_e + x_{p0}), \quad t = 0 \tag{21}$$

$$m_{v2} = \frac{\pi d^2 p_0}{4RT_0}(L_e - x_{p0}), \quad t = 0 \tag{22}$$

3 Latent and Sensible Heat Transfer

3.1 Evaporation Heat Transfer. Figures 2(*a*) and 2(*b*) show wick structure and the meniscus formed between particles. For the wick structure located in the heating section, the thin film region can be divided into (1) nonevaporating film, (2) microfilm, and (3) meniscus regions (see Fig. 2(*c*)). No evaporation occurs in the nonevaporation thin film region because the liquid-vapor interfacial equilibrium temperature is elevated to the wall temperature due to the disjoining pressure effect. Virtually all of the evaporation occurs in the microfilm region where the evaporation process and the disjoining and capillary pressures significantly affect its shape. As the film thickness increases further, the evaporation rate significantly drops and the curvature stays at a constant value. This region of the interface can be referred to as the meniscus and is the third region labeled in Fig. 2(*c*).

Compared with the case without wick that evaporation can only occur in the liquid film left behind by the liquid slug, evaporation heat transfer for the case with sintered particle wick is significantly enhanced due to large number of particles. Ma and Peterson [15] suggested that most of the evaporation heat transfer passes through a small region that is less than 1 μm. The rate of evaporation heat transfer from a particle can be obtained as

$$q_{p,\text{eva}} = 2\pi r_w \sin\theta_{\max,e} k_l (T_e - T_v) \int_0^{10^{-6}} \frac{1}{\delta} dx \tag{23}$$

where $\theta_{\max,e}$ indicates the location of micro region, which was assumed to be $\pi/2$ in Ref. [16] but will be treated as a variable in this work. The film thickness satisfies the following momentum equation

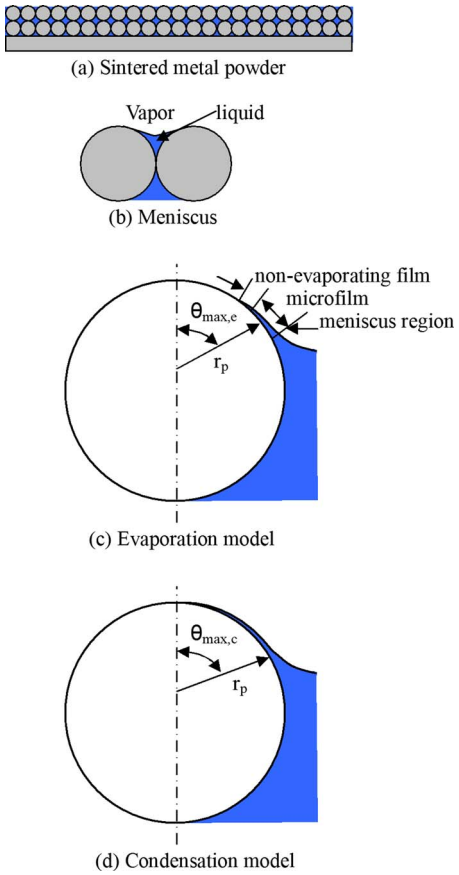

Fig. 2 Wick structure and evaporation/condensation occurred on sintered particles

$$\sigma\frac{dK}{dx} + K\frac{d\sigma}{dx} - \frac{dp_d}{dx} = -\frac{f\,\text{Re}_\delta\,\mu\dot{m}_\delta(x)}{2\delta^3(x)\rho_l} \tag{24}$$

where

$$K = \frac{d^2\delta}{dx^2}\left[1 + \left(\frac{d\delta}{dx}\right)^2\right]^{-3/2} \tag{25}$$

$$p_d = \rho_l R T_{lv} \ln(a\delta^b) \tag{26}$$

are the curvature and disjoining pressure, respectively. For water, the constant in Eq. (26) are $a = 1.5787$ and $b = 0.0243$. $\text{Re}_\delta = \rho u \delta/\mu$ is the Reynolds number with film thickness as characteristic length and $\dot{m}_\delta(x)$ is the mass flow rate of the liquid across the thin film thickness. The corresponding boundary conditions of Eq. (24) are $\delta = \delta_0$, $K = 0$, and $d\delta/dy = 0$ at $x = 0$ where δ_0 is the nonevaporating film thickness that is determined by

$$\delta_0 = \exp\left\{\frac{1}{b}\left[\left(\frac{T_w}{T_v} - 1\right)\frac{h_{lv}}{RT_w} - \ln a\right]\right\} \tag{27}$$

The total evaporating heat transfer may be determined by

$$Q_{\text{eva},p} = N_{p,\text{eva}} q_{p,\text{eva}} \tag{28}$$

where $N_{p,\text{eva}}$ is the total number of particles at the top surface of wicks and it can be found by

$$N_{p,\text{eva}} = \frac{(1-\varepsilon)A_{sp}}{\pi r_w^2} = \frac{(1-\varepsilon)\pi d x_{w,\text{eva}}}{\pi r_w^2} = \frac{4(1-\varepsilon)dx_{w,\text{eva}}}{d_w^2} \tag{29}$$

where $A_{sp} = \pi d x_{w,\text{eva}}$ is the total area of top surface of sintered porous medium, ε is the porosity of the sintered wick, and $x_{w,\text{eva}}$ is

the length of the part expose to evaporation along the tube, which varies with the displacement of the liquid slug. When $x_p>0$, $x_{w,\mathrm{eva},1}=L_e$; $x_{w,\mathrm{eva},2}=L_e-x_p$; when $x_p<0$, $x_{w,\mathrm{eva},1}=L_e+x_p$; $x_{w,\mathrm{eva},2}=L_e$.

Thus, the evaporation heat transfer coefficient is

$$h_e=\frac{Q_{p,\mathrm{eva}}}{A_{sp}(T_e-T_v)}=\frac{N_{p,\mathrm{eva}}q_{p,\mathrm{eva}}}{\pi d x_{w,\mathrm{eva}}(T_e-T_v)} \tag{30}$$

3.2 Condensation Heat Transfer. The physical model of condensation on the sintered wick surface is illustrated in Fig. 2(*d*). Condensation takes place on the entire cap of the particles and the condensate flows into the menisci between particles. The condensation heat transfer in the cooling section is also significantly enhanced due to addition of the wick structure. For condensation on a spherical particle in sintered wick, condensation occurs on only part of the sphere (top portion) $\theta<\theta_{\max,c}$ (see Fig. 2(*d*)). Neglecting the inertia term, the momentum equation for the liquid film is:

$$\mu_\ell\frac{\partial^2 u_\ell}{\partial y^2}=-g\sin\theta(\rho_\ell-\rho_v) \tag{31}$$

where $u=0$ at $y=0$ and $\partial u/\partial y=0$ at $y=\delta$. Equation (31) can be integrated to obtain

$$u_\ell=\frac{g\sin\theta}{\mu_\ell}(\rho_\ell-\rho_v)\left(y\delta-\frac{y^2}{2}\right) \tag{32}$$

By performing mass and energy balances across the thin film, the film thickness [17] can be obtained as

$$\delta=\left\{\frac{8\mu_\ell k_\ell d_w(T_{\mathrm{sat}}-T_w)}{\rho_\ell(\rho_\ell-\rho_v)gh_{\ell v}}\cdot\frac{1}{\sin^{8/3}\theta}\int_0^\theta\sin^{(5/3)}\theta d\theta\right\}^{(1/4)} \tag{33}$$

The total heat transfer rate from one particle is

$$q_{p,\mathrm{con}}=\int_0^{\theta_{\max,c}}\frac{k_\ell(T_{\mathrm{sat}}-T_w)}{\delta}\cdot 2\pi r_w^2\sin\theta d\theta \tag{34}$$

Substituting Eq. (33) into Eq. (34), the rate of condensation heat transfer per particle becomes

$$q_{p,\mathrm{con}}=\frac{\pi}{4}d_w k_\ell(T_{\mathrm{sat}}-T_c)\left[\frac{2\mu_\ell k_\ell(T_{\mathrm{sat}}-T_c)}{\rho_\ell(\rho_\ell-\rho_v)gh_{\ell v}d_p^3}\right]^{(1/4)}\times\int_0^{\theta_{\max,c}}\sin^{(5/3)}\theta\left[\int_0^\theta\sin^{(5/3)}\theta d\theta\right]d\theta \tag{35}$$

which accounts for the condensation occurred on the top of the particle. The condensation occurs on the menisci surface between particles can be neglected. The number of the sintered particle in the condenser section is

$$N_{p,\mathrm{con}}=\frac{(1-\varepsilon)A_{sp}}{\pi r_w^2}=\frac{(1-\varepsilon)\pi d x_{w,\mathrm{con}}}{\pi r_w^2}=\frac{4(1-\varepsilon)dx_{w,\mathrm{con}}}{d_w^2} \tag{36}$$

when $x_p>0$, $x_{w,\mathrm{con},1}=x_p$; $x_{w,\mathrm{con},2}=0$; when $x_p<0$, $x_{w,\mathrm{con},1}=0$; $x_{w,\mathrm{con},2}=-x_p$. The total rate heat transfer is the heat transfer rate per particle times the number of particles in the condenser section. Thus, the condensation heat transfer coefficient is

$$h_c=\frac{N_{\mathrm{con},p}q_p}{\pi d x_{w,\mathrm{con}}(T_v-T_c)} \tag{37}$$

3.3 The Sensible Heat Transfer. The energy equation for the liquid slug in a coordinate system moving with the liquid slug is

$$\frac{1}{\alpha_l}\frac{\partial T_l}{\partial t}=\frac{\partial^2 T_l}{\partial x_l^2}-\frac{h\pi d}{k_l A}(T_l-T_w) \tag{38}$$

which subjects to the following initial and boundary conditions:

$$T=T_c,\quad t=0,\quad 0<x_l<L_p \tag{39}$$

$$T=T_{v1},\quad x_l=0 \tag{40}$$

$$T=T_{v2},\quad x_l=L_p \tag{41}$$

The wall temperature of the tube can be either T_e or T_c depending on the displacement of the liquid slug, i.e., when $x_p>0$

$$T_w=\begin{cases}T_c, & 0<x_l<L_p-x_p\\ T_e, & L_p-x_p<x_l<L_p\end{cases} \tag{42}$$

when $x_p<0$

$$T_w=\begin{cases}T_e, & 0<x_l<|x_p|\\ T_c, & |x_p|<x_l<L_p\end{cases} \tag{43}$$

Since the Reynolds number of the liquid slug varies in a wide range that covers laminar, transition, and turbulent flow, the heat transfer coefficient h of the liquid slug varies from time to time. For laminar regime, the convective heat transfer problem is considered as thermally developing Hagen–Poiseuille flow and the Nusselt number can be obtained analytically [5]. In the transition and turbulent regimes, the Nusselt number can be obtained by using empirical correlations [5]. The sensible heat transfer into and out from the liquid slug can be obtained by integrating the heat transfer over the length of the liquid slug, i.e.,

$$Q_{\mathrm{in},s,l}=\begin{cases}\displaystyle\int_{L_p-x_p}^{L_p}\pi dh(T_e-T_l)dx_l & x_p>0\\ \displaystyle\int_0^{|x_p|}\pi dh(T_e-T_l)dx_l & x_p<0\end{cases} \tag{44}$$

$$Q_{\mathrm{out},s,l}=\begin{cases}\displaystyle\int_0^{L_p-x_p}\pi dh(T_l-T_c)dx_l & x_p>0\\ \displaystyle\int_{|x_p|}^{L_p}\pi dh(T_l-T_c)dx_l & x_p<0\end{cases} \tag{45}$$

4 Numerical Solution

Based on the above governing equations and using an implicit scheme, the results of each time-step can be obtained by following the numerical procedure outlined as follows:

1. Assume the temperatures of the two vapor plugs T_{v1} and T_{v2}.
2. Solve for the vapor pressures p_{v1} and p_{v2} from Eqs. (14) and (15).
3. Solve for x_p from Eqs. (1) and (2).
4. Obtain the new masses of the two vapor plugs m_{v1} and m_{v2} by account for the change in vapor masses from Eqs. (16) and (17).
5. Calculate the pressure of the two vapor plugs p_{v1} and p_{v2} from Eqs. (12) and (13).
6. Solve for T_{v1} and T_{v2} from Eqs. (14) and (15).
7. Compare T_{v1} and T_{v2} obtained in step 6 with assumed values in step 1 and if the differences meet the small tolerance, then go to the step 8; otherwise, the above procedure is repeated until a converged solution is obtained.
8. Obtain the evaporation and condensation heat transfer coefficient from Eqs. (30) and (37).
9. Solve for liquid temperature distribution from Eq. (38) and calculate Q_{sensible}.
10. Use Eqs. (23) and (35) to calculate Q_{latent}.

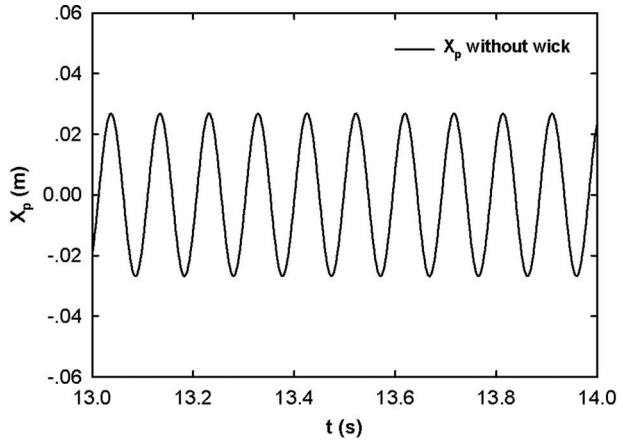

(a) Displacement of liquid slug

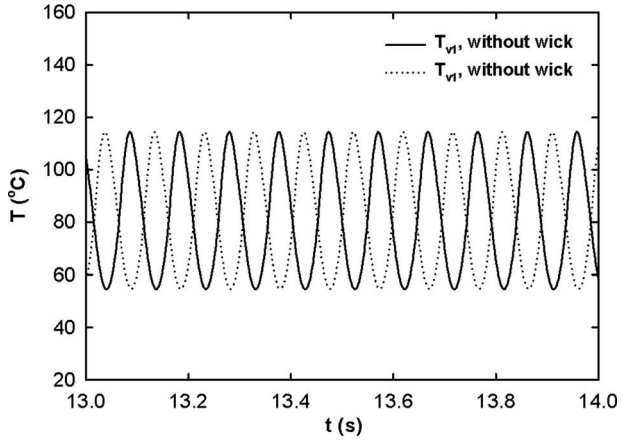

(b) Vapor plug temperatures

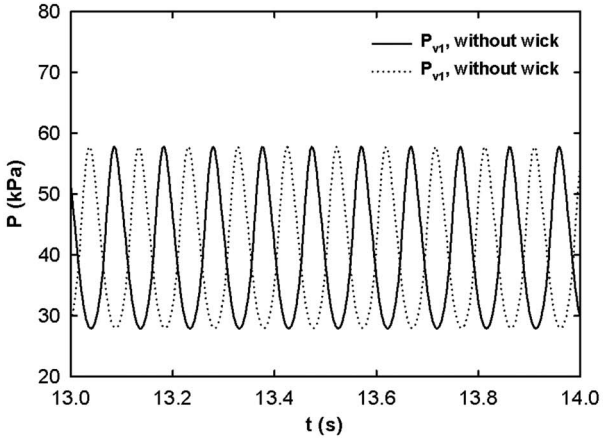

(c) Vapor plug pressures

Fig. 3 Liquid slug displacement and temperature and pressure of vapor plugs without wick

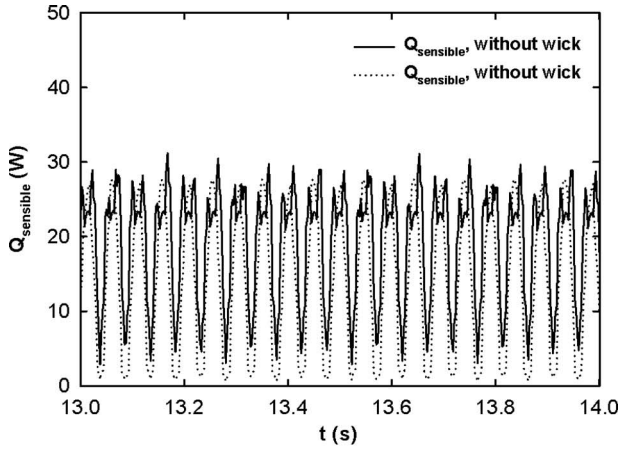

(a) Sensible heat transfer

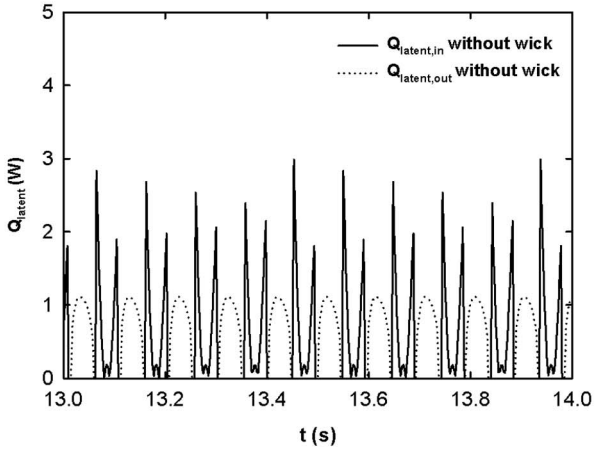

(b) Latent heat transfer

Fig. 4 Sensible and evaporative heat transfer without wick

After the time-step independent test, it was found that the time-step independent solution of the problem can be obtained when time-step is $\Delta t = 1 \times 10^{-4}$, which is used in all numerical simulations.

5 Results and Discussions

To make sure that the comparison between the cases without and with wick structure is fair and objective, the parameters of the *U*-shaped miniature tube without wick structure are based on those used by Shafii et al. [5] who performed thermal modeling of unlooped and looped OHPs with two turns and concluded that the oscillation of the two liquid slugs is symmetric. Simulation is first performed using the parameters same as Ref. [5] and the results are shown in Fig. 3. The parameters of the miniature channel are $L_e = 0.1$ m, $L_c = 0.37$ m, $L_p = 0.35$ m, $d = 0.0015$ m, $T_e = 120°C$, and $T_c = 20°C$. The initial temperature of the vapor plug is $T_{vi} = 35°C$ and the initial pressures of the vapor plugs are $p_{vi} = 5628$ Pa, which is the saturation pressure that corresponds to the initial temperature. The heat transfer coefficient at the heating wall is $h_h = 150$ W/m^2 K and the heat transfer coefficient at the cooling wall is $h_c = 100$ W/m^2 K. The frequency of the displacement of the liquid slug shown in Fig. 3(*a*) is identical as those of Ref. [5] but the amplitude of the liquid displacement obtained in this paper is lower than that in Ref. [5]. The amplitude of oscillation obtained by Shafii et al. [5] was higher because the effective lengths of evaporation and condensation were treated as constants in their model. On the contrary, the lengths of evaporation and condensation in this work were treated as variables depending on the displacement, as indicated by Eqs. (16) and (17). Similarly, the vapor temperatures and pressures shown in Figs. 3(*b*) and 3(*c*), respectively, also have the same frequency as Ref. [5] but the amplitudes are lower due to different effective evaporation and condensation lengths. The sensible and latent transfers are shown in Fig. 4, which also exhibit the similar trend, as seen in Ref. [5].

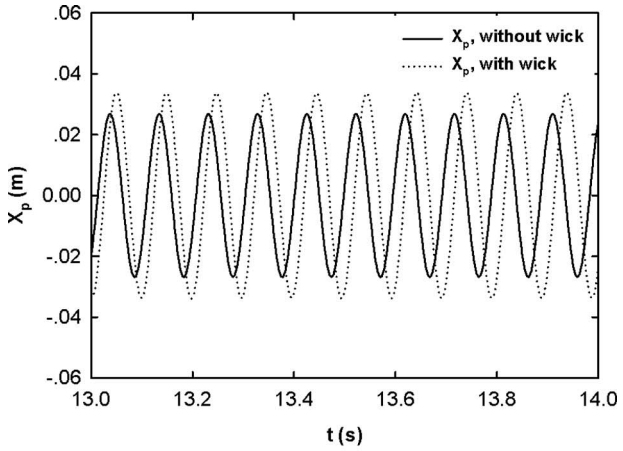

(a) Displacement of liquid slug

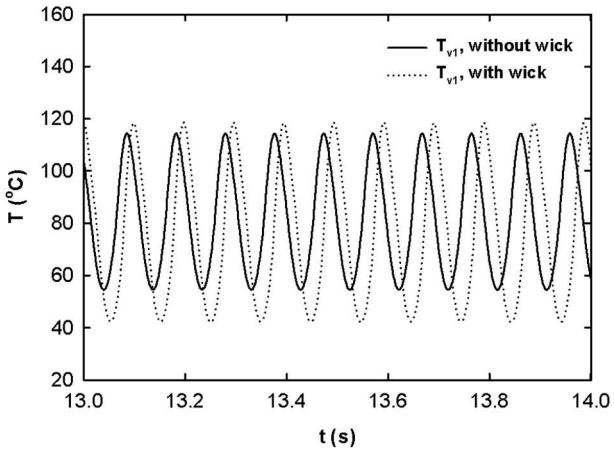

(b) Vapor plug temperatures

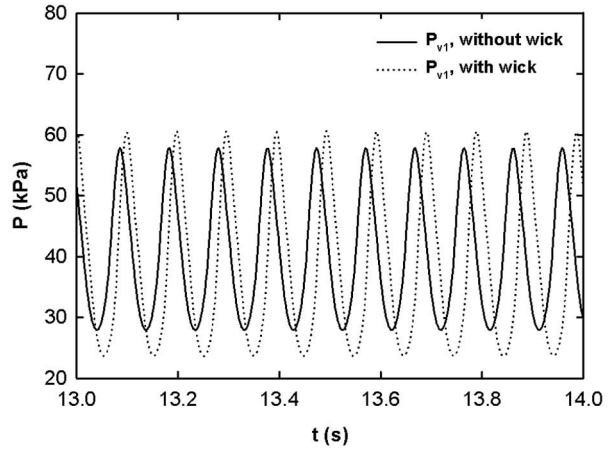

(c) Vapor plug pressure

Fig. 5 Comparison of liquid slug displacement, temperature and pressure of vapor plugs

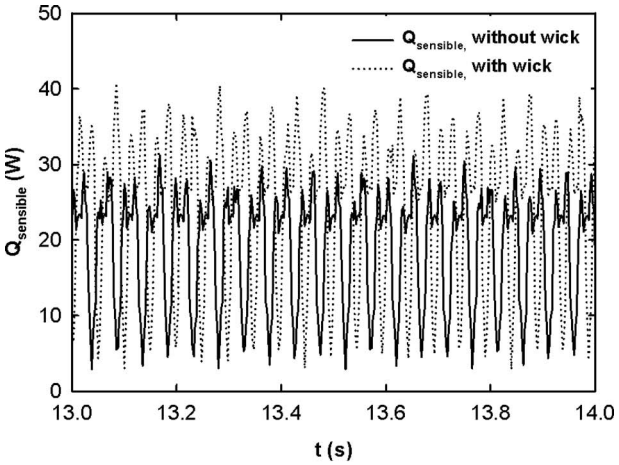

(a) Sensible heat transfer

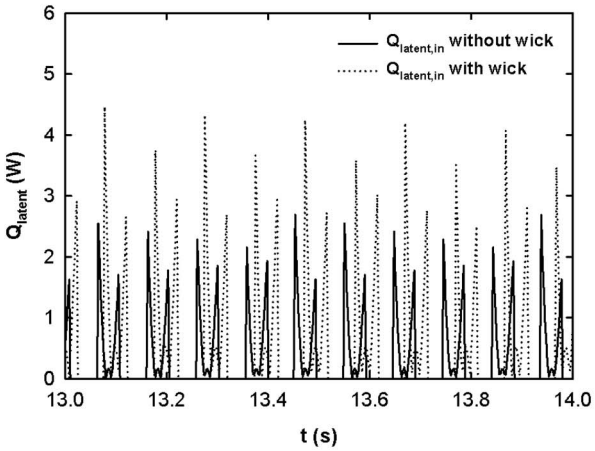

(b) Latent heat transfer

Fig. 6 Comparison of sensible and evaporative heat transfer

The contribution of sensible heat transfer is dominant and the effect of latent heat transfer on the overall heat transfer is relatively insignificant.

Simulation is then carried out for the case with internal wick structures and the results are compared with the case without wick. The inner diameters of the *U*-shaped miniature channels with and without the sintered particles are considered to be the same so that the difference between the two sets of the results are due to the effect of the sintered particles only. The diameter of the sintered particles is $d_w = 0.000135$ m and the porosity of the sintered wick is $\varepsilon = 0.4$. The two angles $\theta_{\max,e}$ and $\theta_{\max,c}$ are set to be equal to 60 deg. Figure 5(*a*) shows the comparison of the displacement for the cases with and without sintered particles. It can be seen that, after wick is added, the magnitude of the liquid slug displacement is increased by 20% and the phase is slightly delayed. The frequency of oscillation for the cases with sintered particles wick is decreased compared with that of the case without wick. Figure 5(*b*) shows the comparison of vapor plug temperatures for the cases with and without sintered particle wick. It can be seen that the temperature of left vapor plug with wick has a much wider temperature range: while the maximum temperature is increased by about 5%, the minimum temperature is decreased from around 55°C to about 40°C. Similar to the trend on liquid slug displacement, there is a slight delay in the phase for the case with sintered particle wick, and the frequency is decreased. The variations in the pressures of the left vapor plugs for the case without and with wick structure are shown in Fig. 5(*c*). It can be seen that the addition of sintered particle wick exhibited the similar trend as the vapor plug temperatures. Therefore, one can conclude that adding the wick will increase the amplitudes of displacement, vapor plug temperature, and pressure while the frequency will slightly decrease.

Figure 6(*a*) shows the comparison of sensible heat transferred into the liquid for the cases with and without wick structure. The phase of the oscillation of sensible heat transfer in and out of the

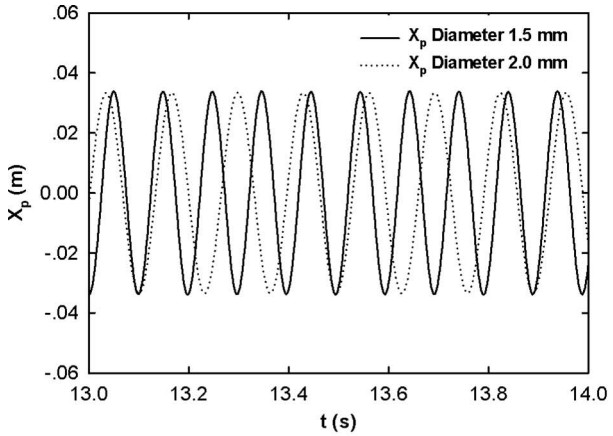

(a) Liquid slug displacement

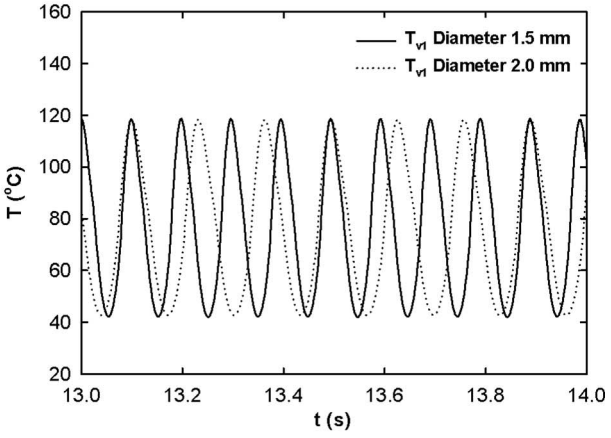

(b) Vapor plug temperatures

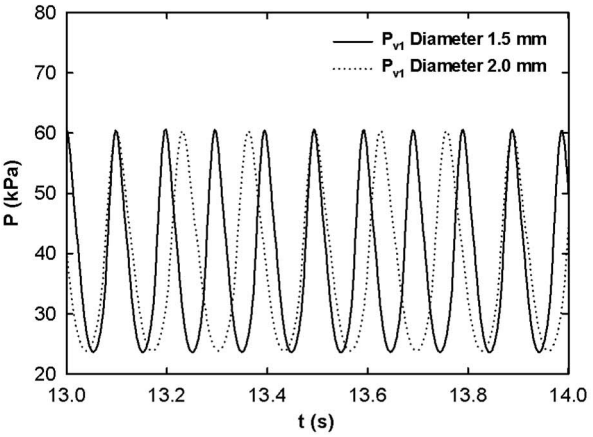

(c) Vapor plug pressures

Fig. 7 Effect of the inner diameter on liquid slug displacement, temperature and pressure of vapor plugs with wick

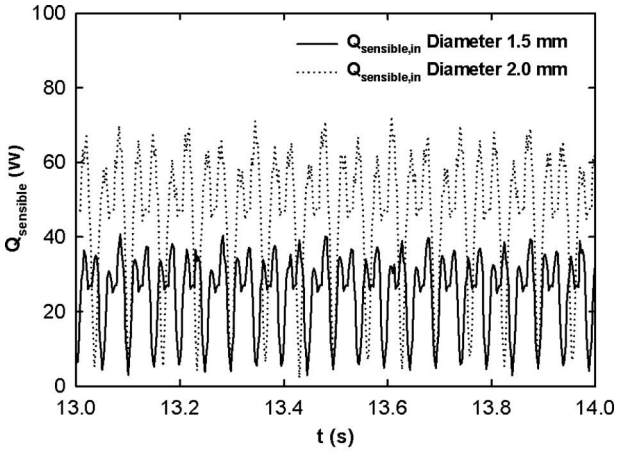

(a) Sensible heat transfer

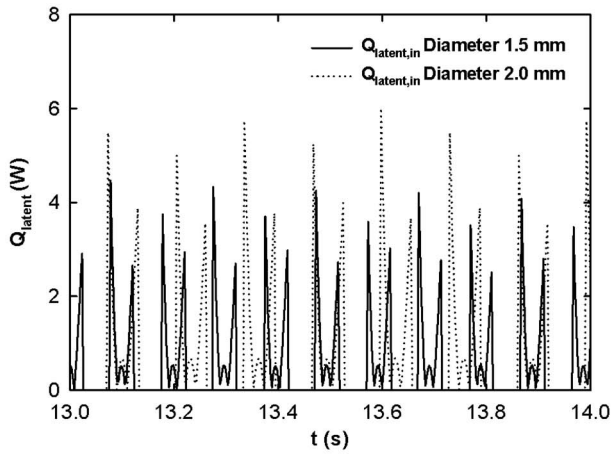

(b) Latent heat transfer

Fig. 8 Effect of the inner diameter on the sensible and evaporative heat transfer with wick

liquid slug is slightly delayed after the addition of the wick. Due to enhanced oscillatory motion of the liquid slug, the average sensible heat transfer rate is increased from 22.39 W without sintered particle wick to 26.57 W with wick, a 19.1% increase. The comparison of latent heat transfer for the cases with and without wick is shown in Fig. 6(*b*). It is seen that the evaporation heat transfer is greatly enhanced with addition of the sintered particle wick. Due to the increase in evaporation area and new evaporation mechanism, the average evaporation heat transfer increases from 0.39 W to 0.64 W, a 90% increase. Thus, the addition of sintered particles changed the evaporation/condensation mechanism in a similar trend as on the other parameters but with a significantly large magnitude. The overall heat transfer enhancement after addition of wick, including both sensible and latent heat transfer, is about 20%.

The effect of the diameter of the channel with sintered particle wick on its oscillatory flow and heat transfer is then studied and the results are shown in Figs. 7 and 8. Figure 7(*a*) shows the effect of the channel diameter on the displacement of the liquid slugs. The increase in inner diameter notably affects the frequency of the liquid slug oscillation but it does not affect the maximum displacement of the liquid slug. The phase of oscillation also advances with increasing channel diameter. The vapor temperature and pressure variations, as shown in Figs. 7(*b*) and 7(*c*), experience similar trends as that of the liquid slug displacement: the magnitudes are not affected by the channel diameter but the frequencies are decreased by about 30%. Figure 8 shows the effect of channel diameter on the sensible and latent heat transfer. It can be seen from Fig. 8(*a*) that the sensible heat transfer experiences an increase in its magnitude: The maximum sensible heat transfer is increased from around 40 W to about 65 W (over 50% increase). Besides, there is also a phase advance after the increase in inner diameter while the frequency of oscillation is also decreased. The performance of the latent heat transfer is shown in Fig. 8(*b*), which has an increase of 15%. The average sensible heat transfer

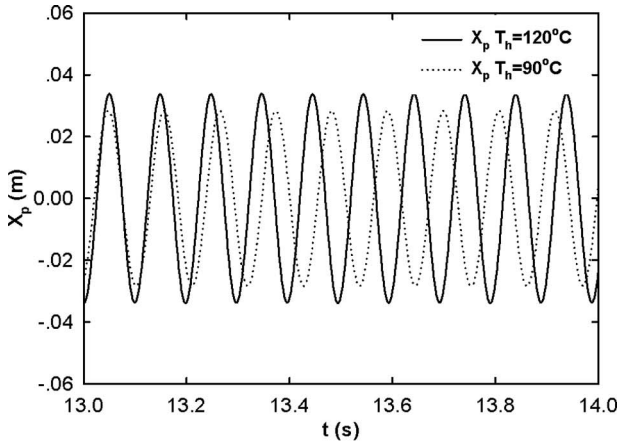

(a) Liquid slug displacement

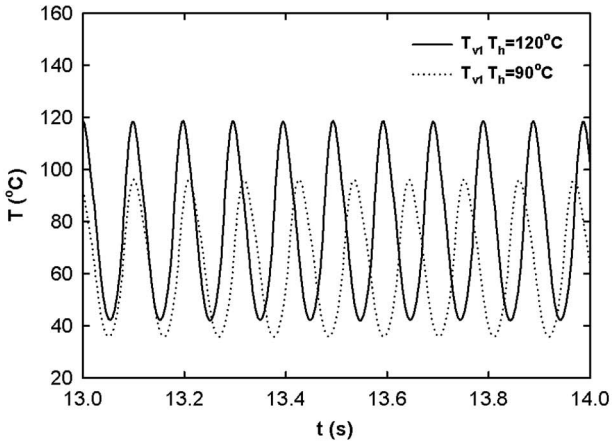

(b) Vapor plug temperatures

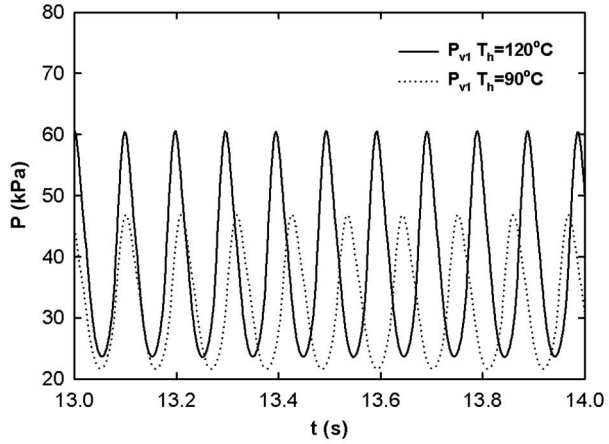

(c) Vapor plug pressure

Fig. 9 Effect of different heating section temperatures on liquid slug displacement, temperature and pressure of vapor plugs with wick

into the liquid slug is around 43.74 W and the evaporation heat transfer of is about 0.85 W. Thus, it can be concluded that the increase in inner diameter helps to increase the both sensible and latent heat transfer.

The effects of heating section temperature on the oscillatory flow and heat transfer performance are studied and the results are plotted in Figs. 9 and 10. When the temperature of heating section is decreased from 120°C to 90°C, the amplitude of the liquid

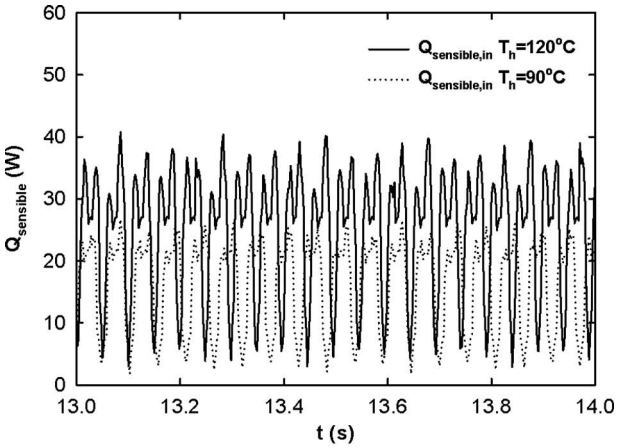

(a) Sensible heat transfer

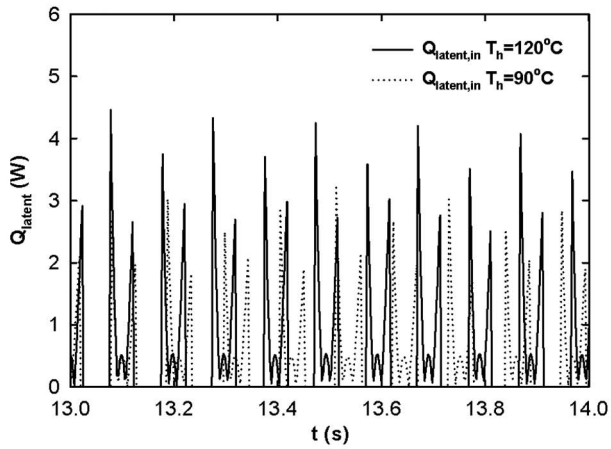

(b) Latent heat transfer

Fig. 10 Effect of different heating section temperatures on sensible and evaporative heat transfer with wick

slug displacement is decreased by about 20% since the latent heat transfer is lowered and the oscillation of liquid slug is weakened. As can be seen from Figs. 9(*b*) and 9(*c*), the temperature and pressure of the two vapor plugs are also decreased, which result less driving force for the oscillation of liquid slug and thus the displacement is shorted. The highest temperature is decreased from around 120°C to around 90°C and the pressure falls from 60 kPa to 45 kPa. Effects of the heating section temperature on both the sensible and latent heat transfer are shown in Fig. 10. The maximum sensible heat transfer is decreased from 40W to about 25 W and the frequency also decreases with decreasing T_h. The maximum latent evaporation heat transfer changed from over 4.5 W to around 3 W, a decrease of about 30%. The averaged sensible and latent heat transfers are around 12.84 W and 0.33 W, respectively. Therefore, the decrease in the temperature of heating section greatly affects the heat transfer performance of the miniature channel by decreasing the inner liquid slug oscillation, temperature/pressure of the two vapor plugs, and the sensible and latent heat transfer.

Figure 11 shows the effect of particle size on the oscillatory flow. It can be clearly seen that the doubling the particle size decreases the range of oscillation but increase the frequency. This trend is attributed to the fact that the increasing the particle size results in lower number of particle. While the amplitude of oscillation for both temperature and pressure decrease with increasing particle size, the minimum vapor plug temperature and pressure

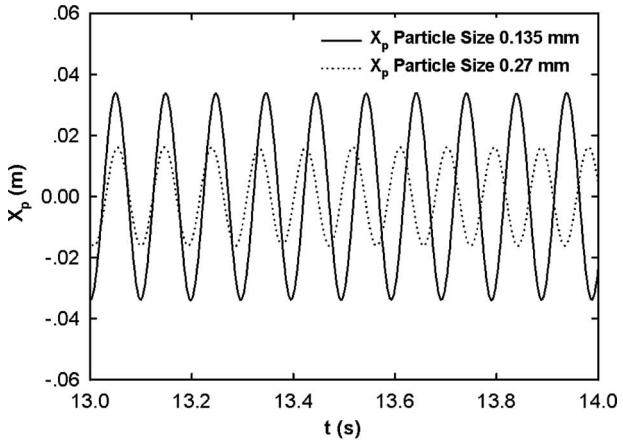

(a) Liquid slug displacement

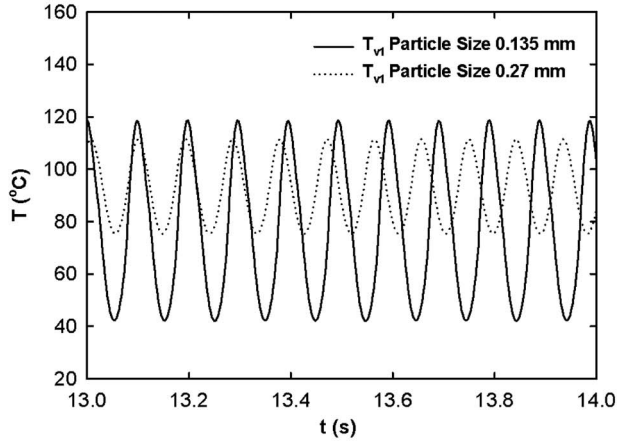

(b) Vapor plug temperatures

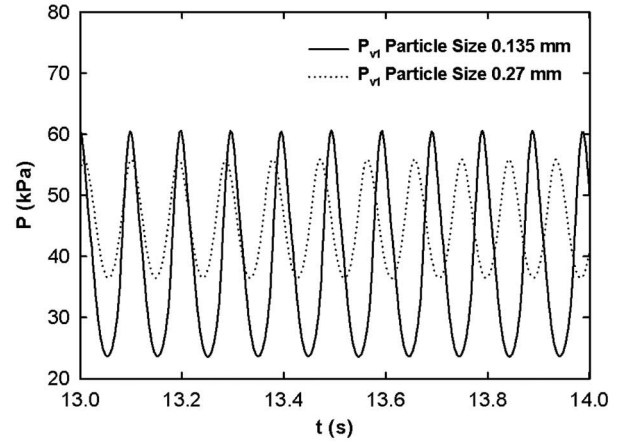

(c) Vapor plug temperature

Fig. 11 Effect of different particle sizes on liquid slug displacement, temperature and pressure of vapor plugs

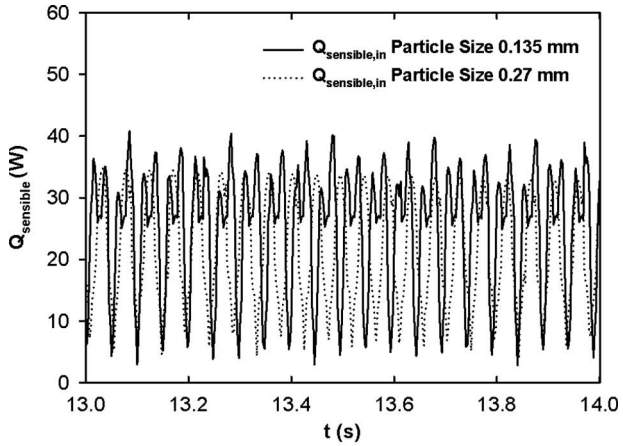

(a) Sensible heat transfer

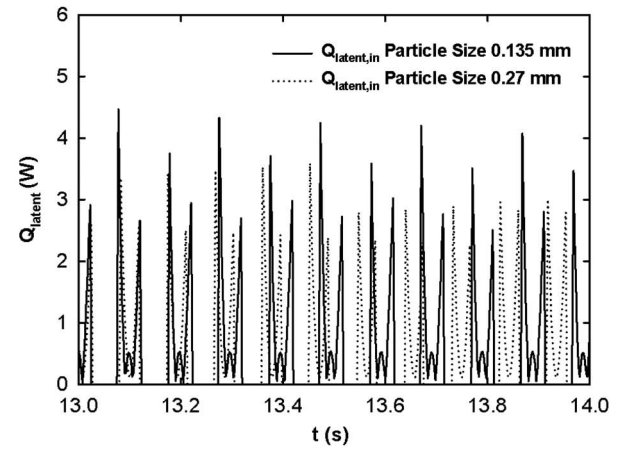

(b) Latent heat transfer

Fig. 12 The effect of different particle sizes on the variation in sensible and evaporative heat transfer with wick

decreased more than the decrease in the maximum temperature and pressure. Figure 12 shows the effect of particle diameter on the sensible and latent heart transfer. It can be seen from Fig. 12(*a*) that the maximum sensible heat transfer shows an apparent decrease from about 40 W to 35 W and the frequency is also increased. Similar variations occur in the latent heat transfer in Fig. 12(*b*), where the maximum latent heat transfer experiences a 30% decrease. The average sensible heat transfer after the doubling the particle size is about 23.68 W while the evaporation heat transfer is around 0.53 W. Thus, doubling the particle size has a negative effect on the heat transfer performance of the tube, which can greatly decrease the latent heat transfer and weaken overall heat transfer. The effects of various parameters on the sensible and latent heat transfer are summarized in Table 1.

6 Conclusions

The effect of internal wick structure on the oscillatory flow and heat transfer performance of an oscillating heat pipe is investigated in this paper. The results show that the addition of the wick greatly increases the latent heat transfer as expected and the sensible heat transfer is also increased. The increase in latent heat transfer causes increases vapor plug temperature and pressure and the amplitude of the liquid slug oscillation as well. The overall

Table 1 Effect of parameters on the performance of the *U*-shaped minichannel

Type of miniature tube	D (mm)	T_h (°C)	Particle size (mm)	$Q_{sensible}$ (W)	Q_{latent} (W)	Q_{total} (W)
Without wick	1.5	120	0.135	22.39	0.39	22.78
With wick	1.5	120	0.135	26.67	0.74	27.41
	2.0	120	0.135	43.74	0.85	44.59
	1.5	90	0.135	12.84	0.33	13.17
	1.5	120	0.27	23.68	0.53	24.21

heat transfer is enhanced by increasing channel diameter but decreased by decreasing heat section temperature and increasing particle diameter.

Acknowledgment

The work presented in this article was funded by the Office of Naval Research Grant No. N00014-06-1-1119 directed by Dr. Mark Spector.

Nomenclature

A = area, m^2
c_p = specific heat at constant pressure, J/kg K
c_v = specific heat at constant volume, J/kg K
d = diameter of the miniature channel, m
h_c = condensation heat transfer coefficient, W/m^2 K
h_e = evaporation heat transfer coefficient, W/m^2 K
h_{lv} = latent heat, J/kg
k = thermal conductivity, W/m
K = curvature of meniscus, 1/m
L = length, m
m = mass of vapor plugs, kg
N = number of the thin film
p_d = disjoining pressure, N/m^2
r = curvature radius of the meniscus, m
p = vapor pressure, Pa
$q_{p,\mathrm{con}}$ = condensation heat transfer on a single particle, W
$q_{p,\mathrm{eva}}$ = evaporation heat transfer on a single particle, W
$Q_{\mathrm{con},p}$ = total condensation heat transfer, W
$Q_{\mathrm{eva},p}$ = total evaporation heat transfer, W
$Q_{\mathrm{in},s,l}$ = sensible heat transfer into the liquid slug, W
$Q_{\mathrm{out},s,l}$ = sensible heat transfer from the liquid slug, W
R = gas constant, J/kg K
t = time, s
T = temperature, K
x_p = displacement of the liquid slug, m
Z = velocity of the liquid slug, m/s

Greek symbols

α = thermal diffusivity, m^2/s
β = contact angle, deg
δ = film thickness, m
ε = porosity
γ = ratio of specific heat
ν = kinematic viscosity, m^2/s
ρ = density, kg/m^3
σ = surface tension, N/m
τ_p = shear stress, N/m^2

Subscripts

0 = initial condition
1 = left vapor plug
2 = right vapor plug
c = condenser
d = disjoining
D = diameter
e = evaporator
l = liquid
p = plug
sp = particle surface
v = vapor
w = the wall of the tube

References

[1] Akachi, H., 1994, "Looped Capillary Heat Pipe," Japanese Patent No. Hei697147.
[2] Zhang, Y., and Faghri, A., 2008, "Advances and Unsolved Issues in Pulsating Heat Pipes," Heat Transfer Eng., **29**(1), pp. 20–44.
[3] Lee, W. H., Jung, H. S., Kim, J. H., and Kim, J. S., 1999, "Flow Visualization of Oscillating Capillary Tube Heat Pipe," *Proceedings of the 11th International Heat Pipe Conference*, Tokyo, Japan, pp. 131–136.
[4] Khandeker, S., Schneider, M., Schafer, P., Kulenovic, R., and Groll, M., 2002, "Thermo-Fluid-Dynamic Study of Flat Plate Closed Loop Pulsating Heat Pipes," Microscale Thermophys. Eng., **6**(4), pp. 303–318.
[5] Shafii, M. B., Faghri, A., and Zhang, Y., 2001, "Thermal Modeling of Unlooped and Looped Pulsating Heat Pipes," ASME J. Heat Transfer, **123**, pp. 1159–1171.
[6] Dobson, R. T., and Harms, T. M., 1999, "Lumped Parameter Analysis of Closed and Open Oscillatory Heat Pipes," *Proceedings of the 11th International Heat Pipe Conference*, Tokyo, Japan, pp. 159–142.
[7] Zhang, Y., and Faghri, A., 2002, "Heat Transfer in a Pulsating Heat Pipe With Open End," Int. J. Heat Mass Transfer, **45**(4), pp. 775–784.
[8] Wong, T. N., Tong, B. Y., Lim, S. M., and Ooi, K. T., 1999, "Theoretical Modeling of Pulsating Heat Pipe," *Proceedings of the 11th International Heat Pipe Conference*, Tokyo, Japan, pp. 159–163.
[9] Hosoda, M., Nishio, S., and Shirakashi, R., 1999, "Meandering Closed-Loop Heat-Transfer Tube (Propagation Phenomena of Vapor Plug)," *Proceedings of the Fifth ASME/JSME Joint Thermal Engineering Conference*, San Diego, CA, March 15–19.
[10] Zhang, Y., Faghri, A., and Shafii, M. B., 2002, "Analysis of Liquid-Vapor Pulsating Flow in a U-Shaped Miniature Tube," Int. J. Heat Mass Transfer, **45**, pp. 2501–2508.
[11] Xu, J., and Zhang, Y., 2009, "Analysis of Heat Transfer during Liquid-Vapor Pulsating Flow in a U-Shaped Miniature Channel," J. Enhanced Heat Transfer, to be published.
[12] Faghri, A., 1995, *Heat Pipe Science and Technology*, Taylor & Francis, Washington, DC.
[13] Zuo, Z. J., North, M. T., and Ray, L., 1999, "Combined Pulsating and Capillary Heat Pipe Mechanism for Cooling of High Heat Flux Electronics," *Proceedings of the ASME Heat Transfer Division*, Nashville, TN.
[14] Holley, B., and Faghri, A., 2005, "Analysis of Pulsating Heat Pipe With Capillary Wick and Varying Channel Diameter," Int. J Heat Mass Transfer, **48**, pp. 2635–2651.
[15] Ma, H. B., and Peterson, G. P., 1997, "Temperature Variation and Heat Transfer in Triangular Grooves With an Evaporating Film," J. Thermophys. Heat Transfer, **11**, pp. 90–97.
[16] Hanlon, M. A., and Ma, H. B., 2003, "Evaporation Heat Transfer in Sintered Porous Media," ASME J. Heat Transfer, **125**, pp. 644–652.
[17] Carey, V. P., 1992, *Liquid-Vapor Phase-Change Phenomena: An Introduction to the Thermophysics of Vaporization and Condensation Processes in Heat Transfer Equipment*, Hemisphere, Washington, DC.

A Statistical Model of Bubble Coalescence and Its Application to Boiling Heat Flux Prediction—Part I: Model Development

Wen Wu
e-mail: wen.wu@gat.com

Barclay G. Jones
e-mail: bgjones@uiuc.edu

Department of Nuclear, Plasma, and Radiological Engineering,
University of Illinois at Urbana Champaign,
Urbana, IL 61801

Ty A. Newell
Department of Mechanical Science and Engineering,
University of Illinois at Urbana Champaign,
Urbana, IL 61801
e-mail: tynewell@uiuc.edu

In this work a statistical model is developed by deriving the probability density function (pdf) of bubble coalescence on boiling surface to describe the distribution of vapor bubble radius. Combining this bubble coalescence model with other existing models in the literature that describe the dynamics of bubble motion and the mechanisms of heat transfer, the surface heat flux in subcooled nucleate boiling can be calculated. By decomposing the surface heat flux into various components due to different heat transfer mechanisms, including forced convection, transient conduction, and evaporation, the effect of the bubble motion is identified and quantified. Predictions of the surface heat flux are validated with R134a data measured in boiling experiments and water data available in the literature, with an overall good agreement observed. Results indicate that there exists a limit of surface heat flux due to the increased bubble coalescence and the reduced vapor bubble lift-off radius as the wall temperature increased. Further investigation confirms the consistency between this limit value and the experimentally measured critical heat flux (CHF), suggesting that a unified mechanistic modeling to predict both the surface heat flux and CHF is possible. In view of the success of this statistical modeling, the authors tend to propose the utilization of probabilistic formulation and stochastic analysis in future modeling attempts on subcooled nucleate boiling.
[DOI: 10.1115/1.4000024]

1 Introduction

Boiling, a type of phase transition, is defined as being the process of the addition of heat to a liquid in such a way that generation of vapor occurs [1]. Liquid boiling can occur within the liquid or at the interface of liquid-to-solid. The former is called homogeneous boiling, while the latter is termed as heterogeneous boiling. Heterogeneous boiling occurs in three characteristic stages, nucleate, transition, and film boiling. These stages generally take place from low to high surface temperatures.

Nucleate boiling is characterized by the incipience and growth of bubbles on a heated surface. The bubbles rise from discrete points on a surface, whose temperature is only slightly above the liquid's saturation temperature. In general, the number of nucleation sites on a surface increases with an increasing surface temperature. An irregular boiling surface (i.e., increased surface roughness) can create additional nucleation sites, while an exceptionally smooth surface, such as glass, tends to reduce this number under the same surface temperature conditions or to require more superheating of the surface for the same number of nucleation sites.

Nucleate boiling provides a means to obtain high heat flux with relatively low wall superheat and is of key importance in a wide range of industrial applications including power generation, chemical and petroleum production, air conditioning, refrigeration, etc. Typically, the forced convective nucleate boiling is encountered in heat exchangers during normal and non-normal modes of operation in pressurized water reactors (PWRs) or boiling water reactors (BWRs), which are popular in many nuclear power plants.

A very wide variety of studies on the prediction of wall heat flux of the nucleate boiling have been performed in the past. Two branches of approaches generally exist. Development of empirical formulas by correlating measured data is often useful for quick design purposes. However, since the formulas lack an accurate representation of the competing heat transfer mechanisms, they can rarely be applied with confidence to new situations. Development of mechanistic models by considering the root cause of boiling is regarded as possibly being able to provide the fundamental explanation for the boiling phenomenon. However, attempts that have been made during the past few decades are of limited success, in part, due to the complexity of the problem itself. Particularly, the existence of vapor bubbles and the coalescence between them impose great difficulties not only in mechanistic modeling but also in direct numerical simulation study. A brief overview of both the empirical correlations and the mechanistic models is first provided below, followed by the details of the model development in this study. Since the empirical correlations are generally not able to completely capture the underlying physics, they are not of particular interest in this study and are not comprehensively reviewed.

In the early studies of heat flux and boiling prediction, numerous correlations specific to water were developed, since water is widely used in forced convection, i.e., in power generation systems. One of the best known correlations was given by Jens and Lottes [2], which relates the wall superheat to the heat flux and pressure in a dimensional form

Manuscript received January 29, 2009; final manuscript revised July 16, 2009; published online October 15, 2009. Assoc. Editor: Yogesh Jaluria.

$$\Delta T_{sat} = 25q^{0.25}e^{-P/62} \tag{1}$$

where ΔT_{sat} is in K, q is in MW/m^2, and P is in bars. An improved equation giving a closer fit to the experimental data was suggested by Thom et al. [3]

$$\Delta T_{sat} = 22.5q^{0.5}e^{-P/87} \tag{2}$$

These equations are valid up to pressures of around 200 bars and may be used for subcooled boiling and forced convection boiling when the nucleate boiling contribution is dominant.

Bowring [4] was the first to identify different heat transfer mechanisms in wall heat flux (q_w) modeling. Observing bubble motion on the heated surface, he proposed that q_w should have three components: single-phase heat transfer (q_{sp}), evaporation (q_{ev}), and the sensible heating of the liquid that occupies the volume vacated by a departing bubble (q_{pump}). Thus, the wall heat flux could be expressed as

$$q_w = q_{sp} + q_{ev} + q_{pump} = q_{sp} + (1+\varepsilon)q_{ev} = h_{sp}(T_{sat} - T_B) + q_{ev}(1+\varepsilon) \tag{3}$$

where $\varepsilon = q_{pump}/q_{ev}$ and was found empirically. The evaporation heat flux q_{ev} was given by the expression

$$q_{ev} = \rho_v h_{fg} V_b f N_a \tag{4}$$

where f is the frequency of the bubbles and N_a is the active nucleation site density. The single-phase component can be calculated from other standard correlations. The ratio ε was then correlated by:

$$\varepsilon = \begin{cases} 1 + 3.2\dfrac{\rho_l c_{pl}\Delta T_{sub}}{\rho_v h_{fg}} & 1 \le P \le 9.5 \\ 2.3 & 9.5 \le P \le 50 \\ 2.6 & P \ge 50 \end{cases} \tag{5}$$

where P is pressure in bars. Taking q_{ev} and q_{sp} from Eq. (3), q_{pump} can be calculated. Bowring used experimental data for vertical upflow in rectangular channels with pressures varying from 1.1 MPa to 13.6 MPa, heat fluxes varying from 30 W/cm^2 to 160 W/cm^2, and velocities varying from 0.8 m/s to 2.0 m/s, and for all ranges of subcooling.

Rouhani and Axelsson [5] extended Bowring's model. In their study q_{sp} was expressed in terms of wall voidage, meaning that this mechanism only works until the surface gets fully covered with vapor bubbles. Unlike Bowring, they expressed q_{pump} independently, proposing that the liquid replacing the departing vapor bubble should be heated through a temperature gradient equal to the mean liquid subcooling. Dix [6] also applied Bowring's model in his study, using R114 as the working fluid for his experiments, while the pressures varied from 0.35 MPa to 0.8 MPa, and mass fluxes varied from 50 kg/m^2 s to 820 kg/m^2 s.

Several other studies [7–9] have adopted Bowring's model. However, most of them have ignored the contribution of heat transfer due to liquid circulation caused by bubbles disrupting the boundary layer, and have only considered q_{sp} and q_{ev} as the two components of the wall heat flux. In most of these models q_{ev} was indirectly calculated using the supplied q_w and q_{sp}. For example, Maroti [8] calculated q_{ev} by assuming the fraction of wall heat flux utilized for vapor generation was proportional to the superheated part of the liquid thermal layer, and applied his model to water pressures ranging from 2.7 MPa to 13.8 MPa. Assuming a linear temperature profile in the liquid, he derived an expression for the evaporation heat flux as

$$q_{ev} = q_w\left(\frac{\Delta T_w}{\Delta T_w + \Delta T_{sub}}\right)^2 \tag{6}$$

The wall heat flux was assumed to be given by

$$q_w = h_{boil}\Delta T_w \tag{7}$$

where $h_{boil} = K\Delta T^n$, with $K = 22P^{0.58}$ and $n = 3.33$. In Eq. (7), pressure P is in atmosphere.

Recent approaches to mechanistic heat flux prediction started to consider bubble motions in addition to the heat flux components due to different heat transfer mechanisms. Sateesh et al. [10] studied the effect of bubble sliding on the heating surface and applied the results to pool boiling heat transfer. Bubble departure and bubble lift-off were incorporated into their model. The liquid circulation caused by bubbles disrupting the boundary layer was taken into account. They considered different mechanisms such as latent heat transfer due to microlayer evaporation (q_{me}), transient conduction due to thermal boundary layer reformation (q_{tc}), natural convection (q_{nc}), and heat transfer due to the sliding bubbles (q_{tcs}). Good agreement was observed when the experimental results of other researchers [11–13] were compared with the validated model. They performed an analytical mechanistic study on the estimation of heat flux components using an area ratio parameter defined as the ratio of available area per nucleation site to the projected area of the bubble at departure, and assuming no coalescence

$$R = \frac{A/N_a}{A_d} \tag{8}$$

to accommodate the effect of bubble coalescence.

From this definition, at any length of time, the number of active nucleation sites became equal to RN_a

$$RN_a = \frac{A/N_a}{A_d}\frac{n_a}{A} = \frac{1}{A_d} \tag{9}$$

Their analysis indicated a high fraction of the heat transfer due to transient conduction and a significant contribution of the sliding bubbles for water boiling on a vertical wall at atmospheric pressure. For an organic liquid, the contribution of microlayer evaporation became comparable with transient conduction at lower pressures, and its contribution dominated at high pressure.

Basu et al. [14] performed a similar wall heat flux partitioning study for subcooled flow boiling. They systematically studied contributions from different heat transfer mechanisms (q_{me}, q_{tc}, and q_{fc}) and considered the effect of bubble sliding. Bubble mergers (coalescence) were considered based on a merge-slide assumption, i.e., after bubbles coalesce, they form a larger bubble, with the new volume equal to the combined volumes of the participating bubbles, and continue to stay on the heated surface until the lift-off criterion is met. Two different cases, bubble merger with and without sliding, were considered, corresponding to low-to-medium heat fluxes and high heat flux cases, respectively.

In the study of Basu et al., a number of dimensional and nondimensional correlations were developed based on their experimental results at a low pressure range (0.1–0.22 MPa) using water to provide the required parameters in their prediction, which included the nucleation site density N_a, bubble departure and bubble lift-off diameters d_d and d_l, bubble waiting time and bubble growth time t_w and t_g, respectively. Model predictions were then compared with their experimental data, as well as other data sets in the literature. Overall good agreement was obtained even at higher pressure ranges up to 3.1 MPa when compared with Morozov's results on water [15]. The authors stated that the critical submodels were believed to be those related to the bubble diameters and bubble release frequency and that it would be essential to acquire additional experimental data covering those conditions.

From the overview above, it is evident that existing models are characterized by their deterministic attempts for the prediction of wall heat flux in pool/flow boiling. In earlier approaches, one or more of the heat flux components were obtained as ratios of other components. In more recent approaches, the division of the wall heat flux was correctly done, while some or all of the underlying subprocess modeling were deterministically performed. The key

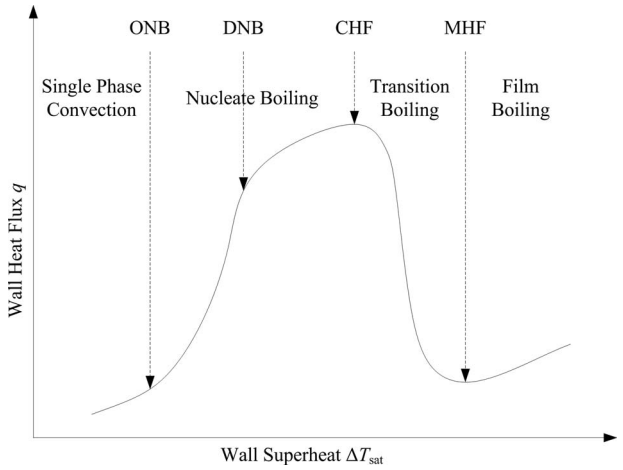

Fig. 1 Typical flow boiling curve

fundamental phenomena of bubble coalescence and its stochastic characteristics were not captured and sufficiently modeled, particularly, in a statistical way. Consequently, no existing models were able to predict the existence of the heat transfer capacity limit, i.e., the critical heat flux (CHF), as the wall superheat increased.

The present investigation attempts to incorporate the effect of stochastic bubble motion in order to obtain a more realistic model of the boiling heat transfer process. To achieve this goal, a probability density function (*pdf*) of the stochastic bubble coalescence on the heated surface is derived and mathematically interpreted as the ratio of bubbles with different radii. A mechanistic model based on basic principles is proposed in which heat flux components contributed by different mechanisms are identified. In conjunction with the formulation of bubble coalescence probability, the total heat flux is evaluated when bubble coalescence is present.

2 Model Development

The model developed in this paper attempts to predict the subcooled nucleate boiling heat flux from given wall superheat, i.e., to predict the boiling curve, from the single-phase forced convection region up to CHF. A qualitative boiling curve in Fig. 1 shows the dependence of the wall heat flux q on the wall superheat $\Delta T_{sat}=T_w-T_{sat}$. Following the increase of the wall superheat along the boiling curve, there are several events that characterize different stages of the boiling.

1. Onset of nucleate boiling (ONB) at which the first bubble forms on the heated surface. ONB characterizes the transition from single-phase forced convection heat transfer to two phase nucleate boiling heat transfer. The surface heat flux increases much faster thereafter compared with the single-phase heat transfer before the ONB.
2. Departure from nucleate boiling (DNB) at which a less rapid surface heat flux rise is observed on the boiling curve. It conveys a signal that the heated surface reaches its peak capacity to transport energy from the surface to the liquid flow.
3. Critical heat flux at which an abrupt decrease in heat flux is observed on a temperature-controlled surface. CHF characterizes the termination of nucleate boiling and initiation of transition to film boiling.
4. Minimum heat flux (MHF) at which a stable vapor film is formed on the heated surface. MHF characterizes the initiation of stable film boiling.

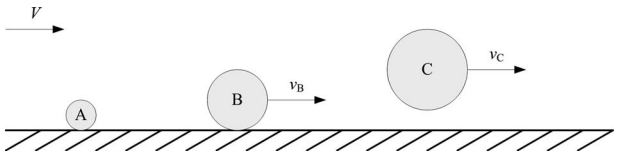

Fig. 2 Bubble in different stages during its life span

The fundamental idea underlying the proposed model is that energy from the heated wall is first transferred to the liquid layer adjacent to the wall, and thereafter from this superheated liquid layer, energy is transferred to the vapor bubble by evaporation while the remainder goes to the bulk liquid [14]. During the process of bubble growth and bubble collapse, a large portion of the energy is transported from the heated surface directly to the highly subcooled bulk region in the form of latent heat. Meanwhile, direct heat transfer to the bulk liquid is also enhanced by the motion of bubbles.

Bubbles on the heated surface typically experience several status changes following their formation until they collapse in the bulk region. As shown in Fig. 2, a bubble can sit/stay on the position where it is generated (A), slide along the heating surface (B), or float in the bulk region (C). Correspondingly, the events that characterize the change of the status of a bubble include bubble generation, bubble departure, and bubble lift-off. Meanwhile, a bubble keeps growing when it remains in contact with the heated surface.

The proposed model couples the heat flux evaluation to the motion of vapor bubbles. Prediction is expected to be only available and valid before reaching CHF because as vapor film starts to build up, the transfer of energy is controlled by completely different mechanisms, e.g., radiation and conduction, and therefore invalidates the basis of the model.

2.1 Statistical Bubble Coalescence. When there are more than one bubble staying on the heated surface, during bubble growth and bubble movement, one may coalesce with another on the heating surface if they are sufficiently close.

Two different types of assumptions can be made when bubbles coalesce, i.e., coalesce-slide or coalesce-lift-off. For coalesce-slide, the newly formed bubble continues to slide and grow on the heated surface. It may coalesce with other bubbles until the criterion for lift-off is reached. For coalesce-lift-off, the newly formed bubble directly leaves the heated surface and enters the bulk region. It is observed in virtually all of our experiments with R134a that the existence of wall generally forces the newly formed bubble to leave the heated surface directly when two or more bubbles coalesce. Only in some rare cases, e.g., when the difference between the two-bubble sizes is great or there exists a suitable local flow field with suitable velocity gradient, the new bubble may remain attached to the heated surface or leave but may be blown back onto the surface to continue its growth. Hence, in this model, the theoretical derivation for bubble coalescence probabilities is based on the coalesce-lift-off assumption.

Bubble coalescence can happen between two stationary bubbles, one stationary bubble and one sliding bubble, or two sliding bubbles. It is also discovered that bubbles after their lift-off stay in the boundary layer for a certain time before they enter the bulk region. Some bubbles during this period may coalesce with bubbles growing on the heated surface. However, due to the small population of this type of event, this coalescence is neglected.

2.1.1 Basic Assumptions. Bubbles are generated from active nucleation sites on the heated surface. The placing of the active nucleation sites is a homogeneous spatial Poisson process, i.e., given the active nucleation site density N_a, the observed number of active nucleation sites n_a on the heated surface has the Poisson distribution [11]

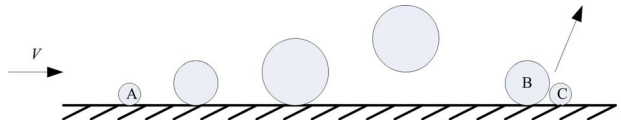

Fig. 3 Bubble life span and bubble coalescence

$$P(n_a) = \frac{e^{-(N_a A_S)}(N_a A_S)^{n_a}}{n_a!} \tag{10}$$

in which A_S is the surface area. From the definition of homogeneous spatial Poisson process, it can be mathematically proven that the active nucleation sites on the heated surface form a uniform distribution (Appendix).

Based on the observation that bubble generation and bubble coalescence are also random processes associated with the randomly distributed active nucleation sites, several basic assumptions are made, from which a statistical model is composed to explain this physical phenomena quantitatively. First, bubbles originating from any single nucleation site are assumed to be generated at a constant frequency f_b, which is calculated from the bubble departure and lift-off model based on the experimental conditions. Second, the condition for two-bubble coalescence is defined as two perfectly spherical bubbles intersecting with each other in three-dimensional (3D) space.

2.1.2 Probabilities of Two-Bubble Coalescence. In order to calculate the probabilities of two-bubble coalescence, it is necessary to first rephrase this problem by using the appropriate mathematical language. Figure 3 illustrates the bubble life span and bubble coalescence phenomena. Consider a flat heated surface, on top of which there exists a flow field with $v>0$. Assume that the surface is sufficiently heated to generate vapor bubbles, starting from bubble generation at $t=0$; the position x and radius r of each bubble can be described by functions $x(t)$ and $r(t)$, respectively, if it is isolated from any other bubbles.

As shown in Fig. 4, starting from bubble generation, each bubble is assumed to stay on its bubble site for t_d and then to slide along the heated surface with a certain sliding velocity from t_d to t_l. The bubble leaves the heated surface at t_l. During its whole life span, the bubble growth rate is controlled by the model discussed in Sec. 2.4.3.

From the uniformly distributed active nucleation sites and the assumption of evenly generated vapor bubbles, the density of bubbles on the heated surface statistically remains at constant N_b and, thus, any single bubble may coalesce with another bubble during any time interval of its life span with a certain finite probability. Once there is coalescence, two bubbles are assumed to leave the heated surface simultaneously and sufficiently fast so

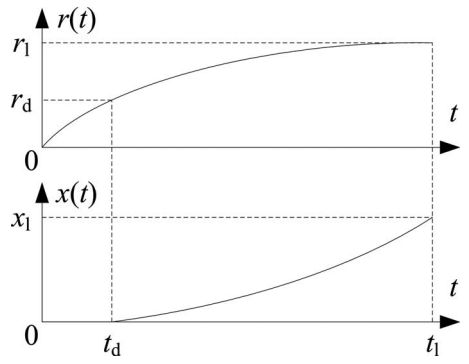

Fig. 4 Simplified bubble growth and bubble sliding curves

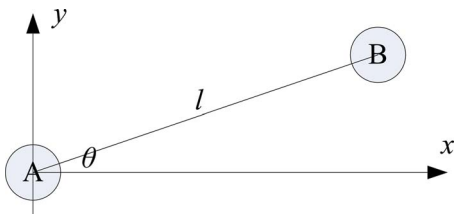

Fig. 5 Bubble relative position

that they do not affect the motion of other bubbles.

This is a continuous probability problem. Therefore, the question is raised as: what is the probability density function (*pdf*) of a bubble coalescing with other bubbles at any time?

Consider the 3D distance between the bubbles shown in Fig. 5 for a bubble A generated at $t=0$, $\boldsymbol{u}=0$, for $t>0$

$$\boldsymbol{u}(t) = \hat{x}\cdot x(t) + \hat{y}\cdot 0 + \hat{z}\cdot r(t) \tag{11}$$

Consider another bubble B generated at $t=\tau$, $\boldsymbol{v}=\hat{x}\cdot l\cos\theta + \hat{y}\cdot l\sin\theta$, for $t>\tau$

$$\boldsymbol{v}(t) = \hat{x}\cdot[x(t-\tau) + l\cos\theta] + \hat{y}\cdot l\sin\theta + \hat{z}\cdot r(t-\tau) \tag{12}$$

The distance between these two bubbles $\boldsymbol{v}(t)-\boldsymbol{u}(t)$ is then

$$\boldsymbol{v}(t) - \boldsymbol{u}(t) = \hat{x}\cdot[x(t-\tau) + l\cos\theta - x(t)] + \hat{y}\cdot l\sin\theta + \hat{z}\cdot[r(t-\tau) - r(t)] \tag{13}$$

The sum of their radii is

$$r(t) + r(t-\tau) \tag{14}$$

According to the assumption made on bubble coalescence, the condition of A coalescing with B at time t is

$$|\boldsymbol{v}(t) - \boldsymbol{u}(t)| \le r(t) + r(t-\tau) \quad \text{for} \quad t - t_l \le \tau \le t \tag{15}$$

Rearrange to obtain

$$l^2 - 2l\cos\theta[x(t) - x(t-\tau)] + [x(t) - x(t-\tau)]^2 - 4r(t)r(t-\tau) \le 0 \tag{16}$$

Therefore, the condition of A coalescing with B at time t is

$$l_1 \le l \le l_2 \tag{17}$$

in which

$$l_{1,2} = \cos\theta[x(t) - x(t-\tau)] \mp \sqrt{4r(t)r(t-\tau) - \sin^2\theta[x(t) - x(t-\tau)]^2} \tag{18}$$

Now if it is assumed that during the life span of A there is another bubble B generated within $[0, x_l]$ with probability of 1, with the uniformly distributed nucleation sites, l is a random variable that is evenly distributed within $[0, x_l]$. Therefore, the probability of A coalescing with B during its life span, which corresponds to l having an appropriate value between l_1 and l_2, is

$$P_{i;B} = \frac{\int_0^{t_l} dt \int_{t-t_l}^{t} d\tau \int_0^{2\pi} d\theta 2\sqrt{4r(t)r(t-\tau) - \sin^2\theta[x(t) - x(t-\tau)]^2}}{\int_0^{t_l} dt \int_{t-t_l}^{t} d\tau \int_0^{2\pi} d\theta x_l} \tag{19}$$

Rearrange to obtain

$$P_{i;B} = \int_0^{t_l} dt \int_{t-t_l}^{t} d\tau \int_0^{2\pi} d\theta \times \left\{ \frac{1}{\pi t_l^2 x_l} \sqrt{4r(t)r(t-\tau) - \sin^2\theta[x(t) - x(t-\tau)]^2} \right\} \tag{20}$$

This probability is calculated based on the assumption that B is generated within the range of $[0, x_l]$. However, it is usually more convenient to perform a calculation based on the assumption of B

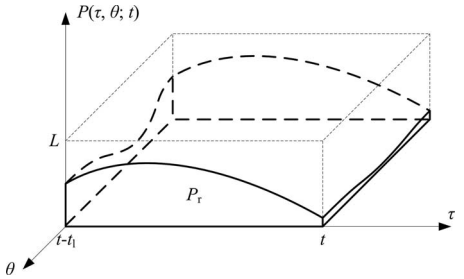

Fig. 6 Bubble coalescence probability

being generated within the range of $[0, L]$, where L is the average distance between two adjacent nucleation sites. In this case, the probability of A coalescing with B during its life span is given as

$$P_i = \int_0^{t_l} dt \int_{t-t_l}^{t} d\tau \int_0^{2\pi} d\theta \times \left\{ \frac{1}{\pi t_l^2 L} \sqrt{4r(t)r(t-\tau) - \sin^2\theta[x(t) - x(t-\tau)]^2} \right\} \quad (21)$$

the probability of A not coalescing with B during its life span is given as

$$\begin{aligned} P_{ni} &= 1 - \int_0^{t_l} dt \int_{t-t_l}^{t} d\tau \int_0^{2\pi} d\theta \times \left\{ \frac{1}{\pi t_l^2 L} \sqrt{4r(t)r(t-\tau) - \sin^2\theta[x(t) - x(t-\tau)]^2} \right\} \\ &= \int_0^{t_l} dt \int_{t-t_l}^{t} d\tau \int_0^{2\pi} d\theta \times \left\{ \frac{0.5L - \sqrt{4r(t)r(t-\tau) - \sin^2\theta[x(t) - x(t-\tau)]^2}}{\pi t_l^2 L} \right\} \end{aligned} \quad (22)$$

Figure 6 illustrates the coalescence probability, which is the total volume of P_r confined by the range of l, divided by the total volume enclosed with the dash line, within which B is assumed to be generated. The probability density function (pdf) of A coalescing with B by definition is

$$p_i(t, \theta, \tau) = \frac{1}{\pi t_l^2 L} \sqrt{4r(t)r(t-\tau) - \sin^2\theta[x(t) - x(t-\tau)]^2} \quad (23)$$

The integral of $p_i(t, \theta, \tau)$ in Eq. (21) is less than 1 because in this problem bubbles may lift-off naturally as a result of bubble growth. By integrating over θ and τ, the pdf of A coalescing with a single bubble is given as

$$p_i(t) = \int_{t-t_l}^{t} d\tau \int_{-\pi}^{\pi} d\theta \cdot p_i(t, \theta, \tau) \quad (24)$$

Correspondingly, the cumulative distribution function is

$$P_i(t) = \int_0^t dt \cdot p_i(t) \quad (25)$$

The probability density function (pdf) of A not coalescing with B by definition is

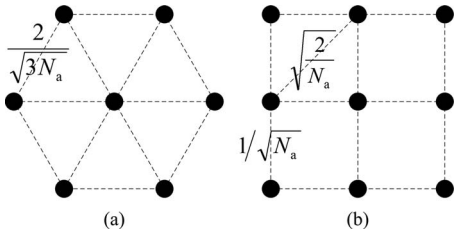

Fig. 7 Nucleation site arrangement and compaction factor

$$p_{ni}(t, \theta, \tau) = \frac{1}{\pi t_l^2 L} \left(\frac{L}{2} - \sqrt{4r(t)r(t-\tau) - \sin^2\theta[x(t) - x(t-\tau)]^2} \right) \quad (26)$$

By integrating over θ and τ, the unconditional pdf of A coalescing with any single bubble is given as

$$p_{ni}(t) = \int_{t-t_l}^{t} d\tau \int_{-\pi}^{\pi} d\theta \cdot p_{ni}(t, \theta, \tau) = \frac{1}{t_l} - p_i(t) \quad (27)$$

The corresponding cumulative distribution function is

$$P_{ni}(t) = \int_0^t dt \cdot p_{ni}(t) \quad (28)$$

2.1.3 Nucleation Site Arrangement and Compaction Factor. On a boiling surface, the average distance of nucleation sites L is defined by the nucleation site density N_a. For a compact two-dimensional (2D) arrangement

$$L = 4/\sqrt{3 \times N_a} \quad (29)$$

as shown in Fig. 7(a). In most literature, however, L was calculated via

$$L = 1/\sqrt{N_a} \quad (30)$$

by assuming a square grid in Fig. 7(b), which is incorrect, as the distances between the neighbor elements in Fig. 7(b) are not uniform. The real average distance should lie in between by taking the average in some manner. By comparing Figs. 7(a) and 7(b), we observe that

$$\frac{1}{\sqrt{N_a}} \leq \frac{2}{\sqrt{3N_a}} \leq \sqrt{\frac{2}{N_a}} \quad (31)$$

which confirms this assertion. Indeed, what Eq. (30) gives is the average nearest-neighbor distance [11].

2.1.4 Probabilities of Multiple Coalescences During Bubble Life Span. With increased wall superheat, ΔT_{sat}, N_a increases and L decreases, while t_l and t_d both increase. As the overall effect, there can be on average more than one bubble existing along the path swept by the sliding bubble A.

The number of bubbles that can potentially coalesce with bubble A can be calculated by

$$N_b \approx \frac{t_l}{t_d + t_w} \cdot \frac{(t_l - t_d)V_s + r_l + \bar{r}_l}{L} \approx \frac{t_l}{t_d + t_w} \cdot \frac{(t_l - t_d)V_s + \frac{5}{3}r_l}{L} \quad (32)$$

The first term is the average number of bubbles that are generated from a nucleation site during the bubble life span, while the second term is the average number of nucleation sites that the trajectory of a sliding bubble covers. The influence of a bubble during sliding is illustrated in Fig. 8.

Therefore, the cumulative distribution function of a bubble not coalescing with one of these N_b bubbles during sliding is

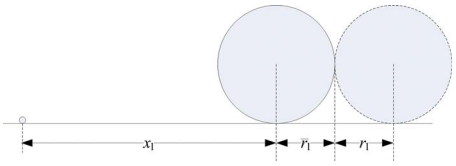

Fig. 8 Influence of bubble during its sliding

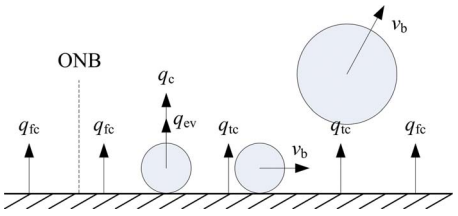

Fig. 9 Heat transfer mechanisms at and near the wall

$$P_{ni,N_b}(t) = P_{ni}^{N_b}(t) \tag{33}$$

The *pdf* of a bubble not coalescing with any of these N_b bubbles during its sliding is

$$p_{ni,N_b}(t) = \frac{d}{dt}P_{ni,N_b}(t) = N_b P_{ni}^{N_b-1}(t)p_{ni}(t) \tag{34}$$

Similarly, the cumulative distribution function of a bubble coalescing with any of these N_b bubbles during sliding is

$$P_{i,N_b}(t) = \left(\frac{t}{t_l}\right)^{N_b} - P_{ni,N_b}(t) \tag{35}$$

The *pdf* of a bubble coalescing with any of these N_b bubbles during sliding is

$$p_{i,N_b}(t) = \frac{d}{dt}P_{i,N_b}(t) = \frac{N_b t^{N_b-1}}{t_l^{N_b}} - \frac{d}{dt}P_{ni,N_b}(t)$$

$$= \frac{N_b t^{N_b-1}}{t_l^{N_b}} - N_b P_{ni}^{N_b-1}(t)p_{ni}(t) \tag{36}$$

2.1.5 Conditional Bubble Coalescence Probability and Ergodic Principle. Based on the coalesce-lift-off assumption, once a bubble coalesces with another bubble, these two bubbles form a new larger bubble and leave the heated surface immediately. Thus, for a bubble that actually coalesces with another bubble at time t, it must satisfy the requirement that it should not coalesce with any bubbles during time interval $(0,t)$. Therefore, the conditional *pdf* of a bubble coalescing with other bubbles is the unconditional *pdf* divided by the probability that it does not coalesce with any of these bubbles during $(0,t)$, which is given by

$$p_{i,c}(t) = \frac{p_{i,N_b}(t)}{P_{ni,N_b}(t)} = \frac{N_b}{t_l^{N_b}}\frac{t^{N_b-1} - t_l^{N_b}P_{ni}^{N_b-1}(t)p_{ni}(t)}{P_{ni}^{N_b}(t)} \tag{37}$$

If we discretize t into $n_g\ \Delta t$ intervals, then

$$p_{i,c} \doteq p_{i,c}(t_i)\Delta t \tag{38}$$

is the probability of a bubble leaving the heated surface during the $(t_i, t_i+\Delta t)$ interval.

From the ergodic principle, if a total of N_b bubbles are observed simultaneously, $p_{i,c}$ can be interpreted as the portion of N_b bubbles in the ith group that leaves the heated surface at t_i as the result of bubble coalescence. From this interpretation, bubbles on the heated surface can be treated as if there are simply n_g groups of bubbles, with each group containing a certain portion $(p_{i,c})$ of the total. In each group, bubbles behave the same by staying on the heated surface for t_i and then lift-off.

2.2 Mechanisms of Flow Boiling Heat Transfer. Following the mechanistic approach of Basu et al., the surface heat flux can be divided into several components due to different heat transfer mechanisms, with each of them being quantified independently. Their proposed fundamental principle is that energy from the wall is first transferred to the liquid layer adjacent to the heated wall and thereafter from this superheated liquid layer, energy is transferred to the vapor bubble by evaporation while the remainder goes to the bulk liquid [14], which is adopted in this study. In this section the energy balance is addressed, followed by the definition and expression of each heat flux component. In combining with the bubble coalescence probability and the bubble grouping information derived from the ergodic principle in Sec. 2.1, the total surface heat flux is quantified in Sec. 2.3.

2.2.1 Energy Conservation. Shown in Fig. 9, several different heat transfer mechanisms are identified in the subcooled nucleate boiling region. Upstream of ONB, the energy is transferred via single-phase forced convection (Q_{fc}) over the whole heated surface. Therefore

$$q_w = \frac{Q_{fc}}{A} = q_l \tag{39}$$

where q_l denotes the heat flux sensed by the liquid. At downstream of ONB, single-phase forced convection continues to occur on the heated surface not occupied by bubbles, which results in sensible heating of the liquid. A thin layer of superheated liquid is, therefore, formed on the heated surface from which bubbles can be generated. During their growth, bubbles continue to obtain energy from this layer (Q_{ev}). Meanwhile, due to the existence of subcooled bulk liquid, condensation (Q_c) may happen near the top of the bubble, which provides an alternate route for heat transfer from the wall to the bulk liquid other than the forced convection.

During bubble sliding and bubble lift-off, the superheated boundary layer is disrupted and the space behind the bubble is filled with colder liquid. Transient conduction (Q_{tc}) is the major mechanism in helping rebuild the superheated thermal boundary layer. As bubbles grow, they lift-up the thermal boundary layer rather than penetrating through it. Besides, the time scale of average bubble life span is short, therefore, the energy transferred due to condensation can be neglected. By omitting the condensation, the energy balance equation can be written as

$$q_w = \frac{Q_{fc}}{A} + \frac{Q_{tc}}{A} + \frac{Q_{ev}}{A} = q_l \tag{40}$$

in which Q_{tc} includes both the contribution due to bubble lift-off and bubble sliding.

2.2.2 Forced Convection. Modeling of forced convection is not part of the tasks in this study. Instead, we borrow the widely accepted formula to compute forced convection heat flux

$$q_{fc} = h_{fc}(T_w - T_B) \tag{41}$$

For a liquid flowing in a straight circular pipe in the turbulent pipe flow range, the Dittus–Boelter equation [16] as given by

$$\mathrm{Nu} = 0.023\ \mathrm{Re}^{0.8}\ \mathrm{Pr}^{0.4} \tag{42}$$

can be used to calculate Nu, the Nusselt number. For asymmetrically heated rectangular duct, Tan and Charters [17,18] suggested

$$\mathrm{Nu} = 0.018\ \mathrm{Re}^{0.8}\ \mathrm{Pr}^{0.4} \tag{43}$$

in the developed-flow region and

$$\mathrm{Nu}_l = \mathrm{Nu}\left(1 + S\frac{D_h}{L}\right) \tag{44}$$

for the local Nusselt numbers in the thermally developing region where

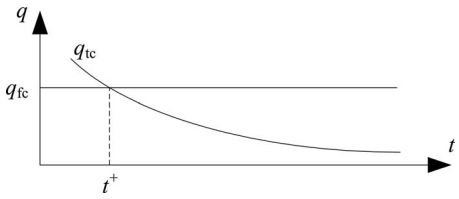

Fig. 10 Transient conduction duration

$$S = \begin{cases} 14.3 \log\left(\dfrac{L}{D_h}\right) - 7.9 & 0 < \dfrac{L}{D_h} \le 60 \\ 17.5 & \dfrac{L}{D_h} > 60 \end{cases} \tag{45}$$

From the definition of Nu, h_{fc} is calculated from

$$h_{fc} = \frac{\mathrm{Nu} \cdot k_l}{D_h} \tag{46}$$

The surface area occupied by the bubbles increases as the wall superheat increases, which causes the decrease in forced convection heat flux component. When the boiling approaches DNB and CHF, the percentage of convection heat transfer approaches zero, as is predicted by the implemented model.

2.2.3 Transient Conduction. Both bubble lift-off and bubble sliding are associated with transient conduction. This is due to the disrupted boundary layer and because a colder liquid comes from the surrounding region with a temperature close to T_{sat} to fill in the region occupied by the moving (including sliding and lift-off) bubble. The transient conduction process is modeled as one-dimensional transient heat conduction into a semi-infinite medium, with the bulk liquid at temperature T_{sat} and heater surface at temperature T_w. Based on the error function solution of the transient temperature profile, the transient conduction heat flux at the wall can be expressed as

$$q_{tc} = \frac{k_l(T_w - T_{sat})}{\sqrt{\pi \alpha_l t}} \tag{47}$$

A basic assumption is made here that at any given moment the local single-phase heat flux at any location is not lower than q_{fc}, or in other words, that q_{fc} is the minimum heat flux that the heated surface experiences [14]. Based on this assumption, we can obtain the characteristic transient conduction period, t^+, which confines the maximum duration of transient conduction, which is calculated by equating q_{tc} and q_{fc}, as shown in Fig. 10

$$t^+ = \left(\frac{k_l}{h_{fc}} \frac{T_w - T_{sat}}{T_w - T_l}\right)^2 \frac{1}{\pi \alpha_l} = \left(\frac{D_h}{\mathrm{Nu}} \frac{T_w - T_{sat}}{T_w - T_l}\right)^2 \frac{1}{\pi \alpha_l} \tag{48}$$

When a vapor bubble accelerates during its sliding and lift-off, acceleration is also imposed on its surrounding fluid flow due to the inertial effect of the fluid. Equivalently, the bubble behaves as if it carries a certain amount of surrounding liquid on its interface with its motion. A concept of "added mass" was proposed to account for this effect and to evaluate the necessary work done to change the kinetic energy associated with the fluid motion [19]. For a purely spherical bubble, the added mass is

$$m_{am} = \frac{2\pi}{3} r_l^3 \rho_l \tag{49}$$

which is one-half of the displaced mass of the fluid.

By assuming that the added liquid mass is uniformly attached to the vapor-liquid interface as an approximation, a virtual bubble radius of $1.5^{1/3} r_l$ is used to replace r_l in calculating the surface area on which transient conduction occurs, in order to incorporate the added-mass effect. In the literature, Judd and Huang [20] suggested a value of $1.8^{1/2}$ to match their experimental data, which was adopted by Sateesh et al. [10] in their modeling approach. In the model of Basu et al. [14], however, this effect was completely neglected.

2.2.4 Evaporation. Bubbles gain vapor from the evaporation of both the microlayer and superheated thermal boundary layer during their growth, while due to the existence of a subcooled bulk liquid, condensation may happen near the bubble cap. The net contribution from evaporation (q_{ev}) upon lift-off of a vapor bubble is, therefore, the amount of latent heat required for generation of the vapor bubble of its size r_l and thus can be expressed as

$$q_{ev} = \frac{4\pi}{3} r_l^3 \cdot \rho_v h_{fg} \tag{50}$$

2.3 Expressions for Each Heat Flux Component. As explained in Sec. 2.1.5, considering the effect of bubble coalescence is equivalent to dividing bubbles into n_g groups, with each group containing $N_a f_i p_{i,c}$ identical bubbles, behaving as if there is no coalescence at all. Based on the n_g groups of identical bubbles, components of the surface heat flux can be calculated as shown below.

For the ith group, the heat flux contributed by evaporation is expressed as

$$q_{i,ev} = \tfrac{4}{3}\pi r_i^3 \rho_v h_{fg} N_a f_i p_{i,c} \tag{51}$$

where $4/3\pi r_i^3 \rho_v h_{fg}$ is the contribution from a single bubble, and $N_a f_i p_{i,c}$ is the total number of bubbles in the group. If the ith group is a nonsliding group, the transient conduction due to bubble lift-off up to its maximum duration is expressed as

$$q_{i,tc} = \frac{2k_l}{\sqrt{\pi \alpha_l}} \Delta T_{sat} N_a f_i p_{i,c} \pi (C_r r_i)^2 \sqrt{\min(t_{i,w}, t^+)} \tag{52}$$

where $t_{i,w}$ is the waiting time, i.e., the interval between bubble lift-off and the next bubble generation. If $t_{i,w} > t^+$, the heat transfer during $t^+ - t_{i,w}$ is governed by the forced convection

$$q_{i,fc} = h_{fc}(T_w - T_l) N_a p_{i,c} \pi (C_r r_i)^2 \max\left(0, 1 - \frac{t^+}{t_{i,w}}\right) \tag{53}$$

If the ith group is a sliding group, there exists transient conduction due both to bubble lift-off and bubble sliding. Similar to the nonsliding group case

$$q_{i,tcs} = \frac{2k_l}{\sqrt{\pi \alpha_l}} \Delta T_{sat} N_a f_i \sqrt{\min(t_g + t_{i,w}, t^+)} \times \left\{ p_{i,c} \pi (C_r r_i)^2 + \sum_{j=i}^{n_g} p_{j,c} 2 (C_r r_i) V_s \Delta t \right\} \tag{54}$$

If $t_g + t_{i,w} > t^+$, the heat transfer during $t^+ - (t_g + t_{i,w})$ is governed by the forced convection

$$q_{i,fcs} = h_{fc}(T_w - T_l) N_a p_{i,c} 2 (C_r r_i) V_s \Delta t \max\left(0, 1 - \frac{t^+}{t_g + t_{i,w}}\right) \tag{55}$$

On the remaining heated surface that is not affected by the bubbles, the forced convection heat transfer is expressed as

$$q_{fc} = h_{fc} A_r (T_w - T_l) \tag{56}$$

The total heat flux is calculated as

$$q_{total} = q_{fc} + \sum_i (q_{i,ev} + q_{i,tc} + q_{i,tcs} + q_{i,fc} + q_{i,fcs}) \tag{57}$$

Table 1 summarizes the expressions for each of the heat transfer mechanisms.

2.4 Underlying Models and Required Parameters. From the discussion in Secs. 2.1–2.3, one needs to know the density of

Table 1 Expressions of different heat flux components

q_{ev}	$\frac{4}{3}\pi r_i^3 \rho_v h_{fg} N_a f_i p_{i,c}$ for each group
q_{tc}	$\frac{2k_l}{\sqrt{\pi\alpha_l}}\Delta T_{sat} N_a f_i p_{i,c} \pi (C_r r_i)^2 \sqrt{\min(t_{i,w}, t^+)}$ for each nonsliding group
q_{tcs}	$\frac{2k_l}{\sqrt{\pi\alpha_l}}\Delta T_{sat} N_a f_i \sqrt{\min(t_g + t_{i,w}, t^+)}\{p_{i,c}\pi(C_r r_i)^2 + \sum_{j=i}^{n_g} p_{j,c} 2(C_r r_i) V_s \Delta t\}$ for each sliding group
q_{fc}	$h_{fc}(T_w - T_l) N_a p_{i,c} \pi (C_r r_i)^2 \max\left(0, 1 - \frac{t^+}{t_{i,w}}\right)$ for each nonsliding group $h_{fc}(T_w - T_l) N_a p_{i,c} 2(C_r r_i) V_s \Delta t \max\left(0, 1 - \frac{t^+}{t_g + t_{i,w}}\right)$ for each sliding group $h_{fc} A_r (T_w - T_l)$ on the remained heated surface not covered by bubbles

active nucleation sites N_a, bubble radius as a function of time $r(t)$ calculated from bubble growth model, and bubble departure radius r_d and lift-off radius r_l calculated from the bubble force balance model, in order to estimate the probabilities of bubble coalescence. It is also necessary to know the velocity and temperature distributions in the flow field. For this purpose, models that are widely accepted and examined or that are developed to be the most up-to-date to the best of authors' knowledge are adopted in this work to provide required parameters.

2.4.1 Turbulent Velocity and Temperature Distribution. The turbulent velocity and temperature profiles in different geometries have been well defined in the literature and are necessary for this modeling approach. The typical Re number ranges from 10,000 to 25,000 in the experiments carried out for this study, ensuring a stabilized fully turbulent flow. With the definition of dimensionless turbulent velocity v^+ and dimensionless distance from the wall y^+, the turbulent velocity profile can be calculated from [21]

$$v^+ = \begin{cases} y^+ & 0 \le y^+ \le 5 \\ -3.05 + 5.00 \ln y^+ & 5 \le y^+ \le 30 \\ 5.5 + 2.5 \ln y^+ & y^+ > 30 \end{cases} \tag{58}$$

in which $v^+ = v/(\sqrt{\tau_w/\rho_l})$, and $y^+ = y(\sqrt{\tau_w/\rho_l}/\nu)$.

The similarity of the velocity and temperature profiles is connected via the Prandtl number, Pr. In his paper, Levy [22] determined the bulk temperature distribution T_B to be

$$T_w - T_B = \begin{cases} Q\ \mathrm{Pr}\ y^+ & 0 \le y^+ \le 5 \\ 5Q\{\mathrm{Pr} + \ln[1 + \mathrm{Pr}(0.2y^+ - 1)]\} & 5 \le y^+ \le 30 \\ 5Q\{\mathrm{Pr} + \ln(1 + 5\ \mathrm{Pr}) + 0.5 \ln(y^+/30)\} & y^+ > 30 \end{cases} \tag{59}$$

in which $Q = q/(\rho_l c_{pl}(\sqrt{\tau_w/\rho_l}))$.

From the turbulent velocity profile, the thickness of the laminar sublayer and the buffer layer, together with the velocity distribution within, is required for the calculation of bubble departure and lift-off radii.

In the model development for bubble coalescence, an assumption is made that the existence of bubbles does not affect the velocity field inside the boundary layers. This assumption is undoubtedly valid when the number of bubbles on the heated surface is small. For a larger number of bubbles with the increase in wall superheat, the effect is unclear. However, the effect of existing bubbles on the temperature field is considered and incorporated into the calculation of different heat flux components, which was described in Sec. 2.2.3.

2.4.2 Active Nucleation Site Density. It is experimentally observed that the increase in the wall superheat activates an increasing number of nucleation sites. Many authors tried to correlate the number of nucleation sites with either the critical cavity size (D_c or r_c) or the wall superheat ΔT_{sat} by setting

$$N_a = \text{const} \times D_c^{-n} \tag{60}$$

or

$$N_a = \text{const} \times \Delta T_{sat}^n \tag{61}$$

in which

$$D_c = \frac{4\sigma T_{sat}}{\rho_v h_{fg} \Delta T_{sat}} \tag{62}$$

n varies from 2 to 6 and is empirically determined by fitting the measured data.

Despite the success of previous experimental studies, the mechanism for an active nucleation site is far from being well understood. No single model to date can give reliable prediction without confirmation or help of experimental data. Very limited experimental studies have been conducted in subcooled flow boiling. The effect of subcooling and velocity has not been quantified, and as such no correlation is available for N_a in subcooled flow boiling. The nucleation site density is critical in this model because it provides the only possible connection between microscopic bubble movement and macroscopic observation of surface heat flux. Since the existing models are insufficient to predict the nucleation site density, measurement is performed and correlated with D_c, expecting that a more precise result on the nucleation site density is available in the future.

2.4.3 Bubble Growth. The governing equation obtained by Mikic et al. [23] in the form of

$$\frac{dR^+}{dt^+} = (t^+ + 1)^{1/2} - (t^+)^{1/2} \tag{63}$$

where

$$R^+ = \frac{A}{B^2}R, \quad t^+ = \frac{A^2}{B^2}t, \quad A^2 = b\frac{h_{fg}\rho_v \Delta T_\infty}{\rho_l T_{sat}}, \quad B = \left(\frac{12}{\pi}\alpha_l\right)^{1/2} \mathrm{Ja}$$

$$\mathrm{Ja} = \frac{\Delta T_\infty c_l \rho_l}{h_{fg}\rho_v}$$

is believed to be one of the best models to predict the bubble growth to date. The validity of Mikic's model has been confirmed experimentally by Lien [24]. For $t^+ \ll 1$ it simplifies to the Rayleigh solution (i.e., inertially controlled bubble growth solution), and for $t^+ \gg 1$ it simplifies to the thermally controlled bubble growth solution and gives Zuber's model [25]

$$R = \frac{2b}{\sqrt{\pi}}\mathrm{Ja}\sqrt{\alpha_l t} \tag{64}$$

where $b = \sqrt{3}$ and $\mathrm{Ja} = (\rho_l c_{pl}\Delta T_{sat})/(\rho_v h_{fg})$.

2.4.4 Bubble Departure and Bubble Lift-Off. Bubble departure and bubble lift-off characterize the change of the status of a bubble on the heated surface, as well as the local heat transfer mechanism associated with a single bubble. Following the analysis on the forces operating on a growing bubble, the general form of the momentum equation governing the bubble motion may be expressed as

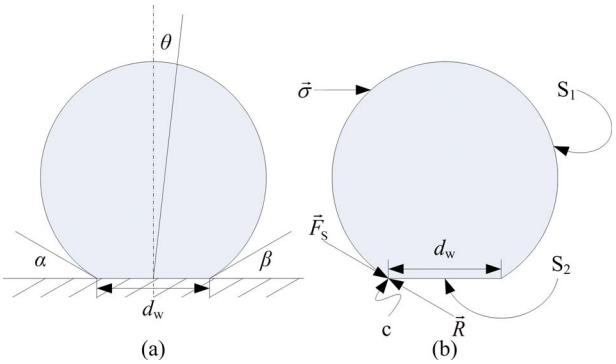

Fig. 11 (*a*) Schematic diagram of vapor bubble; (*b*) free-body diagram of bubble

$$\boldsymbol{F}_{\text{total}} = m_b \frac{d\boldsymbol{V}}{dt} \tag{65}$$

By setting the right hand side to zero, the balance of the bubble forces in the x- and y-directions becomes the criteria for bubble departure and bubble lift-off, respectively.

Consider a growing vapor bubble attached to a wall, as shown in Fig. 11(*a*). A free-body diagram for the bubble is depicted in Fig. 11(*b*), where both the liquid and the solid wall have been removed.

Thorncroft et al. [26] considered the net force acting on an isolated bubble that originates from five sources including a body force, surface tension, liquid stress at the liquid/vapor interface, normal stress due to vapor pressure at the vapor/sold interface, and a reaction force. The net force acting on an isolated bubble may be expressed as

$$\boldsymbol{F} = \boldsymbol{F}_{\text{body}} + \boldsymbol{F}_s + \int_{S_1} \underline{\underline{\sigma}} \cdot \boldsymbol{n} dA + \int_{S_2} p_v(-\boldsymbol{n}) dA + \boldsymbol{R} \tag{66}$$

Different force components are identified from the above expression. To better illustrate this, the main forces on the bubble may be expressed as

$$\boldsymbol{F}_{\text{total}} = \boldsymbol{F}_{\text{body}} + \boldsymbol{F}_s + \boldsymbol{F}_B + \boldsymbol{F}_{\text{cp}} + \boldsymbol{F}_{\text{am}} + \boldsymbol{F}_{\text{qs}} + \boldsymbol{F}_{\text{sl}} + \boldsymbol{R} \tag{67}$$

with the expressions for each force component in Ref. [26] provided below

$$\boldsymbol{F}_{\text{qs}} = 6\pi\rho_l \nu V r \left\{ \frac{2}{3} + \left[\frac{12}{\text{Re}_b} + 0.75\left(1 + \frac{3.315}{\text{Re}_b^{1/2}}\right) \right]^{-1} \right\} \tag{68}$$

$$F_{g,b} = 2\pi\rho_l r^2 V \dot{r} \tag{69}$$

$$F_{g,x} = -\pi\rho_l r^2 (1.64\dot{r}^2 + 0.4 r\ddot{r}) \tag{70}$$

$$F_{s,x} = -1.25 d_w \sigma \frac{\pi(\alpha - \beta)}{\pi^2 - (\alpha - \beta)^2} (\sin\alpha + \sin\beta) \tag{71}$$

$$F_{s,y} = -d_w \sigma \frac{\pi}{(\alpha - \beta)} (\cos\beta - \cos\alpha) \tag{72}$$

$$F_B = \tfrac{4}{3}\pi r^3 (\rho_l - \rho_v) g \tag{73}$$

$$F_{\text{sl}} = \frac{1}{2} V^2 \pi \rho_l r^2 \Gamma^{1/2} \left\{ \left[\frac{1.146 J(\varepsilon)}{\text{Re}_b^{1/2}} \right]^2 + \left(\frac{3}{4}\Gamma^{1/2} \right)^2 \right\}^{1/2} \tag{74}$$

in which $\Gamma = (\partial U/\partial y)(r/V)$

$$J(\varepsilon) \approx \begin{cases} 0.6765\{1 + \tanh[2.5 \log_{10}\varepsilon + 0.191]\} \times \{0.667 + \tanh[6(\varepsilon - 0.32)]\} & 0.1 \le \varepsilon \le 20 \\ 2.255 & \varepsilon > 20 \end{cases}$$

and $\varepsilon = \sqrt{2\Gamma/\text{Re}_b}$.

2.5 Critical Heat Flux. The prediction of CHF is a natural extension of the heat flux prediction in this model. As T_w increases, N_a, r_d, and r_l are all predicted to increase, resulting in an increasingly populated heated surface. Bubbles are inclined to coalesce with others during the earlier stage of their life span. With T_w indefinitely increasing, bubbles are eventually arranged on the heated surface at the most compact pattern with very little sliding allowed. Their average size is confined by the predicted average separation distance of the nucleation sites. This mathematical outcome is consistent with the experimental observations. In this extreme situation, the model indicates a maximum heat flux that the heated surface can deliver.

The application of this model is limited to meeting the CHF condition. It is incapable of predicting the transition boiling and the minimum heat flux because after reaching CHF, blanketing occurs on an increasing portion of the heated surface and restricts its liquid supply, which is not addressed in this study.

2.6 Data Dependency of the Model. This model contains several submodels with each addressing one subprocess. Shown in Fig. 12, a top-down decomposition of this model explains the function of each submodel and the data dependency among them. A computer code written in MATLAB is used to implement this model and to perform predictions based on given experimental conditions. In the first portion of this code, required parameters, e.g., test liquid properties, are prepared from given experimental conditions. Then, combined with the test section geometry, bubble departure/lift-off radii and nucleation site density are calculated, and, in turn, fed into the next portion of the code to compute the conditional bubble interaction probability, giving the information for each group of bubbles. Based on this information, the heat flux components of different mechanisms are calculated to obtain the total heat flux. At sufficiently high wall superheat, the predicted

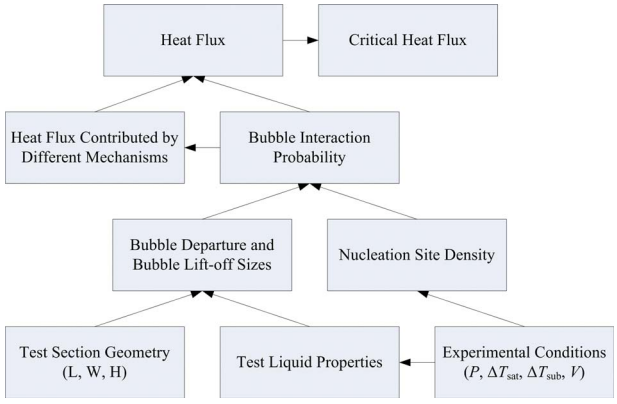

Fig. 12 Data dependency of the model

heat flux remains nearly unchanged with further increase in wall superheat, giving the prediction of CHF.

3 Summary and Discussion

A modeling study conducted of the subcooled boiling heat transfer is explained in this paper. The stochastic nature of bubble motion and bubble coalescence on the boiling surface is captured by deriving the probability density (*pdf*) function of bubble coalescence and developing the bubble lift-off radius distribution. The surface heat flux is decomposed into components contributed by different mechanisms, which are quantified from the bubble lift-off radius distribution. Model prediction indicates the existence of surface heat flux limit as the wall superheat increases, which has not been reported in prior studies before.

Limitations do exist when trying to apply this model to different flow regimes and conditions. This model precludes the effect of vapor bubbles on the continuous bulk liquid phase, which makes it potentially unsuitable for small tubes, when bubbles, during their growth or after their lift-off, may block the cross section and reduce liquid supply to the heated surface. This model has been validated in a horizontal flat heat exchanger and vertical circular tube, as shown in Part II. It is practically hard to apply to horizontal circular tubes because bubbles with different angular positions along the cross section are governed by different force balance equations, making it different to apply the ergodic principle for bubble lift-off radius distribution. Finally, the submodels are selected specifically for turbulent flow in this study; hence, when trying to apply the model to other flow regimes, those flow-specific submodels need to be replaced by their appropriate equivalents.

Acknowledgment

The study is performed in the Air Conditioning and Refrigeration (ACRC) Center at University of Illinois at Urbana-Champaign. The project is sponsored by the U.S. Department of Energy Contract No. DOE DEFG07-00ID14601.

Nomenclature

A = surface area (m^2)
bo = boiling number
co = convection number
c_p = liquid specific heat, constant pressure (J/kg K)
D = diameter (m)
f = frequency of bubbles (Hz)
$\mathrm{Fr_{le}}$ = Froude number
G = mass flow rate (kg/m^2)
h = heat transfer coefficient (W/m^2 K)
h_{fg} = latent heat (J/kg)
k = thermal conductivity (W/m K)
l = distance between two bubbles (m)
L = average distance between nucleation sites or length along duct (m)
m = mass (kg)
n = nucleation site number
N = nucleation site density or bubble density ($1/m^2$)
Nu = Nusselt number
p = probability or probability density function
P = pressure (kPa) or cumulative distribution function
Pr = Prandtl number
q = surface heat flux (W/m^2)
Q = energy (J)
r = bubble radius (m)
Re = Reynolds number
t = time (s)
T = temperature (K)
u, v, and V = velocity (m/s)
x = void fraction or bubble position
y = distance from wall (m)

Greek Symbols

α = thermal diffusivity (m^2/s) or advancing contact angle (deg)
β = receding contact angle (deg)
μ = dynamic viscosity (Pa s)
ν = kinematic viscosity (m^2 s)
ρ = density (kg/m^3)
σ = surface tension (N/m)
τ = shear stress (Pa)

Subscripts

a = active nucleation site
am = added-mass force or added mass (when using with m)
b = bubble
B = bulk region or buoyancy
body = body force
c = cavity or conditional probability
cp = contact pressure force
crit = critical condition
d = departure or bubble diameter
ev = evaporation
fc = forced convection
fs = freestream acceleration force
g = growth or group
g and v = vapor
h = hydrodynamic
i = interaction (coalescence)
l = liquid, local, or lift-off
nc = natural convection
ni = noninteraction
qs = quasisteady drag force
r = radius
s = sliding, or surface tension
sat = saturated condition
sl = shear lift force
sp = single-phase heat transfer
sub = subcooled condition
tc = transient conduction
w = wall/fluid near the wall, or waiting time (when using with t)

Superscripts

$+$ = dimensionless equivalent of the physical property

Appendix

DEFINITION. *A random countable subset* $\mathbf{\Pi} \subset \mathbf{R}^d$ *is called a spatial Poisson process with constant intensity* λ *if the random variables* $N(\mathbf{A}) = \#\mathbf{\Pi} \cap \mathbf{A}, \mathbf{A} \subset \mathbf{R}^d$ *(Borel measurable), satisfy the following*:

(a) For all $n \geq 1$ and disjoint $\mathbf{A}_1, \ldots, \mathbf{A}_n \subset \mathbf{R}^d$, the random variables $N(\mathbf{A}_1), \ldots, N(\mathbf{A}_n)$ are independent.
(b) $N(\mathbf{A}) \sim \mathrm{Poi}(\lambda|\mathbf{A}|)$, where $|\mathbf{A}|$ denotes the volume (Lebesgue measure) of $\mathbf{A}$.

THEOREM. *Consider* $\mathbf{S} \subset \mathbf{R}^d$ *and random events* $a_1, \ldots, a_n \in \mathbf{S}$, *then* $a_1, \ldots, a_n$ *follows uniform distribution on* $\mathbf{S}$.

Proof.

(1) For any randomly selected subset $\mathbf{A} \subset \mathbf{S}$ and event a_i

$$P(a_i \in \mathbf{A} | a_i \in \mathbf{S}) = \frac{P(a_i \in \mathbf{A})}{P(a_i \in \mathbf{S})} = \frac{\sum_{k=1}^{n} \frac{C_{n-1}^{k-1}}{C_n^k} P(N(|\mathbf{A}|) = k, N(|\mathbf{S} \cap \mathbf{A}^C|) = n-k)}{P(N(|\mathbf{S}|) = n)} \frac{\sum_{k=1}^{n} \frac{C_{n-1}^{k-1}}{\frac{n!}{k!\,(n-k)!}} \frac{e^{-\lambda|\mathbf{A}|}(\lambda|\mathbf{A}|)^k}{k!} \frac{e^{-\lambda|\mathbf{S}\cap\mathbf{A}^C|}(\lambda|\mathbf{S} \cap \mathbf{A}^C|)^{n-k}}{(n-k)!}}{\frac{e^{-\lambda|\mathbf{S}|}(\lambda|\mathbf{S}|)^n}{n!}}$$

$$= \frac{\sum_{k=1}^{n} C_{n-1}^{k-1} |\mathbf{A}|^k |\mathbf{S} \cap \mathbf{A}^C|^{n-k}}{|\mathbf{S}|^n} = |\mathbf{A}| \frac{\sum_{k=0}^{n-1} C_{n-1}^{k} |\mathbf{A}|^k |\mathbf{S} \cap \mathbf{A}^C|^{n-1-k}}{|\mathbf{S}|^n} = |\mathbf{A}| \frac{(|\mathbf{A}| + |\mathbf{S} \cap \mathbf{A}^C|)^{n-1}}{|\mathbf{S}|^n} = \frac{|\mathbf{A}|}{|\mathbf{S}|}$$

Therefore, event a_i in $\mathbf{S}$ follows a uniform distribution.

(2) For any randomly selected subset $\mathbf{A} \subset \mathbf{S}$ and event a_i, a_j

$$P(a_i, a_j \in \mathbf{A} | a_i, a_j \in \mathbf{S}) = \frac{P(a_i, a_j \in \mathbf{A})}{P(a_i, a_j \in \mathbf{S})} = \frac{\sum_{k=2}^{n} \frac{C_{n-2}^{k-2}}{C_n^k} P(N(|\mathbf{A}|) = k, N(|\mathbf{S} \cap \mathbf{A}^C|) = n-k)}{P(N(|\mathbf{S}|) = n)}$$

$$= \frac{\sum_{k=2}^{n} \frac{C_{n-2}^{k-2}}{\frac{n!}{k!\,(n-k)!}} \frac{e^{-\lambda|\mathbf{A}|}(\lambda|\mathbf{A}|)^k}{k!} \frac{e^{-\lambda|\mathbf{S}\cap\mathbf{A}^C|}(\lambda|\mathbf{S} \cap \mathbf{A}^C|)^{n-k}}{(n-k)!}}{\frac{e^{-\lambda|\mathbf{S}|}(\lambda|\mathbf{S}|)^n}{n!}} = \frac{\sum_{k=2}^{n} C_{n-2}^{k-2} |\mathbf{A}|^k |\mathbf{S} \cap \mathbf{A}^C|^{n-k}}{|\mathbf{S}|^n} = |\mathbf{A}|^2 \frac{\sum_{k=0}^{n-2} C_{n-2}^{k} |\mathbf{A}|^k |\mathbf{S} \cap \mathbf{A}^C|^{n-2-k}}{|\mathbf{S}|^n}$$

$$= |\mathbf{A}|^2 \frac{(|\mathbf{A}| + |\mathbf{S} \cap \mathbf{A}^C|)^{n-2}}{|\mathbf{S}|^n} = \frac{|\mathbf{A}|^2}{|\mathbf{S}|^2} = P(a_i \in \mathbf{A} | a_i \in \mathbf{S}) P(a_j \in \mathbf{A} | a_j \in \mathbf{S}) = P(a_i \in \mathbf{A} | a_i, a_j \in \mathbf{S}) P(a_j \in \mathbf{A} | a_i, a_j \in \mathbf{S})$$

Therefore, any two events a_i and a_j in $\mathbf{S}$ are independent to each other.

References

[1] Collier, J., and Thome, J., 1994, *Convective Boiling and Condensation*, 3rd ed., Oxford University Press, New York.

[2] Jens, W. H., and Lottes, P. A., 1951, "Analysis of Heat Transfer Burnout, Pressure Drop and Density Data for High Pressure Water," Report No. ANL-4627.

[3] Thom, J. R. S., Walker, W. M., Fallon, T. A., and Reising, G. F. S., 1965, "Boiling in Subcooled Water During Flow Up Heated Tubes or Annuli," *Proceedings of the Symposium on Boiling Heat Transfer in Steam Generating Units and Heat Exchangers*, Vol. 180, pp. 226–246.

[4] Bowring, R. W., 1962, "Physical Model Based on Bubble Detachment and Calculation of Steam Voidage in the Subcooled Region of a Heated Channel," Institute for Atomenergi, Halden, Norway, Report No. HPR-10.

[5] Rouhani, S. Z., and Axelsson, E., 1970, "Calculation of Void Volume Fraction in the Subcooled and Quality Boiling Regions," Int. J. Heat Mass Transfer, **13**, pp. 383–393.

[6] Dix, G. E., 1971, "Vapor Void Fraction for Forced Convection With Subcooled Boiling at Low Flow Rates," Ph.D. thesis, University of California, Berkeley, Berkeley.

[7] Larsen, P. S., and Tong, L. S., 1969, "Void Fractions in Subcooled Flow Boiling," ASME J. Heat Transfer, **91**, pp. 471–476.

[8] Maroti, L., 1977, "Axial Distribution of Void Fraction in Subcooled Boiling," Nucl. Technol., **34**, pp. 8–17.

[9] Chatoorgoon, V., Dimmick, G. R., Carver, M. B., Selander, W. N., and Shoukri, M., 1992, "Application of Generation and Condensation Models to Predict Subcooled Boiling Void at Low Pressures," Nucl. Technol., **98**, pp. 366–378.

[10] Sateesh, G., Sarit, K. D., and Balakrishnan, A. R., 2005, "Analysis of Pool Boiling Heat Transfer: Effect of Bubbles Sliding on the Heating Surface," Int. J. Heat Mass Transfer, **48**, pp. 1543–1553.

[11] Wang, C. H., and Dhir, V. K., 1993, "Effect of Surface Wettability on Active Nucleation Site Density During Pool Boiling of Water on a Vertical Surface," ASME J. Heat Transfer, **115**, pp. 659–669.

[12] Barthau, G., and Hahne, E., 2000, "Nucleation Site Density and Heat Transfer in Nucleate Pool Boiling of Refrigerant R134a in a Wide Pressure Range," *Proceedings of the Third European Thermal Sciences Conference*, Vol. 2, pp. 731–736.

[13] Luke, A., and Gorenflo, D., 2000, "Heat Transfer and Size Distribution of Active Nucleation Sites in Boiling Propane Outside a Tube," Int. J. Therm. Sci., **39**, pp. 919–930.

[14] Basu, N., Warrier, G. R., and Dhir, V. K., 2005, "Wall Heat Flux Partitioning During Subcooled Flow Boiling: Part I—Model Development," ASME J. Heat Transfer, **127**, pp. 131–140.

[15] Morozov, V. G., 1969, *Convective Heat Transfer in Two Phase Flow*, V. M. Borishannskii and I. I. Paleev, eds., Israel Program for Scientific Transactions.

[16] Dittus, F. W., and Boelter, L. M. K., 1930, "Heat Transfer in Automobile Radiators of the Tubular Type," *Publications in Engineering*, Vol. 2, University of California, Berkeley, Berkeley, p. 443.

[17] Tan, H. M., and Charters, W. W. S., 1970, "An Experimental Investigation of Forced-Convective Heat Transfer for Fully-Developed Turbulent Flow in a Rectangular Duct With Asymmetric Heating," Sol. Energy, **13**, pp. 121–125.

[18] Tan, H. M., and Charters, W. W. S., 1969, "Effect of Thermal Entrance Region on Turbulent Forced-Convective Heat Transfer for an Asymmetrically Heated Rectangular Duct With Uniform Heat Flux," Sol. Energy, **12**, pp. 513–516.

[19] Brennen, C. E., 1982, "A Review of Added Mass and Fluid Inertial Forces," Naval Civil Engineering Laboratory, Port Hueneme, CA, Report No. CR82.010.

[20] Judd, R. L., and Hwang, K. S., 1976, "A Comprehensive Model for Nucleate Boiling Heat Transfer Including Microlayer Evaporation," ASME J. Heat Transfer, **98**, pp. 623–629.

[21] Todreas, N. E., and Kazimi, N. S., 1989, *Nuclear Systems I, Thermal Hydraulic Fundamentals*, MIT, Cambridge, MA.

[22] Levy, S., 1967, "Forced Convection Subcooled Boiling—Prediction of Vapor Volumetric Fraction," Int. J. Heat Mass Transfer, **10**, pp. 951–965.

[23] Mikic, B. B., Rohsenow, W. M., and Griffith, P., 1970, "On Bubble Growth Rates," Int. J. Heat Mass Transfer, **13**, pp. 657–666.

[24] Lien, Y., 1969, "Bubble Growth Rates at Reduced Pressure," Sc.D. thesis, MIT, Cambridge, MA.

[25] Zuber, N., 1961, "The Dynamics of Vapor Bubbles in Nonuniform Temperature Fields," Int. J. Heat Mass Transfer, **2**, pp. 83–98.

[26] Thorncroft, G. E., Klausner, J. F., and Mei, R., 2001, "Bubble Forces and Detachment Models," Multiphase Sci. Technol., **13**(3–4), pp. 35–76.

A Statistical Model of Bubble Coalescence and Its Application to Boiling Heat Flux Prediction—Part II: Experimental Validation

Wen Wu[1]
e-mail: wen.wu@gat.com

Barclay G. Jones[2]
e-mail: bgjones@uiuc.edu

Department of Nuclear, Plasma, and Radiological Engineering,
University of Illinois at Urbana-Champaign,
Urbana, IL 61801

Ty A. Newell[3]
Department of Mechanical Science and Engineering,
University of Illinois at Urbana-Champaign,
Urbana, IL 61801
e-mail: tynewell@uiuc.edu

*A mechanistic model for the boiling heat flux prediction proposed in Part I of this two-part paper (2009, "A Statistical Model of Bubble Coalescence and Its Application to Boiling Heat Flux Prediction—Part I: Model Development," ASME J. Heat Transfer, **131**, p. 121013) is verified in this part. In the first step, the model is examined by experiments conducted using R134a covering a range of pressures, inlet subcoolings, and flow velocities. The density of the active nucleation sites is measured and correlated with critical diameter D_c and static contact angle θ. Underlying submodels on bubble growth and bubble departure/lift-off radii are validated. Predictions of heat flux are compared with the experimental data with an overall good agreement observed. This model achieves an average error of $\pm 25\%$ for the prediction of R134a boiling curves, with the predicted maximum surface heat flux staying within $\pm 20\%$ of the experimentally measured critical heat flux. In the second step, the model is applied to water data measured by McAdams et al. (1949, "Heat Transfer at High Rates to Water With Surface Boiling," Ind. Eng. Chem., **41**(9), pp. 1945–1953) in vertical circular tubes. The consistency suggests that the application of this mechanistic model can be extended to other flow conditions if the underlying submodels are appropriately chosen and the assumptions made during model development remain valid.* [DOI: 10.1115/1.4000025]

1 Introduction

A mechanistic model has been proposed in Part I of this paper [1] by developing the distribution of vapor bubble radii on the heated surface to incorporate the effect of stochastic bubble interaction (coalescence) into the modeling and prediction of surface heat flux. The submodels required for the overall model prediction have been introduced and discussed in Part I, and will be validated in this part. Experimental facilities and measuring techniques utilized in this study will be introduced, followed by the validation of the submodels and their dependency.

2 Experimental Facilities and Measuring Techniques

In this section, two-phase flow boiling facilities and measuring techniques used in this study are introduced, which include the experimental apparatus, design of the test section, data acquisition system, and the methodology used to experimentally examine the subcooled flow boiling on a flat surface heat exchanger.

2.1 Subcooled Flow Boiling Experimental Test Facility. The experimental facility consists of a refrigerant loop, a commercial chiller system, and a test section, which are carefully sealed to avoid heat loss. The purpose of the refrigerant loop is to provide a pure, uncontaminated coolant to the test section at desired inlet conditions, including inlet temperature, mass flow rate, pressure, and test section heat flux. R134a, a typical refrigerant, is selected as the working fluid for its low latent heat and moderate saturation temperature.

A schematic diagram of the loop is shown in Fig. 1. Subcooled liquid is drawn from a receiver tank into a variable speed gear pump that drives the coolant flow. This external gear pump is manufactured by Micro-Pump and can provide up to a 4 l/min flow rate. The mass flow rate can be adjusted by setting the pump controller. The exact mass flow rate is examined by a Coriolis-type mass flow meter manufactured by Micro-Motion. Next, the coolant flows through a preheater, which conditions the flow to the desired inlet temperature. Physically, the preheater is three 1.8-m passes of 9.525 mm outer diameter copper tube in a serpentine shape. The outside of the tube is wrapped with twelve electrical heating strips of various capacities. Ten of the strips are controlled by four switches which deliver a constant amount of power to the preheater. The other two strips are controlled by a 115 V Variac to adjust the inlet coolant temperature. The coolant flows into the test section after leaving the preheater, and then back into the receiver tank. When the test section needs to be isolated, a bypass loop allows the coolant to continue circulating.

The test section is installed in the middle of a 1-m long rectangular stainless steel flow channel. One smooth test section is made for heat flux measurement. The smooth flat surface is also used for measuring the active nucleation site density. Eight type-K thermocouples (nickel–chromium positive lead and nickel–aluminum negative lead) shown in Fig. 2 are installed under the heated surface to measure the local wall temperature and heat flux. Figure 2(*a*) shows the details of test section assembly. The height of the channel is adjustable. Two sets of 25.4 mm and 12.7 mm height are used in the experiments. Three quartz windows are installed in the walls of the test section for visualization purposes. The test

[1]Corresponding author. Present address: General Atomics, P.O. Box 85608, San Diego, CA.
[2]Present address: University of Illinois at Urbana-Champaign, Department of Nuclear, Plasma, and Radiological Engineering, 214 Nuclear Engineering Laboratory, 103 South Goodwin Avenue, Urbana, IL 61801-2984.
[3]Present address: University of Illinois at Urbana-Champaign, Department of Mechanical Science and Engineering, 2115 Mechanical Engineering Laboratory, 1206 West Green Street, Urbana, IL 61801.

Manuscript received January 29, 2009; final manuscript received July 16, 2009; published online October 15, 2009. Assoc. Editor: Yogesh Jaluria.

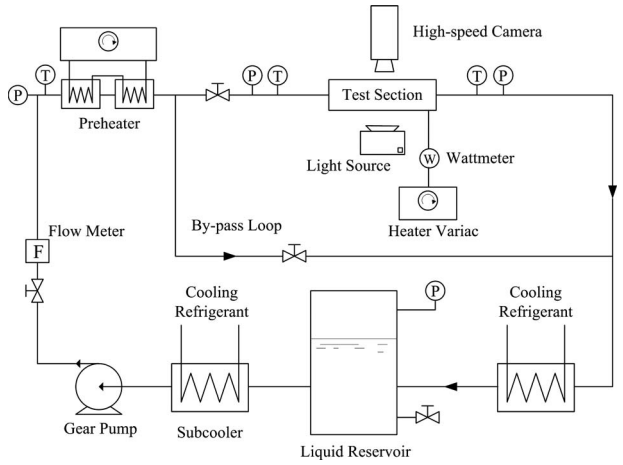

Fig. 1 Schematic diagram of apparatus for flow visualization experiments

section is heated by seven cartridge electric heaters, which provide a maximum total of $750\times7=5050$ W power. The electric power level is controlled by an autotransformer and measured using a voltmeter and an ammeter in the power circuit. Each heater contains one continuous 76.2-mm long heated section. The heater is coated with an INCOLOY sheath to enhance thermal contact with the transition part and to provide high temperature performance.

An array of instruments and techniques are employed in measuring different parameters in the experiment, which include temperature, pressure, mass flow rate, power, and calculated quantities such as heat flux in the two-phase portion of the test section. Type-K thermocouples are used for temperature measurement. These thermocouples are calibrated using an ice bath reference and are considered valid from 5°C to 100°C with an uncertainty of ±0.1°C.

The bulk temperature difference $\Delta T_B=T_w-T_B$ results from measurements of four thermocouples installed under the heating surface and the average of inlet and outlet coolant temperatures.

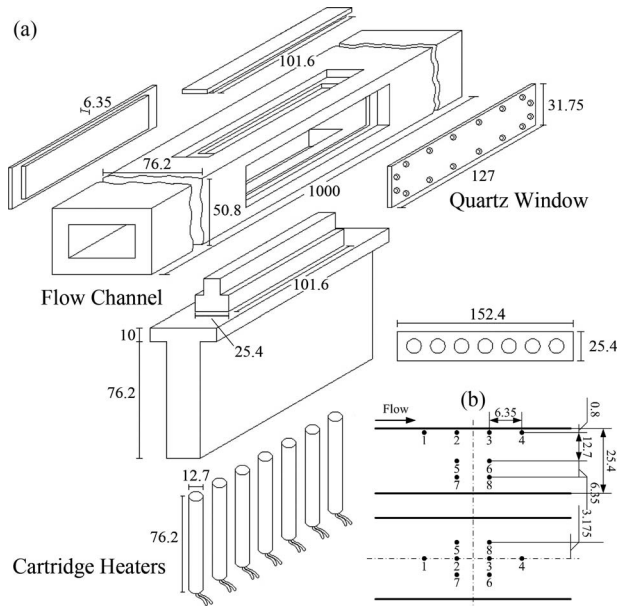

Fig. 2 Structural design of the test section: (*a*) assembly view of the flow channel, the test section, and heaters; and (*b*) thermocouple locations in the test section

The wall superheat $\Delta T_w=T_w-T_{sat}$ is calculated with the measured pressure at the test section inlet, which determines the saturation temperature T_{sat}. The heat flux is determined by the temperature difference between the thermocouples (2, 5 and 3, 6) located in the copper block. The uncertainty for heat flux measurement is estimated to be within $\pm5.0\%$.

Two BEC strain-gauge type pressure transducers are installed immediately before the preheater inlet and the test section inlet. Both transducers are calibrated using a dead weight tester with an uncertainty of ±900 Pa within the range of 0–300 psi (0–2100 kPa).

2.2 Photography System. A Photron FASTCAM Ultima 1024 high-speed video camera system is used to photograph the boiling phenomena on the heated surface from the side window of the test section. In order to achieve the highest possible resolution and eliminate errors in calibration, we mount the camera on a tripod and use a prime lens with a fixed viewing area of approximately 26×13 mm^2. This system can acquire images up to 12,000 frames/s employing a high intensive light supply. In the present experiments, frame rates between 1000 frames/s and 4000 frames/s are used. The high-speed images are recorded in a computer by an IEEE 1394 FireWire connection. Various magnifications are provided by choosing different microlenses, ranging from $0.58\times$ to $7\times$, which allow the detailed observation of the liquid-vapor activity on the heated surface. The accuracy of conversion for different magnification is estimated to be within $\pm1.0\%$.

Another imaging system is used in this study for the measurement of the active nucleation site density from the top view of the test section. A M42 screw mount manual lens Super-Multi-Coated Takuma 55 mm f/1.8 is mounted with a bellows unit on a Canon 20D DSLR camera via a M42-EF adaptor to obtain sufficiently high magnification and feature manual focus adjustment.

2.3 Test Condition and Procedures. The test fluid (R134a) in the loop is de-aerated to remove noncondensable gases prior to each test run. After inlet temperature, outlet pressure, and flow rate are adjusted to desired values, the applied power is incremented starting from low settings. One set of data is recorded at each power setting once hydrodynamic and thermal conditions reach steady levels. Subcooled flow boiling heat transfer results are obtained for each test consisting of an inlet subcooling range from 10°C to 30°C and an inlet pressure range from 400 kPa to 1000 kPa. Three flow rates of 124 kg/m^2 s, 248 kg/m^2 s, and 372 kg/m^2 s are tested, corresponding to single-phase Reynolds numbers from 7266 to 27,641. Considering these values and the fact that the hydrodynamic entry length is measured to be over 150 hydraulic diameters, the fully developed turbulent flow is assumed to exist at the entrance of the heater section. The channel is tested in a horizontal position with the gravity vector oriented normal to the heated surface and perpendicular to bulk motion. Visualization is achieved through the transparent windows of the flow channel while simultaneous local temperature readings are obtained to enable the determination of boiling curves. An overall observation of the flow channel is performed to examine the flow pattern, bubble layer development, including bubble motion and coalescence in the vicinity of the heating surfaces, and distribution of the active nucleation sites on the heated surface.

3 Model Validation

Following the data dependency shown in Part I, each submodel is examined independently in this section with measured experimental data. Results are given for the measurement of the active nucleation site density on the heated surface, followed by bubble growth, critical bubble sizes, and their distributions. In Sec. 3.4, boiling curve predictions are compared with the experimental data.

3.1 Active Nucleation Site Density. Pictures of the active nucleation sites are taken from the top of the heater surface using a Canon 20D Digital SLR camera. The recorded images are then processed via a digital image processing program implemented in MATLAB with varying parameters to obtain quantified reliable results on the average number of active nucleation sites. The active nucleation site density is calculated by dividing the total number of sites by the area over which the camera is focused. The magnification of the camera system is initially calibrated to provide the conversion ratio from pixel to millimeter.

In partial nucleate boiling, where discrete bubbles are present on the surface, the active sites could be easily discerned from the pictures. However, at higher wall superheats, adjacent bubbles begin to coalesce, making it difficult to accurately count the number of individual active sites. To overcome this problem, experiments are conducted under low inlet subcooling conditions with a technique of utilizing long exposures ranging from 2 s to 5 s. The increased subcooling reduces the size of bubbles on the heated surface and accelerates the collapse of bubbles in the bulk region, thereby facilitating a better observation of individual sites. Meanwhile, by introducing long exposure with small aperture, the fast motion of bubbles, including those on the heated surface and in the bulk, are averaged out on the images. By doing this, small errors may be introduced, in that all of the nucleation sites that ever become active during the shutter open interval can be recorded depending on the strength of the signal on the camera charge-coupled device (CCD). However, the error due to site activation and deactivation is expected to be small. This has been assessed by taking snapshots with shorter exposures, on which some individual bubbles are recorded but some effects of the site activations and deactivations are removed, and comparing them against the long exposure results. By counting the bubble sites manually, it is discovered that there is no discernable difference between these two imaging configurations, i.e., the fluctuation is insignificant.

3.1.1 Image Processing Techniques. Various image processing methods have been applied to compute the nucleation site density from the digital images recorded by the Canon 20D digital camera. The major purpose of using these techniques is to remove the background difference partially because of the uneven lighting condition in the experiments. Most noise in the digital image is also filtered out. Key functions and their resulted images are illustrated in Fig. 3.

3.1.2 Results From Nucleation Site Density Measurement. A comparison of the N_a values measured under different pressures with a varying heated surface temperature for $\theta=40$ deg (typical value of the static contact angle for the combination of R134a and copper) is shown in Fig. 4. The size of the symbols represents typical errors during the measurement, which is estimated to be close to 10.0%. Data that are measured at the flow rate of 248 $\mathrm{kg/m^2\,s}$ under different pressures (300 kPa, 400 kPa, and 500 kPa) are displayed with different symbols and fit into the same curve correlated with D_c to incorporate the effect of system pressure. Note that for ΔT_{sat} below 4°C ($D_c \geq 0.7$ μm), measurements are significantly below the fitted curve. This is expected because at very low number densities (~ 10 $\mathrm{sites/cm^2}$) and with the focusing area in the range of 3 $\mathrm{cm^2}$ for a flat plate test surface, missing just one nucleation site during the image processing can cause a large difference. At higher wall superheats, with an increase in N_a, it becomes extremely difficult to measure the exact number of nucleation sites due to bubble motion and bubble coalescence on the heated surface and in the bulk region. Higher vapor quality also leads to a change in the liquid refraction index and in the equivalent object distance, resulting in out-of-focus images. Therefore, most of the experiments are conducted in the range of $3°\mathrm{C} \leq \Delta T_{\mathrm{sat}} \leq 13°\mathrm{C}$ (corresponding to 1 $\mu\mathrm{m} \geq D_c \geq 0.2$ μm).

Based on the present data, a correlation is developed for N_a as a function of both critical diameter D_c and static contact angle θ by borrowing from the formula proposed by Basu et al. [2]. It is given as

$$N_a = 4.114 \times 10^{-6}(1 - \cos\,\theta)D_c^{-2.0} \tag{1}$$

which is very similar to their proposed formula for a low wall superheat range but with a different constant due to the usage of different test liquids.

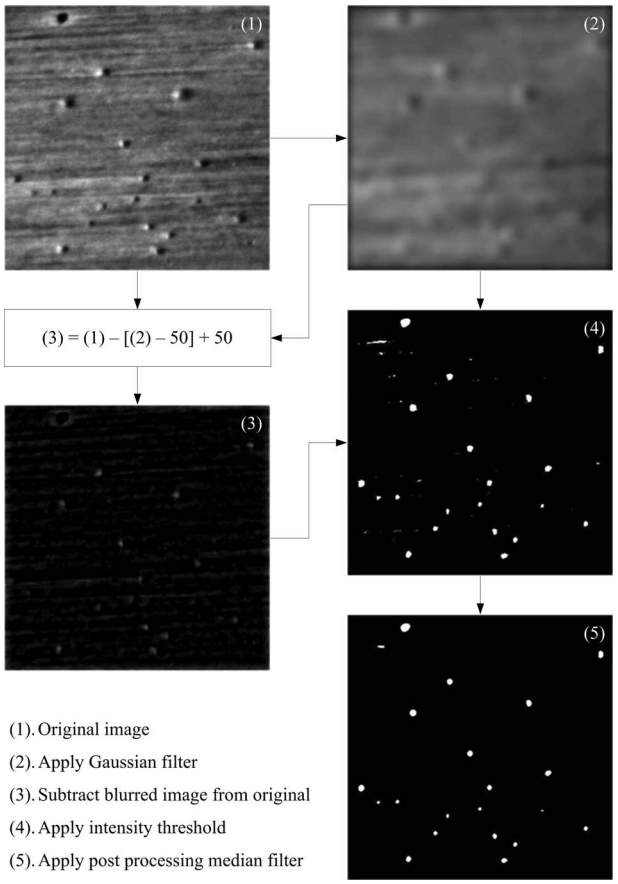

Fig. 3 Image processing flowchart for measuring the active nucleation site density

3.2 Bubble Growth. Experiments are conducted for data collection of bubble growth and critical bubble sizes under a fixed

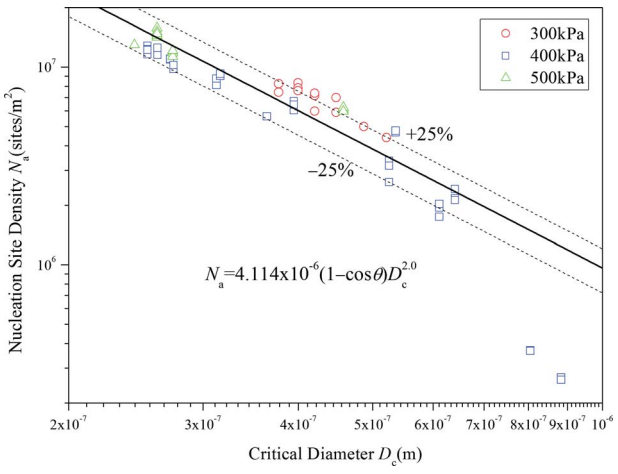

Fig. 4 Measured active nucleation site density

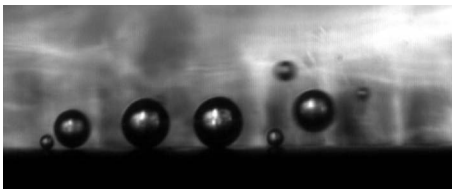

Fig. 5 Flow visualization of bubbles originating from a nucleation site

pressure (300 kPa or 400 kPa) and a wall superheat (typically 4–6 °C), with varying inlet subcooling and flow velocity. Conditions examined in this work are within the nucleate boiling regime for which isolated active nucleation sites are available.

Figure 5 depicts a photograph of a stream of vapor bubbles originating from a single nucleation site. The behavior shown is typical of nucleation at low heat flux. At the nucleation site, bubbles experience a short period of stationary growth, and then depart from the site by sliding downstream. Growth and departure is very regular, and the bubbles appear to be spherical in shape. While sliding along the surface, the bubbles remain attached to the heated surface and continue growing. The pressure is sufficiently high so that the sliding bubbles do not experience significant distortion and remain nearly spherical.

The field depth of the camera lens ranges from 50 μm to 1390 μm. For typical magnification factors used in our studies, the field depth is estimated to be around 150 μm, which ensures a clear and sharp view of the focused bubbles and effectively blurs the out-of-focus bubbles. This feature helps to distinguish the focused bubbles from the background and improves accuracy in edge detection and subsequent calculations for bubble sizes.

The software is developed in VISUAL C++ while employing the MATLAB kernel to process digital images for full quantification of the experimental data with the highest fidelity. Bubbles are approximated as ellipses, whose sizes are calculated by the algorithm of Fitzgibbon et al. [3] or by the algorithm of Taubin [4]. Results also include the inclination angle and a least square error from the ellipse fitting.

3.2.1 Image Processing Techniques. Figure 6 shows the flowchart of data processing. Starting with the original image, an edge detection algorithm is first applied to obtain the edge coordinates

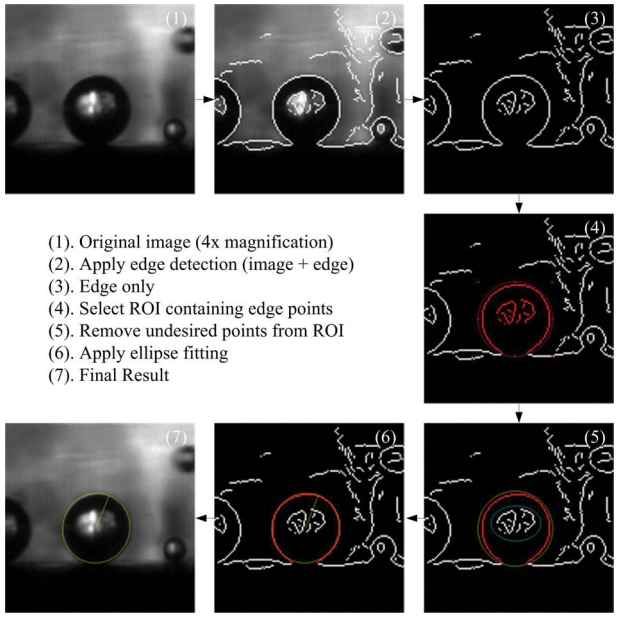

Fig. 6 Image processing flowchart for measuring bubble size

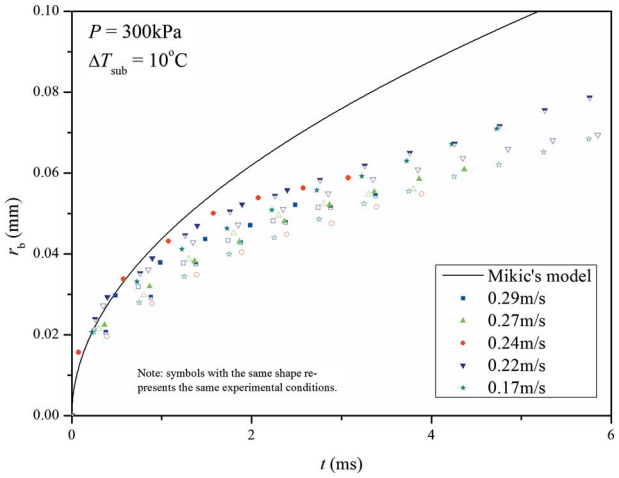

Fig. 7 Measured bubble growth at 300 kPa

in the image. By comparing with the original image, the edge of the desired target bubble can be easily identified and marked with the implemented regions of interest (ROI) selection algorithm. A subset of the code then takes this result as input to the ellipse/circle fitting algorithms to calculate the size, position, and inclination angle of the bubble. Other functions, e.g., image scaling and panning, are provided as aids to accelerate the ROI selection procedure.

3.2.2 Measured Bubble Growth Rate. Two typical sets of experimentally measured bubble growth curves are depicted in Figs. 7 and 8, corresponding to different pressures of 300 kPa and 400 kPa [5], respectively. The growth curve is obtained by measuring the size of individual bubbles from incipience through sliding. The relative error of the measurements is represented by the size of the symbols, which is estimated to be strictly less than 3.9% for a typical bubble radius of 50 μm, assuming a constant error of 0.5 pixels (=1.95 μm) during discretization in the imaging process. The model prediction from Mikic et al. [6] is also shown for comparison.

Because of the stochastic nature of flow and thermal variations, scattered data are expected. For data collected from different nucleation sites, no systematic effect of flow velocity is found within the experimental range. It is observed that the growth of bubbles during their early stages asymptotically matches the

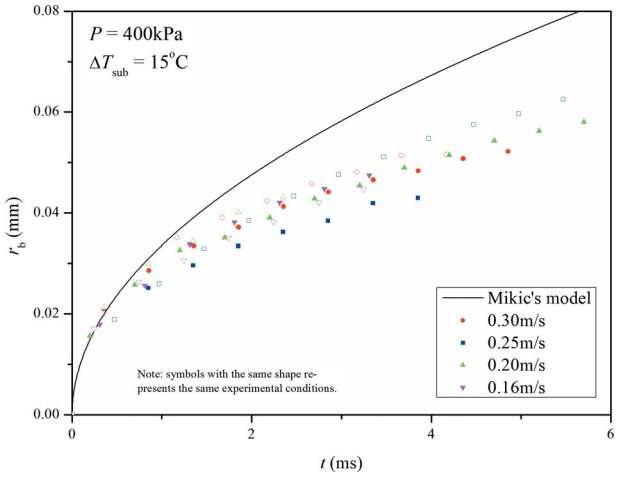

Fig. 8 Measured bubble growth at 400 kPa [5]

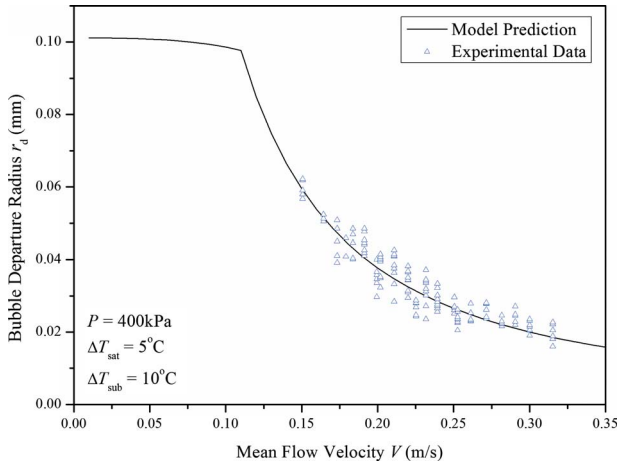

Fig. 9 Bubble departure radius r_d with varying flow velocity

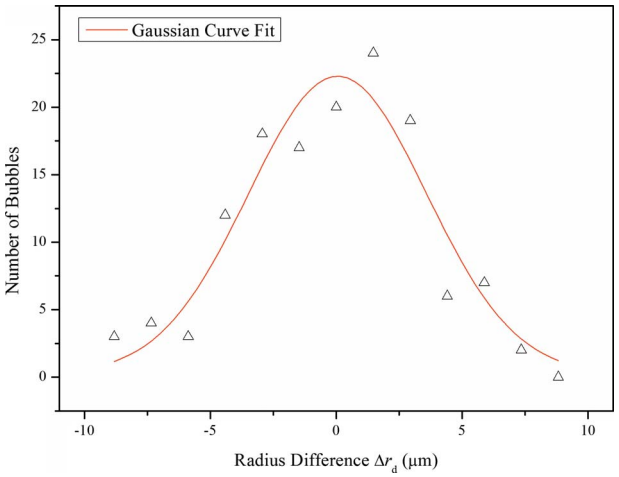

Fig. 11 Bubble departure radius distribution

model prediction from Mikic et al. [6] for a diffusion-controlled result. However, a slower growth than the model prediction is observed thereafter.

3.3 Results on Bubble Departure and Bubble Lift-Off

3.3.1 Bubble Departure Radius. From the model proposed by Thorncroft et al. [7], the vapor bubble radius upon departure can be calculated from the balance of bubble forces. When the wall superheat ΔT_{sat} is fixed, the departure radius is a function of only the mean flow velocity. Figure 9 compares the measurements and the predictions of bubble departure radius as a function of mean flow velocity with the wall superheat maintained in a range of 4.63–5.89°C. Measurements are made at 400 kPa, 10°C inlet subcooling.

Very good agreement is achieved between the model predictions and the measurements. Following the definition of relative deviation $r.d.$, which is given as:

$$r.d. = \frac{1}{N}\sum_{k=1}^{N}\frac{|r_{m,k} - r_{p,k}|}{r_{p,k}} \times 100 \tag{2}$$

where N is the total number of data points, and subscripts "m" and "p" refer to the measured and predicted radii, respectively. It can be obtained that $r.d. = 8.9\%$ for measured departure radii, which is quite acceptable. Figure 10 shows the comparison between predicted and measured data, with most of the data points being within $\pm 10\%$ of the predictions. Another way to compare the model predictions to the experimental results is to observe the distribution of the difference

$$r_{m,k} - r_{p,k} \tag{3}$$

for all available data, shown in Fig. 11. The distribution of the radius difference approximates the Gaussian distribution centered at zero, which means the average of $r_{m,k}$ asymptotically approaches $r_{p,k}$, and that more than 70% of the measured data bear a difference less than 3 μm when compared with the predictions.

3.3.2 Bubble Lift-Off Radius. The prediction of the bubble lift-off radius requires knowledge of bubble sliding velocity to calculate several components of the bubble forces. The uncertainty of the prediction of bubble sliding velocity, however, can be large due to the difficulty in the measurement of the bubble contact area and contact angles, in considering the existence of local eddy and the slight acceleration of bubbles. Therefore, the normalized bubble sliding velocity, defined as the average bubble sliding velocity divided by the bulk velocity at the bubble center in the flow, is measured for the prediction of the bubble lift-off radius. By neglecting the presence of vapor bubbles, the turbulent distribution introduced in Part I is used to provide the velocity profile of the liquid phase.

Figure 12 gives the distribution of the normalized sliding velocity for all measured lift-off bubbles. It is observed that its distribution generally obeys a Gaussian distribution centered at r

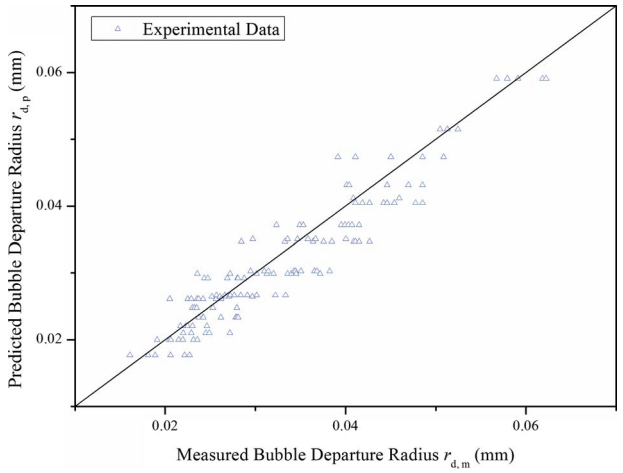

Fig. 10 Comparison between predicted and measured bubble departure radii

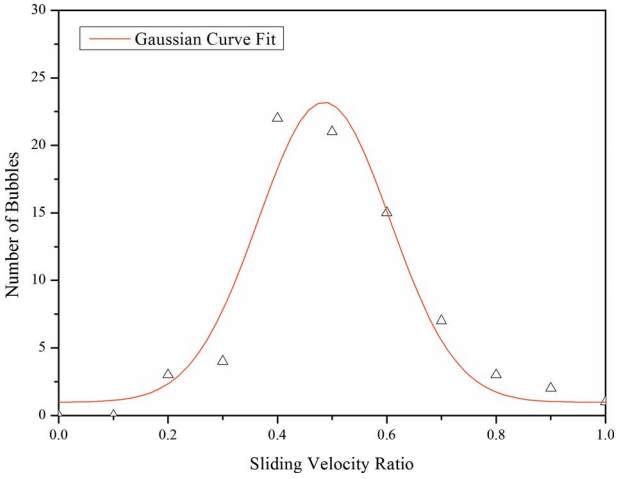

Fig. 12 Bubble sliding velocity distribution

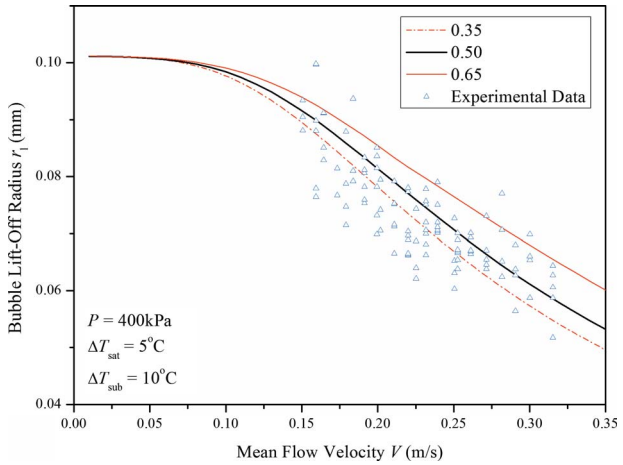

Fig. 13 Bubble lift-off radius r_l with varying flow velocity

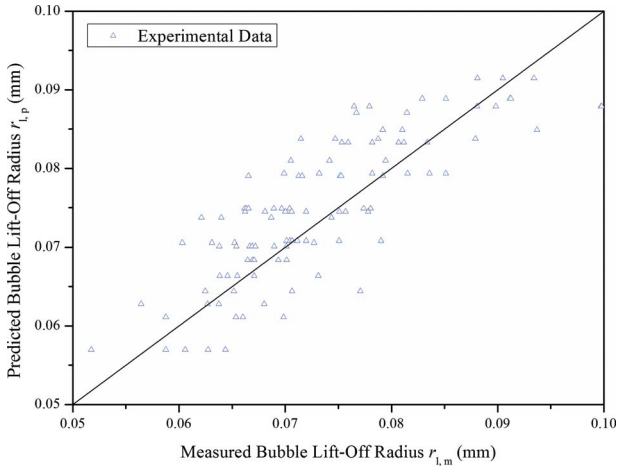

Fig. 15 Comparison between predicted and measured bubble lift-off radii

=0.512 with most data spreading over the range of 0.35–0.65. Figure 13 shows the bubble lift-off radius with a varying mean flow velocity for the ΔT_{sat} range of 4.63–5.89°C, the same as in the bubble departure radius measurement. The prediction is given for a normalized sliding velocity at 0.50. The other two curves, calculated for r being 0.35 and 0.65, are also displayed for reference.

It can be observed that most measured data lie within the range covered by these three curves. Results of the lower bubble lift-off radius are also observed and recorded, which is expected. First of all, the mean bulk velocity and temperature fields are only approximations and ensemble averages to remove the effect of turbulence. It does not reflect the instantaneous local status where the bubbles reside. Second, bubbles starting from their departure experience an acceleration process, which may actually lead to the satisfaction of the lift-off condition but at a lower normalized sliding velocity and result in a bubble lift-off earlier than predicted, as reflected in the measurements. Bubble coalescence generally results in promoting the lift-off of the bubbles and generating large local turbulence, which may in turn contribute to the lift-off of other bubbles in its vicinity.

Figure 14 shows the distribution of a bubble lift-off radius, following a similar definition as in the bubble departure measurement. The mean lift-off radius is 3.78 μm lower than predicted. Due to the stochastic nature of the bubble sliding velocity and the local velocity near the bubble, a wider full-width at half-maximum (FWHM) is also expected, besides its shifted peak to smaller radius range. Comparison of measured and predicted data are shown in Fig. 15, indicating that most data fit within ±10% of the model predictions by assuming a normalized sliding velocity of 0.50.

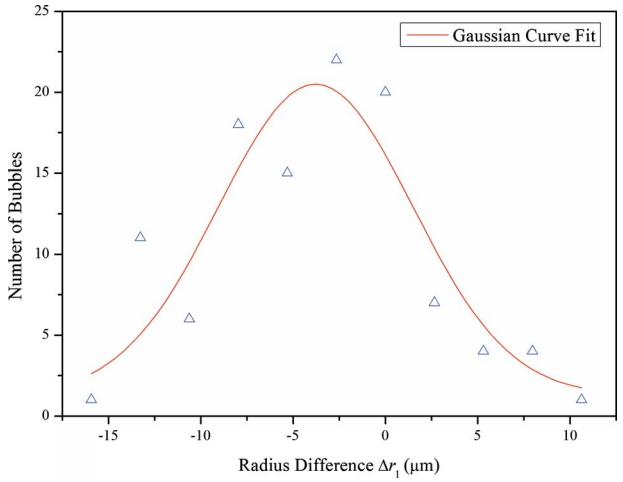

Fig. 14 Bubble lift-off radius distribution

3.4 Model Predictions on Boiling Curves

3.4.1 Experimental Data Overview. Twenty-nine boiling curves corresponding to the test conditions listed in Table 1 are shown in Fig. 16, representing the wall heat flux measurements for a range of pressures, inlet subcoolings, and velocities. Typical error is estimated to be ±0.2°C for $T_w - T_{sat}$ and ±5.0% for q, which is represented by the data symbol size. Under different experimental conditions the boiling curves almost overlap with each other in the subcooled nucleate boiling region and deviate the departure from nucleate boiling (DNB) occurs. This is consistent with existing experimental and modeling results in the literature. The effect of pressure is not reflected by the measured data due to the relatively narrow range of pressures covered in the experiments. Generally speaking, the critical heat flux (CHF) rises with increased pressure and flow velocity, while being less sensitive to inlet subcooling change.

Table 1 Test numbers and their corresponding conditions

$T_w - T_{in}$ (°C)	10			23				33		
				P (MPa)						
V (m/s)	0.4	0.6	0.8	0.4	0.6	0.8	1.0	0.6	0.8	1.0
0.09	EX7	EX16	EX27	EX10	EX8	EX22	–	EX15	EX9	EX21
0.16	EX1	EX17	EX26	EX11	EX2	EX23	EX29	EX14	EX3	EX20
0.25	EX6	EX18	EX25	EX12	EX5	EX24	EX28	EX13	EX4	EX19

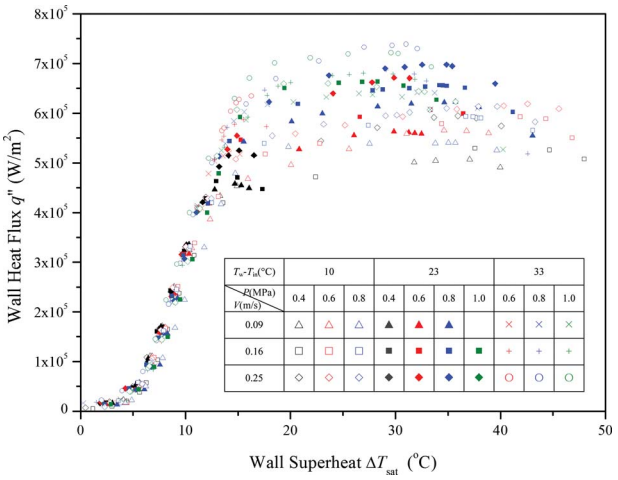

Fig. 16 Measured boiling curves under different experimental conditions

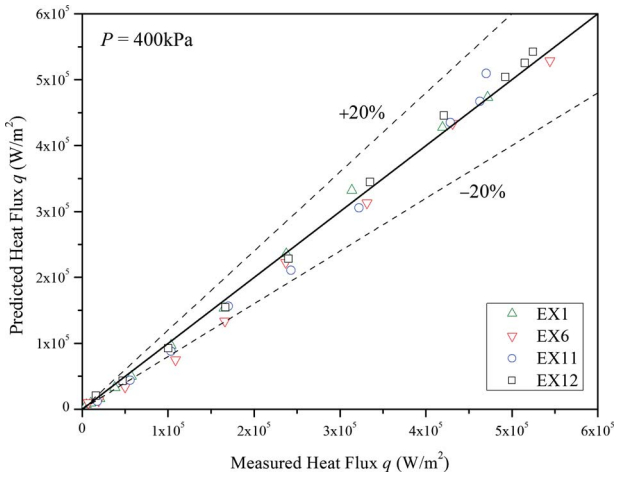

Fig. 18 Comparison of the predicted heat flux with R134a data at 400 kPa

3.4.2 Comparison of Model Predictions With R134a Data at 400 kPa. In this section the model prediction is compared with the collected heat flux data. Figure 17 shows the prediction of boiling curves at 400 kPa, with a varying mean flow velocity and inlet subcooling. This model successfully captures small variances due to the change in the experimental conditions including both inlet subcooling and flow velocity and gives a satisfactory prediction. It matches the experimental results in both single-phase convective heat transfer and subcooled boiling regions, and predicts the location where departure from nucleate boiling occurs based on the bubble coalescence model. The average error within the nucleate boiling range is estimated to be less than 20%, as is shown in Fig. 18. For comparison, the results for EX12 without considering bubble interaction is displayed in Fig. 17. These results are significantly higher than those with bubble interaction considered after the onset of nucleate boiling (ONB).

With a further increase in the wall superheat ΔT_{sat}, the predicted heat flux reaches its maximum and starts to slowly decrease thereafter. What characterizes the maximum capacity of a given heated surface is the CHF, which is identified in this model as the maximum predicted heat flux. As described in Part I, the application of this model is limited upon reaching the CHF. The decreasing trend after the maximum, which mainly results from the decrease in q_{ev} due to the decrease in the most probable bubble radius, does not reflect the transition from CHF to maximum heat flux (MHF) and has weak physical meanings. The assumption that bubbles are immediately removed from the boundary layer upon their coalescence or lift-off excludes the possibility of bubble clustering in the bulk fluid, as well as the resulting blockage of the heated surface and cut-off of liquid supply. Thus, the location of maximum heat flux on the predicted boiling curve should be interpreted, as with a further increase in wall superheat, the surface heat flux is limited by the maximum capacity of the heated surface and remains nearly unchanged until the transition to the film boiling occurs.

Figure 19 shows the bubble lift-off radius distribution under different wall superheats. The bubble departure radii (r_d) under these conditions are also identified for reference. Bubble interaction increases with increased wall temperature. At $\Delta T_{sat}=10°C$, the bubble population on the heated surface has been sufficiently high so that, as a result of bubble interaction, only 15.3% of the bubbles survive to their lift-off sizes ($r_{l10}=0.084$ mm) predicted by the bubble force balance model of Thorncroft et al. [7] and maximizes their contribution to the total heat flux. With a further increase in wall superheat, at $\Delta T_{sat}=20°C$, bubbles are most likely to interact with others and leave the heated surface at $r_b=21.4$ μm. As a comparison, the model of Thorncroft et al. [7]

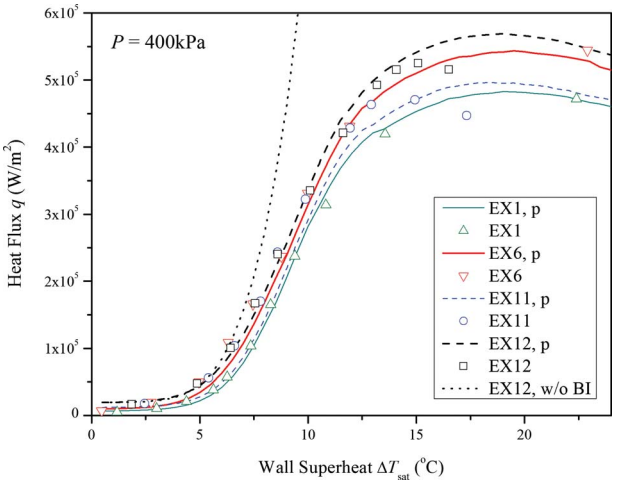

Fig. 17 Predicted R134a boiling curves at 400 kPa

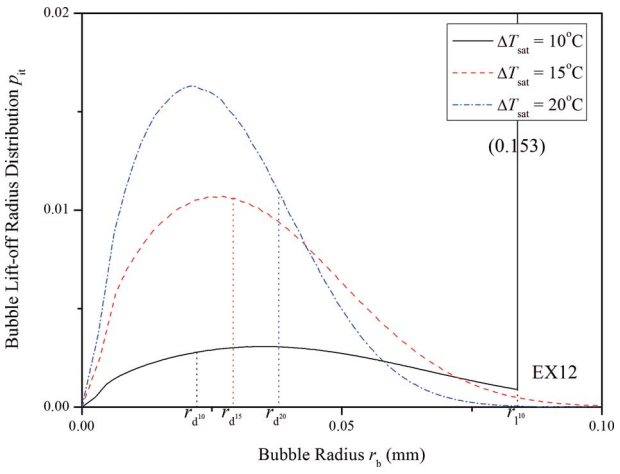

Fig. 19 Bubble lift-off radius distribution at 400 kPa. (The sudden increase in p_{it} for $\Delta T_{sat}=10°C$ at $r_b=r_{l10}=0.084$ mm is governed by the model of Thorncroft et al. [7], which predicts that all bubbles surviving from bubble interactions should lift off at r_l. This also explains the similar behavior of p_{it} in Fig. 22.)

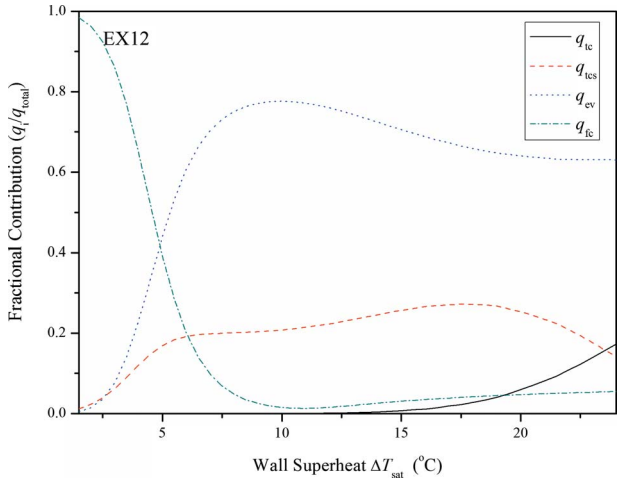

Fig. 20 Fractional contribution of heat flux at 400 kPa

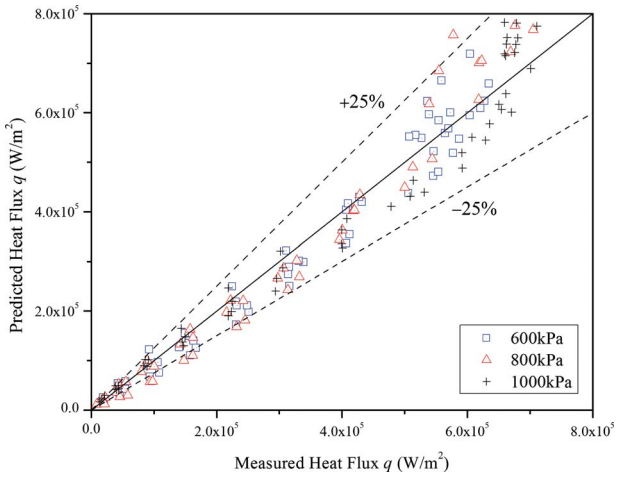

Fig. 21 Comparison of the predicted heat flux with R134a data at higher pressures

gives r_d=37.8 μm and r_l=164.2 μm, indicating that most of the bubbles interact and lift off before they start sliding on the heated surface.

Figure 20 shows the fractional contribution of various heat transfer mechanisms from a model prediction. Heat flux components due to different mechanisms, i.e., q_{ev} (evaporation), q_{tc} (transient conduction due to stationary bubbles), q_{tcs} (transient conduction due to sliding bubbles), and q_{fc} (forced convection) are reported. At low wall superheat, the heat transfer is dominated by the single-phase forced convection, considering that very few bubbles are generated on the heated surface. With an increase in wall superheat, contributions from both evaporation and transient conduction due to sliding bubbles increase dramatically. This is contributed by the rapid increase in the number of bubbles on the heated surface. Because the average separation distance of the nucleation sites is much larger than both the bubble departure and the bubble lift-off radii, bubbles are sparsely displaced on the heated surface. Most bubbles slide from their originating nucleation sites and lift off somewhere downstream. The contribution of transient conduction from stationary bubbles (those bubbles that do not slide before they lift off) remains nearly zero. With a further increase in the wall superheat, q_{ev} remains at 60–70% of the total heat flux, while q_{tc} increases and q_{tcs} decreases due to the increased bubble frequency and the bubble sizes. Bubble interaction probability increases, which results in an increased number of stationary bubbles and a decreased number of sliding bubbles. At predicted CHF, the total contribution of transient conduction is around 35% of the total heat flux with the remaining 65% being contributed by evaporation.

3.4.3 Comparison of Model Predictions With R134a Data at Higher Pressures. Model prediction is also attempted at higher pressures for the test conditions listed in Table 1, with the comparison to the 25 sets of measured R134a boiling curve data shown in Fig. 21. The overall agreement is found to be satisfactory, with most of the predictions staying within ±25% of the experimental measurements. This model gives the best predictions at 400 kPa and 600 kPa, but as the pressure increases, the average error between the predictions and the measurements increases, indicating that this model, being developed and verified at low pressures, may not be fully applicable at high pressures. In Sec. 3.4.4 a detailed comparison will be given on different aspects, followed by an explanation of why the applicability of this model is currently limited to a relatively low pressure range.

3.4.4 Discussion of the Effect of System Pressure. In experiments, with the increase in system pressure, bubble size, bubble generation frequency, and latent heat of the test liquid all decrease, leading to a decreased contribution of a single bubble to the overall heat flux. Although the vapor density does increase, it is not sufficient to compensate for the above changes. Table 2 summarizes the contribution of a single bubble under different pressures, which decreases by 60.0% from 400 kPa to 1000 kPa without considering the bubble interaction. Figures 19 and 22 show the increase in bubble interaction with pressure increase, e.g., at ΔT_{sat}=10°C under 400 kPa, 15.3% of the bubbles lift off without interaction, while under 1000 kPa this ratio decreases to 2.68%. Furthermore, as the pressure increases, bubbles tend to coalesce at smaller radius before reaching their departure radii r_d. All these predict a decreasing trend of the contribution of a single bubble to the overall heat flux during its life span with the increase in system pressure.

The increase in active nucleation sites controlled by the de-

Table 2 Variation in vapor bubble properties with pressure

P (kPa)	r_l (μm)	f_b (Hz)	h_{fg} (kJ/kg)	ρ_v (kg/m^3)	$h_{fg}\cdot\rho_v\cdot V$ (normalized) (%)
400	83.8	6552	191.61	19.529	100.0
600	65.4	4617	180.89	29.155	67.0
800	55.5	2849	171.81	39.025	52.1
1000	47.8	2670	163.66	49.222	40.0

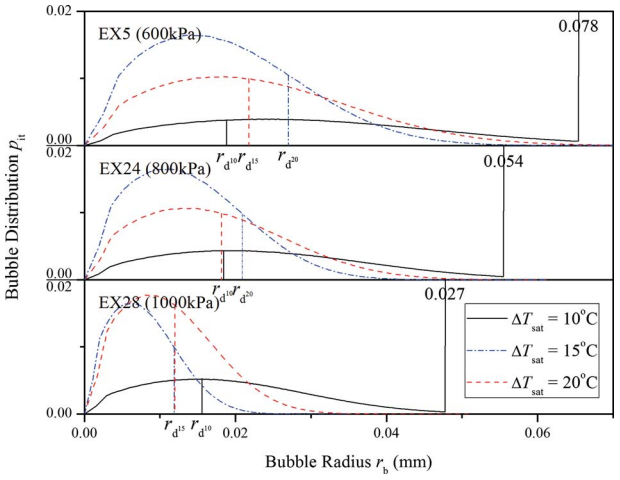

Fig. 22 Bubble lift-off radius distribution at higher pressures

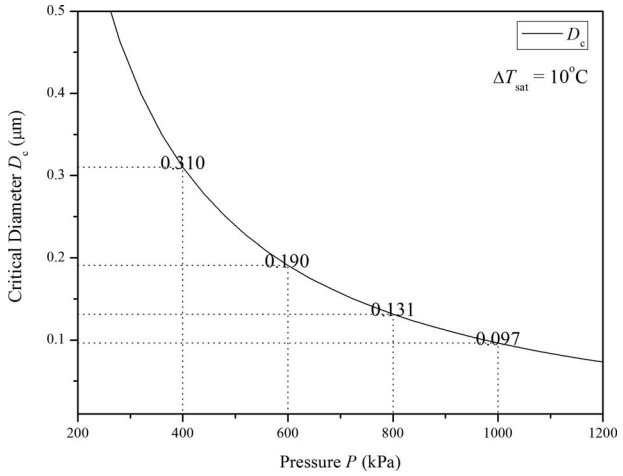

Fig. 23 Variation in critical diameter D_c with pressure

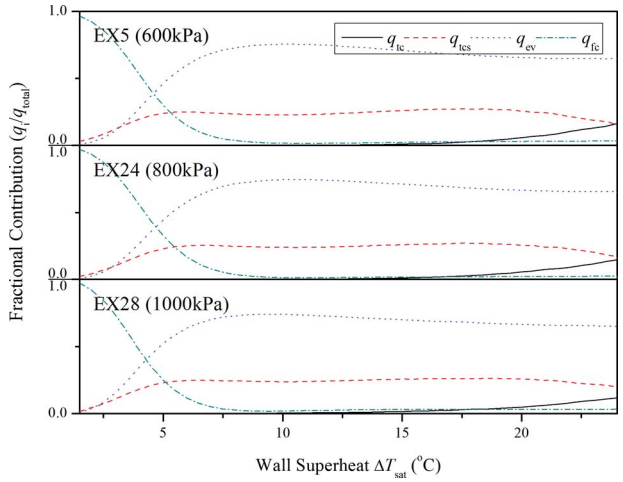

Fig. 24 Fractional contributions of heat flux at higher pressures

crease in critical diameter D_c is the major factor that compensates for this change. Figure 23 shows the variation in D_c with pressure increase. Under the same $\Delta T_{sat}=10°C$, D_c decreases from 0.31 μm to 0.097 μm when the pressure increases from 400 kPa to 1000 kPa due to the change in test fluid property, as is calculated from the expression of D_c

$$D_c = \frac{4\sigma T_{sat}}{\rho_v h_{fg} \Delta T_{sat}} \tag{4}$$

As the nucleation site density N_a is proportional to D_c^{-2}, this change corresponds to 10.26 times of increase in the active nucleation site density under the same wall superheat. Hence, with an increase in pressure, although the single bubble contribution decreases, the total number of bubbles existing on the heated surface during the same period increases to balance this change.

It is hard to precisely estimate the effect of pressure on heat flux due to the currently limited knowledge on the active nucleation site density. It is experimentally established that with an increase in pressure, more bubbles are observed, which is qualitatively explained from the decrease in D_c. However, a reliable expression of the relationship between the increase in nucleation site density and D_c is still unavailable.

Most experiments choose low pressure for low operating cost. However, theories developed based on observation within a low pressure range may become invalid for increased pressures. A comprehensive discussion of the effect of pressure on the active nucleation sites is unavailable. Further study is required to improve the estimation of active nucleation site density at higher pressures.

Figure 24 shows the fractional contribution of heat flux with varying wall superheat under different pressures. In comparing with the fractional contribution at 400 kPa in Fig. 20, it is observed that no major change in the portion of different heat flux components occurs for R134a under different pressures.

3.4.5 Comparison With Measured Critical Heat Flux. As introduced in Part I, the model developed in this work predicts the existence of a maximum heat flux with wall superheat increase as a part of the boiling curve prediction. Figure 25 shows the comparison between the model predictions and the measured critical heat flux from 20 sets of data collected between 400 kPa and 1000 kPa, within which 18 of them lie in the range of $\pm 20\%$ of the predictions. This good agreement is considered representing the success of this modeling approach and suggesting further attention to studies of this kind. As the first attempt to apply stochastic modeling and incorporate random effect of bubble coalescence into the mechanistic boiling curve prediction, this stochastic modeling approach not only predicts the boiling curve, but also realizes the prediction of the maximum nucleate boiling heat flux or critical heat flux as a natural extension of the boiling curve prediction, which has not been successfully achieved before. If such an approach can be further validated, it may effectively unify the existing studies that are currently classified into two categories: (1) those that study the mechanisms of nucleate boiling and (2) those that study the mechanisms of critical heat flux.

3.4.6 Comparison With Water Data in the Literature. The model has also been applied to data available in the literature. Figures 26 and 27 show comparisons between the experimental data published by McAdams et al. [8] and the predicted boiling curves. Experiments were conducted for water boiling on a vertical stainless steel surface. The conditions are: $P=0.413$ MPa, $V=1.22$ m/s (Fig. 26) or 0.34 m/s (Fig. 27), and $\Delta T_{sat}=27.8°C$. Since the value of the static contact angle was not measured in their experiments, a typical value of 38 deg provided by Basu et al. [9] is used in the calculation. Comparison is done within the range of the experimental data with good agreement displayed, in both the prediction of the heat flux and the trend of departure from nucleate boiling (for $V=1.22$ m/s), as is shown in Fig. 26. Modeling predictions made by Basu et al. [9] and Kandlikar [10] are also displayed for comparison, but none of them predicted the DNB. This model gives the best mechanistic prediction to date.

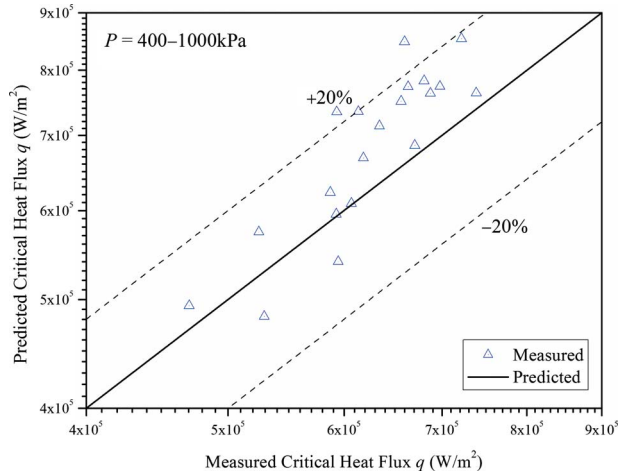

Fig. 25 Comparison of the predicted critical heat flux with R134a data

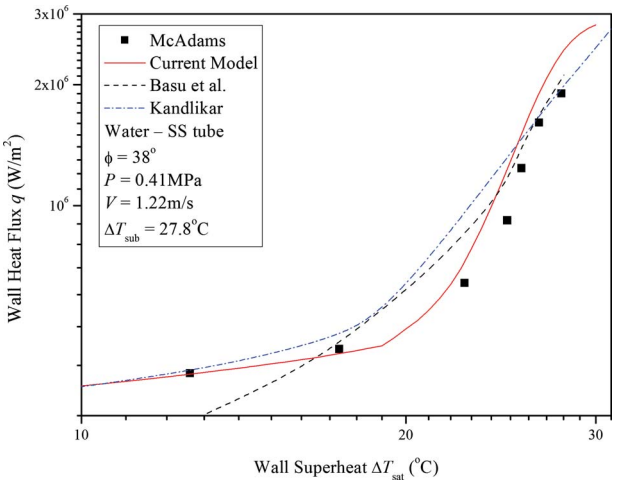

Fig. 26 Boiling curve comparison with the data by McAdams et al. [8]

4 Summary

The validation of a mechanistic model for the boiling curve prediction proposed earlier is discussed in this paper. In the first step of the validation process, the model is applied to experimental data measured on a horizontal heated surface under: (1) inlet pressure of 400–1000 kPa, (2) flow velocity of 0.10–0.25 m/s, and (3) inlet subcooling temperature of 10–30°C. The active nucleation site density N_a is measured and correlated with critical diameter D_c and static contact angle θ by borrowing the form of the formula proposed by Basu et al. [2]. The underlying submodels describing bubble growth and bubble departure/lift-off are compared with experimental measurements, with good agreement achieved.

Comparison between the predicted and measured boiling curves shows an excellent agreement at an average difference of ±25%. The model successfully captures small variances of the heat flux resulting from the different inlet subcoolings and flow velocities. The effect of the system pressure is discussed and explained. Examination of the bubble interaction probability confirms its effect on the surface heat flux. For boiling in R134a as ΔT_{sat} increases, due to bubble growth and bubble interaction, 30–40% of the total heat flux is contributed by the transient conduction resulted from bubble lift-off, with the majority of the rest due to the evaporation.

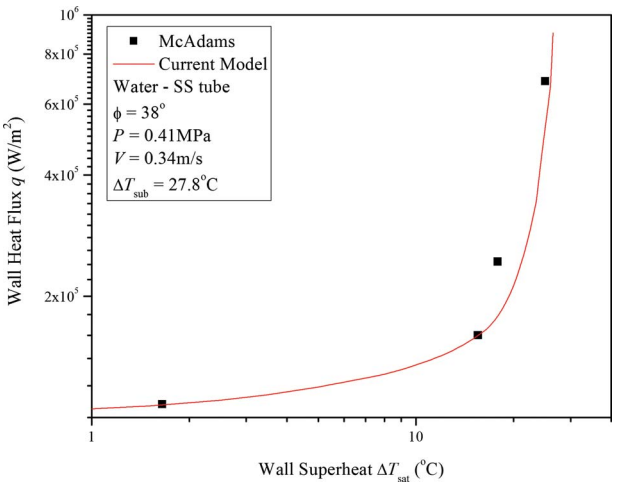

Fig. 27 Boiling curve comparison with the data by McAdams et al. [8]

Twenty predicted maximum heat flux values are benchmarked by the measured critical heat flux, with a difference of ±20% observed. In the second step of validation, predictions are made for water in vertical circular tubes and compared with the data by McAdams et al. [8], with good agreements shown. The result confirms that the application of this model is not limited to horizontal flat heat exchangers. It can be extended to various flow geometries and different test fluids.

Future studies are expected on the effect of system pressure, especially on the prediction of active nucleation sites under varying pressures with the statistical influence of vapor bubbles on the activation of nucleation sites investigated. The bubble motion following their coalescence may be another topic of particular interest. This model assumes immediate bubble lift-off following coalescence based on our experimental observation, while the coalescence-slide assumption was also considered in some studies, e.g., for boiling with water in the modeling approach of Basu et al. [9], although it contradicts our observation. Direct numerical simulation may need to be carried out in order to determine the range of application of these two assumptions. A separate but similar modeling approach with the coalescence-slide assumption may be required for certain system configurations. Finally, a statistical model on the bubble removal from the vicinity of bubble/surface contact upon bubble coalescence is expected to replace the current immediate bubble removal assumption and incorporate into the existing model to improve the prediction of maximum heat flux and explain the transition from nucleate boiling to film boiling.

Acknowledgment

The study is performed in the Air Conditioning and Refrigeration Center (ACRC) at the University of Illinois at Urbana-Champaign. The project is sponsored by the U.S. Department of Energy under Contract No. DOE DEFG07-00ID14601.

Nomenclature

D = diameter (m)
f = frequency of bubbles (Hz)
h = heat transfer coefficient (W/m^2 K)
h_{fg} = latent heat (J/kg)
N = nucleation site density or bubble density ($1/m^2$)
p = probability or probability density function
P = pressure (kPa)
q = surface heat flux (W/m^2)
r = bubble radius (m) or bubble sliding ratio
T = temperature (K)
V = flow velocity

Greek Symbols

θ = surface contact angle (deg)
ρ = density (kg/m^3)
σ = surface tension (N/m)

Subscripts

a = active nucleation site
b = bubble
B = bulk region or buoyancy
c = cavity or conditional probability
d = departure or bubble diameter
ev = evaporation
fc = forced convection
g,v = vapor
l = lift-off
s = sliding
sat = saturated condition
sub = subcooled condition
tc = transient conduction

w = wall/fluid near the wall or waiting time (when using with t)

References

[1] Wu, W., Jones, B. G., and Newell, T. A., 2009, "A Statistical Model of Bubble Coalescence and Its Application to Boiling Heat Flux Prediction—Part I: Model Development," ASME J. Heat Transfer, **131**(12), p. 121013.

[2] Basu, N., Warrier, G. R., and Dhir, V. K., 2002, "Onset of Nucleate Boiling and Active Nucleation Site Density During Subcooled Flow Boiling," ASME J. Heat Transfer, **124**, pp. 717–728.

[3] Fitzgibbon, A., Pilu, M., and Fisher, R. B.1999, "Direct Least Squares Fitting of Ellipses," IEEE Trans. Pattern Anal. Mach. Intell., **21**(5), pp. 476–480.

[4] Taubin, G., 1991, "Estimation of Planar Curves, Surfaces and Non-Planar Space Curves Defined by Implicit Equations, With Applications to Edge and Range Image Segmentation," IEEE Trans. Pattern Anal. Mach. Intell., **13**(11), pp. 1115–1138.

[5] Wu, W., Chen, P., Jones, B. G., and Newell, T. A., 2008, "A Study on Bubble Detachment and the Impact of Heated Surface Structure in Subcooled Nucleate Boiling Flows," Nucl. Eng. Des., **238**(10), pp. 2693–2698.

[6] Mikic, B. B., Rohsenow, W. M., and Griffith, P., 1970, "On Bubble Growth Rates," Int. J. Heat Mass Transfer, **13**, pp. 657–666.

[7] Thorncroft, G. E., Klausner, J. F., and Mei, R., 2001, "Bubble Forces and Detachment Models," Multiphase Sci. Technol., **13**(3&4), pp. 35–76.

[8] McAdams, W. H., Kennel, W. E., Minden, C. S., Carl, R., Picornell, P. M., and Dew, J. E., 1949, "Heat Transfer at High Rates to Water With Surface Boiling," Ind. Eng. Chem., **41**(9), pp. 1945–1953.

[9] Basu, N., Warrier, G. R., and Dhir, V. K., 2005, "Wall Heat Flux Partitioning During Subcooled Flow Boiling: Part II—Model Validation," ASME J. Heat Transfer, **127**, pp. 141–148.

[10] Kandlikar, S. G., 1997, "Further Developments in Subcooled Flow Boiling Heat Transfer," Engineering Foundation Conference on Convective and Pool Boiling, Irsee, Germany, May 18–25.

Modeling Alkaline Liquid Metal (Na) Evaporating Thin Films Using Both Retarded Dispersion and Electronic Force Components

Joseph B. Tipton, Jr.

Kenneth D. Kihm[1]
e-mail: kkihm@utk.edu

Department of Mechanical, Aerospace and Biomedical Engineering,
University of Tennessee,
Knoxville, TN 37996-2210

David M. Pratt
Structures Division, Air Vehicles Directorate,
United States Air Force Research Laboratory,
Wright-Patterson AFB, OH 45433-7542

A new thin-film evaporation model is presented that captures the unsimplified dispersion force along with an electronic disjoining pressure component that is unique to liquid metals. The resulting nonlinear fourth-order ordinary differential equation (ODE) is solved using implicit orthogonal collocation along with the Levenberg–Marquardt method. The electronic component of the disjoining pressure should be considered when modeling liquid metal extended meniscus evaporation for a wide range of work function boundary values, which represent physical properties of different liquid metals. For liquid sodium, as an example test material, variation in the work function produces order-of-magnitude differences in the film thickness and evaporation profile.
[DOI: 10.1115/1.4000022]

Keywords: liquid metal evaporation, sodium, micro/nanoscale, heat transfer, modified disjoining pressure, electronic component by free electrons

1 Introduction

The evaporation of fluids provides an efficient method for heat transfer and passive cooling in devices such as heat pipes and capillary pumped loops. A liquid metal working fluid enables operation in extremely high temperature environments with the added benefits of a high latent heat of evaporation and high heat transfer coefficient. Numerical and experimental studies have applied liquid metal heat pipes and capillary pumped loops in nuclear, hypersonic, and space based systems. In the case of aerospace systems, minimization of system mass calls for a consideration of microscale heat transport devices. Microscale heat pipes have already found applications in the cooling of high performance electronics [1–4]. In microscale systems using conventional coolant fluids, such as water or refrigerants, the thin-film region has been shown to contribute greatly toward meniscus stability and evaporation [5–7].

High temperature liquid metal evaporation on the microscale, however, has received little attention in the literature [8,9]. In analytically studying liquid metal evaporation, one of the main difficulties arises from the presence of free electrons, whereas most conventional coolants are dielectric. To address this knowledge gap, this paper proposes new models for the extended meniscus evaporation of alkaline metal, such as liquid sodium, under capillary and dispersion forces as well as a relatively newly proposed force due to degeneracy of the free electrons in a liquid metal thin film.

As shown in Fig. 1, the interline or contact line region of an evaporating extended meniscus consists of three subregions. In the adsorbed region, a disjoining pressure dominates the local atomic forces. In the intrinsic or bulk meniscus region, the interfacial curvature governs the driving physics through surface tension. The transition or thin-film region exists between the intrinsic meniscus and adsorbed regions where both the disjoining pressure and the interfacial curvature share a comparable influence.

Previous studies addressed numerical heat and mass transfer solutions for steady extended meniscus evaporation. Here, steady connotes a static interline region continually replenished by fluid from the intrinsic meniscus. Wayner and Schonberg [10] developed a governing equation for the film height of a symmetric meniscus as a function of distance between two feed ports. Their development draws upon the pioneering thin-film experiments of Derjaguin et al. [11], Schrage's [12] relationship for net mass flux across a liquid/vapor interface, and the evaporating extended meniscus models of Wayner et al. [13], and Potash and Wayner [14]. Later, Chebaro and Hallinan [15] and Chebaro et al. [16] introduced new nondimensional variables, which re-expressed Wayner and Schonberg's model in a more meaningful manner. They also created an explicit Runge–Kutta numerical solution procedure, which meets the correct system boundary conditions by way of the "shooting method."

London dispersion forces are the only active component of the van der Waals category of long-range atomic forces for the case of neutral atoms and nonpolar molecules. Hamaker [17] first described the London dispersion forces between two media acting in a third medium by considering the microscopic interaction between two molecules and summing under the assumption of additivity. Hamaker's theory does not include the Keesom and Debye forces of polar molecules, the effects of temperature, or time delay effects in the communication of electromagnetic fields between atoms at larger distances (retardation). Lifshitz [18] later pursued a macroscopic approach which modeled the bulk interaction between two media in a vacuum by considering the fluctuation of electromagnetic fields between the two media. Lifshitz's theory incorporates the shortcomings of Hamaker's theory but is limited to interactions in a vacuum. Finally Dzyaloshinskii, Lifshitz, and Pitaevskii (DLP) [19] used quantum electrodynamics to derive the first general theory of van der Waals forces. While much more complex mathematically, the DLP theory successfully includes the interaction of two media in a third medium. The only major restriction is the assumption of planar geometries.

Since the DLP theory originates from a macroscopic perspective, the van der Waals forces can be described using continuum properties of the participating media in the form of their frequency-dependent, dielectric permittivities. When temperature effects can be neglected and when the film thickness is small

[1]Corresponding author.

Manuscript received January 9, 2009; final manuscript received April 7, 2009; published online October 15, 2009. Assoc. Editor: Yogesh Jaluria.

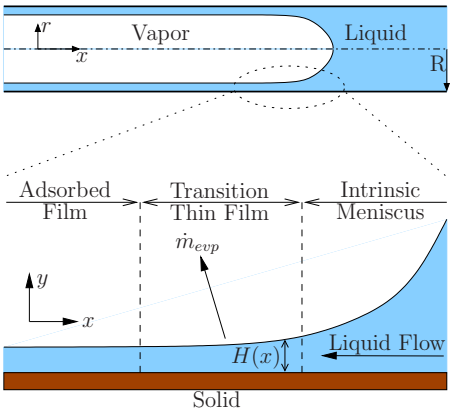

Fig. 1 Schematic of a cylindrical capillary geometry identifying the distinct regions of the extended evaporating meniscus. The majority of heat and mass transfer occurs in the transition thin-film region.

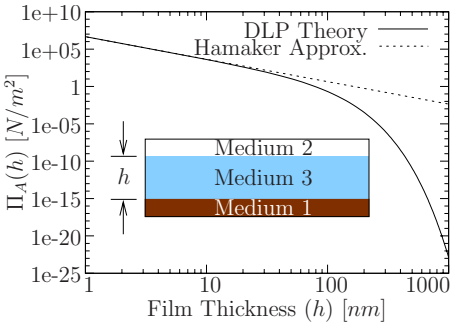

Fig. 2 A comparison of the retarded DLP theory and nonretarded (Hamaker approximation) London dispersion component of the disjoining pressure for the case of type 304 stainless steel (Medium 1) and vapor (Medium 2) interacting across liquid sodium (Medium 3)

compared with the absorption wavelengths of the participating media, the retardation effects of the time delay in the communication of electric fields between atoms may be neglected, and the full DLP theory can be greatly simplified. The resulting nonretarded force is proportional to the inverse cube of the film thickness. This relationship is the macroscopic analog of the microscopic Hamaker theory. It is most often used in the engineering literature in the form of the well known Hamaker constant (Ref. [20], pp. 137–152). Thus, the Hamaker constant represents the limiting case of nonretarded dispersion forces. Prevailing convention assigns a negative value for the Hamaker constant for the case of spreading films, although the literature can be confusing.

At the opposite limit of a thick film, which results in a fully retarded dispersion force, several papers have mentioned an analytical solution proportional to the inverse fourth power of the film thickness [5,21–23]. These works fail to mention the requirements for this solution, namely dielectric materials, film thicknesses much greater than "the wavelengths which characterize the absorptions spectra of the given bodies," and film thicknesses much less than the temperature requirement $H \ll \hbar c/kT$ [19]. Only a select number of working fluids and operating temperatures meet these requirements. The case of a high temperature, liquid metal, evaporating thin film, however, invalidates each of these assumptions.

The original disjoining pressure concept, first proposed by Derjaguin in the 1930s, addresses the additional thin-film pressure created by van der Waals forces. Almost 50 years later, Derjaguin and co-workers [24,25] proposed the existence of an additional form of disjoining pressure in liquid metal films. Inspired by a theoretical prediction of anomalous effects in nanoscale metallic particles [26], they surmised that the free electrons in a thin metal film, modeled as a fermion gas, would experience a confinement in their position. According to Heisenberg's uncertainty principle, this confinement correlates with an increase in momentum. This electron degeneracy creates an increase in the energy density in the thin film and produces an effective "electron pressure" (for a good summary, see Ref. [27]).

Derjaguin and Roldughin [25] assumed films sufficiently thick such that the dispersion forces could be neglected. In addition, they assumed thick films, negligible exchange, correlation, and electrostatic interactions, a perfectly smooth surface, and a model of the electron as a noninteracting particle. In this way, they were able to derive a relationship between the change in kinetic energy of free electrons in the thin film and the disjoining pressure using quantum mechanical theory. The resulting electron degeneracy disjoining pressure varies in intensity and sign depending upon the work function (energy needed to move an electron from the liquid metal to the solid surface) of the system.

Derjaguin et al. [24] indirectly proved the existence of the electronic component to the disjoining pressure by experiment. The DLP Theory of van der Waals forces predict any two identical media will attract each other, regardless of the media in between. Thus, a *free* liquid metal thin film should experience a negative disjoining pressure which would render the film unstable. In contrast, Derjaguin et al. [24] demonstrated the stability of free films of liquid mercury in certain organic liquids, which could only be possible if a larger, positive disjoining pressure component was present.

As far as we can tell, the only previous attempt to model a liquid metal thin film using both the London dispersion force and electron degeneracy force as components of a disjoining pressure was by Ajaev and Willis [28,29]. They were concerned with "thermocapillary flow and rupture in films of molten metal on a substrate" when heated by a Gaussian laser beam. Ajaev and Willis correctly identified the need for both components of the disjoining pressure and, with neither a fundamental physics model nor experimental measurements available, suggested a linear combination of the two. Their paper presented a general parametric study that looked at model trends only. No attempt was made to calculate the appropriate value for either component of the disjoining pressure. In addition, the electronic component was treated under the simplifying assumption of an infinite potential energy well boundary condition.

This paper seeks to model the evaporation of high temperature, liquid metal, thin films and thus distinguishes itself from previous thin-film evaporation studies of more conventional liquids. The novel aspects of this research include (a) an accurate model of the retarded dispersion force component of the disjoining pressure, (b) the incorporation of the electronic component of the disjoining pressure, and (c) a parametric study of the thin-film solution over a range of system work functions that specify the ratio of electronic-to-dispersion components.

2 Modeling of Two-Component Disjoining Pressure

The two components hereby refer to the London van der Waals dispersion component and electronic degeneracy component.

2.1 Expanded van der Waals Contribution (Π_A) Using the Full DLP Theory. London dispersion forces are the only active component of the van der Waals category of long-range atomic forces for the case of substances with neutral atoms and nonpolar molecules [6]. The DLP general theory of van der Waals forces [19] describes the dispersion force per unit area between two smooth media with nonpolluted surfaces (1 and 2) while separated by a gap (H) that is filled with a third medium (3), as illustrated in Fig. 2. The interactions of the long-range atomic forces of the three media produce the dispersion force that is calculated in terms of the macroscopic dielectric permittivities:

$$-\Pi_A(H) = \frac{kT}{\pi c^3}{\sum_{n=0}^{\infty}}' \epsilon_3^{3/2}\omega_n^3 \int_{p=1}^{\infty} p^2 \left\{ \left[\frac{(s_1+p)(s_2+p)}{(s_1-p)(s_2-p)} \exp\left(\frac{2p\omega_n H}{c}\sqrt{\epsilon_3} \right) - 1 \right]^{-1} + \left[\frac{(s_1+p\epsilon_1/\epsilon_3)(s_2+p\epsilon_2/\epsilon_3)}{(s_1-p\epsilon_1/\epsilon_3)(s_2-p\epsilon_2/\epsilon_3)} \exp\left(\frac{2p\omega_n H}{c}\sqrt{\epsilon_3} \right) - 1 \right]^{-1} \right\} dp \tag{1a}$$

where

$$s_1 = \sqrt{\epsilon_1/\epsilon_3 - 1 + p^2} \tag{1b}$$

$$s_2 = \sqrt{\epsilon_2/\epsilon_3 - 1 + p^2} \tag{1c}$$

$$\omega_n = 2\pi nkT/\hbar \tag{1d}$$

$$\epsilon = \epsilon(i\omega_n) \tag{1e}$$

As a formality, the prime notation on the summation symbol serves to indicate that the term with $n=0$ is divided by half.

From the effect of dispersion, the permittivity of a substance is dependent upon the frequency of the incoming electromagnetic radiation. To a first approximation for a metal, one may assume no bound electrons and model the free electrons as classical forced oscillators with negligible dampening. The result, as given by Hecht ([30], pp. 129–130), relates the dielectric permittivity (assuming Maxwell's relation) to the incoming electromagnetic radiation as

$$\epsilon(\omega) \approx n^2(\omega) = 1 - (\omega_e/\omega)^2 \tag{2a}$$

or, in complex form,

$$\epsilon(i\omega) = 1 + (\omega_e/\omega)^2 \tag{2b}$$

where ω_e is the so-called plasma frequency of the free-electron gas,

$$\omega_e = N_e q_e^2/\epsilon_0 m_e \tag{2c}$$

If temperature has little effect on the interactions between the media ($H \ll c\hbar/kT$) and if the film thicknesses are small compared with the absorption wavelength of the participating media ($H \ll \lambda_{1,2,3}$) [19], then the full DLP theory may be simplified such that

$$\Pi_A(H) \approx \frac{A}{6\pi H^3} \tag{3a}$$

where the well-known Hamaker "constant" is incorporated as

$$A = \frac{3\hbar}{4\pi}\int_{\omega=\omega_1}^{\infty} \left(\frac{\epsilon_1(i\omega) - \epsilon_3(i\omega)}{\epsilon_1(i\omega) + \epsilon_3(i\omega)} \right) \left(\frac{\epsilon_2(i\omega) - \epsilon_3(i\omega)}{\epsilon_2(i\omega) + \epsilon_3(i\omega)} \right) d\omega \tag{3b}$$

following the development of Israelachvili (Ref. [20], p. 142). In this form, the dispersion force is said to be nonretarded since any retardation effects of the time delay in the communication of electric fields between atoms may be neglected. This relationship has been most commonly used for the cases of nonmetal thin-film analyses in many previous studies. For the relatively thicker liquid metal films, the corresponding dispersion force cannot be oversimplified by the Hamaker approximation. Instead, the DLP theory in its full must be used in modeling the energy and mass transport in the evaporating liquid metal transition thin film. To our knowledge, this has not been attempted by any research groups to date.

The disjoining pressure of the liquid medium (referred to as 3 in Fig. 2) is interpreted as the negative of the dispersion force per unit area between the planar surfaces (1 and 2). Medium 1 is the solid surface (type 304 stainless steel, smooth and nonpolluted surface, atomic weight: 54.81, 1.79 valence electrons per molecule, density: 8000 kg/m^3, plasma frequency $\nu_{e,1}=2.6620 \times 10^{15}$ Hz). Medium 2 is an inert gas at standard atmospheric pressure approximated by $\epsilon_2=1$. Medium 3 is the alkaline liquid such as pure, perfectly wetting sodium [31,32], $\nu_{e,3}=1.2522 \times 10^{15}$ Hz. Substituting these values and numerically integrating Eq. (3*b*) leads to the Hamaker constant value $A=-1.0199 \times 10^{-19}$ N m. In this configuration, when the dispersion force is negative, media 1 and 2 are repulsive, the disjoining pressure is positive, and the thin film is stable and spreading.

Figure 2 plots the nonretarded (Hamaker approximation) and retarded (full DLP theory) dispersion force for a liquid sodium thin film on a type 304 stainless steel substrate over a range of film thicknesses from 1 nm to 1 μm. Using Eqs. (2*a*)–(2*c*), Eq. (1*a*) was solved numerically with adaptive Lobatto quadrature in the MATLAB© programming environment. The summation was carried out to a relative convergence of 1×10^{-6}. The figure indicates that, for the prevailing stainless steel-sodium film-inert gas configuration, the Hamaker approximation is valid up to about 10-nm thickness but progressively deviates from the full DLP theory thereafter. As we shall see in Fig. 4, the free-electron degeneracy contribution tends to substantially increase the liquid metal film thicknesses in comparison with those of conventional coolants. Consideration of the full DLP theory will be necessary for modeling alkaline evaporating liquid metal thin film.

Since the retarded DLP model for van der Waals contribution (Π_A) is in a form that is quite intractable for use in most common numerical solution methods, we instead express the dispersion force curve of Eq. (1*a*) with a simpler function. Cubic spline interpolation fulfills the requirements of modeling over many orders of magnitude along with second-order differentiability. It furthermore offers a piecewise continuous curve that can be utilized in the collocation solution method, resulting in a continuous solution to the thin-film equation (details can be found in the Appendix).

A cubic spline interpolation model for the retarded dispersion force is bounded to the left by the thickness of the adsorbed film region and to the right by computer-limited round-off errors. Numerical experimentation shows that a good model can be created with negligible error when the retarded dispersion force curve for a domain for 10 nm$\le H \le$771 nm is split into $N=75$ piecewise continuous cubic splines described by

$$\Pi_{A,i}(H) = c_{1,i}(H-H_i)^3 + c_{2,i}(H-H_i)^2 + c_{3,i}(H-H_i) + c_{4,i}, \quad H \in [H_i, H_{i+1}], \quad i = 1,2,\ldots,N \tag{4a}$$

The total spline model then contains $4N$ unknowns (a_i, b_i, c_i, and d_i for $1<i<N$; $N=75$). Continuity through the second derivative provides $4N-2$ constraining equations. The final two constraining equations are specified in the second derivative of the end points

$$\Pi''_{A,1}(H_1) = \frac{2A}{\pi H_0^5} \tag{4b}$$

$$\Pi''_{A,75}(H_{75}) = 0 \tag{4c}$$

where asymptotic analysis at the limit of a thin film gives the Hamaker approximation which can be used for the left end point and the right end point is a so-called "natural" spline. For film thicknesses $H>771$ nm, the dispersion force and its derivatives are treated as negligible.

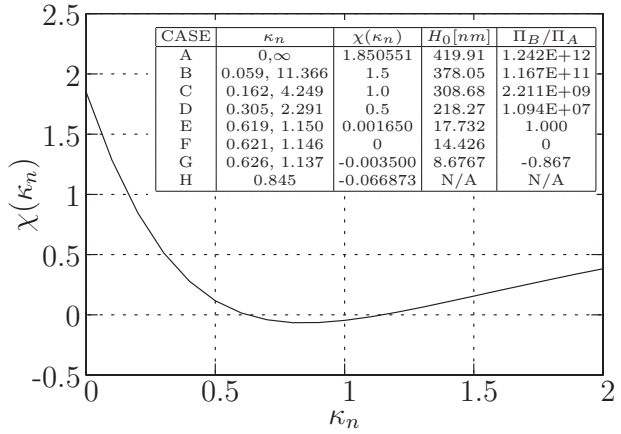

CASE	κ_n	$\chi(\kappa_n)$	$H_0[nm]$	Π_B/Π_A
A	0,∞	1.850551	419.91	1.242E+12
B	0.059, 11.366	1.5	378.05	1.167E+11
C	0.162, 4.249	1.0	308.68	2.211E+09
D	0.305, 2.291	0.5	218.27	1.094E+07
E	0.619, 1.150	0.001650	17.732	1.000
F	0.621, 1.146	0	14.426	0
G	0.626, 1.137	-0.003500	8.6767	-0.867
H	0.845	-0.066873	N/A	N/A

Fig. 3 Dependence of $\chi(\kappa_n)$ on the work function related parameter, κ_n, as related via Eq. (6*a*). This function determines the boundary condition for Derjaguin's electronic component of the disjoining pressure.

2.2 Electronic Degeneracy Contribution (Π_B) as Electronic Component. The free electrons in a thin metal film will experience a confinement in their position and this electron degeneracy creates an increase in the energy density and produces an effective "electron pressure." Therefore, an *additional* contribution to the disjoining pressure needs to be accounted for in the liquid metal thin film. Based on quantum mechanical theory, Derjaguin and Roldughin [25] derived a solution for a disjoining pressure component as a function of the change in kinetic energy of electrons

$$\Pi_B(H) \approx \frac{B}{H^2}, \quad B = \frac{\hbar^2}{2m}\frac{N_e}{V}\chi(\kappa_n) \tag{5}$$

where the parameter χ depends upon the boundary conditions of the system. Important assumptions include (1) thick films, (2) negligible exchange, correlation, and electrostatic interactions, a perfectly smooth surface, and (3) a model of the electron as a noninteracting particle. Roldughin [27] described κ_n as "the distance by which electrons are 'allowed' to go out into the external environment." In so doing, they reduce the energy density of the fermion gas and lower the electronic disjoining pressure.

The parameter κ_n is itself closely related to the work function, W, or energy needed to move an electron from the liquid metal to the solid surface

$$\chi(\kappa_n) = \Sigma_1\Sigma_2 - \frac{1}{4}\Sigma_1^2 \tag{6a}$$

where

$$\Sigma_1 = \frac{\pi}{2} - 2\left[\tan^{-1}(\kappa_n) + \kappa_n - \kappa_n^2 \tan^{-1}\left(\frac{1}{\kappa_n}\right)\right] \tag{6b}$$

$$\Sigma_2 = \frac{\pi}{2} - 2\tan^{-1}(\kappa_n) \tag{6c}$$

$$\kappa_n = \sqrt{1 + \frac{W}{E_F}} \tag{6d}$$

Figure 3 displays this function in graphical form. Depending on the work function of the system, the electronic disjoining pressure can vary in intensity and even become negative, resulting in an unstable film. The minimum value $\chi = -0.066873$ occurs at $\kappa_n = 0.844664$. Also, as κ_n approaches the limits of zero and infinity, the adjusting parameter χ approaches the same limit of $3\pi^2/16$. The infinite limit represents the simplified assumption of an infinitely deep potential pit at the liquid/surface boundary that prevents electrons from emerging from the film as first derived in Derjaguin et al. [24].

Knowledge of the proper work function for a given system proves intractable at the present as this boundary condition depends heavily on a quantum mechanical description of the system that is intimately tied to the surface conditions between the solid and liquid. Instead, we seek to define the range of values which the work function might take in a liquid sodium thin-film system.

The constant part of B, as defined in Eq. (5), is calculated at the melting point of liquid sodium following the method of Derjaguin et al. with the boundary condition parameter χ varying with κ, which is itself a function of the work function.

$$B = \frac{\hbar^2}{2m}\frac{N_e}{V}\chi(\kappa) = 1.1873 \times 10^{-10} \cdot \chi(\kappa) \tag{7}$$

From the discussion surrounding Fig. 3, it is readily apparent that the boundary condition parameter will vary within a set range ($-0.066873 \le \chi(\kappa) \le 1.850551$) which, in turn, yields the range of possible values for B ($-6.837223 \times 10^{-12} \le B \le 1.892039 \times 10^{-10}$).

2.3 Thin Film Equation for Liquid Metal Coolants. Chebaro and co-workers [15,16] used the assumptions of lubrication theory, a simplified curvature, and the augmented Laplace–Young equation to model steady extended meniscus evaporation. Using the following nondimensionalizing variables,

$$\theta = H/H_0, \quad \eta = x/x_0, \quad \bar{\Pi} = \Pi/\Pi_0$$

$$\dot{m}_0 = \rho_l u_0, \quad Ca = \mu_l u_0/\sigma, \quad x_0 = (\sigma H_0/\Pi_0)^{1/2}$$

$$\dot{m}_0 = \left(\frac{2\alpha}{2-\alpha}\right)\left(\frac{\mathcal{M}}{2\pi\mathcal{R}T_v}\right)^{1/2}\left(\frac{P_v\mathcal{M}h_{fg}}{\mathcal{R}T_vT_{lv}}\right)(T_{lv} - T_v)$$

$$\Pi_0 = \frac{\mathcal{M}h_{fg}\Delta T}{V_l T_v}, \quad \Delta T = T_{lv} - T_v$$

they expressed the thin-film interfacial profile as the following nondimensional, nonlinear, inhomogeneous, fourth-order, ordinary differential equation

$$[\theta(\eta)^3\theta(\eta)''' + \theta(\eta)^3\bar{\Pi}(\theta)']' = \frac{-3Ca}{\left(\frac{H_0\Pi_0}{\sigma}\right)^2}[1 - \theta(\eta)'' - \bar{\Pi}(\theta)],$$

$$\eta \in [0,\infty) \tag{8a}$$

where $\eta = 0$ represents the adsorbed film and $\eta = \infty$ represents the bulk meniscus region. The boundary conditions chosen to describe the system were

$$\theta(0) = a_1 \tag{8b}$$

$$\theta'(0) = a_2 \tag{8c}$$

$$\theta''(\infty) = a_3 \tag{8d}$$

$$\theta'''(0) = 0 \tag{8e}$$

The initial perturbations of the dependent variable θ and its first derivative are necessary to avoid a trivial solution and do correspond to physical realities as described in Hallinan et al. [33] (albeit somewhat tenuously), where $a_1 = 1.030$ and $a_2 = 0.0004$. The boundary condition on the second derivative of the dependent variable is $a_3 = K$, where K is the curvature of the bulk meniscus region. Thus, in practice, $\eta = \infty$ is taken to be a point in the far field, $l_{\max}$, where the second derivative approaches an asymptotic value that is the reciprocal of the pore radius $K = 1/R$.

Since Eq. (8*a*) is constructed upon the assumption of lubrica-

tion theory fluid flow, the pressure gradient required to drive the flow and maintain a steady thin-film profile is known to be

$$\frac{dP}{dx} = -\frac{\Pi_0}{x_0}[\theta(\eta)''' + \bar{\Pi}(\theta)'] \tag{9}$$

using the nondimensional variables previously defined. Similarly, the evaporative mass flux along the fluid/vapor interface can be described as

$$\dot{m}_{\text{evp}} = \dot{m}_0[1 - \theta(\eta)'' - \bar{\Pi}(\theta)] \tag{10}$$

which is a direct result of the augmented Laplace–Young equation first derived by Wayner et al. [13] and used by Chebaro et al. [16] to construct Eq. (8*a*).

Following Ajaev and Willis [28], the nondimensionalized total disjoining pressure is treated as an additive combination of the dispersion force and electronic components

$$\bar{\Pi}(\theta) = \frac{\Pi_{A,i}(\theta)}{\Pi_0} + \frac{\Pi_B(\theta)}{\Pi_0}$$

$$\theta \in [\theta_i, \theta_{i+1}], \quad i = 1,2, \ldots, 75 \tag{11}$$

which consists of 75 different equations due to the cubic spline interpolation of the dispersion force. Equations (8*a*) and (11) are combined and solved using orthogonal collocation with Chebyshev polynomials of the first kind as the basis function. The collocation coefficients are found via the Levenberg–Marquardt method. Spatial and iterative studies suggest a 100 term expansion provides an accurate, converged model. The Appendix presents more details on the solution procedure using orthogonal collocation.

3 Results and Discussion

3.1 Dependency of the Electronic Degeneracy Contribution on Work Function. The inset of Fig. 3 gives the parametric variations of the electronic disjoining pressure Π_B resulting from a variation in the system work function boundary condition $\chi(\kappa_n)$ for a given liquid overheat, $\Delta T = 0.0005$ K, and pore radius, $R = 200$ μm. In each case, adsorbed film thicknesses, H_0, are solved by assuming both negligible mass flux and curvature.

Case A represents the upper limit to the electronic disjoining pressure boundary condition $(3\pi^2/16)$ as previously described. It, along with Cases B–D, results in a system where the electronic disjoining pressure (Π_B) dominates over the retarded dispersion component (Π_A). The dispersion component of the disjoining pressure is negligible and can be removed from the governing equation. In cases A–D, the electrons barely penetrate into the substrate, which keeps the electron "pressure" high.

In Case E, the system work function boundary condition parameter $\chi(\kappa_n)$ is chosen such that both components of the disjoining pressure are equal in magnitude. In Case F, the electronic disjoining pressure is zero and the system retains only the dispersion force component of the disjoining pressure. Case G represents the lowest electronic disjoining pressure boundary condition possible for a stable thin-film solution and was obtained by a trial and error approach. This results in a situation where the positive London dispersion disjoining pressure just overcomes the negative (repulsive) electronic disjoining pressure. In cases E–G, electrons readily penetrate into the substrate, effectively lowering the electron pressure.

Finally, Case H represents the lower limit to the electronic disjoining pressure boundary condition as previously described. It results in a negative electronic disjoining pressure that overcomes the positive London dispersion disjoining pressure. As such, no steady thin-film solution is possible.

3.2 Thin Film Solutions for Liquid Sodium Under Different Work Functions. Figure 4 shows the corresponding results of a variation in the electronic disjoining pressure boundary condition parameter, $\chi(\kappa_n)$, on the (a) liquid metal thin-film profile, (b) evaporative mass flux, and (c) liquid pressure gradient. It is interesting to note that the solutions tend to follow two very distinct thin-film profiles. Either the electronic component of the disjoining pressure causes a drastic change in the extended evaporating meniscus or it does not. As a particular consequence, the adsorbed film thickness tends toward two distinct ranges of values that are an order of magnitude apart.

For the majority of work function boundary condition values,

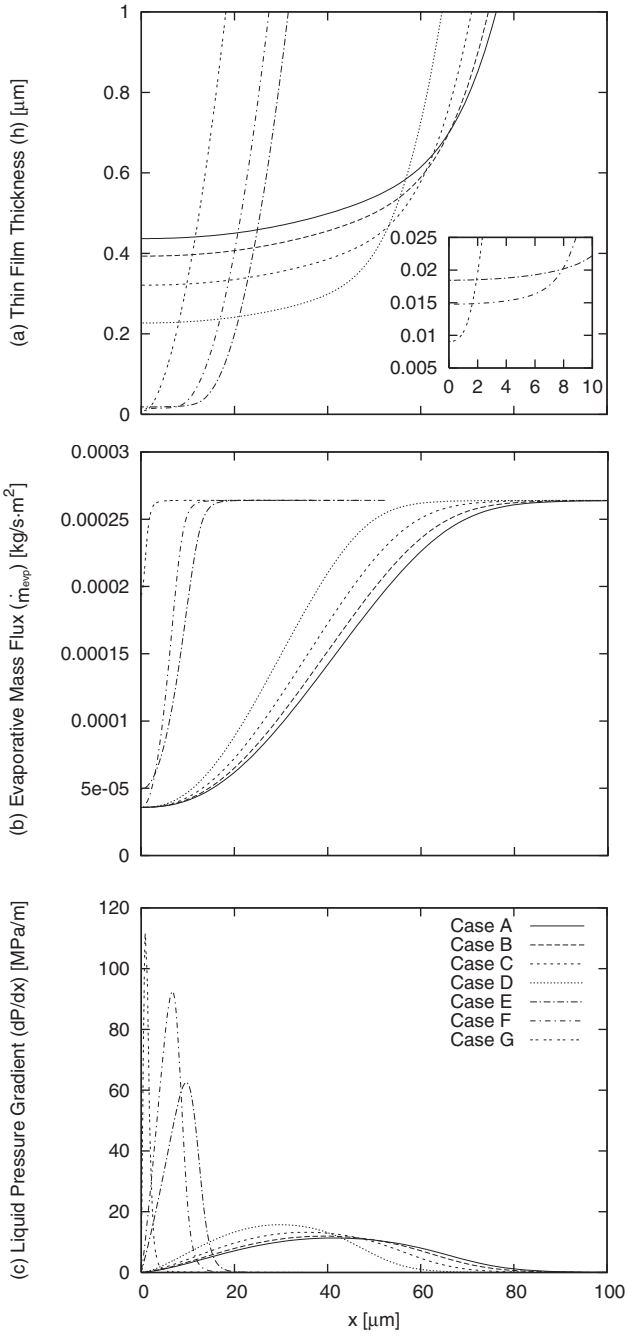

Fig. 4 Steady thin-film evaporation solutions as functions of *x* measured from the absorption thickness H_0 over the range of possible disjoining pressures: (*a*) thin-film thickness, (*b*) evaporative mass flux, and (*c*) liquid pressure gradient. Cases A–G represent the effects of varying strengths of the electron degeneracy component of the disjoining pressure depending upon the electronic work function boundary condition ($R = 200$ μm and $\Delta T = 0.0005$ K).

the electronic component of the disjoining pressure causes a drastic change in the extended evaporating meniscus (Cases A–D in Fig. 4) as compared with the case of no electronic component (Case F). Second, work function boundary conditions near zero (Cases E and G) do not result in drastic deviations from that of Case F in the meniscus profiles. More importantly, the adsorbed film thickness substantially increases, more than 1 order of magnitude from 10 nm to hundreds of nanometers, with increasing work function boundary conditions for the modeled range, in other words, with increasing electron degeneracy contribution.

The evaporative mass flux plot in Fig. 4 shows that all solution curves approach the same asymptotic value ($\dot{m}_{\text{evp}} \approx 0.00027$ kg/s m^2). This is a result of the isothermal film assumption and is clearly evident from Eq. (10). Since the liquid overheat is constant, each case has the same reference evaporative mass flux $\dot{m}_0$. Also, each case has the same pore radius, thus the second derivative of the dependent variable θ will approach the same asymptotic bulk meniscus curvature. Finally, regardless of the work function boundary condition value, the total disjoining pressure $\bar{\Pi}$ quickly falls to zero as the film thickness increases. Thus every case shown reaches the same maximum evaporative heat flux.

Figure 4 shows the liquid pressure gradient that is needed to replenish fluid in the thin film from the bulk meniscus to maintain a steady evaporating thin-film profile. Considering Case F (no electronic component) as the baseline, we see that an increasing work function boundary condition, from Case E to Case A, results in an increasing total disjoining pressure which thickens and lengthens the thin-film profile. This, in turn, broadens the evaporative mass flux curve and the liquid pressure gradient is reduced. It appears that the total evaporated mass (integral of the net evaporative mass flux) decreases with increasing work function boundary condition. For Case G, a negative electronic disjoining pressure component results in a thinner and shorter thin-film profile. This is seen to sharpen the evaporative mass flux curve and, possibly, increase the total evaporated mass. The liquid pressure gradient needed to support this is much higher. Due to the steep thin-film profile and elevated liquid pressure gradient, it is unknown if this evaporating thin-film scenario could be stable.

If heat conduction through the film thickness is included in the governing equation, a nonisothermal temperature distribution will be resulted as a part of the solution. Then, we would expect the evaporative mass flux curves to peak and then decrease as the thickening film would create a heat transfer resistance. However, this would be counteracted to substantial degree by the intrinsically high thermal conductivity of liquid metals. Exploration of this effect is left for future work.

At this point, it remains an open question which of the work function boundary condition cases best represents an experimental reality. The work function for a liquid sodium thin film on a stainless steel substrate is unknown. In experiments with mercury films surrounded by organic fluids, Derjaguin and Roldughin [25] found that organic fluids with approximately the same physical parameters caused extremely different results in mercury film stability. As such, theoretical knowledge of the work function seems improbable and must be obtained experimentally. Even if such a measurement could be made, another obstacle exists as alkaline liquid metals must be isolated in a high temperature, low oxygen environment that is rather inaccessible for delicate and operator intensive operations. The present study, however, leads us to propose a somewhat more tractable binary test. As Fig. 4 illustrates, if the adsorbed film thickness of an evaporating extended meniscus could be measured with just enough accuracy to distinguish between a value that is on the order of tens of nanometers or hundreds of nanometers, this could sufficiently serve to determine the approximate range of work function and resulting magnitude of the electronic component of the disjoining pressure. In our belief, such a work can be regarded as a significant breakthrough in studying alkaline liquid metal evaporating thin films.

4 Conclusions

The present study seeks to expand existing extended meniscus evaporation models to properly capture the unique disjoining pressure characteristics of liquid alkali metals. Where previous studies have only used the nonretarded dispersion force via Hamaker theory, we have incorporated the full (unsimplified) retarded dispersion force (Π_A) using the DLP theory and its representation by cubic spline interpolation. Additionally, we have incorporated an electronic disjoining pressure component (Π_B) that is unique to liquid metals by performing a parametric study on the work function boundary condition. Our results for a liquid sodium thin film in a 200 μm diameter capillary with a 0.0005 K overheat indicate that adsorbed film thicknesses can vary from 8 nm (Case G: $\Pi_B/\Pi_A \approx 0$) to 420 nm (Case A: $\Pi_B/\Pi_A \approx \infty$) depending on the work function boundary condition. Thin film profiles exhibit large changes, as well. The important conceptual results identified from the present work include the following:

1. Accurate high temperature, liquid metal, extended meniscus evaporation models should account for both retarded dispersion force and electronic disjoining pressures.
2. Cubic spline interpolation is an acceptable vehicle to model the retarded dispersion force and can be implemented within the framework of the orthogonal collocation solution method.
3. Results indicate the electronic component of the disjoining pressure is not negligible for a wide range of work function boundary values and must be included in models of liquid metal extended meniscus evaporation.
4. Numerical solutions to the thin-film governing equation for isothermal sodium coolant predicts thin-film thickness profiles, mass flux distributions, and pressure gradient along the substrate of stainless steel.
5. Continuing studies require greater physical insight into the work function for a liquid sodium thin film on a stainless steel substrate.

Acknowledgment

This research was supported partially by the Wright-Patterson Air Force Laboratory in Dayton, OH, partially by the University of Tennessee Grant No. R-011373164, and partially by the WCU (World Class University) Program through the Korea Science and Engineering Foundation (KOSEF) funded by the Ministry of Education, Science and Technology Grant Number R31-2008-000-10083-0.

Nomenclature

- $a_{1,2,3}$ = thin-film boundary conditions
- A = Hamaker constant (J)
- B = disjoining pressure electronic component constant (N)
- c = speed of light in a vacuum (2.99792458×10^8 m/s)
- $c_{1,2,3,4}$ = cubic spline coefficients
- Ca = capillary number ($Ca = \mu_l u_0/\sigma$)
- E_F = Fermi energy (eV)
- f = collocated residual function
- g = forcing function
- $\hbar$ = reduced Planck constant (J s)
- h_{fg} = latent heat of evaporation (J/kg)
- H = film thickness (m)
- H_0 = adsorbed layer thickness (m)
- k = Boltzmann constant ($1.380650277 \times 10^{-23}$ J/K)
- K = curvature of the bulk meniscus region (m^{-1})
- $l_{\max}$ = domain limit (m)
- m = mass (kg)

m_e = electron mass (kg)
$\dot{m}_{evp}$ = evaporative mass flux (kg/s m^2)
$\mathcal{M}$ = molar mass (kg/mol)
n = index of refraction
N_e = valence electron number density (m^{-3})
p = variable of integration
P = pressure (N/m^2)
q_e = electron charge (C)
q_k = orthogonal collocation coefficients
r = radial coordinate (m)
r_m = orthogonal collocation coefficients
$\mathcal{R}$ = universal gas constant (8.31447215 J/K mol)
R = pore radius (m)
R_N = residual function
$s_{1,2}$ = equation placeholders
T = temperature (K)
T_m = Chebyshev polynomials of the first kind
ΔT = liquid overheat (K)
u = velocity (m/s)
V = volume (m^3)
W = work function (eV)
x = axial coordinate (m)
y = vertical coordinate (m)

Greek Symbols

α = evaporation coefficient
δ = Dirac delta function
ϵ = dielectric permittivity
ϵ_0 = permittivity of free space ($8.854187815\times10^{-12}$ s^4 A^2/m^3 kg)
ϵ_1 = dielectric permittivity of container
ϵ_2 = dielectric permittivity of vapor
ϵ_3 = dielectric permittivity of liquid thin film
η = nondimensional axial coordinate ($\eta=x/x_0$)
θ = nondimensional film thickness [$\theta(\eta)=H/H_0$]
$\hat{\theta}$ = nondimensional thin-film thickness in ξ [$\hat{\theta}=\theta(\phi(1+\xi))$]
κ = electronic disjoining pressure work function parameter
λ = wavelength (m)
μ = viscosity (N s/m^2)
ν_e = plasma frequency of an electron gas (Hz)
ξ = nondimensional distance mapped for Chebyshev polynomials
Π = disjoining pressure (N/m^2)
$\bar{\Pi}$ = nondimensional disjoining pressure ($\bar{\Pi}=\Pi/\Pi_0$)
ρ = density (kg/m^3)
σ = surface tension (N/m)
$\Sigma_{1,2}$ = equation placeholders
ϕ = linear domain transformation parameter
χ = electronic disjoining pressure boundary condition
$\hat{\Psi}$ = collocation inhomogeneous, linear, boundary conditions
Ψ_k = collocation Chebyshev polynomials with homogeneous boundary conditions
ω = frequency (rad/s)
ω_e = plasma frequency of an electron gas (rad/s)
ω_n = electromagnetic wave frequency (rad/s)

Subscripts

0 = reference state
A = dispersion component
B = electronic component
i = cubic spline piece
l = liquid
lv = liquid/vapor interface
v = vapor

Appendix

Chebaro and co-workers [15,16] solved the thin-film equation with an explicit Runge–Kutta numerical solution procedure. The far field boundary condition, seen in Eq. (8*c*), is met with the shooting method. Since negligible curvature exists in the interline region, the governing equation reduces to a second order ordinary differential equation (ODE) that is solved with slight perturbations in the independent variable and its first derivative. The end points of this solution then become the boundary conditions for the full, fourth-order ODE. The missing far field boundary condition is satisfied with the shooting method, whereby the second derivative near field boundary condition is iterated upon until the solution approaches an asymptotic value in the far field equal to the curvature of the bulk meniscus (the inverse of a simulated pore radius).

Orthogonal collocation provides a more favorable numerical solution scheme for the problem at hand in that

1. it is fully implicit and thereby eliminates the need for the shooting method.
2. it results in a continuous approximation to the solution (consisting of a series expansion of a basis function operated on by a collocation coefficient) that can later be analytically manipulated for postprocessing needs.
3. it readily handles the possible stiffness problems associated with the high degrees of nonlinearity inherent in the problem.
4. it permits incorporation of the cubic spline interpolation model of the dispersion force.

First we map the domain from $\eta\in[0,l_{max}]$ to $\xi\in[-1,1]$, which later enables easy implementation of the Chebyshev polynomial basis function. A linear transformation accomplishes this task. Applying the chain rule and letting $\hat{\theta}(\xi)=\theta(\phi(1+\xi))$, Eq. (8*a*) can be rewritten as

$$\frac{3}{\phi^4}\hat{\theta}(\xi)^2\hat{\theta}(\xi)'\hat{\theta}(\xi)''' + \frac{1}{\phi^4}\hat{\theta}(\xi)^3\hat{\theta}(\xi)'''' + \frac{3}{\phi}\hat{\theta}(\xi)^2\hat{\theta}(\xi)'\bar{\Pi}(\hat{\theta})' + \hat{\theta}(\xi)^3\bar{\Pi}(\hat{\theta})'' + \frac{3Ca}{\left(\frac{H_0\Pi_0}{\sigma}\right)^2}\left[1-\frac{1}{\phi^2}\hat{\theta}(\xi)''-\bar{\Pi}(\hat{\theta})\right]=0,$$

$$\xi\in[-1,1] \tag{A1a}$$

where

$$\hat{\theta}(-1)=a_1 \tag{A1b}$$

$$\hat{\theta}'(-1)=\phi a_2 \tag{A1c}$$

$$\hat{\theta}''(1)=\phi^2 a_3 \tag{A1d}$$

$$\hat{\theta}''(-1)=0 \tag{A1e}$$

which is amenable to the desired numerical solution scheme.

The disjoining pressure is treated as a linear combination of the dispersion force and electronic components. Thus, Eqs. (4*a*) and (5) are mapped into the new Chebyshev polynomial-friendly domain and added to yield

$$\bar{\Pi}(\hat{\theta})=\frac{\Pi_{A,i}(\hat{\theta})}{\Pi_0}+\frac{\Pi_B(\hat{\theta})}{\Pi_0}=\frac{c_{1,i}H_0^3}{\Pi_0}(\hat{\theta}-\hat{\theta}_i)^3+\frac{c_{2,i}H_0^2}{\Pi_0}(\hat{\theta}-\hat{\theta}_i)^2+\frac{c_{3,i}H_0}{\Pi_0}(\hat{\theta}-\hat{\theta}_i)+\frac{c_{4,i}}{\Pi_0}+\frac{B\chi(\kappa)}{H_0^2\Pi_0}\frac{1}{\hat{\theta}^2}$$

$$\hat{\theta} \in [\hat{\theta}_i, \hat{\theta}_{i+1}], \quad i = 1,2, \ldots, 75 \tag{A2}$$

which consists of 75 different equations due to the cubic spline interpolation of the dispersion force.

With the problem defined in a Chebyshev polynomial-friendly domain, we seek an analytical solution using

$$\hat{\theta}(\xi) = \sum_{m=0}^{\infty} r_m T_m(\xi), \xi \in (-1,1) \tag{A3a}$$

where $\{T_m(\xi)\}_{m=0}^{\infty}$ represents an orthogonal set of basis functions

$$T_0(\xi) = 1 \tag{A3b}$$

$$T_1(\xi) = \xi \tag{A3c}$$

$$T_{m+1}(\xi) = 2\xi T_m(\xi) - T_{m-1}(\xi) \tag{A3d}$$

that are Chebyshev polynomials of the first kind. The approximate analytical solution is obtained by truncating the infinite series of Eq. (A3*a*) to $N+3$ terms such that

$$\hat{\theta}(\xi) \approx \hat{\theta}_{N+3}(\xi) = \sum_{m=0}^{N+3} r_m T_m(\xi), \xi \in (-1,1) \tag{A4}$$

The first four terms in the expansion of Eq. (A4) are obtained explicitly by enforcing the four boundary conditions specified in Eq. (A1*a*). Like terms are gathered and we formally present the approximate analytical solution as a linear combination

$$\hat{\theta}(\xi) \approx \hat{\theta}_N(\xi) = \hat{\Psi}(\xi) + \sum_{k=1}^{N} q_k^N \Psi_k(\xi), \xi \in [-1,1] \tag{A5a}$$

where

$$\hat{\Psi}(\xi) = a_1 + \phi(\xi+1)a_2 + \phi^2\left(\frac{\xi^2}{2} + \xi + \frac{1}{2}\right)a_3 \tag{A5b}$$

satisfies the inhomogeneous, linear, boundary conditions while

$$\Psi(\xi) = T_k(\xi) - T_k(-1) - (\xi+1)T_k'(-1) - \left(\frac{\xi^2}{2} + \xi + \frac{1}{2}\right)T_k''(1) + \frac{1}{6}(-\xi^3 + 3\xi^2 + 9\xi + 5)T_k'''(-1) \tag{A5c}$$

satisfies the original problem statement with homogeneous boundary conditions. This representation uses a reformulated subscript such that $m=k+3$. Thus the k represents N integers and the reason for the earlier truncation to $N+3$ terms becomes clear. Equations for the derivatives of the approximate analytical solution are found by differentiating Eq. (A5*a*).

Since the series truncation produces an *approximate* analytical solution, Eq. (A5*a*) will not fully satisfy Eq. (A1*a*). Instead, we introduce the local residual function $R_N(\hat{\theta}_N(\xi))$ to satisfy the problem statement such that

$$R_N(\hat{\theta}_N(\xi)) + M[\hat{\theta}_N(\xi)] + g = 0, \quad \xi \in [-1,1] \tag{A6a}$$

where $M[\cdot]$ indicates a nonlinear ODE operator and g indicates forcing data as a representation of Eq. (A1*a*). The definition of the residual function becomes

$$R_N(\hat{\theta}_N(\xi)) = -M[\hat{\theta}_N(\xi)] - g, \quad \xi \in [-1,1] \tag{A6b}$$

The collocation method minimizes the local residual function and determines the expansion coefficients $\{q_k^N\}_{k=1}^N$ by way of the sifting property

$$\langle R_N(\hat{\theta}_N(\xi)), \delta(\xi - \xi_j)\rangle_1 = \langle -M[\hat{\theta}_N(\xi)] - g, \delta(\xi - \xi_j)\rangle_1 = 0,$$

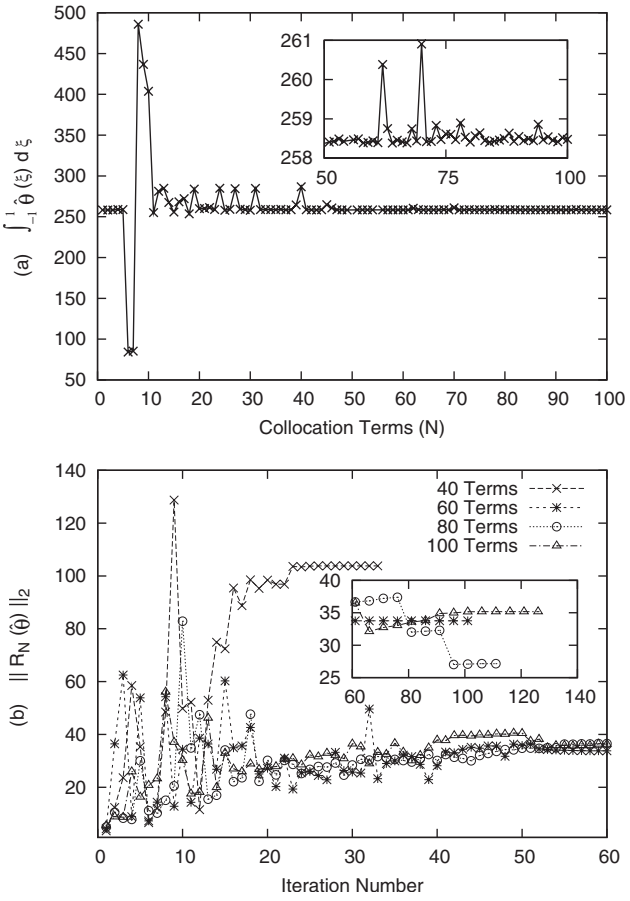

Fig. 5 (*a*) Spatial convergence and (*b*) iterative convergence for $R=200$ μm, $\Delta T=0.0005$ K, and $\chi(\kappa)=0.001650$ (Case E: $\Pi_B/\Pi_A=1.0$)

$$j = 1,2,3, \ldots, N \tag{A7a}$$

where the brackets follow Dirac's notation and denote an inner product of the residual function with a Dirac delta test function with unity weight. As a result, the residual function is evaluated at each of the collocation points to produce a series of algebraic equations

$$R_N(\hat{\theta}_N(\xi_j)) = 0 \tag{A7b}$$

or

$$M[\hat{\theta}_N(\xi_j)] + g = 0 \tag{A7c}$$

where the collocation points are defined by the standard Chebyshev–Gauss–Lobatto open rule formula

$$\xi_j = \cos\left(\frac{2j-1}{2N}\pi\right), \quad j = 1,2, \ldots, N \tag{A7d}$$

The nonlinearities in the residual operator $M[\cdot]$ must be treated before we employ a linear equation solver to obtain the collocation coefficients $\{q_k^N\}_{k=1}^N$. The stiffness associated with a highly nonlinear ODE can cause the Newton–Raphson approach to flounder as the Jacobian becomes poorly conditioned. In such a case the method of steepest descent can be used, albeit with extremely slow convergence. The Levenberg–Marquardt method [34] performs an optimum interpolation between the Newton–Raphson method and the method of steepest descent (or gradient) method. The reader is directed to Henley and Rosen (Ref. [35], pp. 202–204) for further directions as to its implementation.

Spatial convergence is analyzed a posteriori by integrating the approximate analytical solution over the domain of interest. Thus,

$$\int_{-1}^{1} \hat{\theta}_N(\xi)d\xi = \int_{-1}^{1} \hat{\Psi}(\xi)d\xi + \sum_{k=1}^{N} q_k^N \int_{-1}^{1} \Psi_k(\xi)d\xi, \quad \xi \in [-1,1] \tag{A8a}$$

where

$$\int_{-1}^{1} \hat{\Psi}(\xi)d\xi = 2a_1 + 2\phi a_2 + \frac{4}{3}\phi^2 a_3 \tag{A8b}$$

$$\int_{-1}^{1} \Psi_k(\xi)d\xi = \int_{-1}^{1} T_k(\xi)d\xi - 2T_k(-1) - 2T_k'(-1) - \frac{5}{3}T_k''(1) + 2T_k'''(-1) \tag{A8c}$$

and

$$\int_{-1}^{1} T_k(\xi)d\xi = \begin{cases} 0 & \text{if} \quad k = \text{odd} \\ \dfrac{-2}{(k+1)(k-1)} & \text{if} \quad k = \text{even} \end{cases} \tag{A8d}$$

To observe spatial convergence, we increment the number of terms N in the approximate analytical solution, integrate the solution over the domain space using Eq. (A8*a*), and observe the relative error between successive increments.

Figure 5 demonstrates the spatial (Eq. (A8*a*)) and iterative convergences of solutions to the steady extended meniscus evaporation model (Eq. (A1*a*)) using a function (Eq. (A5*a*)) with increasing terms via orthogonal collocation as solved by the Levenberg–Marquardt method. As shown, extending the approximate analytical solution to 100 terms provides an accurate, converged solution.

References

[1] Khrustalev, D., and Faghri, A., 1994, "Thermal Analysis of a Micro Heat Pipe," ASME J. Heat Transfer, **116**, pp. 189–198.

[2] Jiao, A. J., Riegler, R., Ma, H. B., and Peterson, G. P., 2005, "Thin Film Evaporation Effect on Heat Transport Capability in a Grooved Heat Pipe," Microfluid. Nanofluid., **1**, pp. 227–233.

[3] Sobhan, C., Rag, R., and Peterson, G., 2007, "A Review and Comparative Study of the Investigations on Micro Heat Pipes," Int. J. Energy Res., **31**, pp. 664–688.

[4] Jiao, A., Ma, H., and Critser, J., 2008, "Heat Transport Characteristics in a Miniature Flat Heat Pipe With Wire Core Wicks," ASME J. Heat Transfer, **130**, pp. 051501.

[5] Wayner, P. C., Jr., 1999, "Intermolecular Forces in Phase-Change Heat Transfer: 1998 Kern Award Review," AIChE J., **45**, pp. 2055–2068.

[6] Wee, S.-K., Kihm, K. D., and Hallinan, K. P., 2005, "Effects of the Liquid Polarity and the Wall Slip on the Heat and Mass Transport Characteristics of the Micro-Scale Evaporating Transition Film," Int. J. Heat Mass Transfer, **48**, pp. 265–278.

[7] Peterson, G., and Ma, H., 1999, "Temperature Response of Heat Transport in a Micro Heat Pipe," ASME J. Heat Transfer, **121**, pp. 438–445.

[8] Badran, B., Albayyari, J. M., Gerner, F. M., Ramadas, P., Henderson, H. T., and Baker, K. W., 1993, "Liquid-Metal Micro Heat Pipes," *Heat Pipes and Capillary Pumped Loops: Proceedings of the 29th National Heat Transfer Conference*, Atlanta, GA, Aug 8–11, ASME, New York, pp. 71–85.

[9] Ramadas, P., Henderson, H., Badran, B., Gerner, F., and Baker, K., 1993, "Liquid-Metal Micro Heat Pipes Incorporated in Waste-Heat Radiator Panels," *Proceedings of the Tenth Symposium on Space Nuclear Power and Propulsion*, Albuquerque, NM, January 10–14, M. El-Genk and M. D. Hoover, eds., American Institute of Physics, New York, pp. 551–557.

[10] Wayner, P., Jr., and Schonberg, J., 1990, "Heat Transfer and Fluid Flow in an Evaporating Extended Meniscus," *Heat Transfer 1990: Proceedings of the Ninth International Heat Transfer Conference*, Jerusalem, Israel, G. Hestroni, ed., Hemisphere, New York, Vol. 4, pp. 228–234,.

[11] Derjaguin, B., Nerpin, S., and Churaev, N., 1965, "Effect of Film Transfer Upon Evaporation of Liquids From Capillaries," RILEM Bull., **29**, pp. 93–98.

[12] Schrage, R. W., 1953, *A Theoretical Study of Interphase Mass Transfer*, Columbia University Press, New York.

[13] Wayner, P. C., Jr., Kao, Y. K., and LaCroix, L. V., 1976, "The Interline Heat-Transfer Coefficient of an Evaporating Wetting Film," Int. J. Heat Mass Transfer, **19**, pp. 487–491.

[14] Potash, M., Jr., and Wayner, P. C., Jr., 1972, "Evaporation From a Two-Dimensional Extended Meniscus," Int. J. Heat Mass Transfer, **15**, pp. 1851–1863.

[15] Chebaro, H., and Hallinan, K., 1993, "Boundary Conditions for an Evaporating Thin Film for Isothermal Interfacial Conditions," ASME J. Heat Transfer, **115**, pp. 816–819.

[16] Chebaro, H., Hallinan, K., Kim, S., and Chang, W., 1992, "Evaporation From a Porous Wick Heat Pipe for Isothermal Interfacial Conditions," ASME HTD-Vol. 221, pp. 23–28.

[17] Hamaker, H., 1937, "London-Van Der Waals Attraction Between Spherical Particles," Physica, **4**, pp. 1058–1072.

[18] Lifshitz, E., 1955, "The Theory of Molecular Attractive Forces Between Solids," Sov. Phys. JETP, **2**, pp. 73–78.

[19] Dzyaloshinskii, I., Lifshitz, E., and Pitaevskii, L., 1961, "The General Theory of Van Der Waals Forces," Adv. Phys., **10**, pp. 165–209.

[20] Israelachvili, J. N., 1985, *Intermolecular and Surface Forces: With Applications to Colloidal and Biological Systems*, Academic, New York.

[21] Moosman, S., and Homsy, G., 1980, "Evaporating Menisci of Wetting Fluids," J. Colloid Interface Sci., **73**, pp. 212–223.

[22] Truong, J. G., and Wayner, P. C., Jr., 1987, "Effects of Capillary and Van Der Waals Dispersion Forces on the Equilibrium Profile of a Wetting Liquid: Theory and Experiment," J. Chem. Phys., **87**, pp. 4180–4188.

[23] DasGupta, S., Schonberg, J. A., and Wayner, P. C., Jr., 1993, "Investigation of an Evaporating Extended Meniscus Based on the Augmented Young-Laplace Equation," ASME J. Heat Transfer, **115**, pp. 201–208.

[24] Derjaguin, B., Leonov, L., and Roldughin, V., 1985, "Disjoining Pressure in Liquid Metallic Films," J. Colloid Interface Sci., **108**, pp. 207–214.

[25] Derjaguin, B., and Roldughin, V., 1985, "Influence of the Ambient Medium on the Disjoining Pressure of Liquid Metallic Films," Surf. Sci., **159**, pp. 69–82.

[26] Kubo, R., 1962, "Electronic Properties of Metallic Fine Particles," J. Phys. Soc. Jpn., **17**, pp. 975–986.

[27] Roldughin, V., 2000, "Quantum-Size Colloid Metal Systems," Russ. Chem. Rev., **69**, pp. 821–843.

[28] Ajaev, V., and Willis, D., 2003, "Thermocapillary Flow and Rupture in Films of Molten Metal on a Substrate," Phys. Fluids, **15**, pp. 3144–3150.

[29] Ajaev, V. S., and Willis, D. A., 2006, "Heat Transfer, Phase Change, and Thermocapillary Flow in Films of Molten Metal on a Substrate," Numer. Heat Transfer, Part A, **50**, pp. 301–313.

[30] Hecht, E., 2004, *Optics*, 4th ed., Pearson, New York.

[31] Fink, J., and Leibowitz, L., 1996, "A Consistent Assessment of the Thermophysical Properties of Sodium," High Temp. Mater. Sci., **35**, pp. 65–103.

[32] Takens, W., Mischke, W., Korving, J., and Beenakker, J., 1984, "A Spectroscopic Study of Free Evaporation of Sodium," *Rarefied Gas Dynamics: Proceedings of the 14th International Symposium on Rarefied Gas Dynamics*, Tsukuba, Science City, Japan, Jul. 16–20, University of Tokyo Press, Tokyo, pp. 967–974.

[33] Hallinan, K., Chebaro, H., Kim, S., and Chang, W., 1994, "Evaporation From an Extended Meniscus for Nonisothermal Interfacial Conditions," J. Thermophys. Heat Transfer, **8**, pp. 709–716.

[34] Marquardt, D. W., 1963, "An Algorithm for Least-Squares Estimation of Nonlinear Parameters," J. Soc. Ind. Appl. Math., **11**, pp. 431–441.

[35] Henley, E. J., and Rosen, E. M., 1969, *Material and Energy Balance Computations*, Wiley, New York.

Magnetohydrodynamic Correction in Film Boiling Heat Transfer on Liquid Metal in Presence of an Ideal Magnetic Field With Particular Reference to Fusion Reactor Project

F. J. Arias[1]
Department of Physics and Nuclear Engineering,
Technical University of Catalonia,
Avda. Diagonal 647,
08028 Barcelona, Spain
e-mail: frariasm7@fis.ub.edu

The author proposed a magnetohydrodynamic correction from a horizontal surface in liquid-metal in the presence of an ideal magnetic field. The theoretical correction agrees qualitatively with the available experimental measurements made on mercury in a high magnetic field where transition/film boiling is expected.
[DOI: 10.1115/1.3220145]

Keywords: liquid-metal diverters, Tokamak reactors, MHD boiling, ARIES and APEX fusion reactor designs

1 Introduction

The magnetohydrodynamic (MHD) single-phase flow has received considerable attention during the last few years, including studies of the flow properties from Shateyi et al. [1] and Asterios [2], studies of the porous medium from Makinde and Sibanda [3] and Bhadauria [4], a study of the melting behavior from Zhang et al. [5], and so on. With regard to the two-phase flow, where a lot of research has been done, such as the research on the boiling of various fluids from Fujita [6] and Manglik [7] and including the research on the boiling of liquid-metals from Michiyoshi [8], not much work exists on MHD boiling and the phenomenon has received fewer attention than the conventional boiling. Despite it all, the MHD boiling phenomenon may play an important role in technologies such as the blanket design of future fusion reactors. In reality some experiments have been initiated to examine this issue, for example, the Advanced Power Extraction (APEX) project and the evaporation of lithium and vapor extraction (EVOLVE) concept, which is an advanced concept capable of handling high power densities with high power conversion efficiency (see Refs. [9,10]). The objective of the present work was to analyze film boiling heat and mass transfer of a liquid-metal from a horizontal surface in the presence of an ideal magnetic field. A number of models exist for the (MHD) nucleate boiling: Lykoudis [11] considered the slowing down effect of the magnetic field on the growth rate of the bubbles in the case of a horizontal hot plate surrounded by an electrically conducting fluid in the presence of a horizontal magnetic field, and Takahashi et al. [12] studied the effect of a vertical magnetic field on the saturated nucleate pool boiling of mercury on a horizontal surface. With regard to the MHD film boiling, no work exists as far as the author knows. Therefore, the MHD film boiling-type phenomenon appears to be more susceptible to attacks from the theoretical viewpoint; however, in reality a physical model for the effect of the magnetic field on the bubble frequency is still missing.

[1]Corresponding author.
Manuscript received June 20, 2008; final manuscript received March 6, 2009; published online October 15, 2009. Review conducted by Yogesh Jaluria.

2 Basic Assumptions

A film boiling liquid-metal under the Taylor–Helmholtz instability is assumed (Berenson's model in Ref. [13]). Furthermore, a homogeneous and ideal magnetic field is imposed parallel to the heater surface.

Referring to Fig. 1, at a height ξ above the film, the pressure is independent of its radius and equal to p_0. The following relations exist between p_0, p_1, and p_2, where P (upper case) is the pressure and p (lower case) is the pressure identical with the gravity

$$p_2 - p_0 = \rho_l \xi \frac{g}{g_0} \tag{1}$$

$$p_1 - p_0 = \rho_v \xi \frac{g}{g_0} + 2\frac{\sigma}{R} \tag{2}$$

where the second term on the right in the latter equation takes account of the pressure difference due to the curvature of the bubble and the surface tension. Solving the above two equations for the pressure differences gives

$$p_2 - p_1 = \xi(\rho_l - \rho_v)\frac{g}{g_0} - 2\frac{\sigma}{R} \tag{3}$$

Now, when the medium is relatively high in conductivity, the magnetic lines of force are attached to the matter and partaking its streaming motions. So, in the approximation of the frozen field (see Appendix), we know that the curvature generates a magnetic volumetric force on the bubble

$$\frac{\partial P}{\partial r} = \frac{B^2}{\mu R} \tag{4}$$

On the other hand the radius of the bubble R and the average height of the bubble ξ above the vapor film are given semiempirically and are obtained in experimental measurements

$$R = 2.35\sqrt{\frac{g_0\sigma}{g(\rho_l - \rho_v)}}, \quad \xi = 3.2\sqrt{\frac{g_0\sigma}{g(\rho_l - \rho_v)}} \tag{5}$$

Calculating the volume of the bubble and the surface projection in the film boiling we can approximate the magnetic pressure undergone by the bubble of radius R and height ξ (see Fig. 1)

$$\Delta P_{\text{mag}} = \frac{1.54B^2}{\mu} \tag{6}$$

hence, the total external pressure undergone by the bubble is now

$$p_2 - p_1 = \xi(\rho_l - \rho_v)\frac{g}{g_0} - 2\frac{\sigma}{R} - \Delta p_{\text{mag}} \tag{7}$$

where Δp_{mag} is given by Eq. (6). On the other hand Berenson demonstrated that the pressure generated by the vapor flow in the film boiling between r_2 and r_1 in the theory of critical wave (see Fig. 1) is given by

$$p_2 - p_1 = \frac{20.8}{\pi}\frac{\nu_v \kappa_{\text{vl}} \Delta T}{g_0 a^4 \rho_{\text{vl}} \Delta h}\frac{g_0\sigma}{g(\rho_l - \rho_v)} \tag{8}$$

This pressure difference is supplied by the pressure difference given by Eq. (7). Combining Eqs. (5) and (7) gives the available pressure difference

$$p_2 - p_1 = 2.34\frac{g}{g_0}(\rho_l - \rho_v)\sqrt{\frac{g_0\sigma}{g(\rho_l - \rho_v)}} - \Delta p_{\text{mag}} \tag{9}$$

and is equal to Eq. (8). A heat transfer coefficient may be defined by applying the following equation:

$$h = \frac{\kappa_{\text{vl}}}{a} \tag{10}$$

We finally have the heat transfer coefficient corrected by the magnetic field under the imposed assumptions

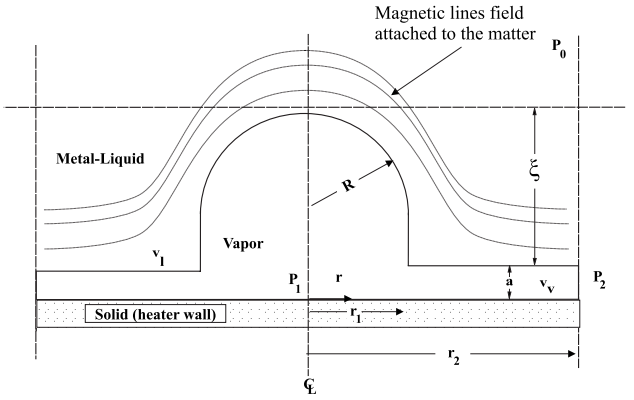

Fig. 1 The physical model of film boiling from the horizontal surface, where in the approximation of the frozen field it shows the lines of force being pushed aside

$$h = h_o\left[1 - \frac{0.66 \times B^2}{\mu g(\rho_l - \rho_v)\sqrt{\dfrac{g_0\sigma}{g(\rho_l - \rho_v)}}}\right]^{1/4} \tag{11}$$

where h_0 is the heat transfer coefficient without the presence of the magnetic field $B=0$ and it naturally corresponds to the value found by Berenson

$$h_0 = 0.62\left[\frac{\kappa_{vl}^3 \Delta h \rho_{vl} g(\rho_l - \rho_v)}{\nu_v \Delta T\sqrt{\dfrac{g_0\sigma}{g(\rho_l - \rho_v)}}}\right]^{1/4} \tag{12}$$

3 Discussion and Experimental Data

When a horizontal magnetic field is applied, the buoyancy will be restrained and more bubbles will remain longer in their nucleation sites, with the possibility of a more direct transition from nucleate to film boiling. Wagner and Lykoudis [14] saw this in an experiment with fields as low as 1.26 T when the temperature of a heating plate rose to 200 °C and above that when the field was not applied indicating the promotion to film boiling that would lead to burnout (Fig. 2). Bertodano et al. [15] noticed the boiling transition by examining the departure frequency with magnetic field strength for a constant wall heat flux shown. Referring to Fig. 3, the experimental data show that the heat transfer coefficient decreases with further increase in the magnetic field, where the qualitatively good agreement between the experimental data and the proposed MHD correction is clear in a high magnetic field where the transition/film boiling regime is expected.

4 Summary and Conclusions

An analytical MHD correction, Eq. (11), is derived, which predicts that magnetic fields have a strong effect (decreases) on the heat transfer coefficient for liquid-metal film and pool boiling. The above equation agrees with the available experimental measurements in a high magnetic field where the transition/film boiling regime is expected, and where the suppression of boiling in film boiling has been thoroughly verified [14,15].

Acknowledgment

The author wishes to thank the anonymous referees and Dr. M. A. Jog of the University of Cincinnati, who called his attention to the ARIES (power core and power cycle engineering project) and APEX fusion reactor designs, for their opportune comments that became determinants in the direction of the present work.

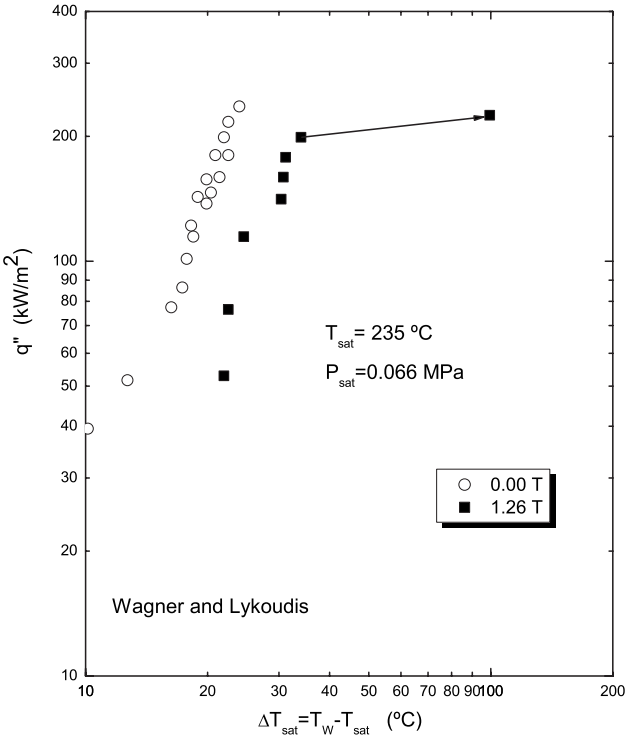

Fig. 2 Indication of the premature onset of critical heat flux with a horizontal magnetic field of 1.26 T applied to a stagnant pool of Hg (reproduced from Ref. [14])

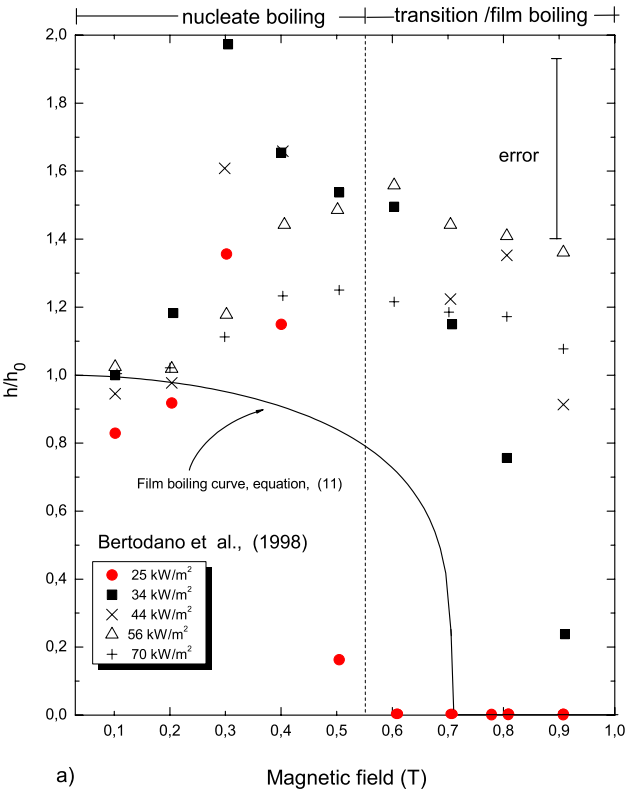

Fig. 3 The heat transfer coefficient as a function of the horizontal magnetic field strength in a stagnant pool of Hg (reproduced from Ref. [15] and in comparison with Eq. (11))

Nomenclature

a = vapor film thickness
B = magnetic field
g = gravity acceleration
g_0 = earth's gravity
h = heat transfer coefficient
J = current density
P = pressure
R = curvature radius
ΔT = superheat temperature
u = velocity
V = volume
Δh = enthalpy of vaporization

Greek Symbols

ξ = average height of the bubble
κ = thermal conductivity of the vapor
μ = magnetic permeability
ν = dynamical viscosity
ρ = density
σ = surface tension, standardized with the gravity
τ_{ij} = magnetic stress tensor

Subscripts

v = vapor
l = liquid
vl = interface vapor-liquid
t = tangential
n = normal
o = earth value
mag = magnetic

Appendix

1 Frozen Magnetic Field. From Ampère's law we may rewrite the Lorentz force in terms of B alone. The vector identity

$$\nabla(\mathbf{B}^2/2) = (\mathbf{B}\times\nabla)\mathbf{B} + \mathbf{B}\times\nabla\times\mathbf{B} \tag{A1}$$

from which, using $\nabla\times\mathbf{B}=\mu\mathbf{J}$

$$\mathbf{J}\times\mathbf{B} = (\mathbf{B}\times\nabla)(\mathbf{B}/\mu) - \nabla(\mathbf{B}^2/2\mu) \tag{A2}$$

The second term on the right of Eq. (A2) acts on the fluid in exactly the same way as the pressure force $-\nabla p$ where the term $\mathbf{B}^2/2\mu$ is called the magnetic pressure and in many, if not most, problems it is of no dynamical significance. The first term on the right, we can write the ith component of this force as

$$\mathbf{B}\times(B_i/\mu) = \frac{\partial}{\partial x_j}\left[\frac{B_iB_j}{\mu}\right] \tag{A3}$$

where there is an implied summation over the index j. From this we may show that the effect of the body force in Eq. (A3) is exactly equivalent to a distributed set of fictitious stresses B_iB_j/μ acting on the surface of fluid elements. This can be established by integrating Eq. (A3) over an arbitrary volume V and invoking Gauss' theorem. Since $\nabla\times(B_i\mathbf{B})=\mathbf{B}\times\nabla B_i+B_i\nabla\times\mathbf{B}=\mathbf{B}\times\nabla B_i$, we find

$$\int[\mathbf{B}\times\nabla(B_i/\mu)]dV = \oint(B_i/\mu)\mathbf{B}\times d\mathbf{S} \tag{A4}$$

The surface integral on the right of Eq. (A4) is equal to the cumulative effect of the distributed stress system B_iB_j/μ acting over the surface of V. The tangential and normal stresses B_tB_n/μ and B_n^2/μ acting on the surface element $d\mathbf{S}$ give rise to a force $\mathbf{B}(\mathbf{B}\times d\mathbf{S})\mu$.

Equation (A4) tells us that this surface tension is, in turn, equivalent to the integrated effect of the volume force $(\mathbf{B}\times\nabla)\times(\mathbf{B}/\mu)$. Since this is true for any volume V, it follows that the body force $(\mathbf{B}\times\nabla)(\mathbf{B}/\mu)$ and the stress system B_iB_j/μ are entirely equivalent in their mechanical action. In summary then, we may replace the Lorentz force $\mathbf{J}\times\mathbf{B}$ by an imaginary set of stresses

$$\tau_{ij} = (B_iB_j/\mu) - (\mathbf{B}^2/2\mu)\delta_{ij} \tag{A5}$$

The second term on the right is the magnetic pressure, and δ_{ij} is the Kronecker delta. These are called the Maxwell stresses and in this manner we can represent the integrated effect of a distributed body force by surfaces stresses alone. Take into account that

$$(u\times\nabla)u = V\frac{\partial V}{\partial s}\hat{\mathbf{e}}_t - \frac{V^2}{R}\hat{\mathbf{e}}_n \tag{A6}$$

Here, $V=|\mathbf{u}|$, s is now a coordinate, measured along a magnetic field line, $\hat{e}_t$ and $\hat{e}_n$ are unit vectors in the tangential and principal normal directions, respectively, $B=|\mathbf{B}|$, and R is the local radius of curvature of the field line. So, the Lorentz force can be written as

$$\mathbf{J}\times\mathbf{B} = \frac{\partial}{\partial s}\left[\frac{B^2}{2\mu}\right]\hat{\mathbf{e}}_t - \frac{B^2}{\mu R}\hat{\mathbf{e}}_n - \nabla(B^2/2\mu) \tag{A7}$$

References

[1] Shateyi, S., Sibanda, P., and Motsa, S. S., 2007, "Magnetohydrodynamic Flow Past a Vertical Plate With Radiative Heat Transfer," ASME J. Heat Transfer, **129**(12), pp. 1708–1713.
[2] Pantokratoras, A., 2009, "Magnetohydrodynamic Flow Past a Vertical Plate With Radiative Heat Transfer," ASME J. Heat Transfer, **131**(2), p. 025503.
[3] Makinde, O. D., and Sibanda, P., 2008, "Magnetohydrodynamic Mixed-Convective Flow and Heat and Mass Transfer Past a Vertical Plate in a Porous Medium With Constant Wall Suction," ASME J. Heat Transfer, **130**(11), p. 112602.
[4] Bhadauria, B. S., 2008, "Combined Effect of Temperature Modulation and Magnetic Field on the Onset of Convection in an Electrically Conducting-Fluid Saturated Porous Medium," ASME J. Heat Transfer, **130**(5), p. 052601.
[5] Zhang, H., Charmchi, M., Veilleux, D., and Faghri, M., 2007, "Numerical and Experimental Investigation of Melting in the Presence of a Magnetic Field: Simulation of Low-Gravity Environment," ASME J. Heat Transfer, **129**(4), pp. 568–576.
[6] Fujita, Y., 1992, "The State of the Art Nucleate Boiling Mechanism," *Proceedings of the Engineering Foundation Conference on Pool and External Flow Boiling*, ASME, Santa Barbara, CA, Mar. 22–27, pp. 83–98.
[7] Manglik, R. M., 2006, "On the Advancements in Boiling, Two-Phase Flow Heat Transfer, and Interfacial Phenomena," ASME J. Heat Transfer, **128**(12), pp. 1237–1242.
[8] Michiyoshi, I., 1988, "Boiling Heat Transfer in Liquid Metals," Appl. Mech. Rev., **41**(3), pp. 129–148.
[9] Abdou, M. A., The APEX TEAM, Ying, A., Morley, N., Gulec, K., Smolentsev, S., Kotschenreuther, M., Malang, S., Zinkle, S., Rognlien, T., Fogarty, P., Nelson, B., Nygren, R., McCarthy, K., Youssef, M. Z., Ghoniem, N., Sze, D., Wong, C., Sawan, M., Khater, H., Woolley, R., Mattas, R., Moir, R., Sharafat, S., Brooks, J., Hassanein, A., Petti, D., Tillack, M., Ulrickson, M., and Uchimoto, T., 2001, "On the Exploration of Innovative Concepts for Fusion Chamber Technology," Fusion Eng. Des., **54**, pp. 181–247.
[10] Wong, C. P. C., Barleon, L., Corradini, M., Fogarty, P., Ghoniem, N., Majumdar, S., Malang, S., Mattas, R., McCarthy, K., Merrill, B., Murphy, J., Nelson, B., Nygren, R., Sawan, M., Sharafat, S., Sviatoslavsky, I., and Zinkle, S., 2001, "Evaluation of the Tungsten Alloy Vaporizing Lithium First Wall and Blanket Concept," Fusion Technol., **39**, pp. 815–822.
[11] Lykoudis, P. S., 1984, "Bubble Growth in a Superheated Liquid Metal in a Uniform Magnetic Field," *Proceedings of the Fourth Beer-Sheva International Seminar on Magneto-hydrodynamic Flows and Turbulence*, Ben-Gurion University of the Negev, Beer-Sheva, Israel, Feb. 27–Mar. 2, pp. 179–292.
[12] Takahashi, M., Inoue, A., and Kaneko, T., 1994, "Pool Boiling Heat Transfer of Mercury in the Presence of a Strong Magnetic Field," Exp. Therm. Fluid Sci., **8**(1), pp. 67–78.
[13] Berenson, P. J., 1961, "Film Boiling Heat Transfer From Horizontal Surface," Trans. ASME, Ser. C: J. Heat Transfer, **83**, pp. 351–356.
[14] Wagner, L., and Lykoudis, P., 1981, "Mercury Pool Boiling Under the Influence of a Horizontal Magnetic Field," Int. J. Heat Mass Transfer, **24**(4), pp. 635–643.
[15] Bertodano, M. A., Leonardi, S., and Lykoudis, P. S., 1998, "Nucleate Pool Boiling of Mercury in the Presence of a Magnetic Field," Int. J. Heat Mass Transfer, **41**, pp. 3491–3500.